

FOR REFERENCE ONLY

✓  
D14  
26/07/09

26 JUL 2002

40 0720628 6



ProQuest Number: 10183108

All rights reserved

INFORMATION TO ALL USERS

The quality of this reproduction is dependent upon the quality of the copy submitted.

In the unlikely event that the author did not send a complete manuscript and there are missing pages, these will be noted. Also, if material had to be removed, a note will indicate the deletion.



ProQuest 10183108

Published by ProQuest LLC (2017). Copyright of the Dissertation is held by the Author.

All rights reserved.

This work is protected against unauthorized copying under Title 17, United States Code  
Microform Edition © ProQuest LLC.

ProQuest LLC.  
789 East Eisenhower Parkway  
P.O. Box 1346  
Ann Arbor, MI 48106 – 1346

# **FLOW VISUALISATION OF IMPINGING AIR AND WATER JETS**

**Uwe Rüdel**

A report submitted in partial fulfilment of the  
requirements of The Nottingham Trent University  
for the degree of Doctor of Philosophy.

This research programme was carried out in the  
Division of Mechanical and Manufacturing Engineering,  
School of Engineering,  
Faculty of Computing and Technology,  
The Nottingham Trent University,  
Burton Street, Nottingham NG1 4BU, UK.

April 2002

## © **Copyright Notice**

This copy of the thesis has been supplied for the purpose of research or private study under the condition that anyone who consults it is understood to recognise that its copyright rests with The Nottingham Trent University and that no quotation from the thesis, and no information derived from it, may be published without proper acknowledgement.

# Contents

|   |      |
|---|------|
| <b>List of Appendices</b> _____   | v    |
| <b>Abstract</b> _____   | vi   |
| <b>Acknowledgements</b> _____   | vii  |
| <b>List of Publications</b> _____                                       | viii |
| <b>List of Figures</b> _____  | ix   |
| <b>Nomenclature</b> _____   | xiii |
| <b>Chapter 1 Introduction</b> _____                                     | 1    |
| 1.1 Background and statement of the problem _____                       | 1    |
| 1.2 Aims and objectives _____   | 5    |
| 1.2.1 Specific aims _____   | 5    |
| 1.2.2 Objectives _____  | 5    |
| 1.2.3 Breakdown of objectives _____                                     | 6    |
| 1.3 Rationale _____   | 8    |
| 1.4 Outline of the investigation _____                                  | 9    |
| <b>Chapter 2 Literature review</b> _____                                | 11   |
| 2.1 Aim and methodology _____   | 12   |
| 2.2 Interpretation of Prandtl number _____                              | 13   |
| 2.3 Effects of Prandtl number in general engineering applications _____ | 18   |
| 2.4 Reviews _____   | 19   |
| 2.5 Effects of Prandtl number in jet impingement literature _____       | 20   |
| 2.6 Flow structure _____  | 21   |
| 2.6.1 Free jet or flow establishment region I _____                     | 22   |
| 2.6.1.1 Centreline velocity decay _____                                 | 24   |
| 2.6.1.2 Vortical structures _____                                       | 26   |
| 2.6.1.3 Mixing and entrainment _____                                    | 28   |
| 2.6.1.4 Thermal structures _____  | 30   |
| 2.6.2 Stagnation or impingement region II _____                         | 32   |
| 2.6.2.1 Flow field _____  | 32   |
| 2.6.2.2 Heat Transfer _____   | 38   |
| 2.6.3 Wall jet region III _____   | 51   |
| 2.6.4 Turbulent Prandtl-number _____                                    | 51   |

|   |           |
|---|-----------|
| 2.7 Experimental techniques for heat transfer testing _____       | 52        |
| 2.8 Conclusions _____   | 54        |
| <b>Chapter 3 Experimental investigation _____</b>                 | <b>57</b> |
| 3.1 Design process _____  | 57        |
| 3.2 Jet flow facility _____                                       | 60        |
| 3.2.1 Introduction _____  | 60        |
| 3.2.2 Description of the Water tunnel _____                       | 61        |
| 3.2.3 Description of the Wind tunnel _____                        | 67        |
| 3.3 Properties of the working fluids _____                        | 69        |
| 3.4 Flow visualisation investigation _____                        | 70        |
| 3.4.1 Quantitative flow visualisation _____                       | 70        |
| 3.4.1.1 Test facility for quantitative flow visualisation _____   | 72        |
| 3.4.1.2 Working fluid and liquid crystals _____                   | 73        |
| 3.4.1.3 Calibration of liquid crystals _____                      | 73        |
| 3.4.2 Qualitative flow visualisation _____                        | 74        |
| 3.4.2.1 Seeding particles _____                                   | 75        |
| 3.5 Heat transfer investigation _____                             | 76        |
| 3.5.1 Comparison and evaluation of experimental techniques _____  | 76        |
| 3.5.1.1 Steady-state techniques _____                             | 77        |
| 3.5.1.2 Transient wall heating technique _____                    | 79        |
| 3.5.1.3 Numerical approach _____                                  | 82        |
| 3.5.2 Selection of the experimental technique _____               | 83        |
| 3.5.3 Experimental set-up _____                                   | 85        |
| 3.5.3.1 Selection of surface cooling or surface heating _____     | 86        |
| 3.5.3.2 Preparation of test surface _____                         | 87        |
| 3.5.3.3 Experimental set-up _____                                 | 88        |
| 3.6 Flow field investigation _____                                | 89        |
| 3.6.1 Basic principles and configuration _____                    | 89        |
| 3.6.1.1 Probe set-up _____  | 92        |
| 3.6.1.2 Seeding _____   | 93        |
| 3.6.1.3 Effects of the window surface _____                       | 94        |
| 3.6.1.4 Determination of the position of the measurement volume _ | 97        |
| 3.6.2 Data reduction and measurement errors _____                 | 98        |
| 3.6.3 Symmetry of the flow field _____                            | 103       |

|  |            |
|--|------------|
| 3.6.4 Measurement procedure _____                      | 105        |
| 3.7 Concluding remarks _____                           | 106        |
| <b>Chapter 4 Numerical investigation _____</b>         | <b>108</b> |
| 4.1 Previous work _____                                | 108        |
| 4.2 Governing equations _____                          | 109        |
| 4.3 Closure of the averaged equations _____            | 110        |
| 4.4 The wall function _____                            | 111        |
| 4.5 Solution procedure _____                           | 113        |
| 4.6 Grid specifications _____                          | 114        |
| 4.7 Boundary and initial conditions _____              | 115        |
| 4.8 Concluding remarks _____                           | 117        |
| <b>Chapter 5 Experimental results _____</b>            | <b>118</b> |
| 5.1 Flow Visualisation _____                           | 118        |
| 5.1.1 Flow field in the test section _____             | 118        |
| 5.1.2 Quantitative flow visualisation _____            | 120        |
| 5.1.3 Qualitative flow visualisation _____             | 121        |
| 5.2 Results of the LDA investigation _____             | 123        |
| 5.2.1 Water results ( $Pr = 7.3$ and $8$ ) _____       | 124        |
| 5.2.1.1 Axial velocity _____                           | 124        |
| 5.2.1.2 Radial velocity _____                          | 126        |
| 5.2.1.3 Axial turbulence _____                         | 128        |
| 5.2.1.4 Radial turbulence _____                        | 130        |
| 5.2.1.5 Reynolds stresses _____                        | 132        |
| 5.2.2 Air results ( $Pr = 0.71$ ) _____                | 134        |
| 5.2.2.1 Axial velocity _____                           | 134        |
| 5.2.2.2 Radial velocity _____                          | 135        |
| 5.2.2.3 Axial turbulence _____                         | 136        |
| 5.2.2.4 Radial turbulence _____                        | 139        |
| 5.2.2.5 Reynolds stresses _____                        | 139        |
| 5.2.3 Combined results ( $0.71 \leq Pr \leq 8$ ) _____ | 142        |
| 5.2.3.1 Velocity profiles at the nozzle exit _____     | 142        |
| 5.2.3.1.1 Exit profile for $Re=20,000$ _____           | 142        |
| 5.2.3.1.2 Exit profile for $Re=10,000$ _____           | 144        |
| 5.2.3.1.3 Exit profile for $Re=2,000$ _____            | 145        |

|  |            |
|--|------------|
| 5.2.3.2 Flow behaviour along the impingement plate _____                 | 147        |
| 5.2.3.2.1 Re=20,000 and Re=10,000 _____                                  | 147        |
| 5.2.3.2.1.1 Flow quantities normal to the plate _____                    | 147        |
| 5.2.3.2.1.2 Flow quantities parallel to the plate _____                  | 155        |
| 5.2.3.2.2 Re=2,000 _____   | 159        |
| 5.2.3.2.2.1 Flow quantities normal to the plate _____                    | 159        |
| 5.2.3.2.2.2 Flow quantities parallel to the plate _____                  | 164        |
| 5.3 Heat transfer results and comparison with flow field data _____      | 171        |
| 5.3.1 Effects of lateral conduction and the finite difference approach _ | 172        |
| 5.3.2 Evolution of the temperature field _____                           | 173        |
| 5.3.3 Qualitative heat transfer results _____                            | 176        |
| 5.3.4 Quantitative heat transfer results _____                           | 178        |
| 5.4 Concluding remarks _____   | 182        |
| <b>Chapter 6 Numerical results _____</b>                                 | <b>186</b> |
| 6.1 Qualitative results _____  | 186        |
| 6.2 Mean velocity profiles _____   | 188        |
| 6.3 Turbulence profiles _____  | 191        |
| 6.4 Concluding remarks _____   | 195        |
| <b>Chapter 7 Conclusions and Further work _____</b>                      | <b>198</b> |
| 7.1 Summary of conclusions _____   | 198        |
| 7.2 Results _____  | 199        |
| 7.2.1 Literature review _____  | 199        |
| 7.2.2 Experimental boundary condition _____                              | 200        |
| 7.2.3 Quantitative temperature field characterisation _____              | 202        |
| 7.2.4 Qualitative flow characterisation _____                            | 202        |
| 7.2.5 Quantitative experimental results _____                            | 203        |
| 7.2.6 Numerical results _____  | 208        |
| 7.3 Practical implications of the work _____                             | 209        |
| 7.4 Recommendations for further work _____                               | 210        |
| <b>References _____</b>  | <b>212</b> |
| <b>Bibliography _____</b>  | <b>246</b> |
| <b>Databases and search facilities _____</b>                             | <b>247</b> |
| <b>Appendices _____</b>  | <b>248</b> |

## LIST OF APPENDICES

### **Appendix A Drawings and design diagrams of the experimental test facility.**

- A.1 List of components
- A.2 Geometry of the Contraction

### **Appendix B Determination of physical properties of seeding particles.**

- B.1 Particle density
- B.2 Effective particle diameter

### **Appendix C Propagation of heat transfer measurement errors and their contribution to the overall uncertainty for three measurement techniques.**

- C.1 Constant *temperature* method
- C.2 Constant *heat flux* method
- C.3 Transient *one-dimensional* technique
- C.4 Transient *two-dimensional* technique
- C.5 Calibration curves of liquid crystals

### **Appendix D C++ Software for One and Two-dimensional transient heat conduction through a semi-infinite solid and for data collection.**

- D.1 One-dimensional transient heat conduction through a solid (numerical approximation)
- D.2 Two dimensional transient heat conduction through a solid (numerical approximation)
- D.3 One-dimensional transient heat conduction through a solid (analytically exact)
- D.4 Data collection from digital multimeter Keithley 2001

### **Appendix E Optical displacement of the measurement volume.**

- E.1 Displacement due to different refractive indices
- E.2 Displacement due to astigmatism

### **Appendix F ANSYS/FLOTRAN data input file for three-dimensional jet impingement model.**

- F.1 Input file

### **Appendix G List of Publications.**

- G.1 Presented at 11<sup>th</sup> Int. Heat Transfer Conf., Kyongju/Korea.
- G.2 Presented at 6<sup>th</sup> Nat. UK Heat Transfer Conf., Edinburgh.
- G.3 Presented at 9<sup>th</sup> Int. Symposium on Flow Visualization, Edinburgh/UK.

# FLOW VISUALISATION OF IMPINGING AIR AND WATER JETS

by

Uwe Rüdell

## ABSTRACT

A detailed study of a single jet impinging orthogonally onto a flat surface has been undertaken for air and water to obtain qualitative and quantitative information of heat transfer and fluid flow characteristics in impinging air and water jets over a Prandtl number range of  $0.71 \leq Pr \leq 8$ . Reynolds numbers of 2000, 10,000 and 20,000 were considered at a nozzle-to-plate spacing of  $z/d=2$ . New experimental data have been obtained using flow visualisation techniques for the mean velocity and turbulence characteristics including Reynolds shear stresses. Particular attention was paid to the near wall characteristics which dominate the heat transfer process. By comparing the flow field data with local heat transfer characteristics (obtained using liquid crystals) an increased physical understanding of the mechanism of jet impingement heat transfer has been attained.

At turbulent Reynolds numbers and all Prandtl numbers, mean and turbulent flow characteristics showed close agreement. The finding of negligible fluid property effects is continued for the flow along the centreline and along the impingement plate. The shear layer that surrounds the core of the approaching jet was identified as the origin of vortical structures, which impinge on the developing wall jet. In due course wavy streamlines between the convected vortices and the impingement surface were observed.

The effects of kinematic viscosity on the flow field are more apparent at the lowest Reynolds number. Quantitative differences in the mean and turbulent intensity profiles normal and parallel to the wall were found in the mixing layer, in close proximity to the wall and further away, in the free stream. The water jet spreads more rapidly than the air jet due to higher levels of shear leading to more entrainment and faster decay of the axial velocity. After impingement the air jet develops a thinner boundary layer. As the flow returns to isotropic behaviour levels of turbulent shear stresses increase rapidly to similar levels as observed in the water jets. For  $Re=2,000$ , the wall jets of both fluids are less stable than at higher Reynolds numbers. The peak in Reynolds shear stress moves away from the stagnation point as the Reynolds number is increased.

Generalised correlations for optimised jet impingement heat transfer which have been derived based on gaseous jets project trends in heat transfer coefficients satisfactorily for higher Prandtl numbers (water jets) at turbulent Reynolds numbers. This is reflected in identical qualitative trends of the radial heat transfer profiles where a primary peak was observed at  $r/d \approx 0.55$  and a secondary peak at  $r/d \approx 1.8$ . This secondary peak in heat transfer coincides with the location of the maxima in the shear stress and turbulence intensity and is attributed to the transition from laminar to turbulent flow.

The Finite Element software package ANSYS/FLOTRAN in conjunction with the Standard k- $\epsilon$  turbulence model has been assessed for the prediction of jet impingement flows. The inherent strong point of the Finite Element technique is its meshing capabilities which was demonstrated by creating 'wedge-shaped' near wall elements to satisfy near-wall model criteria. Despite the inability of the eddy-viscosity model to predict anisotropic flows in the stagnation region, near the wall the mean velocity was over-predicted to within 19%.

## Acknowledgements

During the course of my research work I have received a tremendous amount of support from my friends, colleagues and family for which I am extremely grateful. There are, however, certain persons who deserve a special mention; I would like to thank my Director of Studies, Dr Shirley Ashforth-Frost for her support, encouragement, guidance and for having faith in me throughout this project.

In particular, I would like to extend my sincere gratitude to Dr Martyn Lacey, my mentor, for helping me find this interesting subject, for being such a constant source of motivation, encouragement, backing and feedback and for his tireless backing in the difficult stages of the project.

Thanks are due to the laboratory and technical staff; Messrs. Rob Potter, Ralph James, Keith Adams and Mrs Nicky Mullen for their assistance in manufacturing the experimental facilities. I would like to thank Mr and Mrs Corlett for providing me with urgently needed information for the literature survey and Dr Kay Scarpetta for her exemplary dedication. Mr Chris Shaw deserves a special thankyou for helping with the processing of the liquid crystal data.

Very special thanks are due to my fellow researchers and colleagues; Dr Mark Wakelam, Dr Stephen Ball and Dr Rob Goodson for their friendship, encouragement and advice. Here, Dr Stephen Ball deserves a special mention for his industrious proofreading of this thesis. Thanks also to Mr Matthew Dalton and Mr Brian Cheong for frank discussions and for sharing the laboratory with me.

I am grateful for the education I gained from the Fachhochschule Karlsruhe, University of Applied Sciences, Karlsruhe, Germany, particularly for the support I received from Prof Dr Gottschalk and Prof Dr Reichelt.

I am indebted to my family, especially my parents, Lydia and Erich Rüdél, for their mental and financial support. I am particularly grateful to my Dad for his overwhelming support and great interest he took in my education.

Finally, my greatest thanks go to my beloved wife, Cornelia Rüdél, for her tireless backing throughout my academic education. To follow me to another country and to settle into a new environment was not easy which is why my wife has all my greatest admiration and respect. The thanks I offer here hardly seems enough. Our marriage and our joint life have been my main source of inspiration throughout this project.

## LIST OF PUBLICATIONS

Ashforth-Frost, S and Rüdél, U W, 1998. Flow Visualisation of an impinging water jet using liquid crystals. *Poster presented at the 11<sup>th</sup> Int. Heat Transfer Conf.*, Kyongju, Korea, 23-27 August, Paper AH47.

Rüdél, U, Ashforth-Frost, S and Jambunathan, K, 1999. The effects of boundary conditions on heat transfer testing at moderate Prandtl numbers. *Proc. IMechE 6<sup>th</sup> UK National Conf. Heat Transfer*. Edinburgh, 15-16 Sept., 221-230.

Rüdél, U, Ashforth-Frost, S and Jambunathan, K, 2000. Flow Visualisation of Submerged impinging jets of different Prandtl numbers. *Proc. 9<sup>th</sup> Int. Symp. Flow Visualization*, Edinburgh, 22-25 Aug., Paper 372.

Ashforth-Frost, S and Rüdél, U W, 2001. Flow Visualisation of a water jet impinging in a semi-confined space using liquid crystals. *ASME J. Heat Transfer*. To be Submitted.

Rüdél, U, and Ashforth-Frost, S, 2001. The effects of Prandtl number – a literature review. *Exp. Thermal and Fluids Science*. To be Submitted.

## LIST OF FIGURES

### **Figure:**

- 2.1. Prandtl number of fluids frequently used in jet impingement.
- 2.2. Typical arrangement of jet impingement heating.
- 2.3. Radial and axial temperature distribution in an impinging argon jet ( $z/d=3$ ), Dowd and Maxwell (1978).
- 2.4. Non-dimensionalised Nusselt number distribution at  $z/d=2$ .
- 2.5. Surface tension of fluids for  $0.005 < Pr < 100$ .
- 3.1. Mutual interactions of experimental parameters.
- 3.2. Schematic of the test facility.
- 3.3. Stability of water tunnel.
- 3.4. Shapes of contoured nozzles.
- 3.5. Photograph of the water tunnel.
- 3.6. Stability of air flow at the nozzle exit for  $Re=2000$  and  $Pr=0.71$ .
- 3.7. Schematic of the test facility used for the quantitative flow visualisation.
- 3.8. Temperature-hue calibration of liquid crystals in water:
- 3.9. Range of uncertainty of steady-state techniques.
- 3.10. Range of validity of the 1D-transient technique.
- 3.11. Range of uncertainty of the 1D-transient technique.
- 3.12. Range of validity of the 1D-transient technique (additional heat flux).
- 3.13. Range of uncertainty of the 1d- transient technique (additional heat flux).
- 3.14. Schematic of the LDA-facility.
- 3.15. Schematic of the optical probe set-up with respect to window surface.
- 3.16. Effect of sample size on statistical moments for  $Re=2,000$  ( $Pr=0.71$ ).
- 3.17. Effect of sample size on statistical moments for  $Re=10,000$  ( $Pr=0.71$ ).
- 3.18. Measured and theoretical laminar pipe exit velocity profiles.
- 3.19. Front view of the test section.
- 3.20. Flow symmetry along the impingement surface,  $Re=20,000$  and  $Pr=0.71$ .
- 3.21. Flow symmetry along the impingement surface,  $Re=2,000$  and  $Pr=8$ .

- 3.22 Schematic diagram of the measurement locations for the experimental investigation. a.) coarse mesh, b.) fine mesh.
- 4.1. Three-dimensional computational domain.
- 4.2. Inlet conditions at the nozzle exit for Reynolds number=10,000.
- 5.1. Vector plot of the flow field for  $Re=2,000$  and  $z/d=2$ .
- 5.2. Vector plot of the flow field for  $Re=10,000$  and  $z/d=2$ .
- 5.3. Impinging jet (elapsed time 0:99s).
- 5.4. Impinging jet (elapsed time 1:09s).
- 5.5. Impinging jet (elapsed time 7:51s).
- 5.6. Impinging jet of  $Pr=3.5$  and  $z/d=2$  ( $\mu/\mu_{ref} = 0.54$ ).
- 5.7. Impinging jet of  $Pr=7$  and  $z/d=2$  ( $\mu/\mu_{ref} = 1$ ).
- 5.8. Axial velocity for various Reynolds numbers ( $Pr=7:3$  and  $8$ ).
- 5.9. Radial velocity for various Reynolds numbers ( $Pr=7:3$  and  $8$ ).
- 5.10. Axial turbulence intensity for various Reynolds numbers ( $Pr=7.3$  and  $8$ ).
- 5.11. Radial turbulence intensity for various Reynolds numbers ( $Pr=7:3$  and  $8$ ).
- 5.12. Turbulent shear stresses for various Reynolds numbers ( $Pr=7:3$  and  $8$ ).
- 5.13. Axial velocity for  $Pr=0.71$  for various Reynolds numbers ( $Pr=0.71$ ).
- 5.14. Radial velocity for various Reynolds numbers ( $Pr=0.71$ ).
- 5.15. Axial turbulence intensity for various Reynolds numbers ( $Pr=0.71$ ).
- 5.16. Radial turbulence intensity for various Reynolds numbers ( $Pr=0.71$ ).
- 5.17. Turbulent shear stresses for various Reynolds numbers ( $Pr=0.71$ ).
- 5.18. Velocity profiles at the nozzle exit ( $Re=20,000$ ).
- 5.19. Reynolds stresses at the nozzle exit ( $Re=20,000$ ).
- 5.20. Velocity profiles at the nozzle exit ( $Re=10,000$ ).
- 5.21. Reynolds stresses at the nozzle exit ( $Re=10,000$ ).
- 5.22. Velocity profiles at the nozzle exit ( $Re=2,000$ ).
- 5.23. Reynolds stresses at the nozzle exit ( $Re=2,000$ ).
- 5.24. Axial velocity profile for  $Re=20,000$  (open  $Pr=0.71$ , filled  $Pr=7.3$ ).
- 5.25. Axial velocity profile for  $Re=10,000$  (open  $Pr=0.71$ , filled  $Pr=7.3$ ).
- 5.26. Displacement thickness of the wall jet for  $Re=20,000$ .

- 5.27. Radial velocity profile for  $Re=20,000$  (open  $Pr=0.71$ , filled  $Pr=7.3$ ).
- 5.28. Radial velocity profile for  $Re=10,000$  (open  $Pr=0.71$ , filled  $Pr=8$ ).
- 5.29. Axial turbulence intensity for  $Re=20,000$  (open  $Pr=0.71$ , filled  $Pr=7.3$ ).
- 5.30. Axial turbulence intensity for  $Re=10,000$  (open  $Pr=0.71$ , filled  $Pr=8$ ).
- 5.31. Radial turbulence intensity for  $Re=20,000$  (open  $Pr=0.71$ , filled  $Pr=7.3$ ).
- 5.32. Radial turbulence intensity for  $Re=10,000$  (open  $Pr=0.71$ , filled  $Pr=8$ ).
- 5.33. Reynolds stresses for  $Re=20,000$  (open  $Pr=0.71$ , filled  $Pr=7.3$ ).
- 5.34. Reynolds stresses for  $Re=10,000$  (open  $Pr=0.71$ , filled  $Pr=8$ ).
- 5.35. Mean velocity and turbulence profiles at  $y/d=0.1$  and  $Re=20,000$ .
- 5.36. Reynolds stresses at  $y/d=0.1$  and  $y/d=0.014$  for  $Re=20,000$ .
- 5.37. Mean velocity and turbulence profiles at  $y/d=0.1$  and  $Re=10,000$ .
- 5.38. Reynolds stresses at  $y/d=0.1$  and  $Re=10,000$ .
- 5.39. Schematic of the sign convention for the Reynolds stresses at the nozzle exit.
- 5.40. Radial and axial development of the Reynolds stresses ( $Re=10,000$ ,  $Pr=0.71$ ).
- 5.41. Axial velocity profile for  $Re=2,000$  (open  $Pr=0.71$ , filled  $Pr=8$ ).
- 5.42. Radial velocity profile for  $Re=2,000$  (open  $Pr=0.71$ , filled  $Pr=8$ ).
- 5.43. Displacement thickness of the wall jet for  $Re=2,000$ .
- 5.44. Axial turbulence intensity profile for  $Re=2,000$  (open  $Pr=0.71$ , filled  $Pr=8$ ).
- 5.45. Radial turbulence intensity profile for  $Re=2,000$  (open  $Pr=0.71$ , filled  $Pr=8$ ).
- 5.46. Profiles of Reynolds stresses for  $Re=2,000$  (open  $Pr=0.71$ , filled  $Pr=8$ ).
- 5.47. Mean velocity and turbulence profiles at  $y/d=0.1$  and  $Re=2,000$ .
- 5.48. Reynolds stresses at  $y/d=0.1$  and  $Re=2,000$ .
- 5.49. Radial and axial development of the Reynolds stresses ( $Re=2,000$ ).
- 5.50. Radial and axial development of the mean axial velocity ( $Re=2,000$ ).
- 5.51. Radial development of the mean radial velocity ( $Re=2,000$ ,  $Pr=8$ ).
- 5.52. Ratio of normal stress components on the centreline ( $Re=10,000$  and  $Re=20,000$ ).
- 5.53. Ratio of normal stress components for  $Pr=0.71$  ( $Re=2,000$ ).
- 5.54. Ratio of normal stress components for  $Pr=8$  ( $Re=2,000$ ).
- 5.55. Effect of lateral conduction from the finite difference technique.
- 5.56. Temperature variation of the flow field for  $Re=20,000$  and  $z/d=2$  ( $Pr=0.71$ ).

- 5.57. Temperature variation of the flow field for  $Re=20,000$  and  $z/d=2$  ( $Pr=4.9$ ).
- 5.58 Development of isotherms for an air jet at  $Re=20,000$  and  $Pr=0.71$ .
- 5.59 Typical development of isotherms for a water jet ( $Re=20,000$  and  $Pr=4.9$ ).
- 5.60 Variation of the local Nusselt number for  $Pr=0.71$  and  $Pr=4.9$  ( $Re=20,000$ ).
- 5.61 Variation of peaks in Reynolds stress with  $Re$  ( $Pr=0.71$  and  $7.3$ ).
- 6.1. Qualitative plots of a) Velocity streamlines and b) Turbulent kinetic energy.
- 6.2. Qualitative plots of a) Effective viscosity  $\nu_{eff}$  and b) Dissipation rate.
- 6.3. Radial velocity profiles at  $r/d=0$ .
- 6.4. Radial velocity profiles at  $r/d=0.4$ .
- 6.5. Radial velocity profiles at  $r/d=0.8$ .
- 6.6. Radial velocity profiles at  $r/d=1.2$ .
- 6.7. Radial velocity profiles at  $r/d=1.6$ .
- 6.8. Radial velocity profiles at  $r/d=2$ .
- 6.9. Radial velocity profiles at  $r/d=2.5$ .
- 6.10. Radial profile of  $y^+$  along the impingement plate.
- 6.11 Turbulent kinetic energy profiles at  $r/d=0$ .
- 6.12 Turbulent kinetic energy profiles at  $r/d=0.4$ .
- 6.13 Turbulent kinetic energy profiles at  $r/d=0.8$ .
- 6.14 Turbulent kinetic energy profiles at  $r/d=1.2$ .
- 6.15 Turbulent kinetic energy profiles at  $r/d=1.6$ .
- 6.16 Turbulent kinetic energy profiles at  $r/d=2$ .
- 6.17 Turbulent kinetic energy profiles at  $r/d=2.5$ .

## NOMENCLATURE

| Symbol   | Meaning  | Unit                           |
|--|--|--------------------------------|
| A  | Area of impingement plate  | m <sup>2</sup>                 |
| C <sub>μ</sub> , C <sub>1</sub> , C <sub>2</sub> | Turbulence model constants                                       | 1                              |
| c <sub>p</sub>                                   | Specific heat capacity   | J/(kg.K)                       |
| d  | Nozzle diameter  | m                              |
| f <sub>s,1</sub> , f <sub>s,2</sub>              | Frequency shift on laser beam ½                                  | Hz                             |
| h  | Heat transfer coefficient  | W/(m <sup>2</sup> K)           |
| i  | = $\sqrt{-1}$  | 1                              |
| K  | Coefficient for displacement of measurement volume               | 1                              |
| K <sub>0</sub>                                   | Velocity decay constant  | 1                              |
| k  | Turbulent kinetic energy, (u' <sup>2</sup> + v' <sup>2</sup> )/2 | m <sup>2</sup> /s <sup>2</sup> |
| L  | Characteristic geometric length, (i.e. nozzle, heater)           | m                              |
| m  | Exponent of Prandtl number in heat transfer equations.           | 1                              |
| Nu   | Nusselt number, (=h d/λ)   | 1                              |
| n  | Exponent of Reynolds number in heat transfer equations.          | 1                              |
| n <sub>i</sub>                                   | Refractive index (i=0 air, i=1 Perspex, i=2 water)               | 1                              |
| P  | = -i $\sqrt{\Psi}$   |                                |
| Pr   | Prandtl number, (= ν/α)  | 1                              |
| Pr <sub>t</sub>                                  | Turbulent Prandtl number   | 1                              |
| Q  | Power  | W                              |
| r  | Recovery factor  | 1                              |
| r/d  | Non-dimensional radial distance from the stagnation point        | 1                              |
| Re   | Reynolds number, (= U d/ν)                                       | 1                              |
| ΔS   | Spatial displacement of measurement volume                       | m                              |
| s  | Thickness of impingement plate                                   | m                              |
| Sc   | Schmidt number, (= ν/κ <sub>c</sub> )                            | 1                              |
| St   | Stanton number, (= h/(c <sub>p</sub> ρV))                        | 1                              |
| T  | Temperature  | °C                             |
| T <sub>w</sub>                                   | wall temperature   | °C                             |
| T <sub>aw</sub>                                  | adiabatic wall temperature                                       | °C                             |
| T <sub>0</sub>                                   | Initial temperature  | °C                             |
| T <sub>s</sub>                                   | Temperature at stagnation point                                  | °C                             |

|            |   |                    |
|------------|---|--------------------|
| $T_{x,t}$  | Temperature displayed by liquid crystals                                  | $^{\circ}\text{C}$ |
| $t$        | Time  | s                  |
| $Tu$       | Turbulence intensity, $(=\sqrt{u'^2}/U_{ref})$ , $(=\sqrt{v'^2}/U_{ref})$ | 1                  |
| $\Delta x$ | Spatial horizontal displacement of measurement volume                     | m                  |
| $y$        | Axial distance from the impingement plate.                                | m                  |
| $U$        | Mean axial velocity   | m/s                |
| $U_{exit}$ | Mean axial velocity at nozzle exit  | m/s                |
| $U_{cl}$   | Mean axial velocity at nozzle exit on the centreline                      | m/s                |
| $u'$       | RMS axial velocity fluctuation, $(=\sqrt{u'^2})$                          | m/s                |
| $V$        | Mean radial velocity  | m/s                |
| $v'$       | RMS radial velocity fluctuation, $(=\sqrt{v'^2})$                         | m/s                |
| $V_{NW}$   | Velocity at near wall node  | m/s                |
| $z/d$      | Non-dimensional nozzle-to-plate spacing                                   | 1                  |
| $We$       | Weber number $(=\rho u^2 d/\sigma)$                                       | 1                  |

### Greek symbols

|                                |  |                                     |
|--------------------------------|--|-------------------------------------|
| $\alpha$                       | Thermal diffusivity $(=\lambda/(\rho c_p))$        | $\text{m}^2/\text{s}$               |
| $\beta$                        | Laser beam intersection angle                      | $^{\circ}$                          |
| $\delta$                       | Boundary layer thickness                           | m                                   |
| $\varepsilon$                  | Angle between laser beam and wall                  | $^{\circ}$                          |
| $\varepsilon_h, \varepsilon_t$ | turbulent or eddy thermal conductivity             | $\text{kg}/(\text{m}\cdot\text{s})$ |
| $\phi_m$                       | Coefficient for displacement of measurement volume | 1                                   |
| $\gamma$                       | Ratio of specific heats                            | 1                                   |
| $\eta$                         | $=h^2 t / (\rho c_p \lambda)$                      | 1                                   |
| $\varphi$                      | Laser probe rotation angle                         | $^{\circ}$                          |
| $\kappa$                       | von Karman constant                                | 1                                   |
| $\kappa_K$                     | Molecular diffusivity                              | $\text{m}^2/\text{s}$               |
| $\lambda$                      | Thermal conductivity                               | $\text{W}/(\text{m}\cdot\text{K})$  |
| $\lambda_0$                    | Wavelength of laser beam                           | M                                   |
| $\mu$                          | Dynamic viscosity                                  | $\text{kg}/(\text{m}\cdot\text{s})$ |
| $\nu$                          | Kinematic viscosity                                | $\text{m}^2/\text{s}$               |
| $\theta$                       | Non-dimensional temperature                        | 1                                   |
| $\rho$                         | Density  | $\text{kg}/\text{m}^3$              |

|                                |   |     |
|--------------------------------|---|-----|
| $\sigma$                       | Surface tension                                     | N/m |
| $\tau$                         | inertial decay time constant                        | s   |
| $\xi$                          | Displacement thickness                              | m   |
| $\psi$                         | Decay coefficient                                   | 1/s |
| $\psi_1, \psi_2$               | Coefficients for displacement of measurement volume | 1   |
| $\sigma_k, \sigma_\varepsilon$ | Turbulent Prandtl-Schmidt numbers                   | 1   |

## Subscripts

|          |                           |
|----------|---------------------------|
| aW       | Adiabatic wall            |
| Ax       | Axial direction           |
| B        | Water bath                |
| bP       | beyond potential core     |
| fl       | Fluid                     |
| F        | based on film temperature |
| J        | Jet                       |
| M        | Momentum                  |
| NW       | Near Wall                 |
| 0        | Initial                   |
| P        | Particle                  |
| Rad      | radial direction          |
| ref      | Reference                 |
| S        | Stagnation point          |
| S        | Impingement surface       |
| T        | Thermal                   |
| W        | Wall                      |
| wP       | within potential core     |
| $\infty$ | free stream               |

## **Chapter 1**

### **Introduction**

#### **Introduction**

This Chapter commences with an introduction into the importance of jet impingement and its usefulness for practical and theoretical applications. The brief summary of past research efforts will be followed by an identification of current and future research needs. It will be shown that the choice of the working fluid represents one of the most crucial tasks for the designer in order to effectively achieve the maximum overall efficiency for a given jet impingement heat transfer situation. Based on this problem statement, the specific aims and objectives of this investigation are given, followed by the rationale behind the chosen jet impingement geometry. Finally, a brief outline of the thesis layout is provided.

#### **1.1 Background and statement of the problem**

Due to its excellent heat and mass transfer characteristics, the impinging jet has been exploited extensively in the past for a wide range of industrial applications such as cooling, heating and drying processes. Although jet impingement heat transfer reflects a very complex function of several parameters with different weightings, the high heat transfer rates can be controlled, to a certain degree, by varying the jet geometry and related flow parameters. This gives rise to shortened processing times and improved product quality and uniformity. The highly complex nature of impinging flows is, therefore, of significant interest to the engineering community both from a practical and, more recently, theoretical viewpoint as the impinging jet is used as a test case for turbulence model development. Additionally, the case of an axisymmetric jet discharging into still fluid is frequently employed to understand the fundamental properties of a stationary turbulent field without mean motion, that is turbulence dominated by turbulent diffusion and dissipation.

With recent advances in high-performance semi-conductor components it is anticipated that heat fluxes originating from micro-electronic components and electric circuits will steadily increase. Air, with its inherent thermal limitations, is likely to be

replaced by fluids that are capable of coping with those high thermal loads. In the demand to dissipate these large fluxes, the careful selection of the working fluid and a full understanding of its physical effects has great influence on the performance of the cooling/heating/drying process. Important factors are fluid consumption, overall efficiency, pumping power, weight of the overall system, temperature uniformity, electrical conductivity and the physical size of the component of interest. A further outcome will be a more efficient production cycle with higher capacity, better product quality and higher energy and material savings.

It was only recently that jet impingement researchers began to focus attention on the excellent heat transport properties that can be achieved with liquids. Current applications reflect the diversity and versatility of liquid jet impingement in industrial usage such as the cooling of combustion engines, high-performance electrical circuits, highly reflective optical face plates, the annealing and quenching of metal batches and drying processes, such as those in ink jet printers. To optimise these processes a full understanding of the flow field and its effects on heat transfer is required. Despite jet impingement being a subject of study for decades, the vast majority of correlations have been developed with air as the working fluid, while for other fluids there is a paucity of information. The use of correlations originally derived for air jets can lead to significant errors in designing and optimising processes with fluids other than air. The use of fluids other than air is currently impeded by correlations that fail to represent liquids reliably as they have been developed based mainly on gases, which have entirely different thermophysical properties. These properties are represented by the Prandtl-number ( $Pr$ ) which is the ratio of momentum dissipation to thermal dissipation:

$$Pr = \frac{v}{\alpha} = \frac{c_p \mu}{\lambda} \quad (1.1)$$

To the author's knowledge there exists only one early investigation in the form of a numerical comparison between air and water jets, Sutura *et al.* (1963), where a greater sensitivity of laminar heat transfer to free stream turbulence in water than in air jets was reported. However, to relate recent findings on the complex interactions between the near-wall region and heat transfer to a working fluid other than air, more complementary experimental data are essential.

It becomes apparent from the above, that there exists a considerable lack of detailed knowledge on Prandtl number effects on the flow and temperature fields of impinging jets. The paucity of literature focusing on a fluid other than air and the lack of studies that concentrated on more than one working fluid make the assessment of Prandtl number effects on jet impingement heat transfer a difficult task.

Despite the fact that jet impingement offers some of the highest local heat transfer coefficients, the design of industrial applications often requires high *average* heat transfer coefficients to avoid burnout as a consequence of hotspots. These are caused by the non-uniform distribution of the local heat transfer coefficient which, in turn, is attributable to flow phenomena such as transition, separation or impingement of large scale vortices. Reviewing the literature reveals that these parameters might, in turn, be a function of Prandtl number. Heat transfer coefficients may differ by several orders of magnitude depending on the thermal properties of the fluid. One important question that arises from this fact is the question as to *how* and *where* fluids of different Prandtl numbers affect the flow field and consequently the heat transfer characteristics.

Another potential challenge arises from the fact that increased air traffic demands larger aircrafts with greater passenger capacities. Since the lift induced by an aircraft wing is limited by its physical size other ways of saving weight have to be found. One way of resolving this problem could be the assignment of multiple tasks to pre-existing components onboard an aircraft i.e. using oil for hydraulic control functions and for the cooling of electronic circuits or for heating purposes inside an air refrigeration circuit. In such industrial applications where the type of working fluid cannot be altered without compromising the main objective of the design, the comparatively unfavourable thermal properties not only have to be accepted but have to be investigated in great detail to gain maximum efficiency.

With the advent of the digital computer, numerical fluid dynamics techniques have evolved over the past sixty years from a speciality, reserved to a small group of highly skilled enthusiasts, into a widely used and well accepted engineering tool. Industry was quick to realise the huge potential of the computational fluid dynamics (CFD) method and how it could be used to save valuable resources, time, manpower and to reduce costs. Despite this success, computational fluid modelling cannot, as yet, offer a universal code to reliably solve every flow problem, particularly when it comes to the simulation of

turbulent flow problems where chaotic and random motion prevails. The major difficulty in modelling turbulent flows is the closure of the time-averaged Navier Stokes equations which, despite huge efforts from the research community, has to date not delivered the desired accuracy and reliability. New approaches are currently being developed, such as Direct Numerical Simulation (DNS) or Large Eddy Simulation (LES), but are, to date, not fully explored in that these schemes momentarily require huge computer capacities.

The only way of verifying the validity of numerical turbulence predictions for a given flow geometry is to conduct experiments, which is often difficult to realise so that benchmark cases are employed to adapt numerical solutions to experimental results. Jet impingement has been identified as a suitable test case for the validation of CFD codes due to the stagnant flow character which occurs frequently in engineering applications. Other interesting aspects of jet impingement flow include the high curvature, high heat transfer coefficients, recirculation, separation and developing flow. Therefore, experimental data are needed for quantification, especially in the near wall region where large velocity gradients exist that are somewhat difficult to model numerically but are significant for the performance of a numerical scheme.

The aim of this project is to extend previous gaseous and liquid jet impingement work by studying air and water jets on the same experimental facility to examine the effects of fluid properties, mainly viscosity, on the flow field and on the heat transfer process. This will identify major similarities and differences in the flow field of impinging gaseous and liquid jets so that the huge number of existing correlations derived for air jets may be assessed for their use in liquid jet impingement heat transfer. This will enable a greater understanding of the complex viscous and turbulent interactions that occur during jet impingement heat transfer. To validate existing numerical models, much needed benchmark test case data will be provided.

## **1.2 Aims and objectives**

The specific aims of this study are as follows.

### **1.2.1 Specific aims**

- a) To provide new experimental data for velocity, turbulence and heat transfer in a submerged impinging air jet and a submerged impinging water jet at a low nozzle-to-plate spacing.
- b) To seek a better understanding of the influence of hydrodynamic processes on jet impingement heat transfer.
- c) To assess the suitability of the k- $\epsilon$  turbulence model, available in a commercial Finite Element Computational Fluid Dynamics (CFD) code, in predicting fluid flow characteristics of an impinging jet.

### **1.2.2 Objectives**

The research programme was defined by a consistent pursuit of the following objectives:

- 1.) To compile a literature review on the use of fluids with different thermal properties in jet impingement to give an overall view of Prandtl number research to date and to identify aspects in need of further study.
- 2.) To design, build, validate and calibrate a test rig with the following requirements:
  - ◆ To achieve flow in the test section of low initial turbulence and high uniformity.
  - ◆ To accommodate fluids of different density and viscosity.
  - ◆ To allow different flow velocities to be maintained.
  - ◆ To allow flow visualisation studies.
  - ◆ To facilitate heat transfer, velocity and turbulence measurements.Uncertainty analysis was used throughout the design phase.
- 3.) To assess the suitability of different experimental methods, particularly for use in liquid jet impingement heat transfer, in terms of overall uncertainty, reliability, low safety risk and ease of use.
- 4.) To perform quantitative and qualitative flow visualisation studies of the hydrodynamic and thermal flow field.

- 5.) To undertake experimental measurements of near wall velocity and turbulence intensity (and higher-order statistics if applicable) of the flow field using laser-Doppler anemometry (LDA).
- 6.) To obtain complementary measurements of the heat transfer coefficient using a transient wall heating technique.
- 7.) To analyse the fluid flow and heat transfer results. Determine the effects of Prandtl number on jet impingement heat transfer.
- 8.) To assess the predictive performance of a commercially available Computational Fluid Dynamics (CFD) software package, ANSYS/FLOTRAN, for the present geometry by comparing it to experimental results.

### 1.2.3 Breakdown of objectives

The objectives of this study are best characterised by breaking them down into the following questions:

#### Literature review

What are Prandtl number effects in general flow and heat transfer situations? Which of the three quantities of Prandtl number has the most pronounced effect on jet impingement? What are these effects? Do scalar quantities (Temperature, concentration) show different behaviours from vector quantities (i.e. Velocity)? Are Prandtl number effects more pronounced for roughened surfaces than for smooth surfaces? What is the main mechanism for the heat transfer enhancement in impinging jets and how can different Prandtl numbers display different heat transfer characteristics? What are typical values of the Prandtl number exponent  $m$  and Reynolds number exponent  $n$  in heat transfer correlations?

#### Experimental boundary condition

What are the ranges of validity in terms of uncertainty levels of the three most widely used experimental techniques? How do these experimental techniques compare in terms of overall uncertainty, reliability, repeatability and ease of use? Should some of them only be used for certain Prandtl number regions? What is the most suitable experimental

technique for a combined study of impinging jets of air and water? How does the transient technique compare with steady-state techniques? Can the transient technique be applied for impinging water jets? What are the limitations of the transient approach for air and water jets? Can liquid crystals be used in submerged water jet applications? How does the protective varnish layer affect the heat transfer coefficient?

#### Quantitative temperature field characterisation

Can liquid crystals be used as tracer to map the temperature field of time dependent jet impingement flows? To date, liquid crystals have mainly been used for visualising natural heat convection regimes. Can they be applied for turbulent heat transfer regimes? What are the limitations of the technique? What is a typical calibration curve for liquid crystals? How reliable are liquid crystals for detecting cooling/heating situations? What is a typical time scale for establishing the temperature field for an impinging water jet?

#### Qualitative flow characterisation

What is the main flow pattern in the test section? Are vortices generated at the edges of the jet? Is the flow periodic? Can the flow be characterised quantitatively?

#### Quantitative experimental results

- a) Provided the test apparatus and the flow straightening facility are identical throughout this investigation, are there differences in the velocity profile at the nozzle exit for different Prandtl numbers? What are the effects on the level of turbulence?
- b) For laminar nozzle exit conditions ( $Re=2,000$ ), where effects of viscosity on the flow are expected to be greatest, what are the quantitative differences in the mean and turbulent flow fields for different Prandtl numbers? How do levels of Reynolds stresses compare with each other?
- c) Is the ratio of radial to axial turbulence levels the same for air and water?
- d) How does the flow field change qualitatively for higher Reynolds numbers and for various Prandtl numbers? Do Prandtl number effects in the bulk flow diminish with increasing Reynolds number?
- e) How does the impingement wall affect the approaching jet on the centreline? Is the influence of the wall affected by Reynolds number or Prandtl number?

- f) How does the wall jet behave for different values of Reynolds number or Prandtl number? Are peaks of mean and turbulent quantities affected by Reynolds number or Prandtl number?
- g) Are there any significant disturbances from free stream vortices that might impinge on the boundary layer?
- h) What are differences in the temporal evolution of the temperature field beneath hot impinging air and water jets?
- i) Where do the maximum heat transfer coefficients occur? Are there any qualitative differences in the shape of the radial Nusselt number distribution? Is an overall assessment of the effect of near wall turbulent quantities on the heat transfer possible?

### Numerical results

How well is the mean flow predicted? How do the predictions of the turbulent quantities compare with experimental results? Is the standard k- $\epsilon$  model, with the logarithmic wall function capable of predicting near wall characteristics well? How economical in terms of CPU-time and accuracy is the overall model?

### 1.3 Rationale

The experimental parameters of the present study are summarised in Table 1.1. A jet impingement facility was developed to allow the quantitative and qualitative characterisation of impinging gaseous and liquid jets.

| <b>Parameter</b>   | <b>Range</b>  |
|--------------------|---|
| Jet type           | $\varnothing$ 35mm, semi-confined                   |
| Reynolds number    | 2,000, 10,000 and 20,000                            |
| Pr - heat transfer | 0.71 and 4.9  |
| Pr - flow field    | 0.71, 7.3 and 8                                     |
| $z/d$              | 2   |
| Temperature range  | $15^{\circ}\text{C} \leq T \leq 50^{\circ}\text{C}$ |
| Radial distance    | $0 \leq r/d \leq 2.5$                               |
| Distance from wall | $0 \leq y/d \leq 1.2$                               |

Table 1.1. Experimental parameters.

A semi-confined geometry was chosen due to its relevance for industrial applications where limited space dominates the design, such as in turbine blade cooling, the cooling of electronic components or the drying of ink such as in ink jet printers.

Since Prandtl number effects are dependent on the ratio of inertia to viscous forces, three Reynolds numbers, namely 2,000, 10,000 and 20,000 were chosen. While the highest Reynolds number was to ensure that the secondary maximum in heat transfer was well defined, Gardon and Akfirat (1965), the lower Reynolds numbers were selected to identify viscous effects on the flow field.

For the quantitative flow field investigation, an isothermal jet was used with the working fluids having Prandtl numbers of 0.71 and 8, respectively. Complementary characterisation of the flow field was undertaken for Prandtl numbers of 3.5 and 7 to investigate the effects on the length of the potential core. For the heat transfer investigation, a non-isothermal jet was studied. Here, the flow properties were evaluated at the mean temperature.

In all cases, the impingement plate was placed well within the potential core of the jet,  $z/d=2$ . This coincided with a position where other workers had identified non-monotonous radial heat transfer profiles.

#### **1.4 Outline of the investigation**

This Chapter has provided a brief introduction and statement of the problem. The aims and objectives have been discussed in further detail.

In Chapter 2, relevant literature is reviewed. The literature survey defines Prandtl number and describes different concepts of interpreting it. The most common Prandtl number characteristics are exemplified. To gain an overview of the general effects Prandtl number can have, the literature survey has been expanded to include other fields of engineering. The jet impingement flow structure is divided into three characteristic regions and analysed with respect to effects of fluid properties. Available works on turbulent Prandtl number are also reviewed. The important topic of boundary conditions in jet impingement testing is covered in the final section of the survey. Concluding remarks summarise the survey.

The experimental set-up, procedures and routines for quantitative and qualitative flow visualisation, laser-Doppler Anemometry and liquid crystal thermography are presented in Chapter 3. The design of the experimental facility, the selection process of the experimental technique and the validation of the measurement system are included.

The governing equations for flow and heat transfer and their numerical characterisation are presented in Chapter 4. The k- $\epsilon$  turbulence model is described briefly together with the procedure to obtain the heat transfer coefficient. Attention is paid to the geometry of the three-dimensional model to simulate the flow inside the test section.

The experimental and numerical results are presented in Chapters 5 and 6, respectively. The characteristics of an impinging jet of air and water for Reynolds numbers of 2000, 10000 and 20000 at a nozzle-to-plate spacing of 2 will be discussed. An analysis of the full field flow visualisation results is given first. The emphasise of the Chapter will be placed on the interpretation of detailed flow data at the nozzle exit, along the jet centreline and at various radial positions along the impingement plate. Heat transfer data are directly related to the mean and turbulent flow field. Numerical results will be compared with experimental data.

In the final Chapter 7 a summary and conclusions from this study are discussed and recommendations for further work are given.

## Chapter 2

### Literature review

#### Introduction

Jet impingement is frequently used in industrial applications where high heat transfer coefficients are sought. The circumstance that some of the highest heat transfer coefficients can be achieved with impinging jets, has attracted considerable research attention.

The versatile character of jet impingement is reflected in the wide range of industrial applications, such as the cooling of combustion engines, Kiryu (1986) or highly reflective optical face plates, Palmer (1993). Further applications include cryosurgery, Filippov (1991), drying processes such as in ink jet printers, Can (1998), food processing, Borquez *et al.* (1999) and jet cutting, Alitavoli and McGeough (1998). From a theoretical point of view, the impinging jet serves frequently as test case for understanding principal characteristics of turbulence and its inherent transport mechanisms, Risso and Fabre (1997).

The influence of Prandtl number on convective heat transfer is still one of the least understood aspects of impinging jets, Sun *et al.* (1998). As heat transfer coefficients may differ by several orders of magnitude depending on the thermal properties of the fluid, an important task for researchers is to identify the locations where fluids of different Prandtl numbers show significant differences in the flow field. For example, in unsteady boundary layer flow of water Eswara and Nath (1994) found the point of zero skin friction to move downstream with decreasing Prandtl numbers. Since this point marks the onset of separation when the flow is steady, it can be expected that for heated water flow the transition from laminar to turbulent flow will be delayed. This, in turn, suggests that the location of transition-induced peaks in the local heat transfer profile is a function of Prandtl number.

It becomes apparent from the above, that there exists a strong need for detailed knowledge on Prandtl number effects on the flow and temperature field of impinging jets. The paucity of literature focusing on any one fluid other than air and the lack of studies that concentrated on more than one working fluid make the assessment of Prandtl number effects on jet impingement heat transfer a difficult task. It is the purpose of this literature

survey to review work from the open literature in order to provide an update to the existing knowledge on Prandtl number effects on jet impingement heat transfer.

The publications cited in this survey have been identified using a number of search engines and databases: Details of these services are given in the Section 'References'. Information as to how recent the 185 research articles used in this survey date back to are listed in Table 2.1.

| Year        | Quantity |
|-------------|----------|
| 2001        | 1        |
| 2000        | 2        |
| 1999        | 7        |
| 1998        | 26       |
| 1997        | 18       |
| 1996        | 8        |
| 1995        | 10       |
| 1994        | 17       |
| 1993        | 15       |
| 1953 – 1992 | 82       |

Table 2.1. Number of references and their distribution in this review.

## **2.1 Aim and methodology**

The aim of this survey is to identify heat transfer and flow field characteristics due to the impingement of different fluids. The state of current knowledge will be summarised and areas will be discussed where greater research effort in jet impingement heat transfer is needed. In view of the fact that jet impingement heat transfer is greatly affected by numerous parameters, this work concentrates on those physical principles identified in the literature as being the most relevant, namely nozzle-to-plate spacing, nozzle size, Reynolds number ( $Re$ ) at the nozzle exit and non-dimensionalised distance from the stagnation point. Figure 2.1 illustrates the range of Prandtl number and the corresponding fluids covered in the open literature for specific use in jet impingement heat transfer.

The large differences in Prandtl number are due to the wide range of applications of jet impingement. For the cooling of electronic components the use of a constant heat flux boundary condition provides an almost ideal characterisation of the actual surface condition. The thermal treatment of metals on the other hand is better characterised using a transient boundary condition, Zumbrennen *et al.* (1989, 1990). For air jets, the use of the constant heat flux or constant wall temperature boundary condition can result in heat

transfer deviations of up to 15%, see Taylor *et al.* (1989). Higher heat transfer coefficients associated with liquid jet impingement are expected to yield even greater discrepancies. When conducting an uncertainty analysis it became apparent that each of the most commonly used experimental techniques has its optimum Prandtl number range where it delivers the lowest levels of uncertainty. In a paper on the effects of boundary conditions on jet impingement heat transfer, Rüdél *et al.* (1999) presented results of an uncertainty analysis for the constant temperature, the constant heat flux and the transient boundary condition.

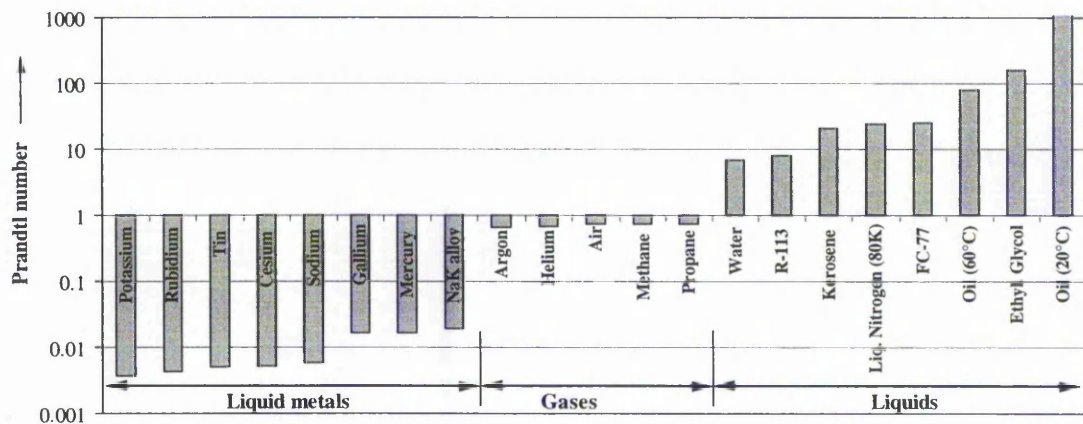


Figure 2.1. Prandtl number of fluids frequently used in jet impingement.

The classification of liquid jets into submerged (i.e. issuing jet is exposed to same fluid) and unsubmerged jets (i.e. issuing jet is exposed to different fluid, usually air) and their inherent different sensitivity to nozzle-to-plate spacing, initial turbulence level and gravity among others requires careful assessment of data. Additionally, the use of characteristic lengths other than nozzle size (i.e. heater dimensions) in correlations reduce their universality to other applications.

To gain a wider overview of relevant factors, the literature review has been expanded to include engineering areas such as heat exchangers, pipe flows and external flows. This allowed conclusions to be drawn as to what extent Prandtl-number effects are considered important.

## 2.2 Interpretation of Prandtl-number

Fluids may be categorised into *Newtonian* and *non-Newtonian* fluids, according to the relationship between shear stress and shear rate. The present work will focus on

Newtonian fluids but for the latter the interested reader is referred to an excellent review on micropolar fluids provided by Ariman *et al.* (1973). The characteristics of a submerged non-Newtonian jet were investigated by Richards and Shekarriz (1997). A new development in enhancing heat transfer characteristics is to suspend small solid particles in a fluid as discussed by Xuan and Li (2000).

According to their state of matter under room conditions (gaseous, liquid, solid), Newtonian fluids can generally be divided into two categories, *gas* or *liquid*. Gases can be described with sufficient accuracy by the kinetic theory of gases while the molecular picture of liquid behaviour is far more complex and less well established. Newtonian liquids may be classified into three different kinds: *liquid metals*, *polar* liquids and *non-polar* liquids. Differences in the ionisation and electrical conductivity are manifested as good (heat) conduction properties (i.e. liquid metals) while *non-polar* liquids represent good insulators.

A *real* fluid, in contrast to an *ideal* fluid, is subjected to perturbations in the form of energy transfer to, or from, the fluid by shear stresses and thermal diffusion effects. The ratio of the transport of momentum by viscous effects to the transport of heat by thermal diffusion is expressed in the Prandtl-number (Pr):

$$\text{Pr} = \frac{\nu}{\alpha} = \frac{c_p \mu}{\lambda} \quad (2.1)$$

Using the analogy to mass transfer the Schmidt number may be likewise expressed as

$$\text{Sc} = \frac{\nu}{\kappa_c} \quad (2.2)$$

Note, that both dimensionless numbers are dependent only on the thermal properties of the fluid. In some cases it is beneficial to consider the numerator and denominator of Prandtl-number separately. Nourgaliev *et al.* (1997), in a paper on Prandtl number effects in internally heated liquid pools, distinguished between two physical mechanisms, i.e. the kinematic viscosity  $\nu$  and thermal diffusivity  $\alpha$ -phenomena, respectively. For the case of low viscosity ( $\nu$ -phenomenon), convection may become the dominant heat transfer mechanism while relatively higher thermal diffusivity ( $\alpha$ -phenomenon) may lead to higher heat conduction rates. The variation of Prandtl-number with temperature has different effects on these two terms. For low temperatures ( $\leq 200^\circ\text{C}$ ) viscosity plays the dominant role in changes of Prandtl-number, Sun and Ma (1998), while in regions of

higher temperatures (up to 7700°C) thermal conductivity and specific heat capacity may exhibit exponential variations with temperature, Ogawa and Hijikata (1996).

As the effects of momentum and diffusive transport processes are confined to a thin layer in the immediate vicinity of a wall, Prandtl number may also be regarded as a proportionality coefficient for the ratio of thermal to hydrodynamic boundary layer thickness. For laminar flow such as in the stagnation region of an impinging jet, Kakaç and Yener (1995) proposed

$$\frac{\delta_t}{\delta_m} = \frac{1}{Pr^{1/3}} \quad (2.3)$$

Perhaps the greatest relevance of Prandtl number for engineering situations is in the field of stagnating flows. Here, aerodynamic cooling or viscous heating affects the measurement of flow quantities (i.e. temperature) in the form of temperature increases due to adiabatic compression or in the form of frictional temperature rises, see Li *et al.* (1997). To account for these effects, the concept of a recovery factor was introduced. The relation between the stream temperature  $T$ , its stagnation temperature  $T_s$  and the adiabatic wall temperature  $T_{aw}$  (temperature adjacent to the wall) is defined as the recovery factor  $r$ :

$$r = \frac{T_{aw} - T}{T_s - T} \quad (2.4)$$

Brodkey (1967) applied the effects of combined friction and heat transfer to define Prandtl number. If the fluid velocity is high,  $T_{aw}$  may be quite different from  $T$  as the wall drag retards the boundary layer so that  $T_{aw}$  approaches  $T_s$ . However, two effects can cause  $T_{aw}$  to differ from  $T_0$ . Firstly, dissipation of kinetic energy from the mainstream to the boundary layer and secondly, heat transfer from the boundary layer to the mainstream. The ratio of these two is the Prandtl number.

For impinging liquid jets which are generally characterised by a negative Joule-Thomson coefficient ( $\partial T/\partial p < 0$ ), this effect manifests itself in a recovery factor that approaches zero at the stagnation point. This is followed by a considerable rise that results in an adiabatic wall temperature in the radial direction that is higher than the free-stream liquid temperature, see Lee *et al.* (1997). Conversely, for gaseous jet impingement heat transfer, the recovery factor at the stagnation point is close to unity, see Goldstein *et al.* (1986). In a subsequent paper, Goldstein *et al.* (1990) studied the radial

distribution of the recovery factor for an impinging air jet and found the recovery factor to be within 20% for  $0 \leq r/d \leq 2$ . In a recent paper, Seol and Goldstein (1997) found in a submerged free air jet that energy separation due to shear work and heat conduction is less significant than energy separation due to pressure fluctuations induced by convective movement of vortices. Generally, it can be stated that the recovery factor is almost independent of  $Re$  and the mass flow rate but sensitive to the nozzle exit velocity profile and the nozzle-to-plate spacing, see Ma *et al.* (1997a). Li *et al.* (1997) compared the radial distribution of the dissipation function with that of the recovery factor and concluded that the heat generating effects of viscous dissipation determines the distribution of the recovery factor.

The close connection between Prandtl number and the recovery factor for different effects of kinematic viscosity and the thermal diffusivity are discussed in the following for various ranges of Prandtl number.

- 1.) **Pr > 1 (i.e. liquids):** For liquids, where Prandtl number may vary by several orders of magnitude, heat transfer enhancement may either be based on the  $\alpha$ -phenomenon as described for water and FC-77 in Womac *et al.* (1993) or on the  $v$ -phenomenon as shown for transformer oil by Ma *et al.* (1997a). In the former case the authors showed that under identical experimental conditions the heat transfer coefficient of water was almost six times that of FC-77. This is due primarily to the thermal conductivity of water being approximately ten times higher than that of FC-77, while the quantities of specific heat capacity and dynamic viscosity have little effect. For high Prandtl number fluids, Lee *et al.* (1997) observed experimentally that a high amount of momentum is dissipated in the form of frictional heat while smaller rates of heat are diffused through the fluid, indicating less loss of frictional heat. Li *et al.* (1997) also observed an increase in recovery factor with Prandtl number due to the difficulty in removing heat through conduction that was generated by viscous dissipation.
- 2.) **Pr = 1 (i.e. steam):** The specific case of  $Pr=1$  is important since it represents the case where viscosity effects are counter-balanced by thermal diffusion. However, this signifies that measurements of any (*real*) fluid even with an *ideal* adiabatic probe will still not result in the *real* total temperature. This is due to the irreversible non-adiabatic character of the stagnation process. To the author's knowledge, no practical

work has been published to date that has studied the effects of counter-balancing transport processes on jet impingement.

- 3.) **0.5 < Pr < 0.75 (i.e. gases):** If the Prandtl number is less than one, more heat is transferred from the boundary layer to the mainstream than would be dissipated from the mainstream to the boundary layer. As a result, the temperature adjacent to the wall will be less than the stagnation temperature. The vast majority of the open literature has focused its attention on gaseous jet impingement, mainly using air. For gases, the thermal boundary layer is generally thicker than the hydrodynamic boundary layer. The impaired process of thermal energy diffusion through the large thermal boundary layer results in a cooling effect of the adiabatic surface. The Prandtl number range of gases is comparatively small so that differences amongst various gases are less pronounced than those amongst liquids. For gases, the thermal conductivity is directly proportional to the kinematic viscosity. Sherman (1990) suggests the use of Eucken's approximation formula  $\lambda = \frac{9\gamma - 5}{4\gamma} \mu c_p$  to infer  $Pr = 2/3$

for monatomic gases ( $\gamma = 5/3$ ) and  $Pr=14/19$  for diatomic gases such as air.

- 4.) **0.5 < Pr (i.e. liquid metals):** In liquid metals, the concept of the thermal boundary layer as representing the total thermal resistance proves impractical. This is attributed to the fact that in high thermal conductivity fluids large quantities of energy are transported through conduction rather than convection. Therefore, the temperature profile within the boundary layer displays almost no temperature gradient and develops much more rapidly than the velocity profile. The low viscosity of liquid metals makes them less adhesive to the wall, therefore exchange of momentum between the free stream and the wall is negligible thus involving almost always turbulent flow. At these low Prandtl numbers, Ruckenstein (1998) regarded the thermal boundary layer  $\delta_h$  as thick and thus regarded it as being generally independent of viscosity.

Another consequence of the strong dependency of Prandtl number on temperature, especially for liquids, is the importance of the choice of the reference temperature for evaluating fluid properties. To account for effects of viscous heating it is essential to use the adiabatic wall temperature instead of the jet temperature when comparing and correlating heat transfer results over a wide range of Prandtl numbers. The issue of varying properties can be avoided by selecting small temperature differences between the surface and the jet, see

Besserman *et al.* (1992), Sun *et al.* (1993) and Womac *et al.* (1993). For higher Prandtl numbers, however, where the viscous dissipation function grows even stronger, especially in the near wall region, the effects of variable properties can no longer be ignored.

From dimensional analysis it can be shown that the velocity field of incompressible and isothermal flow (=constant properties) only depends on the kinematic viscosity. The hydrodynamic flow field is then uncoupled from the temperature field so that Prandtl number does not affect the flow field. However, it has to be noted that Prandtl number is a strong function of viscosity which, in turn, does affect the flow field.

In one of the first investigations on the effects of Prandtl number on jet impingement, Metzger *et al.* (1974) carefully selected  $T_w - T_{aw}$  to be 3.3K and studied the effects of variable properties by increasing the temperature difference up to 17.8K. To prevent distorted velocity and temperature fields that arise when experimental data acquired under large temperature gradients are compared with constant-property-based-correlations, Sun and Ma (1998) suggested two correlation approaches. In each case heat transfer coefficients are evaluated at a reference temperature or are subsequently corrected by a ratio of some pertinent property. Recently, Leland and Pais (1999), when investigating high Prandtl number fluids in unsubmerged jet impingement, accounted for conditions of highly varying fluid properties by using

$$r = Pr^n = \frac{2 c_p (T_{aw} - T_j)}{U_{exit}^2} \quad (2.5)$$

for correlating the recovery factor. The adequacy of this correlation was demonstrated and the exponent  $n=0.47$  was found to compare well with previous work.

### **2.3 Effects of Prandtl number in general engineering applications**

To gain an overview of the general effects that Prandtl-number can have, a literature review in other engineering areas has been conducted. This has allowed conclusions to be drawn as to what extent Prandtl-number effects are considered important. Strong Prandtl-number variations in turbulent layers of the stratosphere can effectively diminish the quality of radar methods, such as used for meteorological forecasts, see Bertin *et al.* (1997). Other examples include the effectiveness of heat exchangers, where an underprediction of the surface temperature for different fluids causes significant design errors, see Hu and Herold (1995). For flow through smooth-tubes, Obot *et al.* (1997)

found effects of Prandtl-number ( $0.7 < Pr < 125$ ) only in the transition region where liquids show considerably lower pressure drop readings with fluid heating than without temperature gradient. This contrasts sharply to the trend documented for air by Obot and Esen (1992). In a study on the performance of enhanced tubes with different surface roughness heights, Ravigururajan and Bergles (1995) found increasing friction factors for water at different Prandtl-numbers. For turbulent flow this study yielded an augmentation in heat transfer of up to 80% for  $Pr=6$  over that of  $Pr=10$ . The improvement was accompanied by an increase in pressure drop, which can significantly deteriorate the overall efficiency of the tubes. For flow through a circular pipe, Büyükalaca and Jackson (1998) obtained enhanced heat transfer data for non-uniform viscosity variations due to increased turbulent diffusion in the near-wall region between the viscous sub-layer and the thermal boundary layer. Harms *et al.* (1998) conducted temperature-dependent studies on viscosity variations in semi-circular duct flow and observed significant deviations from constant-property values of Nu-number. For external flows, Inagaki and Kitamura (1990) found unexpected discrepancies in Nusselt number between water and air in the combined convection region. Goussis and Kelly (1984) analysed the stability of liquid film flow over an inclined surface for the case of heating or cooling. For small values of Prandtl number, cooling stabilised the flow whereas heating destabilised the flow. Large Prandtl number resulted in a reversed trend. For flows of different Prandtl-number in a series of cells of confined geometry, Maurer and Libchaber (1980) found the onset of turbulence to be affected by the change in spatial structure of instabilities. In an analytical work, van Oudheusden (1997) reports the vague nature of the common Prandtl number exponent of  $m=1/3$  for the characterisation of stagnation point heat transfer. A small but fundamental difference between the heat transfer behaviour of axisymmetric stagnation flow and that of plane stagnation flow was found. The Prandtl number exponent for plane stagnation flow heat transfer was slightly higher than its axisymmetric counterpart.

## **2.4 Reviews**

Jet impingement has received a considerable amount of research attention in the past. For air jets Viskanta (1993) and Jambunathan *et al.* (1992) provided comprehensive literature surveys in which various correlations were presented and critically evaluated.

Bibliographies that dated from as far back as 1890 were produced by Button and Jambunathan (1989) and Jambunathan and Button (1994). As one of the first workers to compare several Prandtl number fluids with each other, Martin (1977) presented a comprehensive literature survey in which gaseous and liquid jets are related. Although the presented empirical correlations provide an early analytical link between mainly air and water data, these data only cover a limited range of validity as was later demonstrated by Womac *et al.* (1993). More recently, Faggiani and Grassi (1990), Incropera and Ramadhyani (1994) and Webb and Ma (1995) reviewed characteristics of single-phase liquid jet impingement while Wolf *et al.* (1993) surveyed the literature dealing with liquid jet impingement boiling.

## **2.5 Effects of Prandtl number in jet impingement literature**

Only a few papers are available that directly compare fluids of different Prandtl-number in single jet impingement heat transfer. In an early analytical paper, Suter *et al.* (1963) compared water and air impingement and attributed the higher heat transfer of water in the laminar boundary layer of the stagnation region to a higher sensitivity to free stream turbulence. This greater sensitivity of liquids to disturbances ceased at a Prandtl-number value of 100. Metzger *et al.* (1974) corroborated these findings by comparing the heat transfer data of water ( $Pr=3$ ) with those of synthetic oil ( $84 < Pr < 151$ ). The authors suggested the use of different correlations for liquids whose Prandtl-numbers are below or above a value of 100. Jiji and Dagan (1988) investigated FC-77 and water jets with particular focus on the cooling of electronic chips. A great influence of the heater dimensions was found on overall heat transfer data, which lead him to use the geometric size of the heater as the characteristic length as opposed to nozzle size. Womac *et al.* (1993) compared water and FC-77 jets directly and found slightly higher Nusselt numbers for a dielectric fluid. FC-77 jets were found to be more prone to unsubmerged conditions than comparable water data. In an extensive study on unsubmerged round water jets, Stevens *et al.* (1992) and Pan *et al.* (1992) found negligible dependency on nozzle exit turbulence level and confinement. In one of the few hot-film anemometry studies, Wolf *et al.* (1995a, 1995b) confirmed the above findings and, additionally, investigated the impact of nozzle-to-plate spacing. No striking dependency was noted.

Sun *et al.* (1998) conducted heat transfer measurements of three liquids, R-113, Kerosene and transformer oil, in the Prandtl number range between 7 and 262. The heat transfer profiles compared well with integral solutions which led the authors to conclude their being independent of Prandtl number and insensitive to  $Re$ . In a recent paper on unsubmerged impinging jets, Leland and Pais (1999) conducted a comparative study for high Prandtl number fluids in the range of 48 to 445. Their results show that existing heat transfer correlations under-estimate the heat transfer coefficient by more than 100% as the wall to fluid temperature difference increases.

In one of the few papers on the effects of low Prandtl-number on jet impingement, Palmer (1993) compared the heat transfer coefficient of water jets with those of several liquid metals. While all liquids showed quantitative resemblance at low nozzle exit velocities, (20m/s), for exit velocities of 60m/s liquid metal heat transfer rates exceeded those of water by up to a factor of 2.5. It appears as if there exists little technological interest in the use of liquid metals in jet impingement, except as reactor coolants where they demonstrate their reliability and practicality by achieving high heat transfer coefficients due to their high thermal conductivity. For the hypothetical scenario of a severe accident in a Light Water Reactor, Green *et al.* (1997) conducted heat transfer experiments including phase changes with Cerrobend and Tin as working fluids. The authors pointed out that existing correlations failed to predict heat transfer accurately. The effects of air jet induced transport in a bath were reported by Qian *et al.* (1996). Two heated fluids having widely different Prandtl numbers, silicone oil ( $Pr=990$ ) and a molten metal alloy ( $Pr=0.093$ ), were cooled by an impinging air jet. Results showed that fluids of large thermal diffusivity, high density and low viscosity produced distributions of low temperatures superior to those of high Prandtl number fluids.

## **2.6 Flow structure**

In contrast to the most frequent air jet applications (i.e. submerged), the flow field of an impinging liquid jet can be divided according to whether the jet is exposed to a low (submerged) or high (unsubmerged) viscosity gradient. A submerged jet is characterised by a typical cone shape accompanied by an extensive exchange of momentum with the surroundings. In contrast, unsubmerged jets behave such that the diameter of the jet, after issuing from the nozzle, is almost unaffected by the surrounding fluid and can even

decrease due to gravitational and shear forces. In the following, emphasis will be placed on submerged jets although differences with unsubmerged jets will also be addressed.

Generally, the resulting flow field of an orthogonally impinging semi-confined jet can be divided into three distinct flow regions, see Figure 2.2.

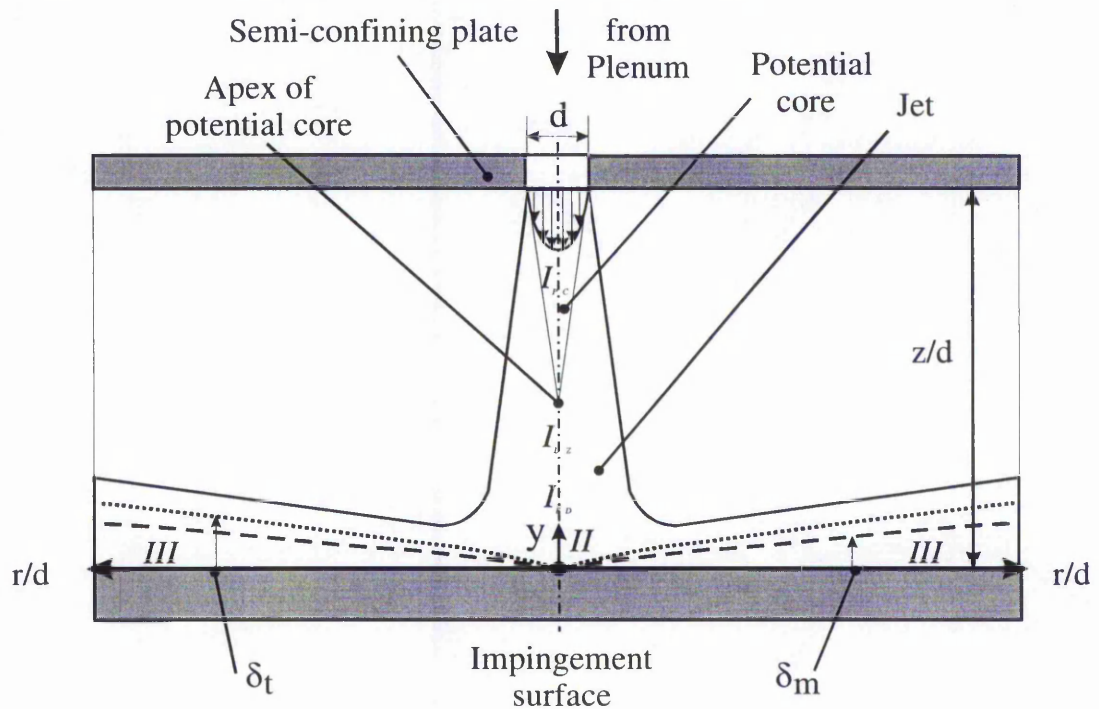


Figure 2.2. Typical arrangement of jet impingement heating.

The free jet region,  $I$ , can further be divided into the potential core zone,  $I_{PC}$ , the developing zone,  $I_{DZ}$ , and the fully developed zone,  $I_{FD}$ . In the potential core zone,  $I_{PC}$ , the flow produces entrainment of mass, momentum and energy, which leads to a gradual velocity decay beginning at the edge of the jet and travelling towards the centreline of the jet. The impingement zone,  $II$ , can be identified as the region in which the jet strikes the surface and where its direction is changed. The wall jet region,  $III$ , is marked by bulk flow moving radially outwards.

### 2.6.1 Free jet or flow establishment region I

The free jet region can be divided into four zones: the *near-field* where the centreline velocity is equal to the nozzle exit velocity, the *transition region* where the velocity starts to decrease, the *zone of similarity* where the flow is fully developed and the *termination zone* which is characterised by a final decay of velocity. For jet impingement

applications the near field region ( $x/d < 10$ ) is of main interest since it is here where maximum mass and heat transfer rates are achieved. Liepmann and Gharib (1992) showed that streamwise in the near field vortex pairs primarily affect entrainment of the jet. Streamwise vorticity was also attributed to play a major role in sustaining flow directed to the centreline and therefore contributing to the growth of the jet. The effects of viscosity on the roll-up of a vortex sheet were analytically studied by Chen and Wang (1991). Results indicate that a viscous vortex sheet is stretched slightly shorter than its inviscid counterpart. In the region of transition ( $15 \leq x/d \leq 30$ ), where the shear layer is exposed to a continuously decreasing velocity difference between the ambient fluid and the high speed core, interaction between remaining vortex dynamics from the near field and the cascade of turbulent motion to smaller scales were observed, Weisgraber and Liepmann (1998). A fundamental link between coherent structures and a statistical model to describe turbulence and its inherent complex unsteady interactions between lateral and streamwise vorticity has yet to be developed. A clear dependence of turbulent velocity and vorticity fields on  $Re$  was identified. It is especially in regions of transition from laminar to turbulent flow and in flows close to a solid wall where viscous stresses reach the same order of magnitude as turbulent stresses and where they contribute considerably to the structure of turbulent flows, see Bradshaw (1971). From this point of view it seems plausible that the choice of the working fluid affects the location of the point where transition from laminar to turbulent flow occurs. In the region of profile similarity the velocity profiles are similar at different distances and the flow is fully developed so that the entire spectrum of Kolmogorov length scales can be found. It has been experimentally known for twenty years that the far field of the jet was dominated by small spatial scales. The work by Dimotakis *et al.* (1983) was the first to identify spatially inhomogeneous flow in the far field of a water jet. For large Schmidt numbers, Dahm and Dimotakis (1990) also observed organised large-scale structures and observed unmixed ambient fluid on the jet centreline. For low Schmidt numbers ( $Sc \approx 1$ ), however, the authors showed no unmixed fluid on the jet centreline, indicating an effect of Schmidt number on mixing in turbulent jets. Yoda *et al.* (1994) confirmed the existence of large-scale structures for the region of  $30 \leq x/d \leq 83$  in the form of 'spots' of different concentrations which extend one jet diameter in the downstream direction. Results corroborated those in water and air jets by Dahm and Dimotakis (1990) and Dowling and Dimotakis (1990).

### 2.6.1.1 Centreline velocity decay

Knowledge of the decay of the centreline velocity is essential in order to position the target surface into the flow field at a location where the velocity starts to decrease and the turbulence level in turn reaches a maximum. Maximum heat transfer rates were found by many authors at the end of the potential core, see i.e. Huber and Viskanta (1994), Chang *et al.* (1995), and Garimella and Rice (1995). For air, several studies have been conducted that investigated centreline velocity decay for air jets as a function of nozzle exit velocity. In an early paper, Hrycak *et al.* (1970) reported measurements on the length of the potential core of impinging isothermal air jets. The potential core length was largest ( $20d$ ) at a Re-number value based on the nozzle exit conditions of 1000. It then decreased sharply until  $3500 \leq Re \leq 5500$ . A subsequent slight increase was observed until the Re reached a value of about 10000. Above this, the length of the potential core was almost unaffected by Re and remained constant ( $5d$ ). However, it has to be noted that Hrycak *et al.* (1970) based their results on a simple axial distance from the nozzle exit. For distances that exceed the near field region, use of the virtual origin,  $x_0$ , and the velocity decay constant,  $K_0$ , are essential. For impinging jets, Livingood and Hrycak (1973) pointed out that for distances of several diameters from the nozzle there is little difference between the virtual origin and the nozzle exit. In a comprehensive study, Malmström *et al.* (1997) examined the flow field of isothermal air jets. For a range of Re less than 50000,  $K_0$  decreased with increasing nozzle diameter. Results corroborated those of George (1989) who reported on the dependency of  $x_0$  and  $K_0$  on the nozzle exit conditions. Values for the decay rate were provided for isothermal air jets by Hussein *et al.* (1994) and agreed well with those of Panchapakesan and Lumley (1993a),  $K_0=5.8$  and  $6.1$ , respectively. Details of experimental conditions for several studies are given in Table 2.2.

Weisgraber and Liepmann (1998) investigated the turbulent flow structure in a free water jet and found the slope of the centreline velocity decay to be lower than in comparable air jets studied by Hussein *et al.* (1994) and Panchapakesan and Lumley (1993a). This suggests that the velocity of water jets decays marginally slower than comparable air jets. For free jets of helium issuing into ambient air, Panchapakesan and Lumley (1993b) reported decay constants that compared favourably with previous air results. However, turbulence levels of axial velocity fluctuations on the jet centreline were almost twice as large as those of the air jet, Panchapakesan and Lumley (1993a).

| Author                              | Fluid              | $\emptyset$<br>[mm]   | Re<br>[ $\times 10^3$ ] | Potential<br>core [ $Z_{pot}/d$ ] | Decay rate $K_0$<br>(decay slope)                        | Tu<br>[%] |
|-------------------------------------|--------------------|-----------------------|-------------------------|-----------------------------------|--|-----------|
| Weisgraber and<br>Liepmann (1998)   | Water              | 25.4                  | 5.5<br>16               | -                                 | $K_0$ : 6.3 (0.158)<br>$K_0$ : 6.7 (0.15)                | 0.5       |
| Romano (1998)                       | Water              | 20                    | 2                       | 1.5                               | -  | 10        |
| Liepmann and<br>Gharib (1992)       | Water              | 25.4                  | 5.5                     | 5                                 | -  | 0.5       |
| Chu <i>et al.</i> (1999)            | Water              | 10.2                  | 8.9 –<br>11.474         | 6.5                               | -  | -         |
| Hussein <i>et al.</i><br>(1994)     | Air                | 25.4                  | 100                     | -                                 | $K_0$ : 5.9<br>( $x_p$ 2.7)                              | 0.58      |
| Cenedese <i>et al.</i><br>(1994)    | Air                | 36                    | 15<br>25                | 4.2<br>3.9                        | -  | -         |
| Malmström <i>et al.</i><br>(1997)   | Air                | 152.4<br>75.8<br>40.1 | 17-97<br>15-46<br>7-84  | $x_p$ 5.2-3<br>1.2-1.2<br>4-2.8   | $K_0$ : 4.01-5.69<br>4.49-5.56<br>3.98-5.86              | 2.5       |
| Panchapakesan and<br>Lumley (1993a) | Air                | 6.12                  | 11                      | -                                 | $K_0$ : 6.06 (0.165)<br>( $\emptyset_{effect} = 0.444$ ) | 0.01      |
| Panchapakesan and<br>Lumley (1993b) | Helium<br>into air | 6.12                  | 30                      | -                                 | $K_0$ : 6.06<br>$\emptyset_{effect} = 0.414$             | 0.2       |
| Knebel, <i>et al.</i><br>(1999)     | Sodium             | 2.5                   | 14 -<br>forced          | $x_p$ -5.24                       | $K_0$ : 6.08   | -         |

Table 2.2. Experimental conditions for free round jet of different working fluids.

In order to compare the decay constants for air and helium data, Panchapakesan and Lumley (1993b) used the concept of effective diameter, given as  $d_{eff.} = (\rho_{air} / \rho_{helium})^{-0.5} d$ . The decay constant of 0.414 for helium compared well with the value of 0.444 from the air jet measurement. Panchapakesan and Lumley (1993b) found, for helium jets, the axial velocity fluctuations to be 80% - 90% higher than radial components, a fact reported earlier by Aihara *et al.* (1974). Carlomagno (1985) used Schlieren interferometry to study the initial region of a two-dimensional helium jet mixing with air. However, this study is limited to a low Re at the nozzle exit. Papadopoulos and Pitts (1998) conducted detailed measurements of the velocity decay of a propane jet and a methane jet issuing into ambient air. By incorporating the concept of effective radius the authors showed that the initial turbulence intensity distribution at the nozzle outlet is the major source for the commonly reported Re effect on the near-field development. Near-field velocity and

concentration centreline distributions were presented and supported the general conclusion that the scalar field (i.e. pressure, temperature and concentration) evolves faster than the velocity field. The results were corroborated by Knebel *et al.* (1998) who performed measurements in a sodium jet and found the decay of the centreline velocity to be the same as for fluids of higher Prandtl number. In contrast, the centreline temperature was reported to decrease with an exponent of  $-1$  compared to that of  $-5/3$  for fluids of higher Prandtl number, such as air and water. The authors also found the integral length scales of the temperature fluctuation to be significantly smaller than turbulent velocity scales. The different behaviour was attributed to heat transport being dominated by molecular diffusion while momentum transport may be characterised by turbulent diffusion. The scalar concentration and velocity field of a round turbulent jet in a co-flow was measured by Chu *et al.* (1999). The length of the potential core was reported to be dependent only on the ambient current to jet velocity ratio ( $U_a/U_0$ ) and the spreading rate of a jet,  $\beta_s$ , in stagnant ambient:

$$\frac{x_e}{d} = \frac{\sqrt{1 + U_a/U_0}}{\beta_s (1 - U_a/U_0)} \quad (2.6)$$

In conclusion, the velocity decay of a jet is not affected by the type of fluid while the temperature decrease depends strongly on the fluid's Prandtl number.

### 2.6.1.2 Vortical structures

Recently, large-scale vortices have been identified as playing a fundamental role in near-field structures of both free air and water jets, Cenedese *et al.* (1994) and Romano (1998). The first author visualised symmetrical vortical recirculating structures at the jet interface and an undisturbed core region close to the nozzle outlet. For an initially laminar water jet, the latter author provided flow images that resembled those of air and revealed double counter-rotating vortices (mushrooms) on the cross-section of the jet. Popiel and Trass (1991) provided an insight into large-scale toroidal vortices of free and impinging air jets in the form of smoke-wire visualisation images. When issuing into ambient fluid, the jet developed initial Kelvin-Helmholtz instabilities, which subsequently evoke, under the influence of viscous forces, a roll-up of the shear layer into primary vortical structures. In an analytical work, Chen and Wang (1991) studied viscous effects on the roll-up of a vortex sheet and revealed that viscosity can significantly delay the evolution

of the roll-up process. Popiel and Trass (1991) observed that the growth of toroidal vortices in air ceases at the end of the potential core while Liepmann and Gharib (1992) noticed, in round water jets, that vortical rings merge until the resultant vortex ring is so large that it breaks down, thus marking the end of the visible potential core. Qualitative agreement was also found in attributing the growth of the primary vortical rings to high strain between the high speed core and still ambient fluid and to an increase of mass flux by entrainment of ambient fluid and to amalgamation processes. Cho *et al.* (1998) pointed out the significance of vortex pairing as affecting flow entrainment, velocity profiles and turbulence intensity of the jet stream.

Due to the essential role of entrainment and toroidal structures on the heat transfer of free and impinging jets it is essential to consider viscosity as a major part in forming the flow and temperature field. Colonius *et al.* (1991) conducted a numerical analysis on the effects of compressibility on free viscous heat-conducting vortices. Although radial velocity in the vortex was found to be generated by viscous effects its overall impact on the decay of vorticity was negligible. Kida *et al.* (1991) studied the behaviour of two lateral vortex rings and found translational motion to be independent of viscosity while collision of interactions of two circular vortex rings was affected by viscosity. When analytically studying viscous effects on the roll-up mechanism of a vortex sheet, Chen and Wang (1991), viscosity was found to delay the evolution of the roll-up process. Values of viscosity studied corresponded to fluids such as Ethylene glycol and transformer oil among others. In addition, a smoothing effect on the velocity field and vorticity distribution was noted. Analytical results on the three-dimensional instability of a counter-rotating vortex pair were provided by Leweke and Williamson (1998). The outcome revealed that viscosity reduces the growth of instabilities of a vortex pair. Trajectories and circulations of vortices were closer examined by Auerbach (1987). The author concluded that once the vortex had disappeared from the edge of a laminar jet, a recirculation vortex had developed. This entrainment process was considered to be of an essentially viscous nature and had been the subject of earlier experimental studies by Taylor (1958) and Kraemer (1971). Viscous diffusion in the jet/ambient interface was characterised by a diffusive length which grows as  $(\nu t)^{0.5}$ . Popiel and Trass (1991) pointed out that mixing and entrainment processes could also be effectively altered by

disturbing the very thin laminar boundary layer of the exiting jet. This in turn would change the formation of large-scale toroidal vortex structures.

### 2.6.1.3 Mixing and entrainment

The cross-section of a free jet in the near field may be characterised as being the locus where three-dimensional instabilities, in the form of vortex pairs (mushrooms), develop out of the so-called 'braid' region and where ambient fluid is entrained through the roll-up of the shear layer. Similar observations depicting an inner ring of entrained fluid surrounded by a distinctive outer ring of unmixed fluid have been reported for air and water jets by McMackin *et al.* (1999) and Liepmann and Gharib (1992), respectively. The latter attributed the biggest effect on the formation of "mushroom" instabilities to  $Re$ . With increasing  $Re$  the downstream location where these vortex pairs form reduced while the number of modes increased. Actual sequences of a visualisation of a heated free air jet can be viewed in McMackin *et al.* (1997). Organised large scale structures about the local jet diameter were found in the far field of air and water jets by Dowling and Dimotakis (1990) and Dahm and Dimotakis (1990). Those structures were in the form of roughly axisymmetric clusters of higher-concentration jet fluid, Yoda *et al.* (1994). The high Schmidt number of liquids ( $Sc_{\text{water}} \approx 600$ ,  $Sc_{\text{air}} \approx 1$ ) with its imposed difficulties has permitted only a very few studies to be conducted on the mixing process of liquids. In an early study, Weddell (see Hottel 1953) investigated mixing between aqueous acid and base solutions. However, these results provide only limited details on the transport processes. With the development of new technologies, more advanced measurement techniques could be employed. Interesting features were revealed by Romano (1998) who investigated a free water jet using Particle Tracking Velocimetry (PTV). Particles at the centreline were found to spread more in the streamwise direction than those in the shear region while the spreading in the cross-section takes place in a similar way along the radial and the tangential direction. Cenedese *et al.* (1994) conducted laser-Doppler Anemometry (LDA) and Particle Image Velocimetry (PIV) measurements in unconfined axisymmetric air jets. They found the length of the potential core to shorten from  $z/d=4.2$  for  $Re=15000$  down to  $z/d=3.9$  for  $Re=25000$ . The spreading angles for these two nozzle exit values were in the range of  $20^\circ$  to  $35^\circ$  and  $10^\circ$  to  $20^\circ$ , respectively. Ashforth-Frost and Rüdél (1998) used liquid crystals as tracer particles to map the development of the

temperature distribution of a turbulent impinging non-isothermal water jet. A spreading angle in the range of  $10^\circ$  to  $25^\circ$  for Re of 35000 was determined. This characteristic agrees well with those of air jets by Cenedese *et al.* (1994).

Liepmann (1991) identified, via flow visualisation and PIV, the impact of "mushroom-shaped" instabilities on the rates of entrainment. Local entrainment rates vary considerably in the core region whereas at a distance of  $r/d > 2$  from the centreline those rates are independent of time. Bhat and Narasimha (1996) reported the effects of jet heating on a liquid jet. Entrainment is reduced due to the significant impact of volumetric heating on large-scale structures.

Panchapakesan and Lumley (1993a, 1993b) compared hot-wire measurements (x-wire probes) of axisymmetric air and helium jets issuing into air. At the edge of the jet, where entrainment caused the density to be close to the ambient density, the intensities of radial and azimuthal fluctuations were equal. However, peaks of Reynolds stresses across the jet were higher for the helium jet than for the air jet. Higher levels of velocity triple moments for the helium jet indicated a highly skewed distribution of velocity fluctuations in the near field of helium jets. Steeper gradients of those values display larger diffusive fluxes, which might be caused by pressure diffusion for the case of the helium jet.

Law and Masllyah (1984) provided both theoretical and experimental descriptions for the effects of confinement of initially laminar air jets. Heat transfer behaviour was found to be similar for a confined and unconfined jet apart from a region far away from the stagnation point. In this region mass transfer for the confined jet was smaller than that of an unconfined jet due to separation along the plate. Ashforth-Frost and Jambunathan (1994) showed that semi-confinement of an air jet led to limited entrainment of ambient fluid thus extending the length of the potential core by up to 20% and reducing heat transfer of the impinging jet. In a study on semi-confined impinging jets, Obot *et al.* (1982) attributed significant reductions in the impingement heat transfer coefficient to the restricted exchange of mass and momentum with ambient fluid. The effect of decreasing peaks in lateral heat transfer distribution became even more pronounced for small nozzle-to-plate spacings. Further, the location of the transition point from laminar to turbulent flow on the target surface was shifted from  $r/d=1.55$  to  $r/d=1.2$ . The contrary was found for FC-77 by Garimella and Rice (1995) who reported semi-confinement to increase the magnitude of secondary peaks in the radial heat transfer distribution. Fitzgerald and

Garimella (1998) showed, in their flow-field analysis, that an increase of Re-number and nozzle-to-plate spacing leads to a shift of the toroidal recirculation regions radially outward and axially closer to the target surface, respectively. This was accompanied by a reduction in the entrainment rate on the centreline of the jet. For the same liquid, Fitzgerald and Garimella (1996) noted a 32% increase in centreline velocity and volume flow rate due to entrainment of ambient fluid. As one of the few researchers to use R-113, Chang *et al.* (1993, 1995) studied the effects of confinement. A reduction of heat transfer was attributed to the interaction of recirculating flow pattern underneath the nozzle-plate and the jet. Generally, it can be said that the major geometric quantity to characterise the effect of semi-confinement is the ratio of the confining plate length to the nozzle-to-plate spacing, as illustrated in Incropera and Ramadhyani (1994). Schroeder and Garimella (1998) attributed different entrainment rates for air and water to differences in heat capacity.

#### 2.6.1.4 Thermal structures

Energy separation in jets is characterised by central regions with higher energy and outer regions of lower energy. This is induced by pressure work caused through moving vortices, Seol and Goldstein (1997). The consequent rearrangement of the temperature field can have a significant impact on heat transfer situations of jets. Seol and Goldstein (1998) visualised the recovery temperature distribution of an impinging air jet using thermochromic liquid crystals and revealed a region of low recovery temperature caused by energy separation at a radial distance between  $1d$  and  $2d$  from the impingement point. For heated air jets, Fox *et al.* (1993) attributed the presence of regions of high or low temperature in free and impinging air jets to the temporal movement of vortex-cores relative to those regions. Instantaneous snapshots of the analytically modelled temperature distribution at the nozzle exit plane revealed the enhancement of the total-temperature separation by the process of vortex pairing. Greater cooling rates than heating rates in the near field of an issuing jet are attributed to longer residence times in regions of lower speed. For a heated air jet, Raghu *et al.* (1990) reported the ejection of heated air from each corner in the form of side jets which resembled the vortical structure reported for isothermal jets. Bhat and Narasimha (1996) exposed a liquid jet to volumetric heating and studied the flow properties in detail. With sufficient heating the jet no longer grew linearly and the decay of

the centreline velocity and the turbulence intensity was arrested. McMackin *et al.* (1997) visualized the inner structure of a heated air jet by using an optical tomography system. Snapshots of the temperature variation across a plane orthogonal to the flow direction revealed images that identified the vortical ring structure of the flow field simultaneously in streamwise and spanwise direction. Rings of hot fluid surrounded rings of cold entrained fluid. The accuracy of the tomographic temperature method was verified by McMackin *et al.* (1999) who presented results that were in quantitative agreement with cold-wire anemometry. Dowd and Maxwell (1978) measured the temperature distribution in an impinging argon jet for  $z/d=6$  jet using spectroscopic techniques. The flattening of the radial temperature distribution towards the target surface is depicted in Figure 2.3. The authors concluded that diffusion processes were responsible for entrainment processes and

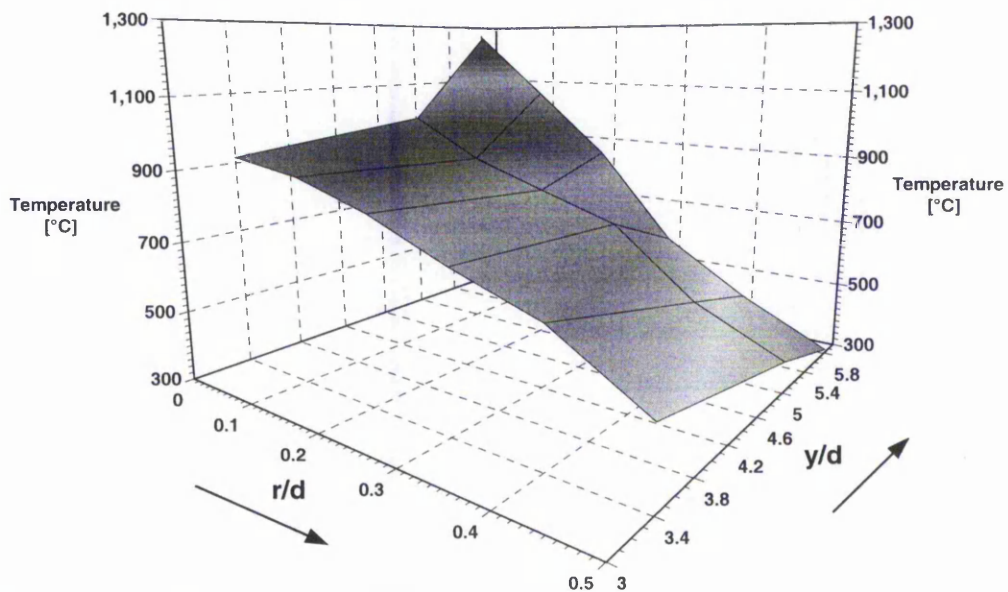


Figure 2.3. Radial and axial temperature distribution in an impinging argon jet ( $z/d=3$ ), Dowd and Maxwell (1978).

therefore were not to be neglected. At an axial distance of approximately  $5d$  from the target surface the profile provoked a slight tendency to peak. Sakakibara *et al.* (1997) visualised the extremely thin thermal boundary layer of an impinging water jet by means of laser-induced Fluorescence (LIF). They report a strong dependency of the counter-rotating vortex pair on the radial position in the stagnation region. The study revealed that due to the thin thermal boundary layer the wall temperature can be assumed to be quantitatively equal to the near wall temperature distribution.

## 2.6.2 Stagnation or impingement region II

In the stagnation region, where the approaching flow experiences a strong deceleration an initially laminar boundary layer subsequently develops in the radial direction. Under the influence of this stagnation pressure gradient the jet gathers the greatest portion of momentum. Though a wall jet only begins to develop in the stagnation region, it is here where viscosity is believed to have its greatest effects on overall heat transfer. Diffusion is seen in the slow growth of laminar shear layers. The flow in the stagnation region is considered laminar up to a radial position of  $r/d \approx 2$ , Gardon and Akfirat (1965) and Incropera and Ramadhyani (1994). It is especially in close vicinity to the stagnation region where the Prandtl-number dominates the process of momentum and heat diffusion.

### 2.6.2.1 Flow field

It is the purpose of this section to clarify the role of the Prandtl number quantities on the flow field of the stagnation region. For air jets, Gauntner *et al.* (1970) defined the impingement region to extend axially from 1.6-2.2 diameters while Giralt *et al.* (1977) proposed the extensions of the region to be 1.2 diameters from the surface for  $z/d \leq 6.8$  and  $0.153(d+z)$  for  $z/d > 6.8$ . Beltaos and Rajaratnam (1977) proposed  $1.2d$  from the target plate as the beginning of the axial impingement region. For an unsubmerged water jet, Stevens *et al.* (1992) found the influence of the plate on the approaching flow to be significant up to a distance of  $0.5d$  from the target plate. Guillard *et al.* (1998) used an LIF-technique to determine the start of the deflection zone of an approaching round water jet in terms of enhanced mixing. A location of  $y/d=1.1$  was identified where lines of constant concentration deviated from the spreading 'cone' of the free jet. Results agreed well with  $y/d=1.3$  computed by Olsson (1997) using a Large-Eddy-Simulation (LES).

The effects of inserting a heated plate into the flow of a free jet are twofold: the large-scale toroidal structures, formed in the free jet region, are affected by the plate some distance upstream and impinge on the target plate. Moreover, interactions between the target plate and oncoming primary vortical rings may significantly change the temperature distribution on the target plate, Fox *et al.* (1993). The authors showed for both air and water jets that at  $z/d=4$  the primary vortex rings struck the surface at a small

radial distance from the stagnation point where the momentum of the boundary layer was not yet strongly developed. This caused the hydrodynamic boundary layer to separate and to eject secondary vortices. For greater values of  $z/d$  the impinging primary vortices hit the surface at a location where the distance from the stagnation point was larger so that the boundary layer has gained more momentum. Consequently, no evidence of any secondary vortices was found. The impingement of large-scale eddies causes an unsteady separation of the stagnation point boundary layer which leads to a surface renewal effect as discussed by Kataoka (1990). Yokobori *et al.* (1983) investigated a plane water jet and observed no counter-rotating vortices in the stagnation region when the nozzle-to-plate distance was shorter than the potential core length. Therefore, it may be conjectured that the effects of impinging large-vortical structures on the target plate are strongly dependent on the discharge height over the target plate and the nozzle shape. Through the work of Lepicovsky *et al.* (1986) who confirmed the existence of primary vortices at a  $Re$  of up to  $2.3 \times 10^6$ , the existence of secondary vortices are, in turn, likely to occur at higher  $Re$ 's, Fox *et al.* (1993). These results contradicted those by Law and Maslyah (1984) who studied contours of stream functions in laminar air jets for different  $Re$ 's and found no secondary vortex at  $Re=400$  whereas at higher  $Re$ 's secondary vortices in opposed directions to primary vortices were noted.

Champion and Libby (1994) divided the stagnation region of an impinging jet into three regions: adjacent to the wall is the viscous sublayer, which is governed by viscous stresses. In region II molecular transport in the form of viscous stresses is no longer existent but is now dominated by turbulent processes such as convection, diffusion, production and dissipation. The outermost region III is the zone where initial turbulence of the jet decays, then grows and becomes eventually anisotropic under the influence of the rate of strain field induced by the directional change of streamlines of the impinging jet. For all three regimes, Champion and Libby (1991) applied a  $k-\epsilon$  turbulence model to model the case of turbulence induced by a slot jet impinging on a wall. The analysis showed that the viscous sublayer and the shear layer differ significantly from those within turbulent boundary layers of parallel flow. Extensional rate of strain in the region of impingement distinguishes the stagnating viscous sublayer substantially from that of a sublayer in parallel flow. Champion and Libby (1994) used an asymptotic analysis and concluded that within the viscous sublayer the entire change in the radial gradient of the radial velocity component and in the mean temperature occurs. Champion and Libby

(1996) extended their earlier asymptotic analysis by mathematically including region II and III. Comparisons were made with experimental data for the intensity of the axial and radial velocities. Agreement was found to be within 15%. Rosén and Trägårdh (1994) found molecular diffusivity in a viscous sublayer to be several orders of magnitude greater than turbulent diffusion, which led him to neglect Reynolds stresses in that region.

In an early study, Hrycak *et al.* (1970) investigated the effects of viscosity in the stagnation region of an impinging round air jet. Increasing nozzle-to-plate distance was found to delay the hydrodynamic boundary layer growth and the dimensionless stagnation pressure decreased. The point of maximum velocity in the wall jet was shifted radially outwards which was attributed to the dominating effects of viscosity outside the stagnation region while viscosity was assumed to exert negligible effects in close proximity to the stagnation point. Contrary results were provided also for an impinging round air jet by Cooper *et al.* (1993) who described the role of the viscous sub-layer in the centre of the stagnation region as confining the thermal boundary layer and therefore suppressing axial turbulence levels. A significant effect of viscosity in the stagnation region was also observed by Ueda *et al.* (1997) who conducted measurements of a round air jet with and without a flat plate in the flow. The wall exerted an effect of decreasing turbulence intensity on the axial flow whereas radial velocity fluctuations were little affected. A closer examination of the near wall region in the centre identified nonlinearities of the axial velocity profile under the influence of viscosity and nozzle characteristics. For higher turbulence levels, the mean velocity decreased with a larger gradient than the low turbulence case and was entirely underpredicted by laminar inviscid theory. More interesting, however, was the fact that profiles of radial and axial r.m.s.-velocity fluctuations increased significantly faster when the initial turbulence level at the nozzle exit was higher. The dissimilar trends of the profiles indicated highly anisotropic turbulence distribution in the centre of the impingement region. Van Fossen *et al.* (1995) concluded that augmentation of gaseous heat transfer in stagnation flow is likely to be a function of turbulence isotropy. For a submerged water jet, Nishino *et al.* (1996) assessed the impact of the impingement plate by comparing axial mean momentum transport between two different axial distances outside the stagnation region. At  $z/d=1.5$  the jet behaved similarly to a free jet since the transport of axial momentum is mainly undertaken by turbulent shear stress and convection. Closer to the wall, at  $z/d=0.06$ , however, most of the turbulent normal stress of the flow is converted into static pressure.

Cooper *et al.* (1993) used hot-wire anemometry instead of Particle-Tracking velocimetry to undertake similar measurements with air jets. Their results exhibited the same trend apart from the near-wall region where fluctuations parallel to the wire introduced perturbations resulting in a higher signal near the wall. Sakakibara *et al.* (1997) provided a detailed insight into the transport mechanisms in the immediate vicinity of the wall. However, in contrast to Nishino *et al.* (1996) who omitted the viscous term in their transport formulations, the authors attributed considerable contribution to viscous dissipation near the stagnation point.

In a study on air and water jets, Sutura *et al.* (1963) reported the dissipation of small scale vorticity before it reaches the boundary layer while large scale vortical filaments are stretched by the divergence of streamlines at the stagnation point. The intensity of the vorticity is amplified through a conservation of angular momentum so that the streamlines reach the boundary layer. When entering the boundary layer substantial three-dimensional effects are induced. Sutura (1965) compared fluids with Prandtl-numbers of 0.71, 7 and 100 with respect to their sensitivity to free stream turbulence. He found that the thermal boundary layer is more sensitive to vortex stretching than the hydrodynamic boundary layer. For air, the thermal boundary layer was about 10 times more sensitive to vorticity than the hydrodynamic boundary layer. This effect is greatest for water ( $Pr=7$ ) and ceases at  $Pr=100$ . Since small scale eddies are destroyed by viscous dissipation before they reach the boundary layer, the effects of viscosity are more pronounced in the laminar region of the stagnation region. Based on a comparison of temporal length scales, Hunt (1973) ignored viscous effects and turbulent eddy interactions in the stagnation region. The proposed rapid-distortion theory assumes turbulent eddies to be distorted more rapidly than they are dissipated by viscous and non-linear inertial forces. In a study on the effects of turbulence on gaseous stagnation point heat transfer, Van Fossen and Simoneau (1987) found no evidence of vorticity in the laminar boundary layer of the stagnation region. Wei and Miao (1992) employed the vortex-stretching model and assumed that vortical structures developed in the stagnation region are evolved from the approaching flow far upstream of the stagnation point. Therefore, the process of vorticity stretching was concluded to be essentially inviscid.

Several authors identified vorticity as the main cause for enhancement of heat transfer in the stagnation region, Yokobori *et al.* (1983) and Sakakibara *et al.* (1997). Van Fossen and Simoneau (1987) attributed enhanced heat transfer to the existence of

vortices in the stagnation region of gas turbine blades and identified experimentally enhanced heat transfer in regions of low turbulent intensities. Vortex pairs whose tangential velocity is directed towards the target surface induce this effect. Based on small-scale vortices being dissipated and large-scale vortical structures not being stretched due to their size, van Fossen *et al.* (1995) suspected the existence of an optimum eddy size. However, no practical evidence was found through experimental airflow studies.

Although knowledge of the viscous boundary layer thickness is inevitable for prediction of jet impingement heat transfer, to the author's knowledge only one study exists that defined quantitatively the thickness of the viscous boundary layer at the stagnation point beneath a confined impinging jet. Law and Masllyah (1984) showed for a confined laminar jet of air that the viscous boundary layer thickness is nearly constant throughout the stagnation region and predictable from radial velocity profiles. Inside the viscous boundary layer the radial velocity exhibited a peak at a radial distance of  $0.65d$  from the stagnation point. Fitzgerald and Garimella (1996, 1998) provided similar trends for a turbulent jet of FC-77. Maximum radial velocities were found at an axial distance of  $0.02d$  from the wall. In an analytical study on the effects of annular confinement on a initially laminar round jet, Hung and Huang (1998) found the nozzle exit conditions to be of dominant influence on the size of the stagnation point boundary layer. Details of the fluid were not further specified apart from assuming their being Newtonian with constant properties. The flow field adjacent to the stagnation point was dominated by the nozzle-to-plate spacing while its influence diminished in the outer portion of the deflection region. With increasing Re-number or increasing length-to-diameter ratio of the nozzle the boundary layer decreased. Generally, it can be concluded that both Re and Prandtl number determine the condition of the boundary layer in the stagnation region. The streamline pattern showed strong resemblance to that obtained for semi-confined FC-77 jets by Garimella and Rice (1995).

Lyell and Huerre (1985) studied unsubmerged stagnation flows showing that plane stagnation flow can be destabilised if velocity fluctuation levels are sufficiently high. Mean flow vorticity leads to relative destabilisation by centrifugal forces but viscous effects were found too strong to allow linear instability to occur.

With the jet approaching the wall, streamwise turbulence intensity increases due to diffusion. The effect of the wall on the mixing layer of the approaching jet is manifested

in a thickening of the mixing layer and in an intense exchange of momentum with surrounding fluid, Guillard *et al.* (1998). Enhanced mixing in close axial vicinity to the wall ( $y=0.7d$  from the wall) was observed. The authors presented images of an instantaneous concentration field that clearly indicates ambient fluid being engulfed at a radial position of  $r/d=0.45$ . The mixing process in the near-wall region was found to be enhanced by the presence of the wall at approximately  $0.7d$  away from the wall. Other authors reported the deceleration of the flow at the same axial location, Sakakibara *et al.* (1997) for water and Cooper *et al.* (1993) for air. It is interesting to note that for the same location Cooper *et al.* (1993) identified a peak in axial velocity fluctuations.

Ueda *et al.* (1997) attributed the peaks of radial rms profiles near the wall to the continuous motion of the stagnation point on a circular trajectory. The histograms of fluctuating velocity in radial direction were characterised by two symmetric peaks around the centre. Landreth and Adrian (1990) used LDV and PIV techniques to analyse a submerged water jet experimentally. Interestingly, a random wandering of the stagnation point during LDV measurements was noted which corroborated Ueda's findings.

With regards to liquid jet impingement, where temperature differences are usually no greater than 60K, changes of Prandtl number are mainly restricted to changes of viscosity since the thermal conductivity and specific heat capacity are relatively independent of temperature, Sun and Ma (1998). The contrary applies for the impingement of plasma jets as used for plasma cutting, welding and spraying where at temperatures beyond 8000K relevant quantities increase exponentially, Ogawa and Hijikata (1996). Chiam (1996) conducted numerical heat transfer studies to analyse the effect of varying thermal conductivity in a stagnation point flow over a flat sheet. The general trend of his results was that increasing values of the thermal conductivity near the wall resulted in decreasing temperature gradients between the wall and the fluid. Particularly for flows of liquid metals the thermal conductivity varies significantly between the wall and the free flow. For the case of an impinging plasma jet, Ogawa and Hijikata (1996) pointed out that all relevant quantities of the Prandtl number are greatly affected by the temperature, particularly for the case of over 8000K. Heat transfer correlations derived for a small temperature difference between fluid and substrate are not applicable for plasma operating temperatures since quantities such as thermal conductivity increase exponentially with temperature.

Outside the impingement region, where turbulent flow prevails, the effects of viscosity are limited to dissipating large-scale eddies into small-scale eddies. The main action of viscosity is restricted to the final stage of eddy-dissipation since the scale of viscous stresses are small compared to Reynolds stresses. However, in the process of transition from laminar to turbulent flow and in the near wall region viscosity effects can no longer be neglected.

### 2.6.2.2 Heat Transfer

It is the purpose of this section to clarify the role of the Prandtl number quantities on heat diffusion in the stagnation region.

The limit of the stagnation zone in the radial direction is taken where the stagnation pressure becomes zero, Polat (1993). Gauntner *et al.* (1970) suggested that the stagnation region extends laterally from 1.6 up to 3 diameters. This value is much higher than  $r/d=1.4$  as proposed by Beltaos and Rajaratnam (1977) and Giralt *et al.* (1977). In studies using water and FC-77, Womac *et al.* (1994) assumed that the impingement region extends to a distance of  $1.9d$ . The vast majority of literature covers stagnation pressure data for air jets while only limited data are available for other fluids, such as those for water by Zumbrunnen *et al.* (1989, 1990) and those of pressure fluctuations in water jets by Yokobori *et al.* (1979). For unsubmerged jets, Liu *et al.* (1991) found the stagnation region extended up to  $r/d=0.787$  while Stevens and Webb (1989) found the same region extended to  $r/d=0.75$ . In an unsubmerged jet, this region is characterised by both the hydrodynamic and thermal boundary layer both being of constant thickness. For  $r/d>0.75$  and for the case of  $Pr > 1$ , the hydrodynamic boundary layer reaches the free surface earlier than the thermal boundary layer. The latter is reversed for the case of  $Pr < 1$ .

Heat transfer in the immediate vicinity of the stagnation point is dominated by laminar flow characteristics. For highly viscous liquids, where nozzle exit velocities are usually in excess of 20m/s, the use of the adiabatic wall temperature can lead to a temperature difference of up to 3K relative to the nozzle exit temperature, Ma *et al.* (1997a). Differences in Nusselt number of up to 14% are likely. It appears that for  $Re$ 's greater than 1900 the effects are believed to become even more pronounced.

The subsequent transition to turbulent flow along the target surface is accompanied by a local peak of lateral Nusselt number. For submerged jets, Webb and Ma (1995) suggested the use of the following correlation for local heat transfer.

$$\text{Nu} / \text{Nu}_s = \left\{ \left[ \frac{\tanh^{0.5}(0.88(r/d))}{(r/d)^{0.5}} \right]^P + [1.69(r/d)^{-1.07}]^P \right\}^{1/P} \quad (2.7)$$

for  $0 < r/d < \infty$

The coefficient P was taken as  $P=-17$  by Sun *et al.* (1993) for water and collapses experimental data to within  $\pm 5\%$ . It can also be adopted for other liquids, such as R-113, transformer oil and ethylene glycol, Webb and Ma (1995).

Sun *et al.* (1998) presented the following correlation for unsubmerged jets of three liquids, namely R-113, Kerosene, transformer oil, as

$$\text{Nu} / \text{Nu}_s = 0.777(r/d)^{-0.5} \quad (2.8)$$

for  $1 < r/d < (0.177 \text{ Re})$

$$\text{Nu} / \text{Nu}_s = 1.85 \text{Re}^{-1/6} \left[ \frac{25.7}{\text{Re}} (r/d)^3 + 0.857 \right]^{-2/3} \quad (2.9)$$

for  $r/d > (0.177 \text{ Re})$

It has been generally accepted for air, water and FC-77 that for low nozzle-to-plate spacings ( $z/d \leq 3$ ) two peaks in radial Nu-number profiles are observed. The inner peak is attributed to a local thinning of the thermal boundary layer by impinging vortex structures. This peak was reported for air jets to occur in the region of  $0.5 < r/d < 0.8$ , Ball (1998), Gillespie *et al.* (1996) and Huber and Viskanta (1994). For dielectric liquid, FC-77, Garimella and Rice (1995) observed primary peaks at  $r/d=0.5$  when  $d \geq 3.18\text{mm}$ . With increasing distance from the nozzle it can be observed that the inner peak is shifted radially outwards until it finally vanishes at  $z/d \approx 4$ . Although the velocity profile at the nozzle exit was not measured, a fully developed velocity profile can be eliminated due to the use of a nozzle with a low aspect ratio ( $L/d$ ). The outer peak is attributed to a region of transition from laminar to turbulent flow at  $r/d=1.6$  to  $r/d=1.8$  and was observed to move radially outwards with increasing values of  $z/d$ , Huber and Viskanta (1994) and Gillespie *et al.* (1996) for air jets. However, in a recent study on round air jets, Ball (1998) found secondary peaks to move towards the stagnation point as  $z/d$  increases. The early transition with increasing  $z/d$  was attributed to increasing levels of axial turbulence.

For low nozzle-to-plate separations ( $z/d=2$ ), low levels of turbulence intensity were measured in the axial and radial region close to the stagnation region. At large nozzle-to-plate distances,  $z/d=6.5$ , the radial near wall turbulence was already high, suggesting that the flow undergoes transition from laminar to turbulent at low values of  $z/d$ . Maximum heat transfer occurred in close proximity to the stagnation point where the thermal boundary layer thickness was a minimum. Garimella and Rice (1995) conducted heat transfer measurements with FC-77 for similar nozzle-to-plate-spacings and showed that the outer peak moves radially outwards with increasing  $z/d$  which corroborated observations made for air by Huber and Viskanta (1994). However, no physical explanation for this occurrence was provided.

It has generally been accepted, that with increasing  $Re$  the stagnation point heat transfer coefficient increases while the secondary peak increases in magnitude and is shifted radially outwards, Lee and Lee (1998) for air and Sun *et al.* (1993) for water. For semi-confined jets, Lytle and Webb (1994) observed the same trend for air and Garimella and Rice (1995) for FC-77. In contrast to that, a monotonic decline of radial Nusselt-number was obtained for confined submerged jets of R-113 by Chang *et al.* (1995).

Figure 2.4 illustrates the non-dimensionalised Nusselt number of four fluids in the range of  $0.7 \leq Pr \leq 24$ . Data were extracted from studies that employed similar experimental boundary conditions and parameters. The graph allows qualitative and limited quantitative assessment of Prandtl number effects such as nozzle diameter and  $Re$  agree to within 38% and 19%, respectively. Filled symbols can be directly compared with each other in terms of  $Re$ . Equally shaped symbols denote equal nozzle diameters. However, to compare the four sets of data, a correction to account for low  $Re$  should be applied since secondary peaks are expected to increase with  $Re$ . Data of FC-77 and air were obtained for the same nozzle size whereas the  $Re$  differed by only 15%. Heat transfer of dielectric fluid decreases by approximately 15% within  $1d$  from the stagnation point. At a radial distance of  $r/d=1.5$  heat transfer levels off and passes through a local (=secondary) peak at  $r/d=2$ . Beyond this location the Nusselt number declines much more slowly. Unlike FC-77, jets of air and water give rise to a much more uniform heat transfer distribution in the region  $r/d \leq 1.5$ . Although the target plate was placed well within the potential core, the water jet only displays a slight tendency towards forming a secondary peak while the air jet produces a strict monotonic bell-shaped distribution.

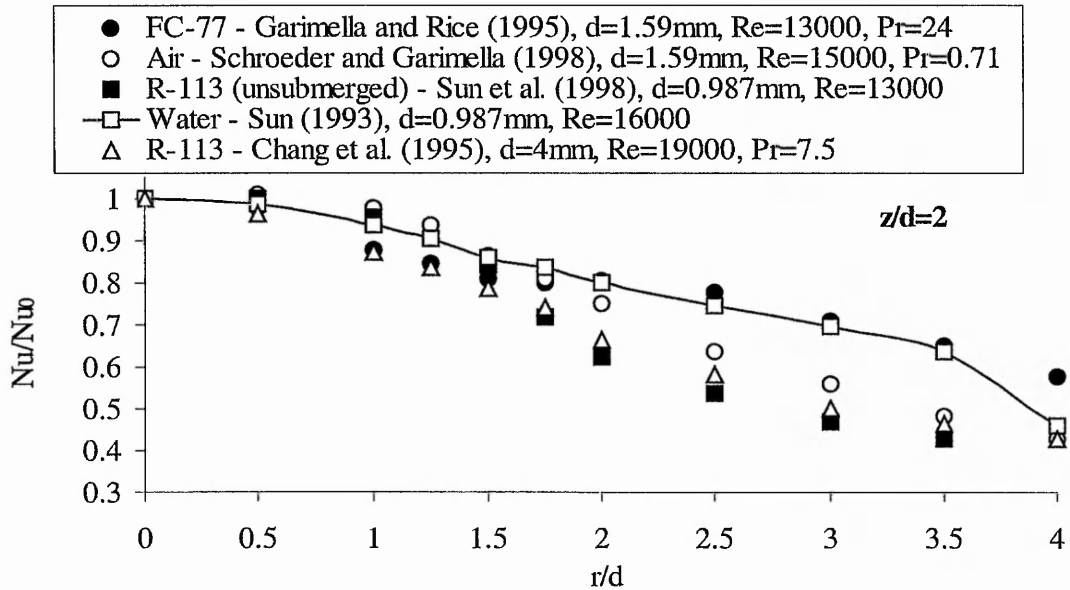


Figure 2.4. Non-dimensionalised Nusselt number distribution at  $z/d=2$ .

Higher average heat transfer rates for FC-77 over those for water were also reported by Womac *et al.* (1993). It is surprising to note that R-113 shows a much more pronounced decline of lateral Nusselt number distribution than water although their Prandtl numbers are almost identical. Reasons for this may originate from the thermal conductivity and specific heat capacity of R-113 being considerably lower than that of water. Data by Chang *et al.* (1995) for a submerged jet were plotted in the same graph and corroborate those of Sun *et al.* (1998). The two sets of data show clearly the same trend with submerged heat transfer data slightly exceeding those for unsubmerged conditions. This trend has also been observed for water by Womac *et al.* (1993). When comparing R-113 data to those of FC-77 the large difference in viscosity (factor 2.2) is likely to account for the two different shapes of radial heat transfer profiles. All other Prandtl-number quantities are identical to within 15%. For airflow with large nozzle diameters,  $d \geq 25$  mm, Ball *et al.* (1998) and Lee and Lee (1998) showed for  $Re > 10000$  the existence of secondary peaks at  $r/d \approx 1.6$ . The same  $Re$  was maintained in Schroeder and Garimella (1998) who reported secondary peaks for  $d = 6.35$  mm but a bell-shaped distribution at nozzle diameters of  $d = 1.59$  mm and  $3.18$  mm. This monotonic Nusselt number profile is in sharp contrast to those of FC-77 presented by Garimella and Rice (1995) who showed a flattening of the heat transfer profile for  $d \geq 3.18$  mm and secondary peaks for  $d \geq 1.59$  mm.

It was the nozzle diameter of  $d=0.79\text{mm}$  that delivered bell-shaped heat transfer profiles. It is therefore reasonable to conclude that the nozzle-diameter threshold for producing secondary peaks is smaller for FC-77 and water than for air.

For unsubmerged jet impingement heat transfer the nozzle diameter can have a significant impact for low Re. Womac *et al.* (1993) found effects of bulk warming of the thin fluid sheet and gravitational influences for small nozzle and large diameters, respectively. For a relatively small nozzle diameter ( $0.978\text{mm}$ ) free water and FC-77 data showed different but almost linear dependencies on Re. For nozzle diameters of  $0.978\text{mm}$  and  $1.59\text{mm}$ , FC-77 jets produced higher heater-average Nusselt numbers than comparable water jets. While the water data showed an almost linear dependency throughout the range of Re, FC-77 heat transfer data exhibited a large reduction with decreasing Re. Incropera and Ramadhyani (1994) attributed this effect to the hydrodynamic boundary layer at the stagnation point being of the same thickness as the film. For greater nozzle diameters ( $d>6.55\text{mm}$ ) the two data exhibit similar trends in that they show an almost constant Nu-number dependency for low Re-number while the slope gradually increases with rising Re. Incropera and Ramadhyani (1994) stated that large nozzle diameters in unsubmerged jets reduce the slope of the heat transfer curve under the action of gravity.

Lytle and Webb (1994) observed more pronounced peaks as Re was increased. Fitzgerald and Garimella (1998) noted for jets of FC-77 that the location of transition to turbulence and thus the location of secondary peaks moves radially outward for increasing  $z/d$ . An increase in nozzle-to-plate spacing was shown to increase axial turbulence and consequently stagnation point heat transfer. Simultaneously, radial turbulence intensities were reduced which smoothed the radial heat transfer distributions.

For water jets of Re's of 6500, Landreth and Adrian (1990) observed a boundary layer separation based on vertical flow reversal at  $r/d=1.6$ . Based on calculations of the displacement thickness secondary vortices are believed to detach regularly. The author pointed out that the velocity characteristics resemble those of Didden and Ho (1985), who found the onset of separation in a jet of higher Re to occur further upstream, at  $r/d=1.1$ .

In comprehensive studies, Wolf *et al.* (1995a, 1995b), Stevens *et al.* (1992) and Pan *et al.* (1992) investigated heat transfer characteristics of unsubmerged planar and unsubmerged round jets. Both studies carefully clarified the role of the hydrodynamic

flow field on the heat transfer characteristics. Stevens found only negligible dependency on turbulence levels of heat transfer coefficient although his paper concentrated on one fixed nozzle-to-plate spacing,  $z/d=1$ . By far the greatest influence on convective heat transfer is  $G$ , the stagnation point velocity gradient. One discrepancy with existing air jet data could, however, be identified. For a small separation distance ( $z/d=1$ ) the Nu-number distribution of Stevens's data showed no secondary peak in the transition region of the wall jet,  $1.25 \leq r/d \leq 2.5$ . The data exhibited, either for fully developed pipe flow or for the contoured nozzle, a clear peak of Nu-number at the edge of the jet, where the developing shear layer enhances mixing.

In one of the few comparative studies, Sun *et al.* (1998) presented Prandtl number effects on jet impingement heat transfer for unsubmerged jets. Three different liquids were used, covering a Prandtl number range of  $7.2 \leq Pr \leq 262$ . It has to be noted, however, that submerged jets may produce marginally higher heat transfer rates than unsubmerged jets depending on operating conditions, as shown for water by Womac *et al.* (1994). For unsubmerged jets of R-113, Kerosene and transformer oil, Sun *et al.* (1998) found no significant change in the shape of normalised Nusselt number profiles for  $7 \leq Pr \leq 262$ . The variation of the Nusselt number at the stagnation point, normalised to the maximum at  $z/d=2$ , was correlated to the nozzle-to-plate spacing by

$$Nu_s / Nu_{s,max} = e^{-0.0000789(z/d)^{1.85}} \quad (2.10)$$

It can be shown that data for unsubmerged water jets of previous works, Elison and Webb (1994) and Stevens and Webb (1991), can be correlated with this equation to within 5%. In one of the early papers, Metzger *et al.* (1974) compared free jets of water and oil and found no dependency on the nozzle-to-plate spacing of Nu-number.

In the generally accepted power-law dependence for the heat transfer coefficient at the stagnation point, heat transfer is generally expressed as

$$Nu_s = C Re^n Pr^m \quad (2.11)$$

where Sun *et al.* (1998), for  $7.2 \leq Pr \leq 262$ , proposed the exponent  $n$  to vary between 0.489 and 0.5,  $m$  between 0.329 and  $1/3$  while  $C$  was in the range between 1.25 and 1.38.

Sun and Ma (1998) proposed a correlation that made use of the reference-temperature method for a Prandtl number range of 0.7 to 348 to predict the local Nusselt number at the stagnation point as

$$\text{Nu}_{s,f} = 1.44 \text{Pr}_f^{0.342} \text{Re}_f^{0.476} \quad (2.12)$$

The concept of using the film temperature as reference temperature was also used by Leland and Pais (1999) who studied over a Prandtl number of 48 to 445 the heat transfer behaviour of an unspecified liquid. For correlating data over such a wide Prandtl number range, the use of the film temperature was critical in achieving a good fit of the data. The authors observed with increasing Prandtl number a converging Nusselt number. If the Prandtl number is sufficiently high a change in Re does not have any significant effects on the heat transfer rate.

The following correlation was suggested by Ma *et al.* (1990) for the case of the target plate being placed beyond the potential core.

$$h_{s,WP} / h_{s,bP} = \left[ \frac{C}{(z/d)} \right]^{0.5} \quad (2.13)$$

Significant heat transfer enhancement was observed, when the jet struck the impingement plate within the potential core length, Gardon and Akfirat (1965), Ma *et al.* (1990) and Sun *et al.* (1993). The non-dimensionalised potential core length C has been determined for water, R-113, kerosene and ethylene glycol. Values can be found elsewhere, Webb and Ma (1995). The data of kerosene, oil and ethylene glycol have been produced using the same rig. The large scatter in experimental parameters such as nozzle diameter and Re impedes the assessment of Prandtl number effects. Direct evaluation in terms of other fluids such as water, R-113 and FC-77 presents a difficult task. Since the length of the potential core is purely a function of nozzle exit conditions further work is necessary to clarify comprehensively the role of high Prandtl number fluids in high Re flows.

Hrycak *et al.* (1970) found the potential core for pipe-type nozzles ( $\text{Re}_{\text{exit}}=52000$ ) with  $l/d=1$  to extend from six to seven diameters. For orifices with  $l/d=1.5$  and  $\text{Re}=6900$ , Huber and Viskanta (1994) estimated the length of the potential core of circular air jets to be close to six diameters. For fully developed pipe flow,  $\text{Re}_{\text{exit}}=22500$  and  $l/d=40$ , Ashforth-Frost and Jambunathan (1994) determined the potential core lengths for the unconfined and the semi-confined jet to 4.8d and 5.8d, respectively. For fully developed water flow with  $l/d=35.5$ , this value was corroborated by Sun *et al.* (1993) who reported the optimum nozzle-to-plate spacing for jets of  $\text{Re}=6000$  to be about  $z/d=5.2$  while it steadily decreased to  $z/d=4.8$  at  $\text{Re}=20000$ . For water and FC-77 jets of larger nozzle diameters ( $d=4.42$  mm, 6.62 mm and 9.27 mm), Besserman *et al.* (1991a) reported

optimum nozzle-to-plate spacings of  $z/d \approx 3$ . The significantly shorter spacing might be attributed to the close proximity of the radial wall confinement and the annular collection of the spent fluid. Those effects are believed to enhance turbulent production and to reduce the length of the potential core. Besserman *et al.* (1992) conducted heat transfer measurements of water jets and found maximum values in the range of  $3 \leq z/d \leq 5$ . Garimella and Rice (1995) conducted FC-77 studies and observed an extending of the potential core length with increasing nozzle-to-plate spacing from  $z/d=4$  to 5 for  $d=1.59\text{mm}$  to  $d=3.18\text{mm}$ , respectively. Using R-113, Chang *et al.* (1995) suggested the length of the potential core to be between 5 and 7d. Ma *et al.* (1990) determined the potential core length of fully developed tube nozzles ( $Re < 750$ ) of transformer oil and ethylene glycol to be 8d.

In contrast to the aforementioned is the study by Filippov (1991) who conducted experiments with impinging jets of liquid nitrogen. For values of  $z/d > 1$  no significant enhancement of heat transfer was observed. Distances in the range of  $1/4 \leq z/d \leq 1$  produced heat fluxes proportional to the square root of  $z$  while spacings of  $z^* \leq z/d \leq 1/4$  enhanced the heat flux according to the power of  $1/4$  where  $z^*$  corresponds to the practical limit of the nozzle-to-plate spacing.

From experiments with geometrically similar nozzles of different diameters, Hollworth and Gero (1985) noted that the local Nusselt number was independent of  $d$  for a given  $z/d$ . Conversely, Besserman *et al.* (1991b) suggested for water and FC-77 that the Nu-number decreases with decreasing nozzle diameter while the contrary is the case for the heat transfer coefficient. These observations were corroborated by Womac *et al.* (1993) for the same liquids and were attributed to a decreasing thermal boundary layer thickness. Physical explanations were presented by Kataoka *et al.* (1987) who observed greater turbulence levels on the centreline of 28mm diameter water jets than in similar 14mm jets. However, it has to be stated that the use of converging nozzles with a constant inlet diameter resulted in a four-fold contraction ratio of the smaller nozzle over that of the bigger nozzle. Significant differences in the turbulence level at the nozzle exit were likely to affect the comparison. Measurements of the potential core lengths resulted in  $z/d=4.5d$ . For the flat unconfined and semi-confined air jet, Ashforth-Frost and Jambunathan (1994) determined the potential core lengths at  $Re_{\text{exit}}=22500$  to be 4.5d and 5.3d, respectively. This suggests that the length of the potential core depends primarily on the nozzle exit

conditions (velocity, nozzle diameter, temperature), the rate of entrainment and on the type of fluid used. To verify the latter further research attention is necessary.

In a study on conjugate heat transfer, Bula *et al.* (2000) studied heat transmitted through a solid body from discrete heat sources when cooled through an impinging oil jet on the opposite side. As the thickness of the disk was increased, the heat transfer coefficient showed a relative peak suggesting that there is an ideal disk thickness for best performance. Furthermore, it was found that a solid of lower thermal conductivity resulted in higher heat transfer coefficients than a target surface of higher thermal conductivity.

Heindel *et al.* (1992) performed measurements to assess the effects of an extended surface when exposed to an impinging FC-77 jet. A five-fold increase of the surface area resulted in more than a three-fold enhancement of heat transfer. In a study on surface roughness, Priedeman *et al.* (1994) found that liquids with higher Prandtl number are more prone to higher surface roughness due to the greater hydrodynamic boundary layer thickness. Increases in the heat transfer coefficient were attributed to surface modifications that thin the hydrodynamic boundary layer and, likewise, the thermal boundary layer. Heat transfer rates of water and FC-77 were enhanced by factors of 1.3 to 3 and 2.2 to nearly 5, respectively. While FC-77 flow is greatly affected through the large fins, a water jet is almost unaffected which is presumably due to the greater thickness of the FC-77 thermal boundary layer. Gabour and Lienhard (1994) investigated the effects of surface roughness on stagnation point heat transfer of an impinging unsubmerged water jet. With decreasing  $Re$  a thickening of the thermal boundary layer was observed which reduced the impact of surface roughness. Increases in the Nusselt number over that of a smooth surface were as large as 50% and corroborated findings of Priedemann *et al.* (1994). Hansen and Webb (1993) conducted similar measurements for air jets and found enhancement of heat transfer rates, as compared to the smooth surface, by a factor ranging from 1.5 to 4.5. However, it has to be noted that enhancement of air heat transfer was attributed to the interactions of 1) the level of turbulence, 2) the fluid velocity at the surface and 3) the ratio between exposed surface area and total area. This is in contrast to the mechanisms observed for water and FC-77 where a 'piercing' of the thermal boundary layer accounted for heat transfer augmentation. In a recent paper, Chakroun *et al.* (1998) corroborated the findings for an air jet by reporting that surface roughness had a strong effect on the flow characteristics such as the mean velocity and turbulence intensity.

For unsubmerged jets, knowledge of the liquid's surface tension is essential since fluid splashing away from the free surface has the effect of reducing heat transfer by up to 20%, Womac *et al.* (1993). In an analytical study Liu *et al.* (1993) modelled the unsubmerged inviscid velocity distribution for a range of Weber numbers. The Weber number characterises the inertial to surface forces:

$$We = \frac{\rho u^2 d}{\sigma} \quad (2.14)$$

A significant reduction of surface deflection was observed as Weber number decreased. The subsequent increase of the velocity gradient at the stagnation point led to an increase of Nusselt number by up to 13%. However, the author pointed out that with common water cooling applications Weber numbers are in the range of several hundred and its practical effects will therefore be negligible. Elison and Webb (1994) observed for low Weber numbers the diameter of the jet immediately after the nozzle exit to be larger than the internal nozzle diameter whereas for higher Weber numbers the jet diameter approached that of the inner diameter of the nozzle. The broadening of the jet for low Weber numbers under the action of surface tension accounted for a  $Nu \sim Re^{0.8}$  relationship observed for  $Re < 2000$ . To the authors knowledge no such work exists with fluids other than water. From Figure 2.5 it can be seen that for some gases the effects of surface tension might even be more pronounced.

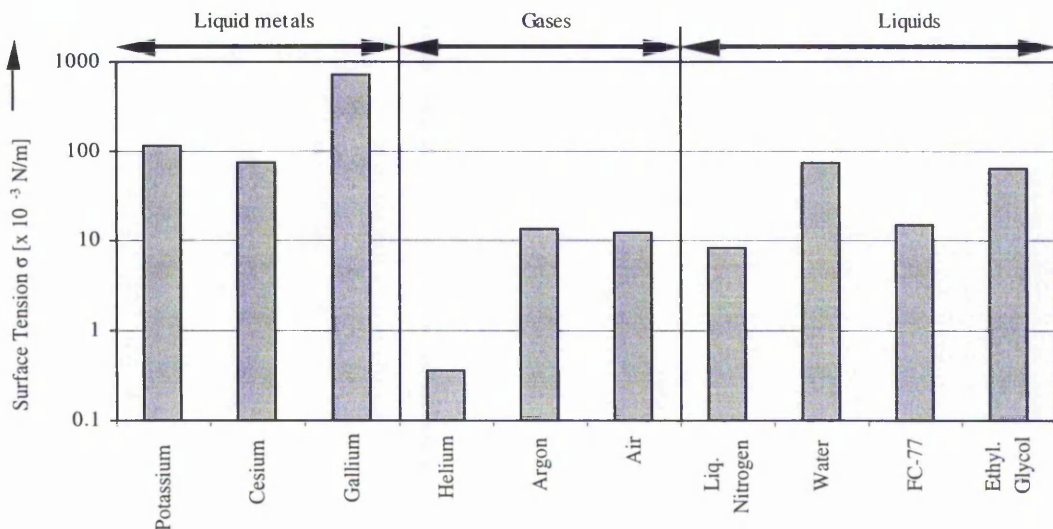


Figure 2.5. Surface tension of fluids for  $0.005 < Pr < 100$ .

Chamkha (1998) examined steady laminar forced convection flow at the stagnation point of an isothermal body. An almost linear increase of the temperature gradient was observed for  $Pr=0.1$  while with increasing Prandtl number the difference between wall and fluid became steeper close to the wall. The author observed a steeper temperature gradient near the wall for  $Pr=6.5$  than for  $Pr=0.7$ . Furthermore, it was obtained from the results that planar nozzles deliver more pronounced temperature gradients than round nozzles.

Sutera (1965) showed that with increasing Prandtl-number the thermal boundary layer thinned relative to the hydrodynamic boundary layer. The subsequent increase in heat transfer was then subject to increased perturbations caused by amplified free stream vortices. Surprisingly, with the Prandtl-number approaching infinity, the infinitesimally thin thermal boundary layer displays no significant effect on heat transfer, in fact, having vanished at a Prandtl-number of 100. Metzger *et al.* (1974) corroborated these findings by comparing the heat transfer data of water ( $Pr=3$ ) with those of synthetic oil ( $85 < Pr < 151$ ). In the generally accepted power-law dependence for the average heat transfer coefficient across the impingement surface, heat transfer is generally expressed as

$$\overline{Nu} = C Re^n Pr^m \quad (2.15)$$

where the authors proposed for the high Prandtl number fluid the exponents  $m$  and  $n$  to be 0.24 and 0.47, respectively. For the lower Prandtl number,  $m$  and  $n$  were suggested as 0.487 and 0.348.

Palmer (1993) conducted a theoretical study to compare the film heat transfer coefficient of water with those of Mercury, Gallium, Cesium, NaK Alloy, Rubidium and Potassium. For the computation of water, an empirical expression by McAdams (1954) for the average film heat transfer coefficient was used:

$$\overline{Nu} = 1.14 Re^{0.5} Pr^{0.4} \quad (2.16)$$

In order to use the same concept for liquid metals, an empirical correlation by Witte (1968) based on spheres in liquid Sodium was employed:

$$\overline{Nu} = \left( 2 + 0.386 Re^{0.6} Pr^{0.6} \right) \quad (2.17)$$

While the water and mercury showed quantitative resemblance at low nozzle exit velocities, (20m/s), liquid metal heat transfer rates exceeded those of water by a factor of up to 2.5 for exit velocities of 60m/s. Further computations showed that the highest heat transfer coefficients were provided by Gallium, followed by Potassium, Rubidium, NaK

Alloy, Cesium and Mercury. It is not surprising that from the point of pressure drop, however, Potassium would be the best selection since it has the lowest density.

Jiji and Dagan (1988) investigated FC-77 and water jets with particular focus on the cooling of electronic chips. A great influence of the heater dimensions was found on overall heat transfer data which lead him to use the geometric size of the heater as the characteristic length as opposed to the nozzle size. The authors proposed the use of  $m=0.4$  for submerged jets. Average heater surface data for a single unsubmerged jet were correlated using a Prandtl number exponent of  $1/3$ :

$$\overline{Nu}_{\text{heater size}} = Re^{0.5} Pr^{1/3} \left[ 3.84 \left( 0.008 \frac{L}{d} + 1 \right) \right] \quad (2.18)$$

Womac *et al.* (1993) compared heat transfer data of submerged and unsubmerged water and FC-77 jets with the correlations of Jiji and Dagan (1988) and Metzger *et al.* (1974). The authors showed that much better agreement is achieved when data for unsubmerged water and FC-77 jets are correlated using a Prandtl-number exponent of  $0.4$ . Further results indicate that FC-77 data generally show greater Nu-numbers than water.

A Prandtl number exponent of  $0.5$  should be used for low Prandtl-number fluids, see Liu *et al.* (1991). The author describes an enhancement in heat transfer for unsubmerged jets by surface waves. The use of a Prandtl-number exponent of  $m=0.4$  is suggested for  $0.157 < Pr < 3$  while  $m=0.33$  promises higher accuracies for  $Pr > 3$ . It can be seen from the literature, that the use of a Prandtl number exponent of  $0.4$  is widely used for jet impingement in literature when only one fluid is used. An exponent of  $0.42$ , as proposed by Martin (1977), is accepted for Prandtl-number fluids in the range of  $7 \leq Pr \leq 25$ . Besserman *et al.* (1991a) used an exponent of  $0.4$  but stated that better fit could be achieved with a larger exponent.

For air jets, Hrycak (1983) and Schroeder and Garimella, (1998) employed an exponent of  $0.4$ . Besserman (1991a) suggested a Prandtl-number exponent of  $0.4$  to collapse both water and FC-77 data since this provided the best fit to the mass transfer study by Sparrow *et al.* (1987). Both studies considered annular collection of the spent fluid. The power-law dependence for heat transfer correlations suggests that fluids with Prandtl number values close to unity display negligible changes with the exponent  $m$ . For the case of air, deviations for the range of  $0.33 < Pr < 0.5$  are less than  $4\%$  relative to  $Pr^{0.4}$ . When comparing the data of water and FC-77 to those of mass transfer of air jets, Besserman *et al.* (1991a) suggested the use of Prandtl-number exponents of  $0.4$  or larger. The choice of  $1/3$  or  $0.4$  as Prandtl number exponent for high Prandtl number fluids can account for differences of up to  $36\%$ .

The exponent of Prandtl-number in the heat transfer correlation drops with increasing Prandtl-number from 0.376 to 0.33, Ma *et al.* (1997b). It is therefore recommended to use values of  $m$  as close to  $1/3$  as possible for high Prandtl number fluids (Ma *et al.* (1997b)) while a value of  $m=0.5$  should lead to best results for gases and liquid metals. For the correlation of different fluids, Sun and Ma (1998) suggested a value of  $m$  equal to 0.342 whereas the  $Re$  exponent was chosen as 0.476. For unsubmerged jet configurations, Sun *et al.* (1998) verified the Prandtl number exponent of  $1/3$  as the most appropriate parameter to correlate wide Prandtl number liquids.

It can be concluded that the exponent of the Prandtl number might be dependent on the turbulence near the wall since the thermal boundary layer is very thin for large Prandtl number fluids, see Ruckenstein (1998). A tabulated overview of the exponents for Prandtl number and  $Re$  for the average Nusselt number is given in Table 2.3.

Recently, Li and Garimella (2001) correlated their heat transfer data over a wide range of  $Pr$  by using non-linear curve fits without constraining the exponents  $m$  and  $n$ . The large discrepancies with respect to the correlation proposed by Sun and Ma (1998) originate from the wider Reynolds number range,  $4000 \leq Re \leq 23,000$  compared to  $200 \leq Re \leq 1,000$  in the latter study.

| Pr exponent $m$ | Re exponent $n$   | Range of Pr                             | Author   |
|-----------------|-------------------|---|--|
| 0.5             | 0.5               | $Pr \ll 1$                              | Liu <i>et al.</i> (1991)                                       |
| 0.42            | 0.5               | $Pr=0.71$ or $Pr=7$                     | Martin (1977)  |
| 0.452           | 0.529             | $0.7 < Pr < 25.2$                       | Li and Garimella (2001)  |
| 0.4             | 0.55              | $Pr=25.2$                               | Garimella and Rice (1994)                                      |
| 0.4             | 0.518 and 0.687   | $Pr=0.71$                               | Schroeder and Garimella (1998)                                 |
| 0.4             | 0.5<br>0.5 or 0.8 | $0.7 < Pr < 25$<br>$7 \leq Pr \leq 25.$ | Besserman <i>et al.</i> (1991a)<br>Womac <i>et al.</i> (1993), |
| 0.342           | 0.476             | $0.7 < Pr < 348$                        | Sun and Ma (1998)  |
| 0.33            | 0.5               | $7 \leq Pr \leq 25.$                    | Jiji and Dagan (1988)  |
| 0.33            | 0.471 or 0.468    | $Pr \gg 1$ (oil)                        | Ma <i>et al.</i> (1997a)                                       |

Table 2.3. Range of Pr exponent as a function of fluid properties for  $\overline{Nu}$ .

### 2.6.3 Wall jet region III

It was at large radial distances from the stagnation point ( $r/d > 13.2$ ), where in an early experimental study, Metzger *et al.* (1974) noticed significant differences in average surface heat transfer behaviour of impinging unsubmerged oil and water jets. While oil results showed a monotonic decrease in heat transfer with increasing heater surface, contrary trends were observed for water results. Heat transfer for water exhibited a similar trend up to  $r/d = 13.2$  and increased at further distance from the stagnation point. The rise for the largest test surface was attributed to a transition from laminar to turbulent flow. Discrepancies were associated with different growth rates of the hydrodynamic and thermal boundary layer thickness and the change in liquid layer thickness. Unfortunately, no local heat transfer data were provided so that the clear identification of the location is obstructed. Interestingly, for a submerged water jet configuration, Sun *et al.* (1993) found at a radial distance of  $r/d = 3.5$  the lateral Nu-number profiles for  $Re > 1.6 \times 10^4$  meet, diverge again beyond this point and collapse beyond  $r/d > 8$ . A similar crossover phenomenon was observed by Garimella and Rice (1995) for FC-77 at  $r/d \approx 3$  and by Huber and Viskanta (1994) for air at  $r/d \approx 2$  to 2.5. The authors postulated this occurrence to an early transition from laminar to turbulent flow.

### 2.6.4 Turbulent Prandtl-number

In jet impingement heat transfer where the flow can be simplified assuming two-dimensionality the concept of the eddy diffusivity for momentum and eddy diffusivity for heat represents a reliable and inexpensive way of turbulent flow modelling. While eddy diffusivity for momentum is commonly evaluated using either a mixing-length model or the  $k-\epsilon$  model, the eddy diffusivity for heat is inferred using the turbulent Prandtl number concept. The turbulent Prandtl number relates variations of time averaged velocity and temperature across a shear flow. For commonly used fluids, such as air and water, the turbulent Prandtl number ( $Pr_t$ ) has been shown empirically to be 0.9, independent of velocity, Kays (1994). In contrast, fluids with a low molecular Prandtl number show a pronounced velocity dependence, Sheriff and O'Kane (1981). In an experimental study on liquid sodium Bremhorst and Krebs (1992) combined unsubmerged jet flow and existing pipe flow data to derive a simple relationship between  $Pr_t$  and eddy diffusivity of

heat. An increase of turbulent Prandtl number with decreasing velocity was noted. It can therefore be concluded that modelling of low Prandtl number fluids for low flow velocities or low diffusivities may not result in satisfactory predictions. Although convective effects are prominent in unsubmerged jet flows, not much literature appears to exist. In fully developed channel flow Kawamura *et al.* (1998), over a Prandtl number range between 0.025 and 5, supported the widely used practice to employ a constant turbulent Prandtl number in the calculation of heat transfer. This trend was found to be inapplicable for Prandtl numbers less than 0.1. Browne and Antonia (1983) presented data of turbulent Prandtl number obtained from a plane air jet. The results show increased levels of Reynolds stresses in the self-preservation region ( $x/d > 20$ ). Chua and Antonia (1990) measured Reynolds stress and heat flux in a round air jet. The self-preserving region was observed to occur earlier,  $x/d > 15$ . This was attributed to the laminar conditions at the jet exit. In a recent paper, Lemoine *et al.* (1999) presented a study using LDA and LIF to determine turbulent flow and temperature characteristics of a free round water jet. In the centreline region, the turbulent Prandtl number exhibited an almost constant value and decreased strongly in the shear layer region. As the distance from the nozzle exit increased the turbulent Prandtl number increased which was found to be in qualitative agreement with results by Chevray and Tutu (1978) and Reynolds (1976).

While  $Pr_t = 0.85$  has been found with sufficient reliability for  $y^+ > 30$  from the wall, only a few studies have been conducted to investigate turbulent Prandtl number in the viscous or transition sublayers. For the case of flow parallel to a smooth wall, Kuznetsov (1991) pointed out that the temperature distribution in turbulent boundary layers along the wall for air, water and transformer oil pass through a peak on approaching the wall. The distance of the peak from the wall reduces with increasing molecular Prandtl number. Chaotic molecular motion between turbulent vortices and ambient fluid reduces heat transfer in the viscous sublayer when the ratios  $\nu/Pr$  and  $\nu_t/Pr_t$  are similar. Further data on turbulent boundary layers can be found in Kays (1994).

## **2.7 Experimental techniques for heat transfer testing**

Only a few papers exist that take into account lateral conduction when obtaining the heat transfer coefficient for transient heat conduction through a solid. Valencia *et al.* (1995) studied

the effects of lateral conduction on heat transfer coefficient using liquid crystal thermography (LCT). For flow in a rectangular channel, where longitudinal vortices generated highly non-uniform heat transfer distributions, three types of measurement methods were considered. Results showed that neglecting lateral conduction can lead to uncertainties of more than 100% for the constant wall heat flux boundary condition whereas the errors for the non-steady thin and thick wall technique are approximately 10% and 20%, respectively.

To overcome the problem of lateral conduction, Vedula *et al.* (1988) suggested the use of anisotropic materials with reduced thermal conductivity relative to the conductivity normal to the target surface. For a heat transfer coefficient of  $400 \text{ Wm}^{-2}\text{K}^{-1}$  numerical solutions in the form of a two-dimensional finite element method were presented that corroborated the accuracy of the exact one-dimensional analytical solution. However, no uncertainty analysis was presented.

In a study on the effects of thermal boundary conditions on heat transfer in an incompressible boundary layer, Taylor *et al.* (1989) pointed out that for air flows at 67m/s a measurable difference exists between total, recovery and static temperature. For high Re's the constant wall heat flux data are 4% to 5% greater than comparable constant wall temperature data. At the boundary layer origin, deviations between the two boundary conditions rose up to 15%. For flows in a turbine blade cooling passage where the heat transfer profile is highly non-uniform and periodic, Chyu *et al.* (1998) compared different methods of evaluating and choosing the appropriate reference temperature. Based on the assumption of invariant local heat flux, the use of the bulk mean temperature as reference temperature rather than the inlet temperature yielded the most accurate results. It is interesting to note that the choice of the reference temperature may account for differences in the heat transfer coefficient of up to 40%.

The vast majority of heat transfer data in liquid jet impingement has been acquired using constant heat flux boundary conditions. With regard to the practical application of liquid jets for cooling of electronic components, this is clearly justified and corresponds to the most realistic simulation of the boundary conditions. There are, however, cases where the transient temperature distribution of a relatively thick impingement plate provides better information than those of comparable steady-state methods. To study the importance of surface motion on the heat transfer beneath a planar jet of water, such as in the hot rolling process of steel strips, Zumbrennen *et al.* (1990) employed a transient two-dimensional method based on a two-dimensional finite difference technique. Heat transfer coefficients in excess of  $25000 \text{ W}/(\text{m}^2\text{K})$  were reported during the initial 12 seconds of a test-run. Using the sequential perturbation

method uncertainties of up to 27% were reported.

A few papers exist that report on the use of the one-dimensional transient heat conduction equation for fluids other than air, such as R-12 by Yan *et al.* (1995), diesel spray by Arcoumanis and Chang (1993) and water by Arjocu and Liburdy (1997). Yan and co-authors studied condensing heat transfer coefficients in a glass tube and justified the one-dimensional character of the problem by referring to a work by Dunne (1983) who has shown that materials with small penetration depths have small lateral conduction.

Arcoumanis and Chang (1993) conducted transient heat transfer measurements between a heated plate and an impinging diesel spray. For short test intervals (<1s) heat transfer rates were inferred from the one-dimensional transient heat conduction equation. This assumption was justified as the temperature gradient normal to the surface was found to be much larger than the lateral one.

Von Wolfersdorf *et al.* (1993) presented a hybrid transient step-heating technique that employed a surface heater and liquid crystal thermography. The most striking feature of this method is the fact that the local surface heat flux and the measurement of surface temperatures were eliminated by providing an additional heat flux using a thin surface heater. Nonuniform heating caused by the likelihood of varying foil thickness of the heater is allowed. Liquid crystals are only used to mark the onset of a chosen temperature (colour).

Arjocu and Liburdy (1997) employed the transient step-heating technique to study heat transfer of impinging liquid water jets. Since the nozzle exit Re was between 300 and 1500, the heat transfer coefficient was less than  $1200 \text{ W}/(\text{m}^2\text{K})$ .

Perera and Baughn (1994) measured variations of the local heat transfer coefficient for sharp edged spirally fluted tubes using the transient heat conduction technique. At the crest and the valley of the flutes, the authors found the effective thickness to be smaller than the penetration depth, which lead them to apply an iterative correction procedure based on a two-dimensional energy balance on a circumferential section of the duct.

## **2.8 Conclusions**

The effects of Prandtl number on fluid flow and heat transfer in general engineering applications and, in particular, in jet impingement have been reviewed. In flow situations, such as heat exchangers or pipe flow, effects of increasing Prandtl number range from higher friction factors over a more stabilised flow to a delay of transition from

laminar to turbulent flow. For jet impingement heat transfer it was revealed that existing literature requires separate consideration of the Prandtl number quantities ( $\nu/\alpha$ -phenomena) in order to clearly identify Prandtl number effects. Although fluids can have almost identical Prandtl numbers (i.e. water and R-113) they can differ significantly in their individual heat transfer characteristics. To relate heat transfer unambiguously to Prandtl number regardless of the relative magnitudes of viscosity in comparison with thermal conductivity, further research effort is needed. To date, numerical models have not been developed that can predict these complex flows with confidence. One way of isolating these properties, and allowing experimental investigations with known uncertainties, can be accomplished by conducting tests using glycerol-water solutions of different concentrations. Thus, a wide range of Prandtl number can be studied while the basic characteristics of the fluid are maintained.

The present review revealed that viscosity has a great effect on the formation of vortex structures, on the sensitivity to turbulence and on the near wall flow characteristics. Recent studies in the free jet region have shown that the behaviour of scalar quantities (i.e. temperature and concentration) in a jet depend strongly on Prandtl number while vector fields (velocity) display almost no dependency on the type of fluid. In addition, the spreading angle of the issuing jet appears to be unaffected by Prandtl number, while reports on the effects of entrainment are somewhat contradictory for fluids of different Prandtl number and need further clarification.

In the stagnation region, where turbulent stresses appear to display the same trend throughout a vast Prandtl number range, heat transfer can be altered significantly by stretching stream lines which are yet again under the influence of viscosity. However, more research effort is needed to further enhance the understanding of the mechanisms that dominate the viscous boundary layer and the stagnation point heat transfer.

When comparing local heat transfer profiles, it becomes obvious that fluids of different Prandtl numbers exhibit different boundary layer mechanisms. This might explain why air with a low Prandtl number exhibits a bell-shaped local heat transfer profile when almost all liquids reviewed displayed a non-monotonic shape of the radial heat transfer curve.

A great effect of Prandtl number on heat transfer is noticeable for roughened target surfaces since the thermal boundary layer is being thinned thus allowing smaller distances for the energy to reach free stream conditions. It would be interesting to know, whether

this 'piercing'-effect may also be encountered for higher Prandtl numbers than that of FC-77.

Practically no research attention has been given to the effects of Prandtl number on surface tension and subsequently on the effects of Weber number on heat transfer. As to the use of the Prandtl number exponent  $m$ , it is well established that a value of  $m < 0.4$  should be used when relating high Prandtl number fluids while liquid metals and gases are best correlated when  $m$  assumes a value of  $0.4 \leq m \leq 0.5$ .

This literature review has identified two main areas of the Prandtl number range that have received the vast majority of research attention. Air, for more than a century, has been traditionally used as working fluid in industrial applications as it is easy to use and, to date, achieved the required cooling effect. With the ever increasing demands for dissipating higher heat fluxes, however, designers have turned their efforts more towards exploiting the better thermal characteristics of liquids. Despite the advances in measurement technology, it could take another decade until liquids have been sufficiently investigated. To provide reliable data more rapidly existing correlations that have been originally derived with air as the working fluid need to be validated for the use of liquids. In a comparison of the hydrodynamic flow fields of air and water, differences and similarities in the flow mechanisms could be identified which would help to increase the physical understanding of these two most commonly used fluids. This would then allow the use of the air related data to investigate further the higher region of the Prandtl number range where liquids differ in their Prandtl number by up to three orders of magnitude.

## **Chapter 3**

### **Experimental investigation**

#### **Introduction**

This Chapter describes the experimental facilities and procedures developed for the practical part of this investigation. This comprises the design, development and validation of the water tunnel, the procedure for the flow visualisation, laser-Doppler anemometry (LDA) and heat transfer testing using liquid crystal thermography. The corresponding calibration and validation procedures are described in further detail. Uncertainty analysis was adopted in the early part of the design process and was used throughout the entire experimental stage to identify sources of uncertainty and to reduce their propagation into the experimental results. Levels of uncertainties associated with the experimental boundary conditions, laser-Doppler anemometry and the calibration routines are quantified and discussed.

#### **3.1 Design process**

The study of heat transfer characteristics of impinging jets over a wide range of Prandtl number required the design of an experimental facility capable of accommodating gases and liquids of different density and viscosity. The design, development and commissioning of a liquid jet impingement test facility formed the major part of the initial stage of the project. The rig had to provide the means to allow flow visualisation studies and to facilitate velocity and heat transfer measurements beneath an isothermal/non-isothermal impinging jet on a flat surface. This section describes the subsequent design process and the test facility and gives further details on the selection of the most important design parameters. During the planning phase, the works by Coleman and Steele (1989), George (1988) and George and Taulbee (1992) were found particularly useful.

In order to ensure industrially relevant flow conditions, the Reynolds number was maintained at a constant value of 2,000, 10,000 and 20,000, based on the nozzle exit conditions:

$$\text{Re} = \frac{U d}{\nu} \quad (3.1)$$

According to the literature review in Chapter 2, the jet configuration of the greatest research interest was identified to be that of a semi-confined and submerged jet. As one of the most important design parameters, the nozzle diameter determines effectively the overall magnitude of the heat transfer coefficient. For a fixed Reynolds number, Besserman *et al.* (1991a) attributed the increase of the average Nusselt number for decreasing nozzle diameters to an increase of the mean velocity at the nozzle exit. As a consequence, the thermal boundary layer in the stagnation-point region thins which reduces the heat transfer resistance. In contrast, Garimella and Nenaydykh (1996) found increasing Nusselt numbers for increasing nozzle diameters and related this effect to an increased level of turbulence for large nozzle diameters. In order to eliminate this discrepancy for estimating the maximum heat transfer coefficient in the present study, a correlation for an impinging water jet proposed by Sun *et al.* (1993) was applied. However, as the nozzle diameter in the present study is significantly larger than that used for deriving the correlation ( $d=1\text{mm}$ ) an alternative work by Yokobori *et al.* (1979) was considered which employed a 40mm round nozzle. Both correlations yielded a heat transfer coefficient of approximately  $3800 \text{ W}/(\text{m}^2\text{K})$ . Discrepancies between the two correlations were less than 4.6%.

For a fixed Reynolds number, the nozzle exit velocity increases with increasing viscosity. With increasing Prandtl number, which is a strong function of viscosity, the nozzle exit velocity would soon become impractical, particularly for the case of liquid jets. A large nozzle diameter allows better spatial resolution for velocity and heat transfer measurements, a circumstance that is particularly important in regions of large velocity and temperature gradients. Low nozzle exit velocities allow a greater Prandtl number range to be covered, especially towards higher Prandtl number fluids. An uncertainty analysis for the experimental technique used in this study (see Chapter 3.5.1.2) revealed that low heat transfer coefficients obtained with large nozzle diameters, were accompanied by low levels of uncertainties. On the other hand, in favour of a small nozzle diameter is the smaller physical size of the test section which would allow greater radial distances to be observed. This would also mean that the wall thickness of the enclosing window of the test section could be thinner thereby reducing the distortion of

the laser beams for LDA measurements. Smaller rig dimensions would lead to a higher average velocity within the rig which in turn reduces the risk of trapped air in the turbulence management section and produces a stronger LDA-signal.

The relatively low uncertainties in the heat transfer measurements for large nozzle diameters and the fact that a greater spatial resolution can be obtained, led to the choice of a nozzle diameter of 0.035m for the impinging jet. The mutual dependency of the decisive experimental parameters can be seen from Figure 3.1.

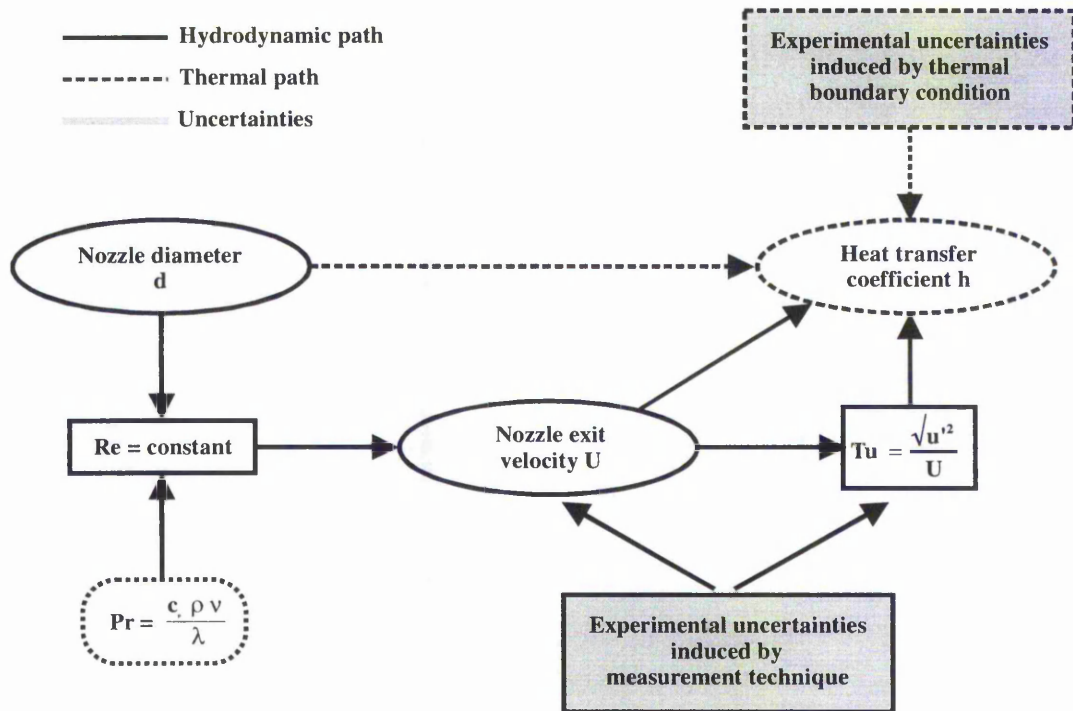


Figure 3.1. Mutual interactions of experimental parameters.

The arrangement of the jet in a horizontal or vertical orientation is not of significant importance for the overall hydrodynamic and thermal performance of the jet since the liquid is injected into the same liquid (submerged configuration) so that no shear is generated and gravitational effects are unimportant, see Webb and Ma (1995). The lower height difference inherent to the horizontal arrangement enables the driving pump to provide a greater pressure potential than the comparable vertical orientation so that, for future studies, a larger Prandtl number range may be covered. Furthermore, the horizontal arrangement ensures easy optical access to the rearside of the impingement surface where the response of the surface mounted liquid crystals was to be observed.

One disadvantage of this arrangement was that evacuation (deaeration) of the flow system becomes more important and has to be carefully maintained at the highest points of the pipe system. The facility and all its components were designed using a fully parametric three-dimensional CAD-package (Pro-Engineer<sup>®</sup>). This allowed a number of different sizes of the test section and the turbulent management section to be evaluated in order to achieve the optimum design. Design drawings and a full list of the rig components can be found in Appendix A.

## **3.2 Jet flow facility**

### **3.2.1 Introduction**

The study of impinging liquid jet heat transfer is dependent upon the development of a water tunnel facility that provides the test section with a steady, non-pulsatile, low turbulent flow of constant temperature and velocity profile. The requirement that any such design should also be able to produce flows of different Reynolds numbers over a range of Prandtl-number makes the design process a difficult one.

There has been considerable research attention to the design of wind tunnels, Mehta (1977), Rae and Pope (1984) and Boyle and Knaub (1988) and turbulence management, Wigeland *et al.* (1978) and Loehrke and Nagib (1976). In contrast, there is a paucity of information on the design of water tunnels and associated flow straightening elements. In the past, recirculating water tunnels were often designed to study boundary layer transition phenomena or cavitation problems, see Ripken (1951) and Domholdt and Moszynski (1964). In a study on the calibration of a hot-film anemometer, Persen and SaeTRAN (1983) described a water tunnel that was operated as a wind tunnel and consequently can be used likewise for such investigations. There exist only a few early papers, that have addressed turbulence management in water tunnels. Robbins (1978) measured the turbulence levels behind a honeycomb and found the turbulence level decreased by up to 48%. In an analysis on the effects of a honeycomb on the turbulence level in a turbulent stream, Lumley and McMahon (1967) condemn the use of screens in water tunnels due to their tendency to “sing”. This singing-effect is caused by operating the screen in the Reynolds number range where vortex shedding occurs. This is in

contrast to the study by Loehrke and Nagib (1976) who suggest that minimum free-stream turbulence levels in air and water flows are achieved by combining honeycomb and screens with the first screen positioned near the downstream end of the honeycomb.

It was only recently that the research community started to appreciate the tremendous usefulness of water channels for the field of hydroacoustics and dynamic stability problems of cylindrical bodies. This is partially due to the excellent visualisation capabilities of water tunnels and the significantly lower dynamic loads exerted on the models. Vogt (1983) described the use of a gravity fed water tunnel to investigate missile stability problems related to unpredicted normal forces and pitching moments. Wetzel and Arndt (1994a) conducted a comprehensive hydrodynamic design study for the evaluation and optimisation of large scale hydroacoustic test facilities. Consideration was given to the design of the contraction section, test section and the turbulence management. The remaining critical components such as the diffuser and turning vanes with their impact on pump flow characteristics was outlined in an accompanying paper, Wetzel and Arndt (1994b). It was only recently, after the design process of the present study had been completed, that Tam and Ghajar (1998) presented the description of a water tunnel that allowed the Reynolds number to be varied from about 280 to 49000 and the Prandtl-number to be varied from 4 to 158.

For the characterisation of a turbulent flow field inside a round confined jet tank, Law *et al.* (1999) suggested that the integral turbulent length scale is proportional to the tank diameter in the region away from the air-water interface. In the same study, the authors evaluated the effects of a shear-free air-water interface on the flow field of a submerged water jet and found that the bulk flow behaviour is only affected at a distance of about  $0.1d$  from the interface.

### 3.2.2 Description of the Water tunnel

The experimental facility consists of a closed recirculating flow loop with a free surface formed in the test region. The main components comprise the main water tank, a centrifugal pump, a filter, a diffuser, the flow straightening section, the nozzle section, the test section, the drainage system and various valves and pipe fittings. The pipe fittings, with exception of the valves and the contraction, were made of PVC-U, specified as Class E. A schematic

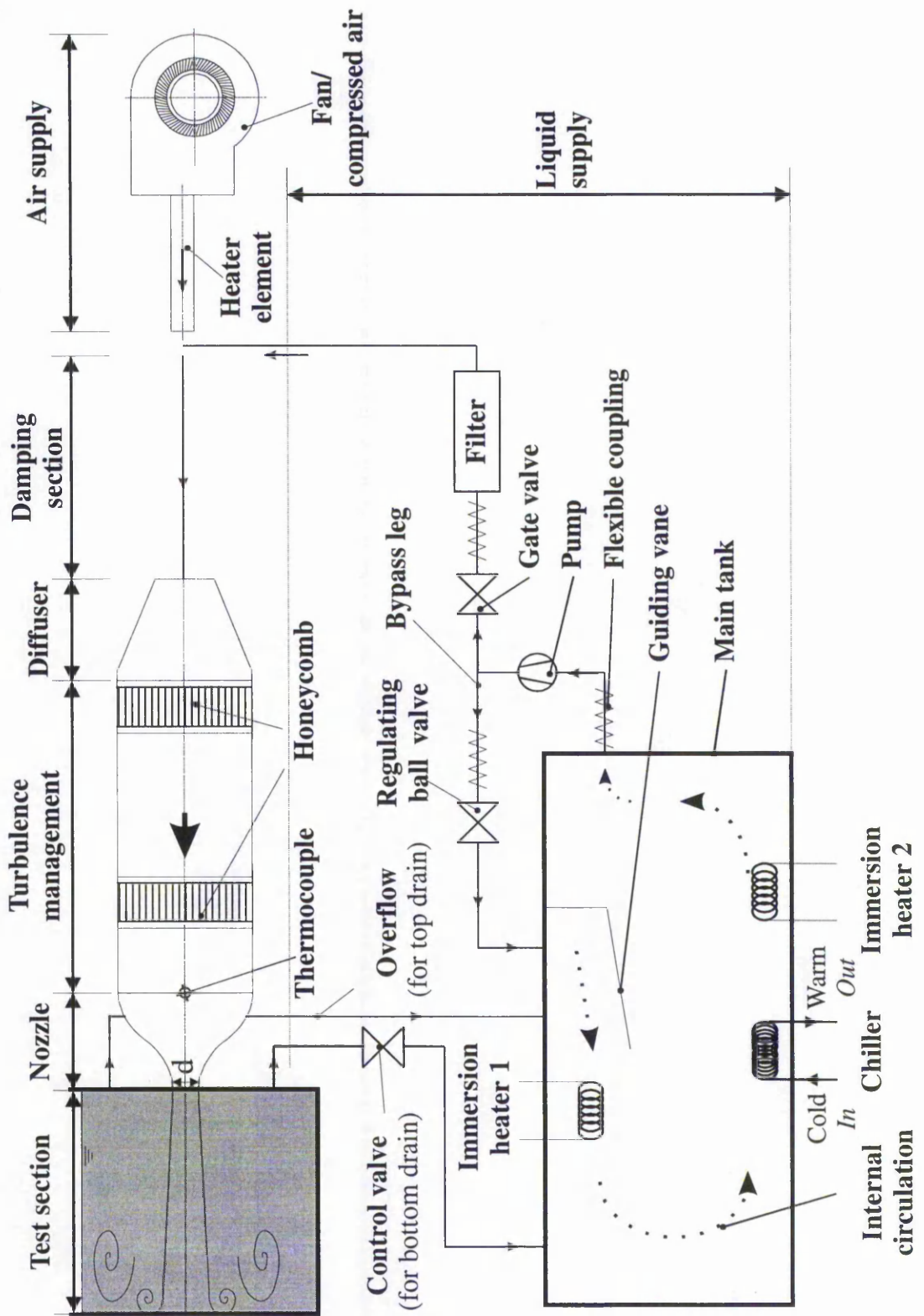


Figure 3.2. Schematic of the test facility.

diagram of the test rig, drawings and a list of suppliers is provided in Figure 3.2. The water tunnel is operated in one of two modes:

1. During *heating* of liquid in the main tank, the pump delivers the flow through a bypass leg straight back into the tank. Through the use of guiding vanes the oncoming flow induces strong vortices in the tank which enhances mixing and reduces the likelihood of temperature gradients.
2. For a *test run* the gate valve is partially opened to pass flow through the main loop into the test section.

The working liquid is stored in a galvanised steel tank with an overall capacity of 270 litres. The internal walls of the tank were covered with a 0.5mm thick PVC foil (pond liner) to maintain a high level of liquid purity throughout the experiments. The main tank was placed on a welded frame. The relatively low position of the centrifugal pump with respect to the liquid level in the water tank reduced the likelihood of cavitation in the suction pipe and eliminated the need for priming the pump prior to each test run. The stainless steel centrifugal pump, model CEA 70/3, supplied by Goulds Pumps Ltd, Ferrybridge, England, was driven by a direct drive motor and had a maximum flow rate of 80 l/min at a head of 14.5m.

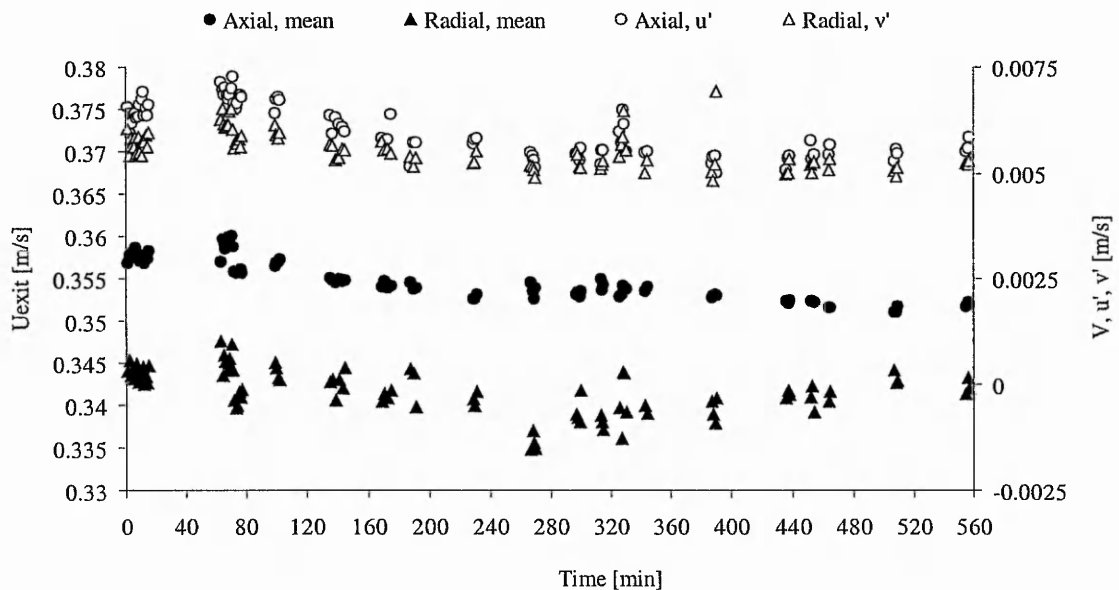


Figure 3.3. Stability of water tunnel.

The pump produced a steady stream which was regulated through a ¼-turn ball valve. Confidence in the stability of the water flow was ascertained from readings of velocity and turbulence at the nozzle exit over a continuous eight hours operating interval. After an initial warm-up period of one hour, measurements were taken using laser-Doppler anemometry. Data from one typical run over a nine hour interval at  $Re=10,000$  are presented in Figure 3.3. The centreline velocity and the axial turbulence were steady to within  $\pm 1\%$  and 7%, respectively. The effects of these variations were reduced by measuring the axial velocity prior to, and after visiting, each measurement region.

To minimise vibrations imposed by the pump it was connected to the rig by means of a flexible coupling and via rubber dampers. Further flexible couplings were installed in the bypass leg and upstream to the filter unit to avoid external forcing frequencies from the pump. Depending on the working mode of the water tunnel, the flow was either carried back to the main tank or directed through a cartridge filter. The filter was fitted with a 100 $\mu$ m PURTEX™ cartridge, delivered by Countywater Softeners Ltd, Wolverhampton, England. Upon leaving the filter the flow passed through two 90°-elbow pipes so that further turbulence damping measures were necessary.

To damp self-induced swirling motion by the fan/pump, a straight pipe of 14 diameters in length was incorporated, according to BS1042:1964. The velocity profile at the pipe exit could be assumed symmetric and fully developed which met an important requirement for the flow condition at the inlet of a diffuser, Mehta (1977). The diffuser section, immediately downstream of the damping section, had an expansion angle of 8° so that the losses were kept to a minimum, White (1979). For the given diffuser area ratio of four this value represented a trade-off between a long diffuser where a thickening of the boundary layer is liable to flow separation and a short diffuser resembling a sudden expansion which leads inevitably to flow separation while introducing high losses.

In the further course of the turbulence management section the flow was straightened by means of a tandem honeycomb design as suggested by Wetzal and Arndt (1994a). The tendency of screens to “sing” in water tunnels eliminated this option in an early stage from further consideration. Honeycombs reduce the turbulence intensity level in water tunnels significantly, Robbins (1978), by breaking up the incoming turbulent motion in the individual cells into flow that is characterised by much smaller longitudinal length scales. After considerable analysis, the first flow manipulator in the calming section was

selected to be formed of tightly packed plastic drinking straws. Friction between straws and the Plexiglas wall held the matrix in place. This low-cost alternative was first proposed by Lumley and McMahon (1967). The solidity  $\sigma$ , defined as the ratio between the solid area to the total area, of the device was inferred to be 0.11. The downstream honeycomb in the calming section was made of aluminium and had a cell diameter of 0.005m and a length of 0.040m. The subsequent overall turbulence reduction justified the increase in pressure drop across the combined manipulator.

At the exit of the turbulence management section the flow diameter was reduced to the effective nozzle diameter using a bell-shaped contraction section. Since the nozzle shape is an important parameter when considering the resulting turbulence level, particularly in respect to the length of the potential core, see Ashforth-Frost and Jambunathan (1994), care was taken in selecting the nozzle section. For a contraction ratio of 2, three different contraction profiles were compared:

- 1.) Optimisation of streamline curvature, Button and Tura (1984).
- 2.) A profile shape proposed by Wille (1963).
- 3.) Design by the author based on a cubic polynomial approach, Own\_2.

Figure 3.4 depicts the profiles of the three considered contoured-nozzle designs. Based on a finite element analysis, the design of Button and Tura (1984) was selected as the most appropriate. The profile co-ordinates are given in Appendix A.

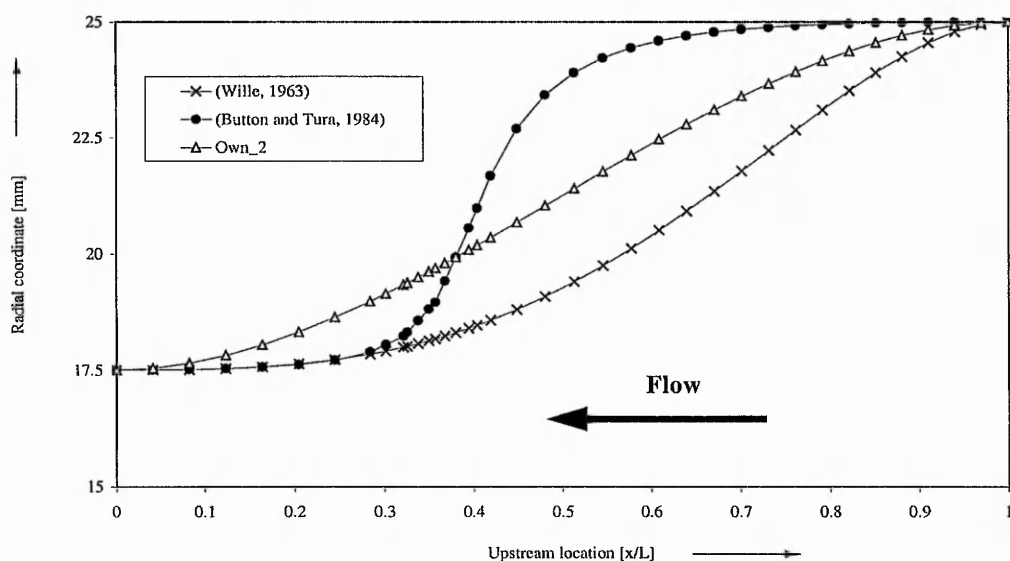


Figure 3.4. Shapes of contoured nozzles.

The nozzle contraction was cast in glass fibre from a wooden mould. To manufacture the mould, a piece of beech was roughly cut to size and machined on a numerical controlled (NC) lathe to achieve high accuracy. The required NC-code was written and tested prior to machining. After finishing the surface with fine sandpaper, it was coated in a thin layer of wood filler, dried and polished. This process was repeated until the effects of surface roughness were eliminated. The accuracy of the manufactured mould was checked using a Shadowgraph and yielded an error of less than 0.9%.

Downstream of the nozzle the flow enters into the test section with the dimensions  $height=14.3d$ ,  $width=8.5d$  and  $length=8.5d$ . The test section is made of 20mm-acrylic sheets and has a base area of 0.3m x 0.3m. This places the centre of the nozzle 4.3 diameters away from the lateral walls and enables nozzle-to-plate spacings,  $z/d$ , of up to 8.5 to be studied. The tank had a height of 500 mm. After impingement onto a flat plate the flow is discharged through four outlets in the semi-confining plate and is controlled through a ball valve to maintain the liquid level in the test section constant. This ensures that during all experiments the nozzle centre is placed 7 diameters from the free surface and the bottom of the test section, respectively. All walls of the test section and most of the pipes of the turbulence management section are made of transparent Perspex to allow direct optical access for flow visualisation studies, LDA measurements and to check for trapped air. A photograph of the experimental test facility is provided in Figure 3.5.

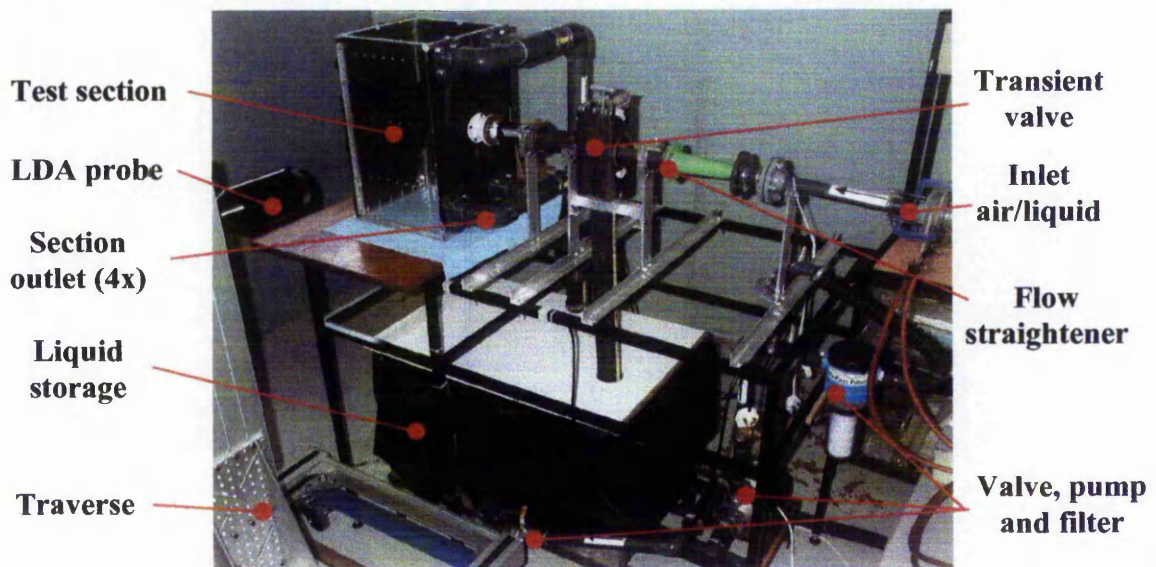


Figure 3.5. Photograph of the water tunnel.

Heating of the liquid in the main tank was accomplished using two immersion heaters, each having a power output of 3kW. The temperature was controlled via an integrated thermostat to within  $\pm 0.5^\circ\text{C}$  and was monitored by thermocouples positioned in the main tank and at entry to the test section. For measurements at room temperature, a 3kW stainless steel heat exchanger was immersed in the main water tank to compensate for the liquid temperature rise induced by the centrifugal pump.

The volume flow rate was metered according to the quantity metering method, as suggested by Goldstein (1996). A calibrated volume of the test tank was filled while the elapsed time was taken. The advantages of this method over the usage of a rated metering technique, such as a Venturi tube, are twofold. Since the measurement volume is placed inside the test section, the need of any additional flow straightening sections upstream and downstream of the flow meter is eliminated, thus reducing the overall pressure drop. This technique offers great repeatability and reliability. An uncertainty analysis yielded uncertainties of 3.5% which is only slightly higher than those of a Venturi tube for a Reynolds number of 20,000 and water as the working fluid.

The most suitable type of water among tap water, soft water, rain water and distilled water in terms of transparency, purity and dissolved air was identified in a trial-and-error analysis. These criteria are vital for the quality of the subsequent flow visualisation studies and laser-Doppler anemometry (LDA) measurements. Results show that tap water, despite a pronounced ageing process after a few weeks of use, was best suited for flow visualisation studies and also delivered the best LDA-signal. Consequently, the water in the main tank was changed every two weeks to eliminate unwanted particles in the water. To reduce the growth of bacteria, bleach was added to the water. This had the additional benefit of improving the seeding characteristics of the water during the LDA tests.

### **3.2.3 Description of the Wind tunnel**

The experimental test facility had been designed to allow fluids of different Prandtl numbers to be investigated. In order to accommodate air as the working fluid, the test facility could be modified by simply attaching the outlet pipe of the air supply to the inlet pipe of the turbulence management section, as can be seen in Figure 3.2.

For the measurement of the velocity field, and for the heat transfer experiments, it was initially intended to use a central compressed air supply. However, when monitoring the velocity at the nozzle exit over a long period of time, there appeared to be a cyclic nature to the flow which resulted in mean velocity fluctuations of up to 15%. This was unacceptable for the velocity measurements but was deemed sufficient for the heat transfer measurements where the focus was placed on a mere qualitative investigation.

Consequently, for the velocity field investigation over the wide range of Reynolds numbers under investigation (2,000, 10,000 and 20,000 respectively) air blowers were used. Details of the air blowers are given in Table 3.1. The quantities of the mean velocity and turbulence intensity represent average values across the diameter of the nozzle exit. Plots of the velocity profiles are presented in Chapter 5 to demonstrate how fluids of different Prandtl numbers are affected when passing through identical flow straightening sections.

| Re     | Manufacturer                    | Mean velocity, $U_{exit}$ | Tu on jet centreline |
|--------|---------------------------------|---------------------------|----------------------|
| 2,000  | Innovative Industrial Col, Ltd. | 0.9 m/s                   | 3.8 %                |
| 10,000 | Air flow Developments Ltd.      | 4.5 m/s                   | 1.5 %                |
| 20,000 | TecQuipment Ltd.                | 8.9 m/s                   | 2.7 %                |

Table 3.1. Characteristics of the air blowers during flow field tests.

The stability of the low Re flow was ascertained from readings over a six hour interval. It can be seen from Figure 3.6 that variations in the centreline velocity and the streamwise turbulence were limited to 2% and 8%, respectively.

For the heat transfer measurements, heating of the flow was accomplished by passing compressed air through a hot air heating element, manufactured by Hawco Ltd, Guildford, England. The required jet temperature was input at the integrated controller and could be maintained to within  $\pm 0.2^\circ\text{C}$ .

Prior to any air measurements being taken, steady-state conditions were ensured by allowing the wind tunnel to settle over a period of 30 minutes. The jet exit velocity on the centreline was measured using a 2.3 mm diameter, 90° bend, Pitot-static tube manufactured according to BS 1042:1983. The dynamic pressure,  $P_U$ , was deduced from a measurement of the fluid displacement using a Perflow Instruments Ltd. analogue

micro-manometer. Where the fluid velocities were outside the range of the Pitot-static tube, LDA measurements were conducted to determine the fluid velocity across the nozzle exit.

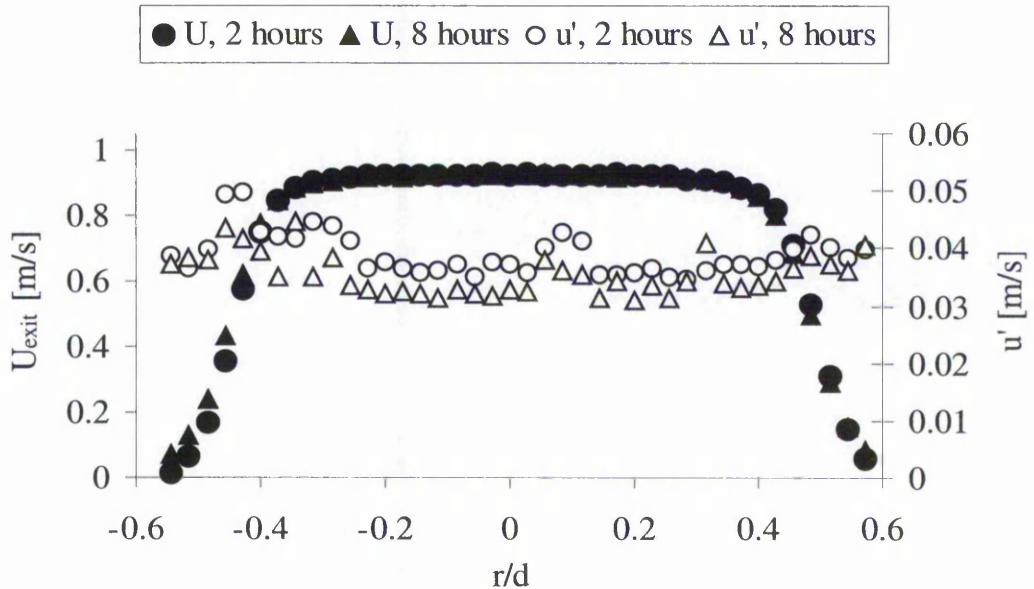


Figure 3.6. Stability of air flow at the nozzle exit for  $Re=2000$  and  $Pr=0.71$ .

### 3.3 Properties of the working fluids

The relevant transport properties of air and water were taken from Kakaç and Yener (1995) and are listed in Table 3.2. All relevant properties were evaluated at the film temperature by averaging the wall and jet static temperature, see Ma *et al.* (1998). For  $Pr > 1$ , the Prandtl number was varied over a temperature range of  $50^{\circ}\text{C} \leq T \leq 15^{\circ}\text{C}$  thus yielding  $3.6 \leq Pr \leq 8$ , respectively. The water temperature was maintained constant to within  $\pm 0.3^{\circ}\text{C}$ . For the Reynolds number of 20,000, the regulating ball valve was closed further which introduced an increased backpressure onto the pump. As a consequence the water temperature was marginally higher than in the lower Reynolds number cases,  $18.4^{\circ}\text{C}$ , instead of  $15^{\circ}\text{C}$ . It is interesting to note that this large variation in Prandtl number is mainly caused by changes of the dynamic viscosity ( $\mu_{50^{\circ}\text{C}}/\mu_{15^{\circ}\text{C}}=0.47$ ) while the thermal conductivity and the specific heat capacity vary by no more than 8.2% and 0.3%, respectively.

| Fluid          | Dynamic viscosity<br>$\mu$ [kg/(m.s)] | Therm. Conduc.<br>$\lambda$ [W/(m.K)] | Spec. heat capacity<br>$c_p$ [J/(kg.K)] | Pr          |
|----------------|---------------------------------------|---------------------------------------|---|-------------|
| Air – 20°C     | $1.81 \times 10^{-6}$                 | 0.026                                 | 1006.1                                  | <b>0.71</b> |
| Water - 50°C   | $0.548 \times 10^{-3}$                | 0.641                                 | 4180.6                                  | <b>3.6</b>  |
| Water – 32.5°C | $0.851 \times 10^{-3}$                | 0.617                                 | 4185.6                                  | <b>5.9</b>  |
| Water – 18.4°C | $1.047 \times 10^{-3}$                | 0.597                                 | 4183.6                                  | <b>7.3</b>  |
| Water - 15°C   | $1.15 \times 10^{-3}$                 | 0.592                                 | 4190.6                                  | <b>8</b>    |

Table 3.2. Properties of the fluids under investigation.

### **3.4 Flow visualisation investigation**

The flow visualisation experiments used a technique based on illuminating tracer particles in the flow with a planar light sheet to highlight the flow pattern. The study comprises the quantitative characterisation of the temperature distribution beneath an impinging water jet as well as identifying the flow field qualitatively over a range of Prandtl-numbers. The temperature distribution of an impinging submerged water jet ( $Pr = 5$ ) was observed on a small-scale gravity-fed test rig using temperature sensitive liquid crystals. This allowed the temporal development of the temperature distribution beneath a submerged semi-confined impinging jet to be mapped. The flow field was studied qualitatively over a range of Prandtl-numbers on the main test rig to observe changes in the flow structure such as flow separation, recirculation, entrainment and regions of vortices. Once these structures had been identified, further investigations in the form of pointwise LDA-measurements were applied to quantify the observations.

#### **3.4.1 Quantitative flow visualisation**

The case of a hot jet impinging on a cold plate is dominated by the effects of fluid that is being re-entrained after circulating along the flow's primary trajectory. The aim of this study was to gain a deeper insight into the temperature distribution and the flow field of a turbulent hot water jet impinging on a cold plate.

The reliable mapping of temperature fields in aqueous flows represents a difficult task because the sensing probe has to be able to withstand high dynamic loads while maintaining its accuracy and dynamic response. For these reasons, the widely used techniques for gaseous flows such as thermocouples or cold wire anemometry (CWA) cannot be employed. In a comprehensive review on optical measuring techniques for momentum heat and mass transfer studies, Durst (1990) provided a classification of widely used techniques for the measurement of transport processes in fluids. The general distinction for temperature measurement techniques in fluids is represented by a) formation of interference patterns (i.e. Holography, Interferometry), b) measurement of light intensity (i.e. Laser induced Fluorescence (LIF), Coherent Anti-Stokes Raman Scattering (CARS)) and c) image formations (i.e. tracer techniques).

The techniques characterised by the *formation of interference patterns* allow the determination of a temperature field from a change in the refractive index which manifests itself in the form of an interference fringe pattern, Herman *et al.* (1998).

With LIF as a typical representative of the *light intensity measurement techniques*, temperature information is obtained from a fluorescing dye that is excited by a laser beam. The temperature is determined as a function of the dye concentration and the intensity of the incident light, see Lemoine *et al.* (1999) and Sakakibara *et al.* (1997).

For the present study, a technique that belongs to the *image formation* group was employed using thermochromic liquid crystals (TLC). This method is frequently used for quantitative temperature measurements in fluids, see Dabiri and Gharib (1991) and Prasad and Koseff (1996), as it is relatively inexpensive, simple to use and allows a whole region to be mapped simultaneously. When illuminated by white light, thermochromic liquid crystals reflect different colours of light at specific wavelengths in response to a change in temperature. The only shortcoming of this technique was the fact that no work existed that had used liquid crystals for visualisation in forced convection/high Reynolds number flows. In one of the scarce papers on mixed convection, Prasad and Koseff (1996) conducted flow visualisation and heat flux measurements in a lid-driven cavity flow. The study reports Re-number flows up to 12000.

### **3.4.1.1 Test facility for quantitative flow visualisation**

The experimental apparatus consists of a gravity driven water channel, the illumination system, the recording and image processing unit and the temperature control facility. Further information can be found in Ashforth-Frost and Rüdél (1998).

The water channel comprises a reservoir, a transparent water tank and the discharge pipe with a  $\frac{1}{4}$  turn valve as well as various pipes and hoses. The velocity profile at the pipe exit was that of a developing flow. The diameter of the discharge pipe was chosen as 10 mm. This represents a compromise between having a pipe diameter that is as close to the final nozzle diameter as possible and the fact that the Reynolds number at the pipe exit increases with larger pipe diameter. The Reynolds number at the pipe exit was 35500 averaged over a time interval of 12 seconds.

A 3-mm thin light sheet was generated using a 1000 W Quartz Tungsten halogen lamp. Since a fan directly discharged the emitted heat from the lamp, the emission of heat from the light source could be neglected. The walls of the water tank were covered with black cardboard to enhance background contrast and to minimise light diffusion. The temperature in the reservoir and in the tank, respectively, was monitored by means of K-type thermocouples.

The images were recorded with a Pulnix CCD-camera having a frame rate of 25 frames/sec and a matrix of 752x582 picture elements. The analogue signal was digitised in real time into 24 bits-per-pixel colour images by a FlashBus MV Plus PCI mastering frame grabber. Colour images were processed using the commercial software "Photo-Paint".

Figure 3.7 gives a schematic of the test facility used for the quantitative flow visualisation study. Initially, the water tank is filled with distilled water up to the semi-confining plate and slowly heated to a temperature of 28.8°C by means of an adjustable portable heating element.

Trapped air beneath the confining plate is carefully removed with a fine thread. In the meantime, water for the reservoir is heated to a temperature of 33°C representing the upper limit of the liquid crystal bandwidth. Then, the liquid crystals are added. This mixture is used to fill the reservoir and allowed to settle for 10 minutes, thus allowing turbulence to be damped out. The jet flow was initiated by opening the  $\frac{1}{4}$  turn-valve and recorded with the camera positioned perpendicularly to the light sheet.

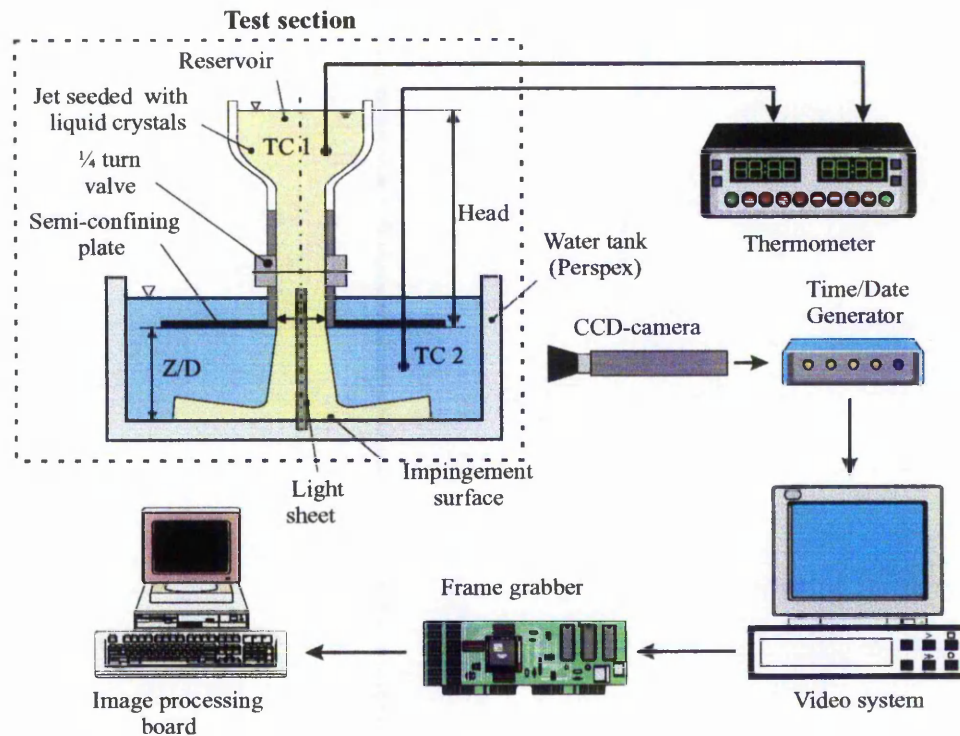


Figure 3.7. Schematic of the test facility used for the quantitative flow visualisation.

#### 3.4.1.2 Working fluid and liquid crystals

The thermochromic liquid crystals employed were R29C4W/S33 encapsulated chiral nematic liquid crystals from Hallcrest Ltd., Poole, England. The crystals had an active colour bandwidth of 4°C, showing red colour at 29°C and blue colour at 33°C. According to the manufacturer's specifications, the diameter of the crystals were between 5 µm and 10 µm. The slurry of the crystals was soluble in water and was added in proportion of 0.08% by volume to distilled and filtered water of 33.2°C in temperature. The optimum concentration had been found by trial-and-error after a number of mixtures had been tested that had resulted in either a poor colour response or a 'milky' over-saturated display of the flow field.

#### 3.4.1.3 Calibration of liquid crystals

The correct interpretation of the perceived colour play required an accurate relationship between temperature and colour. An immersed K-type thermocouple was

connected to a Keithley digital multimeter 2001 with integrated scanner card. The test specimen containing the working fluid was exposed to a rise in temperature of approximately 0.75K/min. After collection of the images a negative temperature gradient was imposed on the test mixture. Special care was taken throughout the experimental phase to keep the viewing angle the same as in the experiment, Farina *et al.* (1994). Temperature-hue curves for heating up and cooling are plotted in Figure 3.8.

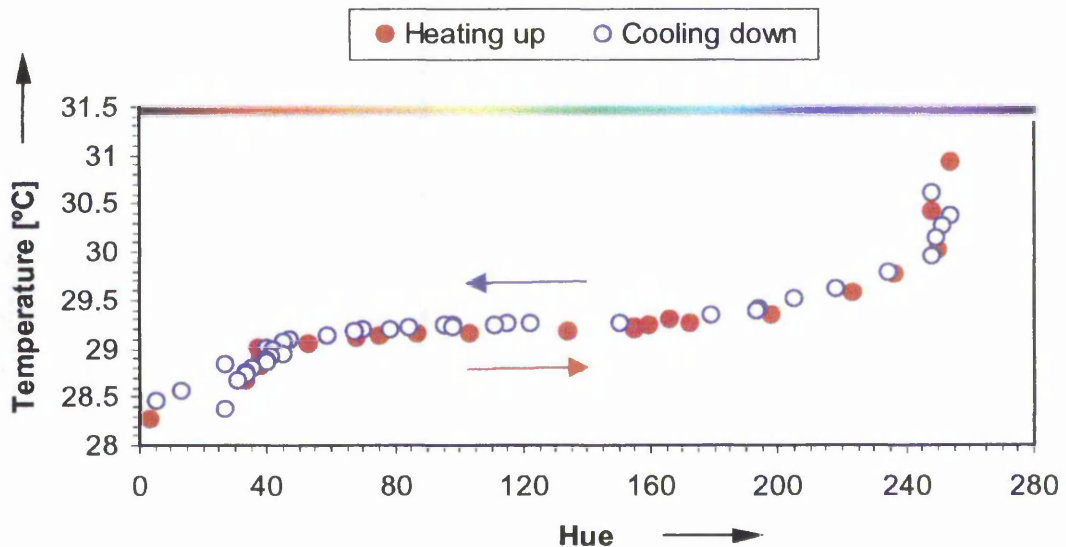


Figure 3.8. Temperature-hue calibration of liquid crystals in water.

From the graph it can be observed that, even when exposed to low temperature differences, a hysteresis effect occurs. This has important implications for quantifying flow field temperatures and is likely to be more pronounced where higher temperature gradients prevail. This phenomenon is an inherent characteristic of liquid crystals and for this reason results can only, at this time, provide a valuable but limited insight to the thermal flow field.

### 3.4.2 Qualitative flow visualisation

The flow dynamics were studied qualitatively by using laser sheet illumination of the seeded flow that allowed the flow field of one half of the jet impingement domain to be observed. Several different techniques exist for the observation of impinging liquid jets that either use hydrogen or air bubbles (Kataoka *et al.* (1987b) or Saripalli (1983) and Barata

(1996)), fluorescent dyes (Chun and Sung (1998) and Barata *et al.* (1993)) or solid tracer particles (Arjocu and Liburdy (1999), Blanchard *et al.* (1999) and Praisner *et al.* (1997)).

Solid particles were used as they were easy to introduce to the recirculating flow, inexpensive and compatible with the available laser in the laboratory. The light sheet was generated using a He-Ne laser ( $\lambda_0 = 632.5$  nm) produced by a circular lens. Still photographs were obtained with a Pentax MX camera using a 50mm lens with a Kodak ISO 400 film at various shutter speeds and apertures between  $f/1.7$  and  $f/2.8$ .

The flow visualisation study concentrated on regions of high velocity gradients or on areas where the flow underwent a change in direction. These regions were at the nozzle exit, in the stagnation region and in the subsequent wall jet region. Due to the varying governing time scales in these regions, it proved difficult to obtain one photograph that covered all areas in the same sharpness.

From the length and direction of the particles streaks the instantaneous variation of the flow field can be deduced. All qualitative flow visualisation tests were conducted under steady state conditions so that each streak on the image represents the instantaneous variation of the flow field.

### 3.4.2.1 Seeding particles

The selection of seeding particles for turbulent flows represents a compromise between two conflicting criteria. A good dynamic response requires small particle size and sufficient small differences between the fluid and particle density while the ability to be recorded on film or tape requires large particle diameters with high refractive indices. The former criteria may be described using the inertial decay time constant of the particle suspension

$$\tau = \frac{\rho_p d_p^2}{18 \mu_f} \quad (3.2)$$

Hollow glass spheres with a mean diameter of  $60\mu\text{m}$  and a relative density of  $573\text{kg/m}^3$  were chosen. The measurement of the particle density is described in Appendix B. Microscope photographs, shown in Appendix B, were obtained using a Scanning Electron Microscope (SEM) and revealed that the average particle diameter was marginally smaller than the stated value of  $60\mu\text{m}$ .

Other solid particles such as aluminium flakes, silver-coated hollow glass spheres, solid glass spheres and polycrystalline seeding powder were tested but were excluded from further considerations due to being irregularly shaped, too small in size, too heavy and not bright enough in the light reflection, respectively. These criteria are based on Mie's scattering theory and are described in detail by Merzkirch (1987).

The optimum flow concentration of 1700 particles/cm<sup>3</sup> was found by trial-and-error and coincides with the value suggested by Praisner *et al.* (1997). From equation (3.2), the resulting inertial decay time constant  $\tau$  was determined to be 193 $\mu$ s for water. This value coincides with the value from Tarbell *et al.* (1986).

### **3.5 Heat transfer investigation**

Heat transfer data were obtained to complement the results from the quantitative flow field investigation. The primary focus lies on the qualitative identification of differences in the local heat transfer profiles which is reflected in the choice of the experimental measurement technique. The transient wall heating technique was adopted for use in the laminar and turbulent flow regimes of the jets since it provides a quick and easy way of testing different heat transfer geometries. The process of comparing and selecting the experimental techniques is described in terms of overall uncertainty, reliability, repeatability and ease of use.

#### **3.5.1 Comparison and evaluation of experimental techniques**

According to the application of impinging jets in industrial applications, there exist many different experimental methods of measuring local heat transfer. The most commonly used boundary conditions are those of uniform heat flux, uniform temperature and the transient wall heating technique. Since the thermal boundary condition can affect the measurement and flow condition significantly, it is essential for the designer to be aware of the characteristics of each method and to interpret the results accordingly. For laminar flow over a flat plate, the choice of the constant temperature or constant heat flux boundary condition can result in differences of up to 36% in local heat transfer, Butler and Baughn (1996). For heat transfer problems that involve liquids, deviations are expected to be even higher. In contrast to this, Kim and Camci (1995) showed, in an

analytical study on jet impingement, that within 2.5 diameters from the stagnation point, local heat transfer is independent of the thermal boundary condition. For liquid jet impingement the boundary conditions may reflect almost ideally the character of real conditions, such as employing the steady state constant heat flux method for modelling the cooling of electronic components. Although this technique has been widely accepted for the modelling of cooling processes, drawbacks such as possible non-uniformities in power dissipation and long experimental settling times make this approach inflexible.

An alternative to the above techniques is represented by the transient wall heating technique, which is well known to be successful in gaseous heat transfer measurements, Ireland and Jones (1985). By exposing the impinging surface to a sudden change in temperature and using liquid crystals as surface temperature indicators, the heat transfer coefficient can be obtained. For the present case of liquid and gaseous jet impingement where heat transfer coefficients can reach values of up to  $3800 \text{ W}/(\text{m}^2\text{K})$ , the one-dimensional assumption of the frequently used transient heat conduction method requires further verification. Furthermore, the objective was to identify an experimental technique capable of providing acceptable levels of uncertainty for both, air and water experiments. While experimental techniques have been well documented and characterised for impinging air jets, the suitability of various experimental techniques for the case of an impinging water jet has not been fully addressed in the open literature. This is attributable to the fact that water jets can be operated in one of two modes, submerged and unsubmerged, and that, to date, a submerged impinging air jet has not been compared to an equivalent water jet under the same conditions. In the following section, several experimental techniques are compared and evaluated in terms of overall levels of uncertainty, reliability, repeatability and ease of use for a submerged impinging jet of air and water. The case of a submerged impinging jet of water has been reported by Rüdél *et al.* (1999). In the following, an uncertainty analysis according to Moffat (1985) was undertaken for the most common characterisation of surface thermal boundary conditions.

### 3.5.1.1 Steady-state techniques

The practicality of the constant temperature boundary condition, as suggested by den Ouden and Hoogendoorn (1974) for air jets, has been assessed. The governing equation for the uncertainty analysis is

$$\frac{\delta h}{h} = \sqrt{\left(\frac{\delta \lambda}{\lambda}\right)^2 + \left(\frac{-\delta s}{s}\right)^2 + \left(\frac{\delta(T_B - T_s)}{(T_B - T_s)}\right)^2 + \left(\frac{\delta(T_s - T_j)}{(T_s - T_j)}\right)^2} \quad (3.3)$$

For a typical anticipated heat transfer coefficient of 500 W/(m<sup>2</sup>K) results of the uncertainty analysis reveal monotonically increasing uncertainties in excess of 25%, see Figure 3.9. This is attributed to the required measurement of surface temperatures to within ±0.001°C, which makes this approach impractical for the use with liquids.

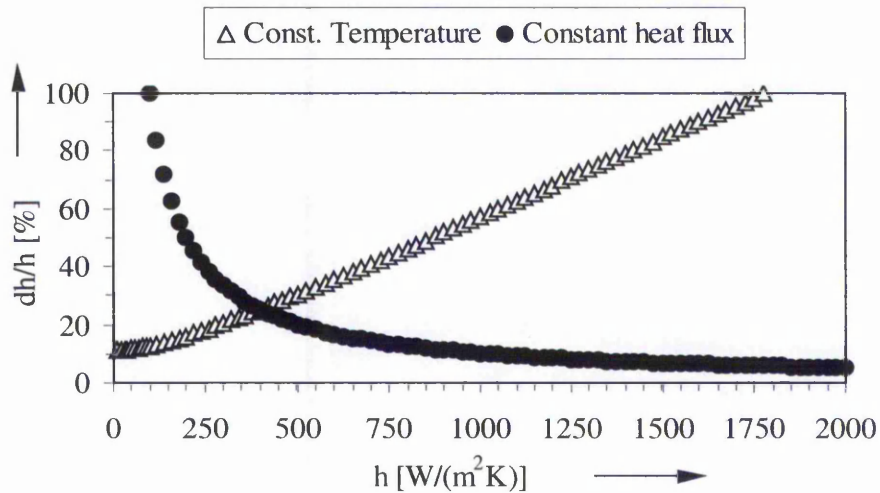


Figure 3.9. Range of uncertainty of steady-state techniques.

For Prandtl numbers where typical heat transfer coefficients are in the range of less than 200 W/(m<sup>2</sup>K), like for gases and other low Prandtl number fluids, except for liquid metals, this technique provides satisfactory levels of uncertainties albeit the practical realisation in terms of maintaining the surface temperature constant, is sometimes difficult to accomplish.

From Figure 3.9 it can also be observed that lower uncertainties in the range of interest are provided by the constant heat flux method. The governing equation for the impingement onto a rectangular plate with the dimensions B.L is

$$\frac{\delta h}{h} = \left\{ \left(\frac{\delta Q}{Q}\right)^2 + \left(\frac{\delta B}{B}\right)^2 + \left(\frac{\delta L}{L}\right)^2 + \left(\frac{\delta(T_{s,ad} - T_j)}{(T_{s,ad} - T_j)}\right)^2 \right\}^{0.5} \quad (3.4)$$

For cooling/heating situations, where heat transfer coefficients are in excess of 1000 W/(m<sup>2</sup>K), this method provides low levels of uncertainties thus providing reliable and

repeatable results. The trend of decreasing uncertainties with increasing heat transfer coefficients makes this technique particularly suitable for turbulent liquid jet impingement heat transfer, see Sun *et al.* (1993) and Leland and Pais (1999). Further details are given in Appendix C where Table C.1 shows that the main contribution to the uncertainty stems from the power source so that particular attention needs to be taken when designing an experiment to avoid operation in this ambiguous section of the chart. Despite its frequent use in determining heat transfer data of liquid jets, the required steady-state mode imposes long experimental settling times and duration times and possible errors caused by the non-uniformities of up to 30% in electrical power dissipation in a heated foil of uniform thickness, Tarasuk and Castle (1983). Of significant importance in the present study was the circumstance, that an experimental method had to be identified that provided acceptable levels of uncertainty for low and relatively high heat transfer coefficients. This led to examination of the transient wall heating technique, where a step change in surface temperature is realised, which relates this technique closely to the constant temperature method. The transient wall heating technique will be briefly discussed in the following.

### 3.5.1.2 Transient wall heating technique

In the transient wall heating technique, the surface is exposed to a sudden change in fluid temperature and the temperature of the surface at any point in time is used to deduce the local heat flux and heat transfer coefficient.

This technique is well established for internal cooling geometries with air as the working fluid, see the detailed description of this technique by Ireland and Jones (1985, 1986). The capability of the transient technique to yield very accurate maps of local surface heat transfer information also led to its application to other fluids, such as R-12, diesel spray and water by Yan *et al.* (1995), Arcoumanis and Chang (1993) and Arjocu and Liburdy (1997), respectively. Yan and co-authors studied condensing heat transfer coefficients in a glass tube and justified the one-dimensional character of the problem by referring to a work by Dunne (1983) who has shown that materials with small penetration depths have small lateral conduction. Arcoumanis and Chang (1993) conducted transient heat transfer measurements between a heated plate and an impinging diesel spray. For

short test intervals (< 1s), heat transfer rates were inferred from the one-dimensional transient heat conduction equation. This assumption was justified as the temperature gradient normal to the surface was found to be much larger than the lateral one. Arjocu and Liburdy (1997) employed the transient step-heating technique to study heat transfer of impinging liquid water jets. Since the nozzle exit Reynolds number was between 300 and 1500, the heat transfer coefficient was less than 1200 W/(m<sup>2</sup>K). In another paper concerned with an impinging water jet, Zumbrennen *et al.* (1990) employed a transient two-dimensional approach based on a two-dimensional finite difference solution to study the importance of surface motion on the heat transfer characteristics such as in the hot rolling process of steel strips. Heat transfer coefficients in excess of 25000 W/(m<sup>2</sup>K) were reported during the initial 12 seconds of a test-run. Using the sequential perturbation method, uncertainties of up to 27% were reported.

While the characteristic heat conduction equation of the transient technique will be shown in the next section, further details for the expression of  $\delta h$  are given in Appendix C and read

$$\frac{\delta h}{h} = \left[ \left( \frac{\delta t}{2t} \right)^2 + \left( \frac{\delta \sqrt{\rho c \lambda}}{\sqrt{\rho c \lambda}} \right)^2 + \left( \frac{1}{\beta(T_j - T_0)} \right)^2 (\delta T_{LC}^2 + (\theta - 1)^2 \delta T_0^2 + \theta^2 \delta T_j^2) \right]^{0.5} \quad (3.5)$$

where  $\beta = 2 \sqrt{\eta} (\pi^{0.5} - \sqrt{\eta}(1 - \theta))$  and  $\sqrt{\eta} = \frac{h \sqrt{t}}{\sqrt{\rho c \lambda}}$ .

Examination of equation 3.5, with regard to short transients, reveals that the highest heat transfer coefficients occur at short transients and at large temperature differences between the initial plate temperature and the surface temperature, Figure 3.10. Figure 3.11 depicts increasing levels of uncertainties at low values of the non-dimensionalised temperature,  $\theta$ . This corroborates observations by Martinez-Botas *et al.* (1995) who reported that for short measurement intervals with high thermal loads, the highest heat transfer rates occur in the initial stage of the process. Butler and Baughn (1996) pointed out that the more the initial conditions resemble those of a uniform wall temperature (in the present study:  $\theta=0$ ) the higher are the uncertainties. In contrast to air measurements, where long durations of the transient may allow the semi-infinite substrate assumption to break down, liquid heat transfer coefficients are inferred from much shorter transients. In cases where  $\theta > 0.6$  the overall uncertainties display significantly lower values. However, Ashforth-Frost (1994) recommended a value of  $\theta \approx 0.5$  to minimise the effects of

erroneous temperature measurements. Ireland (1987) pointed out that a value of  $\theta$  between approximately 0.35 and 0.55 will result in the smallest error in  $h$ .

Measurements in air and water with a variety of different values for  $T_0$  and  $\theta$  and several types of liquid crystal formulations confirmed values for  $\theta$  between 0.35 and 0.55 as most suitable. Different trends depending on the type of fluid became apparent for the selection of the liquid crystal type. While a narrow bandwidth liquid crystal formulation in air measurements yielded the best results in terms of visualising secondary peaks in heat transfer, the contrary was observed for water measurements. Here, the brilliance and brightness of the narrow bandwidth colour display seemed to be significantly impaired by the rapid change in temperature which made their analysis difficult and sensitive to measurement errors. These effects were eliminated in water by using a wide bandwidth liquid crystal formulation which extended the residence time of the isotherms in the stagnation region and displayed a much brighter colour response. In this context it has to be pointed out that the response time of the liquid crystals is in the order of a few milliseconds, Ireland and Jones (1987), and is therefore much shorter than the time interval between two video frames. The contribution to the overall uncertainty for a typical heat transfer situation can be seen from the details given in Appendix C.3.

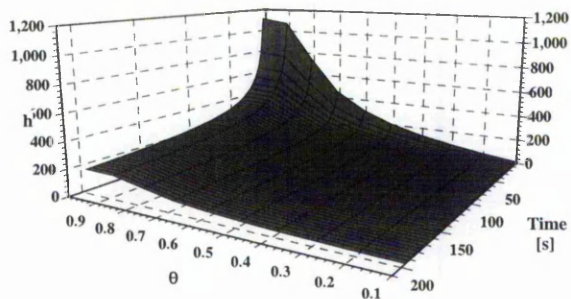


Figure 3.10. Range of validity of the 1D-transient technique.

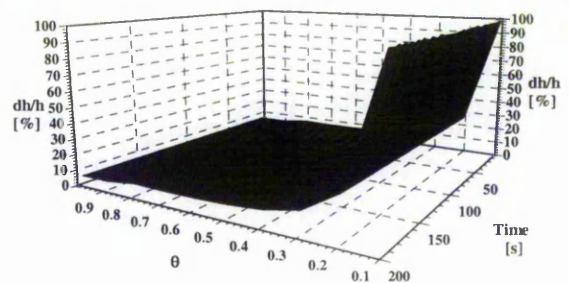


Figure 3.11. Range of uncertainty of the 1D-transient technique.

Stasiek *et al.* (1997) reported that the uncertainty of true-colour based image processing systems using wide-band liquid crystals is approximately of the same order as the uncertainty resulting from human observers using narrow-band crystals. However, in the present study the true colour image processing was applied to both formulations, the narrow-band and the wide-band liquid crystals.

A variation of the transient wall heating technique using a heating foil and liquid crystals was suggested by von Wolfersdorf *et al.* (1993). Elimination of the local heat flux and the requirement of measuring the surface temperature results in a significant increase of the level of uncertainty. Figure 3.12 depicts situations where high heat transfer coefficients are obtained at small temperature differences between the wall and the jet. Results of the uncertainty analysis are plotted in Figure 3.13. Further examination in the initial stage of the test run reveals that the major contribution to the error results from the uncertainty in the start time.

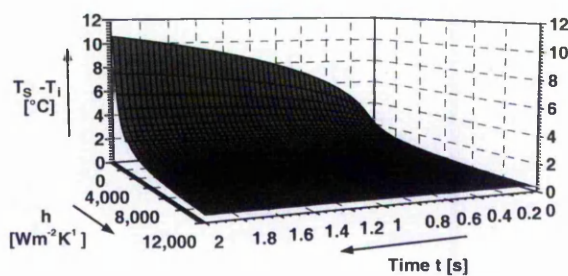


Figure 3.12. Range of validity of the 1D-transient technique (additional heat flux).

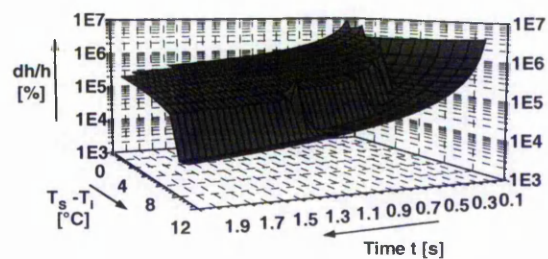


Figure 3.13. Range of uncertainty of the 1D-transient technique (additional heat flux).

### 3.5.1.3 Numerical approach

In cases of high heat transfer coefficients, the heat conduction equation is frequently approximated numerically to deduce the local heat transfer coefficient distribution beneath impinging jets, see Zumbrennen *et al.* (1990). To test the general validity of numerical methods for approximating the solution for the characteristic transient heat conduction equation, the finite-difference method was chosen as a typical representative for computing heat transfer coefficients in jet impingement heat transfer situations. The characteristic equation was expanded into two dimensions by replacing all terms with second-order difference terms which were obtained by truncating the Taylor series after the first derivative. The discretisation of the characteristic equation and the corresponding boundary conditions was performed using the implicit forward-difference scheme, see Kreith and Black (1980). For the governing transient heat conduction equation in axial ( $x$ -) and radial ( $y$ -) direction, this yields

$$\frac{(T_{i+1,j}^{t+\Delta t} - 2T_{i,j}^{t+\Delta t} + T_{i-1,j}^{t+\Delta t})}{\Delta x^2} + \frac{(T_{i,j+1}^{t+\Delta t} - 2T_{i,j}^{t+\Delta t} + T_{i,j-1}^{t+\Delta t})}{\Delta y^2} = \frac{1}{\alpha} \frac{(T_{i,j}^{t+\Delta t} - T_{i,j}^t)}{\Delta t} \quad (3.6)$$

The resulting set of linear equations is solved by the Gauss-elimination method with row pivoting. For the computation of the temperature and heat transfer distribution, a software program was written using the C++ syntax. The code is listed in Appendix D.1. A grid independent solution could only be achieved for the one-dimensional case where 1000 nodes were used.

In the case of the two-dimensional model, the required number to achieve a grid-independent solution exceeded the capabilities of the computational facilities so that finally 625 nodes in each direction were employed. The effects of the grid-independent solution are discussed in Chapter 5. The software program that was developed for its computation is also listed in Appendix D.2.

### 3.5.2 Selection of the experimental technique

Comparing the constant heat flux technique with the constant temperature technique, it was found that the former yields decreasing uncertainties for increasing heat transfer coefficient and thus is particularly suited for high Prandtl number fluids where typical heat transfer coefficients are in excess of 1000 W/(m<sup>2</sup>K). On the other hand, the constant temperature technique reveals relatively low levels of uncertainty for heat transfer coefficients less than 200 W/(m<sup>2</sup>K), thereby making it most attractive for low Prandtl number fluids that are generally characterised by low heat transfer rates. Generally, the transient wall heating technique, which is a variation of the constant temperature technique, can be regarded as providing heat transfer coefficients with uncertainties that lie between those of the constant heat flux and constant temperature technique. To date, the highest heat transfer coefficient determined by the transient technique was approximately 2000 W/(m<sup>2</sup>K) as reported by Sargison *et al.* (2000). For the present study, where high and low heat transfer coefficients were to be determined using the same boundary condition, the transient technique was considered as offering sufficiently low levels of uncertainty for both working fluids, air and water. Another reason for selecting the transient wall heating method was that it does not require any heater elements and also allows full surface heat transfer coefficient distributions to be mapped in a single test.

A test run is initiated by suddenly diverting a heated flow onto the cold impingement plate placed in the test section at ambient temperature. The surface temperature at any point of the plate can be represented, under certain assumptions, by the one-dimensional response of a semi-infinite medium to the sudden step application of a convecting fluid at temperature,  $T_J$ . By using liquid crystals as surface temperature indicators, the heat transfer coefficient can be obtained from the transient equation given in Schneider (1959) with a convection boundary condition. The solution is given as follows:

$$\frac{T_{LC} - T_0}{T_J - T_0} = \theta = 1 - \operatorname{erf} \sqrt{\frac{x^2}{4 \alpha t}} - e^{\frac{hx}{\lambda} + \eta} \left\{ 1 - \operatorname{erf} \left( \sqrt{\frac{x^2}{4 \alpha t}} + \sqrt{\eta} \right) \right\} \quad (3.7)$$

If the target plate is sufficiently thick and initially at a uniform temperature then the heat transfer process can be considered to be one-dimensional into a semi-infinite solid. At the surface of the plate, the co-ordinate  $x = 0$  so that

$$\theta_x = \theta_{ax} = \frac{T_{LC} - T_0}{T_J - T_0} = 1 - e^{\eta} \operatorname{erfc}(\sqrt{\eta}) \quad (3.8)$$

The Gauss error function was implemented using the following series expansion

$$\operatorname{erf}(\sqrt{\eta}) = \frac{2}{\sqrt{\pi}} \sum_{n=0}^{\infty} \frac{(-1)^n \sqrt{\eta}^{2n+1}}{(2n+1) n!} \quad (3.9)$$

A simple C++ program has been developed (see Appendix D.3) to obtain heat transfer coefficients using the above analysis. Equation (3.9) was expanded up to 150 terms since convergence was achieved after approximately 130 terms.

For the important case that the surface will not experience a pure step change in temperature, Bunker *et al.* (1992) suggested the superposition of a set of elemental steps in  $T_J$  as

$$T - T_0 = \sum_{j=1}^N U(t - \tau_j) (T_J - T_0)_j \quad (3.10)$$

where

$$U(t - \tau_j) = 1 - e^{\frac{h^2}{(\rho c_p \lambda)}(t - \tau_j)} \operatorname{erfc} \left( \frac{h}{\sqrt{(\rho c_p \lambda)}} \sqrt{(t - \tau_j)} \right) \quad (3.11)$$

By recording the variation of  $T_J$  with time and approximating it by steps, the local surface heat transfer coefficient can be obtained as the superposition of equations (3.10)

and (3.11). However, it was found that the transient change in jet temperature could be avoided by preheating the nozzle assembly.

In situations where high heat transfer coefficients are anticipated, the aspect of achieving sufficiently short changes in fluid temperature becomes important. Methods used in the past include pneumatically activated ball valves, Martinez-Botas *et al.* (1995), shutter mechanisms, Kumagi *et al.* (1995) and Sargison *et al.* (2000) and manually operating switching valves, Yan *et al.* (1995). The design of the latter was used in this study for its capability of re-diverting the flow within approximately 20ms and also due to its relatively simple design.

The semi-infinite assumption is valid as long as the temperature penetration does not exceed the thickness of the material being used. To maintain the penetration depth much smaller than the effective plate thickness, the guideline for the minimum thickness of the Perspex plate was taken from Schultz and Jones (1973) as

$$s > 4\sqrt{\alpha t} \quad (3.12)$$

In the present investigation the impingement plate was made of Perspex and was 25mm thick. Equation (3.12) yields a maximum test duration of 390 seconds which is much longer than the duration of a typical test run, between 10 to 60 seconds.

### 3.5.3 Experimental set up

To produce the required transient, a special valve was constructed as proposed by Yan (1995). For the heat transfer measurements, all pipework, the nozzle section and the test section were insulated to minimise heat losses.

To produce the necessary transient, the transient valve was closed so that the heated fluid was discharged through the outlet of the valve. The cold impingement plate was then positioned opposite the nozzle exit thereby ensuring that the temperature of the plate was identical to that of the surrounding ambient fluid. The initial surface temperature and the jet temperature were noted. A test run commenced by pushing the slider of the transient valve down thereby activating the time-date generator. The response of the liquid crystal on the plate was recorded on VHS video and was subsequently transferred to the image processing system for analysis.

### 3.5.3.1 Selection of surface cooling or surface heating

When a hot axisymmetric jet impinges onto a cold surface, the heat transfer coefficient can be directly compared to a cold jet cooling a hot surface if the adiabatic wall temperature instead of the fluid temperature is used for the definition of the heat transfer coefficient, see Goldstein *et al.* (1990) and Baughn *et al.* (1991).

The adiabatic wall temperature  $T_{ad,w}$  is defined as

$$T_{ad,w} = T_j + r \frac{U_{exit}^2}{2c_p} \quad (3.13)$$

where the recovery factor,  $r$ , describes the ratio between the frictional temperature increase and the temperature increase due to adiabatic compression, see Li *et al.* (1997). Goldstein and Seol (1991) and Ma *et al.* (1997a) found the recovery factor to be essentially independent of Reynolds number. As a first approximation to estimate the recovery factor for the use of water, the correlation and graphs given by Lee *et al.* (1997) were used as

$$r = 1.2 Pr^{0.5} \quad \text{for } 10 < Pr < 200 \quad (3.14)$$

For air tests, no such correlation exists to date, so that, in order to create a worst case scenario, the recovery factor was estimated to be  $r=1.2$  from Goldstein *et al.* (1990). The authors conducted measurements of a heated jet impinging onto a cold surface and reported the highest values of the recovery factor to occur in the impingement region.

As the maximum nozzle exit velocities for water and air were relatively low, 0.57m/s and 10.1m/s, respectively, equation (3.13) yields discrepancies between the jet exit temperature and the adiabatic wall temperature to be less than 0.01°C and 0.05°C, respectively. This variation is within the measurement uncertainties of the liquid crystals ( $\pm 0.2^\circ\text{C}$ ) so that for the remainder of this study the jet exit temperature will be used as the reference temperature throughout this investigation.

It was shown from the uncertainty analysis that the transient wall heating technique can accommodate both the jet heating and jet cooling modes. Preliminary work with liquid crystals has shown, however, that during surface cooling the liquid crystals may undergo an undesired lag in re-alignment. This manifests itself as simultaneous overlapping of several lower colour bands, thus, making temperature readings in the upper range of the working region difficult and unreliable.

For the heat transfer investigation, it was therefore decided to use a transient liquid crystal technique with a heated jet impinging onto a cold surface.

### 3.5.3.2 Preparation of test surface

The surface temperature was measured using chiral nematic micro-encapsulated liquid crystals of the types BM/R35C15W/C17-10 and BM/R31C1W/C17-10 for water and air, respectively. According to the manufacturer, the wide band and narrow band liquid crystal formulations had a particle size between 5 and 10 $\mu\text{m}$  and an active colour bandwidth of 15 $^{\circ}\text{C}$  and 1 $^{\circ}\text{C}$ , respectively. To ensure an accurate and repeatable temperature-colour relationship of the liquid crystals, a dynamic calibration technique was applied, see Roberts and East (1996). The calibration procedure was performed *in-situ* by continuously comparing the colour response of the crystals with simultaneous measurements from surface-mounted thermocouples. Two foil type T precision thermocouples, with an approximate thickness of 5 $\mu\text{m}$ , were flush mounted on the Perspex substrate at approximately  $r/d=1.05$  and  $r/d=1.5$  using a strain gauge bonding technique. All thermocouples were selected, extended and calibrated according to BS 1041-4:1992. The use of solder for extending the thermocouple wires will not affect the output signal as reported by Moffat (1990). The calibration revealed that the crystals BM/R35C15W/C17-10 and BM/R31C1W/C17-10 displayed red at 35.9 $^{\circ}\text{C}$  (30.1 $^{\circ}\text{C}$ ) and blue at 47.7 $^{\circ}\text{C}$  (31.2 $^{\circ}\text{C}$ ), respectively. The calibration curves are shown in Appendix C.5. Since C17-10 crystals form aqueous acrylic-based coatings and were therefore water soluble, it was essential for their use in water flows that a reliable and durable water resistant coating was used. For this purpose, a water/liquid crystals mixture (ratio 2:1) was sprayed on the surface using an artist's airbrush-gun and coated with a thin layer of Hallcrest BB-M1 black paint, containing AQB-3 Mowilith binder. The black paint was diluted with water in a ratio of 1:1. This layer was top-coated with a mixture of clear, mineral spirits based varnish and thinner, both manufactured by Sericol, Broadstairs, England.

### 3.5.3.3 Experimental set-up

Prior to commencement of the heat transfer tests, the heated fluid was circulated through the test rig to preheat the nozzle assembly and to ensure steady conditions. To mark the start time of the test, the transient valve was fitted with a micro-switch which was activated as soon as the valve's piston had reached its final bottom position. The signal from the micro-switch triggered a time/date generator which was displayed on the VHS-video recorder. The time to switch the flow was estimated to be approximately 40ms which is identical to the frame rate of the CCD-camera used. The warm fluid flow was then diverted by the transient valve to the exhaust position and the impingement plate at ambient temperature quickly positioned in place. The test run was then started and the liquid crystal isotherms recorded on VHS-video. Simultaneously, temperature readings from the surface thermocouples were recorded on a Keithley 2001 digital multimeter which was interfaced to a Pentium 100MHz computer. The software listing for data collection can be found in Appendix D.4.

The time for the flow to travel from the outlet of the transient valve to the impingement surface was calculated based on the mean flow velocity in the respective sections of the rig. For the water flow, this time was computed to be 1.22s which is only 0.08s more than the time observed from the video. The corresponding time interval is approximately 0.09s and can therefore be neglected.

The CCD-camera was positioned normal to the rearside of the heat transfer surface on the same level as the nozzle centre to record the isotherms through the Perspex plate. Illumination was provided by two 150W light bulbs, placed symmetrically off-axis to the position of the CCD-camera. An advantage of this arrangement was the elimination of light reflections and the fact that the camera could be positioned normal to the test surface, Sabatino *et al.* (2000). The illumination and viewing angles were fixed during calibration and experiment.

The images were processed following the procedure as outlined in Richards and Richards (1998). Images of the experimental results were captured from the video and stored as uncompressed Audio Video Interleave (AVI) files. In this form, frames could be viewed in sequence as a movie. In addition, each frame was saved in the Tag Image File Format (TIFF) format for individual processing. White markers scratched into the test surface served as reference points to ensure that each calibration field and subsequent data fields were coincident to within  $\pm 2$  pixels. To transform the Red, Green and Blue

(RGB) values associated with each pixel in an image into Hue, Saturation and intensity (HSI), the hue algorithm proposed by Gonzalez and Woods (1992) was employed.

In the present study, the uncertainty of the heat transfer coefficient is about 10.1%, see Appendix C.4, and compares favourably with typical average uncertainty levels of other turbulence studies, see Son *et al.* (1999) and Stasiak *et al.* (1996).

## **3.6 Flow field investigation**

### **3.6.1 Basic principles and configuration**

The basic principle of laser-Doppler anemometry (LDA) is the non-intrusive measurement of flow velocities by detecting the Doppler frequency shift of a particle moving with the flow. In order to measure the light that is scattered by the particle, the laser beam is split into two coherent (in phase to each other) beams, which cross at an angle. The pulsating light intensity signal that is received by the photomultiplier consists of two components, one for each beam, which have different Doppler shifts due to the angle between the two beams.

For the present investigation, a DANTEC 300mW four-beam two-colour fibre-optic based laser-Doppler anemometer was used. A schematic of the laser-Doppler anemometer set-up is shown in Figure 3.14. In the transmitter, the beam from an Argon-Ion laser is split and one beam is passed through a Bragg cell, where the frequency of the beam is shifted by 40MHz, thus enabling the optical receiver to distinguish between positive and negative velocities and to reduce angle bias. Each beam is then divided into its individual colour components, 488nm (blue) and 514.5nm (green), to allow two-dimensional velocity measurements. The optical signals are transmitted via a 7.5m fibre-optic cable to the laser optics output aperture.

The measurement volume is formed by the intersection of two laser beams at their respective beam waists. The interference produces plane wave fronts, manifested as planes of light and darkness, known as fringes. With the optical transducer head having a beam separation of 38mm, a front lens of 600mm focal length and a beam expander with an expansion ration of 1.95, the diameter of the measurement volume is 0.15mm while its length is 2.4mm in the transverse radial direction. The selection of the front lens represents

a trade-off between optical access to the flow field for the low nozzle-to-plate spacing of  $z/d=2$ , and the size of the measurement volume which affects the overall accuracy of the results. An important advantage of using a lens with a long focal length represents the fact that fringe distortion due to light refraction through particles is reduced, Ruck (1991).

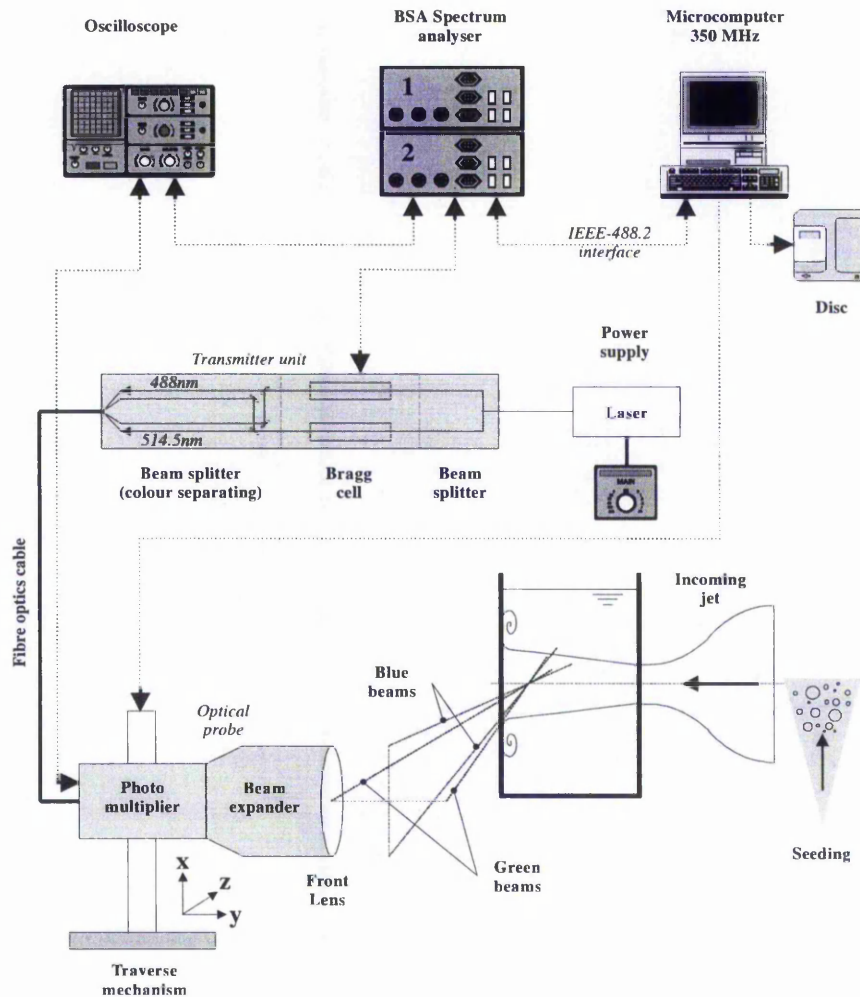


Figure 3.14. Schematic of the LDA-facility.

To facilitate automatic data acquisition and to allow measurements at any point within the flow field, the probe was mounted onto a computer controlled three-dimensional traverse mechanism with a resolution of  $12.5\mu\text{m}$  connected through a GPIB interface to a microcomputer. The microcomputer was not only used to acquire data from the two Burst Spectrum Analysers, but also to analyse, store and display them. Vibration

isolation and stability were accomplished by placing the traverse mechanism onto a rigid frame close to the test section. Careful positioning of the traverse mechanism with respect to the test section assured that the window of the test section was not half way between the centreline of the test section and the lens which would have resulted in a signal ambiguity due to the light refraction back onto the signal detector.

In the interests of reliable and accurate results, considerable time was taken to optimise the settings of the relevant hardware and software parameters in a trial-and-error process. Table 3.3 provides the characteristics of the LDA arrangement employed in this investigation. These settings are regarded as a trade-off between temporal resolution and high accuracy, represented by the data rate and validation, respectively.

The data rate depends on the signal gain and the high voltage supply to the photomultiplier tubes. Careful selection of the high voltage ensured a low noise level while the signal was still strong enough to detect bursts from small seeding particles. It was found that the data rate is a strong function of the fluid velocity.

To avoid electronic noise that may cause both bias and fluctuation in the measured velocity data, the signal processor's validation circuit was employed which detected the distortion of the signal and aborted the sample if the signal showed too much distortion. In order to achieve high validation rates, the record interval was closely matched to the duration of the shortest bursts as monitored on an oscilloscope and by using the histogram function in the software. The record interval, in turn, depends on the record length and on the span of the velocity range.

For determination of the Reynolds stresses the hardware was operated in coincidence mode with the first channel being the clock source master. The different light intensity of the two channels might cause a seeding particle to generate a velocity signal on one channel without simultaneously generating a signal on the other channel. This was eliminated by using coincidence filtering in the software. The largest acceptable time difference between two velocity samples was defined through the record interval window. Its value was determined from dividing the measurement volume diameter,  $dx$ , by the nozzle exit velocity, see Dantec (2000).

|  |   |
|--|---|
| Laser source   | Ar-Ion Laser, 300mW<br>(488nm and 514.5nm)                        |
| Number of fringes (Ch1, Ch2)                         | 35, 35  |
| Fringe spacing (Ch1, Ch2)                            | 4.174 $\mu$ m, 3.959 $\mu$ m                                      |
| Unfocused beam waist diameter                        | 1.35mm  |
| Beam spacing   | 38mm  |
| Beam expansion ratio                                 | 1.95  |
| Focal length of front lens                           | 600mm   |
| Beam intersection angle                              | 7.068°  |
| Measurement volume size [mm]<br>(dx, dy, dz)         | <b>Ch1:</b> 0.15, 0.149, 2.423<br><b>Ch2:</b> 0.142, 0.142, 2.298 |
| Length of the focal region<br>(effect. length of MV) | 0.27mm  |
| Optical frequency shift                              | 40 MHz  |
| Record interval window<br>(for coincidence mode)     | dx/U <sub>cl, exit</sub>  |
| Record interval (Ch1, Ch2)                           | To match transit time   |
| Range of data rate                                   | 5 – 100 Hz  |
| Average validation                                   | 90% – 100%  |

Table 3.3. Parameters for LDA set-up.

### 3.6.1.1 Probe set-up

For the measurement of near wall flow along the impingement plate, it was necessary to move the measurement volume as close to the wall as possible. This was accomplished by inclining the measurement probe by half the intersection angle,  $\beta$ , of the two laser beams in order to make one of them parallel to the solid surface. This measurement requires that all measured velocity components be divided by  $\cos(\beta/2)$ . This was neglected since for small values of  $\beta$  its contribution is less than 0.3%. For higher order statistical moments, this error can propagate to an overall contribution of 0.9% to the overall measurement uncertainties.

In order to achieve a strong signal near the plate surface, the rotation of the probe through an angle  $\phi=45^\circ$  about its longitudinal axis was considered. Since the optical

axes of both beam pairs lie entirely in the plane of the orthogonal velocities, a coordinate transformation was employed to deduce the principal velocities  $u$  and  $v$  from the measured velocities  $u_1$  and  $u_2$ .

$$\begin{bmatrix} u \\ v \end{bmatrix} = \begin{bmatrix} \cos \phi & -\sin \phi \\ \sin \phi & \cos \phi \end{bmatrix} \begin{bmatrix} u_1 \\ u_2 \end{bmatrix} \quad (3.15)$$

The transformation matrix was tested for a typical measurement on the jet centreline downstream of the nozzle exit ( $y/d=1$ ) and close to the wall ( $y/d=0.05$ ). It was found that for the case of the rotated probe,  $\phi=45^\circ$ , the spatial alignment of the two beams, vertically above each other and parallel to the surface, was difficult to accomplish. Furthermore, in the immediate vicinity to the wall, the most crucial parameters for valid data acquisition, data rate and optical noise from reflected light, did not yield the desired improvement. For the final measurements,  $\phi$  was therefore chosen to be  $0^\circ$ .

### 3.6.1.2 Seeding

For the air measurements, a DANTEC seeding generator was employed to provide particles of a 50:50 glycerol/water mixture of approximately  $2\text{--}7\mu\text{m}$  mean diameter. The glycerol/water mixture was replaced every two weeks to avoid an ageing process due to the pressurisation, which would deteriorate its light scatter characteristics.

Seeding of the water flow, particularly for low Reynolds number, represented a more difficult task as the LDA facility operated in backscatter mode. This meant that the light intensity was approximately 2-3 orders of magnitude lower than the forward scattered light intensity, see Vassallo and Kumar (1999). Despite careful consideration of various seeding materials (milk, aluminium powder, glass spheres) and optimisation of the hardware set-up ('High voltage', range of velocity, centre of velocity range, record length, etc.), the maximum data rate was in the order of 10Hz. A  $100\mu\text{m}$ -cartridge filter was incorporated into the flow loop as it was found that the particle size distribution could be narrowed down. A further outcome was the reduced scatter in the obtained results. To compensate for the relatively low data rate at this Reynolds number, a measurement interval of 5 minutes per measurement point was maintained. Finally, the water was seeded with Spherichel<sup>®</sup> hollow glass spheres (manufactured by Potters

Ballotini, Bury St. Edmunds, England) due to their high reflective surface and neutral buoyancy ( $\rho_{\text{rel}}=1.1$ ).

The particle seeding methods for both fluids were considered as not affecting the flow or the modulation of the signal when passing through the measurement volume.

### 3.6.1.3 Effects of the window surface

The measurement of the internal liquid flow required the presence of a transparent window between the LDA optics and the flow field. The effects of plane and curved window surfaces on the displacement of the measurement volume have been addressed by several workers, i.e. Doukelis et al. (1994) and Parry et al. (1990). Zhang and Eisele (1995) presented a simplified method of quantifying errors when aligning a LDA probe off-axis. The authors concluded that for three-dimensional measurements, where one probe must be mounted off-axis in order to resolve the third velocity component, the refraction of laser beams through the plane window and through fluids of different refractive indices can have severe effects on the measurement of flows in terms of accuracy and reliability of the results. These include

- a) the displacement of the measurement volume,
- b) astigmatism (=loss of the unique focusing point of a light bundle after refraction),
- c) changes in the fringe spacing and distortion of fringe pattern,
- d) changes in the path of the measurement volume when traversing,
- e) changes to the maximum data rate.

Although in the present study only a 2D-probe was used, the implications are still valid for general off-axis alignments of an optical probe. In the following, these aspects and their consequences on the present investigation will be discussed.

a) The refraction of a laser beam on a plane window surface leads to a deflection of the incident beam which is expressed by an angle measured between the refracted light beam and the surface normal. See also Figure 3.15 for further details. In the present study, the optical probe was inclined by half the intersection angle,  $\varphi=\beta/2$ , so that one of the green laser beams, green 1, was aligned parallel to the wall while the second beam, green 2, was inclined by the intersection angle,  $\beta$ , with respect to the surface normal. The pair of blue beams was inclined in both planes ('x-y' and 'x-z') by half the intersection

angle,  $\beta/2$ . The displacement of the measurement volume due to the Perspex window was calculated using optical geometric relationships. Results of the calculation can be found in Appendix E.1. It is shown that the two measurement volumes in water are only 0.0175mm apart from each other which is 11% of the size of the measurement volume in this direction. In this context it has to be noted that the photomultiplier only focuses onto a part of the measurement volume. As the photomultiplier focuses at the central region of the measurement volume, the effects of the small inclination angle,  $\phi$ , are considered negligible. For the situation where the measurement volumes are located at different spatial positions, Dantec (1996) suggested setting the hardware to the coincidence private mode while the software carries out the coincidence filtering. This procedure, however, resulted in insignificant differences in Reynolds stresses when compared to the conventional method.

b) Astigmatism is an optical aberration in lens optics and occurs when a focused light bundle is refracted on the interface of two media with different refractive indices. Zhang and Eisele (1996) studied the effects of astigmatism on the formation of the measurement volume and found that the largest effects were encountered for large off-axis angles, while for angles next to half the beam intersection angle the effects were negligible. Based on Zhang and Eisele (1995), the displacement between the two measurement volumes caused by astigmatism was determined for both working fluids, air and water. Results are given in Appendix E.2. It is shown that the small off-axis angle indeed results in a negligible difference, 0.008mm, between the intersection points of the green and the blue beams. Compared to the diameter of the measurement volume this was regarded as being insignificant.

c) Fringe distortion can occur if the beam waist is not located exactly in the centre of the beam intersection region. It can also be caused by astigmatism which in turn leads to a reduction in data rate. The uniformity of fringe spacing in the measurement volume is an essential condition for accurate LDA measurements and may be achieved if the laser beams intersect with their respective beam waists. For measurements in internal flows, which are bounded by solid windows, this condition can no longer be maintained. Fringe distortion due to improper optical layout has been investigated by Durst and Stevenson (1975) and Miles and Witze (1996). In order to estimate the error in turbulence measurement due to fringe distortion, Zhang and Eisele (1998a) considered its effects



high intensity. For the present investigation, a lens with a focal length of 600mm was used in favour of one with a focal length of 310mm.

#### 3.6.1.4 Determination of the position of the measurement volume

The location of the centre of the measurement volume was determined using the window surface/photomultiplier current method, as described in Dantec (2000). The location of the measurement volume with reference to the radial and transverse radial direction was determined prior to each test run by inserting a transparent block 500mm high into the test section. The block had a surface area of 20mm x 290mm and had been machined to within  $\pm 0.1$ mm, so that all edges were considered straight. To determine the location of the measurement volume along the *transverse radial direction*, a window surface of the reference block was positioned on the centreline of the test section which coincides with the centreline of the jet flow. The LDA measurement volume was then traversed from the probe-side towards this window while the detected Doppler signal and the signal from the photomultiplier were displayed on an oscilloscope. When the anode current limiter was turned on, the signal on the oscilloscope increased in magnitude and the measurement volume was touching the reference window surface. Further traversing of the probe led to a maximum of the Doppler signal which indicated that the centre of the measurement volume was at the surface of the window and thus on the centreline of the jet. The location of the centre of the measurement volume in the *radial direction* was determined by traversing the measurement volume from inside the block out of the top surface until the maximum signal indicated the location of the centre of the measurement volume. The described procedures for locating the centre of the measurement volume in the radial and transverse radial direction, respectively, ensured that fringe distortion in the measurement volume due to refraction of focused light on the interface of two media with different refractive indices was taken into account. For measurements in the axial direction, perpendicular to the surface, the position of the measurement volume was determined by placing the measurement volume in the wall and traversing out of it in 0.1mm increments until a sufficiently strong signal was detected on the oscilloscope. This procedure was applied prior to each measurement near the wall, thereby assuring minimum uncertainty levels and a high confidence level in all near wall measurements.

All of the above steps were repeated three times. Each time the spatial increments were reduced until the position was established to within  $\pm 0.2\text{mm}$  and  $\pm 0.1\text{mm}$  in the transverse radial direction and radial direction, respectively. Due to the length of the measurement volume, the positioning in the radial transverse direction was less accurate.

### 3.6.2 Data reduction and measurement errors

The analogue signal from the photodetector was sent directly to the processor where the instantaneous particle velocity for each detected Doppler-burst was calculated from the frequency shift according to

$$u = \frac{\lambda_0 (f_{s,1} - f_{s,2})}{2 \sin(\varphi/2)} \quad (3.16)$$

The subsequent data analysis was performed to compute the statistical moments of the data. The mean velocity was calculated from

$$U = \sum_{i=0}^{N-1} \eta_i u_i \quad (3.17)$$

The standard deviation was given by

$$\sigma^2 = \sum_{i=0}^{N-1} \eta_i (u_i - U)^2 \quad (3.18)$$

which was used to deduce the velocity fluctuation  $u'$

$$u' = u'_{\text{RMS}} = \sqrt{\sigma^2} = \sqrt{\sum_{i=0}^{N-1} \eta_i (u_i - U)^2} \quad (3.19)$$

The third and fourth order moments, Skewness and Flatness, were computed from

$$S = \frac{1}{\sigma^3} \sum_{i=0}^{N-1} \eta_i (u_i - U)^3 \quad (3.20)$$

and

$$F = \frac{1}{\sigma^4} \sum_{i=0}^{N-1} \eta_i (u_i - U)^4 \quad (3.21)$$

Equations 3.17 to 3.21 apply likewise to the velocity in the radial direction,  $V$ . The Reynolds stresses were computed from the cross-moments as

$$u'v' = (UV) + \sum_{i=0}^{N-1} \eta_i (u_i - U)(v_i - V) \quad (3.22)$$

To avoid the problem of Doppler ambiguity as a consequence of continuous LDA processing, the signal from the photomultiplier was processed in a Fourier signal analyzer operated in the burst mode as recommended by George and Taulbee (1992). The intrinsic problem of the burst mode-processing, the velocity bias due to the sampling and sampled process not being statistically independent from each other, was corrected by using residence-time weighted statistics, see Buchhave (2000).

In LDA sampling, bias may strongly affect the computation of statistical quantities. This is due to the fact that the main assumption of the sampling process being independent of the measured quantity can no longer be maintained. The most important of these correlations is the *velocity bias* where fast particles tend to contribute more towards the signal than slower particles as more fast moving particles are swept through the measurement volume. In the *directional bias* sampling is reduced if the direction of a particle is close to the fringe plane so that fewer fringes will be crossed.

To compensate for velocity bias and directional bias, slower particles have to be given more weight than fast particles when computing the statistical moments. This was considered by using the so-called transit weighting factor  $\eta_i$

$$\eta_i = \frac{t_i}{\sum_{j=0}^{N-1} t_j} \quad (3.23)$$

Despite the longer time that it takes to perform the computation, results are regarded as being free of velocity bias and directional bias, Buchhave (2000).

For ensemble averaging of the data, the optimum number of samples per measurement point was determined as a compromise between accuracy and duration of the sampling process. In the interest of reliable and reproducible results, more emphasis

was placed on acquiring data with a high validity rate rather than aiming for a high data sampling rate.

Various different data collection modes (dead time and transit-time averaging) were investigated. The measurement volume was positioned at the exit of the nozzle on the centreline and readings of various sample sizes were taken for each individual data collection mode. The differences between transit-time averaging and dead time mode were negligible. Figure 3.16 and Figure 3.17 show the effects of the number of samples on the mean velocity and turbulence level for Reynolds numbers of 2,000 and 10,000 respectively. It can be seen from the graphs that in both cases no appreciable variations in the velocity and turbulence intensity curves exist. The odd statistical moment, the mean velocity, showed marginal scatter, less than  $\pm 0.7\%$ .

For the measurements in air, at least 2500 counted and validated samples were collected at each data point. Data were sampled at an average data rate of 25-80Hz over a sampling period of 60 to 120s. For the three Reynolds numbers, 2500, 3500 and 5000 samples were collected, respectively. The effects of seeding concentration on the mean velocity and turbulence intensity were tested and yielded no significant differences.

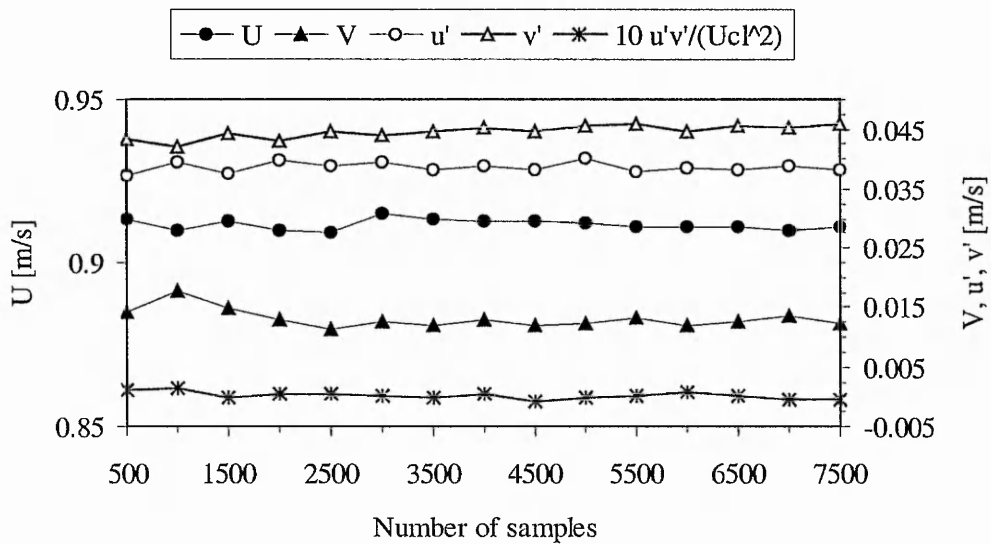


Figure 3.16. Effect of sample size on statistical moments for Re=2,000 (Pr=0.71).

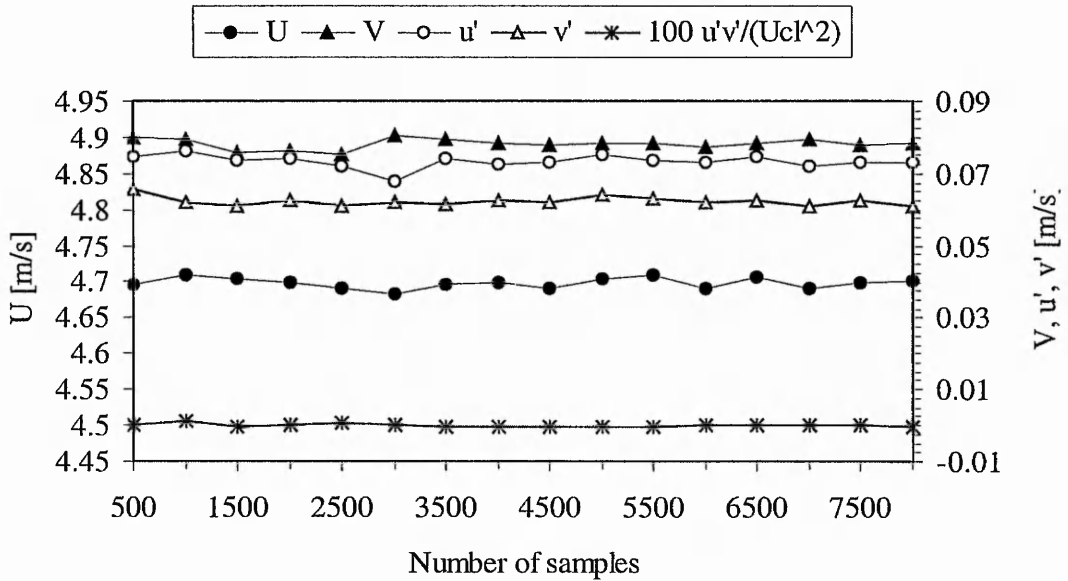


Figure 3.17. Effect of sample size on statistical moments for  $Re=10,000$  ( $Pr=0.71$ ).

In water, the signal was weaker due to the inherent characteristics of the backscatter operating mode. For the low Reynolds number case, data were sampled at a sampling rate of 5-15 Hz over a time period of up to 240s. This assured a minimum number of 1000 validated counts. A sampling rate of 15 to 25 Hz was obtained for the Reynolds number of 10,000 during a typical sampling period of 150s. This yielded approximately 2000 samples per data point. The least problematic was the fastest flow where 5000 samples could be collected thus allowing valid information on Skewness and Flatness to be obtained. The stated numbers of samples coincide with the LDA-manufacturer's recommendation to ensure sufficient statistical certainty in moments processing, Dantec (2000). Other authors, Zhang (1999) and Muto and Ishigaki (1999), collected fewer and similar numbers of samples for air and water flows, respectively.

The bias or systematic error of the LDA-system was assessed by comparing measured velocities obtained at the exit of a fully developed laminar pipe flow with the exact solution of the one-dimensional Navier-Stokes equation. From Figure 3.18 it can be seen that for non-dimensional velocities  $U/U_{c1}$  greater than 0.2 the results agree to within 0.7%. Towards the edge of the pipe, where mixing effects become more significant, deviations increase while the symmetric character of the flow is unaffected.

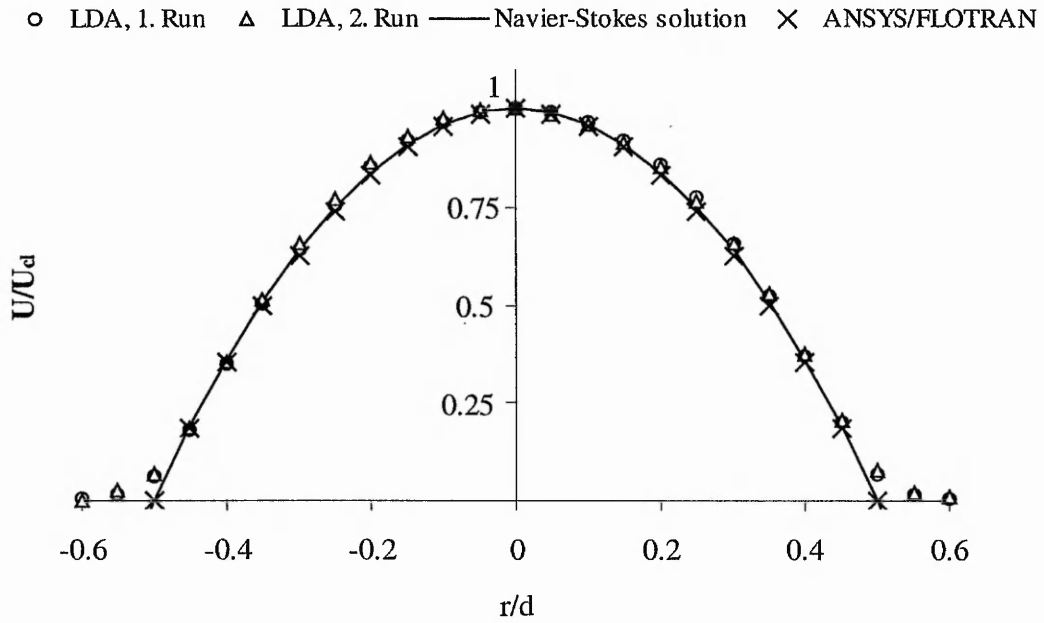


Figure 3.18. Measured and theoretical laminar pipe exit velocity profiles.

The uncertainties in the measurements of the mean velocity, turbulence intensity and Reynolds stresses were estimated based on a 95% confidence interval. The employed procedure was proposed by Benedict and Gould (1996) and reads as follows:

$$\text{Error}_{\text{mean}} = 1.96 \frac{\sqrt{\overline{u'^2}}}{u} \cdot \frac{100}{U} \tag{3.24}$$

$$\text{Error}_{\text{RMS}} = 1.96 \sqrt{\frac{\overline{u'^4 - u'^2}}{4 N \overline{u'^2}}} \cdot \frac{100}{\overline{u'^2}} \tag{3.25}$$

$$\text{Error}_{\overline{u'v'}} = 1.96 \sqrt{\frac{\overline{u'^2 v'^2 - \overline{u'v'}^2}}{N}} \cdot \frac{100}{\overline{u'v'}} \tag{3.26}$$

The calculated uncertainties using the above equations are listed in Table 3.4.

In a paper on measurements in a turbulent boundary layer, Zhang (1999) reported similar magnitudes of the uncertainties in measuring Reynolds stresses in water flows, i.e.  $\overline{u'v'} < 16\%$ . The above numbers represent the worst case, the actual measurement results suggest that the uncertainties are lower than the numbers quoted in Table 3.4.

|                                      | <b>Re=2,000</b> | <b>Re=10,000</b> | <b>Re=20,000</b> |
|--------------------------------------|-----------------|------------------|------------------|
| <b>Air</b> (N=2500, 3500 and 5000)   |                 |                  |                  |
| Error U, V                           | 4.4%, 4.6%      | 3.6%, 3.9%       | 2.7%, 2.9%       |
| Error $u', v'$                       | 5.2%, 5.5%      | 4.4%, 4.7%       | 3.2%, 3.5%       |
| Error $\overline{u'v'}$              | 11.6%           | 8.6%             | 6.9%             |
| <b>Water</b> (N=1000, 2000 and 5000) |                 |                  |                  |
| Error U, V                           | 5.6%, 5.9%      | 3.9%, 4.3%       | 2.9%, 3.2%       |
| Error $u', v'$                       | 8.5%, 8.8%      | 7.6%, 7.9%       | 4.0%, 4.3%       |
| Error $\overline{u'v'}$              | 14.8%           | 11.5%            | 7.1%             |

Table 3.4. Calculated uncertainties over the measurement range.

### 3.6.3 Symmetry of the flow field

To ensure that the flow field in the test section was symmetric about the radial and transverse radial axis and that the confining geometry together with the four outlets was not affecting the flow through end effects or unwanted three-dimensional recirculation vortices, the degree of flow symmetry along the impingement surface was ascertained. Measurements were taken at a distance of  $0.1d$  from the plate with air at ambient temperature as the working fluid. The Reynolds number at the jet exit was 20,000. The two-dimensional character of the LDA-system allowed measurements in the axial and radial direction but was not sensitive along the transverse radial axis. Data were therefore collected in  $0.14d$  steps along diagonals across the region of interest, centred  $2.5d$  around the stagnation point in the radial and transverse radial direction, respectively. The impingement plate was divided into four quadrants, which are numbered in an anti-clockwise direction when viewed downstream from the exit of the nozzle, see Figure 3.19.

The first set of data was collected when traversing from the top of the I. quadrant to the bottom of the III. quadrant. A second set of measurements were then made by starting at the top of the II. quadrant and propagating through the test field to the bottom of the IV quadrant. The results are presented in Figure 3.20.

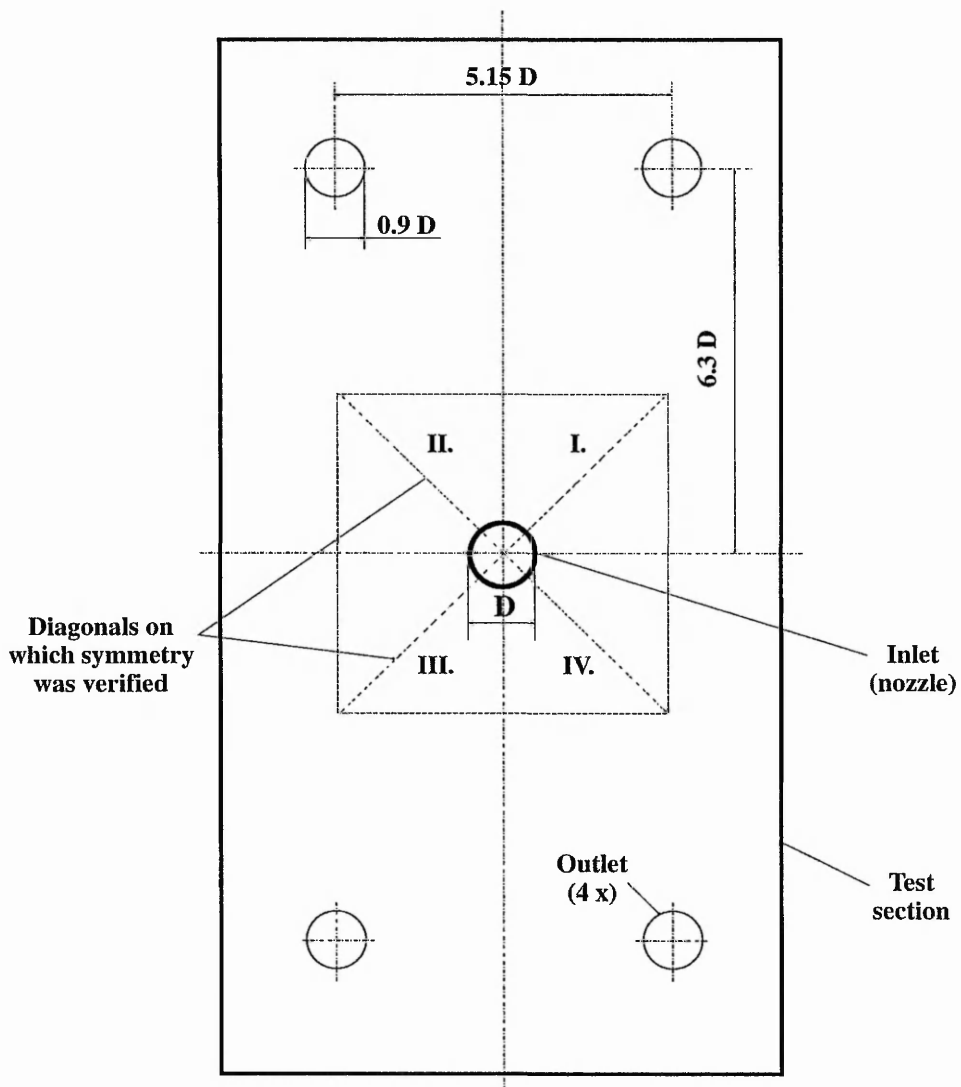


Figure 3.19. Front view of the test section.

It can be seen from the graph that, within the stated experimental uncertainties, the curves for the radial velocity show almost identical behaviour in all four quadrants. Similar trends are found for the axial velocity component which diminishes to almost zero outside the stagnation region where the flow is dominated by the characteristic wall jet. Almost identical trends were observed for the case of water and  $Re=2,000$  and are shown in Figure 3.21.

It was concluded that the flow is sufficiently symmetric and that effects of the outlets and the radial walls on the region of interest are negligible.

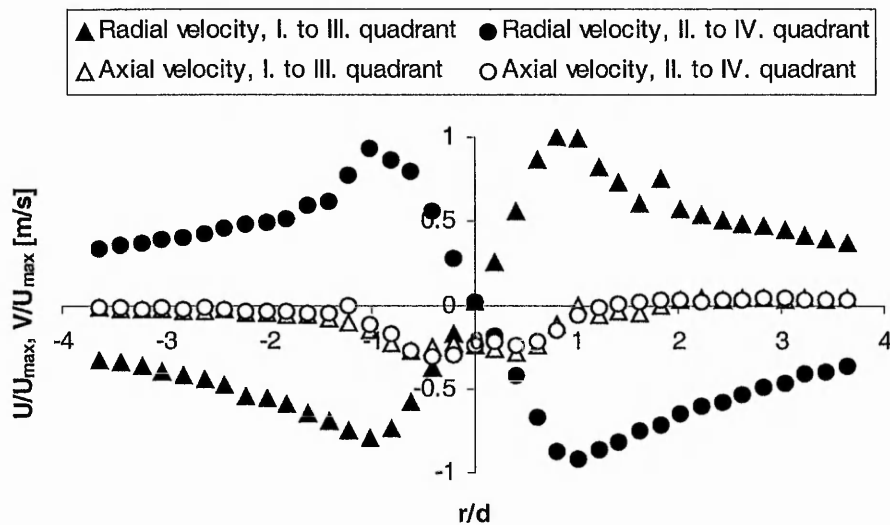


Figure 3.20. Flow symmetry along the impingement surface,  $Re=20,000$  and  $Pr=0.71$ .

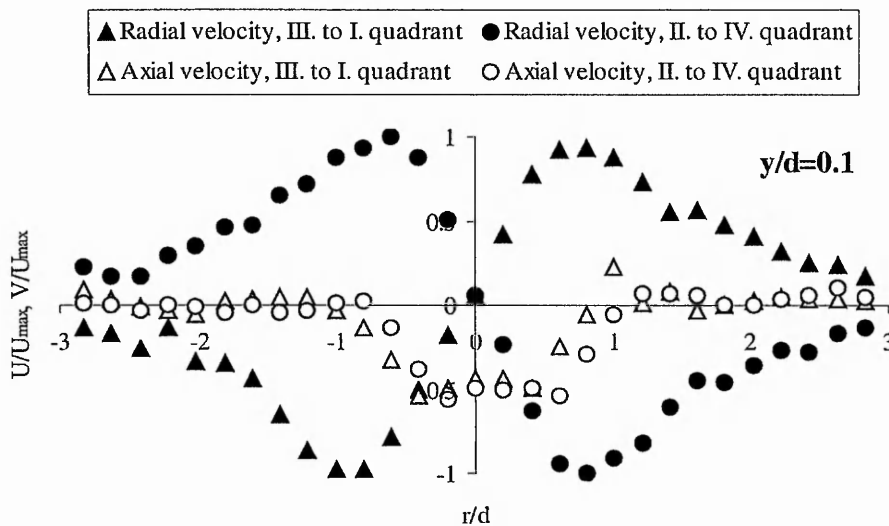


Figure 3.21. Flow symmetry along the impingement surface,  $Re=2,000$  and  $Pr=8$ .

### 3.6.4 Measurement procedure

Prior to each measurement, the position of the measurement volume was established using the routine as described in Section 3.6.1.4. The centrifugal pump and the air blower were allowed to run for at least one hour before measurements were taken. Measurements in the flow were performed at seven radial positions ( $0 \leq r/d \leq 2.5$ ), orthogonal to the impingement surface ( $0 \leq y/d \leq 1.35$ ). An axial measurement path was

then divided into four sections to adapt the number of measurement points, the measurement interval and the photomultiplier high voltage to the local flow conditions (i.e. near the wall and at the edge of the jet). A schematic diagram of the measurement locations is given in Figure 3.22.

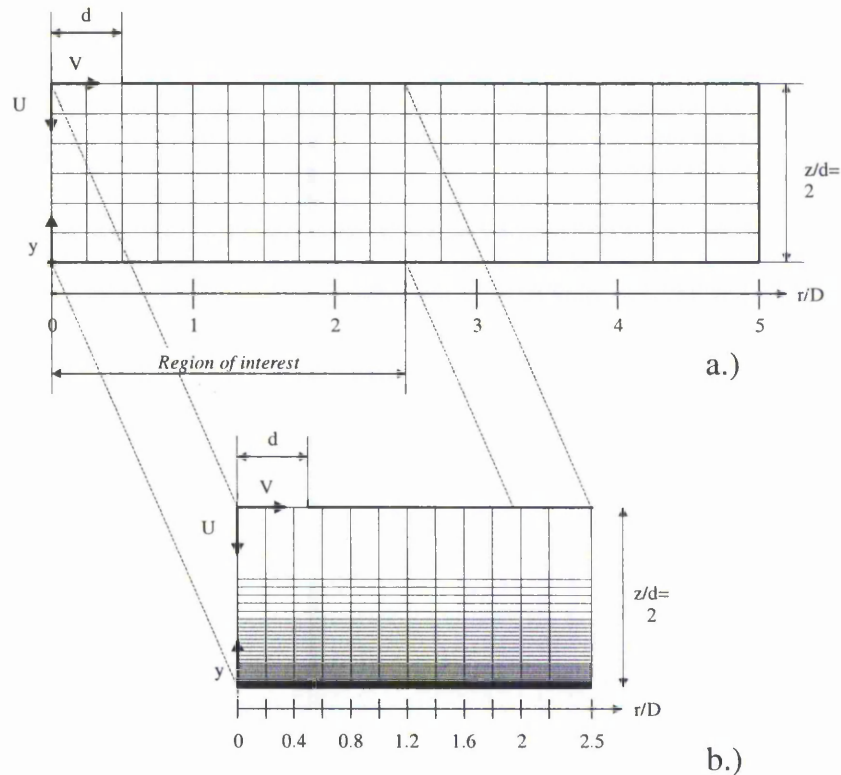


Figure 3.22. Schematic diagram of the measurement locations for the experimental investigation. a.) coarse mesh, b.) fine mesh.

Before and after visiting each section, the nozzle exit velocity on the centreline of the jet was measured to ensure steady conditions and to determine the factor against which the data were normalised. For every measurement point, the position of the probe as mounted on the traverse mechanism was manually checked with a ruler for its exact position.

### 3.7 Concluding remarks

The design and development of the experimental test facilities, their validation and the corresponding procedures adopted for flow visualisation, laser-Doppler Anemometry and liquid crystal thermography have been described in detail. The quantitative and

qualitative flow visualisation investigation has been outlined. The principal set-up of the laser-Doppler Anemometry system, the seeding, the influence of the window surface, the positioning of the measurement volume and the measurement of the statistical moments of the flow have all received particular attention.

The experimental uncertainties in the mean axial velocity, mean radial velocity, axial turbulence intensity, radial turbulence intensity and the shear stresses are estimated to be less than 5.7%, 6.0%, 8.5%, 8.8% and 14.8%, respectively. Uncertainties are lower in air than in water due to the intrinsic disadvantages of the backscatter mode in terms of signal quality for low flow velocities.

Based on a detailed uncertainty analysis among the three most widely used boundary conditions, the transient wall heating technique was selected for the heat transfer tests. This technique has been explained along with its careful selection of the experimental parameters that are necessary to ensure low levels of uncertainty. The heat transfer coefficients for air are estimated to have uncertainties of less than 10.2%.

## **Chapter 4**

### **Numerical investigation**

#### **Introduction**

This Chapter describes the numerical investigation that was performed in order to simulate the impingement flow. The standard high Reynolds number  $k$ - $\epsilon$  turbulence model embodied in the commercially available computational fluid dynamics (CFD) package ANSYS/FLOTRAN was used. In order to accurately compare findings from the experimental investigation with the numerical results, the geometry of the test section was modelled by employing a three-dimensional grid. The great flexibility in mesh building, offered by the finite element method, was exploited to create 'wedge-shaped' elements near the wall that maintained the non-dimensional thickness of the viscous sublayer in excess of the minimum value. For this geometry, the grid specification, boundary and initial conditions and the computational procedures employed to obtain a converged solution are described.

#### **4.1 Previous work**

In the following, numerical studies of impinging jets relevant to the present study are presented. Despite its inherent weakness of assuming local isotropy, recent works have successfully employed the  $k$ - $\epsilon$  turbulence model for predicting flow fields and heat transfer beneath impinging jets. Examples include studies by Davies and Carter (1998), Ashforth-Frost and Jambunathan (1996), Morris *et al.* (1996) and Dianat *et al.* (1996) and are due to the model's numerical stability and low requirements on computational resources. Bradshaw (1996) pointed out, that even the most advanced turbulence models seem unable to predict the effects of streamline curvature, as in an impinging jet, accurately.

Computational grids can play a crucial role in accurate CFD simulations. Péniguel (1998) pointed out that grid generation constitutes a real bottleneck for most industrial studies as this step often requires up to 80% of the overall model development time. Kumar (1999) suggested the use of a flow consistent grid where the length scales are compatible with that of the flow. An alternative to this approach which gives the designer

more flexibility in creating the mesh more quickly, represents the finite element method, Shaw (1992). Since in the finite element method the numerical equations are produced from data at known points on the element, there is no restriction on how complex the geometry is shaped. This circumstance has found increased attention by researchers who applied the finite element method for computing flow situations in complex geometries. Rabbit (1997) used a three-dimensional finite element software package to validate several linear and non-linear k-ε turbulence models for the case of an impinging jet. Ross and Larock (1997) tested the finite element method in conjunction with various eddy-viscosity turbulence models and recommended the use of this numerical scheme for the computation of three-dimensional turbulent flows.

## 4.2 Governing equations

The description of the motion of steady, incompressible turbulent flow can be described by the continuity equation

$$\frac{\partial \bar{u}}{\partial x} + \frac{\partial \bar{v}}{\partial y} + \frac{\partial \bar{w}}{\partial z} = 0 \quad (4.1)$$

and the time-averaged Navier-Stokes equations. These equations of motion in three-dimensional Cartesian coordinates read, Schlichting (1979),

$$\bar{u} \frac{\partial \bar{u}}{\partial x} + \bar{v} \frac{\partial \bar{u}}{\partial y} + \bar{w} \frac{\partial \bar{u}}{\partial z} = -\frac{1}{\rho} \frac{\partial \bar{p}}{\partial x} + \nu \left( \frac{\partial^2 \bar{u}}{\partial x^2} + \frac{\partial^2 \bar{u}}{\partial y^2} + \frac{\partial^2 \bar{u}}{\partial z^2} \right) - \left( \frac{\partial \overline{u'^2}}{\partial x} + \frac{\partial \overline{u'v'}}{\partial y} + \frac{\partial \overline{u'w'}}{\partial z} \right) \quad (4.2)$$

$$\bar{u} \frac{\partial \bar{v}}{\partial x} + \bar{v} \frac{\partial \bar{v}}{\partial y} + \bar{w} \frac{\partial \bar{v}}{\partial z} = -\frac{1}{\rho} \frac{\partial \bar{p}}{\partial y} + \nu \left( \frac{\partial^2 \bar{v}}{\partial x^2} + \frac{\partial^2 \bar{v}}{\partial y^2} + \frac{\partial^2 \bar{v}}{\partial z^2} \right) - \left( \frac{\partial \overline{u'v'}}{\partial x} + \frac{\partial \overline{v'^2}}{\partial y} + \frac{\partial \overline{v'w'}}{\partial z} \right) \quad (4.3)$$

$$\bar{u} \frac{\partial \bar{w}}{\partial x} + \bar{v} \frac{\partial \bar{w}}{\partial y} + \bar{w} \frac{\partial \bar{w}}{\partial z} = -\frac{1}{\rho} \frac{\partial \bar{p}}{\partial z} + \nu \left( \frac{\partial^2 \bar{w}}{\partial x^2} + \frac{\partial^2 \bar{w}}{\partial y^2} + \frac{\partial^2 \bar{w}}{\partial z^2} \right) - \left( \frac{\partial \overline{u'w'}}{\partial x} + \frac{\partial \overline{v'w'}}{\partial y} + \frac{\partial \overline{w'^2}}{\partial z} \right) \quad (4.4)$$

The latter terms on the right-hand side of the equations describe the extra stresses due to velocity fluctuations produced by the turbulence in the flow.

In direct analogy to the transport of turbulent momentum, the time averaged *energy equation* reads, Kakaç and Yener (1995),

$$\bar{u} \frac{\partial \bar{T}}{\partial x} + \bar{v} \frac{\partial \bar{T}}{\partial y} + \bar{w} \frac{\partial \bar{T}}{\partial z} = \frac{\lambda}{\rho c_p} \left( \frac{\partial^2 \bar{T}}{\partial x^2} + \frac{\partial^2 \bar{T}}{\partial y^2} + \frac{\partial^2 \bar{T}}{\partial z^2} \right) - \left( \frac{\partial \overline{u'T'}}{\partial x} + \frac{\partial \overline{v'T'}}{\partial y} + \frac{\partial \overline{w'T'}}{\partial z} \right) \quad (4.5)$$

To solve the above set of equations for momentum and heat, the Reynolds stresses and the turbulent heat diffusion terms are approximated through the use of a turbulence model.

### **4.3 Closure of the averaged equations**

For the modeling of the turbulent flow, the standard  $k-\varepsilon$  turbulence model by Launder and Spalding (1974) was employed in this work. The main advantages of this model is its simplicity and low requirements on computational resources for complex geometries. The standard  $k-\varepsilon$  model's constants are obtained empirically. In a two-dimensional case study on impinging jets of different Prandtl numbers, Rüdél *et al.* (2000) compared the standard high Reynolds number  $k-\varepsilon$  model with the  $k-\varepsilon$  model based on renormalization theory (RNG) and found very close quantitative and qualitative agreement between the two. An exception to this was in the stagnation region where the RNG model predicted lower levels of  $k$ , thus reducing one of the main shortcomings of the standard  $k-\varepsilon$  model.

The  $k-\varepsilon$  model employs the concept of eddy-viscosity where the Reynolds stresses are treated as additional viscous stresses which are only a function of the mean velocity gradient, one turbulent length scale and one turbulent time scale, Bauer *et al.* (2000). One of the shortcomings of the eddy-viscosity concept for the use in stagnating flows is the assumption of isotropy, i.e. the Reynolds stresses are the same in all directions.

The equations (4.1) to (4.5) present fourteen unknowns but only five equations. To resolve this disparity in number between unknowns and equations, the kinematic eddy-viscosity is assumed to be linearly dependent on the mean rate of strain. This yields, in Cartesian tensor form,

$$\overline{u_i u_i} = \frac{2}{3} \delta_{ij} k - \nu_t \left( \frac{\partial \bar{u}_i}{\partial x_j} + \frac{\partial \bar{u}_j}{\partial x_i} \right) \quad (4.6)$$

where the turbulent kinetic energy  $k$  is

$$k = \frac{1}{2} \sum_i^{i=j} \overline{u_i'^2} \quad (4.7)$$

The reader is reminded here that  $k$  in the above equation is based on a three-dimensional numerical analysis while  $k$  from the experimental study was obtained using only a two-dimensional LDA system. For this reason discrepancies between numerical predictions and experimental results are expected.

The *turbulent* or *eddy kinematic viscosity* is

$$\nu_t = C_\mu \frac{k^2}{\varepsilon} \quad (4.8)$$

The turbulent heat transport is related to the temperature gradient through

$$-\overline{u_i' T'} = \frac{\lambda_t}{\rho c_p} \left( \frac{\partial \overline{T}}{\partial x_i} \right) \quad (4.9)$$

where  $\lambda_t/c_p$  is the *turbulent* or *eddy thermal conductivity*,  $\varepsilon_h$ . For turbulent flow, *Reynolds's analogy* connects the similar exchange mechanisms between momentum and heat transfer. The exchange coefficient for momentum  $\varepsilon_m$  is defined as  $\rho \nu_t$  so that the *turbulent Prandtl number* may be defined as

$$Pr_t = \frac{\varepsilon_m}{\varepsilon_h} \quad (4.10)$$

Values for  $k$  and  $\varepsilon$  are obtained from the modelled transport equations, Abbott and Basco (1989)

$$\frac{\partial k}{\partial t} + \overline{u_i} \frac{\partial k}{\partial x_i} = \frac{\partial}{\partial x_i} \left( \frac{\nu_t}{\sigma_k} \frac{\partial k}{\partial x_i} \right) + \nu_t \left( \frac{\partial \overline{u_i}}{\partial x_j} + \frac{\partial \overline{u_j}}{\partial x_i} \right) \frac{\partial \overline{u_i}}{\partial x_j} - \varepsilon \quad (4.11)$$

$$\frac{\partial \varepsilon}{\partial t} + \overline{u_i} \frac{\partial \varepsilon}{\partial x_i} = \frac{\partial}{\partial x_i} \left( \frac{\nu_t}{\sigma_\varepsilon} \frac{\partial \varepsilon}{\partial x_i} \right) + C_{1,\varepsilon} \frac{\varepsilon}{k} \nu_t \left( \frac{\partial \overline{u_i}}{\partial x_j} + \frac{\partial \overline{u_j}}{\partial x_i} \right) \frac{\partial \overline{u_i}}{\partial x_j} - C_{2,\varepsilon} \frac{\varepsilon^2}{k} \quad (4.12)$$

The following values of the empirical turbulence model constants have been used for the  $k$ - $\varepsilon$  model owing to their good agreement with jet flows and mixing layer flows, Launder and Spalding (1974):  $C_\mu = 0.09$ ,  $C_{1,\varepsilon} = 1.44$ ,  $C_{2,\varepsilon} = 1.92$ ,  $\sigma_k = 1.0$ ,  $\sigma_\varepsilon = 1.314$ ,  $Pr_t = 1.0$ .

#### **4.4 The wall function**

Near solid walls, where the Reynolds number tends to zero, the model required the application of universal velocity and temperature profiles. To bridge the viscous sublayer

where viscous and turbulent effects were significant, an empirical formula, called the wall function, was employed. The turbulent kinetic energy in the near-wall element is computed from the transport equation for  $k$ . The production and dissipation of the turbulent kinetic energy was assumed to be in local equilibrium in the wall adjacent element. Heyerichs and Pollard (1996) gave a detailed overview of existing wall functions and how they are implemented in the  $k$ - $\epsilon$  model. In the present study, the generation and dissipation terms over which the governing equations are integrated, were assumed constant throughout the near-wall cell.

The thickness of the viscous sublayer was defined through

$$y^+ = \frac{C_\mu^{1/4} \rho k^{1/2} \delta}{\mu} = \frac{\delta_{NW} \rho}{\mu} \sqrt{\frac{\tau_{NW}}{\rho}} \quad (4.13)$$

In the present study, the near wall nodes were placed outside the viscous sublayer,  $y^+ \geq 11.5$ . For these values of  $y^+$  the wall element effective viscosity was computed from

$$\mu_{\text{eff}} = \frac{\mu y^+}{\frac{1}{\kappa} \ln(E y^+)} \quad (4.14)$$

and the effective thermal conductivity from

$$\lambda_{\text{eff}} = \frac{C_P}{Pr_t} \frac{\mu y^+}{\left[ \frac{1}{\kappa} \ln(E y^+) + P_{fn} \right]} \quad (4.15)$$

where

$$P_{fn} = \frac{\pi/4}{\sin(\pi/4)} \frac{\left( \frac{A}{\kappa} \right)^{1/2} \left( \frac{Pr}{\sigma_1} - 1 \right)}{\left( \frac{Pr}{\sigma_1} \right)^{1/4}} \quad (4.16)$$

For  $y^+ < 11.5$ , these quantities become

$$\mu_{\text{eff}} = \mu \quad (4.17)$$

and

$$\lambda_{\text{eff}} = \lambda \quad (4.18)$$

## **4.5 Solution Procedure**

The partial differential equations governing the velocity and temperature field of a flow situation have to be digitised before being solved by a digital computer. The discretisation technique used in the present study is the *finite element* method.

The general finite element technique has established itself as the standard technique for structural analysis where stress and strain predictions in solids are sought. With the more general development of this method, the finite element technique has only recently emerged as a serious alternative to the more established finite volume method for use in complex flow problems. A detailed description of this technique is given in the standard reference on the finite element method for fluid applications by Zienkiewicz and Taylor (1991). The commercially available CFD-package used in the present study was ANSYS/FLOTRAN 5.2. A more detailed description of the features of this software package can be found in the ANSYS/FLOTRAN manual, Ansys (2000), so that only the most important features will be briefly given in the following sections.

The solution procedure commenced by splitting the computational domain into a finite number of elements, which were treated as separate sub-domains. The variation of the independent variable was approximated through a simple function over the element whereby a residual was defined to measure the errors. In the discretisation process the element matrices were formed, assembled and the resulting system solved for each degree of freedom separately using a segregated sequential solution algorithm. Galerkin's method of weighted residuals was employed to minimise the residuals to form the element integrals. In the *global iteration* process, the equations were solved in turn and subsequently the properties were updated. The advection term was handled using a Monotone Streamline Upwind Approach (MSU) to produce smooth and monotone solutions. For the mean velocity components the Tri-Diagonal Matrix Algorithm (TDMA), as described by Patankar (1980), was used while all other quantities such as pressure, temperature, turbulent kinetic energy and dissipation rate were solved using the preconditioned conjugate residual method, see Ansys (2000). To stabilise the solution, relaxation was applied to all parameters by the default values (temperature: 0.8, all other variables 0.5). Overall convergence of the segregated solver was measured through the convergence monitoring parameters which were calculated for each degree of freedom at

each global iteration. For a convergent solution, typically 20,000 sweeps were necessary which used about 144 hours of CPU-time on a PENTIUM 800MHz computer.

#### **4.6 Grid specification**

Since the flow at the nozzle exit was symmetric with respect to the horizontal and vertical centreline, only one quarter of the test section was modelled with the target plate being positioned at  $z/d=2$ . The flow was analysed under steady-state conditions in a Cartesian co-ordinate system. The size of the numerical mesh was selected based on the three-dimensional grid dependency study conducted by Barata *et al.* (1987) for an impinging jet with crossflow. The authors had found that the axial velocity profile is well predicted by both a fine mesh of 60x34x34 nodes and a coarse mesh of 30x17x17 nodes. In contrast to this, it was reported that the predicted radial velocity and turbulence levels were considerably improved by grid refinement. However, it was noted that even with the fine mesh the predictions of the Reynolds stresses close to the stagnation point are overpredicted due to the inapplicability of the turbulent viscosity assumption close to the target plate.

For the present study the computational domain was divided into two regions.

1. The actual region of interest where computational results will be compared with experimental results extends to a radial distance of 2.5 diameters from the stagnation point. A fine grid with 52 elements in the axial direction and 47 elements in the radial direction was employed. In the transverse radial direction, approximately 30 elements were used over the length of the region of interest, see Figure 4.1.
2. For the remainder of the domain, the focus was to simulate the effects of the confining geometry of the test section on the flow field. Therefore, a coarse grid was used that decreased in element number with increasing distance from the stagnation point. One exception to this represented the outlet where the grid was locally denser.

The computational domain had a total number of 116,350 elements which represented the highest number of elements that could be used with the computer storage available. The grid was non-uniform with finer grid spacings along the axis of the jet, at the edge of the jet and in the immediate vicinity of the target plate where large velocity gradients were anticipated. The solution was estimated to be grid-independent to within  $\pm 12.5\%$ .

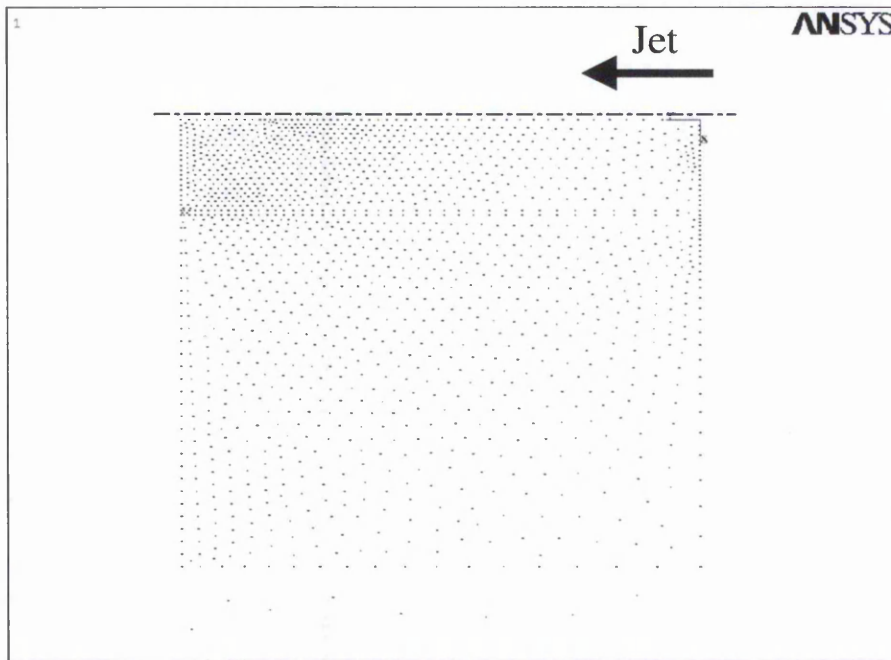


Figure 4.1. Computational grid.

The most critical criterion for successful turbulence flow modelling was the positioning of the near-wall node outside the viscous sublayer,  $y_t^+ > 11.5$ . In this context it should be mentioned that the reason for choosing the finite element method over the finite volume technique for this study was its greater flexibility in mesh building. The mesh generated by the finite difference/finite volume technique requires that the formation of the grid points is somewhat cuboid in a topological sense, Shaw (1992). For the case of an impinging jet, the maximum radial velocity is expected to occur at  $r/d \approx 1$ . However, since the non-dimensional thickness of the viscous sublayer,  $y^+$ , is a linear function of the flow velocity parallel to the wall, the value of  $y^+$  can be expected to decrease for  $r/d > 1$ . This was eliminated by arranging the near-wall nodes on a straight line with positive slope, thereby maintaining the condition of  $y_t^+ > 11.5$ . The computational domain is shown in Figure 4.2.

#### **4.7 Boundary and initial conditions**

The computational domain had six boundaries where dependent variable values were specified. The velocities at the four solid walls, namely the semi-confining plate, the

impingement surface, the lateral and bottom walls, were set to zero (non-slip condition). Furthermore, the turbulent kinetic energy,  $k$ , and the dissipation,  $\epsilon$ , were set to zero at the walls. The velocity and turbulence at the inlet were taken from measurements at the nozzle exit while the dissipation,  $\epsilon$ , was determined from

$$\epsilon_{\text{inlet}} = \frac{C_{\mu} k^{3/2}}{0.05R} \quad (4.19)$$

Figure 4.3 shows a plot of the turbulence parameters at the nozzle exit. At the outlet a zero pressure boundary condition was applied.

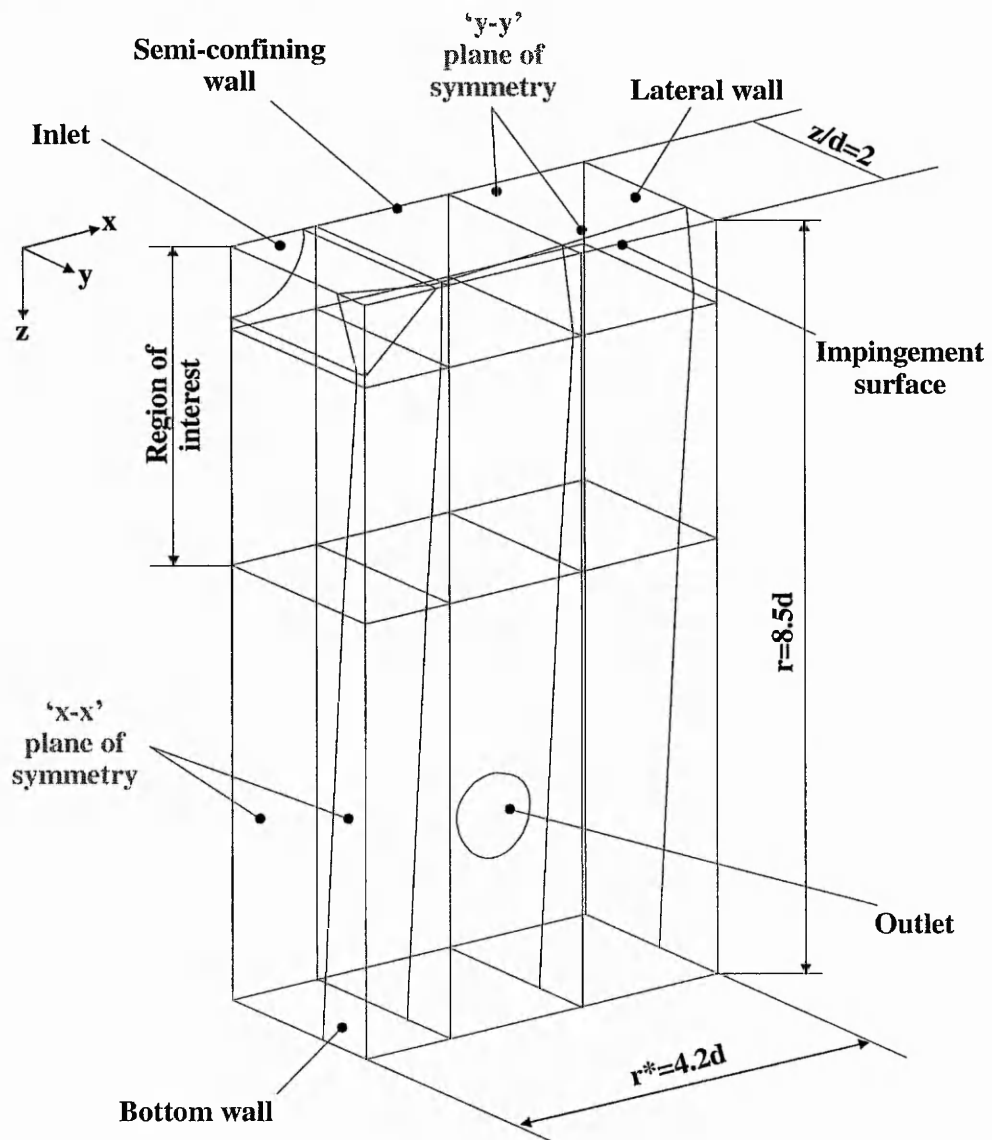


Figure 4.2. Three-dimensional computational domain.

Computations were performed at a nozzle exit Reynolds number of 10,000 with air as the working fluid. The fluid properties were allowed to vary so that the energy equation was solved even though heat transfer was not considered. The variation of the relevant fluid properties were accounted for by using ANSYS/FLOTRAN's internal fluid property tables.

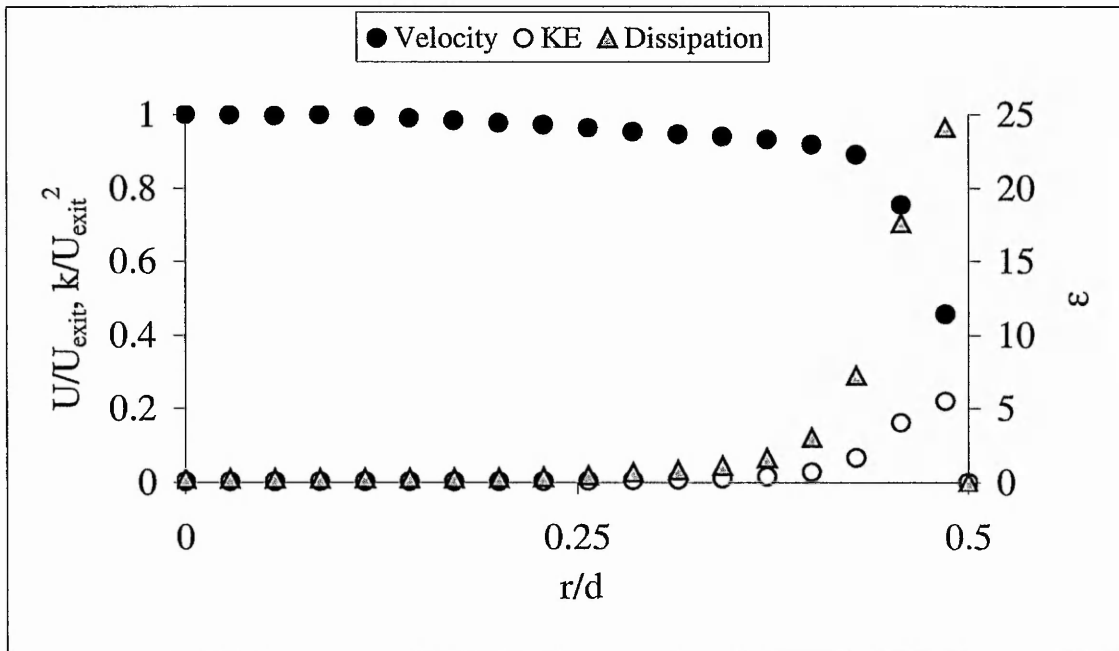


Figure 4.3. Inlet conditions at the nozzle exit for Reynolds number=10,000.

#### 4.8 Concluding remarks

The governing time-averaged equations of motion and their computation through the standard k-ε turbulence model have been presented. The three-dimensional grid, modelled to reproduce the geometry in the test section, has been discussed together with the measures taken to ensure that the near wall nodes are located outside the viscous sublayer. Furthermore, the initial and boundary conditions and the computational procedures to obtain a convergent solution have been described.

## **Chapter 5**

### **Presentation and Discussion of Experimental Results**

#### **Introduction**

Experimental results obtained from an investigation into the effects of near wall velocity and turbulence on the heat transfer distribution beneath semi-confined impinging jets of air and water are presented and analysed in this Chapter. Jets discharged from a round 35mm nozzle over a range of Reynolds numbers (2,000, 10,000 and 20,000) and impinged onto a smooth flat surface positioned two diameters away from the nozzle exit.

Some insight into the flow structure of the submerged impinging jet was obtained by performing full field flow visualisation. In a preliminary study, the temperature field was captured using liquid crystals as tracer particles. A selection of these results are presented in the first Section. The majority of this Chapter is dedicated to the presentation of new experimental near wall velocity and turbulence data for three different Reynolds numbers which have been obtained using laser-Doppler anemometry. Possible effects of turbulent flow structures on the heat transfer mechanism are investigated and presented in the second Section of this Chapter. To associate the turbulence flow data directly to the heat transfer characteristics of each working fluid, the evolution of the temperature field at two points along the jet centreline and on the impingement surface was determined on the same test facility. The observation of the time-dependent development of the surface isotherms using liquid crystal thermography allowed the heat transfer characteristics to be obtained quantitatively and qualitatively for air and water, respectively. Heat transfer data are presented in the third Section before finally, a brief summary of the main conclusions drawn from the experimental study closes the Chapter.

#### **5.1 Flow Visualisation**

##### **5.1.1 Flow field in the test section**

As part of the flow visualisation study, this Section quantifies the general flow field inside the test section induced by an impinging jet. The observed toroidal recirculation patterns represent a unique feature of submerged and confined jets and were also reported by Fitzgerald and Garimella (1998). Figure 5.1 and Figure 5.2 show vector

plots of the flow field and the recirculation zones for  $Pr=0.71$  at Reynolds numbers of 2,000 and 10,000, respectively. In both cases, the jet issues from the nozzle and travels towards the impingement plate where its direction is changed by  $90^\circ$ . The flow then develops into the typical wall jet, which is characterised by a region of maximum radial velocity. For the laminar nozzle exit conditions,  $Re=2,000$ , this region extends further into the free flow than in the turbulent flow. Flow vectors in the immediate vicinity to the impingement plate and the confining wall are shorter in length than those farther away from the wall and thus indicate a relatively thick boundary layer compared to  $Re=10,000$ . Generally, it can be seen that the flow field is much smoother than in the laminar case where the vector's directions seem to be spread more diffusely.

It becomes apparent from Figure 5.2 that the recirculating flow at the higher Reynolds number is transported back along the semi-confining plate towards the edge of the jet where it finally mixes with the incoming jet flow. This is in contrast to the slower flow field, depicted in Figure 5.1, which produces a recirculation pattern where the spent fluid appears to have less momentum so that the bulk of the recirculating flow mixes earlier with the incoming flow by impinging on the developing wall jet, approximately at  $r/d=0.5$  to  $1.5$ . The centre of the recirculation region moves radially outward and marginally closer to the target plate as the Reynolds number is increased. As the Reynolds number is increased from 2,000 to 10,000 the toroid moves radially outward from  $r/d=3.13$  to 4.41.

In all subsequent jet impingement heat transfer experiments, these recirculating vortices cause fluid cooled by the target plate to recirculate and become entrained into the impinging hot jet, thus reducing the temperature difference between the jet and target plate. This intense mixing has a contributing effect on the lower heat transfer coefficients obtained in confined jets relative to unconfined jets, see also Obot *et al.* (1992) and Ashforth-Frost (1994).

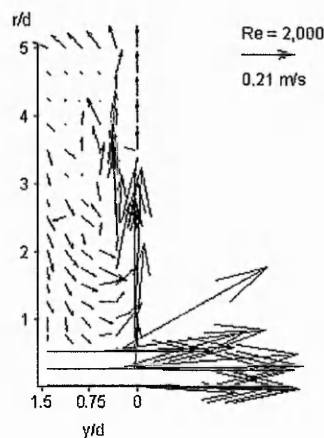


Figure 5.1 Vector plot of the flow field for  $Re=2,000$  and  $z/d=2$  ( $Pr=0.71$ ).

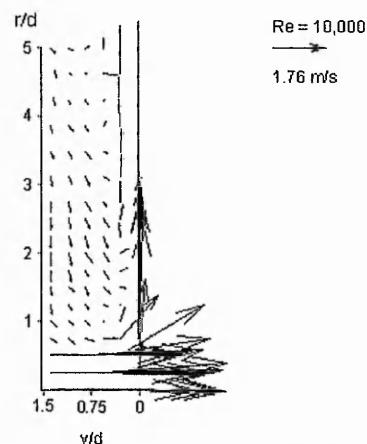


Figure 5.2 Vector plot of the flow field for  $Re=10,000$  and  $z/d=2$  ( $Pr=0.71$ ).

### 5.1.2 Quantitative flow visualisation

Results of a preliminary quantitative flow visualisation study using liquid crystals are presented below. The nature of the liquid crystal tracer technique allows the flow and temperature field to be visualised simultaneously. The impinging water jet ( $Pr=5.4$ ) was investigated at a mean Reynolds number of 35000 and  $z/d=3$ . The times given in Figure 5.3 to Figure 5.5 are measured from initiation of the test run while temperature information is inferred from the temperature-hue curve given in Figure 3.8. Details of the technique are provided in Ashforth-Frost and Rüdél (1998).

With the flat surface placed within the potential core, the hot jet ( $\equiv$ violet) issues from the pipe into the cold test section ( $\equiv$ dark red) and moves axially downstream (see Figure 5.3). The jet is exposed to a sudden temperature change, which reduces the temperature of the jet with distance from the nozzle exit. The jet develops and impinges on the cold surface where its direction is changed under the influence of the stagnation pressure. Along the wall, heat transfer is enhanced so that the temperature of the wall jet decays faster.

From Figure 5.4, the development of the wall jet can be observed. The separation point moves continuously downstream manifesting a thickening of the boundary layer. At  $r/d \approx 0.6$ , a temporary thinning of the wall bound flow is observed.

Figure 5.5 illustrates the path followed by the liquid crystals between the parallel plates. Due to entrainment of spent (i.e. already heated) fluid the space between the parallel plates is gradually heated. The separated flow field develops radially inwards by rolling back along the confining plate towards the centreline.



Figure 5.3. Impinging jet (elapsed time 0:99s).

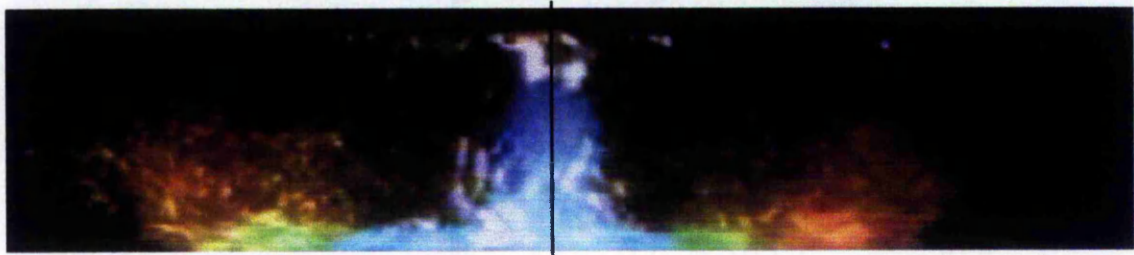


Figure 5.4. Impinging jet (elapsed time 1:09s).

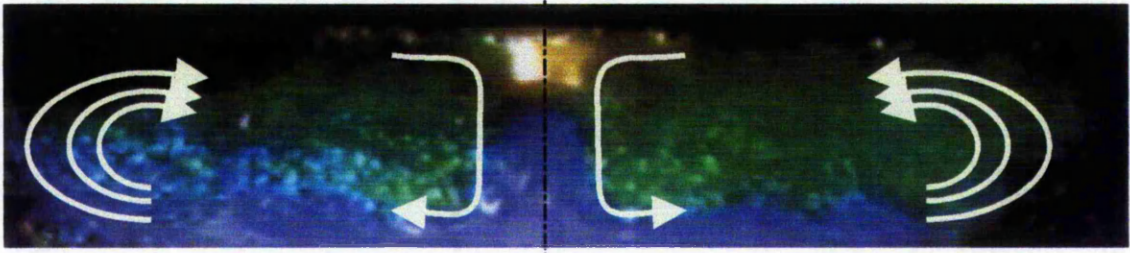


Figure 5.5. Impinging jet (elapsed time 7:51s).

### 5.1.3 Qualitative flow visualisation

The similarities in flow patterns at a nozzle-to-plate spacing of  $z/d=2$  for Prandtl numbers of 3.5 and 7 are shown in Figure 5.6 and Figure 5.7, respectively. Since the flow along the impingement plate is unsteady, the instantaneous exposure of the flow provides a pattern of streak lines. After issuing from the nozzle, the jet moves axially downstream in an ordered manner and is seen to be surrounded by a thin shear layer that is intrinsically unstable. The jet does not exhibit any well-formed vortex structures at its edge before striking the surface because the vortex structures have not had time to develop for this low value of  $z/d$ , Cornaro *et al.* (1999). Another explanation for the absence of any large-scale vortices at the edge of the jet is attributed to the low aspect diameter ratio of the contraction nozzle which prevents a flat velocity profile developing at the nozzle exit. Instead, the velocity profile is regarded as being intermediate between a flat velocity profile and a turbulent pipe flow profile. This will be further discussed in Section 5.2 and can be observed in Figure 5.18. Popiel and Trass (1991) stressed that large-scale discrete toroidal vortices can exist only in a jet issuing from a bell-shaped convergent nozzle. This was also shown by Kataoka *et al.* (1987b) and Landreth and Adrian (1990). For jets that issued from straight pipes, Ashforth-Frost (1994) and Cornaro *et al.* (1999) reported similar small vortices at the edge of the jet, as observed in the present study.

As the jet approaches the wall, the static pressure increases until it reaches a peak at the stagnation point. For  $Re > 10,000$  and small  $z/d$  ratios, this pressure distribution matches a Gaussian distribution, see Zumbrennen *et al.* (1990) for an impinging water jet and Colucci and Viskanta (1996) for an impinging air jet. Under the influence of this favourable pressure gradient the direction of the flow is changed through  $90^\circ$  and accelerates along the target surface. Observations of the flow revealed no radial

oscillating movement of the stagnation point which is in contrast to the findings of Ueda *et al.* (1997) for  $z/d=2$ .

After impingement, the pressure gradient helps to 'laminarise' the developing wall jet and the streamlines, in close proximity to the surface, appear almost parallel to the impingement plate. As discussed in the previous paragraph, the formation of small vortices at the edge of the jet are observed. These vortices are transported through the shear layer towards the impingement surface where they impinge at  $r/d=0.6$  to  $0.8$ . At this position, small circular vortex structures can be seen in both photographs and coincide with the location where the first isotherms during the heat transfer tests occurred. This is where the present study revealed a primary peak in the heat transfer profile, see Figure 5.60.

Both photographs in Figure 5.6 and Figure 5.7 reveal a region further away from the wall, where the flow appears as wavy streamlines between the convected vortices and the impingement surface. It is here, at approximately  $r/d \approx 2$ , where the present study and other researchers have reported secondary peaks in the local heat transfer profile. For example, Gardon and Akfirat (1965) for air and Garimella and Rice (1995) for FC-77.

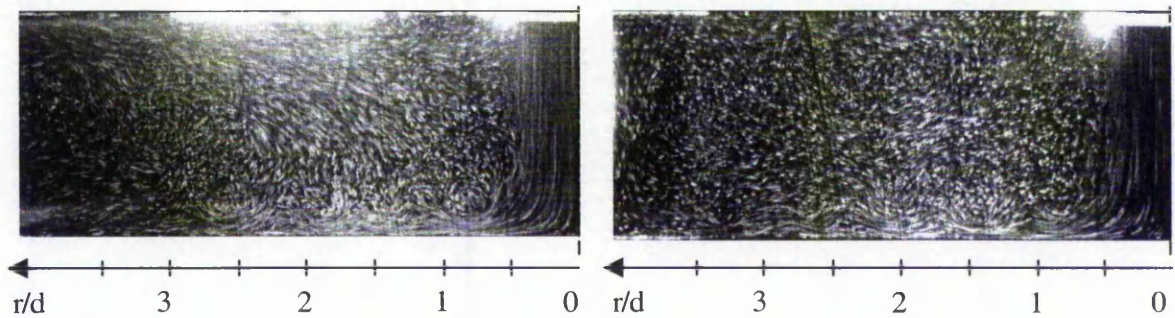


Figure 5.6 Impinging jet of  $Pr=3.5$  and  $z/d=2$   
( $\mu/\mu_{ref} = 0.54$ ).

Figure 5.7 Impinging jet of  $Pr=7$  and  $z/d=2$   
( $\mu/\mu_{ref} = 1$ ).

It is interesting to note that Meola *et al.* (2000), in a paper on the fluid dynamics of impinging air jets, observed instantaneous streakline fields that showed strong resemblance to the wavy streamlines from the present findings. However, the authors attributed this behaviour to flow separation at  $r/d \approx 1.2$  as a consequence of a thinning of the boundary layer at  $r/d \approx 0.6$ . The subsequent evolution of primary and secondary vortices in the wall jet region was swept away by the flow moving downstream and led to flow re-attachment at  $r/d \approx 2$ . When the mean velocity field was obtained by time averaging the instantaneous vorticity field, no significant mean vortical structures could be discerned.

Didden and Ho (1985) observed an unsteady separation of the wall jet boundary layer caused by secondary vortices which in turn is a direct consequence of the

impingement of primary ring vortices on the boundary layer. Despite the fact that in the present study vortical structures were seen to impinge on the developing wall jet, which transported them further downstream, no separating boundary layer flow was identified. In the further course of the study, this will be further examined for both fluids using LDA measurements.

Entrainment of spent fluid can be observed where the recirculating vortex transports fluid back towards the centre of the jet. For the two Prandtl-number photographs shown above, the centres of the toroids are at almost identical radial and axial positions, 6.4 and 2.4, respectively. Over the studied Prandtl-number range ( $0.71 \leq Pr \leq 8$ ), no shift in the centre of the recirculation vortex becomes apparent.

For the same Reynolds number,  $Re=20,000$ , Cornaro *et al.* (1999) reported an increase of the vortical structures along the impingement plate and at the jet edge when the non-dimensional nozzle-to-plate spacing was increased from 1 to 4. The case of  $z/d=6$  was studied in the present study but is not shown here as the dynamics of the flow field were difficult to capture via photograph. However, an increase in the dynamics of the vortical structures at the edge of the jet and the radial oscillation of the stagnation point were clearly identified.

During the LDA measurements, the flow field of the impinging water jet at  $Re=2,000$  was observed. Although results were not captured on video, the flow field showed strong similarity to the results for laminar air jets by Popiel *et al.* (1980). The flow in the immediate vicinity to the stagnation point was undisturbed and showed a gradual thickening in the developing stage of the wall jet. At  $r/d \approx 1.5$ , large scale coherent eddies were seen to evolve and quickly grow in size until a break-up was observed further downstream.

## **5.2 Results of the LDA investigation**

In this Section, velocity and turbulence measurements are presented to describe the flow field and the near wall flow phenomena of impinging jets of air and water. The temperature difference between the issuing jet and the fluid in the section was maintained at  $<0.2^\circ\text{C}$ . Firstly, results for water and air are presented individually. Secondly, water results are related directly with corresponding air data by plotting them on the same graphs. To begin with, a description of the velocity and turbulence profiles at the nozzle exit is given. The flow field is then characterised at seven radial positions along the impingement surface before results from measurements parallel to

the target plate are shown. The geometry was that of a semi-confined configuration where the target plate was placed two diameters from the nozzle exit. This distance was studied to identify differences in the physics of the flow which, at  $r/d \approx 2$ , have been reported to yield high *average* heat transfer coefficients due to the existence of secondary peaks in the radial heat transfer profile. The primary objective was to determine the effects of Prandtl number over a range of  $0.71 \leq Pr \leq 8$  on the flow field and the heat transfer of impinging jets.

All mean velocity data are normalised by the centreline velocity at the nozzle exit,  $U_{\text{exit}}$ . The turbulence intensity is defined as the ratio of the RMS of the fluctuating component of the respective velocity over the centreline velocity at the jet exit, see Cornaro *et al.* (1999). The axial (U) and radial (V) velocity components refer to their directions with respect to the jet centreline and are normal and parallel to the impingement plate, respectively.

### 5.2.1 Water results (Pr = 7.3 and 8)

In the following, flow field data for impinging water jets are presented. The data for  $Re=2,000$  and  $Re=10,000$  were obtained for  $Pr=8$  while a Prandtl number of 7.3 was maintained for  $Re=20,000$ .

#### 5.2.1.1 Axial velocity

The non-dimensionalised axial velocity profiles,  $U/U_{\text{exit}}$ , are shown in Figure 5.8 for seven radial positions,  $0 \leq r/d \leq 2.5$ . Data are presented as a function of the distance orthogonally from the plate,  $0.003 \leq y/d \leq 1.2$ . After issuing from the nozzle, the jet propagates towards the wall and is gradually decelerated as the effects of the target plate increase. Towards the shear layer at the edge of the jet,  $r/d=0.4$ , the axial velocity extends closer to the wall thus indicating a thinning of the boundary layer. After impingement, the axial velocity decays quickly along the surface. For  $r/d > 1.2$ , the axial flow component has diminished to less than 3% of its initial value at the nozzle exit flow field. An exception to this is the low Reynolds number case ( $Re=2,000$ ) where the axial velocity is preserved to 10% of its starting value until a distance of approximately 1.6 diameters away from the stagnation point.

It can be seen from Figure 5.8 that the effects of the target plate on the velocity decay, based on a 95% criterion, are most pronounced for  $Re=2000$  where this condition is satisfied at approximately 0.88 diameters from the wall. The two higher

○  $r/d = 0$    □  $r/d = 0.4$    △  $r/d = 0.8$    ●  $r/d = 1.2$    ■  $r/d = 1.6$    ▲  $r/d = 2.0$    ◆  $r/d = 2.5$

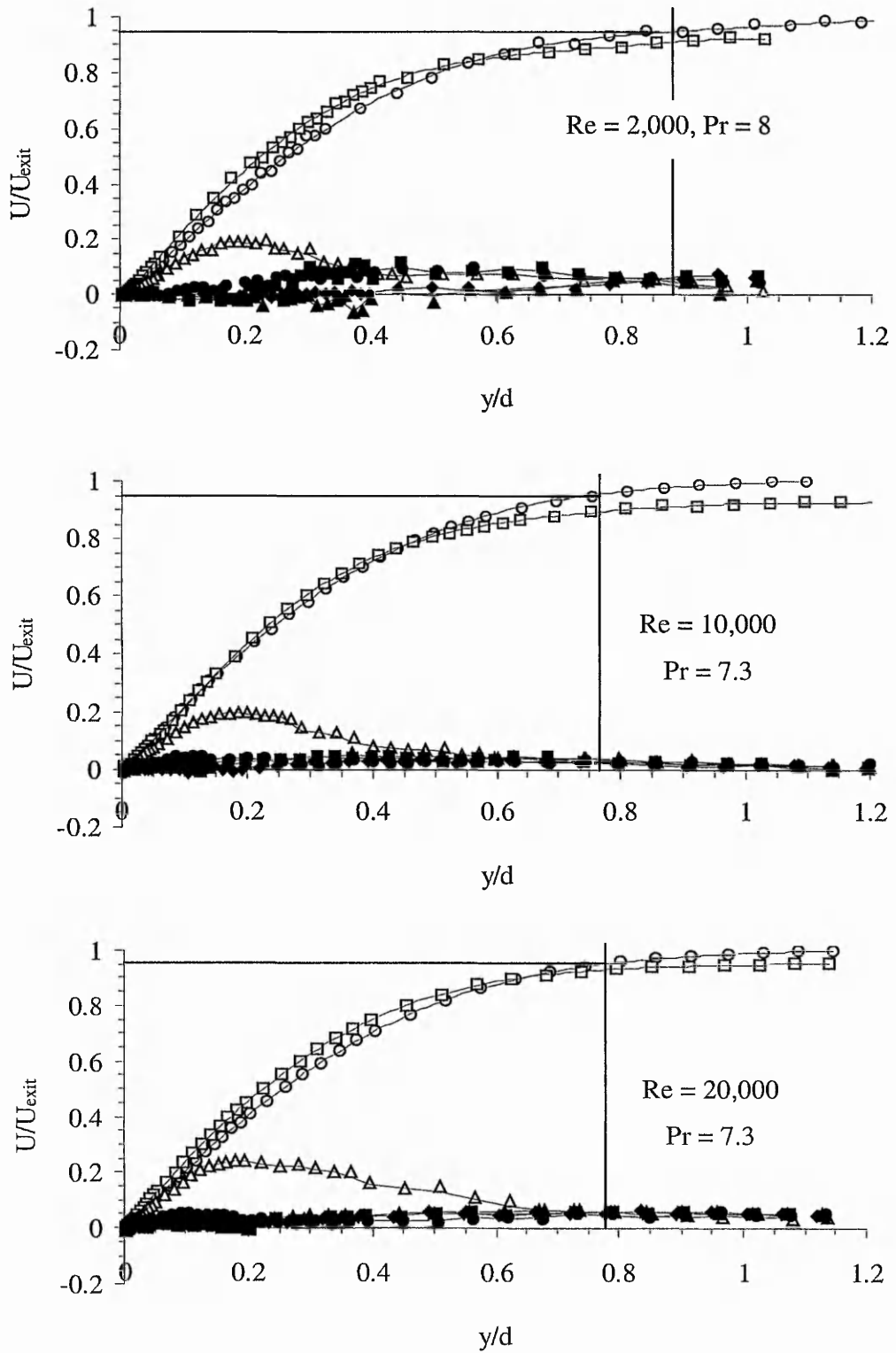


Figure 5.8. Axial velocity for various Reynolds numbers ( $Pr=7.3$  and  $8$ ).

Reynolds numbers are less affected by the damping effect of the wall in that the corresponding axial distances from the wall are approximately 0.76 diameters. Both these two cases show only little quantitative differences. This suggests that an increase in the Reynolds number from 2,000 to 20,000 results in a reduction of the effects of the target plate on the flow field.

The cases of  $Re=10,000$  and  $Re=20,000$  share the common feature of the centreline velocities at  $y/d > 1$  being marginally higher than the respective nozzle exit velocities. This is attributed to the confined geometry where surrounding fluid, that is returning from the far wall, is entrained back into the incoming flow thereby exchanging mass and momentum. As the width of the jet narrows, the axial velocity increases.

### 5.2.1.2 Radial velocity

The distribution of the radial velocity along the impingement surface is presented in Figure 5.9. The radial velocity,  $V$ , is normalised by  $U_{\text{exit}}$  and is shown as a function of the non-dimensionalised distance from the plate between  $y/d=0.003$  and  $y/d=1.2$ . On the centreline, where the axial velocity is maximum the contribution of the radial velocity component to the flow field is insignificant. With increasing distance from the stagnation point, the radial velocity increases rapidly to form the characteristic wall jet. With increasing distance from the stagnation point, the boundary layer thickens. This is shown as a shift of the peak away from the surface.

Since the mean flow field at  $Re=2,000$  extends the furthest into the free stream among the three considered cases, turbulence levels are expected to be greatest for this Reynolds number because the rate of supply of kinetic energy to the turbulence is proportional to the mean flow kinetic energy, Bradshaw (1971). This behaviour is associated with the position of the outlet holes with respect to the nozzle location.

The low Reynolds number jet produces a wall jet that is characterised by a steep initial velocity gradient at  $r/d \approx 0.8$  followed by a very strong deceleration. This 'spiky' velocity profile is in contrast to the smoother wall jet profile of the higher Reynolds number flows. As the Reynolds number increases, the wall jet preserves more momentum which can be seen from the radial profiles at  $r/d=0.8$ , 1.2 and 1.6 where the radial velocities exceed 78% of the nozzle exit velocity.

At a distance of  $r/d=2.5$ , the low  $Re$  number flow reaches only 30% of the initial nozzle exit velocity whereas at Reynolds numbers of 10,000 and 20,000, the attained peak values are 50% and 54% respectively.

○  $r/d = 0$    □  $r/d = 0.4$    △  $r/d = 0.8$    ●  $r/d = 1.2$    ■  $r/d = 1.6$    ▲  $r/d = 2.0$    ◆  $r/d = 2.5$

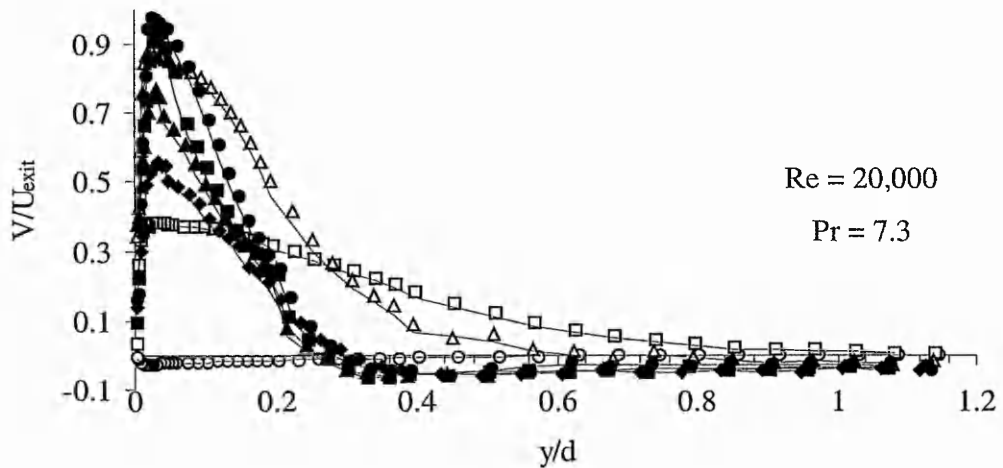
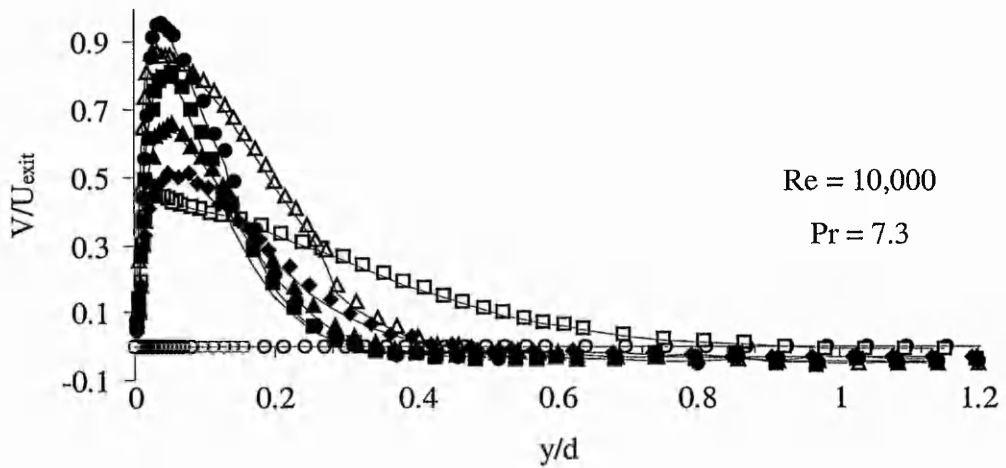
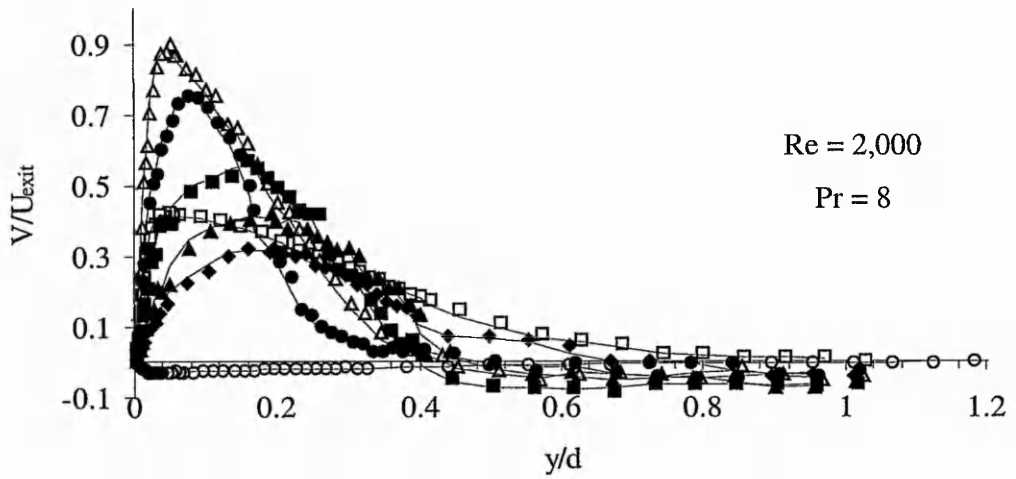


Figure 5.9. Radial velocity for various Reynolds numbers (Pr=7.3 and 8).

### 5.2.1.3 Axial turbulence

The distribution of axial turbulence,  $u'/U_{\text{exit}}$ , at radial positions  $0 \leq r/d \leq 2.5$  normal to the plate is shown in Figure 5.10. The root mean square value of the fluctuating velocity component has been normalised with respect to the mean velocity at the nozzle exit. All three Reynolds number cases have in common that the lowest levels of axial turbulence are found on the centreline. For  $r/d=0$  and  $Re=2,000$ , axial turbulence intensity of approximately 8.5% is preserved from the nozzle exit up to a distance of  $y/d \approx 0.4$ . This is in contrast to the higher Reynolds numbers, where the decrease starts at  $y/d \approx 0.24$  and  $y/d \approx 0.16$  for  $Re=10,000$  and  $Re=20,000$ , respectively. In the immediate vicinity of the wall, axial turbulence reaches a minimum. The consistency of the turbulence data at  $y/d=1.2$  can be validated for  $r/d=0$  and 0.4 by referring to turbulence levels obtained at the nozzle exit, see Figure 5.18 and Figure 5.20 in Section 5.2.3.1. As the shear layer at the edge of the jet is approached, radial turbulence levels rise. Outside the immediate region of impingement of the jet,  $0.8 \leq r/d \leq 2$ , the turbulence profiles develop a peak that moves closer to the wall as the radial position from the stagnation point increases.

When comparing levels of axial turbulence among the three Reynolds numbers, it can be seen that the highest turbulence levels occur for  $Re=2,000$  while the maximum values for  $Re=10,000$  and  $20,000$  decrease to approximately 16% and 13.5%, respectively. This is consistent with the vector plots shown in Figure 5.1 and Figure 5.2 where a more diffuse flow field was observed for  $Re=2,000$ . Higher turbulence levels at low  $Re$ 's were also found when the RMS fluctuating component was normalised by the local mean velocity,  $U$ .

The low Reynolds number case in Figure 5.10 is characterised by a gradual increase in the turbulence level to 20% at  $r/d=1.2$  which subsequently rises to a maximum value of approximately 29% at  $r/d=1.6$ . At  $r/d=2$ , the peak has maintained its value but has shifted further away from the surface. By  $r/d=2.5$ , the turbulence level has decreased to 15%.

While for  $r/d \leq 0.4$  turbulence features are almost identical for all three Reynolds numbers, differences in the development of axial turbulence become apparent for increasing distances away from the stagnation point in the form of rapidly increasing axial turbulence levels. This can be seen for  $Re=10,000$  where at  $r/d=0.8$  the turbulence level has reached almost 78% of its maximum value which is finally attained at  $r/d=1.6$ . A similar situation as for  $Re=2,000$  is encountered for  $Re=10,000$  since the same turbulence levels are observed for  $r/d=1.6$  and  $r/d=2$ . In contrast to  $Re=2,000$ , however, the wall jet at  $r/d=2.5$  displays still a relatively high turbulence level, namely 13.5%.

○  $r/d = 0$    □  $r/d = 0.4$    △  $r/d = 0.8$    ●  $r/d = 1.2$    ■  $r/d = 1.6$    ▲  $r/d = 2.0$    ◆  $r/d = 2.5$

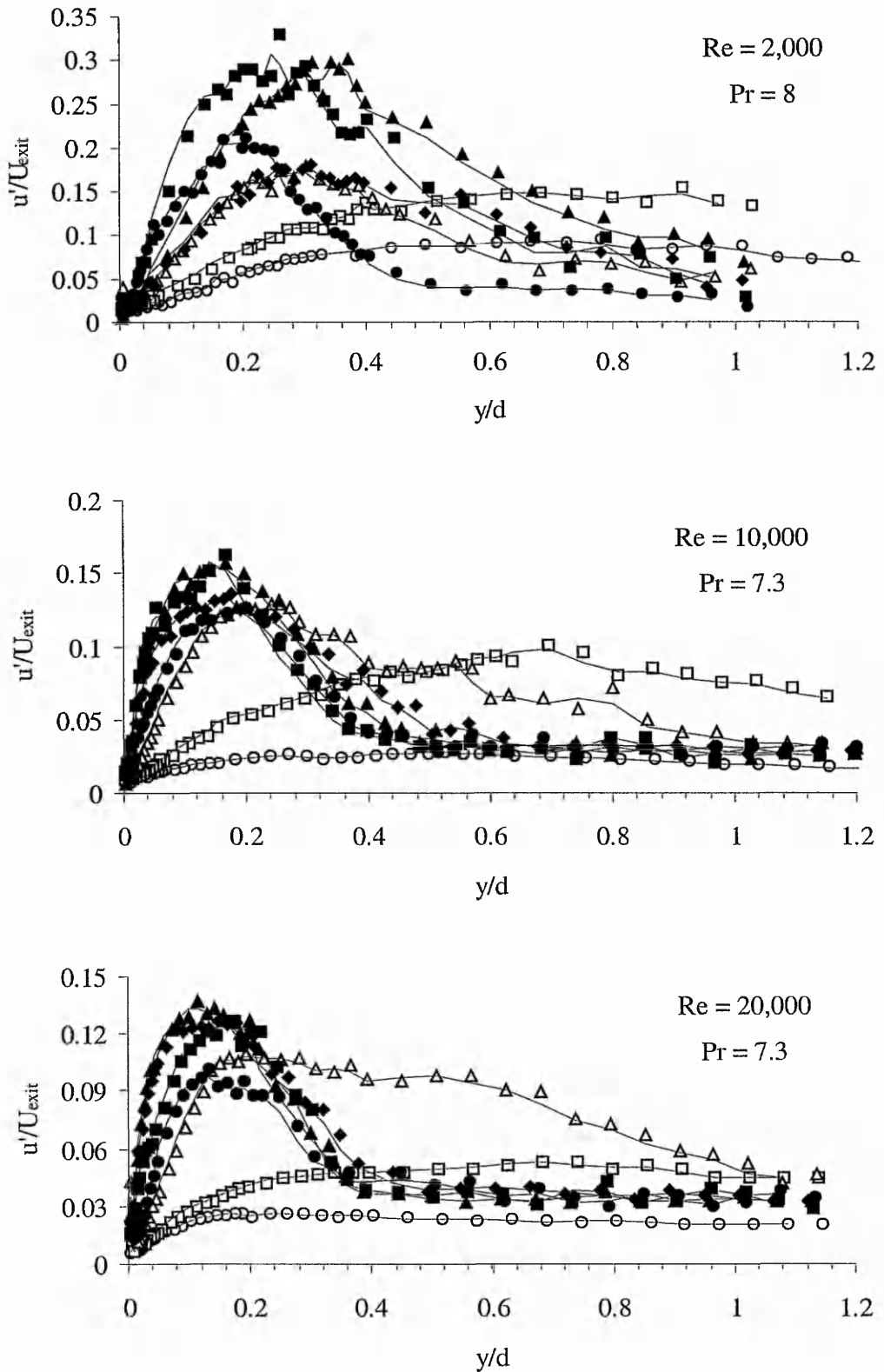


Figure 5.10. Axial turbulence intensity for various Reynolds numbers ( $Pr=7.3$  and 8).

The case of  $Re=20,000$  is different from  $Re=10,000$  in the way that the axial turbulence evolves along the impingement plate. At  $r/d=1.2$ , the turbulence level is almost identical to that attained at  $r/d=0.8$  but still has not reached its peak value. At  $r/d=1.6$ , the turbulence level is still growing and reaches its peak value at  $r/d=2$  whereby a shift of the peak towards the surface is observed. At  $r/d=2.5$ , the near wall flow is still dominated by relatively high levels of turbulence. Further details will be given in Section 5.2.3.2.

#### 5.2.1.4 Radial turbulence

The development of near wall radial turbulence,  $v'/U_{\text{exit}}$ , along the impingement surface for all three considered Reynolds numbers is shown in Figure 5.11. Data are plotted against non-dimensional distance from the wall in the range  $0.003 \leq y/d \leq 1.2$ . On the centreline of the jet, the turbulence generated at the nozzle exit is transported towards the impingement surface where it decreases before reaching a local peak in the immediate vicinity of the wall. This rise in radial turbulence near the wall is in contrast to the variation of the axial turbulence and could be attributed to the errors caused by the finite length of the LDA measurement volume and near wall reflections, see also Ashforth-Frost (1994). For  $r/d > 0.4$ ,  $v'/U_{\text{exit}}$  continues to rise as the wall jet develops with the maximum values being attained at  $1.6 \leq r/d \leq 2$ .

The low Reynolds number wall jet displays the highest level of turbulence intensity of approximately 25.5% at a radial position of  $r/d=1.2$ . It can also be seen that the near wall peak is shifted from  $y/d=0.03$  at  $r/d=1.2$  to  $y/d=0.05$  at  $r/d=1.6$ . Despite the fact that the steep turbulence gradients near the wall are preserved up to  $r/d=1.6$ , turbulence levels are beginning to fall rapidly for  $y/d > 0.082$ . By  $r/d=2$ , near wall peaks in the turbulence profiles have disappeared and the curves for  $r/d=2$  and  $r/d=2.5$  level off with increasing distance away from the target plate.

With increasing Reynolds number, the overall near-wall turbulence levels drop and display a shift of their peaks towards the wall. The most pronounced feature when approaching the wall is the local increase in radial turbulence followed by a 25% reduction at approximately  $y/d=0.04$  to  $y/d=0.08$ . In addition, a peak very close to the wall can be seen. This is consistent throughout the wall jet region and in contrast to the axial turbulence profiles.

The wall jet reaches a peak in radial turbulence at  $r/d=1.6$  when  $Re=10,000$ . Doubling the Reynolds number yields a slight reduction in the peak level and tends to shift the radial position where the peak level occurs. This is evident from the graph for  $Re=20,000$  where the maximum value can be seen at  $r/d=2$ .

○  $r/d = 0$    □  $r/d = 0.4$    △  $r/d = 0.8$    ●  $r/d = 1.2$    ■  $r/d = 1.6$    ▲  $r/d = 2.0$    ◆  $r/d = 2.5$

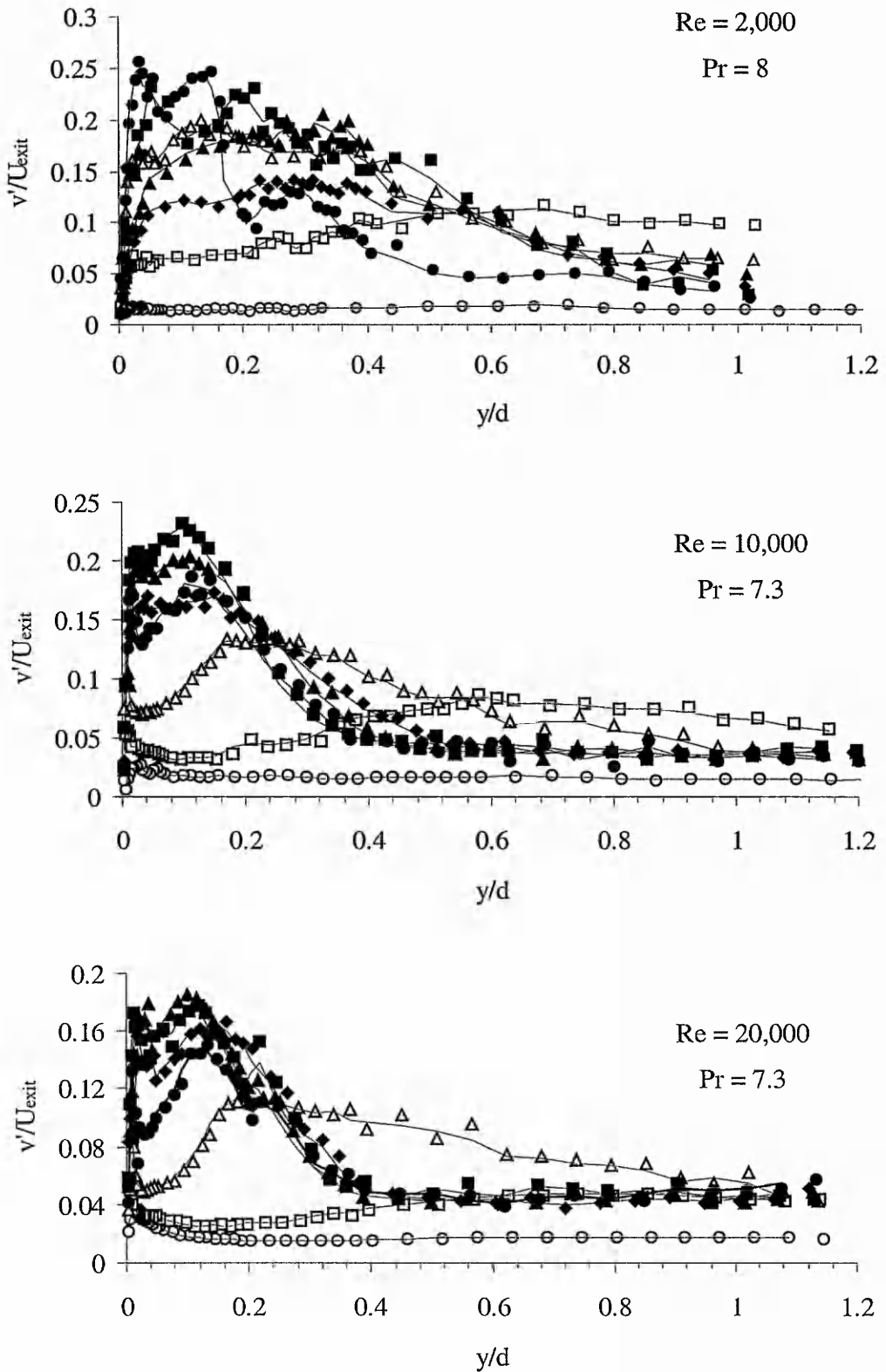


Figure 5.11. Radial turbulence intensity for various Reynolds numbers (Pr=7.3 and 8).

### 5.2.1.5 Reynolds stresses

In the following, the contribution of the turbulent motion to the mean stress in the form of shear stress is presented. Reynolds stresses play an important role in the transfer of mean momentum through turbulent motion. Measurements of the turbulent shear stress were normalised by the square of the nozzle exit velocity and are presented in Figure 5.12. The overall levels of the shear stress component confirm the findings from the axial and radial turbulence profiles, described in the previous Sections, in that the turbulence of the flow field decreases in magnitude as the Reynolds number increases. This is indicated by a decrease of the absolute maximum levels from 0.04 to 0.0115 for  $Re=2,000$  and  $Re=20,000$ , respectively.

For all Reynolds numbers, the shear stresses show zero values at the wall and non-zero values in the region between  $0.01 \leq y/d \leq 0.4$ . While the shear stresses are negligible on the centreline of the jet, their levels rise towards the shear layer, thus indicating that fluid is moving radially outwards. With increasing radial distance, the shear stresses assume negative values in the wall jet which indicates that fluid moves orthogonally away from the target plate. The peak in the turbulent shear stresses moves closer to the wall and further away from the stagnation point as the Reynolds number is increased.

At the low Reynolds number, the profiles are characterised by relatively large quantitative differences among them. The Reynolds stresses reach a maximum value  $1.6d$  away from the stagnation point, at  $y/d=0.21$ . While the radial turbulence profile reaches its peak further upstream ( $r/d=1.2$ ), the axial turbulence profiles peak in approximately the same region, between  $0.2 \leq y/d \leq 0.28$ . It appears therefore, that the Reynolds stresses are dominated by the course of the axial turbulence.

This trend continues for the case of  $Re=10,000$ , where the position of the peak level coincides with that of the axial turbulence profile at  $y/d=0.17$ . For  $Re=20,000$ , the peak levels also occur at the same location as the peaks of the axial turbulence profiles, approximately  $y/d=0.115$ . Since the radial levels display their peak closer to the wall, at  $y/d=0.11$ , and  $y/d=0.1$  for  $Re=10,000$  and  $Re=20,000$  respectively, this suggests that the peaks of the Reynolds stresses are closely related to those of the axial turbulence profiles if  $Re \geq 10,000$ .

○  $r/d = 0$    □  $r/d = 0.4$    △  $r/d = 0.8$    ●  $r/d = 1.2$    ■  $r/d = 1.6$    ▲  $r/d = 2.0$    ◆  $r/d = 2.5$

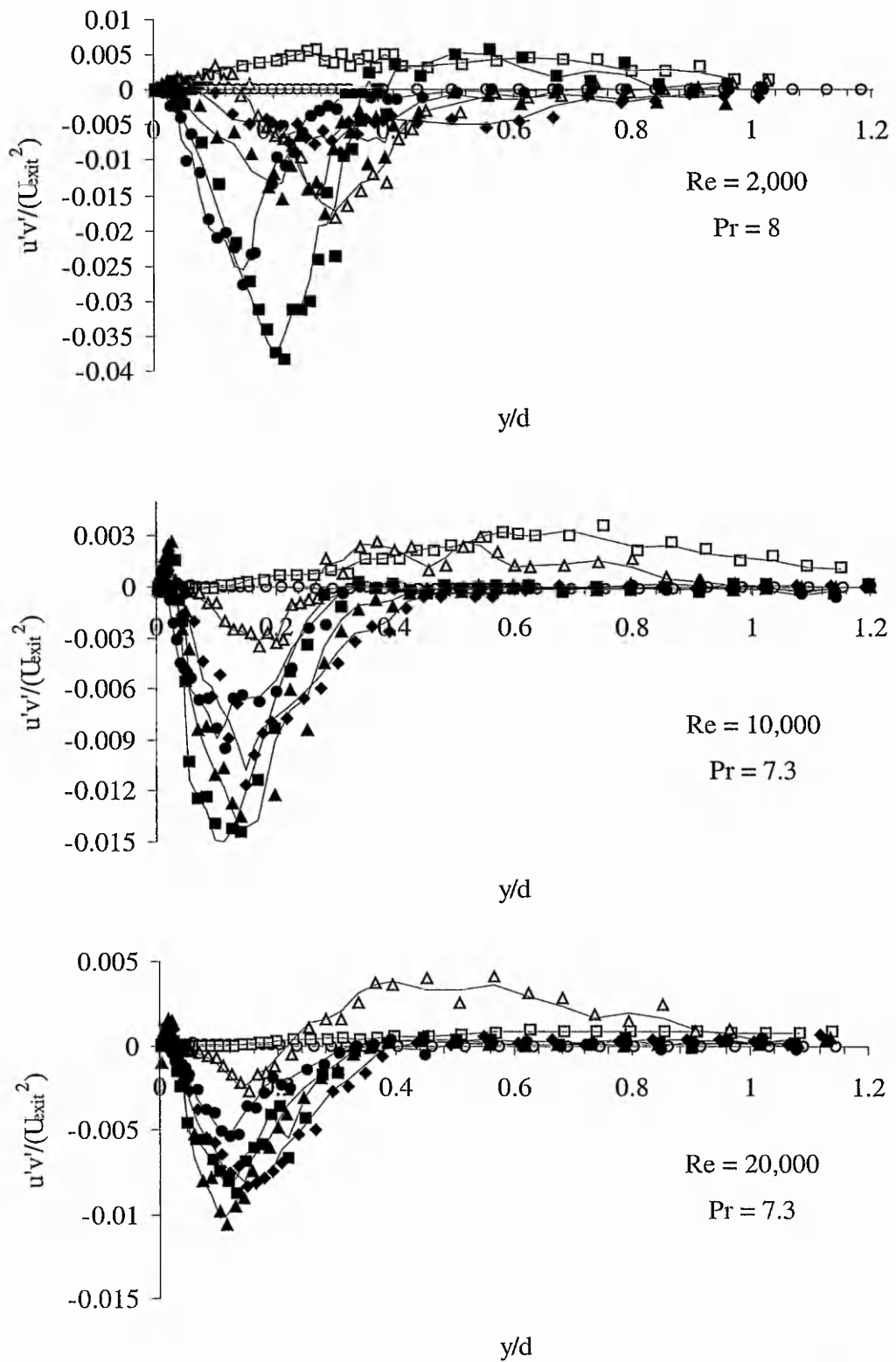


Figure 5.12. Turbulent shear stresses for various Reynolds numbers ( $Pr=7.3$  and  $8$ ).

## 5.2.2 Air results ( $Pr = 0.71$ )

In the following, LDA measurements of the flow field beneath an impinging air jet for Reynolds numbers of 2,000, 10,000 and 20,000 are presented. The fact that air jets have been subject to many experimental studies will be exploited to verify the results from the present study. However, no work could be identified that reported on the flow field of a confined jet resembling that in the present study. Ashforth-Frost (1994) studied a semi-confined jet that was formed from a fully developed velocity profile at the exit of the pipe. Cooper et al. (1993) characterised the flow field of an unconfined impinging air jet using a hot-wire anemometry technique. More recently, Dianat *et al.* (1996) and Kim et al. (1994) compared measurements of Reynolds stresses beneath unconfined impinging air jets with numerical predictions.

### 5.2.2.1 Axial velocity

The variation of the axial velocity profile for impinging air jets of  $Re=2,000$  and  $20,000$  is shown in Figure 5.13. Since the axial velocity profile for  $Re=10,000$  will be used in Chapter 6 to validate the results from the numerical model, it is omitted from presentation in the current Section. However, it will be seen that the profile closely resembles that of  $Re=20,000$ .

As the flow approaches the stagnation point, the wall affects the flow, based on a 95% criterion, at increasing values of  $y/d$  as the Reynolds number is increased. This indicates that with increasing Reynolds number, the distance downstream from the nozzle exit over which 95% of the nozzle exit velocity is preserved, decreases. It becomes evident that after impingement, where the axial velocity was transferred into radial momentum, both Reynolds numbers show different behaviours in the way the axial velocity declines along the wall. Throughout the wall jet region and in close proximity to the wall, the  $Re=2,000$  case shows no contribution of the axial velocity component to the wall jet but develops a local peak at approximately  $y/d \approx 0.4$  and  $r/d = 1.6$ . It can be noted that the same trend was observed for the corresponding water jet ( $Pr=8$ ). This suggests that the flow field can be divided into a *wall bound flow* dominated by a radially outwards directed velocity component and a *free stream flow*, which is strongly affected by the flow reversals and entrainment processes induced by the confining character of the test section. The axial velocity component of the high Reynolds number jet continues to decline steadily with increasing values of  $r/d$  which can be seen as a gradual decrease of the peaks close to the target plate. Eventually, at

$r/d=1.6$ , the axial velocity component has declined to such an extent that its value remains constant throughout the wall bound flow and the free stream flow.

○  $r/d = 0$    □  $r/d = 0.4$    △  $r/d = 0.8$    ●  $r/d = 1.2$    ■  $r/d = 1.6$    ▲  $r/d = 2.0$    ◆  $r/d = 2.5$

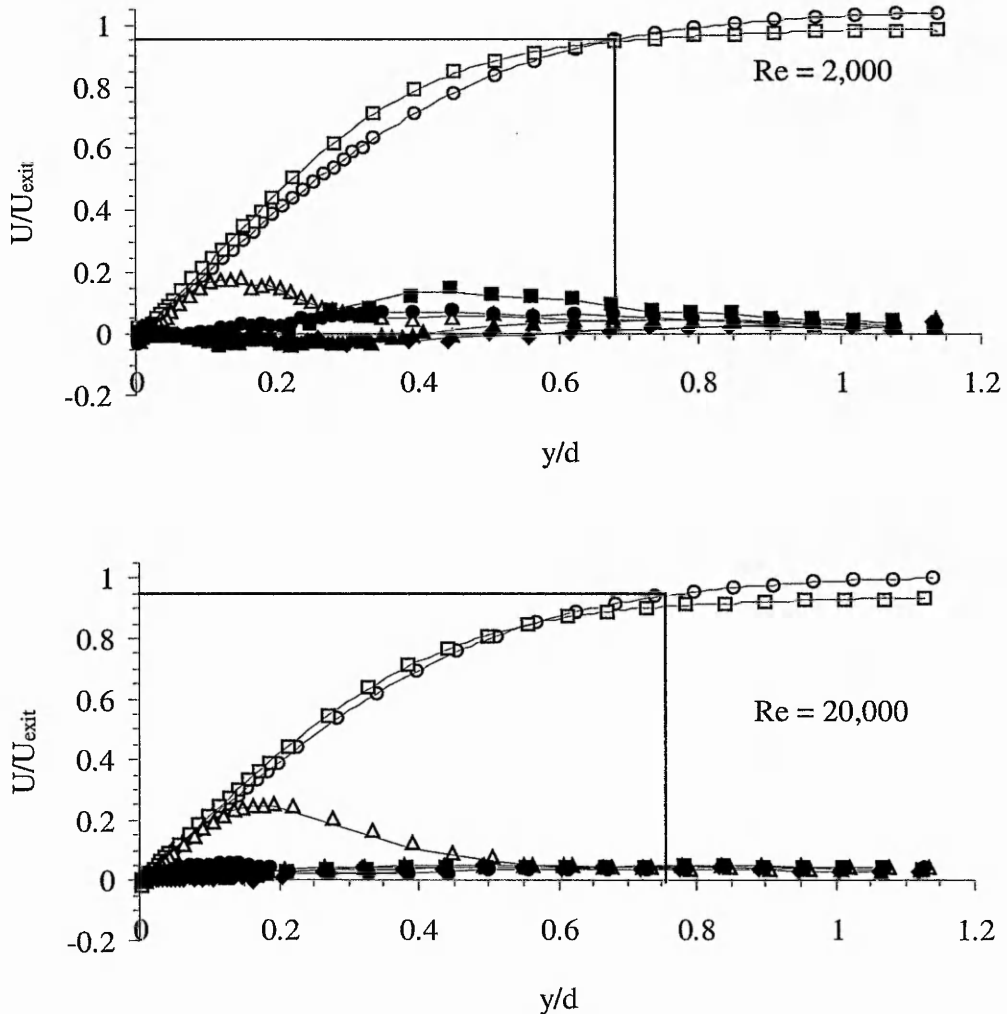


Figure 5.13. Axial velocity for  $Pr=0.71$  for various Reynolds numbers.

### 5.2.2.2 Radial velocity

The development of the wall jet,  $V/U_{exit}$ , is illustrated in Figure 5.14. Data are plotted against non-dimensional distance from the wall in the range  $0.003 \leq y/d \leq 0.4$ . At the stagnation point, the radial velocity component is zero but grows rapidly as the flow moves in the radial direction under the influence of a favourable pressure gradient. The extension of this static wall pressure region beneath a round air jet was identified by Ball (1998) to be  $r/d=1.35$ . For  $Re=20,000$ , the present study reveals that the peak of the radial velocity occurs well within this region, at  $r/d=1$ , and

compares favourably with the value reported by Ball (1998). It is interesting to note, that throughout the variation of the Reynolds number these peaks occur at the same radial position,  $r/d=1$ .

The velocity profiles for  $Re=2,000$  display shallow gradients for  $r/d>1.2$  with the peaks extending deep into the free stream flow, thus indicating a thickening of the boundary layer. In contrast, the  $Re=20,000$  case shows much greater confinement of the velocity peaks within the thin near wall layer. By  $r/d=1.2$  and  $Re=20,000$ , the wall jet has reached free stream conditions at  $y/d=0.3$ .

### 5.2.2.3 Axial turbulence

The distribution of axial turbulence,  $u'/U_{\text{exit}}$ , along the impingement surface is presented in Figure 5.15 as a function of non-dimensional distance from the wall,  $y/d$ . Measurements of the low Reynolds number flow reveal a highly diffuse distribution of turbulence along the wall jet, with the peak occurring at  $r/d=2$  and  $y/d=0.32$ . The overall turbulence level is reduced as the Reynolds number is increased while the radial position where the maximum turbulence level occurs remains unchanged. Both higher Reynolds number jets exhibit a more ordered distribution of axial turbulence in that their wall jets become constantly more turbulent as their distance from the stagnation point increases. The turbulence levels attain a peak value at  $r/d=2$  with the value of  $y/d$  being smaller for  $Re=20,000$  than in the case of  $Re=10,000$ . Similar quantitative and qualitative characteristics of the axial turbulence were found by Ashforth-Frost (1994).

While the axial velocity for  $Re=2,000$  shows a local maximum at  $r/d=1.6$  and  $y/d=0.44$ , the axial velocity fluctuation shows a distinct peak further downstream and closer to the wall,  $r/d=2$  and  $y/d=0.36$ , respectively. This confirms that a decoupling between axial velocity and axial turbulence exists.

○  $r/d = 0$    □  $r/d = 0.4$    △  $r/d = 0.8$    ●  $r/d = 1.2$    ■  $r/d = 1.6$    ▲  $r/d = 2.0$    ◆  $r/d = 2.5$

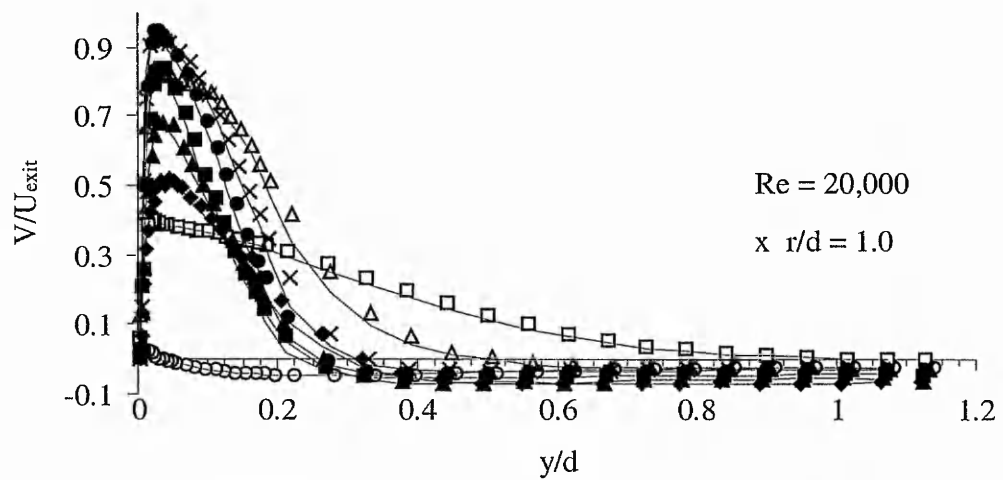
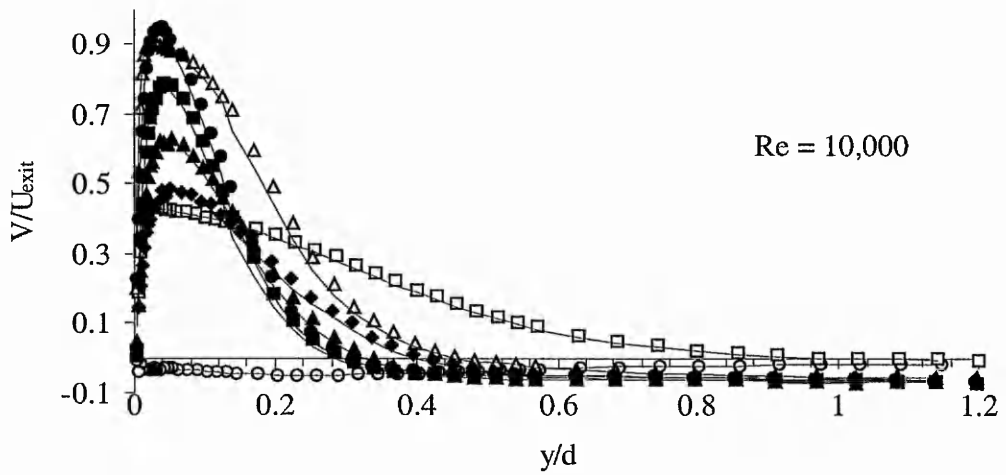
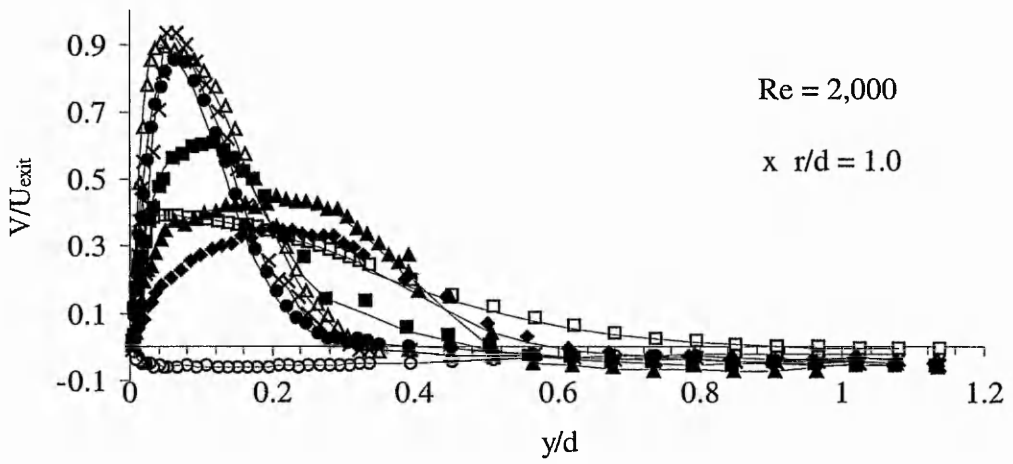


Figure 5.14. Radial velocity for various Reynolds numbers ( $Pr=0.71$ ).

○  $r/d = 0$    □  $r/d = 0.4$    △  $r/d = 0.8$    ●  $r/d = 1.2$    ■  $r/d = 1.6$    ▲  $r/d = 2.0$    ◆  $r/d = 2.5$

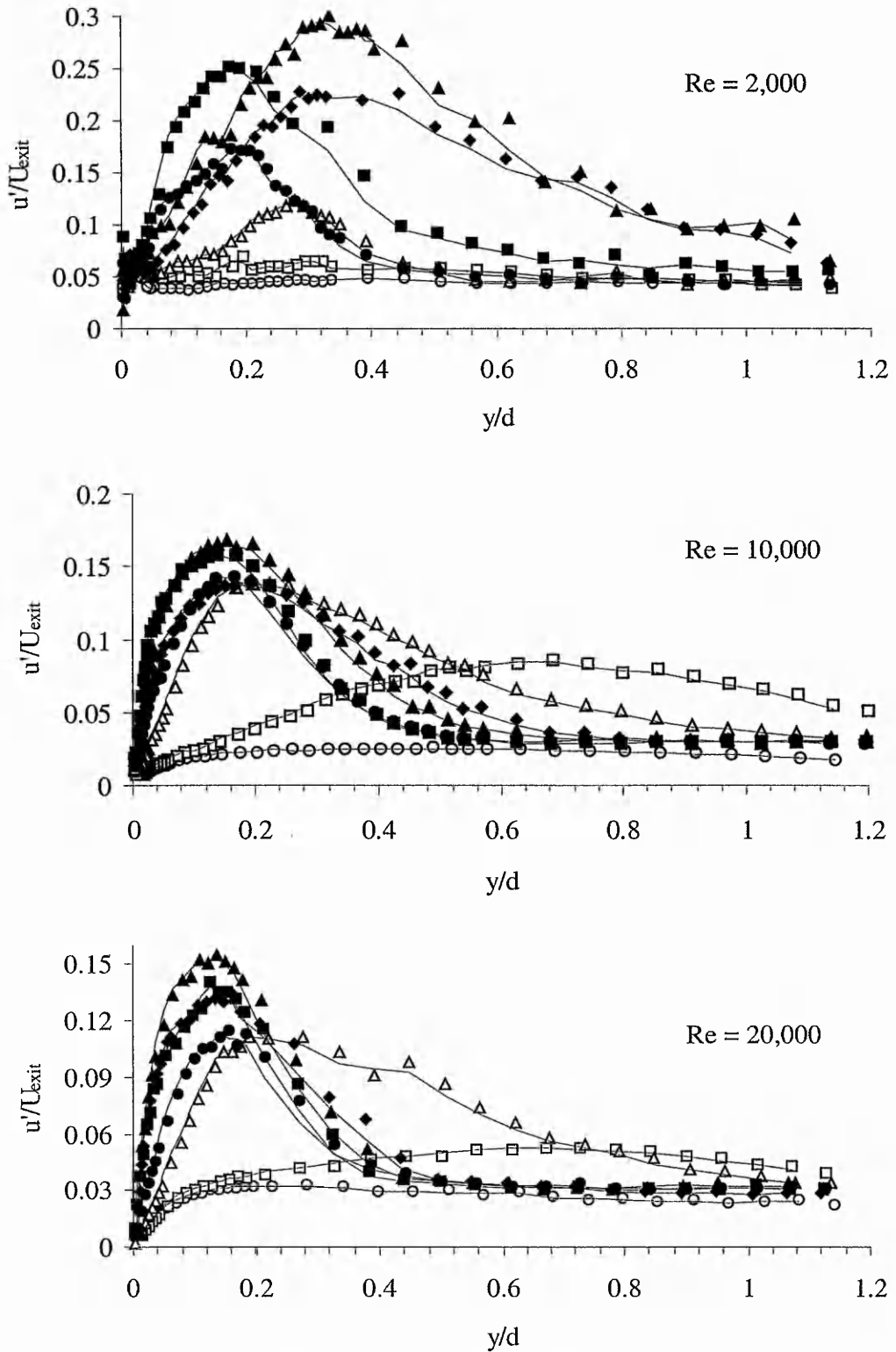


Figure 5.15. Axial turbulence intensity for various Reynolds numbers ( $Pr=0.71$ ).

#### 5.2.2.4 Radial turbulence

The development of radial turbulence,  $v'/U_{\text{exit}}$ , is presented in Figure 5.16. The fluctuating component normal to the surface is, on the whole, around 72% of the parallel component. This ratio represents a good means to check the reliability of measurement data in shearing flows over a smooth surface and is in accordance with a value of 60% suggested by Knowles and Myszko (1998) and 75% reported by Ashforth-Frost (1994). The trend of shifting peaks towards the wall as the Reynolds number increases was already noted for axial turbulence and is continued for the radial turbulence parallel to the wall.

#### 5.2.2.5 Reynolds stresses

Reynolds stresses,  $u'v'$ , for various Reynolds numbers are presented in Figure 5.17 and are normalised by the square of the nozzle exit velocity,  $U_{\text{exit}}^2$ . Similar trends were observed by Ashforth-Frost (1994) and Dianat *et al.* (1996). Both authors observed the highest levels of the Reynolds shear stresses at  $r/d=2$  which coincides with present results.

It is striking that, with the exception of the region near the jet shear layer and in close proximity to the wall, the sign of the shear stresses is negative throughout the Reynolds number range. This implies that for impinging air jets the direction in which mean momentum is transported through turbulent motion with respect to the wall, is independent of the nozzle exit conditions. For  $Re=2,000$ , this will be further discussed in Section 5.2.3.2.2.2.

○  $r/d = 0$    □  $r/d = 0.4$    △  $r/d = 0.8$    ●  $r/d = 1.2$    ■  $r/d = 1.6$    ▲  $r/d = 2.0$    ◆  $r/d = 2.5$

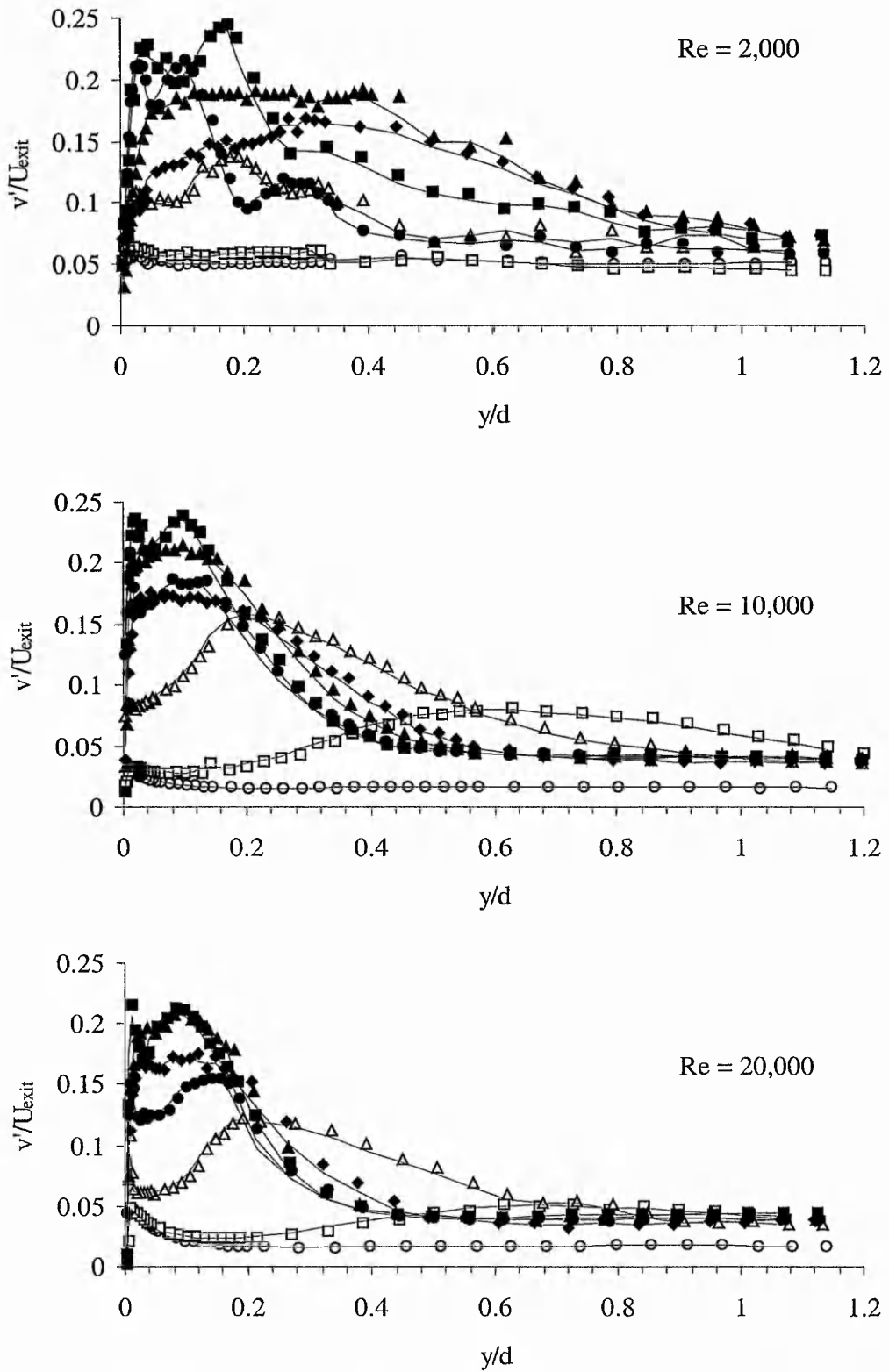


Figure 5.16. Radial turbulence intensity for various Reynolds numbers ( $Pr=0.71$ ).

○  $r/d = 0$    □  $r/d = 0.4$    △  $r/d = 0.8$    ●  $r/d = 1.2$    ■  $r/d = 1.6$    ▲  $r/d = 2.0$    ◆  $r/d = 2.5$

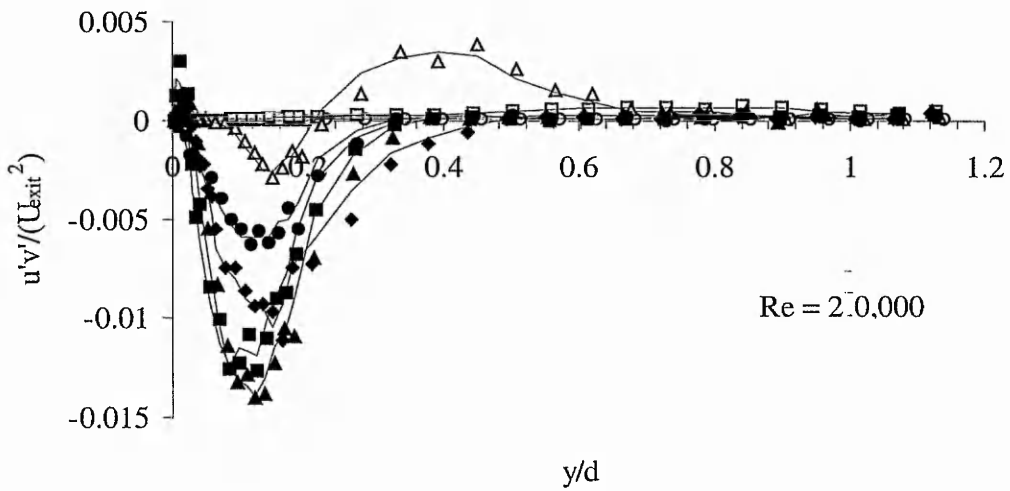
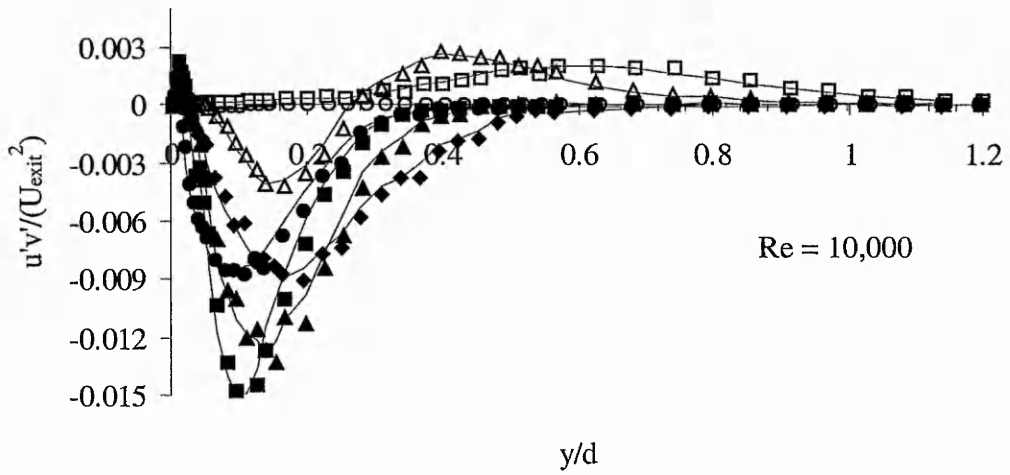
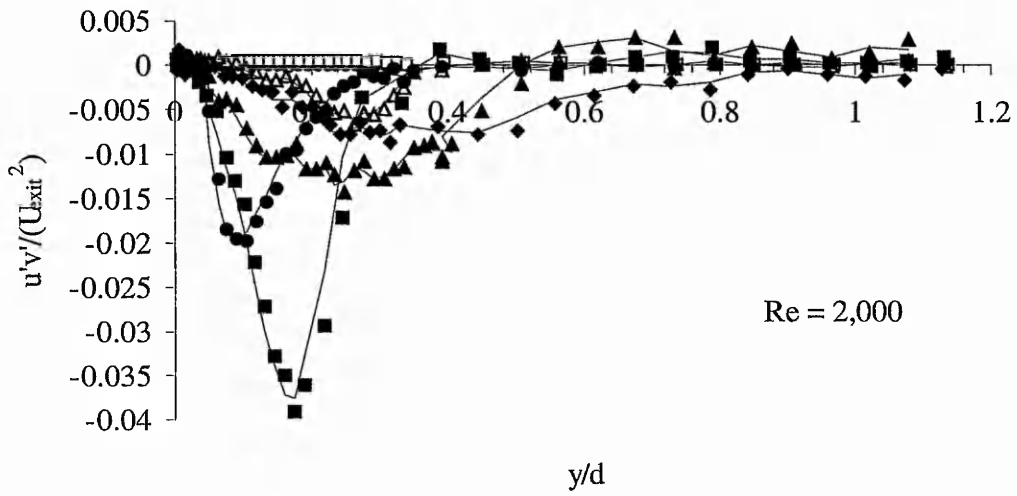


Figure 5.17. Turbulent shear stresses for various Reynolds numbers ( $Pr=0.71$ ).

### 5.2.3 Combined results ( $0.71 \leq Pr \leq 8$ )

In the previous Sections, Chapter 5.2.1 and 5.2.2, the respective hydrodynamic results of the flow fields generated by impinging water jets and air jets were individually presented. In this Section, velocity data of both working fluids are compared directly to easily identify Prandtl number effects. As the flow field beneath an impinging jet is a strong function of the initial flow conditions, the velocity profiles from the nozzle exit are shown first. Velocity data from measurements normal to the surface are presented along the target plate. This is followed by a characterisation of the near wall flow field along the impingement surface.

#### 5.2.3.1 Velocity profiles at the nozzle exit

##### 5.2.3.1.1 Exit profile for $Re=20,000$

To understand the dynamics of the flow and to clarify the evolution of the flow field it is necessary to quantify the distribution of the velocity and turbulence intensity at the nozzle exit. Furthermore, the effects of the turbulence management section on air and water flows can be assessed.

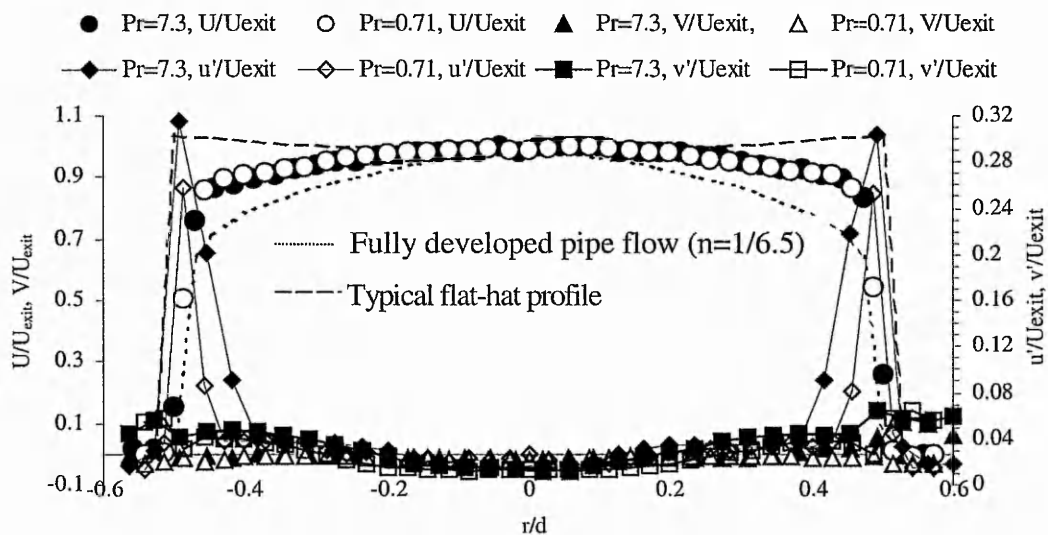


Figure 5.18. Velocity profiles at the nozzle exit ( $Re=20,000$ ).

Velocity profiles were obtained at a distance of  $0.5 d$  from the nozzle exit and are presented as ratios of streamwise velocity and RMS of the fluctuating component over the centreline velocity at the nozzle exit, see Figure 5.18. Both working fluids show identical characteristics in that the maximum is reached at the jet centreline with a monotonical and symmetrical decrease in the radial direction. Quantitative

discrepancies between the two fluids are minimal and are well within the estimated experimental uncertainty intervals. The surrounding boundary layer is very thin and produces axial turbulence intensity levels of 31% and 25% for water and air, respectively. In the radial direction, the turbulence levels are significantly lower, approximately 6%, and are therefore assumed to be only of minor significance for the further development of the flow field. It is interesting to note that in a recent paper, Cornaro *et al.* (1999) attributed the existence of large scale vortices at the edge of the jet to the level of turbulence intensity in the shear layer. The authors reported that well organized large vortex structures were not present for  $Tu > 14\%$  which corroborates the present findings of the flow visualization photographs in Figure 5.6 and Figure 5.7.

To demonstrate the intermediate nature of the nozzle contraction with its low area aspect ratio, typical profiles of fully developed pipe flow and of a ‘flat’ profile as used by Ashforth-Frost (1994) and Cho *et al.* (1998), respectively, are plotted on the same graph. Hung and Huang (1998) pointed out that parabolic and uniform velocity profiles at the nozzle exit not only differ in the jet spreading rate but also in the thickness of the boundary layer at the stagnation point. A parabolic velocity profile produces a thinner boundary layer at  $r/d=0$ .

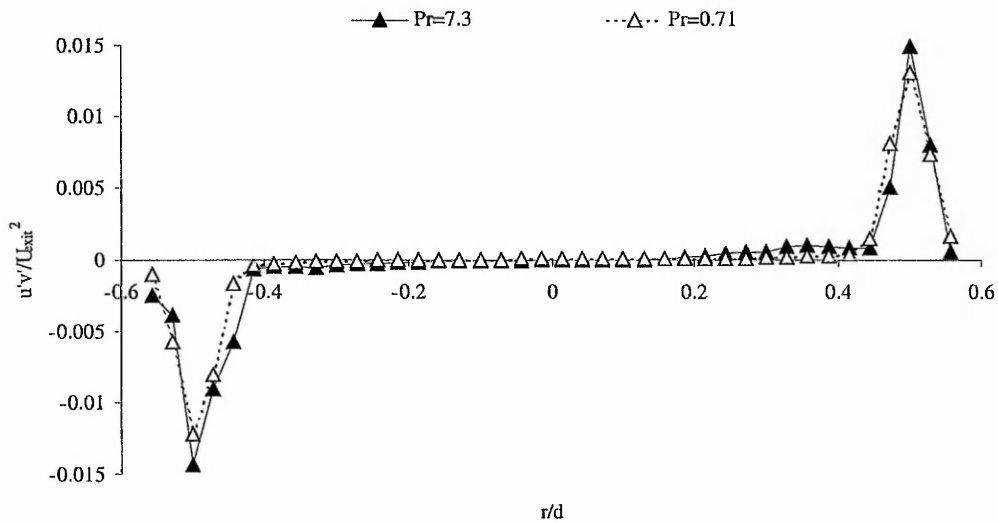


Figure 5.19. Reynolds stresses at the nozzle exit ( $Re=20,000$ ).

Both fluids have a zero level of Reynolds shear stress when the mean velocity reaches its maximum as is shown in Figure 5.19. Maximum shear stress occurs at about  $r/d=0.5$  and coincides with the position of maximum axial turbulence intensity.

5.2.3.1.2 Exit profile for Re=10,000

Figure 5.20 compares the mean velocity profiles for Pr=0.71 and Pr=8 together with the characteristics of turbulence intensity for Re=10,000. The peak values of the mean velocity occur on the jet centreline where the velocity gradients are approximately zero and the turbulence intensity show minimum values. In contrast, the relative maximum values of turbulence intensity are found at the edge of the jet where changes in velocity are the greatest. Here, turbulence levels for air and water are 16% and 18%, respectively. One further significant difference to Re=20,000 is the small difference in turbulence intensity between the axial and radial fluctuating velocity component; both fluids show discrepancies of less than 20% between these two directions.

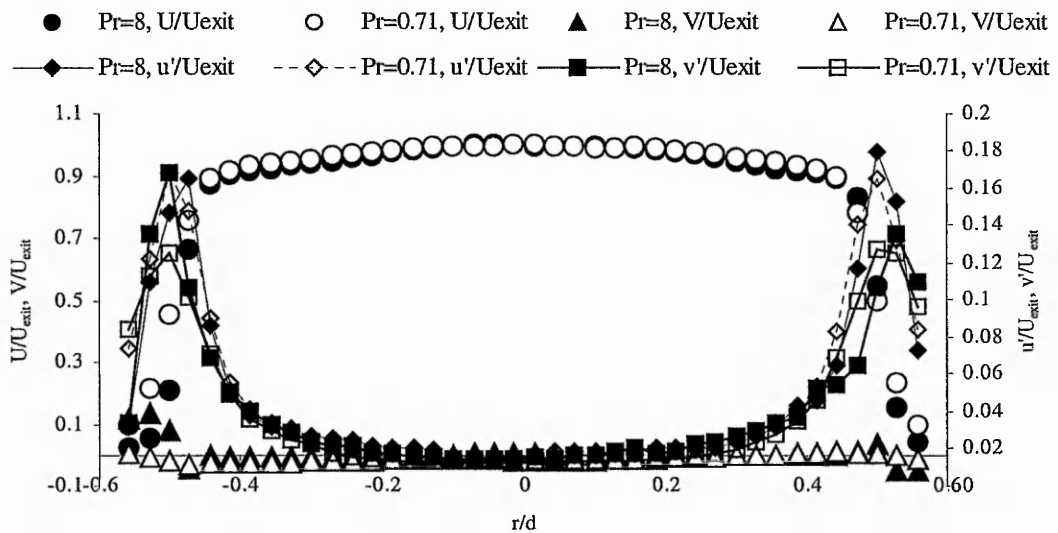


Figure 5.20. Velocity profiles at the nozzle exit (Re=10,000).

When compared to the higher Reynolds number of Re=20,000, no major change in the variation of mean velocity is apparent whereas the turbulence levels in the shear layers of both fluids have dropped and now display almost identical values. Despite the relatively large difference in Prandtl number, both fluids display almost identical exit conditions which suggest that inertia effects far outweigh viscous or other effects of fluid properties.

Profiles of turbulent shear stresses are shown in Figure 5.21. The levels are insignificantly lower than those for Re=20,000 but, again, show almost identical quantitative and qualitative resemblance. Peak values are attained at the edge of the jet and have opposite signs on either side of the nozzle. This change of sign over the cross section of the nozzle is a consequence of the fluid particles that leave the nozzle

with mean velocity,  $U$ , and travel radially outwards in view of the turbulent fluctuation (i.e.  $v' < 0$  for  $r/d > 0$ ). They arrive at a region where a smaller mean velocity prevails so that this layer is accelerated due to the conservation of momentum. For  $r/d > 0$ , this results in a positive axial turbulent fluctuation which leads, overall, to a positive product of  $u'v'$ . The reader is referred to Figure 5.39 where a schematic of the sign convention for the Reynolds stress is provided.

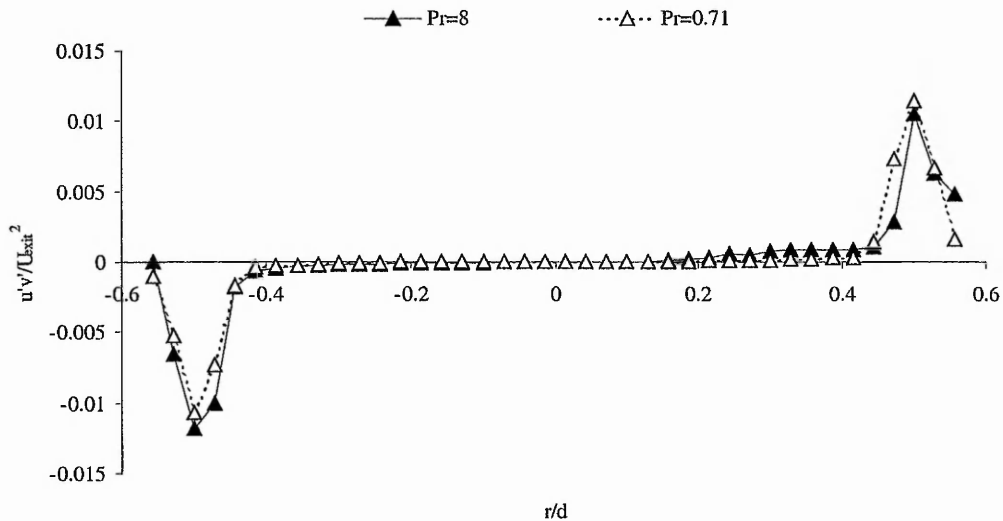


Figure 5.21. Reynolds stresses at the nozzle exit ( $Re=10,000$ ).

### 5.2.3.1.3 Exit profile for $Re=2,000$

Uniform velocity profiles associated with relatively low turbulence intensity levels, compared to the higher Reynolds numbers, were measured across the nozzle exit for  $Re=2,000$ . Figure 5.22 depicts the normalised mean velocity and the development of axial and radial turbulence intensities for the two working fluids. Despite the relatively large difference in Prandtl number, both fluids display almost identical exit conditions in terms of mean velocity. Although the air jet displays almost an identical axial velocity gradient at the jet edge as the water jet, it does not produce sharp rises of turbulence intensity in the same region. Instead, the fluctuating velocity in both directions remains at an almost constant level of approximately 4.5% across the nozzle diameter. Conversely, the water jet develops a much higher axial velocity fluctuation on the centreline than its radial counterpart. Since the turbulence intensity levels give an indication of the relative mixing rates, the anisotropic behaviour of the water jet suggests a faster decay in the axial direction when compared with the spreading of the jet in the radial direction. Despite this quantitative

discrepancy at  $r/d=0$ , both components grow equally strong near the nozzle edge resulting in two distinct peaks which have identical values at  $r/d=\pm 0.5$ . This discrepancy in the behaviour of air and water leads to the conclusion that the mean velocity is de-coupled from the variation of turbulence intensity.

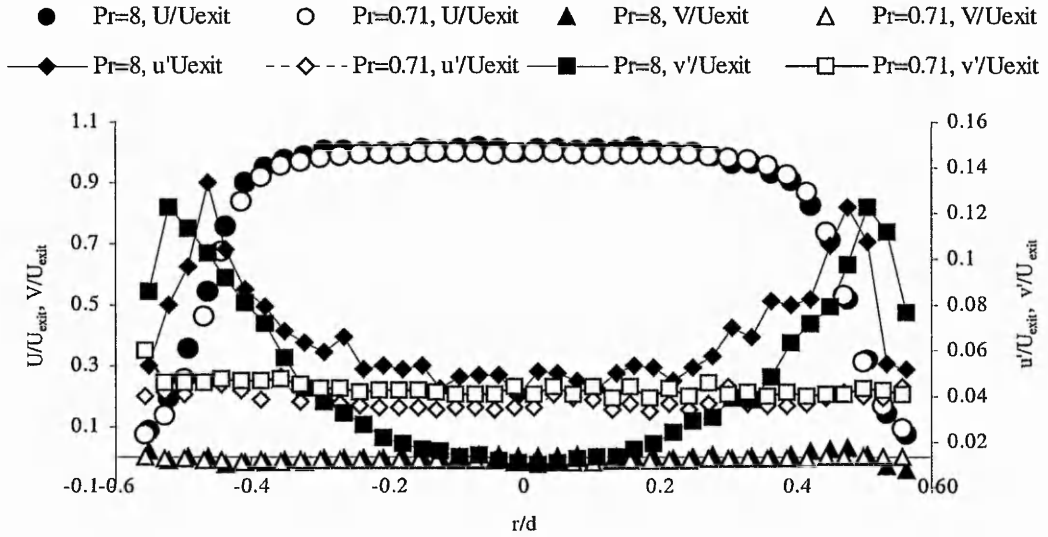


Figure 5.22. Velocity profiles at the nozzle exit ( $Re=2,000$ ).

Profiles of Reynolds shear stress in water show qualitatively similar shapes to those obtained in higher  $Re$  flows. This is in contrast to air where at  $Re=2,000$  levels of shear stress show almost zero levels throughout the cross-section, thereby confirming that the mean velocity is related to the Reynolds shear stress. Among the three studied Reynolds numbers, the value of  $Re=2,000$  and  $Pr=8$  represents the lowest peak level.

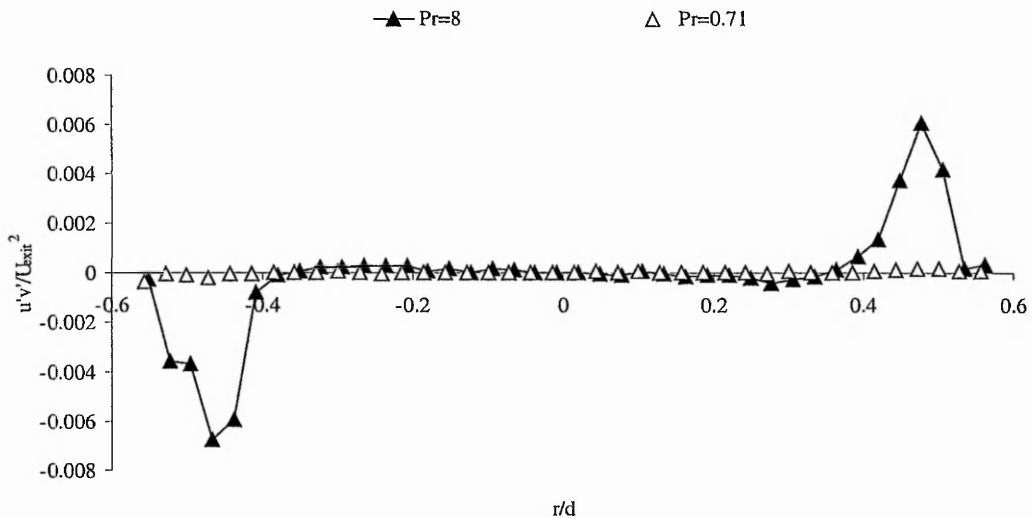


Figure 5.23. Reynolds stresses at the nozzle exit ( $Re=2,000$ ).

### 5.2.3.2 Flow behaviour along the impingement plate

Results from measurements in air and water jets normal to the impingement surface are presented in the following by plotting non-dimensional data of mean velocity, turbulence intensity and turbulent shear stresses against their respective radial distance from the stagnation point. This will be followed by a presentation of the results obtained from measurements parallel to the plate.

#### 5.2.3.2.1 $Re=20,000$ and $Re=10,000$

##### 5.2.3.2.1.1 Flow quantities normal to the plate

The emphasis is placed on identifying differences between the two Prandtl number fluids. As both working fluids show almost exact quantitative agreement under highly turbulent conditions, data for each flow quantity will be presented and discussed jointly for  $Re=20,000$  and  $Re=10,000$ , respectively. This close agreement is not surprising in view of the fact that under these flow conditions inertia forces are 20,000 and 10,000 times greater than the respective viscous forces. Nevertheless, a quantitative inspection of the flow fields induced by both working fluids is necessary to relate turbulence features with complementary respective heat transfer data.

To examine the wall jet for flow reversal, the axial velocity profiles are studied in more detail, as suggested by Landreth and Adrian (1990). Graphs for  $Re=10,000$  and  $Re=20,000$  are presented in Figure 5.24 and Figure 5.25, respectively. They show the fast decay of the axial velocity component as the wall jet proceeds along the target plate. By  $r/d=1.2$ , less than 10% of the initial axial momentum is preserved in the wall jet.

While the water jet for  $Re=20,000$  shows flow reversal in the immediate vicinity of the wall at  $r/d=0.8$ ,  $r/d=1.2$  and  $r/d=1.6$ , the air wall jet shows axial flow reversal at  $r/d=0.8$  and  $r/d=1.6$ . However, it has to be pointed out that in any of these flow reversals only at one node, the one located closest to the wall at  $y/d=0.003$ , was a negative velocity determined. This is in contrast to Landreth and Adrian (1990) who detected a region of flow reversal over a length of about  $0.1d$  in the immediate vicinity of the wall. For this reason, the occurrence of negative flow in the present tests has to be treated with caution when its implications on heat transfer are evaluated. To clarify the existence of flow reversal due to unsteady separation, the variation of the mean velocity defect in the wall jet boundary layer was determined from the displacement thickness, similar to the analysis of Landreth and Adrian (1990).

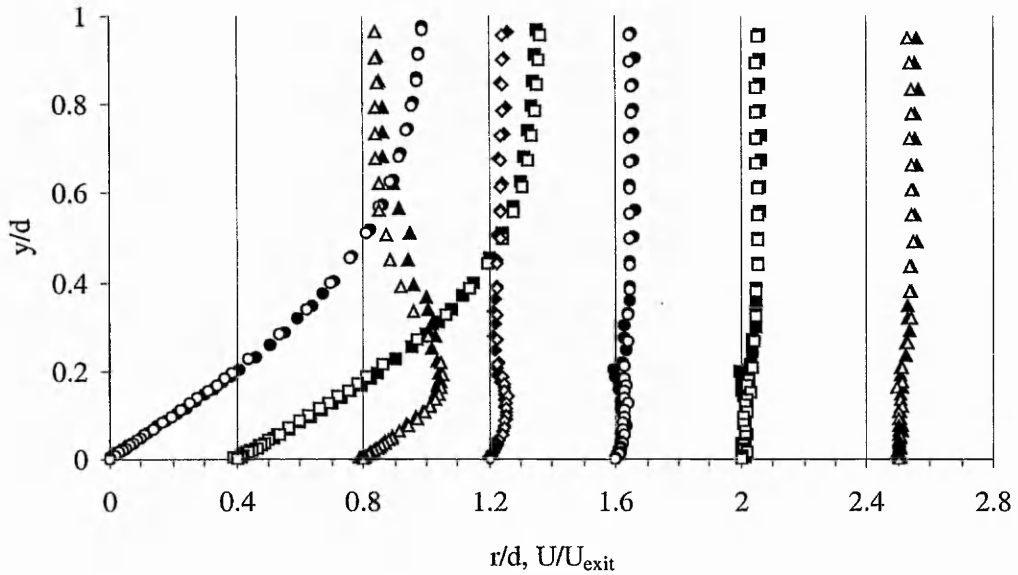


Figure 5.24. Axial velocity profile for Re=20,000 (open Pr=0.71, filled Pr=7.3).

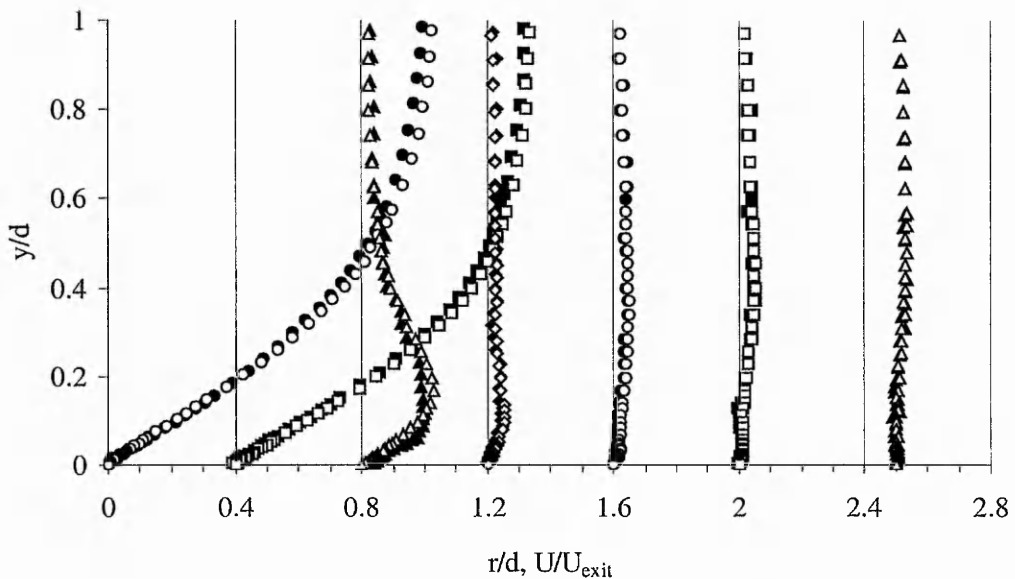


Figure 5.25. Axial velocity profile for Re=10,000 (open Pr=0.71, filled Pr=8).

This serves as an indicator for the distance by which the external streamlines are shifted owing to the formation of the boundary layer. Its value was determined from

$$\xi_{d(y)} = \int_{y_1=0}^{y_2=y_{\max}} \left( 1 - \frac{V}{V_{\max}} \right) dy \quad (5.1)$$

where the subscript max refers to the edge of the boundary layer, positioned at  $y_{\max}$  normal from the plate. For the integration of the wall profiles, Simpson's rule was used. In Figure 5.26 the calculated displacement thickness of the mean flow for Re=20,000 can be seen.

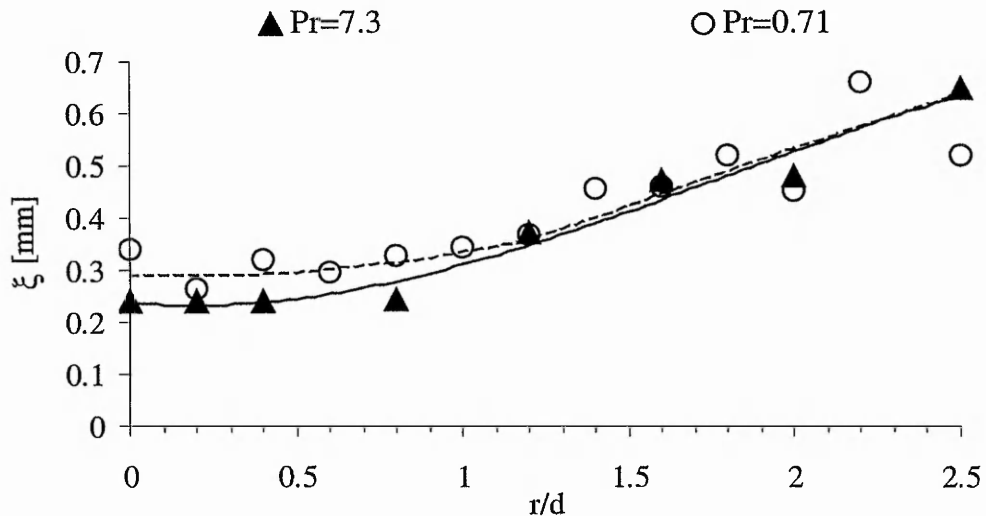


Figure 5.26. Displacement thickness of the wall jet for  $Re=20,000$ .

For  $r/d \leq 0.8$ , the displacement thickness for air varies irregularly about a level of 0.3 while water displays an almost constant, albeit lower, displacement thickness. This value signifies an attached boundary layer over the length of the stagnation region and corroborates the findings by Landreth and Adrian (1990). At approximately  $r/d=1.2$ , the displacement thickness starts to rise gradually throughout the Prandtl number range which indicates a growth of the boundary layer, thereby allowing vortices to undergo breakaway.

Figure 5.27 and Figure 5.28 depict the evolution of the wall jets in terms of radial velocity for  $Re=20,000$  and  $Re=10,000$ , respectively. It can be seen that the maximum values for both Reynolds numbers occur between  $0.8 \leq r/d \leq 1.2$ . Since both Prandtl numbers show excellent agreement, the measurement results for air at  $r/d=1$  may be used to identify the location of the peak value for both Prandtl numbers. This corroborates the findings from Fitzgerald and Garimella (1998) for FC-77 at  $Re=23,000$  and  $Re=13,000$ . At  $r/d=1.6$  and  $r/d=2$  minor discrepancies at  $y/d \approx 0.2$  are visible which are due to a temporary low data rate in the water jet at  $Re=20,000$ . This is a consequence of the subdivision of the measurement region where, towards the end of the innermost sub-region, the LDA-signal was weakened.

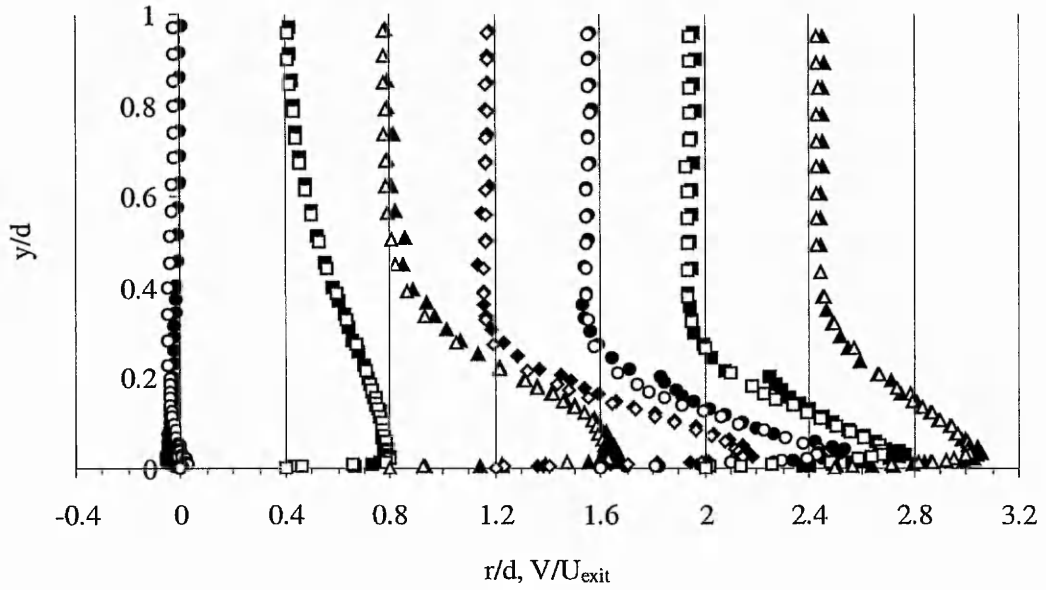


Figure 5.27. Radial velocity profile for  $Re=20,000$  (open  $Pr=0.71$ , filled  $Pr=7.3$ ).

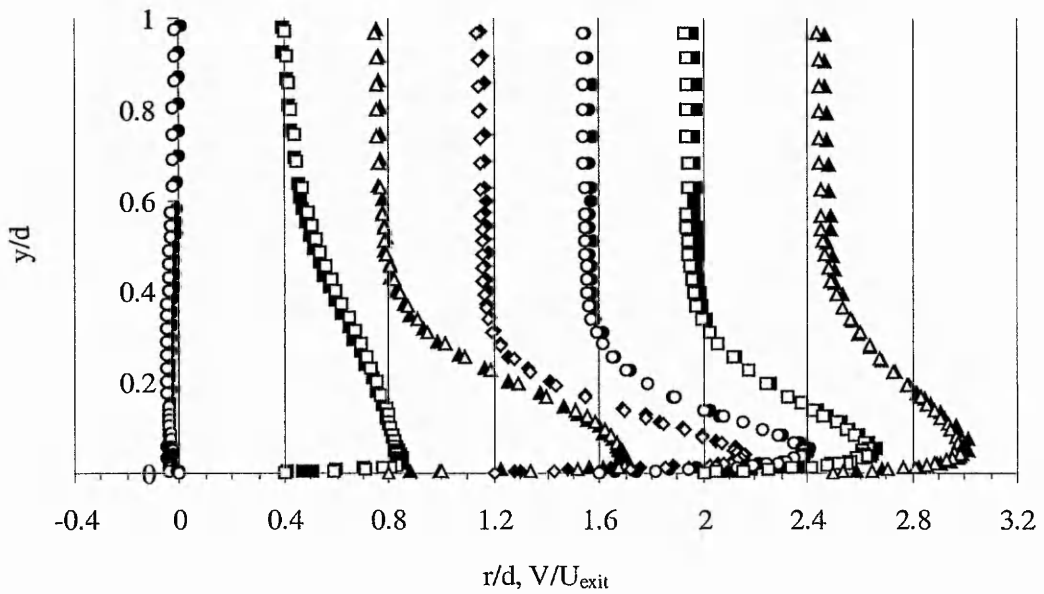


Figure 5.28. Radial velocity profile for  $Re=10,000$  (open  $Pr=0.71$ , filled  $Pr=8$ ).

Axial turbulence levels for  $Re=20,000$  and  $Re=10,000$  are presented in Figure 5.29 and Figure 5.30, respectively. In the stagnation region ( $r/d \leq 0.8$ ) and for all studied distances normal to the plate,  $y/d \leq 1$ , where the spreading of the jet prevails, both Prandtl numbers show identical axial turbulence intensities to within  $\pm 5\%$ . From both graphs it can be observed that with increasing radial distance, the profiles show steeper gradients at the wall while the peaks move closer to the target surface.

Measurements in the air jet at  $r/d=1.8$  (not shown here) revealed that the axial turbulence levels were still growing, finally peaking at  $r/d=2$ . This is consistent throughout the Prandtl number range and for  $Re=20,000$  and  $Re=10,000$ , with peak values of 15.5% and 16.3%, respectively. The radial position of the peak axial velocity fluctuations at  $r/d=2$  was also found by Cooper *et al.* (1993) for air.

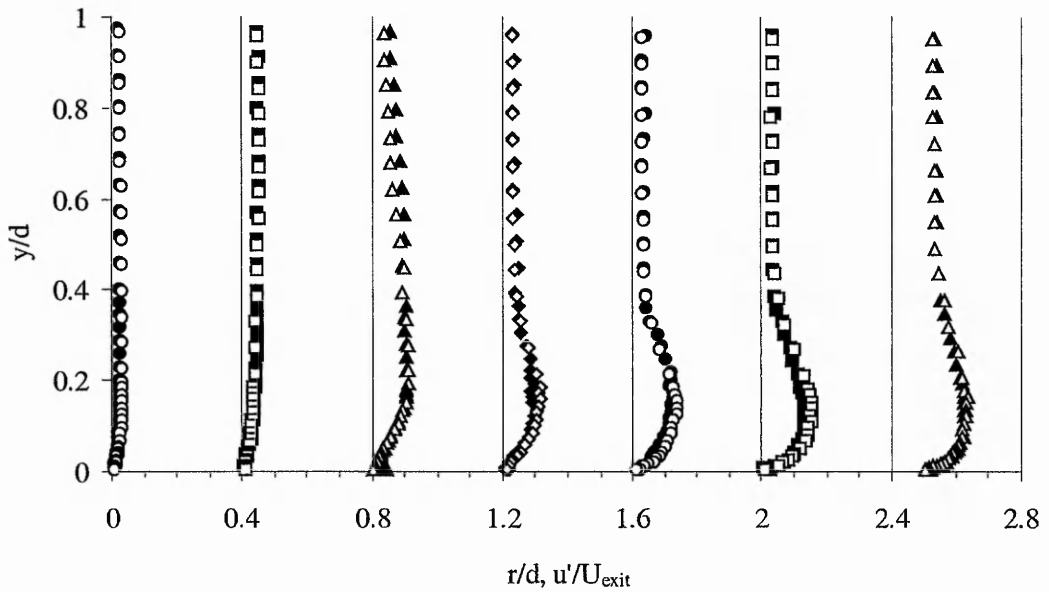


Figure 5.29. Axial turbulence intensity for  $Re=20,000$  (open  $Pr=0.71$ , filled  $Pr=7.3$ ).

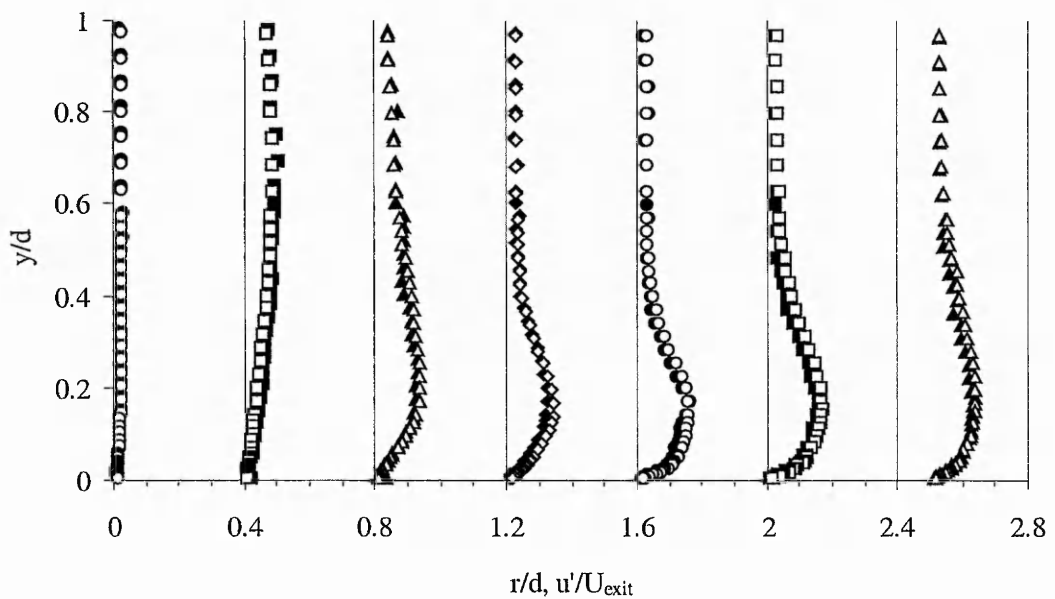


Figure 5.30. Axial turbulence intensity for  $Re=10,000$  (open  $Pr=0.71$ , filled  $Pr=8$ ).

An entirely different behaviour near the wall was observed for the radial turbulence intensity, as shown in Figure 5.31 and Figure 5.32. Here, the radial turbulence levels show non-zero values indicated by a steep velocity rise which is followed by a local minimum at about  $y/d=0.03$ . This reduction is probably due to the wall exerting a damping effect and suppressing the turbulence fluctuation. While for large values of  $y/d$  the radial turbulence intensity is about 25% higher than that of the axial intensity, this difference rises to about 35% in the immediate vicinity of the wall.

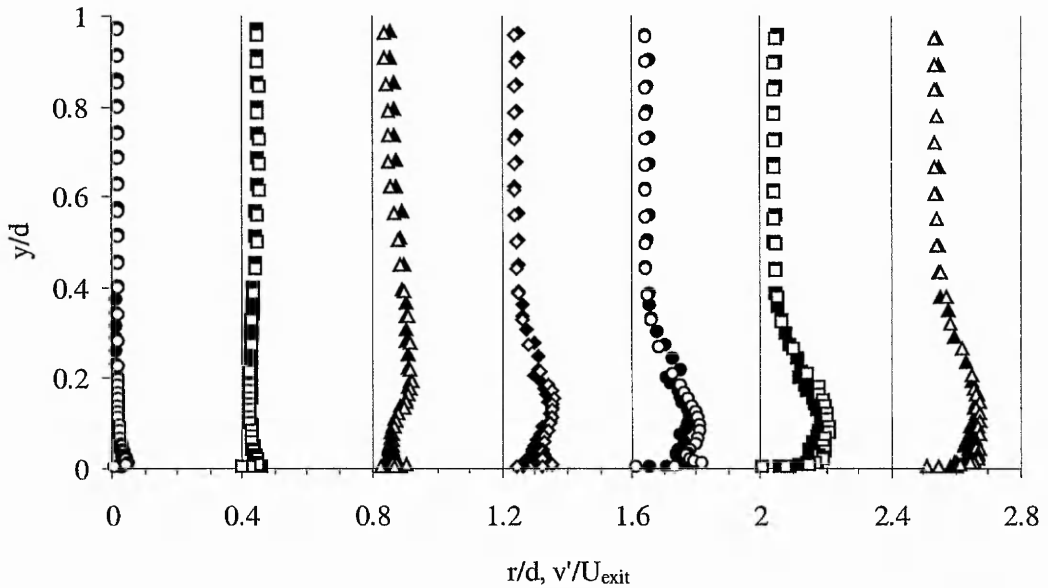


Figure 5.31. Radial turbulence intensity for  $Re=20,000$  (open  $Pr=0.71$ , filled  $Pr=7.3$ ).

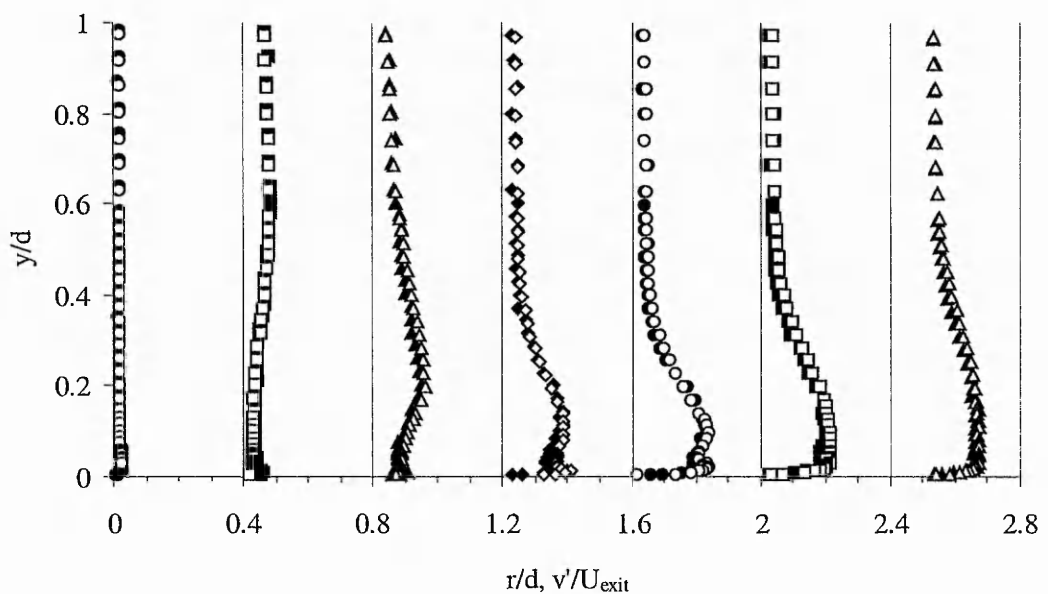


Figure 5.32. Radial turbulence intensity for  $Re=10,000$  (open  $Pr=0.71$ , filled  $Pr=8$ ).

Further measurements near the wall show, for both Reynolds number flows, that the maximum level in radial turbulence intensity is approximately 20% and is attained at  $r/d=2$ . This value is still higher than that of 17.8% obtained for FC-77 by Fitzgerald and Garimella (1998) at the same radial location. The difference is attributed to the nozzle exit conditions (developing velocity profile) and stronger entrainment effects due to the test section geometry in the present investigation. Hung and Huang (1998) attributed changes in flow fields induced by a uniform or a parabolic velocity profile to a greater outward transfer of momentum owing to the high velocity gradient at the edge of the flat jet. The uniform jet spreads faster and seems to develop higher levels of turbulence along the target plate. Since the radial turbulence intensity for  $Re=10,000$  and  $Re=20,000$  peaks at  $r/d=2$ , it can be concluded that the magnitude of the radial turbulence levels is not affected by a change in Reynolds numbers. This corroborates findings by Fitzgerald and Garimella (1998). For a more accurate determination of the position in the turbulence peaks, the reader is referred to Section 5.2.3.2.1.2.

Profiles of the turbulent shear stresses are plotted in Figure 5.33 and Figure 5.34 for  $Re=20,000$  and  $Re=10,000$ , respectively. Identical quantitative trends between the two fluids for  $r/d < 0.8$  confirm the absence of significant turbulent motion directly beneath the impinging jet. At  $r/d=0.8$ , the developing wall jet shows a non-monotonic behaviour with a change of sign at  $y/d \approx 0.23$  and  $y/d \approx 0.26$  for  $Re=20,000$  and  $Re=10,000$ , respectively. This position moves normally away from the target surface as the radial distance increases.

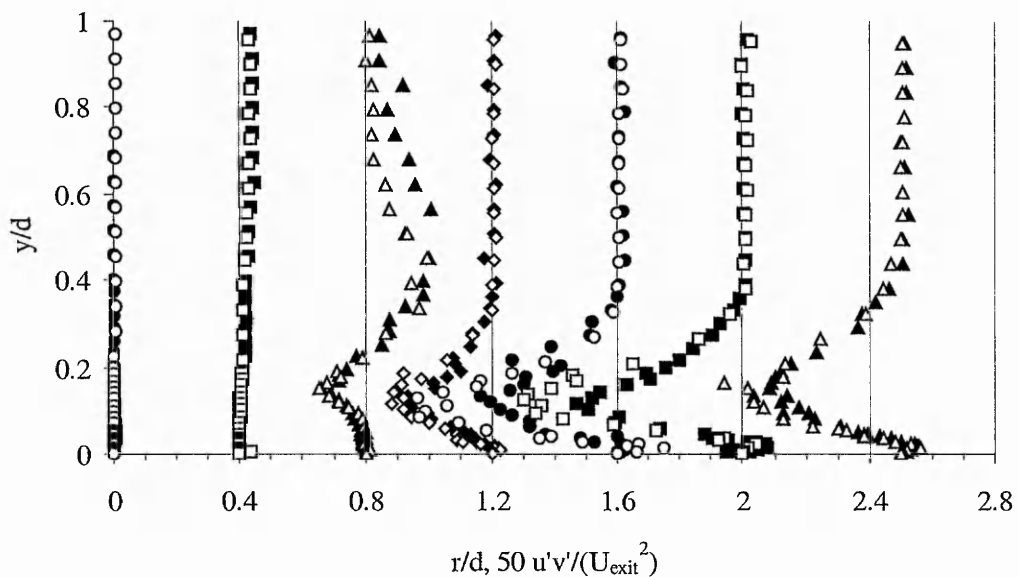


Figure 5.33. Reynolds stresses for  $Re=20,000$  (open  $Pr=0.71$ , filled  $Pr=7.3$ ).

Since information about the entrainment and mixing characteristics may be inferred from measurements of the Reynolds stress field, see Schneider *et al.* (1997), this change of sign is attributed to the increasing effects of re-circulating free stream flow that interacts with the wall-bound flow. With increasing radial distance, levels of turbulent shear stress rise steadily to peak at a position of  $r/d=2$ . With the Reynolds stresses expressing the contribution of turbulent motion to the mean stress, peaks in turbulent shear stresses correspond to regions where the mean velocity gradients are largest, see also Figure 5.27 and Figure 5.28.

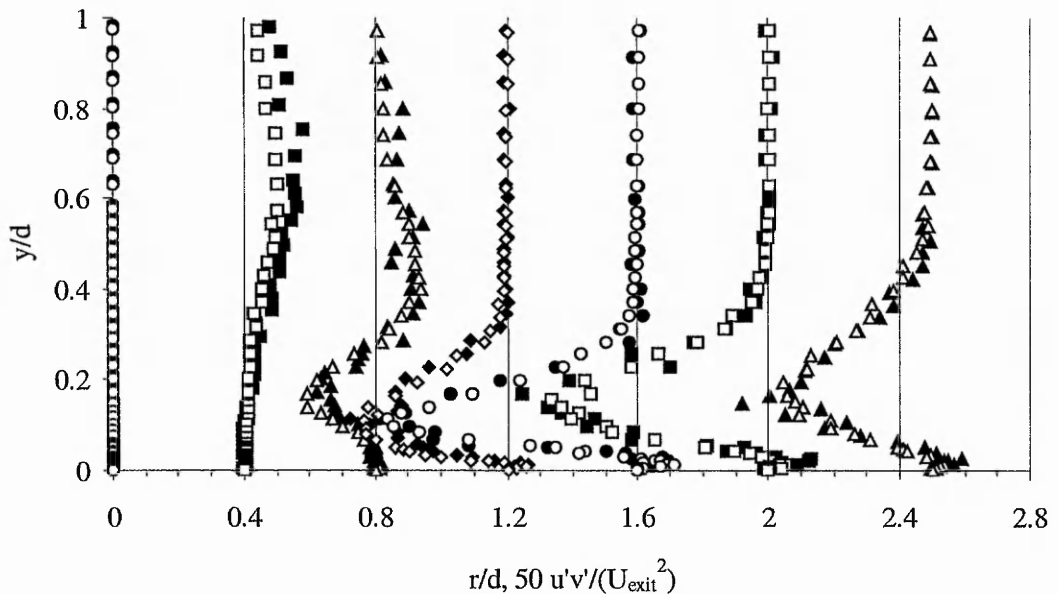


Figure 5.34. Reynolds stresses for  $Re=10,000$  (open  $Pr=0.71$ , filled  $Pr=8$ ).

Another noteworthy feature is that for  $Re \geq 10,000$  and close to the wall, for  $y/d < 0.04$ , the Reynolds stresses exhibit a positive peak with a subsequent change of sign for increasing values of  $y/d$ . It may be noted that these observations coincide with those by Ashforth-Frost (1994) and were attributed to relatively small negative velocity profiles of the axial velocity components, see also Figure 5.24 and Figure 5.25 in the present study. Here, for  $r/d \geq 1.2$ , the axial velocity profiles show a weak tendency to flow lifting (normal to the wall) for both Prandtl numbers, which manifests itself either as negative axial shear strain ( $\partial U / \partial Y < 0$  at  $r/d=2$ ) near the wall or as zero slope of the axial velocity profile ( $\partial U / \partial Y = 0$  at  $r/d=0.8$ ). For a schematic of the sign convention the reader is referred to Figure 5.39.

5.2.3.2.1.2 Flow quantities parallel to the plate

In order to accurately locate the position where the maxima in the measured turbulence variables occur, the development of the axial and radial mean velocity is plotted in Figure 5.35 to Figure 5.38, along with the respective turbulence intensities and turbulent shear stresses. All measurements parallel to the wall were performed at  $y/d=0.1$  because at this location all flow quantities display between 80% and 100% of their maximum values.

- Pr=7.3,  $U/U_{exit}$     ▲ Pr=7.3,  $V/U_{exit}$     — — Pr=0.71    - - - - Pr=0.71
- ◆ Pr=7.3,  $u'/U_{exit}$     ■ Pr=7.3,  $v'/U_{exit}$     - - - Pr=0.71    — — Pr=0.71

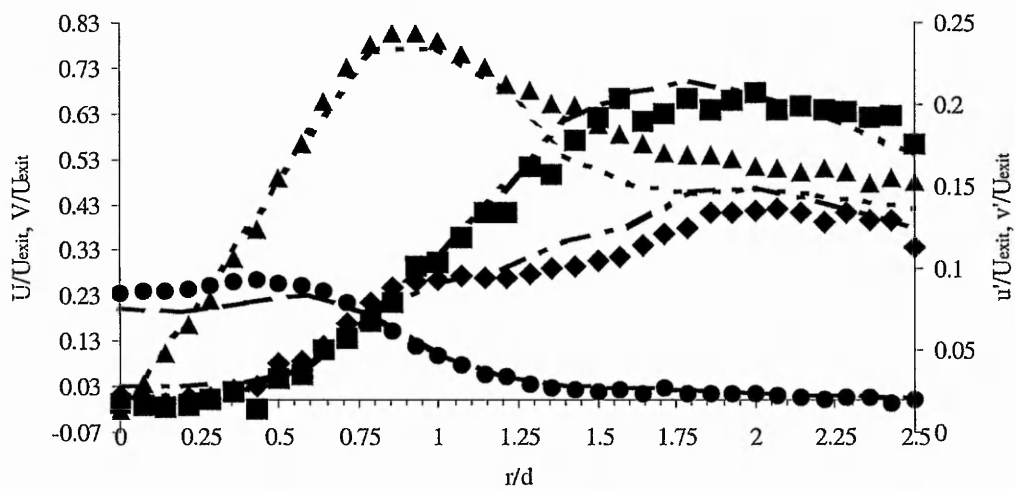


Figure 5.35. Radial velocity and turbulence profiles at  $y/d=0.1$  for  $Re=20,000$ .

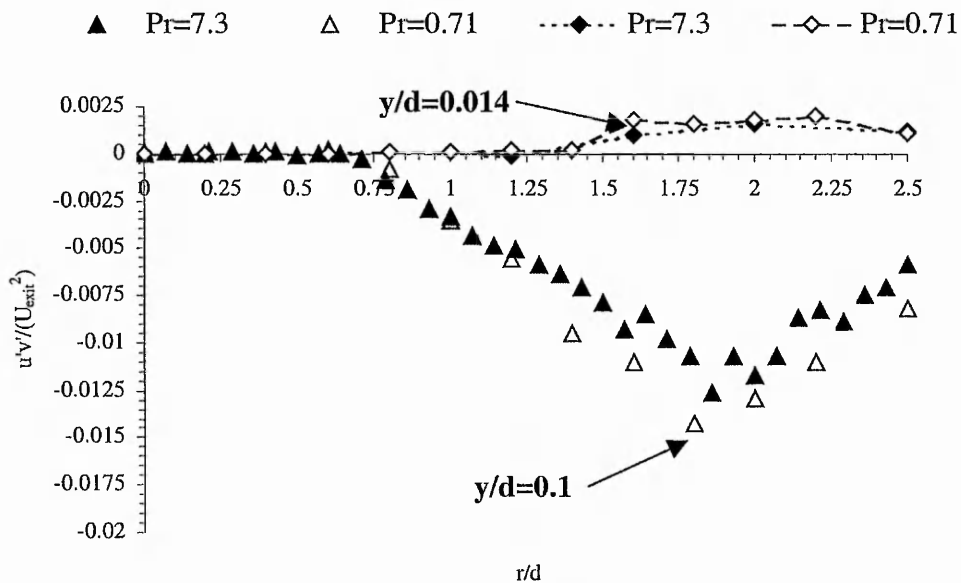


Figure 5.36. Reynolds stresses at  $y/d=0.1$  and  $y/d=0.014$  for  $Re=20,000$ .

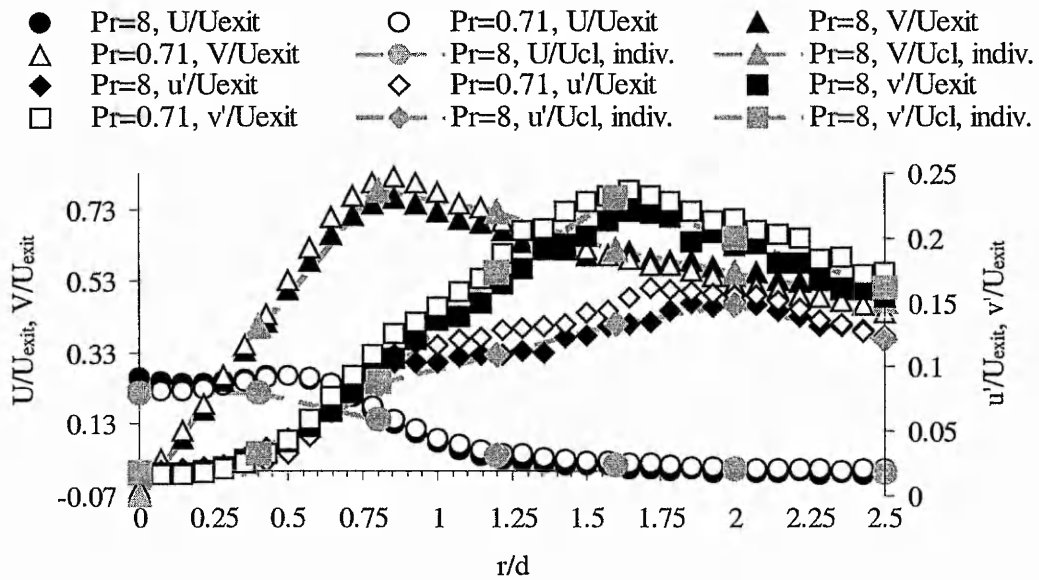


Figure 5.37. Radial velocity and turbulence profiles at  $y/d=0.1$  for  $Re=10,000$ .

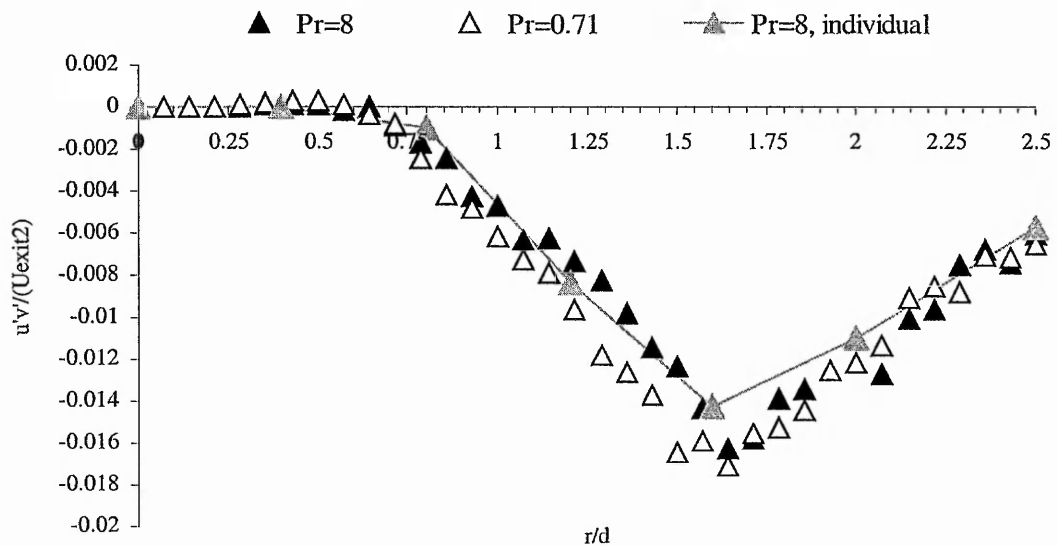


Figure 5.38. Reynolds stresses at  $y/d=0.1$  for  $Re=10,000$ .

In Figure 5.37, the variation in the axial velocity displays a local peak at  $r/d=0.5$  due to the entrainment of re-circulating fluid which leads to an exchange of mass and momentum. A further indication for the strong effects of entrainment in the present geometry is reflected in the somewhat stretched lateral decay curve. While Fitzgerald and Garimella (1998) determined the axial velocity to be zero at  $r/d \approx 1.2$ , the present results indicate that at  $r/d=1.4$  the axial velocity has been preserved to 10% of its centreline value,  $U_{exit}$ . For both high Reynolds number cases,  $Re=10,000$  and  $Re=20,000$ , the radial velocity reaches a maximum at  $r/d=0.85$  and declines thereafter to

almost zero levels. Both jets ( $Re=10,000$  and  $Re=20,000$ ) are characterised by equal turbulence levels in the axial and radial direction on the centreline which immediately start to rise as the edge of the jet is approached. The axial turbulence profile exhibits a distinct kink which is shifted from  $r/d \approx 0.85$  to  $r/d \approx 0.92$  as the Reynolds number is doubled. This is followed by a reduction in its radial growth and leads to a peak at  $r/d \approx 1.85$  and  $r/d \approx 1.92$  for  $Re=10,000$  and  $Re=20,000$ , respectively. Note that only the axial turbulence component is affected by a change in slope, while the fluctuating velocity parallel to the wall rises without significant changes until it reaches a maximum at  $r/d \approx 1.64$  and  $r/d \approx 1.8$  for  $Re=10,000$  and  $Re=20,000$ , respectively. The peaks in axial turbulence are approximately 68% of the radial turbulence levels, thus confirming the previously mentioned typical value of approximately 65% for shearing flows over smooth surfaces. A possible explanation for maximum turbulence levels at this radial location is that the eddies that originate from the mixing layer surrounding the jet core, are transported downstream, being deflected due to impingement and then penetrate into the wall jet, thus giving rise to a peak in turbulence quantities.

A schematic of the sign convention for the shear stress is given in Figure 5.39 and illustrates the positive values of the turbulent shear stress for positive  $r/d$ 's at the nozzle exit, Figure 5.19 and Figure 5.21. A positive sign of the turbulent shear indicates that fluid particles with a negative radial velocity fluctuation move outward thereby giving rise to negative axial velocity fluctuations. In the following, positive values of the turbulent shear stress for  $r/d \leq 0.6$  will, therefore, be associated with fluid that is moving in the radial direction dominated by axial shear strain, while negative Reynolds stress parallel to the impingement surface,  $r/d \geq 0.6$ , indicates fluid moving orthogonally away from the target plate.

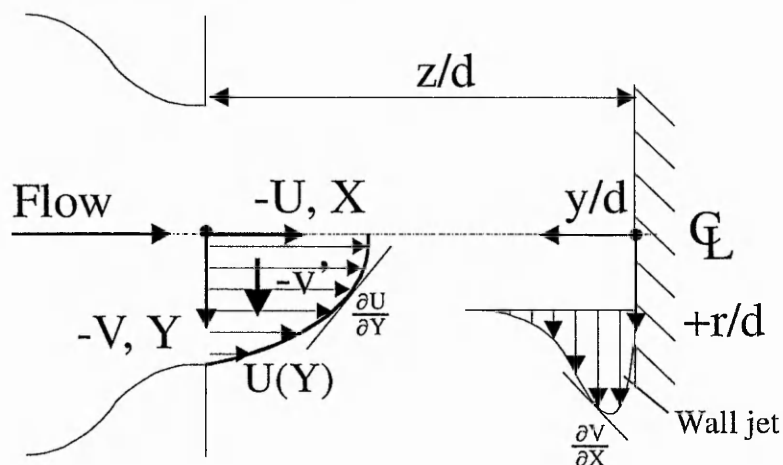


Figure 5.39. Schematic of the sign convention for the Reynolds stresses at the nozzle exit.

From Figure 5.36 and Figure 5.38 it can be seen that as long as the developing wall jet is directly beneath the nozzle,  $r/d \leq 0.5$ , the shear stress is zero. At  $r/d \approx 0.65$ , both Reynolds numbers begin to increase negative values of the normalised shear stress. At the position where the axial and normal turbulence intensity profiles peak, the Reynolds stresses display extreme values, at  $r/d \approx 1.64$  and  $r/d \approx 1.85$  for  $Re=10,000$  and  $Re=20,000$ , respectively. This will be further discussed in Section 5.2.3.2.2.

The evolution of the turbulent shear stress through various non-dimensional distances normal to the plate,  $y/d$ , is exemplified for  $Re=10,000$  and  $Pr=0.71$  in Figure 5.40. At a position of  $y/d=1$ , the profile resembles that from the nozzle exit which was recorded at  $y/d=1.5$ . Along the developing jet ( $0.4 \leq y/d \leq 1$ ) the sign of the shear stress is in accordance with that at the nozzle exit. Up to  $y/d=0.4$ , the magnitude does not change and the axial shear strain is greater than the radial shear strain, i.e.  $\partial U/\partial Y > \partial V/\partial X$ . With increasing distance from the nozzle exit, at  $y/d=0.4$ , the effects of the wall grow stronger so that the Reynolds stresses beneath the rim of the nozzle start to decrease.

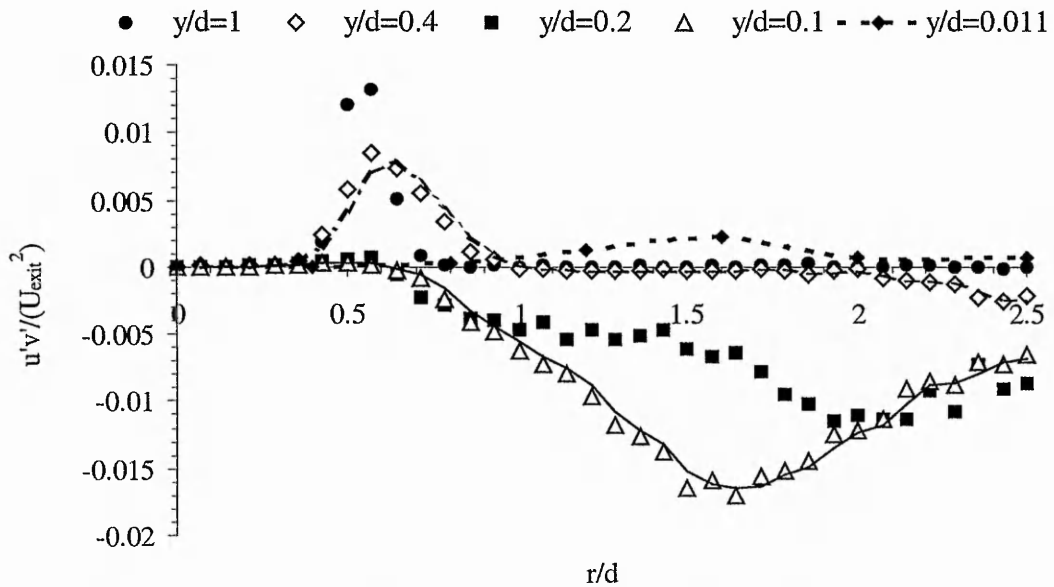


Figure 5.40. Streamwise development of the Reynolds stresses ( $Re=10,000$ ,  $Pr=0.71$ ).

With the approach of the target plate, at  $y/d=0.2$ , the shear strain  $\partial V/\partial X$  increases due to the streamline curvature and circumferential stretching which affects the shear stress more than the turbulence intensity, see Barata *et al.* (1993). Beyond the edge of the jet, the shear strain  $\partial V/\partial X$  is now greater than  $\partial U/\partial Y$  so that the decreasing shear stress changes its sign. This becomes noticeable as a suppression of the positive peak at the edge of the jet with a subsequent reversed rise in magnitude for greater  $r/d$ 's. For a distance closer to the wall,  $y/d=0.1$ , the peak is observed at a

position of  $r/d=1.8$  and  $r/d=1.65$ , for  $Re=20,000$  and  $Re=10,000$ , respectively. According to Schlichting (1979), these extreme values of turbulent shear stress can be directly linked to local maxima in skin friction. This will be further discussed in Section 5.3.4 where its implications on heat transfer are analysed.

In the immediate vicinity of the wall, at  $y/d=0.014$ , Figure 5.36 and Figure 5.40 show positive values of turbulent shear stress for  $r/d>0.9$ . This occurrence was also reported by Ashforth-Frost (1994) and Knowles and Myszko (1998).

### 5.2.3.2.2 $Re=2,000$

#### 5.2.3.2.2.1 Flow quantities normal to the plate

The results presented in this Section include mean and turbulent velocity characteristics along the impingement plate when laminar flow conditions ( $Re=2,000$ ) prevail at the nozzle exit.

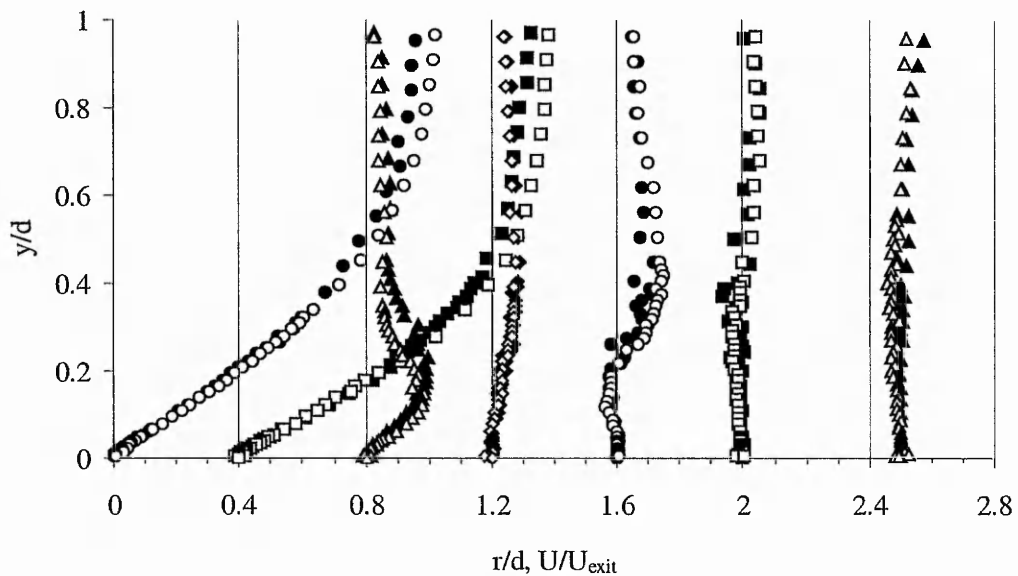


Figure 5.41. Axial velocity profile for  $Re=2,000$  (open  $Pr=0.71$ , filled  $Pr=8$ ).

Features of the mean axial and radial flow are quantified in Figure 5.41 and Figure 5.42, respectively. Results suggest that for  $Re=2,000$ , fluid properties have by far the strongest effects on the flow fields of all the investigated Reynolds numbers. The graphs indicate that the development of the radial wall jet depends on Prandtl number, while the decay of the axial velocity component shows similarities between air and water. However, based on a 95% criterion, the approaching water jet decays faster than the air jet, see also Figure 5.8 and Figure 5.13. In the immediate vicinity of

the stagnation point,  $r/d \leq 0.4$ , the developing wall jets of both working fluids show close agreement in that they display much thicker wall jet profiles at  $r/d=0.4$  than at their respective higher Reynolds numbers. At  $r/d=0.8$ , quantitative discrepancies start to evolve as the air jet begins to form a wall jet with a higher radial velocity and a smaller thickness than its liquid counterpart. This trend prevails until  $r/d=1.6$ , where the profiles of both fluids deviate qualitatively from their previous shapes in that their peaks are shifted away from the wall. This is accompanied by a simultaneous growth of the wall jet thickness. At  $r/d=2$ , both fluids form peaks in the radial velocity at positions that have almost doubled their distance from the target plate ( $y/d=0.22$ ) compared to the distance of  $y/d=0.11$  at  $r/d=1.6$ . The dissimilarities in the near wall region appear to have vanished by  $r/d=2$ , while the two fluids display ongoing differences in their sensitivity towards the re-circulation pattern of the free stream. In contrast to the position of  $r/d \leq 1.6$ , however, the radial wall jet with  $Pr=0.71$  now exhibits a greater sensitivity to re-circulation effects than the water wall jet.

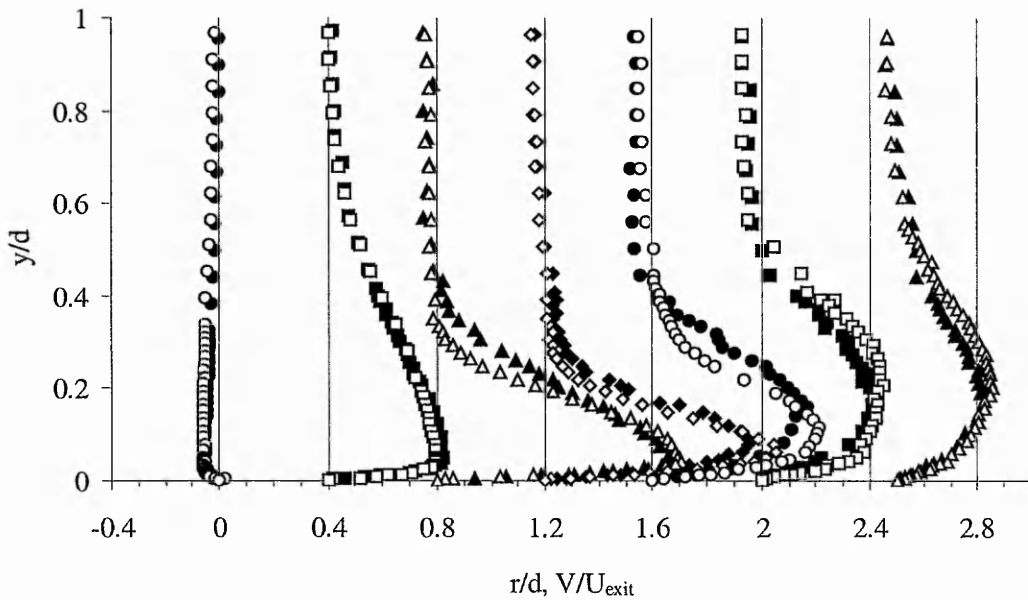


Figure 5.42. Radial velocity profile for  $Re=2,000$  (open  $Pr=0.71$ , filled  $Pr=8$ ).

In the above, the position of  $r/d=2$  was identified as the location where the two Prandtl numbers begin to produce similar near wall behaviours. This trend is further investigated in Figure 5.43 by plotting the displacement thickness inferred from equation (5.1). The fact that the boundary layer along the impingement plate is much thicker for  $Re=2,000$  than for the higher Reynolds numbers, is reflected in the displacement thickness  $\theta_{Re=2,000}=2.35\text{mm}$  which is about four times greater at  $r/d=2.5$  than  $\theta_{Re=20,000}$ , see also Figure 5.26. The displacement thickness of the air jet remains

constant for  $r/d \leq 0.8$  and begins to grow steadily beyond this location. For  $Pr=8$ , this region of constant displacement thickness is extended to  $r/d \leq 1.2$ . The slightly larger displacement thickness for water over that of the air jet for  $r/d \leq 1.2$  confirms the findings from Figure 5.42 in that the streamlines in the water wall jet are displaced earlier due to the thicker boundary layer. Beyond this region, at  $r/d=1.6$ , the water jet appears to develop a sharper rise in near wall profile thickness, which levels off further downstream. For  $Pr=8$ , this can be interpreted as a sudden shift of the streamlines away from the impingement plate due to the formation of the boundary layer.

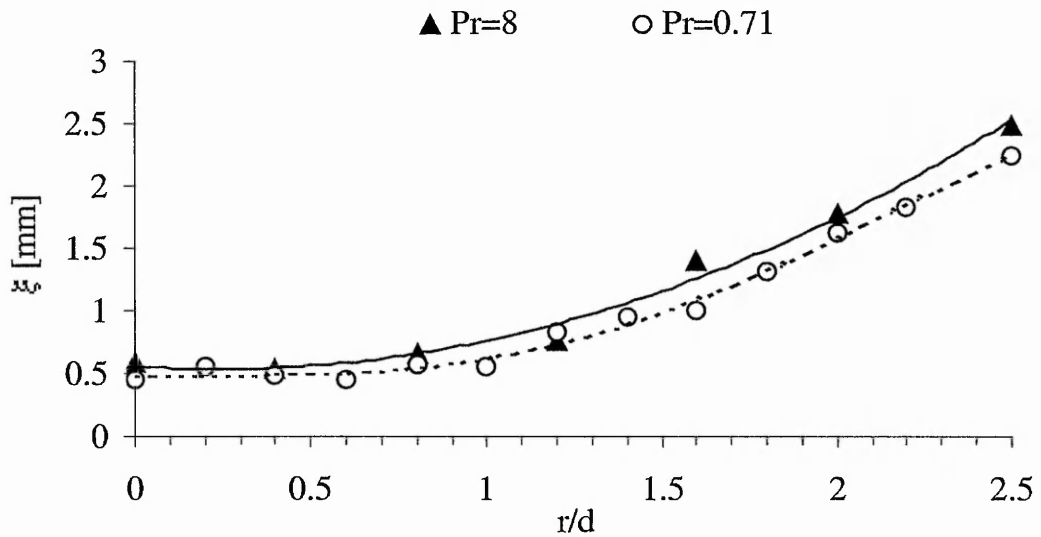


Figure 5.43. Displacement thickness of the wall jet for  $Re=2,000$ .

Turning now to the turbulence characteristics, Figure 5.44 and Figure 5.45 highlight the development of the axial turbulence intensity. At the stagnation point and along the jet centreline,  $r/d=0$ , axial turbulence levels of both jets show an almost constant variation with the water jet displaying higher turbulence levels. For  $r/d > 0.4$  jets of air and water form peaks at almost identical radial positions. In the region of  $0.8 \leq r/d \leq 1.6$ , the peaks for both Prandtl number fluids move closer to the wall,  $y/d \approx 0.2$ , while for  $r/d \geq 2$  the peaks are shifted further away from the wall, to  $y/d \approx 0.33$ . Further away from the wall,  $y/d > 0.08$ , the approaching water jet displays higher axial mixing rates which prevail until  $r/d=1.6$ . At  $r/d=2$  the water jet displays similar axial turbulence characteristics than the air while this trend is reversed for  $r/d=2.5$ . By the time the effects of the wall become significant, the approaching air jet has preserved more of its initial conditions from the nozzle exit. Very close to the wall and throughout the radial region of interest,  $0 \leq r/d \leq 2.5$ , the air jet produces a much steeper increase in axial turbulence with significantly higher turbulence levels than the water jet. Here, for

$y/d \leq 0.08$ , the air jet shows levels of axial turbulence that are approximately threefold higher than those of the water jet. These results corroborate those from Figure 5.8 and Figure 5.13 where the air jet was found to preserve 95% of its centreline velocity for longer (i.e. closer to the wall) than the water jet.

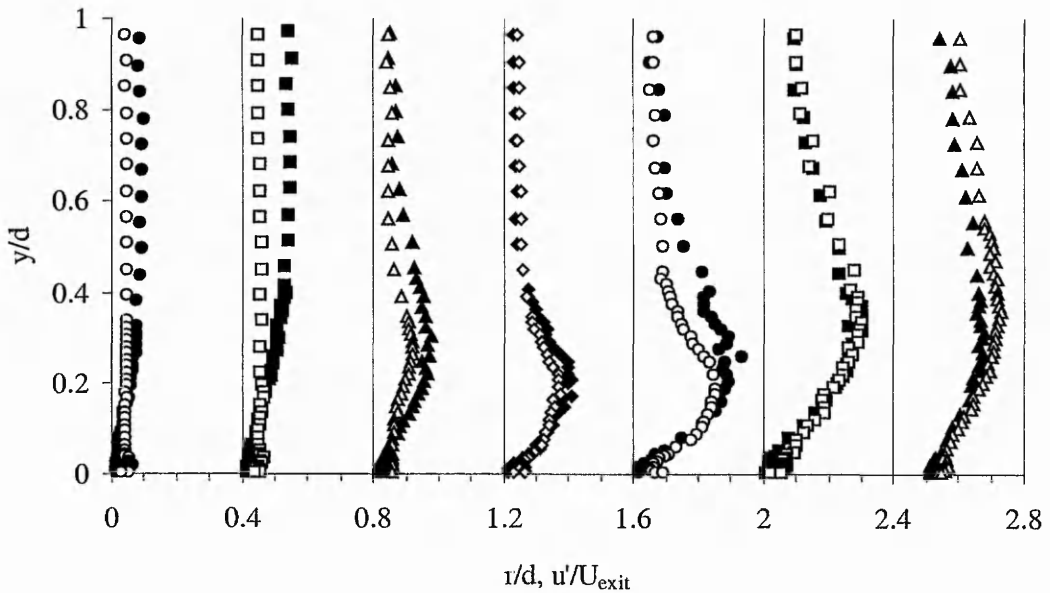


Figure 5.44. Axial turbulence intensity profile for  $Re=2,000$  (open  $Pr=0.71$ , filled  $Pr=8$ ).

Differences in the radial turbulence intensity between air and water are not apparent on the centreline and for  $r/d=0.4$ , since the radial component is only beginning to develop. In contrast to the axial turbulence profiles, the radial turbulence data display local peaks in the immediate vicinity to the wall while further into the free stream the graphs level off more gradually than the axial component. Note that the radial turbulence intensity is several times higher at the wall than the axial velocity fluctuation so that its effects on heat transfer augmentation could be greater than its axial counterpart. Due to the greater fluctuating velocity gradients near the wall,  $r/d=0.8$  and  $r/d=1.2$ , water will induce greater turbulence related heat transfer rates. For greater values of  $y/d$ ,  $0.02 \leq y/d \leq 0.2$ , the spreading rate of the water jet is greater thereby enhancing entrainment of surrounding fluid. By  $r/d=1.6$ , both fluids show almost identical levels of radial turbulence which continue for greater  $r/d$ 's.

Figures 5.44 and 5.45 show that higher turbulence levels prevail in the mixing layer of the water jet. Barata *et al.* (1993) identified this region as the location of maximum turbulence production by shear stress which is likely to be balanced by turbulent dissipation. For this reason differences in the turbulence characteristics between both fluids are expected to be largest here. Another aspect is the fact that, in

turbulent flow of an incompressible fluid, where the contribution of pressure to deformation work is zero, the rate of turbulent kinetic energy supplied from the large scale to the small scale eddies (“cascade” of energy) is directly proportional to the presence of Reynolds stresses, Arpaci (1997) and Bradshaw (1971).

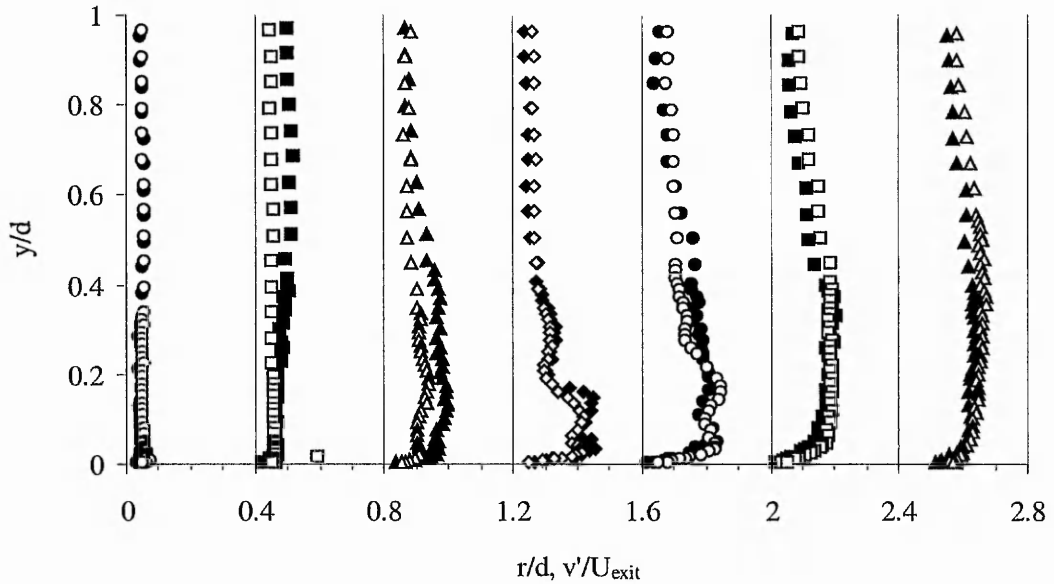


Figure 5.45. Radial turbulence intensity profile for  $Re=2,000$  (open  $Pr=0.71$ , filled  $Pr=8$ ).

The higher level of turbulent shear stress in the water jet is documented in Figure 5.46, where the air wall jet shows almost zero turbulent shear stress in the early developing stages, for  $r/d \leq 0.4$ . By  $r/d=0.8$ , the air wall jet seems to have overcome the quantitative differences to the water wall jet that prevailed at the nozzle exit. Very close to the wall and up to  $y/d \approx 0.2$ , results for both working fluids collapse onto a single profile. Further into the free stream, however, the water wall jet produces higher shear stress levels at its edges than the air jet. Since these differences exceed experimental uncertainties, differences are attributed to the lower kinematic viscosity of water.

Results at  $r/d=0.8$  have to be regarded as an intermediate stage between the impingement region directly beneath the jet edge and the subsequent development into a wall jet. The water jet spreads more rapidly than the air jet, thus giving rise to higher shear stress levels in the mixing layer. Indeed, profiles of turbulent shear stress are qualitatively identical from  $r/d=1.2$  onwards and continue to develop maximum values at  $r/d=1.6$ . As was observed for the mean flow, close agreement between the two fluids is attained for  $r/d \geq 1.6$ .

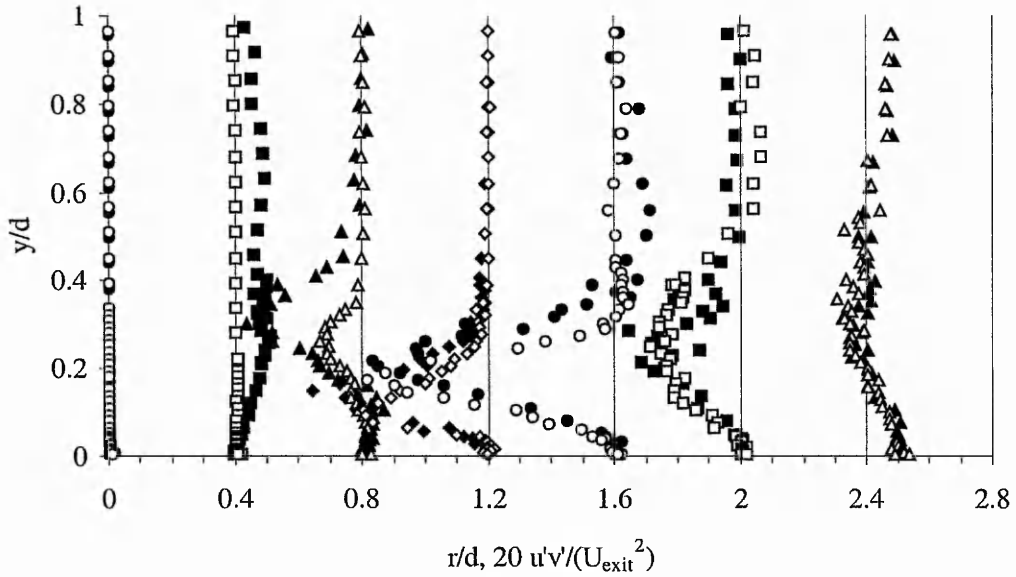


Figure 5.46. Profiles of Reynolds stresses for  $Re=2,000$  (open  $Pr=0.71$ , filled  $Pr=8$ ).

**5.2.3.2.2.2 Flow quantities parallel to the plate**

The axial and radial mean velocity and turbulence quantities from measurements parallel to the surface at  $y/d=0.1$  are plotted in Figure 5.47. To verify data for  $Pr=8$ , results from measurements previously presented in Section 5.2.3.2.2.1 are also included.

While axial velocity profiles show identical variations along the surface for  $0 \leq r/d \leq 2.5$ , the radial velocity of the air wall jet displays a peak value that is approximately 9% higher than that of the water jet, thereby confirming the trend that was observed in Figure 5.42.

Directly beneath the jet, at  $r/d \leq 0.5$  and  $y/d=0.1$ , the turbulence levels of both fluctuating components are greater in the air jet than in the water jet. Compared to the nozzle exit conditions, Figure 5.22, this represents higher turbulence mixing rates of the air jet in both directions while the water jet shows almost identical values to those from the nozzle exit. A cross-over of the two fluctuating velocity components can be seen at  $r/d \approx 0.5$ . Despite the axial turbulence on the centreline of the air jet being 67% higher than that of the water jet, by  $r/d=0.65$  data for the two fluids have collapsed onto a single curve. The turbulence levels normal to the wall continue to rise monotonically until they reach a peak at  $r/d \approx 1.5$ . The pronounced kink that was observed for  $Re=10,000$  and  $Re=20,000$  at  $r/d \approx 0.85$  and  $r/d \approx 0.92$  respectively, does not exist for the low Reynolds number. Since the peak in radial velocity occurs at the identical location as for higher Reynolds numbers,  $r/d \approx 0.85$ , this occurrence is not

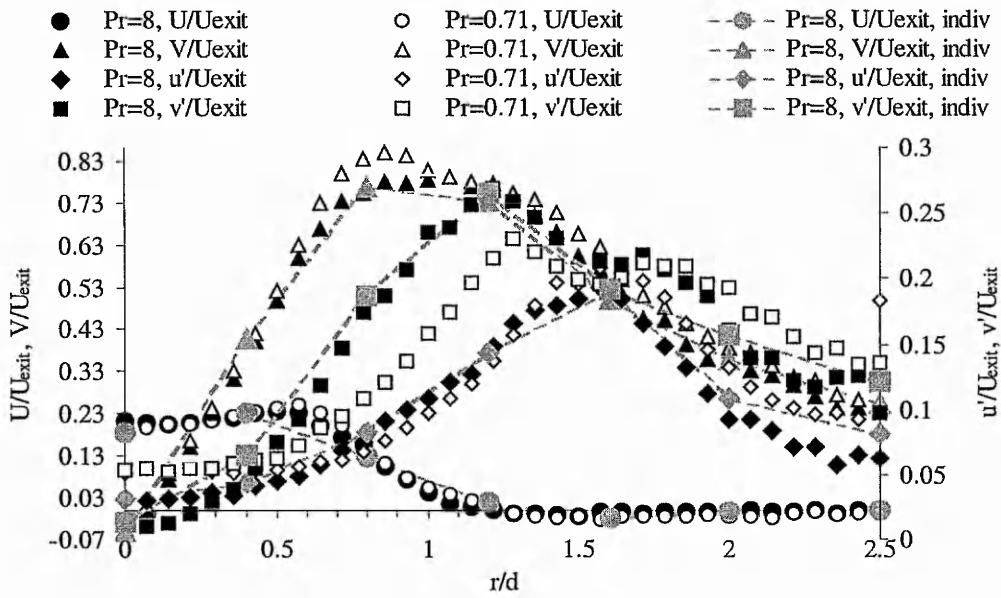


Figure 5.47. Radial velocity and turbulence profiles at  $y/d=0.1$  and  $Re=2,000$ .

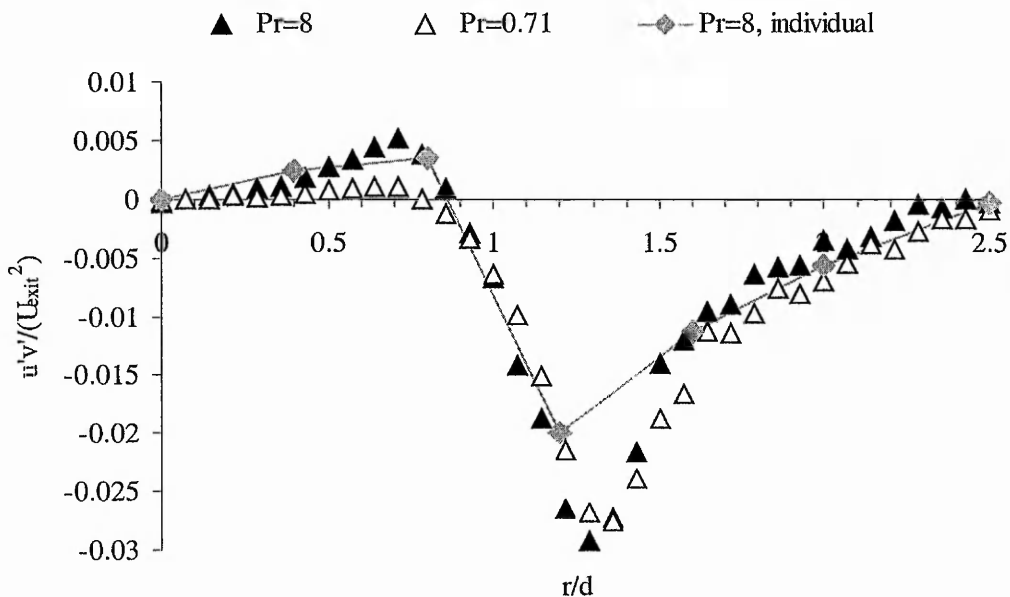


Figure 5.48. Reynolds stresses at  $y/d=0.1$  and  $Re=2,000$ .

associated with the radial mean velocity. Moreover, a Reynolds number dependency is also noticed for the development of the radial turbulence intensity. After leaving the stagnation region,  $r/d \leq 0.8$ , the water jet rises more steeply to reach the peak value at approximately the same radial location as the air jet but with a 20% higher magnitude. While the higher Reynolds numbers display a continuous increase in radial turbulence intensity which peaks at  $r/d \approx 1.64$  and  $r/d \approx 1.71$  for  $Re=10,000$  and  $Re=20,000$ , respectively, the low Reynolds number flow shows two local peaks, at  $r/d \approx 1.28$  and  $r/d \approx 1.78$ , respectively.

To investigate the lack of the 'kink' in axial turbulence intensity, the variation of Reynolds stresses along the impingement plate at  $y/d=0.1$  is plotted in Figure 5.48. Differences in Reynolds stresses between air and water that prevailed at the nozzle exit are preserved, albeit reduced in magnitude, up to the region where the mixing layer of the jet strikes the target surface at  $r/d \approx 0.7$ . At this location, the shear stress induced by the water jet is about five times as high as that produced by the air jet. However, both jets agree qualitatively in that the shear stress is positive before it changes its sign further downstream at almost identical radial positions,  $r/d \approx 0.85$ . This is in contrast to the higher Reynolds number flows, which had zero shear stress levels up to  $r/d \approx 0.6$  until stress levels started to assume negative values.

The influence of dynamic viscosity,  $\mu$ , near the wall increases with decreasing local Reynolds number and tends to stabilise laminar flow. However, due to the very high levels of turbulence, the question arises as to whether the present flow field beneath the laminar jet is laminar or turbulent. To answer this question, the development of the turbulent shear stress for various distances away from the impingement plate is depicted in Figure 5.49.

Despite similar qualitative trends, as in the higher Reynolds number cases, it has to be noted that turbulent shear stress levels of the  $Re=2,000$  case are about 50% greater. With decreasing values of  $y/d$ , the axial velocity forms a peak at the edge of the jet due to entrainment of re-circulating fluid. This peak shifts radially outwards and causes the velocity gradient to drop which decreases the Reynolds stress while the radial positions of zero values are shifted downstream. These findings are supported for four normal distances from the impingement plate and are presented in Figure 5.50 and Figure 5.51 for the axial and radial velocity, respectively.

At  $y/d=1$ , the largest axial velocity gradient in water occurs at  $r/d=0.57$  which coincides with the peak in turbulent shear stress, see Figure 5.49 and Figure 5.50. Shear stress levels in air are significantly lower at  $y/d=1$  but show increased levels by  $y/d=0.4$ . At this location, the turbulent shear in water begins to decrease under the effect of the target plate. The change in sign observed for both Prandtl numbers at  $r/d \approx 0.65$  for  $y/d=0.4$  is attributed to the decay of the axial velocity while the subsequent rise of the mean radial velocity dominates the occurrence of negative shear stress. The shear stress is almost zero for  $1 \leq r/d \leq 1.5$ . At  $r/d \approx 1.65$ , where the radial mean velocity starts to exceed the axial velocity component in magnitude, the shear stress changes its sign again from positive to negative. This suggests that

turbulent shear stress characteristics are not only affected by mean velocity gradients but also by the magnitude of the mean velocity. It explains why levels of turbulent shear stress are almost zero for  $y/d=0.014$ . By  $r/d \approx 0.9$  and at various distances away from the impingement plate, both Prandtl numbers show quantitative and qualitative agreement in their Reynolds stress characteristics which is maintained up until  $r/d=2.5$ .

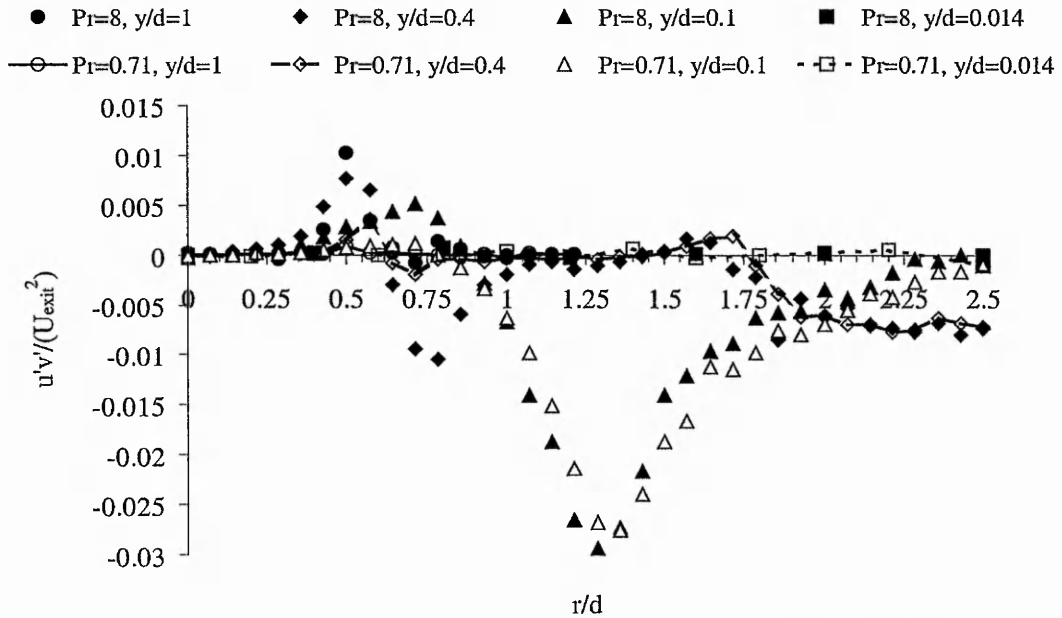


Figure 5.49. Radial and axial development of the Reynolds stresses (Re=2,000).

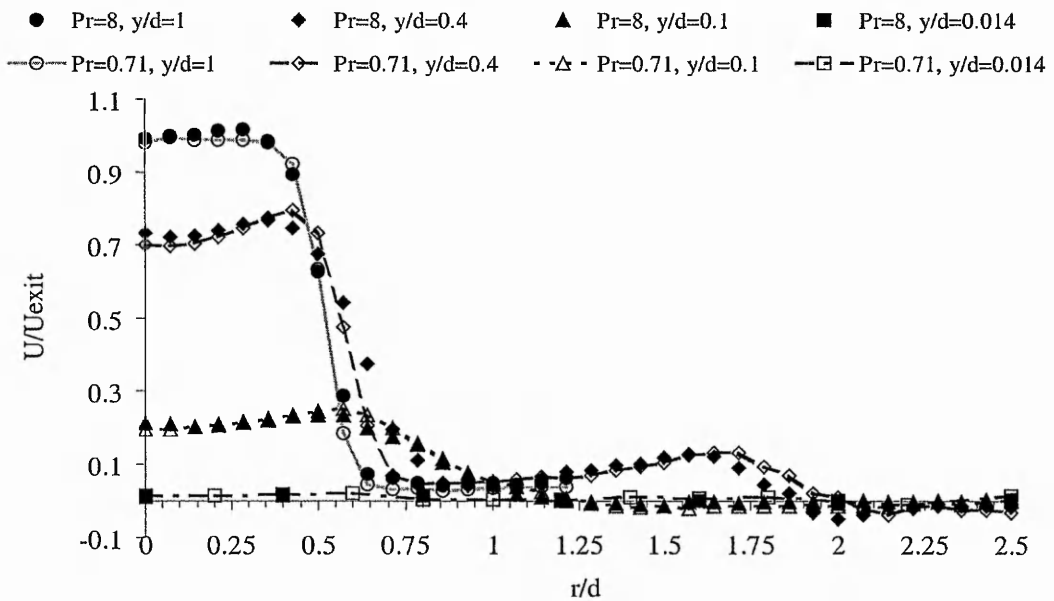


Figure 5.50. Radial and axial development of the mean axial velocity (Re=2,000).

It was shown in Figure 5.40 that jets of  $Re=10,000$  and  $Re=20,000$  form positive peaks in shear stress at the edge of the jet. As the impingement plate is approached, at  $y/d=0.4$ , the region, where the shear stress is dominated by the axial velocity gradient,  $\partial U/\partial Y$ , extends to  $r/d \approx 0.9$ , thus confirming the spreading of the jet. With reduced distance from the wall,  $y/d=0.2$ , the shear stress normal to the wall has reduced to zero levels and only the normal stresses  $u'$  and  $v'$  display local peaks. Here, for  $r/d > 0.65$  the gradient of the mean velocity parallel to the wall,  $\partial V/\partial X$ , begins to dominate the turbulence production of the wall jet. A different behaviour is observed in Figure 5.49 for  $Re=2,000$  at  $y/d=0.4$  where the edge of the approaching jet first experiences axial strain  $\partial U/\partial Y$  before, at  $r/d \approx 0.62$ , the shear stress changes its sign thereby indicating that the turbulent motion of the flow is driven by the velocity gradient parallel to the wall. As the distance from the wall is further reduced,  $y/d=0.1$ , the axial velocity gradient has extended its influence in the radial flow direction. The developing wall jets of air and water show relatively high levels of positive shear stress (induced by axial strain) in the region  $0 \leq r/d \leq 0.85$  before the shear changes its sign at  $r/d \approx 0.8$ . The missing 'kink' in axial turbulence intensity is therefore attributed to the preservation of axial strain in the mixing layer of the jet which prevails until very close to the impingement wall. This indicates that for  $Re=2,000$  the approaching jet has a greater effect on the development of the subsequent wall jet than for higher Reynolds numbers where the radial strain,  $\partial V/\partial X$ , is the only source of shear stress production.

In the further development of the wall jet, Figure 5.48, at  $r/d \approx 1.28$ , the shear stress displays a peak at the same location where the radial turbulence intensity exhibits a maximum. This is consistent with the trend observed in Section 5.2.3.2.1.2 in that the location of the radial turbulence intensity peak shifts downstream along the impingement plate as the Reynolds number is increased. At  $r/d \approx 1.71$ , a less pronounced maximum in radial turbulence intensity can be seen which is accompanied by a change in the rate at which the shear stress decays.

The conclusions that can be drawn from this are threefold: For  $Re=2,000$ , the wall jet is less stable than its high Reynolds number counterpart since the edges of the approaching jet at  $y/d=0.4$  are strongly affected by flow normal *and* parallel to the wall, thus indicating that a strong re-circulating flow in the test section exists. Secondly, in contrast to the higher Reynolds number flows, the case of  $Re=2,000$  displays higher levels of axial shear strain at  $y/d=0.1$ . This identifies the mixing layer at the edge of the jet as the location where Reynolds number effects and Prandtl number effects occur.

Finally, the peak in Reynolds shear stress, which causes secondary peak in heat transfer, moves away from the stagnation point as the Reynolds number is increased.

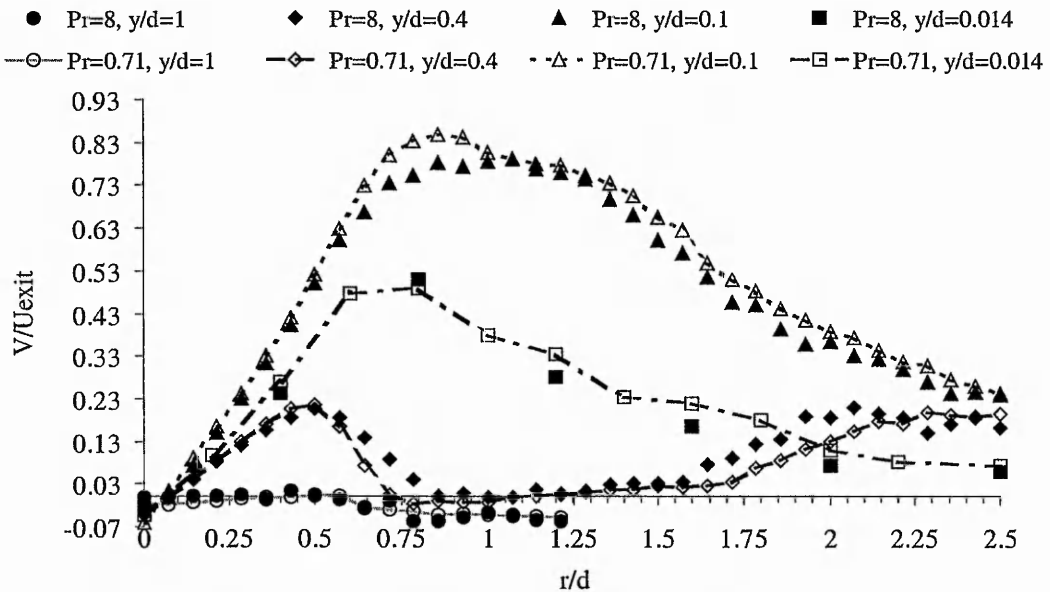


Figure 5.51. Radial development of the mean radial velocity ( $Re=2,000, Pr=8$ ).

Variations in initial conditions between water and air at the nozzle exit diminish continuously as the jet propagates towards the impingement plate so that it can be concluded that the flow field begins to become turbulent where both flow fields are identical to within the measurement uncertainty. This is indicated at the location near the wall where the Reynolds stresses agree closely, namely at  $r/d \approx 0.9$  in Figure 5.49. Furthermore, high levels of turbulence corroborate findings by McNaughton and Sinclair (1966) who classified the flow field produced by a laminar jet as semi-turbulent in contrast to a laminar description given by Polat *et al.* (1989).

An interesting feature for  $Re=2,000$  is highlighted when both working fluids are compared in terms of the anisotropic behaviour in the stagnation region at  $r/d=0$ . To assess the implications with respect to other Reynolds number flows, first of all a typical example for the close agreement in the ratio of the axial stress component to the radial stress component,  $u'/v'$ , is given in Figure 5.52 for  $Re=10,000$ . Here, the anisotropy increases as the plate is approached and decreases linearly in the immediate vicinity of the wall. At  $y/d=0.4$ , the value of  $u'$  reaches 160% of  $v'$  thereby implying that the flow is dominated by the axial velocity component. The actual change in flow direction from axial to radial (i.e. normal to parallel) takes place in the region  $y/d < 0.09$ . Although not shown here, results for  $Re=20,000$  corroborate this trend qualitatively in that the ratio of normal stress components is increased to two. With increasing distance from the

stagnation point, this ratio decreases in magnitude thus indicating a return of the wall jet to isotropy.

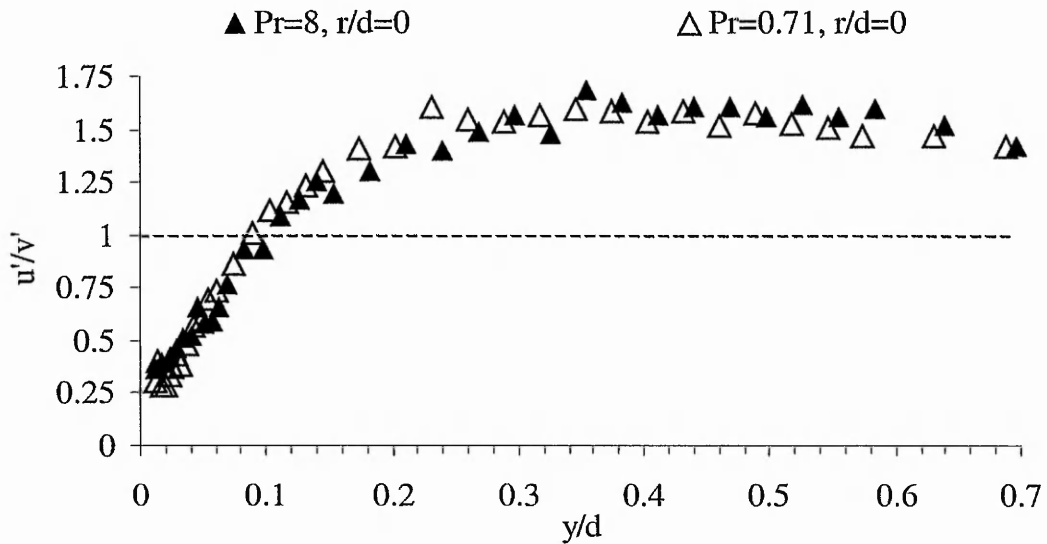


Figure 5.52. Ratio of normal stress components on the centreline ( $Re=10,000$ ).

In Figure 5.53 and Figure 5.54, the anisotropic behaviour of both working fluids in the region  $0 \leq r/d \leq 2.5$  is characterised for  $Re=2,000$ . Air follows the trend of the larger Reynolds numbers in that the ratio between the axial and radial normal stress reaches a maximum at  $y/d \approx 0.3$  and decreases as the impingement plate is approached. In close vicinity to the wall, at  $y/d \approx 0.02$ , a local maximum of  $u'/v'=1.15$  is observed. A different behaviour is observed for water, where on the centreline the axial fluctuating velocity component is up to 5.6 times as high as its radial counterpart. As the wall is approached, the jet slowly returns to isotropy which is finally reached close to the wall. With respect to the nozzle exit conditions, see Figure 5.22, where the ratio  $u'/v'$  was 3.65, the flow anisotropy has increased by 53%. Since for air this increase is 16%, it can be concluded that nozzle exit conditions have a greater effect on the water jet than for the air jet.

In the region surrounding the shear layer of the jet,  $r/d=0.4$  and  $r/d=0.8$ , the air jet shows almost isotropic behavior while the water jet is dominated by radial turbulence. With increasing distance from the stagnation point and, as the wall jet continues to develop, differences between the two fluids diminish and the flow tends to isotropy. In the near wall region, the radial velocity component is greater than the axial one, see also Figure 5.47.

It can be concluded that for  $Re=2,000$  differences in anisotropy exist which confirm that the flow fields for air and water, particularly on the centreline, are

affected by fluid properties and nozzle exit conditions. This highly disturbed flow field can therefore best be described as *quasi-turbulent*.

○  $r/d = 0$    □  $r/d = 0.4$    △  $r/d = 0.8$    ●  $r/d = 1.2$    ■  $r/d = 1.6$    ▲  $r/d = 2.0$    ◆  $r/d = 2.5$

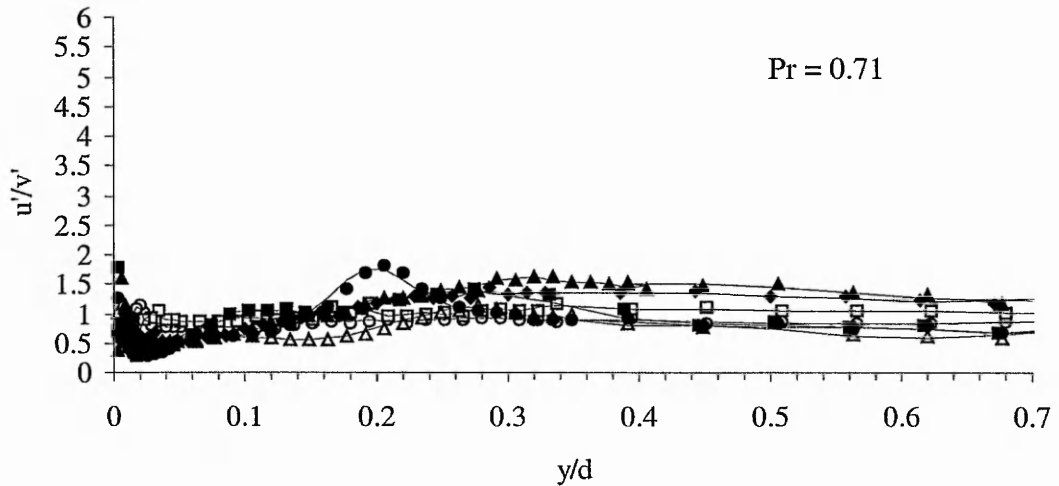


Figure 5.53. Ratio of normal stress components for  $Pr=0.71$  ( $Re=2,000$ ).

○  $r/d = 0$    □  $r/d = 0.4$    △  $r/d = 0.8$    ●  $r/d = 1.2$    ■  $r/d = 1.6$    ▲  $r/d = 2.0$    ◆  $r/d = 2.5$

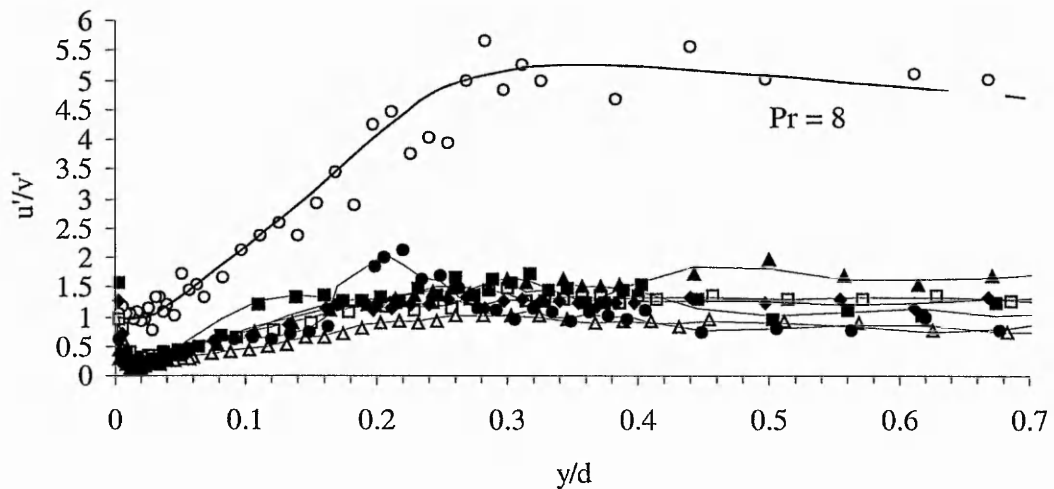


Figure 5.54. Ratio of normal stress components for  $Pr=8$  ( $Re=2,000$ ).

### 5.3 Heat transfer results and comparison with flow field data

Heat transfer data for turbulent impinging jets ( $Re=20,000$ ) of air and water are presented. Firstly, the general validity of numerical methods for approximating the solution for the characteristic transient heat conduction equation is tested by comparing results of a one-and two-dimensional finite difference scheme with those

from the exact analytical solution. This includes a brief discussion of the effects of lateral conduction. Secondly, the temperature fields of the two working fluids are described through thermocouple measurements. Finally, heat transfer characteristics between the air and water jet will be compared qualitatively by considering liquid crystal isotherms that were recorded on video with respect to time. The heat transfer data for the impinging air jet will be further analysed by presenting the distribution of the radial heat transfer coefficient. For the impinging water jet, the variation of local heat transfer is given qualitatively. Throughout the discussion, mean velocity and turbulence data presented previously will be referred to where appropriate.

### 5.3.1 Effects of lateral conduction and the finite difference approach

To account for lateral conduction in transient testing, the heat conduction equation was solved using the finite difference method in one and two dimensions. Results were compared to the analytically exact solution to assess the predictive character of the finite difference technique. The range of the computed heat transfer coefficients corresponds to a typical impinging jet heat transfer situation for which the adequacy of the one-dimensional exact analytical solution has been proven, Ireland and Jones (1985) and Yan (1995) among others. It can be seen from Figure 5.55 that the exact solution of the one-dimensional transient heat conduction equation, for the temperature profile shown, predicts a monotonic heat transfer coefficient distribution with the highest heat transfer coefficient at the stagnation point. This trend is closely reproduced by the one-dimensional numerical approach, however, quantitative discrepancies account to up to 39% at the stagnation point,  $r/d=0$ . When applying the two-dimensional finite difference technique, it is interesting to note that quantitative and qualitative discrepancies between the two numerical approaches are only of marginal nature. However, it has to be pointed out that, despite all computational efforts, no grid-independent solution could be achieved. Amongst other intrinsic shortcomings (truncation error, round-off error and greater computation time), this represents a disadvantage of the two-dimensional model. The fact remains that the one-dimensional model does not differ greatly from the two-dimensional model, which suggests that the use of Perspex as material for the impingement plate effectively suppresses lateral heat conduction, see Valencia *et al.* (1995). Since the numerical approach over-predicts the heat transfer coefficient by unacceptable levels and no differences between the one- and two-dimensional solution were found, the exact solution was used for the remainder of

this investigation. In general, it can be said that the finite difference method has to be applied with caution to the specific problem of jet impingement.

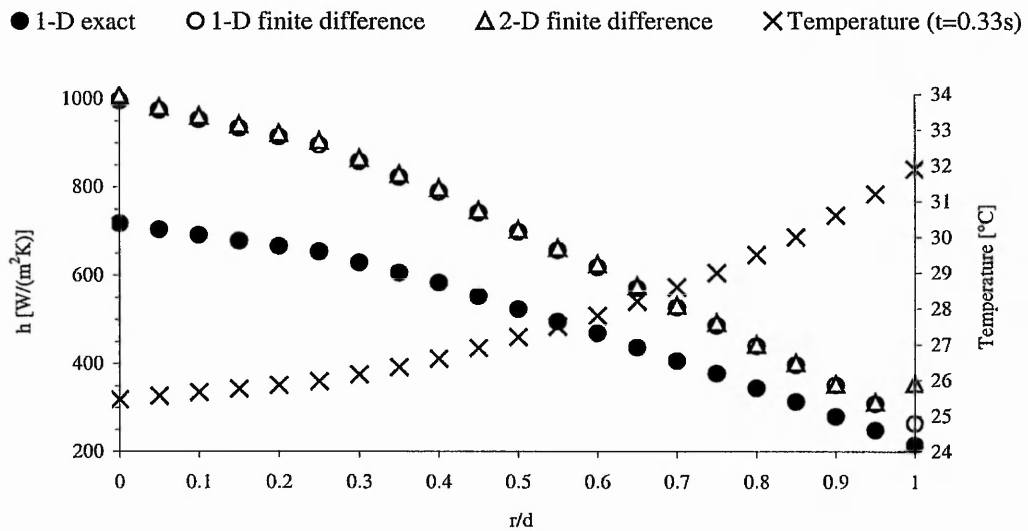


Figure 5.55. Effect of lateral conduction from the finite difference technique.

### 5.3.2 Evolution of the temperature fields

The temporal development of temperature at two points on the jet centreline ( $y/d=2$  and  $y/d=0.86$  or  $y/d=0.54$ ) is shown in Figure 5.56 and Figure 5.57 for  $Pr=0.71$  and  $Pr=4.9$ , respectively. Note that the thermal properties were evaluated at the film temperature by averaging the initial temperature in the test section and the incoming fluid temperature. For the air jet, the hot temperature induces an increase in thermal conductivity and dynamic viscosity. From the definition of Prandtl number, these two trends are counterproductive and therefore lead to a change in Prandtl number of less than 0.5%. This is in contrast to the hot water case where the rise in thermal conductivity is accompanied by a drop in viscosity, thus resulting in a drop of Prandtl number from 8 to 4.9. While the specific heat capacity does not undergo a significant change throughout the temperature variation, the thermal conductivity plays an important role in the temporal evolution of the temperature field. The graphs show that the water temperature at the nozzle exit reaches 95% of its final value within 2.7s, whereas the corresponding time for the air jet is 9.7s.

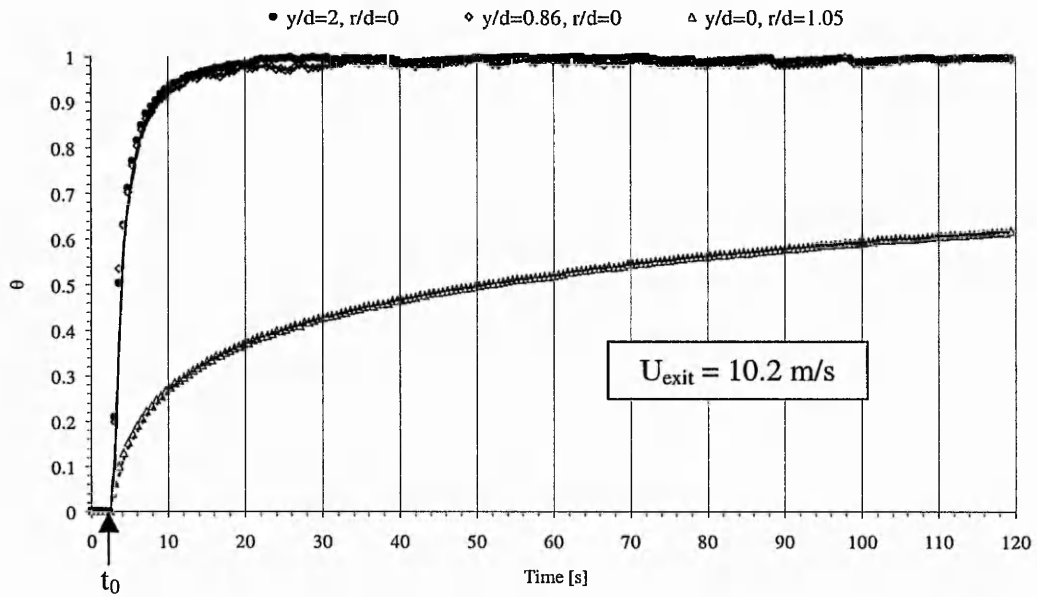


Figure 5.56. Temperature variation of the flow field for  $Re=20,000$  and  $z/d=2$  ( $Pr=0.71$ ).

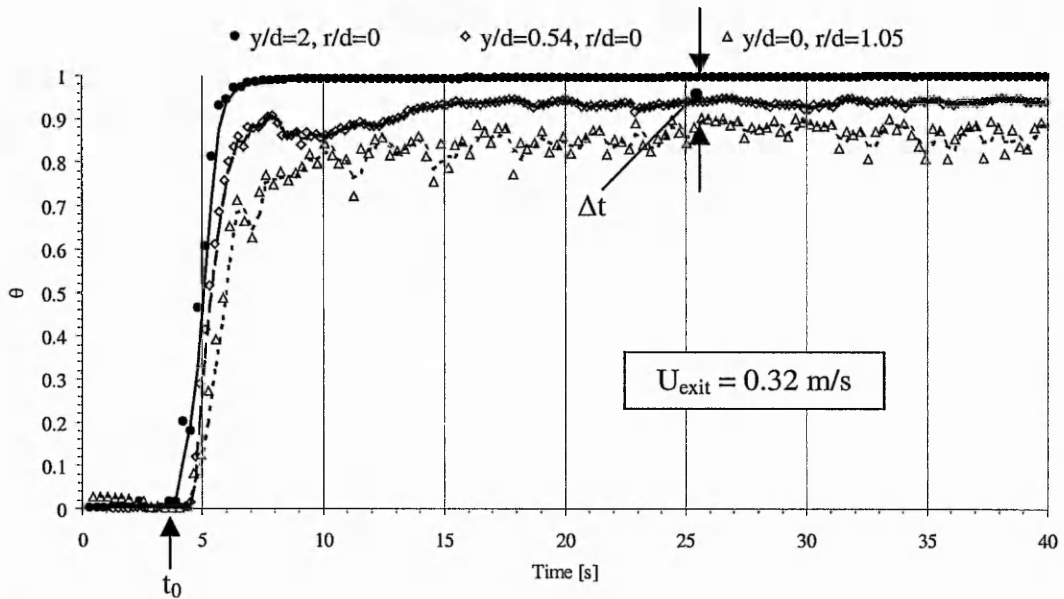


Figure 5.57. Temperature variation of the flow field for  $Re=20,000$  and  $z/d=2$  ( $Pr=4.9$ ).

Since the Reynolds number is identical for both Prandtl numbers, this mismatch in response time can be attributed to a difference in the thermal time constants, as defined by Iacovides *et al.* (1999):

$$\tau = \frac{\rho c_p \lambda}{h^2} \tag{5.2}$$

Substituting the fluid properties into Equation (5.2) yields a ratio of

$$\frac{\tau_{\text{Water}}}{\tau_{\text{Air}}} \approx \frac{868 \rho_{\text{Air}} 4.1 c_{p, \text{Air}} 23.1 \lambda_{\text{Air}} h_{\text{Air}}^2}{\rho_{\text{Air}} c_{p, \text{Air}} \lambda_{\text{Air}} h_{\text{Water}}^2} \approx 83000 \frac{h_{\text{Air}}^2}{h_{\text{Water}}^2} \tag{5.3}$$

Inspection of equation (5.2) and (5.3) identifies the dominance of the fluid properties of water over those of air as the main factor for the difference in response time.

Further evidence of the importance of the thermal conductivity for the evolution of the temperature field is shown further downstream of the nozzle exit. While the air jet appears to preserve its temperature at this axial position, the water jet displays a much greater diffusion of thermal energy into the cold surrounding fluid. This suggests that thermal conductivity plays an important role in the mixing and entrainment processes that occur when a jet flow is issued into a surrounding that has a different temperature. Measurements of the surface temperature at  $r/d=1.05$  show pronounced qualitative differences between  $Pr=0.71$  and  $Pr=4.9$ . While the temperature rise in the airflow is smooth and steady, the temperature field induced by the water jet is much more diffuse and appears to be more turbulent. The observation that the temperatures at  $y/d=0.54$  and at  $r/d=1.05$  do not reach the initial jet temperature at the nozzle exit, points to the fact that the incoming jet undergoes strong mixing with the surrounding fluid so that the temperature field spreads quickly within the confining geometry of the test section.

The temperatures of the surface and the fluid for  $t-t_0>7s$  and  $Pr=4.9$  display an almost constant difference  $\Delta t$ , see Figure 5.57. This suggests that due to the high thermal conductivity of water, the thermal energy of the incoming jet flow is quickly transported through the entire flow domain, thereby, gradually raising the temperature of the fluid in the test section. Measurements showed that for a typical transient test duration of 120s, the average water temperature in the test section was increased by approximately 18°C. With regards to the thermal properties of air, this process of heat conduction through the fluid is impeded by the higher value of specific heat capacity for water. Water can 'store' four times the amount of thermal energy relative to air before its temperature is increased by 1°C.

As a consequence of the favourable thermal transport properties of water, the flow temperature is the highest in the immediate vicinity of the nozzle exit and decays gradually with increasing distance from the incoming jet flow. This temporal dependency of the surface temperature prevented the accurate determination of the convective heat transfer coefficient in water. However, qualitative results have been obtained which provide a new insight into the distribution of the heat transfer coefficient beneath a water jet. Conversely, the air jet confines its thermal energy much more effectively to within its flow field so that a quantitative analysis can be performed.

### 5.3.3 Qualitative heat transfer results

This Section details the temporal development of liquid crystal isotherms for  $Pr=0.71$  and  $Pr=4.9$  when a hot jet of  $Re=20,000$  impinges on an initially cold impingement surface. Areas of high local heat transfer are indicated by their early change of liquid crystal colour. A measure of the temperature gradient is provided by observing the width of the isotherm under study.

Both working fluids agree in their display of qualitative trends, in that the first liquid crystal colour change appears at the edge of the jet,  $r/d \approx 0.5$ . This region of high heat transfer is characterised by a relatively low temperature gradient. Its occurrence is attributed to both the fluid accelerating out of the stagnation region which thins the local boundary layer and the influence of the turbulence generated by the shear layer surrounding the approaching jet, Huber and Viskanta (1994). The isotherm then divides into two, one moving towards the centre of the jet while the second one propagates radially outwards.

A third isotherm is produced by the air jet in the region of  $1.2 \leq r/d \leq 2$  and is also divided into two. Figure 5.58 presents a typical series of the time-dependent development of isotherms for  $Pr=0.71$ . This zone of small temperature gradient is constantly reduced by the approaching second isotherm as the temperature of the impingement plate continues to increase radially outwards.

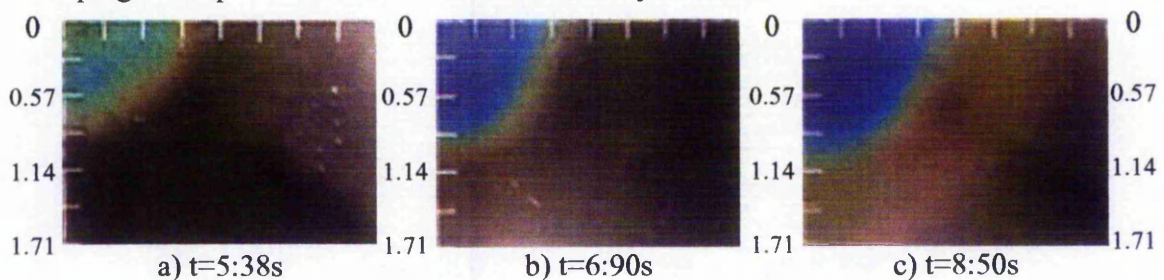


Figure 5.58. Development of isotherms for an air jet at  $Re=20,000$  and  $Pr=0.71$ .

While the air jet produces a very smooth variation in surface temperature, the heat transfer induced by the water jet is dominated by strong spatial fluctuations of the isotherms. A typical example for the evolution of these unsteady isotherms for  $Pr=4.9$  is shown in Figure 5.59. The stated times refer to the instant when the jet first strikes the surface. The first image, Figure 5.59a) confirms the first occurrence of an isotherm at  $r/d \approx 0.55$ . Note, that a narrow bandwidth liquid crystal was used for this test in contrast to all later tests where the wide bandwidth formulation was used. In due course, the series of images show pockets of fluid emerging from an initially smooth and evenly distributed temperature field at  $r/d \approx 0.8$ . At  $t=7:59s$ , spots of cooler temperature become visible at  $r/d \approx 1$  and continue to grow in size while they continue

to propagate radially outwards. These instantaneous temperature fluctuations produce areas of high and low temperature in the region  $1.5 \leq r/d \leq 2$ , see Figure 5.59 f). Although not shown here, the temperature eventually returns back to a temperature distribution similar to that in Figure 5.59 b).

The unsteady nature of the above mentioned pockets of fluid and the resulting occurrence of fluctuating surface temperature were observed at several random times for varying intervals and did not show any periodicity. This phenomenon suggests a possible link to unsteady boundary layer separation as observed in the present flow visualisation and by Didden and Ho (1985), Landreth and Adrian (1990) and Meola *et al.* (2000).

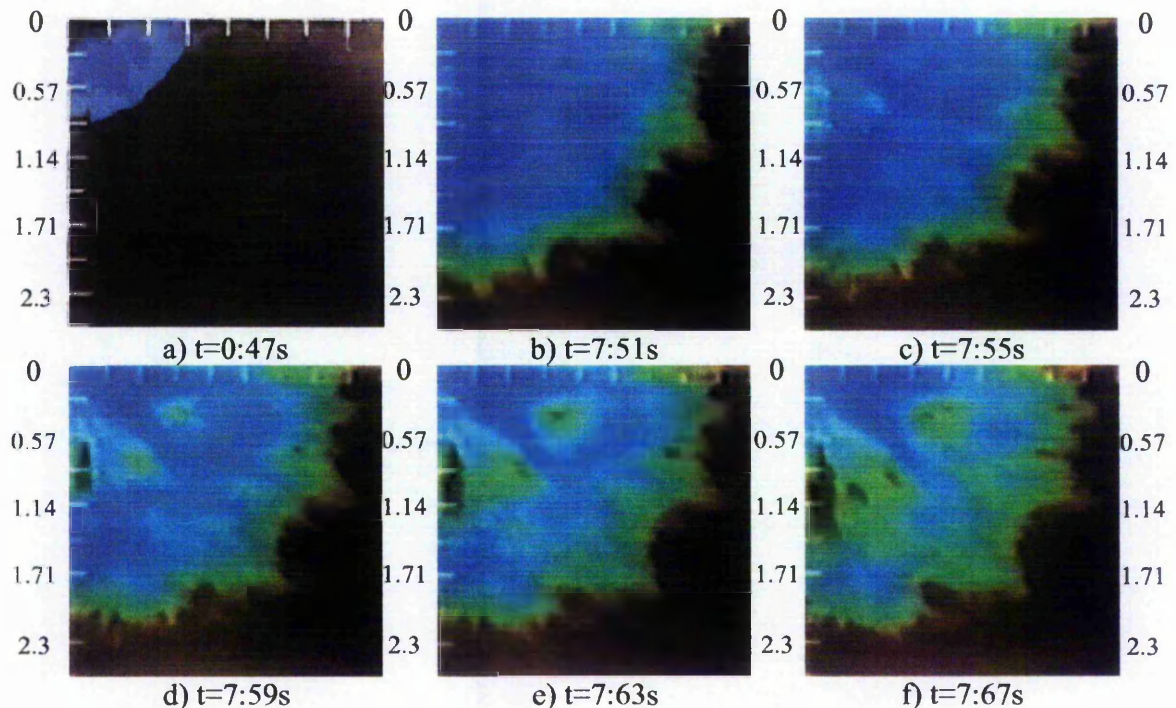


Figure 5.59. Typical development of isotherms for a water jet ( $Re=20,000$  and  $Pr=4.9$ ).

Existing results for impinging air jets, i.e. by Gardon and Akfirat (1965), Lee and Lee (1999) and Meola *et al.* (2000) corroborate the present findings qualitatively. However, although the above liquid crystal results showed identical temperature trends for water and air, namely primary and secondary peaks in the temperature distribution, this is not reflected in currently available heat transfer data for liquids. One possible explanation for this could be size effects in the nozzle which make a direct comparison difficult. No primary (inner) peaks in the radial heat transfer distribution were reported by Sun *et al.* (1993) for an impinging water jet with a nozzle diameter of 0.987mm. Garimella and Rice (1995) studied jets of FC-77 with nozzle diameters of up to 6.35mm and found only a flattening of the heat transfer profile at the stagnation point. Chang *et al.* (1995) reported a monotonic heat transfer

profile for an impinging jet of Freon R-113 with a nozzle diameter of  $d=4\text{mm}$ . To the authors knowledge, the only study that presented results for a submerged water jet with a nozzle diameter similar to that of the present study,  $40\text{mm}$ , is that by Yokobori *et al.* (1979). However, no local heat transfer data were presented.

### 5.3.4 Quantitative heat transfer results

The Nusselt number distribution for air as a function of the radial distance from the stagnation point is shown for a Reynolds number of 20,000 in Figure 5.60. Since the impingement plate was located within the potential core of the jet, at  $z/d=2$ , the resulting heat transfer profile is non-monotonic and displays two local peaks. At the stagnation point, values of Nusselt number are minimal and begin to increase towards the edge of the jet, where the primary peak is formed at  $r/d \approx 0.5$ . This peak is approximately 7% higher than the stagnation point value and lies well within the range of 5-14% suggested by Lee and Lee (1999). As the radial distance increases, a slight flattening is observed before the non-dimensionalised heat transfer coefficient decreases to 78% of its stagnation point value which is reached at a position of  $r/d \approx 1.2$ . By  $r/d \approx 1.7$ , the Nusselt number has recovered to approximately 88% of the stagnation point value before it finally decreases monotonically, thereby, indicating developing flow of the wall jet.

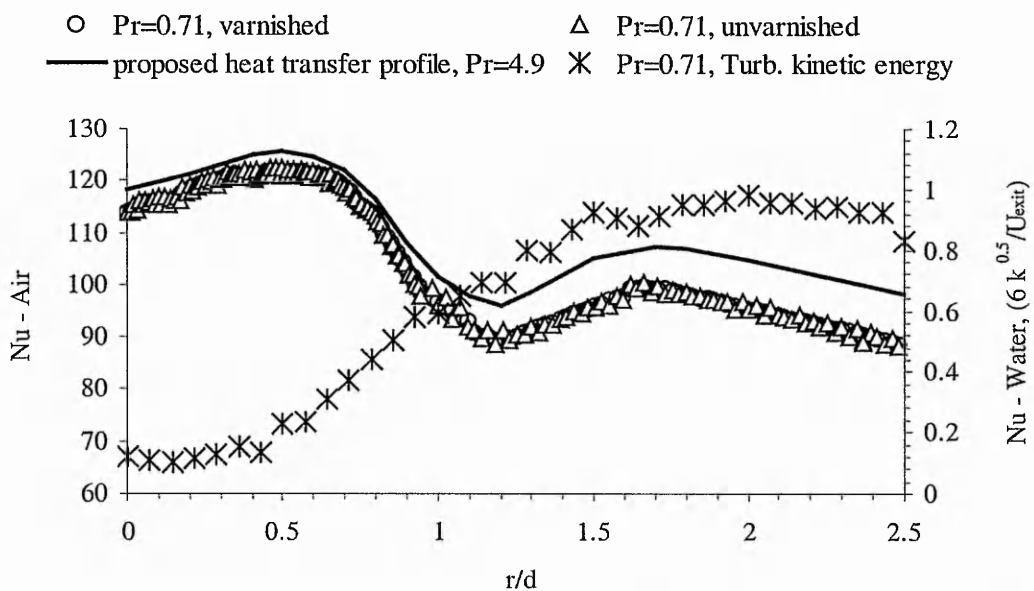


Figure 5.60. Variation of the local Nusselt number for  $Pr=0.71$  and  $Pr=4.9$  ( $Re=20,000$ ).

Heat transfer characteristics of the impinging air and water jet were studied using two types of liquid crystals, BM/R31C1W/C17-10 and BM/R35C15W/C17-10,

respectively. To protect the liquid crystals from being washed off, a thin top layer of varnish was applied. As this coat represents an additional resistance against heat transfer, the effects of the varnish layer were quantified for an impinging air jet by plotting results of the unvarnished plate together with those from the varnished plate, see Figure 5.60. It becomes apparent from the graph that the effects of two thin coats of varnish, applied with a conventional artist's airbrush, on the convective heat transfer coefficient are negligible. Furthermore, the varnish protected the liquid crystals sufficiently from being washed off in water so that the plate was re-used for measurements in air without loss of response time.

The existence of peaks in the local heat transfer profile is important as they lead to high average surface heat transfer coefficients. Here, for air, the average heat transfer is  $107.1 \text{ W}/(\text{m}^2\text{K})$  and agrees well with the value of  $103.5 \text{ W}/(\text{m}^2\text{K})$  reported by Ball (1998) for an impinging semi-confined jet with a diameter of  $d=0.1\text{m}$ . Viskanta (1993) refers to the following correlation

$$\overline{Nu} = 0.0233 \text{ Re}^{0.87} \text{ Pr}^{0.33} \tag{5.4}$$

which yields a value of  $114.8 \text{ W}/(\text{m}^2\text{K})$ , thus over-predicting present results by 6.7%.

The minimum in heat transfer at the stagnation point,  $r/d=0$ , is accompanied by the lowest level in axial and radial turbulence throughout the wall jet region, see Figure 5.61.

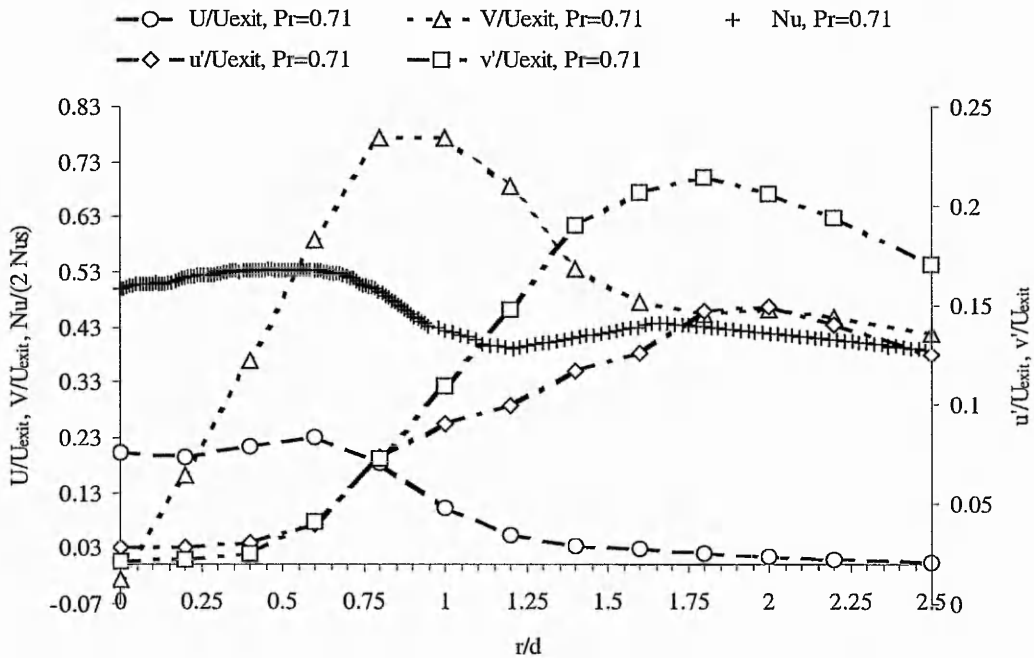


Figure 5.61 Variation of the local Nusselt number for  $Pr=0.71$  and  $Pr=4.9$  ( $Re=20,000$ ).

It has to be noted that Figure 5.61 contains the flow quantities as presented in Figure 5.35. As the edge of the jet is approached and the axial velocity attains a local maximum, the Nusselt number displays a primary peak which is well documented for impinging air jets, Huber and Viskanta (1994), Lee and Lee (1999) and Meola *et al.* (2000). As is shown in Figure 5.40, immediately after issuing from the nozzle, a positive peak in turbulent shear stress at the edge of the approaching jet is formed, which diminishes as the target surface is approached. This occurrence corroborates findings of the flow situation depicted in Figure 5.6 where small circular vortex structures appear close to the deflection zone of the axial flow,  $r/d=0.6$  to  $0.7$ . Kezios (1956) and Ball (1998) attributed the primary peak in the local heat transfer to a thinning of the boundary layer. Although such an occurrence could not be discriminated from present LDA-results, it can be seen in Figure 5.4, for an impinging water jet of  $Pr=5.4$ , that at  $r/d\approx 0.6$  the near wall flow shows some thinning.

Referring once again to Figure 5.61, the minimum in Nusselt number at  $r/d\approx 1.1$  coincides with a region of high radial velocity and relatively low local turbulence intensity. In fact, the axial turbulence in particular shows a local flattening while velocity gradients are shallow.

There is much speculation as to the cause of the secondary peak in local heat transfer. While some workers attributed the local maximum to a transition from laminar to turbulent flow, see Gardon and Akfirat (1965) and Gillespie *et al.* (1996), other researchers observed unsteady separation of the wall jet where the subsequent re-attachment of the flow coincided with the position of the secondary peak, Meola *et al.* (2000) and Landreth and Adrian (1990). It has to be borne in mind, however, that the latter observation was only made when a PIV-technique was used which emphasises its unsteady character. The results of the present study, see Figure 5.6, confirm some of the findings by Meola *et al.* (2000) in that the qualitative flow field shows similarities in the streamline behavior. The unsteadiness of the flow field was demonstrated through instantaneous hot spots in the liquid crystal isotherms. Furthermore, the normalised turbulent kinetic energy along the impingement surface displays almost constant levels for  $1.5 \leq r/d \leq 2.5$ . However, in terms of the more important aspect of unsteady separation in the region of  $0.8 \leq r/d \leq 1.2$  with subsequent re-attachment of the wall jet, flow reversal was not observed. The occasional occurrence of negative flow vectors was confined to the immediate vicinity of the wall and is due to errors caused by the finite length of the LDA measurement volume and near wall reflections.

Clear evidence of laminar flow in the region,  $0 \leq r/d \leq 0.5$ , has been presented which developed further along the plate, thereby increasing its turbulence levels. As the flow approached the region  $1.5 \leq r/d \leq 2$ , maximum levels of axial and radial turbulence intensity and shear stress were observed which coincided with the secondary peak in the heat transfer coefficient profile. This region is downstream from the location where Gillespie *et al.* (1996) reported that transition from laminar to turbulent flow is complete,  $r/d \approx 1.2$ . It can therefore be concluded that the secondary peak in heat transfer is attributed to the transition from laminar to turbulent flow.

The location of the peak in turbulent shear stress from the present data agrees well with the correlation for the secondary peak in heat transfer, as proposed for air by Lee and Lee (1999).

$$(r/d)_{2\text{nd peak}} = 0.137 \text{ Re}^{0.267} \quad (5.5)$$

It can be seen from equation (5.5) that this is independent of the working fluid. In fact, the good agreement between the correlation and the present results was also confirmed by the position of the secondary peak isotherm for the impinging water jet, see Figure 5.58. The position of the peaks in Reynolds stress together with the correlation from equation (5.5) are plotted in Figure 5.62.

Schlichting (1979) attributed maximum values of turbulent shear stress to extreme values of skin friction. Indeed, Alekseenko and Markovich (1996) showed, for the case of an impinging jet of potassium ferricyanide and ferrocyanide, that peaks in skin friction coincided with those of the local heat transfer coefficient, namely at  $r/d = 1.75$ . Since the Reynolds number of 24800 was close to that of the present study, it appears that peaks in turbulent shear stress contribute, among other turbulent intensity components, strongly to the shape of the local heat transfer profile.

Figure 5.62 summarises the qualitative results from the previous Section and includes a plot of equation (5.5). An important observation during the water tests concerns the occurrence of pronounced primary and secondary peaks in the local heat transfer distribution. These peaks manifest themselves as an early appearance of isotherms and as an unsteady occurrence of isotherms in the region  $0.5 \leq r/d \leq 0.7$  and  $1.5 \leq r/d \leq 2$ , respectively. To the author's knowledge, the primary peak in the heat transfer distribution of an impinging water jet has not been previously reported in the open literature. This could be related to the fact that existing work on local heat transfer distributions has not involved nozzle diameters larger than 12.7mm.

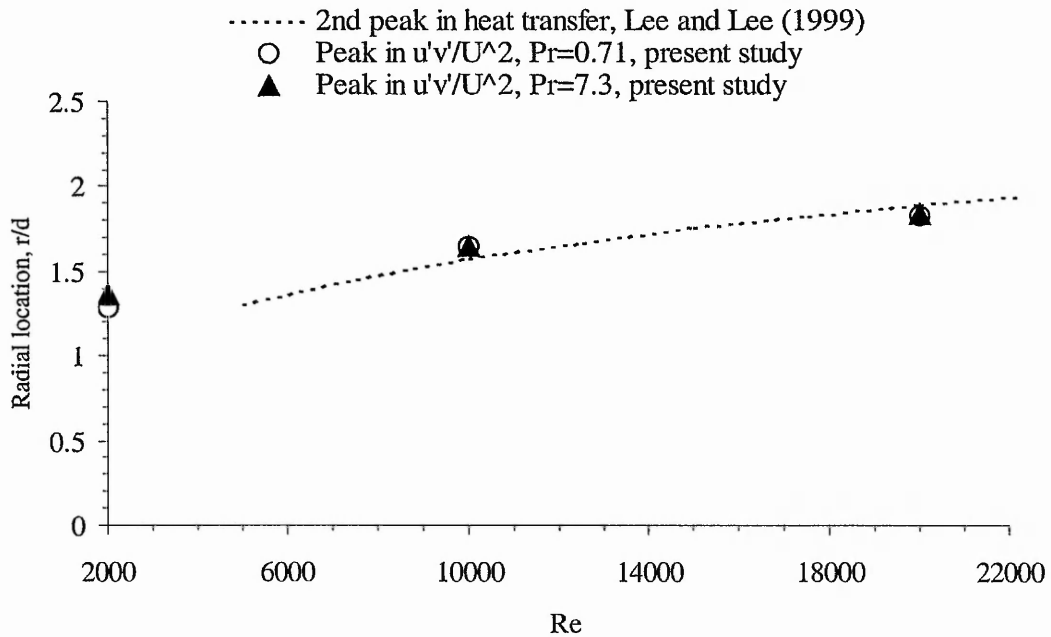


Figure 5.62. Variation of peaks in Reynolds stress with Re (Pr=0.71 and 7.3).

#### **5.4 Concluding remarks**

An experimental investigation was carried out to study the flow field of a semi-confined, submerged jet impinging onto a flat surface over a range of Prandtl numbers. Effects of fluid properties on turbulent impinging jet flow were studied for three Reynolds numbers based on the nozzle exit conditions, namely Re=2,000, 10,000 and 20,000. Water, at different temperatures, and air were used as working fluids, so that  $0.71 \leq Pr \leq 8$ . The impingement plate was positioned at a non-dimensional spacing of  $z/d=2$  and therefore well within the potential core of the jet. Quantitative and qualitative flow visualisation, laser-Doppler anemometry (LDA) and liquid crystal thermography have been used to obtain new detailed fluid flow and heat transfer data. The reliability and consistency of the results has been demonstrated by comparing, wherever possible, data with other authors' works.

The full field flow visualisation of impinging water jets of various Prandtl numbers revealed that vortical structures originate in the shear layer surrounding the jet core and impinge on the developing wall jet at  $r/d \approx 0.6-0.7$ . Further downstream, at a radial position of approximately  $r/d \approx 2$ , the flow develops wavy streamlines between the convected vortices and the impingement surface. The centres of the recirculating vortices that transport spent fluid back to the jet centreline are independent of Prandtl number.

The nozzle exit conditions have been characterised for all three Reynolds numbers,  $Re=2,000$ ,  $Re=10,000$  and  $Re=20,000$ , to enable test results to be reproduced. Results for  $Re=10,000$  were used as input boundary conditions to a numerical model. For  $Re=2,000$ , the nozzle exit conditions for air and water differ in that the air jet shows almost constant levels of axial and radial turbulence levels across the nozzle exit, while the water jet develops distinct peaks of turbulence intensity in both directions at the edge of the nozzle. This leads to a markedly higher level of turbulent shear stress when compared to the air jet. In the air jet, the turbulence intensity levels are almost identical in the axial and radial direction, while the water jet develops a much higher axial velocity fluctuation on the centreline than its radial counterpart. This gives rise to different mixing rates in axial and radial direction for the water jet. For this Reynolds number, the effects of the impingement plate on the approaching jet are strongest on the water jet ( $y/d \approx 0.9$ ) while the air jet is unaffected until a distance of  $y/d \approx 0.67$  from the plate is reached.

Variations of the turbulent flow field with respect to near wall axial and radial velocity, turbulent normal and shear stress components have been described in detail. The flow fields produced by the high Reynolds number jets,  $Re=10,000$  and  $20,000$ , show almost identical quantitative agreement for all studied velocity components, which suggests that Prandtl number effects are negligible if the Reynolds number is sufficiently high,  $Re \geq 10,000$ . This agreement has also been observed for their anisotropic behaviour in the stagnation region.

For the flow in the test section, it has been shown that among the three Reynolds numbers, the case of  $Re=2,000$  produces the largest levels of turbulence. For these laminar nozzle exit conditions, air and water show quantitative differences in the development of the mean and turbulence components which were found in the mixing layer at the edge of the approaching jet and along the impingement plate and in close proximity to the wall. In the developing region of the wall jet, air produces a faster wall jet with a thinner boundary layer. Up to a radial distance of  $r/d \approx 1.6$ , the water jet shows generally greater levels of axial and radial turbulence intensity and turbulent shear stress, which is due to differences in kinematic viscosity. An exception to the above is represented by the region in the immediate vicinity of the wall where the air jet displays consistently higher axial turbulence levels than the water jet, for  $0 \leq r/d \leq 2.5$ . For  $r/d > 1.6$ , the wall jets of air and water approach close similarity in their mean velocity and turbulence profiles, with the air jet slightly exceeding turbulence levels of the water jet.

From the development of the shear stress normal and parallel to the wall, the following conclusions can be drawn: For  $Re=2,000$ , the wall jet is less stable than its high Reynolds number counterpart since the edges of the approaching jet at  $y/d=0.4$  are strongly affected by flow normal *and* parallel to the wall, thus indicating that a strong recirculating flow in the test section exists. Secondly, in contrast to the higher Reynolds number flows, the case of  $Re=2,000$  displays higher levels of axial shear strain at  $y/d=0.1$ . This identifies the mixing layer at the edge of the jet as the location where Reynolds number effects and Prandtl number effects occur. Finally, the peak in Reynolds shear stress, which causes the secondary peak in heat transfer, moves away from the stagnation point as the Reynolds number is increased.

Since it was shown for  $Re=2,000$  that shear stress levels are well preserved from the nozzle exit to the location where the jet impinges on the plate, nozzle exit conditions are very important for low Reynolds number jets if maximum heat transfer coefficients are to be achieved.

For  $Re=2,000$ , differences in anisotropy between air and water jets exist, particularly on the centreline, which confirm that the flow field is affected by fluid properties and nozzle exit conditions. For  $r/d>0.9$ , differences in the mean and turbulent flow quantities have diminished to within the measurement uncertainties so that the flow field can be best described as *quasi-turbulent*.

The inadequacy of using the finite difference approach in solving the transient one-dimensional heat conduction equation through a semi-infinite body has been demonstrated. Heat transfer coefficients inferred from this approach are over-predicted by up to 39% when compared to the exact solution. Effects of lateral conduction are seen to be negligible.

Thermal conductivity of the stationary fluid in the test section prior to a test has been shown to play the most important role in the evolution of the transient temperature field. While the air jet appears to preserve its temperature along the centreline, the water jet displays a much greater diffusion of thermal energy into the cold surrounding fluid. This difference in entrainment behaviour between the two fluids is also reflected in the development of the isotherms. The temperature rise in the airflow is smooth and steady and is in contrast to the temperature field induced by the water jet, which is more diffuse and appears to be more turbulent.

Qualitative results using liquid crystals have shown identical temperature trends for impinging turbulent jets of water and air, namely primary and secondary peaks in

the temperature distribution at  $r/d \approx 0.55$  and in the region  $1.5 \leq r/d \leq 2$ .

The radial Nusselt number profile for the impinging air jet confirms the non-monotonic nature when the impingement plate is positioned well within the potential core of the jet. The primary peak in heat transfer could be attributed to the impingement of vortical structures on the developing wall jet which was accompanied by a simultaneous thinning of the near wall flow at this radial location.

The minimum in Nusselt number at  $r/d \approx 1.1$  coincides with a region of high radial velocity and relatively low local turbulence intensity.

The secondary maximum in the radial heat transfer profile has been attributed to maximum values of all of the turbulence components, axial and radial turbulence intensity and turbulent shear stress, in the region  $1.5 \leq r/d \leq 2$ . As the flow was shown to be laminar in the region,  $0 \leq r/d \leq 0.5$ , the occurrence of maximum turbulence quantities at  $1.5 \leq r/d \leq 2$  and the secondary peak in heat transfer is attributed to transition from laminar to turbulent flow. For both working fluids, it was found that the location of the peak in turbulent shear stress coincides well with the correlation for the secondary peak in heat transfer, as proposed by Lee and Lee (1999).

## **Chapter 6**

### **Presentation and Discussion of Numerical Results**

#### **Introduction**

Results of the computational simulation of jet impingement inside the test section will be discussed and compared to results from experimental measurements. An isothermal jet at a Reynolds number of 10,000 impinging onto a flat surface positioned  $2d$  away from the nozzle exit is considered. As was shown in Chapter 5, velocity profiles for  $Re \geq 10,000$  are identical over the considered Prandtl number range, so that for the verification of the numerical model, air was used as the representative working fluid. A three-dimensional model has been developed which allowed the near wall nodes to be placed just outside the viscous sublayer, irrespective of their distance from the stagnation point. The initial boundary conditions to the numerical model were specified using the measured velocity and turbulence profiles at the nozzle exit as presented in Chapter 5. A turbulence model was used to solve the transport equations for the individual Reynolds stresses. Based on a preliminary study on the performance of the standard  $k-\varepsilon$  model against the RNG  $k-\varepsilon$  model, no significant quantitative differences between the two models were identified. Thus, the standard  $k-\varepsilon$  model was employed in view of its requirements for less computational resources, see Rüdél *et al.* (2000). The high Reynolds number standard  $k-\varepsilon$  model, as implemented in the commercial Finite Element software package ANSYS/FLOTRAN, has been employed. The purpose of this study is not to improve numerical codes, but to verify the performance of the Finite Element scheme in a typical CFD-situation and to assess the reliability of the most widely used turbulence model in predicting the velocity and turbulence field beneath an impinging jet.

#### **6.1 Qualitative results**

To gain a qualitative impression of the nature of the numerical flow prediction, plots of the velocity streamlines and the effective viscosity are given in Figure 6.1 while contours of turbulent kinetic energy and dissipation rate are presented in Figure 6.2. Predictions of the mean flow characteristics compare well with experimental results shown in Figure 5.6 and Figure 5.7. Despite the observation that the model estimates

trends of turbulent kinetic energy correctly, it fails to capture impinging vortical structures in the mixing layer of the jet and wavy streamlines in the wall jet. Furthermore, it can be seen that the model is well capable of predicting large scale eddies and large scale recirculation patterns while small scale eddies are not discernable.

In accordance with expectations, highest levels of turbulent kinetic energy occur at the edge of the approaching jet and in the immediate vicinity of the impingement surface. In contrast to the distribution of turbulent kinetic energy, the map of effective viscosity, which is the sum of molecular and turbulent viscosity, shows a more uniform distribution across the entire flow domain. The mutual relationship between the turbulent kinetic energy and the dissipation rate becomes apparent close to the stagnation point in a region,  $0 \leq r/d \leq 0.5$ , where both parameters show identical qualitative trends which result in peak values at the same radial location.

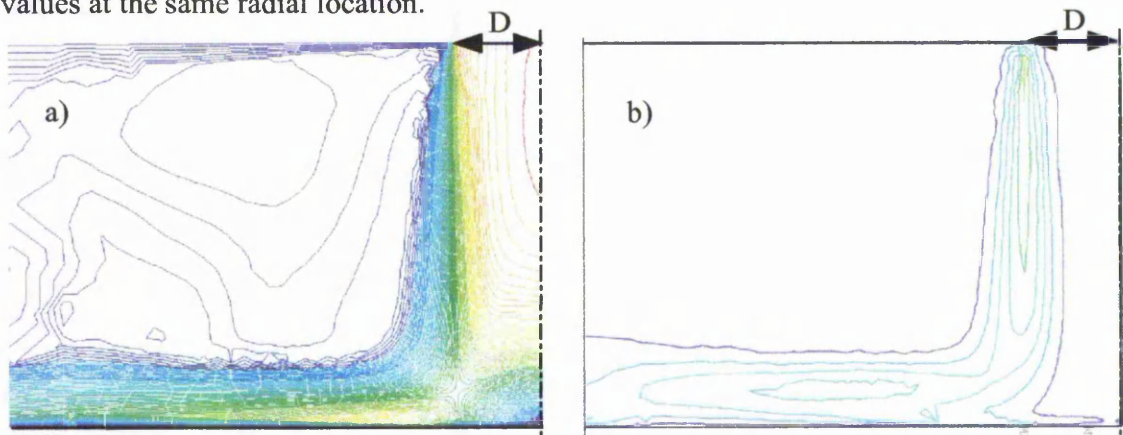


Figure 6.1. Qualitative plots of a) Velocity streamlines and b) Turbulent kinetic energy.

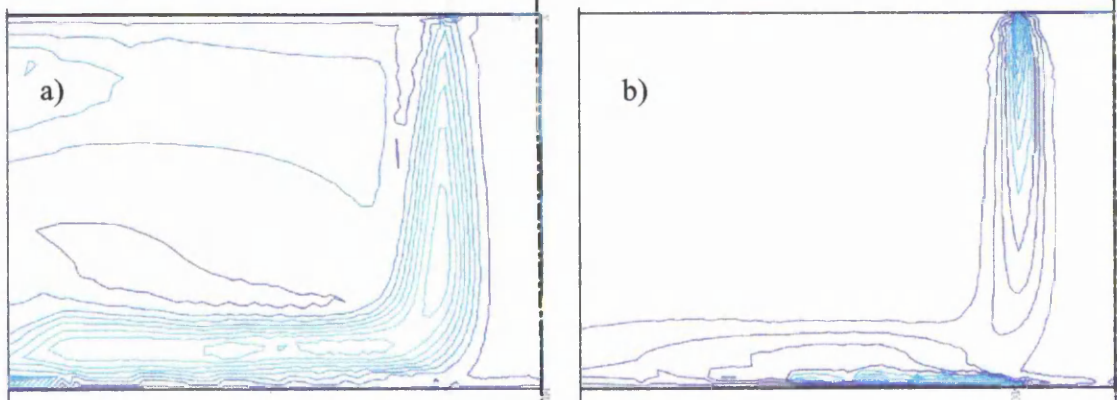


Figure 6.2. Qualitative plots of a) Effective viscosity  $v_{eff}$  and b) Dissipation rate.

### 6.2 Mean velocity profiles

The numerical prediction of the mean axial velocity decay is shown in Figure 6.3. A comparison with experiment reveals excellent agreement along the entire jet centreline. Predictions of the development of the mean radial velocity along the impingement surface are presented in Figure 6.4 to 6.9, together with measurements of the flow field using Laser Doppler-Anemometry (LDA).

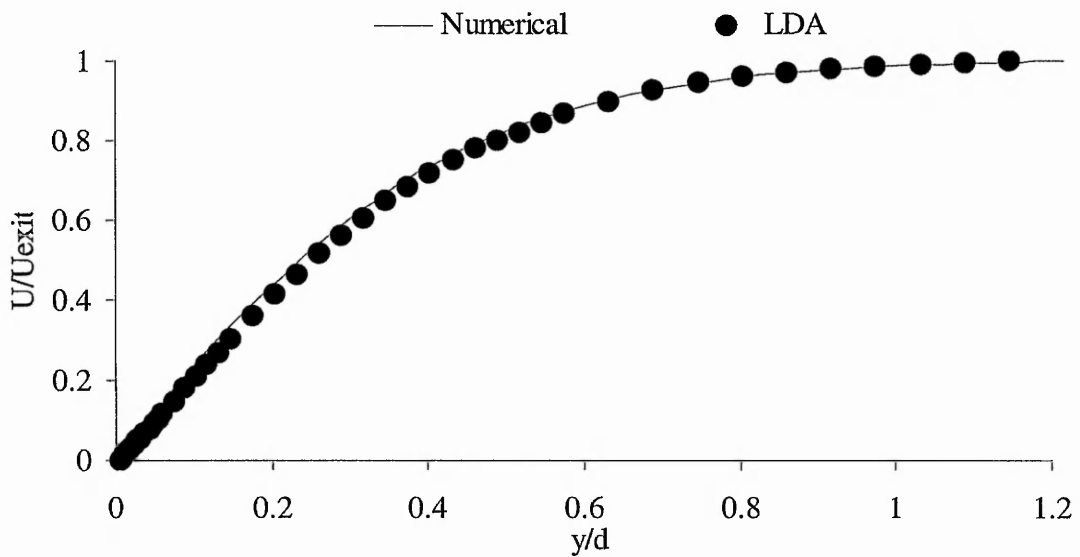


Figure 6.3. Axial velocity profiles at  $r/d=0$ .

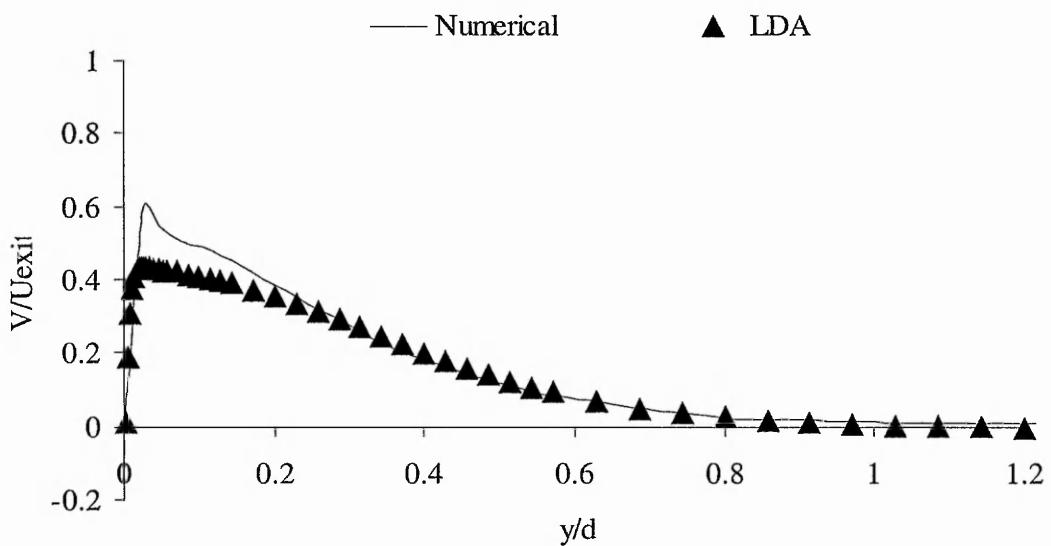


Figure 6.4. Radial velocity profiles at  $r/d=0.4$ .

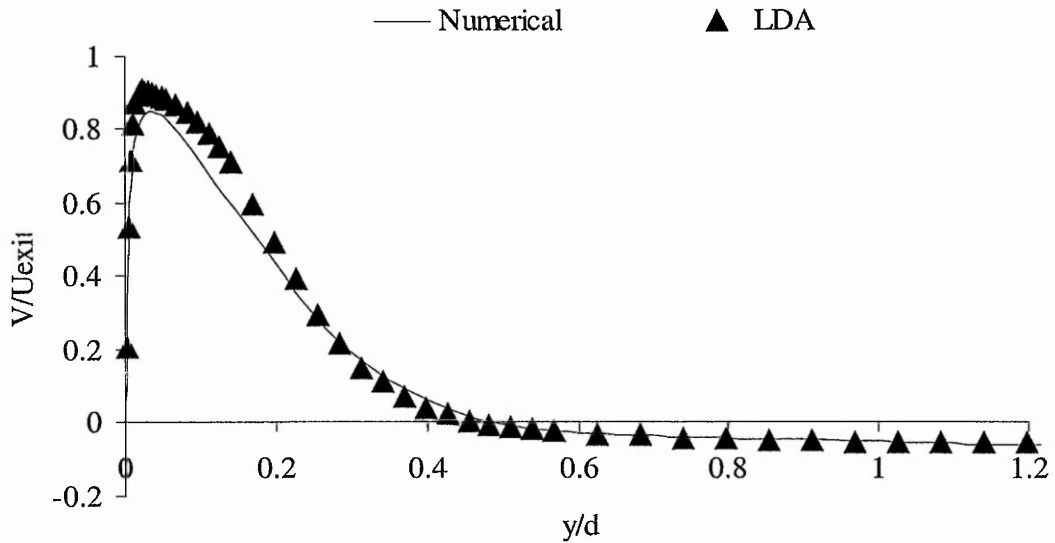


Figure 6.5. Radial velocity profiles at  $r/d=0.8$ .

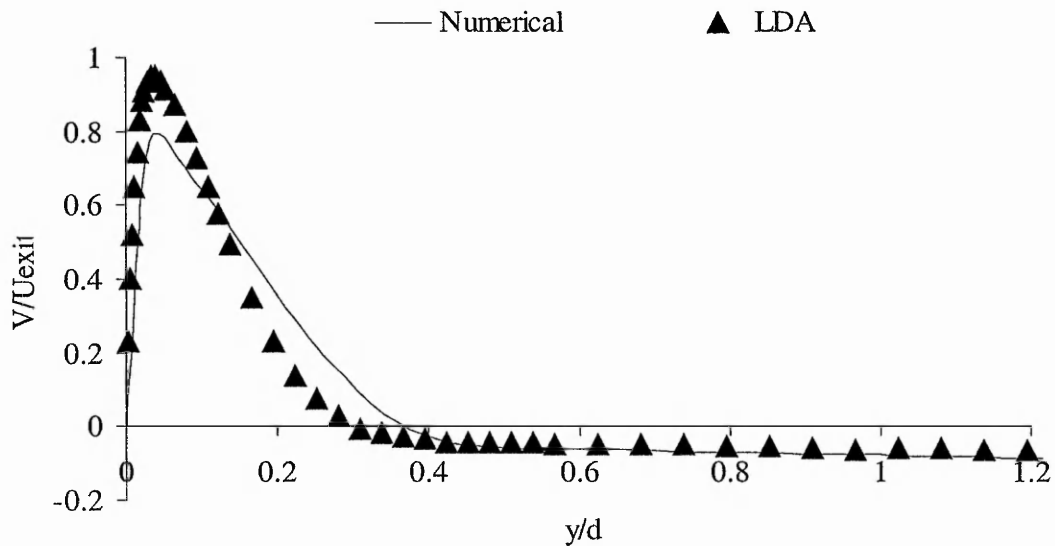


Figure 6.6. Radial velocity profiles at  $r/d=1.2$ .

Trends in the radial velocity profiles are generally predicted correctly by the numerical model in that the velocity of the wall jet steadily increases in the stagnation region,  $0 \leq r/d \leq 0.8$ , before a peak develops between  $r/d=0.8$  and  $r/d=1.2$ . In due course, the spreading rate of the jet, described by the levels in peak velocity, is under-predicted up until  $r/d=1.6$ . At  $r/d=2$ , the numerical model predictions coincide with experimental results but by  $r/d=2.5$ , the  $k-\epsilon$  model over-estimates peak velocities near the wall. It is here where the turbulence model displays a quantitative mismatch with experimental data

in that the location of the velocity peak is too far away from the impingement plate. With respect to the reduction in radial velocity, it can be noted that for distances,  $r/d > 0.8$ , the radial velocity decay is over-predicted in the region  $0.14 \leq y/d \leq 0.6$ . Further away from the impingement plate, the near zero radial velocities, for  $y/d > 0.6$ , are correctly predicted.

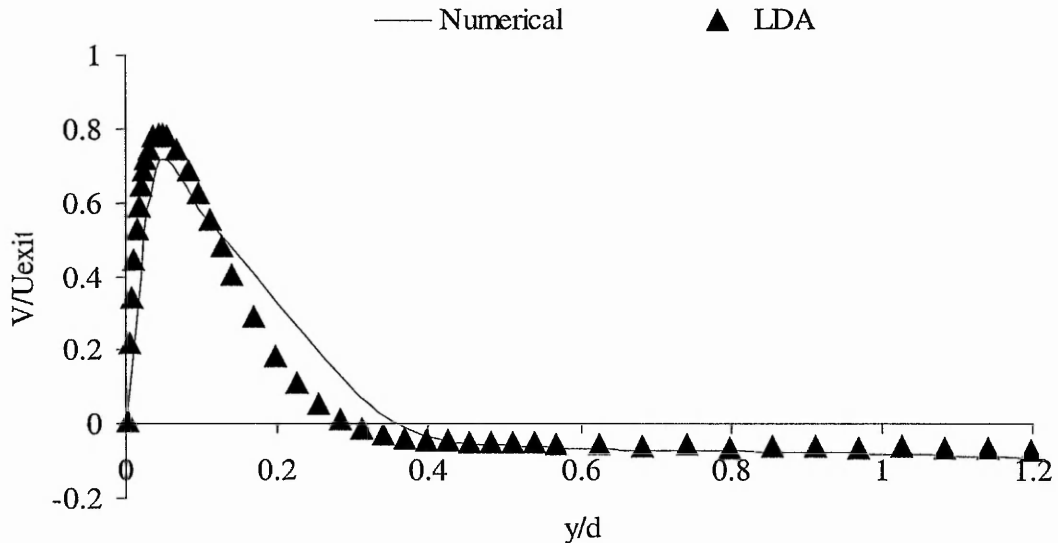


Figure 6.7. Radial velocity profiles at  $r/d=1.6$ .

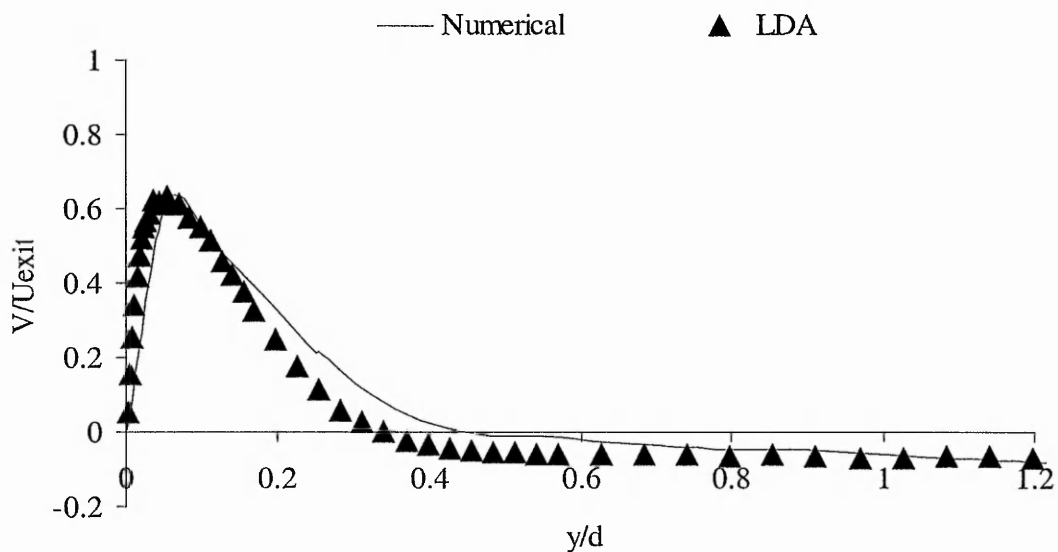


Figure 6.8. Radial velocity profiles at  $r/d=2$ .

Throughout the impingement region under study, the predicted wall jet was found to be too thick when compared to the equivalent experimental data. While the latter show zero values of  $V/U_{exit}$  at approximately  $y/d=0.3$ , the numerical results suggest negative

values for  $y/d \geq 0.4$ . This trend was also reported by Ashforth-Frost (1994) for an impinging air jet at  $Re=20,000$  using the  $k-\epsilon$  turbulence model.

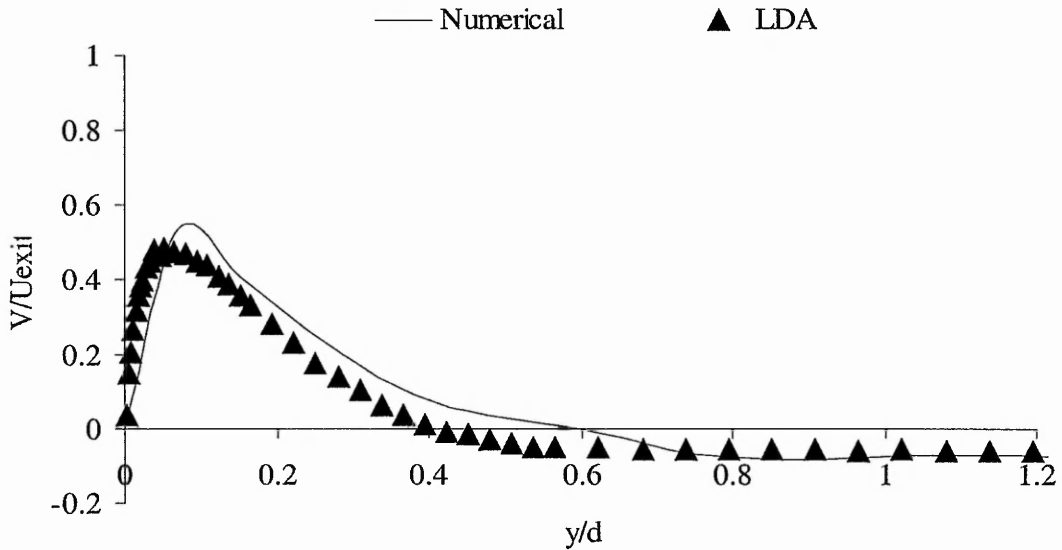


Figure 6.9. Radial velocity profiles at  $r/d=2.5$ .

### 6.3 Turbulence profiles

To reduce the number of nodes required to model the boundary layer flow, the standard  $k-\epsilon$  model employs a universal wall function. As the turbulent kinetic energy,  $k$ , and the dissipation rate,  $\epsilon$ , for the area between the near wall node and the wall are obtained, based on the equilibrium wall function, the near wall node was positioned to satisfy the condition  $y^+ > 11.5$ . This non-dimensional distance, calculated at the near wall nodes is plotted for  $0 \leq r/d \leq 2.5$  in Figure 6.10. It becomes clear that the criterion for the wall function is met for  $r/d \geq 0.25$  so that reliable predictions of  $k$  are expected beyond this region.

While the numerical model is three-dimensional, the experimental results are based on a two-dimensional characterisation of the flow field due to the two-component Laser-Doppler Anemometer, see also Chapter 3. Despite this discrepancy in the number of axes, quantitative differences are estimated to account to less than 10% due to the axisymmetric nature of the nozzle.

Figure 6.11 to 6.16 depict numerical predictions of the radial development of the turbulent kinetic energy,  $k$ , together with measured levels of turbulent kinetic energy. Recall

from Chapter 4, that the turbulent kinetic energy has been calculated using  $k=1/2(u'^2 + v'^2)$ .

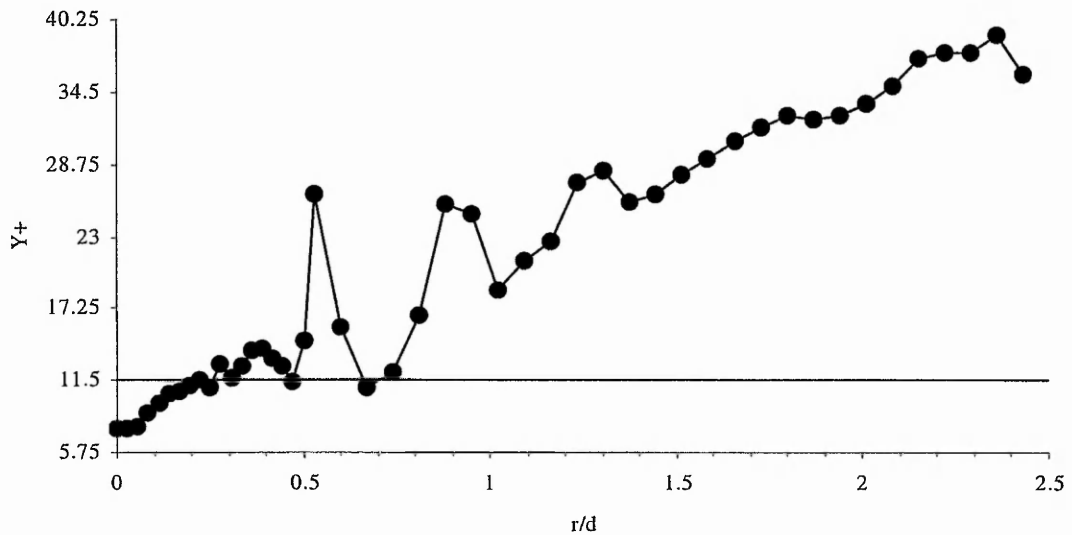


Figure 6.10. Radial profile of  $y^+$  along the impingement plate.

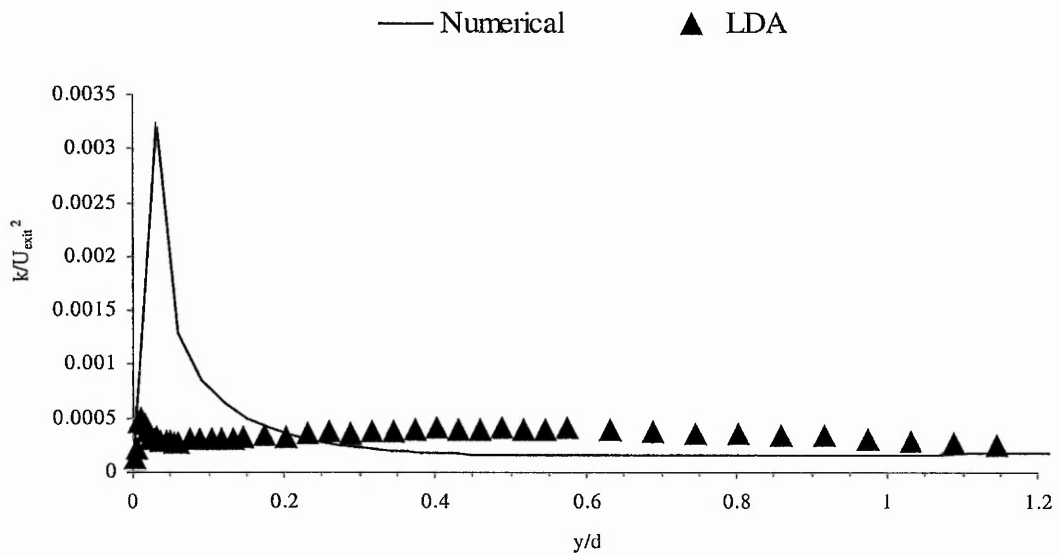


Figure 6.11. Turbulent kinetic energy profiles at  $r/d=0$ .

The numerically predicted turbulence profiles in the stagnation zone,  $0 \leq r/d \leq 0.8$ , show poor agreement with experimental results, particularly in the region where the effects of the wall become pronounced,  $y/d \leq 0.8$ . Here, in close proximity to the wall, numerical data are over-predicted by up to 950%.

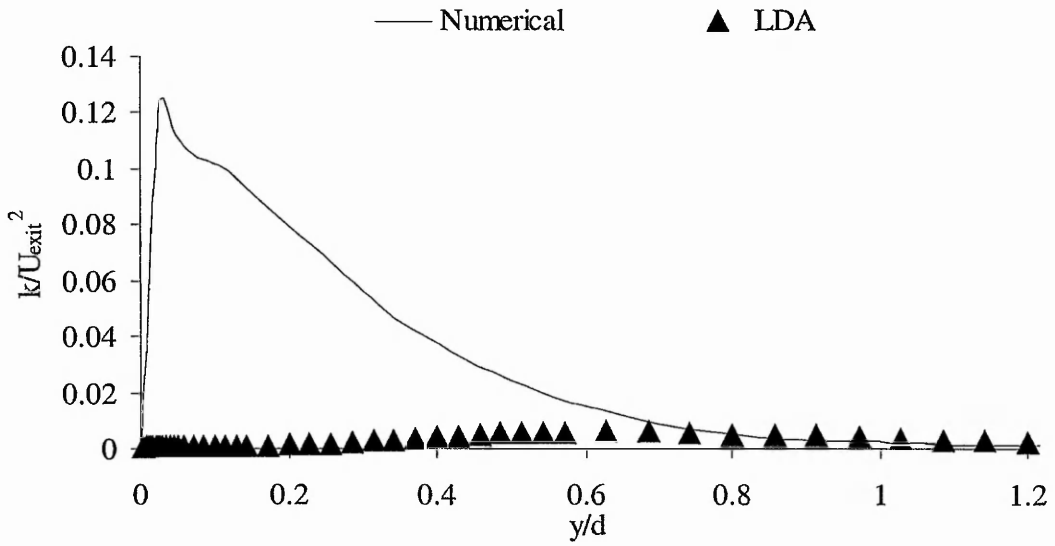


Figure 6.12. Turbulent kinetic energy profiles at  $r/d=0.4$ .

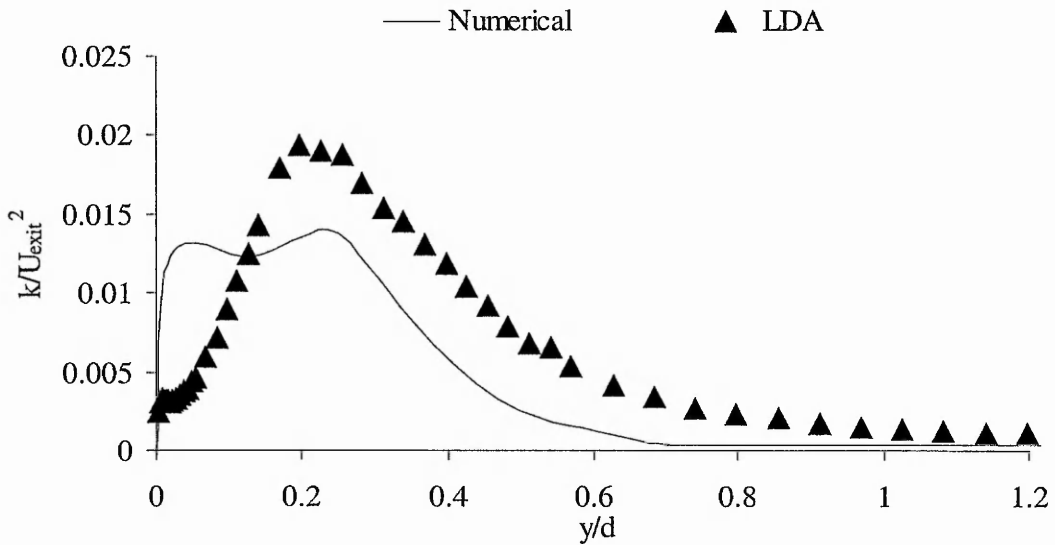


Figure 6.13. Turbulent kinetic energy profiles at  $r/d=0.8$ .

With increasing distance from the stagnation point, quantitative agreement improves until at  $r/d=1.2$  the predictions in peak values compare to within 20% with experiment. Despite the reasonable quantitative prediction of the peak levels, the model shows them too far away from the target plate,  $y/d=0.23$  compared to  $y/d=0.14$  from experiment. This, in turn, leads to the same observation as for the corresponding mean radial velocity in that the turbulent kinetic energy is over-predicted in the region,  $0.2 \leq y/d \leq 0.4$ , see also Figure 6.6.

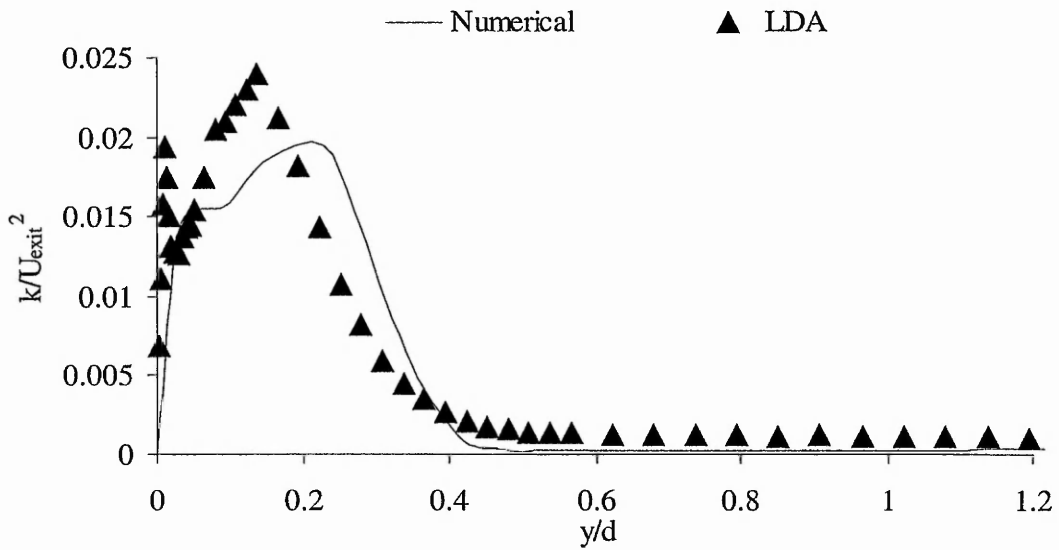


Figure 6.14. Turbulent kinetic energy profiles at  $r/d=1.2$ .

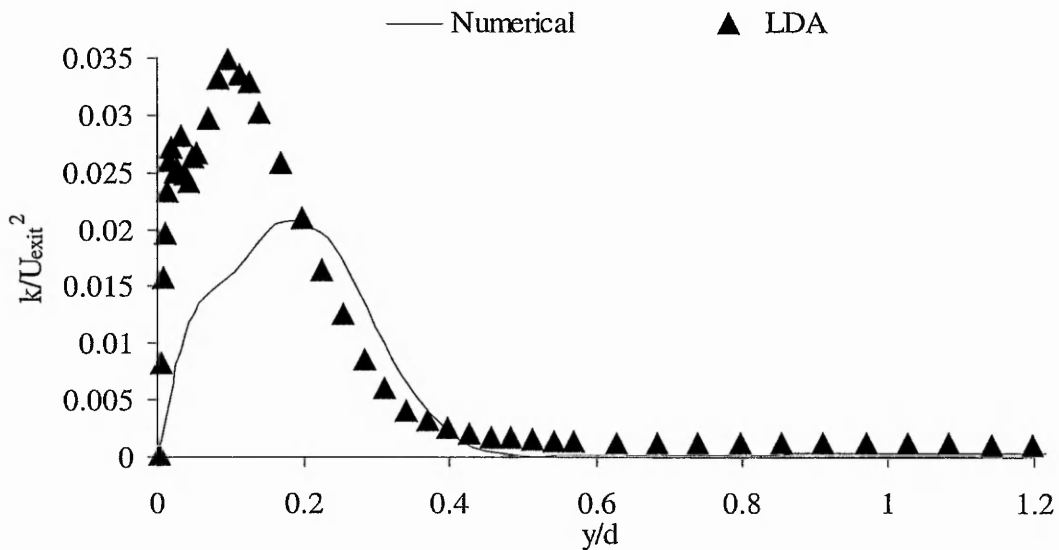


Figure 6.15. Turbulent kinetic energy profiles at  $r/d=1.6$ .

With increasing radial distances,  $r/d \geq 1.6$ , turbulence levels are under-predicted with the closest match occurring at  $r/d=2.5$ . It is interesting to note that here, the location of the peak is predicted correctly while quantitative differences are approximately 35%. The incorrect prediction of  $k$  is observed in regions where the flow is anisotropic and can be explained by the use of the eddy-viscosity concept which assumes that turbulence is isotropic. This will lead to inaccurate values of the individual shear stresses such that the anisotropic flow in the stagnation region cannot be accounted for by the  $k-\epsilon$  turbulence model.

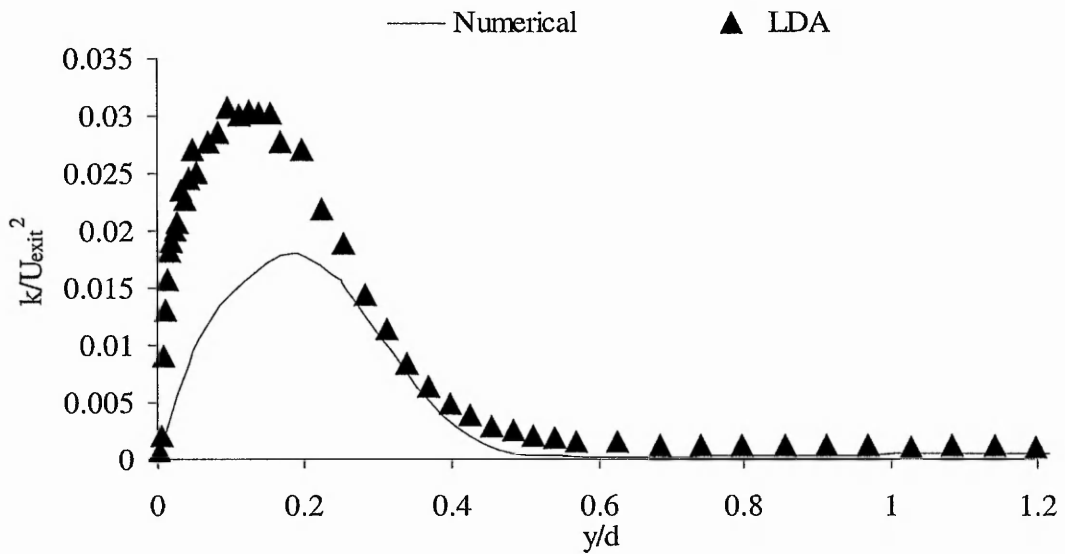


Figure 6.16. Turbulent kinetic energy profiles at  $r/d=2$ .

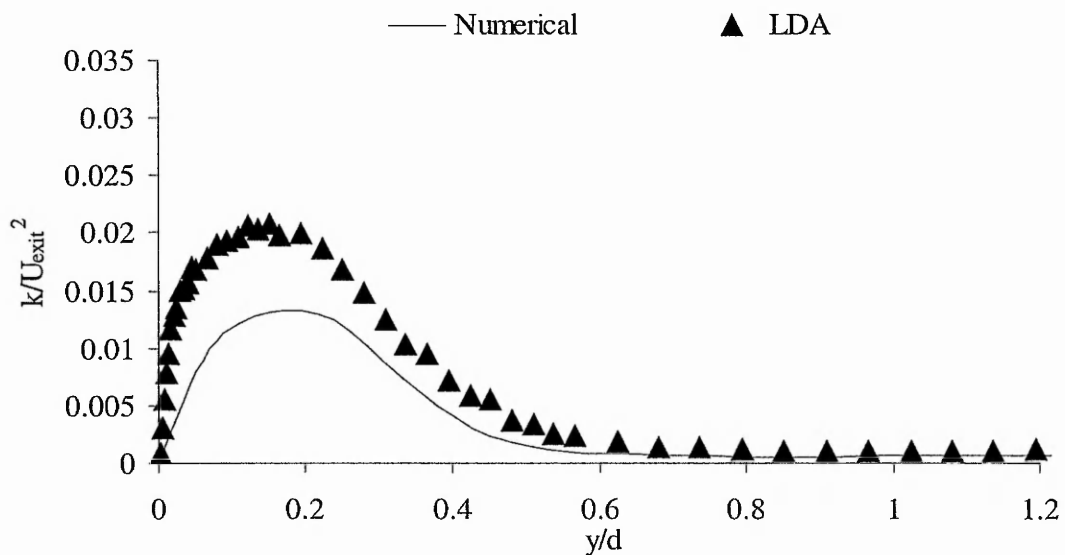


Figure 6.17. Turbulent kinetic energy profiles at  $r/d=2.5$ .

### 6.4 Concluding remarks

The commercial CFD package ANSYS/FLOTRAN has been employed to model the flow field of a turbulent submerged jet impinging onto a flat surface. To the author's knowledge this study is the first work that assesses the performance of the Finite Element

scheme in conjunction with the k- $\epsilon$  model against detailed experimental jet impingement data. From comparisons with other authors works, it has been shown that the Finite-Element scheme of the software code predicts jet impingement to the same level of accuracy as the more established Finite Volume scheme. Furthermore, its versatile meshing potential gives the designer great flexibility in adjusting the mesh to the often complex requirements of turbulence modelling.

The test facility that was used to obtain experimental data was modelled by considering one quarter of the geometry, thereby, exploiting symmetrical conditions. Air ( $Pr=0.71$ ) was used as the working fluid with a Reynolds number of 10,000 at the nozzle exit.

It has been shown during the course of the project that differences in two turbulence models, namely the standard k- $\epsilon$  model and the RNG k- $\epsilon$  model were negligible such that the former was used for the final model as it took less computational time and resources. Numerical predictions of the axial velocity decay agree very well with experimental data and acceptable levels of conformity are found for the mean radial velocity along the impingement plate. In close proximity to the wall and at all radial stations, except for  $r/d=0.4$  and  $r/d=2.5$ , excellent qualitative agreement was found while quantitative discrepancies were no more than 19%. At  $r/d=0.4$ , the model over-predicts experimental peak values by up to 40%, while at  $r/d=2.5$ , the peak in radial velocity is given too far away from the impingement surface. At all radial stations, the model over-predicts experimental results in the region of,  $0.14 \leq y/d \leq 0.6$ , by up to 50%.

For  $r/d \leq 0.4$ , the turbulent kinetic energy is over-predicted by up to 950%. This leads to an over-prediction of the boundary layer thickness and also relates to the under-prediction of the spreading rate. Shortcomings in the predictive quality of the numerical model, identified during the present study, are the well known intrinsic features of the k- $\epsilon$  standard turbulence model, i.e. the assumption of isotropic turbulence in the stagnation region and in near-wall regions and the use of the eddy-viscosity concept which in turn leads to too high values of the Reynolds stress. In addition, as the wall function employed by the turbulence model is invalid in the stagnation region, the failure of correct simulation cannot be attributed to the k- $\epsilon$  turbulence model alone.

Overall, it can be said that the k- $\epsilon$  turbulence model predicts the mean flow and turbulence characteristics reasonably well. However, since Chapter 5 of this study showed that the Reynolds stress significantly affects the radial heat transfer distribution, the k- $\epsilon$

model's predictions have to be treated with caution, see also Cooper *et al.* (1993). Another aspect is the fact that the  $k$ - $\varepsilon$  turbulence model was developed for two-dimensional (channel) flow as opposed to the present flow situation where the cross-section of the radial flow increases radially.

## **Chapter 7**

### **Conclusions and Recommendations**

#### **Introduction**

The final Chapter presents conclusions drawn from the research programme and gives recommendations for further work. It commences with a summary of the work undertaken with reference to the aims and objectives detailed in Section 1.2. The conclusions derived from the experimental and numerical investigation are then discussed in detail. Finally, the practical significance of the findings is outlined.

#### **7.1 Summary of conclusions**

A comprehensive literature review on the use of fluids of different Prandtl numbers in jet impingement has been completed to identify areas where more research attention is required. An experimental test facility has been successfully designed and built to accommodate air and water as working fluids over a range of Reynolds numbers. The jet discharged from a contoured round nozzle of 35mm diameter and impinged into a semi-confined space with a non-dimensional nozzle-to-plate spacing of  $2d$ . Reynolds numbers at the nozzle exit were maintained at 20,000, 10,000 and 2,000. Flow visualisation studies using liquid crystals and hollow glass spheres provided a preliminary insight to the flow field and complemented velocity field and heat transfer results. A two-component backward collection laser-Doppler anemometry system has been used to obtain velocity and turbulence characteristics in the far and near wall region of the impingement surface. The effects of the transparent window surface on the mean velocity and turbulence data were thoroughly investigated and found to be negligible. In the heat transfer tests, particular attention has been paid to the use of the experimental boundary condition in terms of overall uncertainty, reliability, low safety risk and ease of use. The transient wall heating technique in conjunction with liquid crystals and a true colour image processing system has been finally chosen to obtain quantitative and qualitative heat transfer results for air and water, respectively. Software has been developed that showed that the heat transfer coefficient from a finite-difference solution of the governing equation over-predicted the analytically exact solution by up to 39%.

The commercially available Computational Fluid Dynamics (CFD) software package, ANSYS/FLOTRAN, has been used to assess the performance of a typical Finite Element code in predicting the fluid flow characteristics of a semi-confined impinging air jet. Numerical simulations have been compared directly to experimental findings. To the author's knowledge no previous attempts have been made to apply the intrinsic features of the Finite Element code to the modelling of the near wall region of the impingement surface.

As a direct result of this investigation new data for velocity, turbulence and Reynolds stress components have been obtained for semi-confined impinging jets of air and water for Reynolds numbers of 2,000, 10,000 and 20,000. Heat transfer data for air have corroborated previous studies while those with water as working fluid yield a local Nusselt number distribution which has previously not been reported. No other similar fluid flow measurements were found in the open literature that compared water and air on the same experimental test rig.

## **7.2 Results**

### **7.2.1 Literature review**

Depending on the application, Prandtl number effects can manifest themselves as higher friction factors, more stabilised flow fields and a delay of transitions from laminar to turbulent flow.

The literature review revealed that based on the definition of Prandtl number in equation (1.1), the  $\nu$ -phenomenon (i.e. kinematic viscosity) has been shown to have the greatest effect on the flow field as it affects the formation of vortex structures, sensitivity to turbulence and near wall flow characteristics. The  $\alpha$ -phenomenon, consisting mainly of the specific heat capacity and thermal conductivity plays an important role only in the high temperature range (up to 7700°C). Furthermore, fluids with identical Prandtl numbers can have entirely different heat transfer characteristics due to different relative values of the  $\nu$ - and  $\alpha$ -phenomena.

It has been shown in the free jet region that the behaviour of scalar quantities (i.e. temperature and concentration) in a turbulent jet depend strongly on Prandtl number while

vector fields (velocity) display almost no dependency on the type of fluid. The spreading angle of the issuing jet seems to be unaffected by Prandtl number, while reports on the effects of entrainment are somewhat contradictory for fluids of different Prandtl number.

Jets of water and FC-77 that impinged on roughened surfaces showed an enhancement of the heat transfer coefficient since the thermal boundary layer is being pierced which allows for a smaller distances for the energy to reach free stream conditions.

Heat transfer augmentation in the stagnation region of impinging jets is widely believed to be caused by vorticity amplification due to the stretching of vortical filaments under the influence of diverging streamlines. The process of vortex stretching appears to be independent of viscosity and is accompanied by the appearance of an unsteady large-scale vortex pair. In the stagnation region, fluids of different Prandtl numbers display different ratios of the thermal boundary layer thickness to the thickness of the hydrodynamic boundary layer.

Over the last few decades values for  $n$  have been set to 0.5 to express laminar flow in the stagnation region while the exponent  $m$  varied according to the fluid Prandtl number and the number of fluids to be correlated. A value of  $m=0.33$  was recommended when relating high Prandtl number fluids while liquid metals and gases were best correlated when  $m$  assumed values of 0.4, 0.42 or 0.5. It was only recently that better data fits were achieved when the exponents  $m$  and  $n$  were determined from a non-linear curve fit without initially constraining their respective values. This leads to  $m$  assuming values in the range  $0.33 \leq m \leq 0.5$ .

### 7.2.2 Experimental boundary condition

An uncertainty analysis was undertaken and revealed that the constant temperature technique shows lowest value of approximately 10% uncertainty when the heat transfer coefficient is less than  $120\text{W}/(\text{m}^2\text{K})$ . Although these levels might be acceptable for certain impinging air jet heat transfer situations, the monotonic increase makes this technique unsuitable for impinging liquid jets ( $\text{Pr}>1$ ) and jets of liquid metals ( $\text{Pr}\ll 1$ ) where typical heat transfer coefficients are in excess of  $1,000\text{W}/(\text{m}^2\text{K})$ . These high heat transfer coefficients are best measured by employing the constant heat flux method since

the uncertainty decrease inversely with increasing heat transfer coefficient. A compromise between the two steady-state techniques is represented by the transient technique. It is not surprising that the technique shows the same qualitative trend in uncertainty levels as the constant temperature technique with the exception that here the 10% threshold in uncertainties is reached for heat transfer coefficients of  $3,000\text{W}/(\text{m}^2\text{K})$ . This makes this technique particularly attractive for jet impingement heat transfer involving large nozzle sizes and fluids in relatively close proximity to  $Pr=1$  (i.e. air and water). Overall, the transient technique is comparatively simple to use as it does not require any electric heater elements and it cuts down the experimental time considerably. It allows the whole region of interest to be mapped in a single test run which usually lasts no more than 120s. In contrast, both steady-state techniques require about 20 minutes to settle before *one* data point can be taken. Another feature in favour of the transient technique is the circumstance that low uncertainty levels require only accurate time measurements which is comparatively easy to achieve. To extend the applicability of the constant temperature technique for higher heat transfer coefficients, tolerances in temperature measurements are required to be better than  $\pm 0.01^\circ\text{C}$  which is impractical.

For the combined study of impinging air and water jets the transient technique was found to be the most suitable experimental technique due to its relatively low uncertainty levels for both fluids, its simplicity, ease of use and its potential of running a large number of test runs within a short period of time. However, it has to be pointed out that despite the satisfactory levels of uncertainty limitations to the technique exist in the form of a mixing process that takes place within the first few seconds of the test run between the incoming jet flow and the stationary fluid. The heat transfer characteristics of this mixing process is very difficult to obtain, especially quantitatively. However, new qualitative flow visualisation of the heat transfer characteristics has been achieved.

It can therefore be concluded that the transient technique can be successfully applied for the characterisation of heat transfer characteristics induced by impinging air and water jets if only qualitative trends of the water jet are required. The multiple use of sprayable liquid crystals as temperature indicators in air and water was demonstrated. Furthermore, it was shown that the protective varnish layer imposes a negligible thermal resistance to the heat transfer process.

### 7.2.3 Quantitative temperature field characterisation

For the first time liquid crystals have been used successfully as tracer particles for the simultaneous visualisation of the flow field and temperature distribution in high Reynolds number jet impingement. In the studied case the temperature difference between the cold impingement surface and the hot jet was 4°C. It was observed that during the initial 12 seconds of the test and at a mean Reynolds number of 35,000, the space between the semi-confining plate and the impingement surface ( $z/d=2$ ) was heated up to the jet temperature. Despite the relatively high levels of uncertainty in the present study, roughly estimated to be approximately 18%, the technique provides great potential for combining liquid crystal thermography (LCT) with Particle Image Velocimetry (PIV). This combination represents a simple but powerful technique for the detection of fluid temperature and velocity because an entire flow domain can be deduced from only two consecutive video frames. Limitations to this technique include the requirement for optical access to the geometry and a match of refractive indices of the working fluid and the liquid crystals. The calibration of the 'seeding' liquid crystals reveals a similar profile as for the conventional 'sprayable' crystals, with a linear region over the working range. The calibration was undertaken under heating and cooling conditions and revealed a hysteresis effect in the order of  $\pm 0.1^\circ\text{C}$ . This has even greater implications for situations where the temperature gradient is larger than in the present case.

### 7.2.4 Qualitative flow characterisation

After discharging from the nozzle, the jet propagates towards the impingement surface where the flow is decelerated, changed in direction and accelerated under the influence of the favorable pressure gradient. The flow then develops into the typical wall jet, which is characterised by a region of maximum radial velocity. The flow is then transported back along the semi-confining plate towards the edge of the jet where it mixes with the incoming jet flow. This toroidal recirculation pattern represents a typical feature of confined submerged jets. The jet does not exhibit any well-formed vortex structures at its edge before striking the surface because the vortex structures have not had time to develop for the relatively low value of  $z/d=2$ . The lack of distinct vortex structures may

also be explained by the low aspect diameter ratio of the contraction which prevented a flat velocity profile from developing at the nozzle exit.

The jet is well mixed prior to impingement and no radial oscillating movement of the stagnation point was observed. The observed vortical structure appeared randomly and had no prescribed order. Further downstream from the stagnation point, the flow appears turbulent in the form of wavy streamlines between the convected vortices and the impingement surface. Although no boundary layer separation was observed, it is believed that these vortical structures are the governing mechanism of the development of secondary peaks in the local heat transfer profile.

### 7.2.5 Quantitative experimental results

- a) The distribution of the velocity and turbulence intensity at the nozzle exit has been characterised for three Reynolds numbers,  $Re=2,000$ ,  $Re=10,000$  and  $Re=20,000$ . For the latter two, almost identical nozzle exit conditions in terms of mean and turbulent flow for the two Prandtl number fluids were observed, thereby suggesting that Prandtl number effects are negligible if the Reynolds number is sufficiently high,  $Re \geq 10,000$ . Among the three considered Reynolds numbers, highest levels of turbulence intensity were observed for the highest Reynolds number. For  $Re=2,000$ , the mean velocity profiles for air and water at the nozzle exit showed very close quantitative agreement but this was in contrast to the variation in axial and radial turbulence intensity levels which differed through a distinct peak developing only at the edge of the water jet whereas the air jet showed an almost constant turbulence level across the nozzle exit. This led to a markedly higher level of turbulent shear stress in the water jet when compared to the air jet. Furthermore, the water jet develops a much higher axial velocity fluctuation on the centreline than in the radial direction. This anisotropic behaviour of the water jet implies a faster decay in axial direction when compared to the spreading of the jet in the radial direction.
- b) For the studied fluids of air and water,  $0.7 \leq Pr \leq 8$ , kinematic viscosity displays the strongest effects at  $Re=2,000$  and affects all measured mean and turbulent flow quantities. Close to the stagnation point,  $r/d \leq 0.4$ , results highlight strong similarities in the axial and radial mean velocity profiles. However, based on a 95% criterion, the

axial velocity of the approaching water jet decays faster than that of the air jet. In the immediate vicinity of the stagnation point,  $r/d \leq 0.4$ , the developing wall jets of both working fluids show close agreement in that they display much thicker wall jet profiles at  $r/d=0.4$  than at their respective higher Reynolds numbers. At  $r/d=0.8$ , quantitative discrepancies start to evolve as the air jet begins to form a wall jet with a higher radial velocity and a smaller thickness than its liquid counterpart. This trend prevails until  $r/d=1.6$  where the profiles of both fluids deviate qualitatively from their previous shapes in that their peaks are shifted away from the wall. This is accompanied by a simultaneous growth of the wall jet thickness. At  $r/d=2$ , both fluids form peaks in the radial velocity at positions that have almost doubled their distance from the target plate ( $y/d=0.22$ ) compared to the distance of  $y/d=0.11$  at  $r/d=1.6$ . The dissimilarities in the near wall region appear to have vanished by  $r/d=2$ , while the two fluids display ongoing differences in their sensitivity towards the recirculation pattern of the free stream.

Prandtl number effects are also apparent for the development of turbulence intensity throughout the flow field. However, it is interesting to note that discrepancies in axial turbulence intensity exist in other regions than those of radial turbulence intensity. At the stagnation region and along the jet centreline,  $r/d=0$ , axial turbulence levels of both jets show an almost constant variation with the water jet displaying higher turbulence levels. For  $r/d > 0.4$  jets of air and water form peaks at almost identical radial positions. Away from the wall,  $y/d > 0.08$ , the approaching water jet displays higher axial mixing rates until  $r/d=1.6$ . At  $r/d=2$ , the water jet displays similar axial turbulence characteristics as the air jet while this trend is reversed at  $r/d=2.5$ . Very close to the wall and throughout the radial region of interest,  $0 \leq r/d \leq 2.5$ , the air jet produces a much steeper increase in axial turbulence with significantly higher turbulence levels than the water jet. Here, for  $y/d \leq 0.08$ , the air jet shows levels of axial turbulence that are approximately threefold higher than those of water.

Differences in the radial turbulence intensity between air and water are not apparent on the centreline and at  $r/d=0.4$ , since the radial component is only beginning to develop. In contrast to the axial turbulence profiles, the radial turbulence data display local peaks in the immediate vicinity to the wall while further into the free stream the graphs level off more gradually than the axial component. Note that the radial turbulence

intensity is several times higher at the wall than the axial velocity fluctuation so that its effects on heat transfer augmentation could be greater than those of its axial counterpart. Due to the greater fluctuating velocity gradients near the wall,  $r/d=0.8$  and  $r/d=1.2$ , water will induce greater turbulence related heat transfer rates. For greater values of  $y/d$ ,  $0.02 \leq y/d \leq 0.2$ , the spreading rate of the water jet is greater thereby enhancing entrainment of surrounding fluid. By  $r/d=1.6$ , both fluids show almost identical levels of radial turbulence which continue for greater  $r/d$ 's.

Differences between air and water in the variation of the turbulence shear stress were found in the early stages of the developing wall jet,  $r/d < 0.8$ . Since these differences exceed experimental uncertainties, discrepancies are attributed to the lower kinematic viscosity of water. Furthermore, the following conclusions can be drawn: For  $Re=2,000$ , the wall jet is less stable than its high Reynolds number counterpart since the edges of the approaching jet at  $y/d=0.4$  are strongly affected by flow normal *and* parallel to the wall, thus indicating that a strong re-circulating flow in the test section exists. Secondly, in contrast to the higher Reynolds number flows, the case of  $Re=2,000$  displays higher levels of axial shear strain at  $y/d=0.1$ . This identifies the mixing layer at the edge of the jet as the location where Reynolds number effects and Prandtl number effects occur. Finally, the peak in Reynolds shear stress, which is associated with the secondary peak in heat transfer, moves away from the stagnation point as the Reynolds number is increased.

- c) For  $Re=10,000$  and  $Re=20,000$  it was found that the anisotropy increases equally for both Prandtl number fluids as the jet approaches the impingement plate. The axial turbulence intensity is up to 2 times higher than the radial turbulence intensity while for  $Re=10,000$  this factor decreases to 1.6. With increasing normal distance from the wall,  $y/d > 0.4$ , these ratios decrease.

For  $Re=2,000$ , air follows the trend of larger Reynolds numbers in that the ratio between the axial and radial normal stress reaches a maximum at  $y/d \approx 0.3$  and decreases as the impingement plate is approached. In close vicinity to the wall, at  $y/d \approx 0.2$ , a local maximum of  $u'/v'=1.15$  is observed. A different behaviour is observed for water, where on the centreline the axial fluctuating velocity component is up to 5.6 times as high as its radial counterpart. As the wall is approached, the jet slowly returns to isotropy which is finally reached close to the wall.

- d) As the Reynolds number decreases from  $Re=20,000$  to  $Re=2,000$ , the overall turbulence level of the flow field inside the test section increases. This is in contrast to the turbulence levels obtained at the nozzle exit which showed the reversed trend. This is attributed to the remote position of the four exit holes with respect to the central position of the nozzle. For  $Re \geq 10,000$ , discrepancies in the mean and turbulent flow quantities between the water and air jet are well within the measurement uncertainties so that Prandtl number effects can be neglected.
- e) The effects of the target plate on the approaching jet for  $Re=10,000$  and  $Re=20,000$  are identical for air and water and become pronounced, based on a 95% criterion, at  $y/d \approx 0.75$  and  $y/d \approx 0.78$ , respectively. It can be concluded that the effects of the target plate on the flow field are only little affected by an increase in Reynolds number. However, more pronounced effects were found for  $Re=2,000$  where this distance is  $y/d \approx 0.9$  for the water jet and  $y/d \approx 0.67$  for the air jet.
- f) For all three Reynolds numbers,  $Re=2,000$ ,  $10,000$  and  $20,000$ , and for air and water, the peaks in radial velocity occur at the same radial distance from the stagnation point,  $r/d=0.85$ .

The radial positions where peaks in the turbulent quantities (axial turbulence intensity, radial turbulence intensity and turbulent shear stress) occur, increase with increasing Reynolds number and are independent of the working fluid. Peaks of all three turbulence quantities occur at  $r/d \approx 1.65$  for  $Re=10,000$  and at  $r/d \approx 1.85$  for  $Re=20,000$ . For  $Re=2,000$  the peak locations of the individual turbulent quantities differ from each other in that the radial turbulent intensity and the turbulent shear stress reach a peak at  $r/d \approx 1.3$  while the axial turbulence intensity shows a maximum at  $r/d \approx 1.58$ .

- g) The most likely explanation for the maximum in turbulence levels at  $r/d \approx 1.6$  and  $r/d \approx 1.8$  for  $Re=10,000$  and  $Re=20,000$ , respectively, is transition from laminar to turbulent flow. Based on the flow visualisation study, however, it is possible that eddies that originate from the mixing layer surrounding the jet core, are transported downstream, being deflected due to impingement and then penetrate into the wall jet, thus giving rise to a peak in turbulence intensity.
- h) The temporal evolution of the temperature field induced by a hot impinging jet was compared for air and water when the impingement surface was immersed in initially cold fluid. It was shown that the temperature field is dominated by a mixing and

entrainment process which in turn depends on the thermal properties (i.e. thermal conductivity and specific heat capacity) of the working fluid. The air jet preserves its thermal energy on the centreline within a relatively small spatial region which results in an almost instantaneous increase in jet centreline temperature. This is in contrast to the water jet which displays a strong mixing process with greater spatial diffusion of thermal energy into the cold surrounding fluid. Therefore, for a fixed point on the jet centreline, the temperature beneath the water jet fluctuates and does not reach the nozzle exit temperature until the temperature of the whole domain is equal to the nozzle exit temperature.

This is also reflected in the temporal temperature response of the impingement surface as measured by liquid crystals. The implications on the surface temperature are such that the air cooled impingement plate undergoes a smooth and monotonic temperature rise while the water cooled plate experiences a much more diffuse and non-monotonic temperature increase.

- i) For the air and the water jet, identical qualitative trends in the radial distribution of the respective heat transfer coefficients were identified. At the edge of the jet, at  $r/d \approx 0.55$ , a primary peak was found which is consistent with previously published work for air jets. For water, this occurrence has previously not been reported for nozzle diameters larger than 12.7mm. In due course, both working fluids produce areas of high heat transfer in the region  $1.5 \leq r/d \leq 2$ , which manifest themselves as secondary peaks in the radial distribution of the heat transfer coefficient.

The present study identifies for both Prandtl number fluids the existence of laminar flow at the stagnation point. At this point of zero velocity, the Nusselt number shows a local minimum. In due course, at the edge of the jet, a well-documented thinning of the boundary layer manifests itself as a primary peak in the radial heat transfer distribution. In this region,  $0.6 \leq r/d \leq 0.8$ , the impingement of small-scale vortices was observed which appears to mark the onset of an increase in levels of turbulent kinetic energy,  $k$ . At  $r/d \approx 1.1$ , the minimum in Nusselt number corresponds to a region of high radial velocity which leads to relatively low turbulence intensity levels.

The secondary maximum in the radial heat transfer profile has been attributed to maximum values of all of the turbulence components, axial and radial turbulence intensity and turbulent shear stress, in the region  $1.5 \leq r/d \leq 2$ . As the flow was shown to be laminar in the region  $0 \leq r/d \leq 0.5$ , the occurrence of maximum turbulence quantities at  $1.5 \leq r/d \leq 2$  and the secondary peak in heat transfer are attributed to transition from laminar to turbulent flow. For both working fluids, it was found that the location of the peak in turbulent shear stress coincides well with correlations from the open literature for the secondary peak in heat transfer.

### 7.2.6 Numerical results

The finite element based commercial CFD based software package ANSYS/FLOTRAN has been shown to predict the flow field of an impinging air jet to the same level of accuracy as a conventional finite volume based code, see Ashforth-Frost (1994).

The widely used  $k$ - $\epsilon$  turbulence model employed in the present study predicted the axial velocity decay of the impinging jet very well and also showed a reasonable prediction of the radial mean velocity profiles. While levels in peak velocity are under-predicted outside the stagnation region and up to  $r/d=1.6$ , the numerical model predictions coincide with experimental results at  $r/d=2$ . By  $r/d=2.5$ , the  $k$ - $\epsilon$  model over-estimates peak velocities near the wall. The velocity profile in the immediate vicinity to the wall,  $y/d < 0.5$ , is matched well by the turbulence model, thereby confirming the predictive quality of the logarithmic wall function.

The calculated levels of turbulent kinetic energy,  $k$ , showed poor agreement with experimental data in the stagnation region,  $r/d \leq 0.8$ , but increased in accuracy as the radial distance from the stagnation point increased. The reason for the large quantitative discrepancy of  $k$  in the stagnation region is the anisotropic behaviour of the stagnating flow.

Despite the relatively long CPU-time required for achieving a convergent solution, the present model provides an inexpensive, three-dimensional insight into the mean and turbulent velocity field of an impinging jet.

### **7.3 Practical implications of the work**

Results have shown that the mean and turbulent flow fields beneath impinging semi-confined jets of air and water for  $10,000 \leq Re \leq 20,000$  are identical and are therefore interchangeable. For design purposes where preliminary estimates of the turbulent flow field are often required under low cost aspects, experiments with air as working fluid can be easily conducted due to its large availability, low weight, low pumping power and the absence of any sealing requirements. Water, on the other hand, could be used to reduce the dynamic loads acting on the object due to the lower characteristic velocity involved.

The present study has demonstrated the great potential of using liquid crystals as tracer particles for mapping the temperature distribution inside a flow field. This technique is particularly well suited for situations where temperatures are to be obtained to within  $\pm 0.25^\circ\text{C}$  and where a complex shaped geometry limits the use of other methods such as holography.

Relatively high values of average Nusselt number occur when the impingement plate is positioned at  $z/d=2$ . However, this configuration is not recommended if a uniform temperature distribution is required as hot spots exist where the heat transfer distribution shows local peaks, at  $r/d \approx 0.6$  and  $r/d \approx 1.8$ .

If maximum heat transfer coefficients are to be achieved, nozzle exit conditions are of great importance for relatively low Reynolds number jets. After issuing from the nozzle, water jets were shown to induce greater turbulence levels than air jets.

Present findings have provided a detailed two-dimensional characterisation of the turbulent flow field beneath impinging air and water jets along the jet centreline and in the near wall region. Data of mean velocity, turbulence intensity and particularly Reynolds stress over a range of Reynolds numbers can be used by numerical modellers to assess the predictive character of CFD codes. The experimental data are available in Data file format upon request.

#### **7.4 Recommendations for further work**

Heat transfer characteristics for an impinging water jet at  $Re=20,000$  and for both fluids at  $Re=10,000$  and  $Re=2,000$  need still to be quantified to verify the validity of existing heat transfer correlations.

For a nozzle diameter of 35mm, the present study has identified very close qualitative agreement of the respective radial heat transfer profiles for jets of air and water in that primary and secondary peaks were observed. Previous studies used nozzle diameters of less than 3.2mm and found the heat transfer coefficient to decrease monotonically with increasing distance from the stagnation point. To avoid unwanted hot spots in the wall jet region,  $1.5 \leq r/d \leq 2$ , that critical diameter needs to be determined which produces a distinct secondary peak in heat transfer.

The cause of the secondary peak in heat transfer was shown to be due to transition from laminar to turbulent flow. However, to date, to the author's knowledge there exists only one study that obtained fluctuating temperature data beneath impinging jets to unambiguously attribute a change in the flow regime to the secondary peak in heat transfer. As the considered Reynolds number for the heat transfer investigation was well in the turbulent range, an investigation into flows of lower Reynolds numbers (i.e. 2000, 5000) would increase the understanding of the underlying heat transfer mechanism.

Growing passenger numbers in civil aviation are likely to lead to an increasing optimisation process of existing components on board an aircraft in terms of their overall efficiency-weight distribution. For the hydraulic fluid, oil, the optimum flow and heat transfer regime require further research attention. Furthermore, the question arises if there exists an asymptotic value of Prandtl number beyond which a further Reynolds number increase does not result in a significant heat transfer improvement.

The use of liquid crystals as tracer particles for mapping temperature fields could be extended by incorporating PIV-techniques in the post-analysis. This would relate the temperature distribution unambiguously with the corresponding velocity field. Additionally, liquid crystals could be applied to the present geometry to visualise the thermal entrainment of different Prandtl number fluids.

Varying fluid properties can have a great impact on the overall heat transfer characteristics when the temperature difference between the adiabatic wall and the fluid

are greater than approximately 20°C or when the nozzle exit velocities are high. Currently available heat transfer correlations do not account for these effects and need further research attention.

To overcome the weakness of the linear eddy viscosity model, while still maintaining its computational efficiency and robustness, the use of a non-linear eddy-viscosity could represent a real alternative to a second moment closure turbulence model, see Bauer *et al.* (2000).

Further effects of Prandtl number may become important for the heat transfer enhancement of nanofluids where the thermal conductivities are improved by suspending small solid particles in fluids of low thermal conductivity such as energy transmission or process fluids, see Xuan and Li (2000).

Micropolar fluids, which have Non-Newtonian behaviour, contain minute amounts of polymeric additives and display a reduction in skin friction near a rigid body, see Hassanien *et al.* (1999). Due to their increasing importance in the process industry their heat transfer characteristics require quantification.

## References

- Abbott, M B and Basco, D R, 1989. *Computational Fluid Dynamics - An Introduction for Engineers*. Longman Scientific & Technical.
- Aihara, Y, Koyama, H and Morishita, E, 1974. Effects of an air stream on turbulent diffusion of helium jet from a small nozzle. *Phys. Fluids*, **17**, 665-673.
- Alekseenko, S V and Markovich, D M, 1996. Local characteristics of impinging round jets. In: Rodi, W and Bergeles, G, eds., *Engineering Turbulence Modelling and Experiments*, **3**, Elsevier Sciences, 633-642.
- Alitavoli, M and McGeough, J A, 1998. Expert process planning system for meat cutting by high pressure water jet. *J. Materials Processing Technology*, **76**(1-3), 146-152.
- Ansys, 1999, Ansys User's Manual, Vols. 1-4, Release 5.5, SAS IP, Inc.
- Arcoumanis, C and Chang, J-C, 1993. Heat transfer between a heated plate and an impinging transient diesel spray. *Experiments in Fluids*, **16**, 105-119.
- Ariman, T, Turk, M A and Sylvester, N D, 1973. Microcontinuum Fluid Mechanics – A Review. *Int. J. Engineering Science*, **11**, 905-930.
- Arjocu, S C and Liburdy, J A, 1997. Influence of elliptical structure on impinging jet array heat transfer performances. *SPIE*, **3172**, 130-140.
- Arjocu, S C and Liburdy, J A, 1999. Near Surface Characterization of an Impinging Elliptic Jet Array. *J. Fluids Engineering*, **121**, 384-390.
- Arpaci, V S, 1997. *Microscales of Turbulence*. Gordon and Breach Science Publishers.

- Ashforth-Frost, S A, 1994. *Flow visualisation of semi-confined jet impingement*. Ph.D. Thesis, The Nottingham Trent University, England.
- Ashforth-Frost, S A and Jambunathan, K, 1994. Effect of nozzle geometry and semi-confinement on the potential core of a turbulent axisymmetric free jet. *Proc. 10<sup>th</sup> Int. Heat Transfer Conf.*, Brighton, England, 14-18 August, paper 63.
- Ashforth-Frost, S and Jambunathan, K, 1996. Numerical Prediction of Semi-Confined Jet Impingement and Comparison with Experimental Data. *Int. J. Numerical Methods in Fluids*, **23**, 295-306.
- Ashforth-Frost, S and Rüdell, U W, 1998. Flow Visualisation of an impinging water jet using liquid crystals. *11<sup>th</sup> Int. Heat Transfer Conf.*, Kyongju, Korea, 23-27 August, Paper AH47.
- Auerbach, D, 1987. Experiments on the trajectory and circulation of the starting vortex. *J. Fluid Mechanics*, **183**, 185-196.
- Ball, S J, 1998. *Near wall flow characteristics in jet impingement heat transfer*. Ph.D. Thesis, The Nottingham Trent University, England.
- Ball, S J, Ashforth-Frost, S A, Jambunathan, N and Whitney, C F, 1998. Orthogonally impinging axisymmetric jet investigation – Heat transfer and near wall thermal flow field characteristics. *Proc. 11<sup>th</sup> Int. Heat Transfer Conf.*, Kyongju, Korea, 23-28 August, **5**, 457-462.
- Barata, J M M, 1996. Fountain Flows Produced by Multiple Impinging Jets in a Crossflow. *AIAA Journal*, **34**(12), 2523-2530.
- Barata, J M M, Durão, D F G, Heitor, M V and McGuirk, J J, 1987. The Turbulence Characteristics of a single impinging jet through a crossflow. *Proc. 6th Symp. Turbulent Shear Flows*, Toulouse, France, 13-5-1 to 13-5-11.

- Barata, J M M, Durão, D F G, Heitor, M V and McGuirk, J J, 1993. On the analysis of an impinging jet on ground effects. *Experiments in Fluids*, **15**, 117-129.
- Bauer, W, Haag, O and Hennecke, D K, 2000. Accuracy and robustness of nonlinear eddy viscosity models. *Int. J. Heat Fluid Flow*, **21**, 312-319.
- Baughn, J W, Hechanova, A E and Yan, X, 1991. An Experimental Study of Entrainment Effects on the Heat Transfer From a Flat Surface to a Heated Circular Impinging Jet. *ASME J. Heat Transfer*, **113**, 1023-1025.
- Beltaos, S and Rajaratnam, N, 1977. Impingement of axisymmetric developing jets. *J. Hydraulic Research*, **15**(4), 311-326.
- Benedict, L H and Gould, R D, 1996. Towards better uncertainty estimates for turbulence statistics. *Experiments in Fluids*, **22**(2), 129-136.
- Bertin, F, Barat, J and Wilson, R, 1997. Energy dissipation rates, eddy diffusivity, and the Prandtl-number: An in situ experimental approach and its consequences on radar estimate of turbulent parameters. *Radio Science*, **32**, No. 2, 791-804.
- Besserman, D L, Incropera, F P and Ramadhani, S, 1991a. Experimental study of heat transfer from a discrete source to a circular liquid jet with annular collection of the spent fluid. *Experimental Heat Transfer*, **4**(1), 41-57.
- Besserman, D L, Incropera, F P and Ramadhani, S, 1992. Heat transfer from a square source to an impinging liquid jet confined by an annular wall. *ASME J. Heat Transfer*, **114**(1), 284-287.
- Besserman, D L, Ramadhani, S and Incropera, F P, 1991b. Numerical simulation of laminar flow and heat transfer for liquid jet impingement cooling of a circular heat source with annular collection of the spent fluid. *Numerical Heat Transfer*, **20**(A), 263-278.

Bhat, G S and Narasimha, R, 1996. A volumetrically heated jet: Large-eddy structure and entrainment characteristics. *J. Fluid Mechanics*, **325**, 303-330.

Blanchard, J N, Brunet, Y and Merlen, A, 1999. Influence of a counter rotating vortex pair on the stability of a jet in a cross flow: an experimental study by flow visualizations. *Experiments in Fluids*, **26**, 63-74.

Borquez, R, Wolf, W, Koller, W D and Spiess, W E L, 1999. Impinging jet drying of pressed fish cake. *J. Food Engineering*, **40**(1/2), 113-120.

Boyle, M T and Knaub, C, 1988. Low speed wind tunnel testing. *Proc. 4th Annual IEEE Semiconduction Thermal and Temperature Measurement Symposium*, San Diego/USA, 31-39.

Bradshaw, P, 1971. *An Introduction to Turbulence and its Measurement*. Pergamon Press.

Bradshaw, P, 1996. Understanding and prediction of turbulent flow – 1996. *Int. J. Heat Fluid Flow*, **18**:45-54.

Bremhorst, K and Krebs, L, 1992. Experimentally determined turbulent Prandtl numbers in liquid sodium at low Reynolds numbers. *Int. J. Heat Mass Transfer*, **35**(2), 351-359.

BRITISH STANDARDS INSTITUTION, 1964. BS1042: Part 1: 1964. *Methods for the measurement of fluid flow in pipes. Orifice Plates, Nozzles and Venturi Tubes*.

BRITISH STANDARDS INSTITUTION, 1992. BS1041-4: 1992. *Temperature measurement. Guide to the selection and use of thermocouples*.

Brodkey, R S, 1967. *The Phenomena of Fluid Motions*. Dover Publications Inc., New York.

- Browne, L W B and Antonia, R A, 1983. Measurements of Turbulent Prandtl number in a plane jet. *ASME J. Heat Transfer*, **105**, 663-665.
- Buchhave, P, 2000. Course notes on LDA measurement considerations, *Seminar on Experimental Fluid Dynamics and Data Interpretation*, Lyngby, Denmark, 13-21 June.
- Bula, A J, Rahman, M M and Leland, J E, 2000. Axial steady free surface jet impinging over a flat disk with discrete heat sources. *Int. J. Heat and Fluid Flow*, **21**, 11-21.
- Bunker, R S, Metzger, D E and Wittig, S, 1992. Local Heat Transfer in Turbine Disk Cavities: Part 1 – Rotor and Stator cooling with Hub Injection of Coolant. *ASME J. Turbomachinery*, **114**, 211-220.
- Butler, R J and Baughn, J W, 1996. The effect of the thermal boundary condition on transient method heat transfer measurements on a flat plate with a laminar boundary layer. *ASME J. Heat Transfer*, **118**, 831-837.
- Button, B L and Jambunathan, K, 1989. Jet impingement heat transfer: a bibliography 1976-1985. *Previews Heat Mass Transfer*, **15**(2), 149-178.
- Button, B L, Tura, R, 1984. Design of a blower type low speed thermal wind tunnel. Coventry (Lanchester) Polytechnic, *Report ME383*.
- Büyükalaca, O and Jackson, J D, 1998. The correction to take account of variable property effects on turbulent forced convection to water in a pipe. *Int. J. Heat Mass Transfer*, **41**(4-5), 665-669.
- Can, M, 1998. Simultaneous convective heat and mass transfer in impingement ink drying. *Int. Comm. Heat Mass Transfer*, **25**(6), 863-874.

- Carlomagno, G M, 1985. Schlieren interferometry in the mass diffusion of a two-dimensional jet. *Experiments in Fluids*, **3**, 137-141.
- Cenedese, A, Doglia, G, Romano, G P, de Michele, G and Tanzini, G, 1994. LDA and PIV velocity measurements in free jets. *Experimental Thermal and Fluid Science*, **9**:125-134.
- Chakroun, W M, AbdelRahman, A A and AlFahed, S F, 1998. Heat transfer augmentation for air jet impinged on a rough surface. *Applied Thermal Engineering*, **18**(2), 1225-1241.
- Chamkha, A J, 1998. Hydromagnetic plane and axisymmetric flow near a stagnation point with heat generation. *Int. Comm. Heat Mass Transfer*, **25**(2), 269-278.
- Champion, M and Libby, P A, 1991. Asymptotic analysis of stagnating turbulent flows. *AIAA Journal*, **29**(1), 16-24.
- Champion, M and Libby, P A, 1994. Reynolds stress description of opposed and impinging turbulent jets. II, Axisymmetric jets impinging on nearby walls. *Phys. Fluids*, **6**(5), 1805-1819.
- Champion, M and Libby, P A, 1996. Asymptotic and computational results for a turbulent jet impinging on a nearby wall. *Fluid Mechanics and its Applications*, **37**, 133-140.
- Chang, C T, Kocamustafaogullari, G, Landis, F and Downing, S, 1993. Single and multiple liquid jet-impingement heat transfer. *ASME, Heat Transfer Division*, **HTD-246**, 43-52.
- Chang, C T, Kojasoy, G, and Landis, F, 1995. Confined single- and multiple-jet impingement heat transfer – I. Turbulent submerged liquid jets. *Int. J. Heat Mass Transfer*, **38**(5), 833-842.

- Chen, P H, and Wang, W L, 1991. Roll-up of a viscous vortex sheet. *J. Chinese Institute of Engineers*, **14**(5), 507-517.
- Chevray, R and Tutu, N K, 1978. Intermittency and preferential transport of heat in a round jet. *J. Fluid Mechanics*, **88**, 3321-339.
- Chiam, T C, 1996. Heat transfer with variable conductivity in a stagnation-point flow towards a stretching sheet. *Int. Comm. Heat Mass Transfer*, **23**(2), 239-248.
- Cho, H H, Lee C H and Kim, Y S, 1998. Characteristics of heat transfer in impinging jets by control of vortex pairing. *ASME paper 98-GT-276*.
- Chu, P C K, Lee, J H and Chu V H, 1999. Spreading of Turbulent Round Jet in Coflow. *J. Hydraulic Eng.*, **125**(2), 193-204.
- Chua, L P and Antonia, R A, 1990. Turbulent Prandtl-number in a circular jet. *Int. J. Heat Mass Transfer*, **33**(2), 331-339.
- Chun, K B and Sung, H J, 1998. Visualization of a locally-forced separated flow over a backward-facing step. *Experiments in Fluids*, **25**, 133-142.
- Chyu, M K, Ding, H, Downs, J P and Soechting, F O, 1998. Determination of local heat transfer coefficient based on bulk mean temperature using a transient liquid crystals technique. *Experimental Thermal and Fluid Science*, **18**, 142-149.
- Coleman, H W and Steele, W G, 1989. *Experimentation and Uncertainty Analysis for Engineers*. John Wiley & Sons Inc., New York.
- Colonius, T, Lele, S K and Moin, P, 1991. The free compressible viscous vortex. *J. Fluid Mechanics*, **230**, 45-73.

- Colucci, D W and Viskanta, R, 1996. Effect of Nozzle Geometry on Local Convective Heat Transfer to a Confined Impinging Air Jet. *Experimental Thermal and Fluid Science*, **13**, 71-80.
- Cooper, D, Jackson, D C, Launder, B E and Liao, G X, 1993. Impinging jet studies for turbulence model assessment – 1. Flow field experiments. *Int. J. Heat Mass Transfer*, **36**(10), 2675-2684.
- Cornaro, C, Fleischer, A S and Goldstein, R J, 1999. Flow visualization of a round jet impinging on cylindrical surfaces. *Experimental Thermal and Fluid Science*, **20**, 66-78.
- Dabiri, D and Gharib, M, 1991. Digital particle image thermometry: The method and implementation. *Experiments in Fluids*, **11**, 77-86.
- Dahm, W J A and Dimotakis, P E, 1990. Mixing at large Schmidt number in the self-similar far field of turbulent jets. *J. Fluid Mech.*, **217**, 299-330.
- Dantec, 1996. *BSA. Installation & User's guide*, DANTEC Measurement Technology A/S, Denmark.
- Dantec, 2000. *BSA/FVA Flow software, Installation & User's guide, Vol. 1+2*, DANTEC Measurement Technology A/S, Denmark.
- Davies, T W and Carter, M C, 1998. Convective heat transfer from a hot rotating cylinder with jet impingement. *The Phoenix Journal*, **11**(1), 81-96.
- den Ouden, C and Hoogendoorn, C J, 1974. Local convective heat transfer coefficients for jets impinging on a plate; experiments using a liquid crystal technique. *Proc. 5<sup>th</sup> Int. Heat Transfer Conf.*, Tokyo, 3 – 7 Sept., **5**, 293-297.
- Dianat, M, Fairweather, M and Jones, W P, 1996. Predictions of axisymmetric and two-dimensional impinging turbulent jets. *Int. J. Heat and Fluid Flow*, **17**:530-538.

Didden, N and Ho, C-M, 1985. Unsteady separation in a boundary layer produced by an impinging jet. *J. Fluid Mech.*, **160**, 235-256330.

Dimotakis, P E, Miake-Lye, R C and Papantoniou, D A, 1983. Structure and dynamics of round turbulent jets. *Phys. Fluids*, **26**, 3185-3192.

Domholdt, L C and Moszynski, J R, 1964. A low turbulence water tunnel – Design and Performance. *ASME Paper 64-FE-21*, 2-11.

Doukelis, A, Founti, M, Mathioudakis, K and Papailiou, K, 1994. A general procedure for calculating and correcting the displacement of laser beams passing through plane and cylindrical windows using a three component laser Doppler anemometer for turbomachinery applications. *Proc. 7th Int. Symp. Applications of Laser Techniques to Fluid Mechanics*. Lisbon, Portugal, Paper no. 17.4.1-17.4.7.

Dowd, A and Maxwell, R W, 1978. Temperature in an impinging argon jet. *Proc. 5<sup>th</sup> Int. Conf. on Gas Discharges*, Univ. Liverpool, England, 11-14 Sept, 67-69.

Dowling, D R and Dimotakis, P E, 1990. Similarity of the concentration field of gas-phase turbulent jets. *J. Fluid Mech.*, **218**, 109-141.

Dunne, S T, 1983. *A study of flow and heat transfer in gas turbine cooling passages*, D. Phil. Thesis, Oxford University, Oxford, United Kingdom.

Durst, F and Stevenson, W H, 1975. Moire pattern to visually model laser-Doppler signals. The accuracy of Flow measurements by laser Doppler Methods. *Proc. of the LDA-Symp.*, Copenhagen, pp. 183-205.

Durst, F, 1990. Optical Techniques for Fluid Flow and Heat Transfer. *Experimental Thermal and Fluid Science*, **3**:33-51.

- Elison, B and Webb, B W, 1994. Local heat transfer to impinging liquid jets in the initially laminar, transitional, and turbulent regimes. *Int. J. Heat Mass Transfer*, **37**(8), 1207-1216.
- Eswara, A T and Nath, G, 1994. Unsteady nonsimilar two-dimensional and axisymmetric water boundary layers with variable viscosity and Prandtl number. *Int. J. Engineering Science*, **32**(2), 267-279.
- Faggioli, S and Grassi, W, 1990. Impinging liquid jets on heated surfaces. *Proc. 9<sup>th</sup> Int. Heat Transfer Conf.*, Jerusalem, 19-24 August, **1**, 275-285.
- Farina, D J, Hacker, J M, Moffat, R J and Eaton, J K, 1994. Illuminant invariant calibration of thermochromic liquid crystals. *Experimental Thermal and Fluid Science*, **9**, 1-12.
- Filippov, Y P, 1991. Removal of intensive heat flux with liquid nitrogen jet impingement. In: Fast, R W, ed., *Advances in Cryogenic Engineering*, **37**(A), Plenum Press, 189-196.
- Fitzgerald, J A and Garimella, S V, 1996. Flow field measurements in confined and submerged jet impingement. *ASME, Heat Transfer Division*, **HTD-333**, **2**, 121-129.
- Fitzgerald, J A and Garimella, S V, 1998. A study of the flow field of a confined and submerged impinging jet. *ASME J. Heat Transfer*, **41**(8-9), 1025-1034.
- Fox, M D, Kurosaka, M, Hedges, L and Hirano, K, 1993. The influence of vortical structures on the thermal fields of jets. *J. Fluid Mech.*, **255**, 447-472.
- Gabour, L A and Lienhard V, J H, 1994. Wall Roughness Effects on Stagnation Point heat transfer beneath an impinging liquid jet. *J. Heat Transfer*, **116**, 81-87.

- Gardon, R and Akfirat, J C, 1965. The role of turbulence in determining the heat transfer characteristics of impinging jets. *Int. J. Heat Mass Transfer*, **8**, 1261-1272.
- Garimella, S V and Nenaydykh, B, 1996. Nozzle geometry effects in liquid jet impingement heat transfer. *Int. J. Heat Mass Transfer*, **39**(14), 2915-2923.
- Garimella, S V and Rice, R A, 1995. Confined and submerged liquid impingement heat transfer. *ASME J. Heat Transfer*, **117**(4), 871-877.
- Gauntner, J W, Livingood, J N B and Hrycak, P, 1970. Survey of literature of flow characteristics of a single turbulent jet impinging on a flat plate. *NASA TM D-5652*.
- George, W K and Taulbee, D B, 1992. Designing Experiments to Test Closure Hypotheses. *Experimental Thermal and Fluid Science*, **5**:249-259.
- George, W K, 1988. The Role of Experimentation in Thermal and Fluid Science Applications. *Experimental Thermal and Fluid Science*, **1**:109-110.
- George, W K, 1989. The self-preservation of turbulent flows and its relation to initial conditions and coherent structures. In: George, W K and Arndt, R E A, eds., *Advances in Turbulence*, Hemisphere, 39-72.
- Gillespie, D R H, Guo, S M, Wang, Z, Ireland, P T and Kohler, S T, 1996. A Comparison of Full Surface local Heat Transfer Coefficient and Flow Field Studies beneath sharp-edged and radiused entry impinging jets. *ASME paper 96-GT-428*.
- Giralt, F, Chi C J and Trass, O, 1977. Characterisation of the impingement region in an axisymmetric turbulent jet. *Ind. Eng. Chem. Fundam.*, **16**(1), 21-28.
- Goldstein, R J, 1996. *Fluid Mechanics Measurements*, 2nd ed., Taylor & Francis, London.

- Goldstein, R , Sobolik, K A and Seol, W S, 1990. Effects of Entrainment on the Heat Transfer to a Heated Circular Air Jet impinging on a Flat Surface. *ASME J. Heat Transfer*, **112**, 608-611.
- Goldstein, R J and Seol, W S, 1991. Heat transfer to a row of impinging circular air jets including the effect of entrainment. *Int. J. Heat Mass Transfer*, **34(8)**, 2133-2147.
- Goldstein, R J, Behbahani, A I, Heppelmann, K, 1986. Streamwise Distribution of the Recovery Factor and the local heat transfer coefficient to an impinging circular air jet. *Int. J. Heat Mass Transfer*, **29(8)**, 1227-1235.
- Gonzalez, R C and Woods, R E, 1992. *Digital image processing*. Addison-Wesley, Reading, MA, 229-235.
- Goussis, D and Kelly, R E, 1984. Effects of viscosity variation on the stability of film flow over heated or cooled inclined surfaces. *AIChE Symposium Series*, **80(236)**, paper 10.
- Green, J A, Dinh, T N and Sehgal, B R, 1997. Molten-metal jet impingement: Insights from experiments and analysis. *Proc. 5<sup>th</sup> Int. Conf. on Nuclear Engineering*, Nice, France, 26-30 May, ICONE5-2421.
- Guillard, F, Fritzon, R, Revstedt, J, Trägårdh, C, Alden, M and Fuchs, L, 1998. Mixing in a confined turbulent impinging jet using planar laser-induced fluorescence. *Experiments in Fluids*, **25**, 143-150.
- Hansen, L G and Webb, B W, 1993. Air jet impingement heat transfer from modified surfaces. *Int. J. Heat Mass Transfer*, **36(4)**, 989-997.
- Harms, T M, Jog, M A and Manglik, R M, 1998. Effects of temperature-dependent Viscosity Variations and Boundary Conditions on fully developed laminar forced Convection in a Semicircular Duct. *ASME J. Heat Transfer*, **120**, 600-605.

- Hassanien, I A, Shamardan, A, Moursy, N M and Gorla, R S R, 1999. Flow and Heat transfer in the boundary layer of a micropolar fluid on a continuous moving surface. *Int. J. Numerical Methods for Heat and Fluid Flow*, **9**(6), 643-659.
- Heindel, T J, Ramadhyani, S, Incropera, F P and Campo, A, 1992. Surface Enhancement of a Heat Source exposed to a circular liquid jet with annular collection of the spent fluid. *ASME HTD-206-2, Topics in Heat Transfer*, **2**, 111-118.
- Herman, C, Kang, E and Wetzel, M, 1998. Expanding the applications of holographic interferometry to the quantitative visualization of oscillatory thermofluid processes using temperature as tracer. *Experiments in Fluids*, **24**, 431-446.
- Heyerichs, K and Pollard, A, 1996. Heat transfer in separated and impinging turbulent flows. *Int. J. Heat Mass Transfer*, **39**(12), 2385-2400.
- Hollworth, B R and Gero, L R, 1985. Entrainment effects on impingement heat transfer. Part 2. Local heat transfer measurements. *ASME J. Heat Transfer*, **107**(4), 910-915.
- Hottel, H C, 1953, Burning in laminar and turbulent fuel jets. *Proc. 4<sup>th</sup> Int. Symposium on Combustion*, The Williams and Wilkins Co., 97-113.
- Hrycak, P, 1983. Heat transfer from round impinging jets to a flat plate. *Int. J. Heat Mass Transfer*, **26**(12), 1857-1865.
- Hrycak, P, Lee, D T, Gauntner, J W and Livingood, J N B, 1970. Experimental flow characteristics of a single turbulent jet impinging on a flat plate. *NASA-TN-D-5690. NTIS N70-20567*.
- Hu, S and Herold, K E, 1995. Prandtl-number effect on offset fin heat exchanger performance: experimental results. *Int. Comm. Heat Mass Transfer*, **38**(6), 1053-1061.

- Huber, A M and Viskanta, R, 1994. Effect of jet-jet spacing on convective heat transfer to confined, impinging arrays of axisymmetric air jets. *Int. J. Heat Mass Transfer*, **37**(18), 2859-2869.
- Hung, Y H and Huang, L S, 1998. Hydrodynamic characteristics for a round jet impingement with annular confinement. *Int. J. Modelling Simulation*, **18**(3), 180-189.
- Hunt, J C R, 1973. A theory of turbulent flow around two-dimensional bluff bodies. *J. Fluid Mechanics*, **6**(41), 625-7061.
- Hussein, H J, Capp, S P and George, W K, 1994. Velocity measurements in a high-Reynolds-number, momentum-conserving, axisymmetric, turbulent jet. *J. Fluid Mech.*, **258**, 31-75.
- Iacovides, H, Jackson, D C, Kelemenis, G and Launder, B E, 1999. The measurement of local wall heat transfer in stationary U-ducts of strong curvature, with smooth and rib roughened walls. *Proc. 4<sup>th</sup> Int. Symp. Engineering Turbulence Modelling and Experiments*, Corsica, France, 433-442.
- Inagaki, T and Kitamura, K, 1990. Turbulent heat transfer with combined forced and natural convection along a vertical flat plate (Effect of Prandtl-number). *Heat Transfer - Japanese Research*, **19**(2), 70-80.
- Incropera, F P and Ramadhyani, S, 1994. Single-phase, liquid jet impingement cooling of high-performance chips. In: Kakaç, S *et al.* (eds.), *Cooling of Electronic Systems*, Kluwer Academic Publishers, 457-506.
- Ireland, P, 1987. *Internal Cooling of Turbine Blades*. Ph.D. Thesis, University of Oxford, England.
- Ireland, P T and Jones, T V, 1985. The measurement of local heat transfer coefficients in blade cooling geometries. *AGARD Conf. Proc.*, **390**, paper 28.

Ireland, P T and Jones, T V, 1986. Detailed measurements of heat transfer on and around a pedestal in fully developed passage flow. *Proc. 8th Int. Heat Transfer Conf.*, San Francisco, **3**, 975-980.

Ireland, P T and Jones, T V, 1987. The response time of a surface thermometer employing encapsulated thermochromic liquid crystals. *J. Phys. E: Sci. Instrum.*, **20**, 1195-1199.

Jambunathan, K and Button, B L, 1994. Jet impingement heat transfer: a bibliography 1986 – 1991. *Previews Heat Mass Transfer*, **20(5)**, 385-413.

Jambunathan, K, Lai, E, Moss, M A and Button, B L, 1992. A review of heat transfer data for single circular jet impingement. *Int. J. Heat and Fluid Flow*, **13(2)**, 106-115.

Jiji, L M and Dagan, Z, 1988. Experimental investigation of single-phase multijet impingement cooling of an array of microelectronic heat sources. In: Aung, W., ed., *Cooling Technology for Electronic Equipment*. Hemisphere, 333-351.

Kakaç, S and Yener, Y, 1995. *Convective Heat Transfer*. CRC Press, London.

Kataoka, K, 1990. Impingement Heat Transfer augmentation due to large scale eddies. *Proc. 9<sup>th</sup> Int. Heat Transfer Conf.*, Jerusalem, 19-24 August, **1**, 255-273.

Kataoka, K, Sahara, R, Ase, H and Harada, T, 1987a. Role of large-scale coherent structures in impinging jet heat transfer. *J. Chemical Engineering Japan*, **20(1)**, 71-76.

Kataoka, K, Sahara, R, Ase, H and Harada, T, 1987b. The effect of surface renewal due to large-scale eddies on jet impingement heat transfer. *Int. J. Heat Mass Transfer*, **30(3)**, 559-567.

- Kawamura, H, Ohsaka, K, Abe H and Yamamoto, K, 1998. DNS of turbulent heat transfer in channel flow with low to medium-high Prandtl number fluid. *Int. J. Heat and Fluid Flow*, **19**:482-491.
- Kays, W M, 1994. Turbulent Prandtl number – Where are we? *ASME J. Heat Transfer*, **116**, 284-295.
- Kezios, S P, 1956. *Heat Transfer in the Flow of a Cylindrical Air Jet Normal to an Infinite Plane*. Ph.D. Thesis, Illinois Institute of Technology, Chicago, U.S.A.
- Kida, S, Takaoka, M and Hussain, F, 1991. Collision of two vortex rings. *J. Fluid Mechanics*, **230**, 583-646.
- Kim, K and Camci, C, 1995. Fluid Dynamics and convective heat transfer in impinging jets through implementation of a high resolution liquid crystal technique, Part I: Flow and Heat Transfer Experiments. *Int. J. Turbo and Jet Engines*, **12**, 1-12.
- Kim, K, and Camci, C, 1995. Fluid dynamics and convective heat transfer in impinging jets through implementation of a high resolution liquid crystal technique, Part II: Navier–Stokes computation of impulsively starting heat transfer experiments. *Int. J. Turbo and Jet Engines*, **12**, 13-19.
- Kiryu, M, 1986. Development of oil-cooled 750cc motorcycle engine. *Auto. Technol.*, **40**, 1154-1158.
- Kline, S and McClintock, 1953. Describing uncertainties in single sample experiments. *Mechanical Engineering*, **75**, 3-8.
- Knebel, J U, Krebs, L, and Müller, U, 1999. Turbulent Convection in Buoyant Sodium Jets. *Experimental Thermal and Fluid Science*, **8**:149-157.

- Knebel, J U, Krebs, L, Müller, U and Axcell, B P, 1998. Experimental investigation of a confined heated sodium jet in a co-flow. *J. Fluid Mechanics*, **368**, 51-79.
- Knowles, K and Myszko, M, 1998. Turbulence measurements in radial wall-jets. *Experimental Thermal and Fluid Science*, **17**:71-78.
- Kraemer, K, 1971. Die Potentialströmung in der Umgebung von Freistrahlen. *Z. Flugwiss*, **19**, 94-104.
- Kreith, F and Black, W Z, 1980. *Basic Heat Transfer*. Harper and Row, New York.
- Kumagi, S, Suzuki, S and Kubo, R, 1995. Transient Cooling of a Hot Metal Plate with an Impinging Water Jet. *Heat Transfer – Japanese Research*, **24**(6), 538-550.
- Kumar, A, 1999. Role of flow-consistent grid in CFD. *Computers & Fluids*, **28**, 265-280.
- Kuznetsov, V A, 1991. Turbulent Heat Transfer by liquid with low thermal conductivity near smooth wall. *Theoretical Foundations of Chemical Engineering* (English Translation of *Teoreticheskie Osnovy Khimicheskoi Tekhnologii*), **25**(2), 230-232.
- Landreth, C C and Adrian, R J, 1990. Impingement of a low Reynolds number turbulent circular jet onto a flat plate at normal incidence. *Experiments in Fluids*, **9**, 74-84.
- Launder, B E and Spalding, D B, 1974. The numerical computation of turbulent flows. *Comput. Meths. Appl. Mech. Eng.*, **3**, 269-289.
- Law, C N S, Khoo, B C and Chew, T C, 1999. Turbulence structure in the immediate vicinity of the shear-free air-water interface induced by a deeply submerged jet. *Experiments in Fluids*, **27**, 321-331.

- Law, H S and Maslyah, J H, 1984. Mass Transfer due to a confined laminar impinging axisymmetric jet. *Ind Eng Chem Fundam*, **23**, 446-454.
- Lee, J and Lee S-J, 1998. Turbulent heat transfer characteristics in a stagnation region of axi-symmetric jet impingement. *Proc. 11<sup>th</sup> Int. Heat Transfer Conf.*, Kyongju, Korea, 23-28 August, **5**, 433-438.
- Lee, J and Lee S-J, 1999. Stagnation region heat transfer of a turbulent axisymmetric jet impingement. *Experimental Heat Transfer*, **12**:137-156.
- Lee, X C, Ma, C F, Zheng, Q, Zhuang, Y and Tian, Y Q, 1997. Numerical study of recovery effect and impingement heat transfer with submerged circular jets of large Prandtl number liquid. *Int. J. Heat Mass Transfer*, **40**(11), 2647-2653.
- Leland, J E and Pais, M R, 1999. Free Jet Impingement Heat Transfer of a High Prandtl number fluid under Conditions of Highly Varying Properties. *ASME J. Heat Transfer*, **121**, 592-597.
- Lemoine, F, Antoine, Y, Wolff, M and Lebouche, M, 1999. Simultaneous temperature and 2D-velocity measurements in a turbulent heated jet using combined laser-induced fluorescence and LDA. *Experiments in Fluids*, **26**, 315-323.
- Lepicovsky, J, Ahuja, K K, Brown, W H and Burrin, R H, 1986. *AIAA Paper 86-1941*.
- Leweke, T and Williamson, C H K, 1998. Cooperative elliptic instability of a vortex pair. *J. Fluid Mechanics*, **360**, 85-119.
- Li, C-Y and Garimella, S V, 2001. Prandtl number effects and generalized correlations for confined and submerged jet impingement. *Int. J. Heat and Mass Transfer*, **44**, 3471-3480.

- Li, D-Y, Guo, Z-Y and Ma, C-F, 1997. Relationship between the recovery factor and the viscous dissipation in a confined impinging, circular jet of high-Prandtl number liquid. *Int. J. Heat and Fluid Flow*, **18**, 585-590.
- Liepmann, D and Gharib, M, 1992. The role of streamwise vorticity in the near-field entrainment of round jets. *J. Fluid Mech.*, **245**, 643-668.
- Liepmann, D, 1991. Streamwise vorticity and entrainment in the near field of a round jet. *Phys. Fluids A*, **3**(5), 1179-1185.
- Liu, X, Gabour, A and Lienhard V, J H, 1993. Stagnation point heat transfer during impingement of laminar liquid jets: analysis including surface tension, *ASME J. Heat Transfer*, **115**,99-105.
- Liu, X, Lienhard V, J H and Lombara, J S, 1991. Convective Heat Transfer by Impingement of Circular liquid jets. *ASME J. Heat Transfer*, **113**, 571-582.
- Livingood, J N B and Hrycak, P, 1973. Impingement heat transfer from turbulent air jets to flat plates – a literature survey. *NASA TM X-2778, NTIS N73-24927*.
- Loehrke, R I and Nagib, H M, 1976. Control of Free-stream Turbulence by Means of Honeycombs: A Balance between Suppression and Generation. *J. Fluids Engineering*, **98**(38), 342-355.
- Lumley, J L and McMahon, J F, 1967. Reducing Water Tunnel Turbulence by Means of a Honeycomb. *ASME J. Basic Engineering*, **89**, 764-770.
- Lyell, M J and Huerre, P, 1985. Linear and nonlinear stability of plane stagnation flow. *J. Fluid Mech.*, **161**, 295-312.
- Lytle, D and Webb, B W, 1994. Air Jet impingement Heat Transfer at low Nozzle-Plate spacings. *Int. J. Heat Mass Transfer*, **37**, 1687-1697.

- Ma, C F, Sun, H, Auracher, H, and Gomi, T, 1990. Local convective heat transfer from vertical heated surfaces to impinging circular jets of large Prandtl-number fluid. *Proc. 9<sup>th</sup> Int. Heat Transfer Conf.*, Jerusalem, **2**, 441-446.
- Ma, C F, Zheng, Q, Lee, S C and Gomi, T, 1997a Impingement heat transfer and recovery effect with submerged jets of large Prandtl number liquid – 1. Unconfined circular jets. *Int. J. Heat Mass Transfer*, **40**(6), 1481-1490.
- Ma, C F, Zhuang, Y, and Lee, S C, 1997b. Impingement heat transfer and recovery effect with submerged jets of large Prandtl-number liquid – II.. Initially laminar confined slot jets. *Int. J. Heat Mass Transfer*, **40**(6), 1490-1500.
- Ma, C F, Zheng, Q, Sun, H, Wu, K and Horii, K, 1998. Local convective heat transfer from a vertical flat surface to oblique submerged impinging jets to large Prandtl-number liquid. *Experimental Thermal and Fluid Science*, **17**, 238-247.
- Malmström, T G, Kirkpatrick, A T, Christensen, B and Knappmiller, K D, 1997. Centreline velocity decay measurements in low-velocity axisymmetric jets. *J. Fluid Mech.*, **246**, 363-377.
- Martin, H, 1977. Heat and mass transfer between impinging gas jets and solid surfaces. *Advances in Heat Transfer*, **13**, 1-60.
- Martinez-Botas, R F, Lock, G D and Jones, T V, 1995. Heat transfer measurements in an annular cascade of transonic gas turbine blades using the transient liquid crystal technique. *J. Turbomachinery*, **117**, 425-431.
- Maurer, J and Libchaber, A, 1980. Effect of the Prandtl-number on the onset of turbulence in liquid He. *Journal de Physique (Paris) Lettres*, **41**(21), L515-L518.

- McAdams, W H, 1954. *Heat Transmission*. 3rd ed., McGraw-Hill Book Company, New York.
- McMackin, L, Hugo, R J, Bishop, K P, Chen, E Y, Pierson, R E and Truman, C R, 1999. High speed optical tomography system for quantitative measurement and visualisation of dynamic features in a round jet. *Experiments in Fluids*, **26**, 249-256.
- McMackin, L, Hugo, R J, Pierson, R E and Truman, C R, 1997. High speed optical tomography system for imaging dynamic transparent media. *Opt Express*, **1**, 302-311, <http://epubs.osa.org/oearchive/source/2360.htm>.
- McNaughton, K J and Sinclair, C G, 1966. Submerged Jets in Short Cylindrical Flow Vessels. *J. Fluid Mech.*, **25**(2), 367-375.
- Mehta, R D, 1977. The Aerodynamic Design of Blower Tunnels with Wide-angle Diffusers. *Prog. Aerospace Sci.*, **18**, 59-120.
- Meola, C, Cardone, G, Carmicino, C and Carlomagno, G M, 2000. Fluid Dynamics and Heat Transfer in an impinging air jet. *Proc. 9<sup>th</sup> Int. Symp. Flow Visualization*, Edinburgh, 22-25 Aug., Paper 429.
- Merzkirch, W, 1987. *Flow Visualization*, 2nd ed., Academic Press Inc., London.
- Metzger, D E, Cummings, K N and Ruby, W A, 1974. Effects of Prandtl number on heat transfer characteristics of impinging liquid jets. *Proc. 5<sup>th</sup> Int. Heat Transfer Conf.*, Tokyo, **2**, 20-24.
- Miles, P C and Witze, P O, 1996. Fringe field quantification in an LDA probe volume by use of a magnified image. *Experiments in Fluids*, **16**, 330-335.
- Moffat, R J, 1985. Using Uncertainty Analysis in the Planning of an Experiment. *J. Fluids Engineering*, **107**, 173-180.

- Moffat, R J, 1990. Some Experimental Methods for Heat Transfer Studies. *Experimental Thermal and Fluid Science*, **3**:14-32.
- Morris, G K, Garimella, S V and Amano, R S, 1996. Prediction of jet impingement heat transfer using a hybrid wall treatment with different turbulent Prandtl number functions. *ASME J Heat Transfer*, **118**(3), 562-569.
- Muto, Y and Ishigaki, T, 1999. Secondary flow in compound sinuous/meandering channels. *Proc. 4<sup>th</sup> Int. Symp. Engineering Turbulence Modelling and Experiments*, Corsica, France, 511-520.
- Nishino, K, Samada, M, Kasuya, K and Torii, K, 1996. Turbulence statistics in the stagnation region of an axisymmetric impinging jet flow. *Int. J. Heat and Fluid Flow*, **17**:193-201.
- Nourgaliev, R R, Dinh, T N and Sehgal, B R, 1997. Effect of fluid Prandtl number on heat transfer characteristics in internally heated liquid pools with Rayleigh numbers up to  $10^{12}$ . *Nuclear Engineering and Design*, **169**(1-3), 165-184.
- Obot, N T and Esen, E B, 1992. Smooth tube friction and heat transfer in laminar and transitional flow. *Int. Comm. Heat Mass Transfer*, **19**(3), 299-310.
- Obot, N T, Das, L, Vakili, D E and Green, R A, 1997. Effect of Prandtl-number on smooth-tube heat transfer and pressure drop. *Int. Comm. Heat Mass Transfer*, **24**(6), 889-896.
- Obot, N T, Douglas, W J M and Mujumdar, A S, 1982. Effect of semi-confinement on impingement heat transfer. *Proc. 7<sup>th</sup> Int. Heat Transfer Conf.*, Munich, 6-10 September, **3**, 395-400.

- Ogawa, K and Hijikata, K, 1996. Experimental and Theoretical Study on Heat transfer of an Impinging Plasma Jet. *ASME, Transport Phenomena in Material Processing and Manufacturing*, **HTD-336**, 1-8.
- Olsson, M, 1997. *Large Eddy Simulation of a circular impinging jet. using a Large-Eddy-Simulation (LES)*. Ph.D. Thesis, Royal Institute of Technology, Sweden.
- Palmer, J R, 1993. Theoretical model for high power diamond laser optics using high velocity liquid metal jet. *SPIE High Heat Flux Engineering*, **1739(58)**, 86-115.
- Pan, Y, Stevens, J and Webb, B W, 1992. Effect of Nozzle Configuration on Transport in the Stagnation Zone of Axisymmetric, Impinging free-Surface liquid jets: Part 2 – Local Heat Transfer. *ASME J. Heat Transfer*, **114(4)**, 880-886.
- Panchapakesan, N R and Lumley, J L, 1993a. Turbulence measurements in axisymmetric jets of air and helium. Part 1. Air jet. *J. Fluid Mech.*, **246**, 197-223.
- Panchapakesan, N R and Lumley, J L, 1993b. Turbulence measurements in axisymmetric jets of air and helium. Part 2. Helium jet. *J. Fluid Mech.*, **246**, 225-247.
- Papadopoulos, G and Pitts, M, 1998. Scaling the near-field centreline mixing behavior of axisymmetric turbulent jets. *AIAA Journal*. **36(9)**, 1635-16421.
- Parry, A J, Lalor, M J, Tridimas, Y D and Woolley, N H; 1990: Refraction corrections for laser-Doppler anemometry in a pipe bend. Dantec Information No. 09:4-6.
- Patankar, S V, 1980. *Numerical Heat Transfer and Fluid Flow*. Hemisphere Publishing Co., New York.
- Péniguel, C, 1998. Heat Transfer simulation for industrial applications: needs, limitations, expectations. *Int. J. Heat and Fluid Flow*, **19**, 102-114.

- Perera, K K and Baughn, J W, 1994. The effect of pitch angle and Reynolds number on local heat transfer in spirally fluted tubes. *ASME, Heat Transfer Division*, **HTD-279**, 99-112.
- Persen, L N and Saetran, L R, 1983. Hot-film measurements in a Water Tunnel. *J Hydraulic Research*, **21(5)**, 379-389.
- Polat, S, 1993. Heat and mass transfer in impingement drying. *Drying technology*, **11(6)**, 1147-1176.
- Polat, S, Huang, B, Mujumdar, A S and Douglas, W J M, 1989. Numerical Flow and Heat Transfer Under Impinging Jets: A Review. *Ann. Rev. of Num. Fluid Mechanics and Heat Transfer*, **2**, Hemishpere, New York, 157-197.
- Popiel, C and Trass, O, 1991. Visualization of a free and impinging round jet. *Experimental Thermal and Fluid Science*, **4**:253-264.
- Popiel, O, Van Der Meer, Th H, Hoogendoorn, C J, 1980. Convective Heat Transfer on a Plate in an Impinging round hot gas jet of low Reynolds number. *Int. J. Heat Mass Transfer*, **23**, 1055-1068.
- Praisner, T J, Seal, C V, Takmaz, L and Smith, C R, 1997. Spatial-temporal turbulent flow-field and heat transfer behavior in end-wall junctions. *Int. J. Heat and Fluid Flow*, **18**:142-151.
- Prasad, A K and Koseff, J R, 1996. Combined forced and natural convection heat transfer in a deep lid-driven cavity flow. *Int. J. Heat and Fluid Flow*, **17**:460-467.
- Priedeman, D, Callahan, V and Webb, B W, 1994. Enhancement of liquid jet impingement heat transfer with surface modifications. *ASME J. Heat Transfer*, **116**, 486-489.

- Qian, F, Farouk, B, Mutharasan, R and Macken, N, 1996. Heat transfer from a liquid bath due to an impinging gas jet: effect of liquid Prandtl-number. *ASME, Heat Transfer Division*, **HTD-333**, 181-195.
- Rabbitt, M J, 1997. Some Validation of Standard, Modified and Non-Linear k- $\epsilon$  Turbulence Models. *Int. J. Num. Methods in Fluids*, **24**, 965-986.
- Rae W H and Pope, A, 1984. *Low Speed Wind tunnel testing*. 2nd ed., John Wiley, New York.
- Raghu, S, Lehmann, B and Monkewitz, P A, 1990. On the mechanism of 'side-jets' generation in periodically excited axisymmetric jets. In: *Advances in Turbulence*, **3**, Springer, Berlin, 221-226.
- Ravigururajan, T S and Bergles, A E, 1995. Prandtl-number influence on heat transfer enhancement in turbulent flow of water at low temperatures. *ASME J. Heat Transfer*, **117**, 276-282.
- Reynolds, A J, 1976. The variation of turbulent Prandtl number and Schmidt number in wakes and jets. *Int. J. Heat Mass Transfer*, **19**, 757-764.
- Richards, C and Shekarriz, A, 1997. Characteristics of a Submerged Non-Newtonian Jet. *Proc. ASME Fluids Engineering Division*, **FEDSM97-3076**.
- Richards, C D and Richards, R F, 1998. Transient temperature measurements in a convectively cooled droplet. *Experiments in Fluids*, **25**, 392-400.
- Ripken, J F, 1951. Design Studies for a Closed-Jet Water Tunnel. University of Minnesota, St Anthony Falls Hydraulic Laboratory, Paper No. 9, Series B.
- Risso, F and Fabre, J, 1997. Diffusive turbulence in a confined jet experiment. *J. Fluid Mech.*, **337**, 233-261.

- Robbins, B E, 1978. Water Tunnel Turbulence Measurements Behind a Honeycomb. *J. Hydronautics*, **12**(3), 122-128.
- Roberts, G T and East, R A, 1996. Liquid crystal thermography for heat transfer measurement in hypersonic flows: a review. *J. Spacecraft Rockets*, **33**(6), 761-768.
- Romano, G P, 1998. Investigation on particle trajectories and lagrangian statistics at the outlet of a circular jet. *Experimental Thermal and Fluid Science*, **17**:116-123.
- Rosén C and Trägårdh, C, 1994.  $\overline{u'v'}$  Reynolds stress in the viscous sublayer over a wide range of Re numbers. *AIChE Journal*, **40**(1), 29-39.
- Ross, J A and Larock, B E, 1997. An Algebraic Stress Finite Element Model of Turbulent Flow. *Int. J. Num. Methods in Fluids*, **24**, 693-714.
- Ruck, B, 1991. Distortion of LDA fringe pattern by tracer particles. *Experiments in Fluids*, **10**(6), 349-354.
- Ruckenstein, E, 1998. On the Laminar and Turbulent Free convection Heat Transfer from a Vertical Plate over the entire Range of Prandtl numbers. *Int. J. Heat Mass Transfer*, **25**(7), 1009-1018.
- Rüdel, U, Ashforth-Frost, S and Jambunathan, K, 1999. The effect of boundary conditions on heat transfer testing at moderate Prandtl numbers. *Proc. IMechE 6<sup>th</sup> UK National Conf. Heat Transfer*. Edinburgh, 15-16 Sept., 221-230.
- Rüdel, U, Ashforth-Frost, S and Jambunathan, K, 2000. Flow Visualisation of Submerged impinging jets of different Prandtl numbers. *Proc. 9<sup>th</sup> Int. Symp. Flow Visualization*, Edinburgh, 22-25 Aug., Paper 372.

Sabatino, D R, Praisner, T J and Smith, C R, 2000. A high-accuracy calibration technique for thermochromic liquid crystal temperature measurements. *Experiments in Fluids*, **28**, 497-505.

Sakakibara, J, Hishida, K and Maeda, M, 1997. Vortex structure and heat transfer in the stagnation region of an impinging plane jet (simultaneous measurements of velocity and temperature fields by Digital Particle Image Velocimetry and Laser-induced Fluorescence). *Int. J Heat Mass Transfer*, **40**(13), 3163-3176.

Sargison, J E, Guo, S M, Lai, C C, Oldfield, M L G, Lock, G D and Rawlinson, A J, 2000. Use of Liquid Crystal techniques for Gas Turbine Film Cooling in a Transonic Tunnel. *Proc. 9<sup>th</sup> Int. Symp. Flow Visualization*, Edinburgh, 22-25 Aug., Paper 409.

Saripalli, K R, 1983. Visualization of Flow Patterns induced by an Impinging Jet issuing from a Circular Platform. *AIAA Journal*, **21**(12), 1764-1766.

Schlichting, H, 1979. *Boundary Layer Theory*. McGraw-Hill, New York.

Schneider, P J, 1959. *Conduction Heat Transfer*, Addison-Wesley Publishing Co. Inc., Reading, Mass.

Schneider, G M, Hooper, J D, Musgrove, A R, Nathan, G J and Luxton, R E, 1997. Velocity and Reynolds stresses in a precessing jet flow. *Experiments in Fluids*, **22**, 489-495.

Schroeder, V P and Garimella, S V, 1998. Heat transfer from a discrete heat source in confined air jet impingement. *Proc. 11<sup>th</sup> Int. Heat Transfer Conf.*, Kyongju, Korea, 23-28 August, **5**, 451-456. 4

Schultz, D L and Jones, T V, 1973. Heat transfer measurements in short-duration hypersonic facilities. *AGARD-AG-165*.

- Seol, W S and Goldstein, R J, 1997. Energy Separation in a Jet Flow. *ASME J. Fluids Engineering*, **119**, 74-82.
- Seol, W S and Goldstein, R J, 1998. Visualization of the effect of acoustic excitation on vortex structure and energy separation in jets. *Proc. 11<sup>th</sup> Int. Heat Transfer Conf.*, Kyongju, Korea, 23-27 August, **5**, 491-496.
- Shaw, C T, 1992. *Using Computational Fluid Dynamics*. Prentice Hall, London.
- Sheriff, N and O'Kane, D T, 1981. Sodium eddy diffusivity of heat measurements in a circular duct. *Int. J. Heat Mass Transfer*, **24**, 205-211.
- Sherman, F, 1990. *Viscous Flow*. McGraw-Hill, New York.
- Son, C, Michaelis, M, Ireland, P and Bather, S, 1999. Detailed Heat Transfer Measurements in an Engine Representative Impingement Cooling System using Liquid Crystals. *Proc. ASME Heat Transfer Division*, **HTD-361-3**, 389-397.
- Sparrow, E M, Xu, Z X and Azevedo, L F A, 1987. Heat (Mass) Transfer for Circular Jet Impingement on a confined Disk with Annular Collection of the Spent Air. *Int. J. Heat Mass Transfer*, **109**, 329-335.
- Stasiek, J, Mikielwicz, D, Mikielwicz, J and Collins, M W, 1997. A new method of heat transfer coefficient measurements by liquid crystal and digital processing. *Trans IChemE*, **75(A)**, 657-662.
- Stasiek, J, Collins, M W, Ciofalo, M and Chew, P E, 1996. Investigation of flow and heat transfer in corrugated passages – I. Experimental results. *Int. J. Heat Mass Transfer*, **39(1)**, 149-164.

- Stevens, J and Webb, B W, 1989. Local heat transfer coefficients under an axisymmetric, single-phase liquid jet. In: Shah, R K, ed., *ASME Heat Transfer in Electronics 1989*, New York, 113-119.
- Stevens, J and Webb, B W, 1991. The effect of inclination on local heat transfer under an axisymmetric, free liquid jet. *Int. J. Heat Mass Transfer*, **34**(4/5), 1227-1236.
- Stevens, J, Pan, Y and Webb, B W, 1992. Effect of Nozzle Configuration on Transport in the Stagnation Zone of Axisymmetric, Impinging free-Surface liquid jets: Part 1 – Flow Structure. *ASME J. Heat Transfer*, **114**(4), 874-879.
- Sun, H and Ma, C F, 1998. Effect of variable fluid properties on impingement heat transfer with submerged circular jets. *Int. J. Heat Mass Transfer*, **41**(10), 1363-1366.
- Sun, H, Ma, C F and Chen, C, 1998. Prandtl number dependence of impingement heat transfer with circular free-surface liquid jets. *Int. J. Heat Mass Transfer*, **41**(10), 1360-1363.
- Sun, H, Ma, C F and Nakayama, W, 1993. Local characteristics of convective heat transfer from simulated microelectronic chips to impinging submerged round water jets. *J. Electronic Packaging*, **115**(1), 71-77.
- Sutera, S P, 1965. Vorticity amplification in stagnation-point flow and its effect on heat transfer. *J. Fluid Mechanics*, **21**(3), 513-534.
- Sutera, S P, Maeder, P F and Kestin, J, 1963. On the sensitivity of heat transfer in the stagnation point boundary layer to free-stream vorticity. *J. Fluid Mechanics*, **16**, 497-520.
- Tam, L-M and Ghajar, A J, 1998. The unusual behaviour of local heat transfer coefficient in a circular tube with a bell-mouth inlet. *Experimental Thermal and Fluid Science*, **16**, 187-194.

- Tarasuk, J D and Castle, G S P, 1983. Temperature distribution in an electrically heated wide metallic foil. *ASME J. Heat Transfer*, **105**, 210-212.
- Tarbell, J M, Gunshinan, J P, Qeselowitz, D B, Rosenberg, G, Shung, K K and Pierce W S, 1986. Pulsed Ultrasonic Doppler Velocity measurements inside a Left Ventricular Assist Device. *J. Biomechanical Eng.*, **108**, 232-238.
- Taylor, G I, 1958. Flow induced by jets. *J. Aero/Space Sci*, **25**, 464-465.
- Taylor, R P, Coleman, H W, Hosni, M H and Love, P H, 1989. Thermal boundary condition effects on heat transfer in the turbulent incompressible flat plate boundary layer. *Int. J. Heat Mass Transfer*, **32**(6), 1165-1174.
- Ueda, T, Imaizumi, H, Mizomoto, M and Shepherd, I G, 1997. Velocity statistics along the stagnation line of an axi-symmetric stagnating turbulent flow. *Experiments in Fluids*, **22**, 473-481.
- Valencia, A, Fiebig, M and Mitra, N K, 1995. Influence of heat conduction on determination of heat transfer coefficient by liquid crystal thermography. *Experimental Heat Transfer*, **8**:271-279.
- Van Fossen, G J and Simoneau, R J, 1987. A Study of the Relationship between Free-Stream Turbulence and Stagnation Region Heat Transfer. *ASME J. Heat Transfer*, **109**, 10-15.
- Van Fossen, G J, Simoneau, R J and Ching, C Y, 1995. Influence of Turbulence Parameters, Reynolds numbers, and Body Shape on Stagnation region Heat Transfer. *ASME J. Heat Transfer*, **117**, 597-603.
- Van Oudheusden, B W, 1997. A note on the Prandtl-number effect on laminar heat transfer and recovery. *The Aeronautical Journal*, **101**(1008), 371-374.

- Vassallo, P F and Kumar, R, 1999. Liquid and gas velocity measurements using LDV in air-water duct flow. *Experimental Thermal and Fluid Science*, **19**, 85-92.
- Vedula, R P, Metzger, D E and Bickford, W B, 1988. Effects of lateral and anisotropic conduction on determination of local convection heat transfer characteristics with transient tests and surface coatings. *ASME Heat Transfer Division*, **104**, 21-28.
- Viskanta, R, 1993. Heat transfer to impinging isothermal gas and flame jets. *Experimental Thermal and Fluid Science*, **6**, 111-134.
- Vogt, G L, 1983. Water Tunnel construction for continuous mode flow visualization. *Proc. 21st Aerospace Sci. Meeting*, Reno, Nevada/USA, 10-13 Jan., AIAA paper, 1-11.
- von Wolfersdorf, J, Hoecker, R and Sattelmayer, T, 1993. A hybrid transient step-heating heat transfer measurement technique using heater foils and liquid-crystal thermography. *ASME J. Heat Transfer*, **115**, 319-324.
- Webb, B W and Ma, C F, 1995. Single-Phase liquid jet impingement heat transfer. *Advances in Heat Transfer*, **26**, 105-217.
- Wei, C Y and Miao, J, 1992. Stretching of Freestream Turbulence in the stagnation region. *J. AIAA*, **30**(9), 2196-2203.
- Weisgraber, T H and Liepmann, D, 1998. Turbulent structure during transition to self-similarity in a round jet. *Experiments in Fluids*, **24**, 210-224.
- Wetzel, J M and Arndt, R E A, 1994a. Hydrodynamic design considerations for Hydroacoustic facilities: Part 1 - Flow quality. *ASME J. Fluids Engineering*, **116**, 324-331.

- Wetzel, J M and Arndt, R E A, 1994b. Hydrodynamic design considerations for Hydroacoustic facilities: Part 2 – Pump design factors. *ASME J. Fluids Engineering*, **116**, 332-337.
- White, F W, 1979. *Fluid Mechanics*. McGraw-Hill, New York.
- Wigeland, R A, Ahmed, M and Nagib, H M, 1978. Management of Swirling Flows with Application to Wind Tunnel Design. *AIAA Journal*, **16**(11), 1125-1131.
- Wille, R, 1963. Beiträge zur Phänomenologie der Freistrahlen. *Zeitschrift für Flugwissenschaften*, Band 11, 222-233.
- Witte, L C, 1968. An experimental study on forced convection heat transfer from a sphere to liquid sodium. *ASME J. Heat Transfer*, **90**, 9-12.
- Wolf, D H, Incropera, F P and Viskanta, R, 1993. Jet impingement boiling. In: *Advances in Heat Transfer*, **23**, 1-132.
- Wolf, D H, Viskanta, R and Incropera, F P, 1995a. Turbulence dissipation in a free-surface jet of water and its effect on local Impingement heat transfer from a heated surface: Part 1 - Flow structure. *ASME J. Heat Transfer*, **117**(1), 85-94.
- Wolf, D H, Viskanta, R and Incropera, F P, 1995b. Turbulence dissipation in a free-surface jet of water and its effect on local Impingement heat transfer from a heated surface: Part 2 – Local heat transfer. *ASME J. Heat Transfer*, **117**(1), 95-103.
- Womac, D J, Incropera, F P and Ramadhyani, S, 1994. Correlating equations for impingement cooling of small heat sources with multiple circular liquid jets. *ASME J. Heat Transfer*, **116**(2), 482-486.

- Womac, F P, Ramadhyani, S and Incropera, F P, 1993. Correlating equations for impingement cooling of small heat sources with single circular liquid jets. *ASME J. Heat Transfer*, **115**(1), 106-115.
- Xuan, Y and Li, Q, 2000. Heat transfer enhancement of nanofluids. *Int. J. Heat and Fluid Flow*, **21**, 58-64.
- Yan, X, Baughn, J W, Rabas, T J and Arman, B, 1995. Liquid-crystal transient technique for measurement of in-tube local condensing heat transfer coefficients. *Experimental Heat Transfer*, **8**, 17-32.
- Yoda, M, Hesselink, L and Mungal, M G, 1994. Instantaneous three-dimensional concentration measurements in the self-similar region of a round high-Schmidt-number jet. *J. Fluid Mech.*, **279**, 313-350.
- Yokobori, S, Kasagi, N, Hirata, M, Nakamaru, M and Haramura, Y, 1979. Characteristic behaviour of turbulence and transport phenomena at the stagnation region of an axisymmetrical impinging jet. *Proc. 2<sup>nd</sup> Symp. Turbulent Shear Flow, London*, **4**, 4.12-4.17.
- Yokobori, S, Kasagi, N and Hirata, M, 1983. Transport phenomena at the stagnation region of a two-dimensional impinging jet. *Transactions of JSME B*, **49**(441), 1029-1039.
- Zhang, X, 1999. Turbulence measurements of an inclined rectangular jet in a boundary layer. *Proc. 4<sup>th</sup> Int. Symp. Engineering Turbulence Modelling and Experiments*, Corsica, France, 433-442.
- Zhang, Z and Eisele, K, 1995. Off-axis alignment of an LDA probe and the effect of astigmatism on measurements. *Experiments in Fluids*, **19**, 89-94.

Zhang, Z and Eisele, K, 1996. The effects of astigmatism due to beam refractions on the formation of the measurement volume in LDA measurements. *Experiments in Fluids*, **20**, 466-471.

Zhang, Z and Eisele, K, 1998a. On the overestimation of the flow turbulence due to fringe distortion in LDA measurements. *Experiments in Fluids*, **25**, 371-374.

Zhang, Z and Eisele, K, 1998b. Further considerations of the astigmatism error associated with off-axis alignment of an LDA-probe. *Experiments in Fluids*, **24**, 83-89.

Zumbrunnen, D A, Incropera, F P and Viskanta, R, 1992. A laminar boundary layer model of heat transfer due to a nonuniform planar jet impinging on a moving plate. *Wärme- und Stoffübertragung*, **27**, 311-319.

Zumbrunnen, D A, Incropera, F P and Viskanta, R, 1989. Convective Heat Transfer distributions on a Plate Cooled by Planar water jets. *ASME J. Heat Transfer*, **111**(4), 889-896.

Zumbrunnen, D A, Incropera, F P and Viskanta, R, 1990. Method and Apparatus for Measuring Heat Transfer Distributions on Moving and Stationary Plates Cooled by a Planar liquid jet. *Experimental Thermal and Fluid Science*, **3**, 202-213.

Zienkiewicz, O C and Taylor, R L, 1991. *The Finite Element Method - Vol. 2: Solid and Fluid Mechanics*, McGraw-Hill, New York.

## **Bibliography**

Akai, T J, 1994. *Applied Numerical Methods for Engineers*. John Wiley & Sons Inc., New York.

Adams, W H, 1954. *Heat Transmission*. McGraw-Hill Book Co., New York.

Incropera, F P and DeWitt, D P, 1996. *Introduction to Heat Transfer*. John Wiley & Sons Inc., New York.

Kettner, P, 1993. *Strömungstechnik*, Lecture notes, Fachhochschule Karlsruhe, University of Applied Technology, Karlsruhe, Germany.

Schmidt, F W, Henderson, R E and Wolgemuth, C H, 1993. *Introduction to Thermal Sciences*. 2nd ed., John Wiley & Sons Inc., New York.

Versteeg, H K and Malalasekera, W, 1995. *An introduction to Computational Fluid Dynamics - The Finite Volume Method*. John Wiley & Sons Inc., New York.

## **Databases and search facilities**

During the course of this project, the following databases and search engines on the Internet have been used.

ATHENS on <http://www.athens.ac.uk/> provides access to the following databases:

- ANTE Plus on <http://www.antenet.co.uk/>
- BIDS on <http://www.bids.ac.uk/>
- COMPENDEX on <http://edina.ed.ac.uk/compendex/>
- EMERALD on <http://www.emerald-library.com/>
- INSPEC on <http://www.edina.ed.ac.uk/inspec/>

Edinburgh Engineering Virtual Library (EVVL) on <http://www.eevl.ac.uk>

The following databases are maintained by the Department of Mechanical and Manufacturing Engineering at The Nottingham Trent University.

- Jet Impingement Database on <http://www.eevl.ac.uk/jet/>
- Liquid Crystal database on <http://www.eevl.ac.uk/lcd/>

ZETOC on <http://zetoc.mimas.ac.uk/> allows access to the British Library's Electronic Table of Contents (ETOC).

MetaCrawler on <http://www.metacrawler.com>

**Appendix A –  
Drawings and design diagrams  
for the experimental test facility**

**A.1 List of components**<sup>1</sup>

| <b>No.</b> | <b>Name of Component</b>                     | <b>Material</b>  | <b>Quantity</b> |
|------------|--|------------------|-----------------|
| 1          | Welded frame                                 | Angle iron       | 6000mm          |
| 2          | Main frame (□ 25mm)                          | Steel tube       | 8000mm          |
| 3          | Centrifugal pump,<br>(LOWARA CE KM70/3)      | Stainless steel  | 1               |
| 4          | Radiator hose (Ø=31.75mm)                    | Rubber           | 500mm           |
| 5          | Pipe, straight, plain (Ø=25.4mm)             | PVC              | 500mm           |
| 6          | Gate valve (Ø=25.4mm)                        | Bronze           | 1               |
| 7          | Bypass-filter (Ø=25.4mm)                     | PVC              | 1               |
| 8          | Flexible coupling (Ø=25.4mm)                 | Rubber           | 300mm           |
| 9          | Pipe, Bend, 90° (Ø=25.4mm, R=85mm)           | PVC              | 3               |
| 10         | Pipe, Straight (Ø=25.4mm)                    | PVC              | 200mm           |
| 11         | Diffuser (AR=4, α=8°)                        | Glassfibre       | 1               |
| 12         | Pipe, straight (Ø=50mm)                      | Perspex          | 750mm           |
| 13         | Valve housing                                | Perspex          | 1               |
| 14         | Valve plunger                                | Perspex          | 1               |
| 15         | Flow straightening element (honeycomb)       | Aluminium        | 1               |
| 16         | Flow straightening element (drinking straws) | PVC              | 1               |
| 17         | Nozzle (AR=2, φ=0.8)                         | Glassfibre       | 1               |
| 18         | Bracket (U-profile)                          | Aluminium        | 500mm           |
| 19         | Impingement plate (20mm thick)               | Perspex          | 1               |
| 20         | Test tank (capacity=45 litre)                | Perspex          | 1               |
| 21         | Discharge pipe (Ø=50.4mm)                    | PVC              | 500mm           |
| 22         | Ball valve (Ø=50.8mm, in Discharge leg)      | Stainless steel  | 1               |
| 23         | Radiator hose (Ø=50.4mm)                     | Rubber           | 500mm           |
| 24         | Water tank (capacity=270 litre)              | Galvanised steel | 1               |
| 25         | Ball valve (Ø=25.4mm, in By-pass leg)        | Steel            | 1               |

<sup>1</sup> see DRG No. 2/2

## A.2 Geometry of the Contraction

In the following, the co-ordinates of the contraction are given. To facilitate the manufacturing process, the mould was extended by 5mm on either side. After casting the excess material was parted off on a lathe.

|                   |           |               |             |
|-------------------|-----------|---------------|-------------|
| Inlet width       | = 50 mm   | Q(inlet)      | = -0.935175 |
| Outlet width      | = 35 mm   | Q(outlet)     | = 0.935078  |
| Contraction ratio | = 2.04    | True length   | = 82.997344 |
| Stream function   | = 0.8     | Target length | = 82.997344 |
| Epsilon           | = 0.51572 | Computations  | = 11572     |

| No. | Axial direction<br>[mm] | Radial direction<br>[mm] | Shadowgraph<br>measurements [mm] |
|-----|-------------------------|--------------------------|----------------------------------|
| 1   | 0.000                   | 17.500                   | 17.498                           |
| 2   | 5.000                   | 17.500                   | 17.463                           |
| 3   | 8.416                   | 17.503                   | 17.457                           |
| 4   | 11.829                  | 17.511                   | 17.477                           |
| 5   | 15.233                  | 17.529                   | 17.479                           |
| 6   | 18.621                  | 17.561                   | 17.490                           |
| 7   | 21.981                  | 17.615                   | 17.537                           |
| 8   | 25.296                  | 17.710                   | 17.628                           |
| 9   | 28.535                  | 17.884                   | 17.829                           |
| 10  | 30.000                  | 18.043                   | 17.927                           |
| 11  | 31.651                  | 18.222                   | 18.104                           |
| 12  | 32.000                  | 18.308                   | 18.155                           |
| 13  | 33.000                  | 18.553                   | 18.374                           |
| 14  | 34.000                  | 18.799                   | 18.649                           |
| 15  | 34.610                  | 18.949                   | 18.856                           |
| 16  | 35.500                  | 19.406                   | 19.279                           |
| 17  | 36.500                  | 19.919                   | 19.788                           |
| 18  | 37.731                  | 20.552                   | 20.416                           |
| 19  | 38.500                  | 20.977                   | 20.796                           |
| 20  | 39.759                  | 21.673                   | 21.476                           |
| 21  | 42.209                  | 22.685                   | 22.507                           |
| 22  | 44.881                  | 23.414                   | 23.249                           |
| 23  | 47.594                  | 23.899                   | ./.                              |
| 24  | 50.282                  | 24.221                   | ./.                              |
| 25  | 52.927                  | 24.439                   | 24.308                           |
| 26  | 55.533                  | 24.592                   | ./.                              |
| 27  | 58.107                  | 24.700                   | ./.                              |
| 28  | 60.654                  | 24.780                   | 24.662                           |
| 29  | 63.181                  | 24.839                   | ./.                              |
| 30  | 65.693                  | 24.882                   | ./.                              |
| 31  | 68.193                  | 24.916                   | 24.813                           |
| 32  | 70.684                  | 24.940                   | ./.                              |

|    |        |        |        |
|----|--------|--------|--------|
| 33 | 73.168 | 24.959 | ./.    |
| 34 | 75.646 | 24.973 | 24.827 |
| 35 | 78.121 | 24.983 | ./.    |
| 36 | 80.592 | 24.991 | ./.    |
| 37 | 83.062 | 24.996 | 24.852 |
| 38 | 85.530 | 24.999 | ./.    |
| 39 | 87.997 | 25.000 | ./.    |
| 40 | 92.997 | 25.000 | 25.002 |

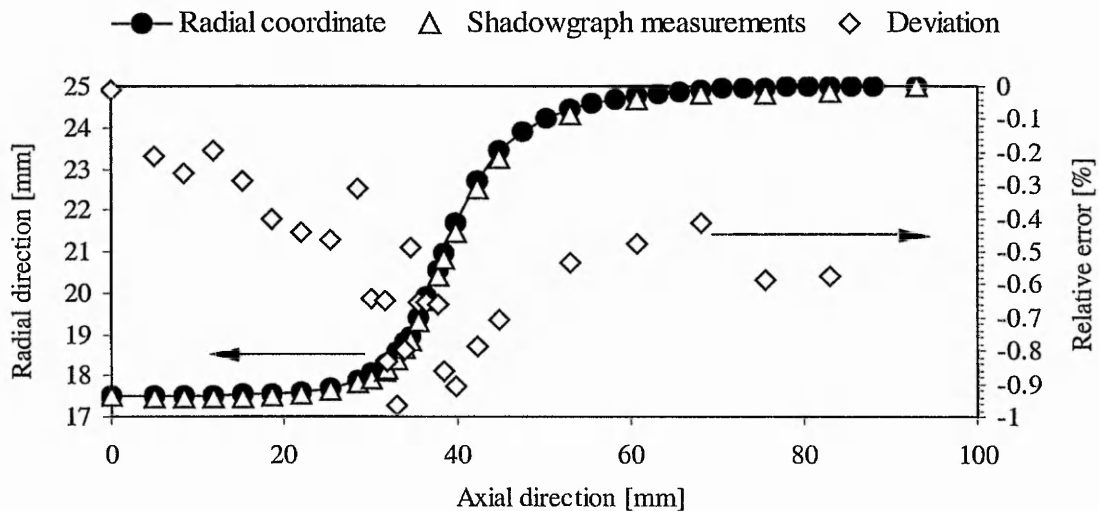
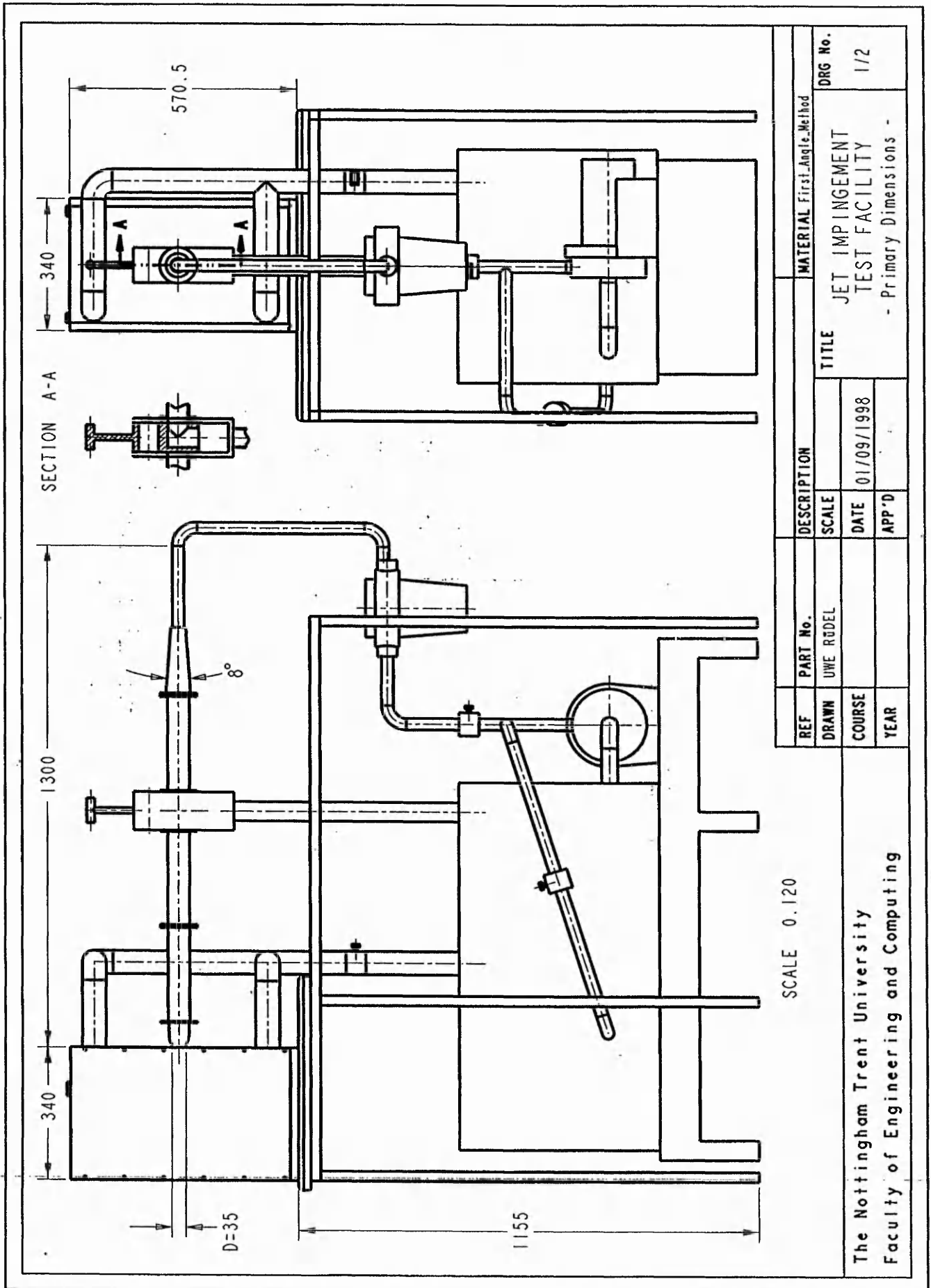


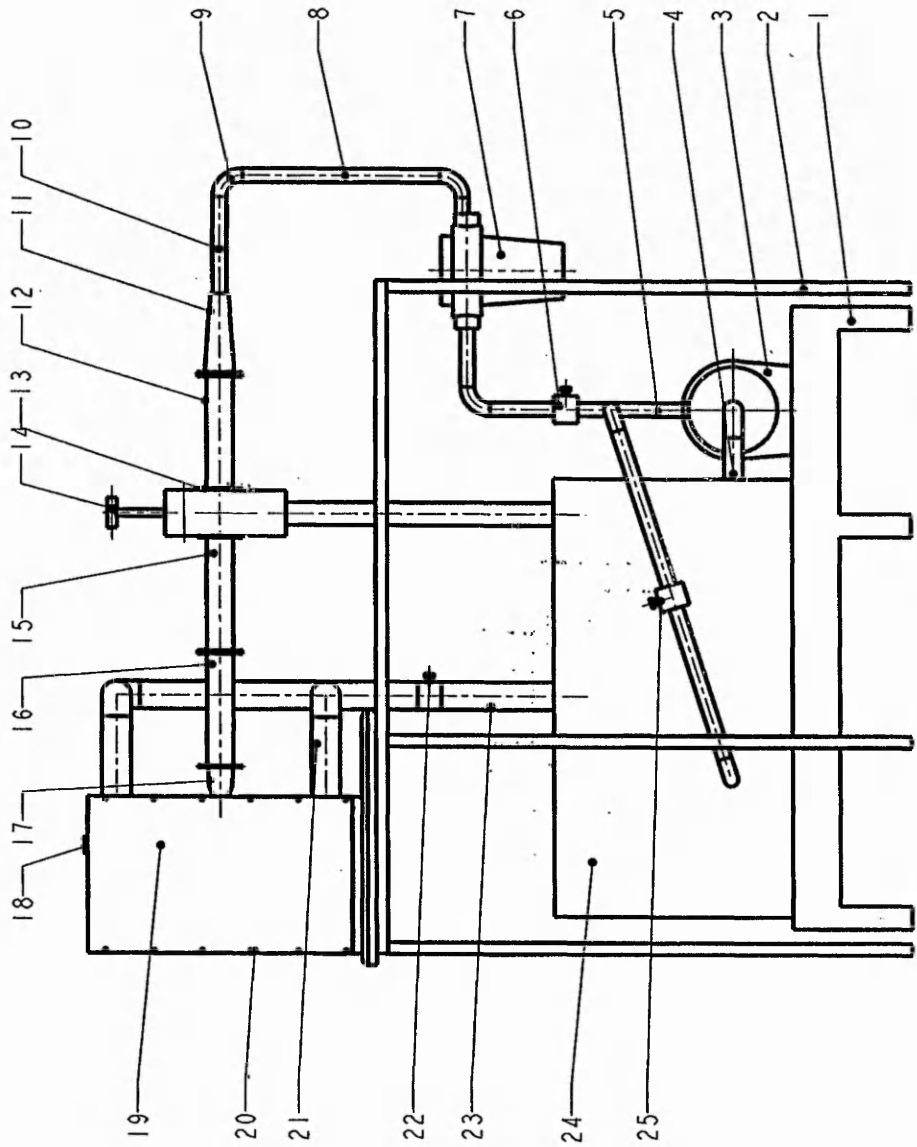
Figure A1. Actual and theoretical shape of nozzle.



SCALE 0.120

The Nottingham Trent University  
Faculty of Engineering and Computing

| REF    | PART No.  | DESCRIPTION | MATERIAL                      | First_Angle_Method | DRG No. |
|--------|-----------|-------------|-------------------------------|--------------------|---------|
| DRAWN  | UWE RUDEL | SCALE       | JET IMPINGEMENT TEST FACILITY |                    |         |
| COURSE |           | DATE        | - Primary Dimensions -        |                    |         |
| YEAR   |           | APP'D       | 1/2                           |                    |         |
|        |           |             | 01/09/1998                    |                    |         |



SCALE 0.100

|        |          |             |            |       |       |        |                                  |
|--------|----------|-------------|------------|-------|-------|--------|----------------------------------|
| REF    | PART No. | DESCRIPTION | MATERIAL   | First | Angle | Method | DRG No.                          |
| DRAWN  | UWE      | RDELD       |            |       |       |        | 2/2                              |
| COURSE |          |             |            |       |       |        | JET IMPINGEMENT<br>TEST FACILITY |
| YEAR   |          |             |            |       |       |        | - Components -                   |
|        |          | SCALE       | DATE       | APP'D |       |        |                                  |
|        |          |             | 01/09/1998 |       |       |        |                                  |

The Nottingham Trent University  
Faculty of Engineering and Computing

**Appendix B –  
Determination of physical properties of seeding particles**

### **B.1 Particle density**

The density of the seeding particles was determined according to BS 733-1:1983 and BS 733-2:1987 using a Gay-Lussac density bottle. The procedure consists mainly of three steps. The capacity of the bottle is calculated from precise measurements of its mass and the bottled water, followed by measurements of the mass of the sample and determination of the amount of water required to fill the residual volume of the bottle. All measurements were being made in an air-conditioned room at a constant temperature of 20.4°C. The density bottle, also called pycnometer, and its stopper are made of borosilicate glass and have low thermal conductivities. The bottle has a capacity of 100ml.

First, the pycnometer was cleaned with surfactant cleaning fluid and then thoroughly rinsed with Isopropanol. After drying the bottle by means of blowing warm air through it, the bottle and the stopper were allowed to achieve thermal equilibrium with the environment. The bottle and the stopper were weighed ( $m_1$ ) and the sample placed inside and reweighed ( $m_2$ ). The stopper was removed, the bottle topped up to the neck with distilled water and the stopper inserted by allowing it to sink under its own weight, so displacing the excess water. Any surplus water on the outside surface of the pycnometer was carefully removed by drying with a cloth and filter paper. Care was taken not to draw any liquid out from the bottle by capillary action. The filled bottle was weighed ( $m_3$ ) and then washed out thoroughly. After cleaning, rinsing and drying the bottle and the stopper, the capacity of the bottle was determined by topping it up to the neck with distilled water and reweighing ( $m_4$ ). Table B.1 gives values for a typical experiment.

$$\rho_{\text{Sample}} = \frac{m_{\text{Sample}}}{V_{\text{Sample}}} \quad (\text{B.1})$$

$$\rho_{\text{Sample}} = \frac{\rho_{\text{Water}} m_{21}}{(m_{41} - m_{32})} \quad (\text{B.2})$$

|       | <b>Description</b>                | <b>Value [g]</b> | <b>Uncertainty interval</b> |
|-------|-----------------------------------|------------------|-----------------------------|
| $m_1$ | Mass of bottle + stopper          | 34.887           |                             |
| $m_2$ | Mass of bottle + stopper + sample | 37.363           |                             |

|                       |   |         |                                 |
|-----------------------|---|---------|---------------------------------|
| $m_3$                 | Mass of bottle + stopper + sample + water             | 134.173 |                                 |
| $m_4$                 | Mass of bottle + stopper + water                      | 136.01  |                                 |
| $m_{21}$              | Mass of sample ( $m_2 - m_1$ )                        | 2.476   | $\delta m_{21} = 0.005\text{g}$ |
| $m_{32}$              | Mass of residual volume ( $m_3 - m_2$ )               | 96.81   | $\delta m_{32} = 0.04\text{g}$  |
| $m_{41}$              | Mass of bottle volume ( $m_4 - m_1$ )                 | 101.123 | $\delta m_{41} = 0.04\text{g}$  |
| $\rho_{\text{Water}}$ | Density of water at 20.4°C [ $\text{kg}/\text{m}^3$ ] | 998.204 |                                 |

Figure B.1 Experimental parameters, typical values and uncertainty intervals.

Substituting the values from Table 1 into equation B.2 yields  $\rho_{\text{Sample}} = 573 \text{ kg}/\text{m}^3$ . This value corresponds favourably with the manufacturer's specifications of  $\rho = 600 \text{ kg}/\text{m}^3$ . Applying the procedure described by Moffat (1985) the uncertainty in  $\rho_{\text{Sample}}$  for the present experiment can be found from

$$\frac{d\rho_{\text{Sample}}}{\rho_{\text{Sample}}} = \left[ \left( \frac{\delta m_{21}}{m_{21}} \right)^2 + \left( \frac{\delta m_{41}}{(m_{41} - m_{32})} \right)^2 + \left( \frac{\delta m_{32}}{(m_{41} - m_{32})} \right)^2 \right]^{0.5} \quad (\text{B.3})$$

This yields an uncertainty of 1.3% which was considered sufficiently accurate.

## **B.2 Effective particle diameter**

The spherical shape of the particles can be observed from Figure B.1 which shows a photographs obtained with a scanning electron microscope (SEM) and a magnification of 1700. Due to the depth of field, the size distribution could only be estimated to range from 25 $\mu\text{m}$  to 70 $\mu\text{m}$ .

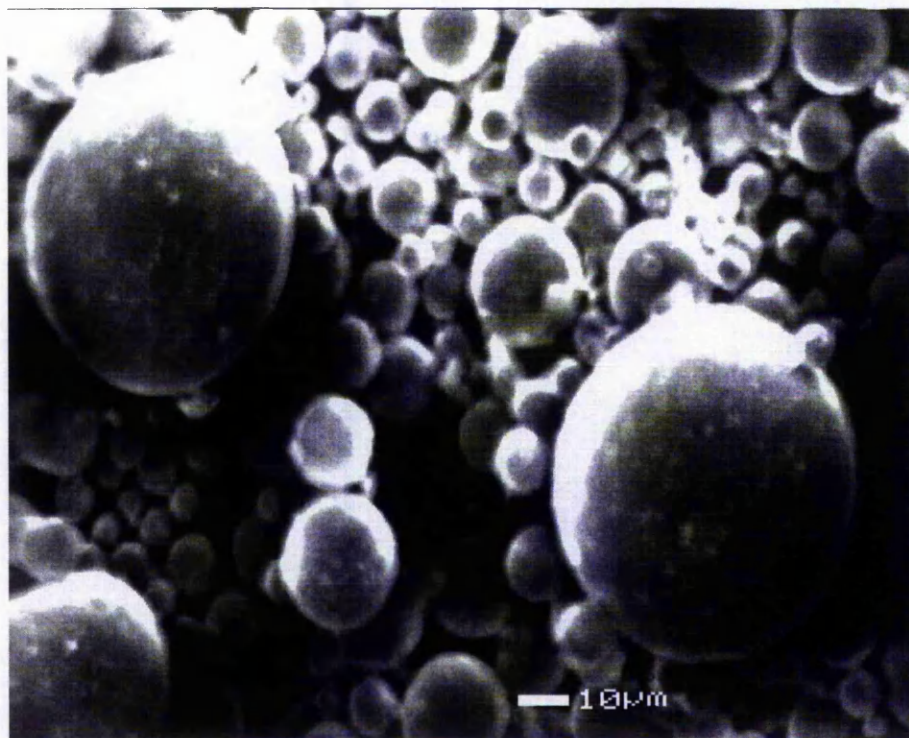


Figure B.1. SEM photograph of seeding particles (factor of magnification = 1700).

**Appendix C –  
Propagation of heat transfer measurement errors  
and their contribution to the overall uncertainty  
for three experimental techniques**

## Uncertainty of various techniques for heat transfer measurements

According to Kline and McClintock (1953) the uncertainty interval of a result  $r = f(x_1, x_2, x_3, \dots, x_n)$  is given by

$$\delta h = \left[ \left( \frac{\partial h}{\partial x_1} \delta x_1 \right)^2 + \left( \frac{\partial h}{\partial x_2} \delta x_2 \right)^2 + \dots + \left( \frac{\partial h}{\partial x_n} \delta x_n \right)^2 \right]^{0.5} \quad (\text{C.1})$$

where  $\delta_i$  are the uncertainties in measuring the variables  $x_i$ . Equation (C.1) is valid under the assumption that the individual variables were a) observed independently, b) from a Gaussian population and c) based on the same interval width of the Gaussian distribution.

### C.1 Constant temperature method

The governing equation reads as

$$h = \frac{\lambda \cdot A (T_B - T_S)}{s \cdot A (T_S - T_J)} = \frac{\lambda (T_B - T_S)}{s (T_S - T_J)} \quad (\text{C.2})$$

while the uncertainty analysis for the constant temperature method yields

$$\frac{\delta h}{h} = \left[ \left( \frac{\delta \lambda}{\lambda} \right)^2 + \left( \frac{-\delta s}{s} \right)^2 + \left( \frac{\delta (T_B - T_S)}{(T_B - T_S)} \right)^2 + \left( \frac{\delta (T_S - T_J)}{(T_S - T_J)} \right)^2 \right]^{0.5} \quad (\text{C.3})$$

### C.2 Constant heat flux technique

For the governing equation

$$h = \frac{Q}{A \cdot (T - T_{\text{Wall}, \infty})} = \frac{Q}{(B \cdot L) \cdot (T_{S, \text{ad}} - T_J)} \quad (\text{C.4})$$

an uncertainty analysis for the constant heat flux method ( $A=B \cdot L$ ) reveals

$$\frac{\delta h}{h} = \left[ \left( \frac{\delta Q}{Q} \right)^2 + \left( \frac{\delta B}{B} \right)^2 + \left( \frac{\delta L}{L} \right)^2 + \left( \frac{\delta (T_{S, \text{ad}} - T_J)}{(T_{S, \text{ad}} - T_J)} \right)^2 \right]^{0.5} \quad (\text{C.5})$$

The contribution of the individual quantities can be seen from Table C.1.

| Measured Parameter | Typical value | $\pm \delta x$ | $[(\partial h/\partial x)\delta x]/(dh/h)$ [%] |
|--------------------|---------------|----------------|--|
| Q                  | 5000 W        | 500 W          | 98.76  |
| B, L               | 0.5 m         | 0.0001 m       | $\sum < 0.001$                                 |
| $T_{S, ad}$        | 40°C          | 0.2°C          | 0.25   |
| $T_J$              | 20°C          | 0.2°C          | 0.99   |

Table C.1. Contribution to overall uncertainty of 10.1% ( $h=1000 \text{ W}/(\text{m}^2\text{K})$ ).

### C.3 Transient one-dimensional transient technique

The governing equation is

$$\frac{\partial^2 T}{\partial x^2} + \frac{\partial^2 T}{\partial y^2} = \frac{1}{\alpha} \frac{\partial T}{\partial t} \quad (\text{C.6})$$

with the following boundary conditions

$$T(t=0, x=0) = T_0$$

$$T(t=0, x=a) = T_0$$

$$T(t=0, y=0) = T_0$$

$$T(t=0, y=b) = T_0$$

(C.7)

$$\lambda \frac{\partial T}{\partial x} = h(T - T_\infty) \text{ at } x=0$$

The energy equation for this problem is linear so that (C.6) can be solved as product of two one-dimensional solutions, see Carslaw and Jaeger (1959) and Incropera and DeWitt (1996).

$$T_{\text{Total}} = T_x \cdot T_y \quad (\text{C.7.1})$$

$$\frac{\partial^2 T_x}{\partial x^2} = \frac{1}{\alpha} \frac{\partial T_x}{\partial t} \quad (\text{C.8})$$

$$\frac{\partial^2 T_y}{\partial y^2} = \frac{1}{\alpha} \frac{\partial T_y}{\partial t} \quad (\text{C.9})$$

In the following, the solution to equation (C.8) will be determined first. Since  $T_x$  is a function of the spatial variable  $x$  and the time  $t$ , the Laplace transformation is applied by multiplying equation (C.8) by  $e^{-pt}$ . This yields

$$\int_0^{\infty} e^{-pt} \frac{\partial^2 T_x}{\partial x^2} dt - \frac{1}{\alpha} \int_0^{\infty} e^{-pt} \frac{\partial T_x}{\partial t} dt = 0 \quad (C.10)$$

The following Laplace theorems are used, see Carslaw and Jaeger (1959):

$$\mathcal{L} \left\{ \frac{\partial^2 T_x}{\partial x^2} \right\} = \frac{\partial^2 \hat{T}_x}{\partial x^2} \quad (C.11)$$

$$\mathcal{L} \left\{ \frac{\partial T_x}{\partial t} \right\} = w \mathcal{L}\{T_x\} - T_{x,0} \quad (C.12)$$

so that with (C.11) and (C.12) into (C.10) the subsidiary equation becomes

$$\frac{d^2 \hat{T}_x}{dx^2} - \frac{w}{\alpha} \hat{T}_x = -\frac{1}{\alpha} T_{x,0} \quad (C.13)$$

with  $a < x < b$  and  $w/\alpha = c^2$ .

Thus, the partial differential equation (C.6) has been reduced to an ordinary differential equation. It can be solved by determining the *complementary function* of the homogenous equation first.

$$\frac{d^2 \hat{T}_x}{dx^2} - c^2 \hat{T}_x = 0 \quad (C.14)$$

(C.14) is solved by assuming that the solution has the following form.

$$\hat{T}_x = e^{dx} \quad (C.15)$$

$$\frac{d\hat{T}_x}{dx} = de^{dx} \quad (C.16)$$

$$\frac{d^2 \hat{T}_x}{dx^2} = d^2 e^{dx} \quad (C.17)$$

(C.15) and (C.17) into (C.14) yields

$$d^2 e^{dx} - c^2 e^{dx} = 0 \quad (C.18)$$

and therefore

$d_1 = c$  (not applicable as  $x$  is bounded between 0 and  $\infty$  only).

$$\underline{d_2 = -c} \quad (C.19)$$

The *complementary function* is therefore

$$\hat{T}_{x, \text{Compl}} = C e^{-c x} \quad (C.20)$$

The general solution is now obtained by finding the *particular integral* to the inhomogeneous equation (C.13). The *particular integral* is assumed to be of the form

$$\hat{T}_{x, \text{pl}} = \underbrace{a_1}_{=0} x^2 + \underbrace{a_2}_{=0} x + a_3 \quad (C.21)$$

$$\frac{d \hat{T}_{x, \text{pl}}}{d x} = \frac{d^2 \hat{T}_{x, \text{pl}}}{d x^2} = 0 \quad (C.22)$$

and will be used to equate coefficients. With (C.21) and C.(22) into (C.13)

$$0 - c^2 a_3 = -\frac{1}{\alpha} T_{x,0} \quad (C.23)$$

$$a_3 = \frac{1}{w} T_{x,0} \quad (C.24)$$

The general solution to equation (C.13) comprises of the *complementary function* and the *particular integral* and reads as

$$\underline{\underline{\hat{T}_{x, \text{total}} = C e^{-c x} + \frac{1}{w} T_{x,0}}} \quad (C.25)$$

The coefficient  $C$  is determined from the convective boundary condition (C.7) which is transformed into the Laplace domain

$$\frac{\partial \hat{T}_x}{\partial x} = \frac{h}{\lambda} \left( \hat{T}_x - \frac{T_\infty}{w} \right) \quad (C.26)$$

With (C.7) in (C.26)

$$\frac{\partial \left[ C e^{-c x} + \frac{1}{w} T_{x,0} \right]}{\partial x} = \frac{h}{\lambda} \left( \left[ C e^{-c x} + \frac{1}{w} T_{x,0} \right] - \frac{T_\infty}{w} \right) \quad (C.27)$$

$$-c C e^{-c x} - \frac{h}{\lambda} C e^{-c x} = \frac{h}{\lambda} \left( \frac{1}{w} T_{x,0} - \frac{T_\infty}{w} \right) \quad (C.28)$$

$$C e^{-c x} \left( -c - \frac{h}{\lambda} \right) = \frac{h}{\lambda} \left( \frac{1}{w} T_{x,0} - \frac{T_{\infty}}{w} \right) \quad (C.29)$$

with  $x = 0$  and  $w = c^2 \alpha$

$$C = \frac{\frac{h}{\lambda} (T_{\infty} - T_{x,0})}{w \left( c + \frac{h}{\lambda} \right)} \quad (C.30)$$

Finally, with (C.25) and (C.30)

$$\hat{T}_{x,\text{total}} = \frac{\frac{h}{\lambda} (T_{\infty} - T_{x,0})}{w \left( c + \frac{h}{\lambda} \right)} e^{-c x} + \frac{T_{x,0}}{w} \quad (C.31)$$

Back-substitution yields

$$T_x = \frac{\lambda}{h} \operatorname{erfc} \left( \frac{x}{2 \sqrt{\alpha t}} \right) - \frac{\lambda}{h} e^{\frac{hx}{\lambda} + \frac{t h^2}{(\lambda \rho c \lambda)}} \operatorname{erfc} \left( \frac{x}{2 \sqrt{\alpha t}} + \frac{h}{\lambda} \sqrt{\alpha t} \right) \quad (C.32)$$

With  $x = 0$  and

$$\sqrt{\eta} = \frac{h \sqrt{t}}{\sqrt{\rho c \lambda}} \quad (C.33)$$

this yields

$$T_x = T_{x,LC} = \frac{\lambda}{h} \left[ 1 - e^{\eta} \operatorname{erfc}(\sqrt{\eta}) \right] \quad (C.34)$$

Finally,

$$\theta_x = \frac{T_{x,LC} - T_0}{T_J - T_0} = 1 - e^{\eta} \operatorname{erfc}(\sqrt{\eta}) \quad (C.35)$$

When applying the procedure suggested by Kline and Clintock (1953) to equation (C.35), it follows for the uncertainty that

$$\delta h = \left[ \left( \frac{\partial h}{\partial t} \delta t \right)^2 + \left( \frac{\partial h}{\partial \sqrt{\rho c \lambda}} \delta \sqrt{\rho c \lambda} \right)^2 + \left( \frac{\partial h}{\partial T_{LC}} \delta T_{x,LC} \right)^2 + \left( \frac{\partial h}{\partial T_0} \delta T_0 \right)^2 + \left( \frac{\partial h}{\partial T_J} \delta T_J \right)^2 \right]^{0.5} \quad (C.36)$$

The partial derivatives are differentiated from equation (C.35) and yield

$$\frac{\partial h}{\partial t} = \frac{-h}{2t} \quad (\text{C.37})$$

$$\frac{\partial h}{\partial \sqrt{\rho c \lambda}} = \frac{h}{\sqrt{\rho c \lambda}} \quad (\text{C.38})$$

$$\frac{\partial h}{\partial T_{x,LC}} = \frac{\partial h}{\partial \theta} \frac{\partial \theta}{\partial T_{x,LC}} = \frac{h}{\beta(T_J - T_0)} \quad (\text{C.39})$$

$$\frac{\partial h}{\partial T_0} = \frac{\partial h}{\partial \theta} \frac{\partial \theta}{\partial T_0} = \frac{h(T_{x,LC} - T_J)}{\beta(T_J - T_0)^2} \quad (\text{C.40})$$

$$\frac{\partial h}{\partial T_J} = \frac{\partial h}{\partial \theta} \frac{\partial \theta}{\partial T_J} = \frac{-h(T_{x,LC} - T_0)}{\beta(T_J - T_0)^2} \quad (\text{C.41})$$

where  $\beta = 2 \sqrt{\eta} (\pi^{0.5} - \sqrt{\eta}(1-\theta))$ .

Substituting equations (C.37) to (C.41) yields

$$\frac{\delta h}{h} = \left[ \left( \frac{\delta t}{2t} \right)^2 + \left( \frac{\delta \sqrt{\rho c \lambda}}{\sqrt{\rho c \lambda}} \right)^2 + \left( \frac{1}{\beta(T_J - T_0)} \right)^2 (\delta T_{x,LC}^2 + (\theta-1)^2 \delta T_0^2 + \theta^2 \delta T_J^2) \right]^{0.5} \quad (\text{C.42})$$

The contribution of the individual quantities to the overall uncertainty can be seen from Table C.2

| Measured parameter x        | Typical value                             | $\pm \delta x$                           | $[(\partial h/\partial x)\delta x]/(dh/h)$<br>[%] |
|-----------------------------|---|--|---|
| t                           | 5.49 s                                    | 0.1 s                                    | 0.81  |
| $\sqrt{(\rho c_p \lambda)}$ | 569 J/(m <sup>2</sup> Ks <sup>0.5</sup> ) | 29 J/(m <sup>2</sup> Ks <sup>0.5</sup> ) | 25.31   |
| $T_{x,LC}, T_J, T_0$        | 30.65, 53, 19.65 °C                       | 0.1, 0.2, 0.1 °C                         | $\Sigma 73.88$                                    |

Table C.2. Contribution to overall uncertainty of 10.1% (Pr=0.71, h=113.8 W/(m<sup>2</sup>K)).

## C.4 Transient two-dimensional transient technique

In the direction normal to the plate surface, the one-dimensional solution is the well-known equation (3.8) of transient heat conduction through a semi-infinite solid. Lateral conduction can be accounted for by applying the solution given in Carslaw and Jaeger (1959) for a semi-infinite solid with initial temperature  $T_0$  and time-dependent surface temperature  $\phi = \phi(t)$ . Due to the axisymmetric character of round jet impingement heat

transfer, only one half of the plate was considered.

In the same manner as described in Appendix C.3, equation (C.9) is solved by considering (C.25). For the case of the hot target plate being cooled by the jet, the coefficient C is determined by assuming that the surface temperature is an exponential function of time. Therefore,

$$\phi(t) = e^{-\zeta t} \tag{C.43}$$

In the Laplace domain, this becomes

$$\hat{\phi}(w) = \frac{1}{w - \zeta} \tag{C.44}$$

So that the solution to (C.9) reads as

$$\hat{T}_{y, \text{total}} = \frac{e^{-c y}}{w - \zeta} + \frac{1}{w} T_0 \tag{C.45}$$

Back-substitution yields

$$\hat{T}_{y, \text{total}} = \frac{1}{2} e^{-\zeta t} \left\{ e^{-y\sqrt{\zeta/\alpha}} \operatorname{erfc} \left( \frac{y}{2\sqrt{\alpha t}} - \sqrt{\alpha t} \right) + e^{y\sqrt{\zeta/\alpha}} \operatorname{erfc} \left( \frac{y}{2\sqrt{\alpha t}} + \sqrt{\alpha t} \right) \right\} \tag{C.46}$$

To determine the lateral temperature, the surface temperature is assumed as

$$\phi = T_0 e^{\lambda t} \quad \lambda < 0 \tag{C.47}$$

Then from (C.7.1), it follows that  $\theta_{\text{Total}} = \theta_x \cdot \theta_y$  where  $\theta_x$  is given by (C.35) and

$$\theta_y = \frac{T_y}{T_0} \tag{C.48} \quad \text{with} \quad T_y = T_1 + T_2 \tag{C.49}$$

where

$$T_1 = T_0 \operatorname{erf} \left( \frac{y}{2\sqrt{(\alpha t)}} \right) \tag{C.50}$$

and

$$T_2 = \frac{T_0}{2} e^{\lambda t} \left\{ \left[ e^{-y\sqrt{(\lambda/\alpha)}} \right] \operatorname{erfc} \left( \frac{y}{2\sqrt{(\alpha t)}} - \sqrt{(\lambda t)} \right) + \left[ e^{y\sqrt{(\lambda/\alpha)}} \right] \operatorname{erfc} \left( \frac{y}{2\sqrt{(\alpha t)}} + \sqrt{(\lambda t)} \right) \right\} \tag{C.51}$$

Let  $\lambda = -p^2$ , where  $p$  is a real number so that  $p = -i\sqrt{\lambda}$ . It follows that

$$T_2 = \frac{T_0}{2} e^{-p^2 t} \left\{ \left[ e^{-iy_p \sqrt{(1/\alpha)}} \right] \operatorname{erfc} \left( \frac{y}{2\sqrt{(\alpha t)}} - i p \sqrt{t} \right) + \left[ e^{iy_p \sqrt{(1/\alpha)}} \right] \operatorname{erfc} \left( \frac{y}{2\sqrt{(\alpha t)}} + i p \sqrt{t} \right) \right\} \quad (C.52)$$

Let  $a = \frac{y}{2\sqrt{(\alpha t)}}$  and  $b = p\sqrt{t}$ . Also put

$$e^{\pm i[y_p \sqrt{(1/\alpha)}]} = \cos(y_p \sqrt{(1/\alpha)}) \pm i \sin(y_p \sqrt{(1/\alpha)}) = \cos \gamma \pm i \sin \gamma \quad (C.53)$$

and

$$\operatorname{erfc}(z) = \operatorname{erfc}(a + ib) = 1 - \operatorname{erf}(a + ib) = 1 - P - iQ \quad (C.54)$$

$$\operatorname{erfc}(\bar{z}) = \operatorname{erfc}(a - ib) = 1 - \operatorname{erf}(a - ib) = 1 - P + iQ \quad (C.55)$$

The Gauss error function was implemented using the sum of the following series expansions:

$$P(r, \beta) = \frac{2}{\sqrt{\pi}} \sum_{n=0}^{\infty} \frac{(-1)^n r^{2n+1} T_{2n+1}(\cos \beta)}{(2n+1) n!} \quad (C.56)$$

$$Q(r, \beta) = \frac{2r \sin \beta}{\sqrt{\pi}} \sum_{n=0}^{\infty} \frac{(-1)^n r^{2n} T_{2n}(\cos \beta)}{(2n+1) n!} \quad (C.57)$$

where  $T_{2n+1}(\cos \beta)$  and  $U_{2n}(\cos \beta)$  are the *Chebyshev's* polynomials of the first and second kind, respectively. The expressions  $P$  and  $Q$  are now calculated by using the recurrence equations and the starting values given in Gradshteyn and Ryzhik (1980).

Substituting equations (C.53), (C.54) and (C.55) into (C.52) yields

$$T_2 = \frac{T_0}{2} e^{-p^2 t} \left\{ [\cos \gamma - i \sin \gamma][1 - P + iQ] + [\cos \gamma + i \sin \gamma][1 - P - iQ] \right\} \quad (C.58)$$

Finally, substituting (C.49), (C.50) and (C.58) into (C.48) leads to

$$\theta_y = \frac{T_y}{T_0} = T_1 + T_2 = \left\{ \operatorname{erf} \left( \frac{y}{2\sqrt{(\alpha t)}} \right) + e^{-p^2 t} [(1 - P)\cos \gamma + Q \sin \gamma] \right\} \quad (C.59)$$

To determine the decay coefficient  $\lambda$  experimentally a round semi-confined submerged jet impinging on a heated plate was considered. For the case of air ( $Pr = 0.7$ ) the nozzle diameter was 0.1m while the water jet had similar nozzle exit conditions ( $Re = 20000$ ) at a nozzle diameter of 0.02m. The experiments were conducted by suddenly exposing a hot impingement plate to a cold jet. In the case of the water jet the test run was initiated by dropping the plate guided by rails along the wall. The surface

temperature was measured via a thermocouple attached at the stagnation point of the Perspex plate.

A least square fit was used to determine the decay coefficient  $\lambda$  for the air jet to 0.0014 whereas for the water jet  $\lambda$  was determined to be 2.

### C.5 Calibration curves of liquid crystals

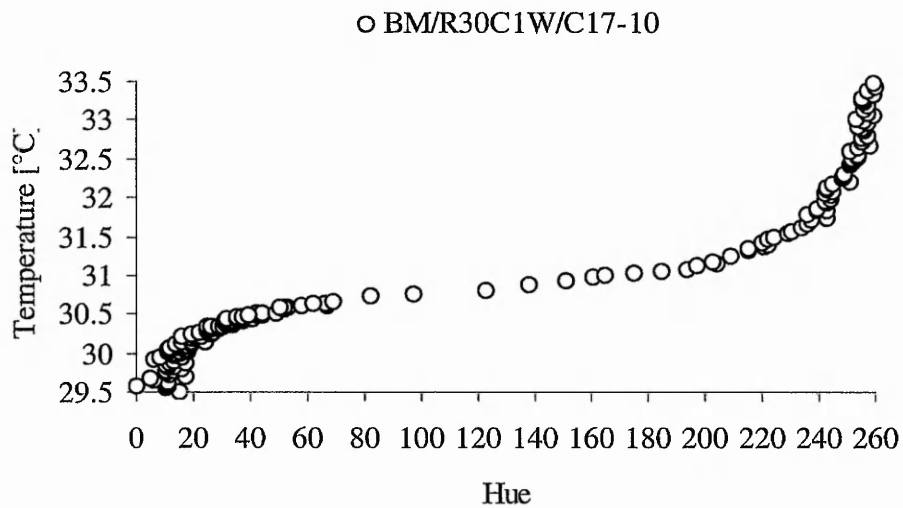


Figure C.1. Liquid crystal temperature-hue calibration curve for air measurements.

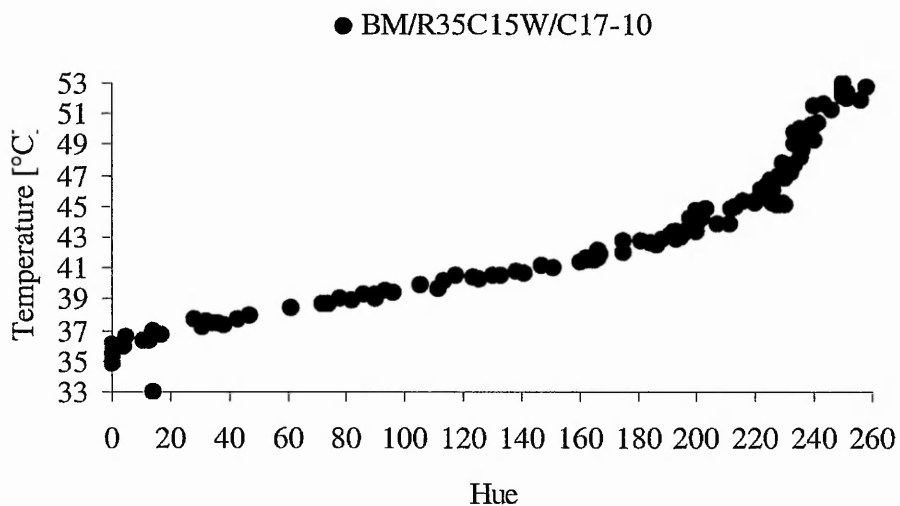


Figure C.2. Liquid crystal temperature-hue calibration curve for water tests.

**Appendix D –  
C++ Software for One and Two-dimensional transient heat conduction  
through a semi-infinite solid and for data collection.**

## D.1 One-dimensional transient heat conduction through a solid (numerical approximation)

```

#include <conio.h>           //for getch()
#include <iostream.h>       //basic library function
#include <math.h>           //for pow(Nx,2)
#include <process.h>       //for 'exit'-function
#include <fstream.h>       //for file functions

const long double dx=long double (0.00005);
const long double Alph=long double (1.00925E-7); // k=0.18; Ro=1189; cp=1500;
const float k=float (0.18);
const int size=2000; //32500 is the maximum size of an array, 32500^(1/2)=180=xx=yy

//One-dimensional transient conduction through a semi-infinite body using the finite
difference technique, Uwe Rüdell, 11th April 1999

void Input_Data (long double &Th, float &He, int &B, int &Nx, int &Ny, double
T[9001], long double &Fo, int &C, long double &Tfl, float &T0);
void Erect_Matrix (int Nx, int Ny, double T[9001], long double Fo, long double &Tfl, int
B, int C, float T0);

void main ()
{
    int Nx=0, Ny=0, B=1;
    double T[9001];
    float T0=float (0);
    float He=0;
    int C=0;
    long double Fo=long double (0), Th=long double (0), Tfl=long double (0);
    Input_Data (Th, He, B, Nx, Ny, T, Fo, C, Tfl, T0);
    Erect_Matrix (Nx, Ny, T, Fo, Tfl, B, C, T0);
    //getche();
}

void Input_Data (long double &Th, float &He, int &B, int &Nx, int &Ny, double
T[9001], long double &Fo, int &C, long double &Tfl, float &T0)
{
    float dt;
    cout << "Please enter the elapsed time: ";
    cin >> dt;
    cout << "Please enter the fluid temperature: ";
    cin >> Tfl;
    cout << "Enter temperature of the plate (°C): ";
    cin >> T0;
    Fo=long double (((Alph*dt)/(dx*dx)));
    cout << "Fourier number is " << Fo << " " << endl;
}

```

```

T[0]=float (T0);
cout << "Please enter the number of internal nodes: ";
cin >> Ny;
cout <<"Enter T[1]: ";
cin >> T[1];
}

long double** Alloc2D(long double** M, long double nln, long double nout)
{
M=new long double* [nln];
for (int i=1; i<nln; i++)
    {
M[i]=new long double [nout];
    }
return M;
}

void Erect_Matrix (int Nx, int Ny, double T[9001], long double Fo, long double &Tfl, int
B, int C, float T0)
{
ofstream transfer;
transfer.open("HTC2d990405.txt", ios::app | ios :: out);
long double P=long double (0);
long double S[size+1];
long double Z=long double (0), ZZ=long double (0);
long double** M;
M=Alloc2D(M,size+1,size+1);
}

//Matrix solver, Gauss elimination, Uwe Rüdell, 19th October 1998
//modified on 7th April 1999

int Y=int(0);

for (int m=1; m<Ny+1; m++) //to fill the matrix initially with zero elements
    {
    for (int l=1; l<Ny+2; l++)
        {
M[m][l]=0;
        }
    }

for (int i=1; i<Ny+1; i++)
    {
    for (int j=1; j<(Ny+2); j++)
        {
        if (i < (1+1)) //to fill the row of surfaces nodes
            {

```

```

if (j == i)
{
    M[i][j]=((Tf1-T[1])*2*Fo*dx/k);
}
if (j == (i+1))
{
    M[i][j]=(2*Fo);
}
if (j == (Ny+1))
{
    M[i][j]=(((2*Fo)+1)*T[1]-T0);
}
}

if (i == 2) //to specify the second column of nodes
{
    if (j == i)
    {
        M[i][j]=((2*Fo)+1);
    }
    if (j == (i+1))
    {
        M[i][j]=(-Fo);
    }
    if (j == Ny+1)
    {
        M[i][j]=(T0+(T[i-1]*Fo));
    }
}

if (i > 2)
{
    if (i == Ny)
    {
        if (j == i)
        {
            M[i][j]=((2*Fo)+1);
        }
        if (j == (i-1))
        {
            M[i][j]=(-Fo);
        }
        if (j == Ny+1)
        {
            M[i][j]=(T0+(T0*Fo));
        }
    }
    else

```

```

        {
        if (j == i)
            {
                M[i][j]=((2*Fo)+1);
            }
        if (j == (i-1))
            {
                M[i][j]=(-Fo);
            }
        if (j == (i+1))
            {
                M[i][j]=(-Fo);
            }
        if (j == Ny+1)
            {
                M[i][j]=(T0);
            }
        }
    }
}

transfer << "***** After erecting matrix *****" << endl;
for (i=1; i<(Ny+1); i++) //to print out the final matrice
    {
        for (int j=1; j<(Ny+2); j++)
            {
                transfer << "\t\t" << M[i][j];
            }
        transfer << endl;
    }

transfer << "***** New matrix *****" << endl;
for (int j=1; j<(Ny+2); j++) //to swap lines to get pivot line
    {
        for (int i=1; i<(Ny+1); i++)
            {
                if (i > j)
                    {
                        if (M[i][j] > M[j][j])
                            {
                                if (M[i][j] != 0)
                                    {
                                        for (int p=1; p<(Ny+2); p++)
                                            //to exchange line with pivot line
                                                {
                                                    P=long double (M[i][p]);
                                                    //to create pivot element on diagonal

```

```

M[i][p]=long double (M[i-1][p]);
//to bring highest value element within
M[i-1][p]=long double (P);
//column on diagonal position
}
}
}
if (M[i][j] < M[j][j])
{
if (M[i][j] != 0) //brings
value beneath diagonal element
{ //equal to zero
long double pivot = long double (M[i][j]);
for (int p=j; p<(Ny+2); p++)
{
M[i][p] = long double ((M[i][p] -
((M[j][p]*pivot)/M[j][j]));
}
}
}
}

for (int e=1; e<(Ny+1); e++) //to print out the final matrix
{
for (int f=1; f<(Ny+2); f++)
{
transfer << "\t\t"<<M[e][f];
}
transfer << endl;
}

for (j=1; j<Ny; j++)
{
S[j]=long double (0);
}

for (i=1; i<(Ny); i++)
{
S[i]=long double (0);
}

for (i=(Ny); i>0; i--) //Backsubstitution
{
if (i == (Ny))

```

```

        {
        S[(Ny)]=long double (M[i][i+1]/M[i][i]);
        }
else
    {
    for (j=(Ny); j>i; j--)
        {
        Z = long double (M[i][j]*S[j]);
        ZZ += long double (Z);
        }
    S[i]=long double ((1/M[i][i])*(M[i][(Ny+1)]-ZZ));
    ZZ=long double (0);
    }
}

for (i=1; i<(Ny+1); i++)    //print final solution vector
    {
    transfer <<" S["<<i<<" = "<<S[i]<<endl;
    cout <<" S["<<i<<" = "<<S[i]<<endl;
    }
transfer.close();
delete M;
}

```

## D.2 Two dimensional transient heat conduction through a solid (numerical approximation)

```

#include <conio.h>                //for getch()
#include <iostream.h>            //basic library function
#include <math.h>                //for pow(Nx,2)
#include <process.h>            //for 'exit'-function
#include <fstream.h>            //for file functions

const long double Alph=long double (1.00925E-7); // k=0.18; Ro=1189; cp=1500;
const float k=float (0.18);
const int size=5000;

//Two-dimensional transient conduction through a semi-infinite body using the finite
difference technique, Uwe Rüdell, 5th April 1999

void Input_Data (long double &Th, float &He, int &B, int &Nx, int &Ny, double
T[9001], long double &Fo, int &C, long double &Tfl, float &T0, float &dx);
void Erect_Matrix (int Nx, int Ny, double T[9001], long double Fo, long double &Tfl, int
B, int C, float T0, float dx);

void main ()
{
    int Nx=0, Ny=0, B=1;
    double T[9001];
    float T0=float (0);
    float He=0, dx=0;
    int C=0;
    long double Fo=long double (0), Th=long double (0), Tfl=long double (0);
    Input_Data (Th, He, B, Nx, Ny, T, Fo, C, Tfl, T0, dx);
    for (int x=1; x<(Ny+2); x++)
        {
            cout << "T["<<x<<"] = "<<T[x]<<endl;
        }

    Erect_Matrix (Nx, Ny, T, Fo, Tfl, B, C, T0, dx);
    getch();
}

void Input_Data (long double &Th, float &He, int &B, int &Nx, int &Ny, double
T[9001], long double &Fo, int &C, long double &Tfl, float &T0, float &dx)
{
    float dt; /
    cout << "\nPlease enter the dimensions of the rectangular plate [in m]:";
    cout << "\nThickness: ";
    cin >> Th;
    cout << "Height:  ";

```

```

cin >> He;
cout << "Please enter the fluid temperature: ";
cin >> Tfl;
cout << "Enter temperature of the plate (°C): ";
cin >> T0;
T[0]=float (T0);
cout << "Please enter the elapsed time: ";
cin >> dt;
cout << "What distance between the nodes [metre]? ";
cin >> dx;
cout << "dx=dy=" << dx << " [m] " << endl;
Fo=long double (((Alph*dt)/(dx*dx)));
cout << "Fourier number is " << Fo << "" << endl;
cout << "Please enter the number of internal nodes along the (vertical) y-axis: ";
cin >> Ny;
cout << "You will have " << Ny+1 << " nodes along the (vertical) y-axis ";
Nx=Th/dx;
cout << "and " << Nx+1 << " nodes along the (horizontal) x-axis.";
C= int (Nx*Ny);
if (C>9000)
    {
        cout << "\nNumber of unknowns exceeds capacity of solver matrix
(9000x9000)";
        exit(0);
    }
cout << "\nEnter the surface temperature in the following fashion: ";
cout << "\n(T[n=1], T[n=2],.. T[n=" << Ny << "]). " << endl;

for (int y=(Ny+1); y<((Nx*Ny)+2); y=y+(Ny+1))
    {
        T[y]=T0;
        //cout << "T[" << y << "]=" << T[y] << "";
    }

for (int x=1; x<(Ny+1); x++)
    {
        cout << "Enter T[" << x << "]: ";
        cin >> T[x];
    }
}

long double** Alloc2D(long double** M, long double nln, long double nout)
{
    M=new long double* [nln];
    for (int i=1; i<nln; i++)
        {
            M[i]=new long double [nout];
        }
    return M;
}

```

```

}

void Erect_Matrix (int Nx, int Ny, double T[9001], long double Fo, long double &Tfl, int
B, int C, float T0, float dx)
{
  ofstream transfer;
  transfer.open("HTC2d990405.txt", ios::app | ios :: out);
  long double P=long double (0);
  long double S[size+1];
  long double Z=long double (0), ZZ=long double (0);
  long double** M;
  M=Alloc2D(M,size+1,size+1);
}

```

```

//Matrix solver, Gauss elimination, Uwe Rüdell, 19th October 1998
//modified on 7th April 1999

```

```

int A=int (Ny*Nx);
int C2=int (Nx);
int Y=int(0);

for (int m=1; m<A+1; m++)
  {
    for (int l=1; l<A+2; l++)
      {
        M[m][l]=0;
      }
  }

for (int i=1; i<A+1; i++)
  {
    for (int j=1; j<(A+2); j++)
      {
        if (i < (Ny+1))
          {
            if (j == i)
              {
                M[i][j]=(Tfl-T[i])*2*Fo*dx/k;
              }
            if (j == (i+Ny))
              {
                M[i][j]=(2*Fo);
              }
            if (j == (A+1))
              {
                if ((i%Ny) == 1)
                  {
                    M[i][j]=(((4*Fo)+1)*T[i])-((2*Fo)*T[i+1])-T0);

```

```

T0);
    }
    else
    {
        M[i][j]=(((4*Fo)+1)*T[i])-(Fo*(T[i-1]+T[i+1]))-
    }
}

if (i > Ny)
{
    if (i < ((2*Ny)+1))
    {
        if (j == i)
        {
            M[i][j]=((4*Fo)+1);
        }
        if (j == (i+1))
        {
            if ((i%Ny) == 1)
            {
                M[i][j]=((-2)*Fo);
            }
            else
            {
                if ((i%Ny) == 0)
                {
                    M[i][j-2]=((-1)*Fo);
                }
                else
                {
                    M[i][j]=((-1)*Fo);
                    M[i][j-2]=((-1)*Fo);
                }
            }
        }
    }
    if (j == (i+Ny))
    {
        M[i][j]=(-Fo);
    }
    if (j == (A+1))
    {
        if ((i%Ny) == 0)
        {
            M[i][j]=(T0+(Fo*(T[i-Ny]+T[i+2])));
        }
        else

```

```

        {
            M[i][j]=(T0+(Fo*T[i-Ny]));
        }
    }
else
{
    if (i > ((Nx*Ny)-Ny))
    {
        if (j == i)
        {
            M[i][j]=((4*Fo)+1);
        }
        if (j == (i+1))
        {
            if ((i%Ny) == 1)
            {
                M[i][j]=((-1)*Fo);
            }
            else
            {
                M[i][j]=((-1)*Fo);
                M[i][j-2]=((-1)*Fo);
            }
        }
        if (j == (i-Ny))
        {
            M[i][i-Ny]=(-Fo);
        }
        if (j == (A+1))
        {
            if ((i%Ny) == 0)
            {
                M[i][j]=(T0+(Fo*(T0+T0)));
            }
            else
            {
                M[i][j]=(T0+(Fo*T0));
            }
        }
    }
else
{
    if (j == i)
    {
        M[i][j]=((4*Fo)+1);
    }
    if (j == (i+1))

```

```

        {
        if ((i%Ny) == 1)
            {
                M[i][j]=((-2)*Fo);
            }
        else
            {
                if ((i%Ny) == 0)
                    {
                        M[i][j-2]=((-1)*Fo);;
                    }
                else
                    {
                        M[i][j]=((-1)*Fo);
                        M[i][j-2]=((-1)*Fo);
                    }
            }
        }
    if (j == (i-Ny))
        {
            M[i][i-Ny]=(-Fo);
        }
    if (j == (i+Ny))
        {
            M[i][j]=(-Fo);
        }

    if (j == (A+1))
        {
            if ((i%Ny) == 0)
                {
                    M[i][j]=T0+(Fo*T0);
                }
            else
                {
                    M[i][j]=(T0);
                }
        }
    }
}
}
}
}

for (int j=1; j<((Nx*Ny)+2); j++) //to swap lines to get pivot line
{
    for (int i=1; i<((Nx*Ny)+1); i++)
        {
            if (i > j)

```

```

    {
    if (M[i][j] > M[j][j])
        {
        if (M[i][j] != 0)
            {
            for (int p=1; p<((Nx*Ny)+2); p++)
                {
                P=long double (M[i][p]);
                M[i][p]=long double (M[i-1][p]);
                M[i-1][p]=long double (P);
                }
            }
        }
    if (M[i][j] < M[j][j])
        {
        if (M[i][j] != 0)
            {
            long double pivot = long double (M[i][j]);
            for (int p=j; p<((Nx*Ny)+2); p++)
                {
                M[i][p] = long double ((M[i][p] -
((M[j][p]*pivot)/M[j][j]));
                }
            }
        }
    }
}

for (j=1; j<(Nx*Ny); j++)
    {
    S[j]=long double (0);
    }

for (i=1; i<(Nx*Ny); i++)
    {
    S[i]=long double (0);
    }

for (i=(Nx*Ny); i>0; i--) //Backsubstitution
    {
    if (i == (Nx*Ny))
        {
        S[(Nx*Ny)]=long double (M[i][i+1]/M[i][i]);
        }
    else
        {
        for (j=(Nx*Ny); j>i; j--)

```

```

        {
            Z = long double (M[i][j]*S[j]);
            ZZ += long double (Z);
        }
        S[i]=long double ((1/M[i][i])*(M[i][((Nx*Ny)+1)]-ZZ));
        ZZ=long double (0);
    }
}

transfer << dx << " " << Fo << " " << T0 << " " << Tfl << endl;
for (i=1; i<((Nx*Ny)+1); i++)
    //print final solution vector
    {
        transfer << " S["<<i<<"] = "<< S[i] << " at " << T[i] << endl;
    }
transfer.close();
delete M;
}

```

### **D.3 One-dimensional transient heat conduction** **through a solid (analytically exact)**

```

#include <stdlib.h>
#include <string.h>
#include <stdio.h>
#include <conio.h>
#include <iostream.h>
#include <math.h>
#include <fstream.h>          // for file functions
#include <process.h>         // for exit

#define PI 3.14159265359

//One-dimensional continuous transient Heat Transfer, Uwe Rüdell, 9th April 1999
//HTCtran1contin.cpp

void Input_Data (float &Time, float &T0, float &Tfl);
void Calculation (float &Non_Dimensional_Temp, float Time, float Tlc[201], int &k);

void main ()
{
    float Time=float (0), T0=float (0), Tfl=float (0), Tlc[201],
    Non_Dimensional_Temp=float (0);
    int x=0;

    char Option;
    int ContinueFlag=0;

    do
    {
        Input_Data (Time, T0, Tfl); //, Tlc);
        cout << "How many HTC's would you like to get computed?" << " ";
        cin >> x;
        for (int m=1; m<(x+1); m++)
            {
                cout << "Enter liquid crystals event temperature: ";
                cin >> Tlc[m];
            }
        for (int k=1; k<(x+1); k++)
            {
                Non_Dimensional_Temp=(Tlc[k]-T0)/(Tfl-T0);
                Calculation (Non_Dimensional_Temp, Time, Tlc, k);
                //getch();
            }
    }
}

```

```

        //return 0;
        }

        cout << "\nWould you like to process further data (Y/N)?\n";
        cin >> Option;
        if (Option=='y' || Option=='Y')
            {
                ContinueFlag=0;
            }
        else if (Option=='n' || Option=='N')
            {
                exit(-1);
            }
        }
    while (ContinueFlag==0);
    //return 0;
}

```

```

void Input_Data (float &Time, float &T0, float &Tfl)
{
    cout << "          Program to determine the Heat Transfer Coefficient (HTC) ";
    cout << "          when a cold plate is heated by a hot jet          ";
    cout << "          (see Yan et al. (1995))          "<<endl;
    cout << "Enter the elapsed time:          ";
    cin >> Time;
    cout << "Enter initial plate temperature T0:  ";
    cin >> T0;
    cout << "Enter jet temperature Tfl:          ";
    cin >> Tfl;
    /*if (T0 > Tfl)
        {
            cout << " Program terminated since Ffl " << endl;
            cout << "          than T0 (Tfl>T0).          " << endl;
            exit(0);
        }
    */
}

```

```

void Calculation (float &Non_Dimensional_Temp, float Time, float Tlc[201], int &k)
{
    float Eta=float (0), Root_Eta=float (0), HTC=float (0), Increment=float (0),
    ERF=float (0), n=float (0), j=float (0);
    long double ERF_1=0, ERF_2=0, Calculated_NDT=0, fact=1;

    ofstream transfer;
    transfer.open("HTCtran1contin.txt", ios::app | ios::out); //app to add to file
    do

```

```

{
HTC=HTC+Increment;
Eta=float ((pow(HTC,2)*Time)/pow(569,2));
Root_Eta=float (sqrt(Eta));
for(n=float (1); n<150; n++)
{
if (n > 1)
{
fact=1;
for (j=(n-1); j>0; j--)
{
fact *= j;
}
}
ERF_1=((pow(Root_Eta,((2*n)-1)))/(((2*n)-1)*fact))*(pow(-
1,(n+1)));
ERF_2=ERF_2+ERF_1;
}
ERF=float (ERF_2*(2/sqrt(PI)));
ERF_1=0;
ERF_2=0;
fact=1;
Calculated_NDT=1-(exp(Eta)*(1-ERF));
Increment=float (0.01);
}
while ((fabs(Non_Dimensional_Temp-Calculated_NDT)>0.0001));
cout << "\n Time t = " << Time << "";
//transfer << "\n Time t = " << Time << "";
cout << " Tlc[" << k << "] = " << Tlc[k] << "";
//transfer << " Tlc[" << k << "] = " << Tlc[k] << "";
cout << " NDT, Calc.DT" << Non_Dimensional_Temp << ", " <<
Calculated_NDT << "";
cout << " HTC = " << HTC << "";
//transfer << " HTC = " << HTC << "";
transfer << HTC << endl;
transfer.close();
//return 0;
}

```

**D.4 Data collection from digital multimeter Keithley 2001**

```

#include <conio.h>                //for getch()
#include <iostream.h>            //basic declaration file
#include <fstream.h>            //for file functions
#include <malloc.h>              //for pointer management
#include <stdio.h>               //for printf()
#include <string.h>              //for strepy
#include "c:\borlandc\bin\decl.h" //declares the GPIB-card functions

#define Mybuffsize 64000        //sufficient for 400 full readings or 5800 compact
readings

int TALK (void);
int LISTEN (void);
int INFO (void);
int FaultStatus (int Board);

const int leng=50;
unsigned char* Buffer_K;

void main ()
{
    cout << "\n\t\tThis program collects data from Keithley 2001." << "";
    cout << "\n\t\t    Developed by Uwe Ruedel, October 1999.    " << "";
    TALK ();
    LISTEN ();
    /INFO ();
    out << "\n\t\t\tEnd of program." << "";
    eturn;

int TALK ()
{
    char A[28][leng]={ "*CLS", "*RST", ":init:cont 0;:abort", ":sens:volt:dc:nplc 1",
    ":sens:volt:dc:rang 0.2", ":sens:volt:dc:aver:stat off", ":func 'volt:dc'", ":form:elem
    READ, TIME, RNUM, CHAN, UNIT", ":arm:lay1:sour imm", ":arm:lay1:coun
    1", ":arm:lay1:tcon:dir sour", ":arm:lay2:sour imm", ":arm:lay2:coun 1",
    ":arm:lay2:tcon:dir sour", ":trig:sour tim;tim 0.01", ":trig:coun 400",
    ":trig:tcon:dir sour", ":trac:clear", ":trac:feed sens", ":trac:poin 400", ":trac:egr
    full", ":form:data Ascii", ":trac:feed:cont next", ":rout:scan:int (@1,2)",
    ":rout:scan:lsel int", "*SRE 1", ":stat:meas:PTR 32767;NTR 0;ENAB 512",
    ":init"};
    //NPLC=0.1 high accuracy-f=30Hz, NPLC=0.01
    fast response, f=90Hz/Channel

    char Command[leng];
    int StringLength1;
    int Device, Board;

```

```

Board=ibfind ("GPIB0");
ibsic(Board);
ibsre(Board,1);
ibcac(Board,0);
ibtmo(Board,T10s); //T10us
ibclr(Board);

Device=ibfind ("2001");
ibclr(Device);
for (int i=0; i<29; i++)
    {
        strcpy(Command,A[i]);
        StringLength1=strlen(Command);
        cout << "\n" << Command <<"";
        ibwrt(Device,Command,StringLength1); //board works through all
                                                commands consecutively.
    }
getche(); //waits until 2001 is ready!!
FaultStatus(Board);
turn 0;
}

int FaultStatus (int Board)
{
    char Command[10],Buffer[100];
    strcpy(Command,"\x5f\x20\x50\x64");
    ibcmd(Board,Command,4);
    ibrd(Board,Buffer,100);
    if (((int)Buffer[0]&15)==0)
        {
            printf("\nNo Error! %d\n", Buffer[0]);
        }
    return 0;
}

int LISTEN (void) //function reads from 2001
{
    int Device;
    Buffer_K= new unsigned char [64001];

    Device=ibfind ("2001");
    ibwrt(Device,":trac:data?",11); //len of command=11
    cout << "\n\n\t2001 has been requested to send data to its internal buffer. " <<"";
    ibrd(Device,Buffer_K,Mybuffsize); // board has been prepared to data
                                        reception while the command was
                                        written to 2001.

    cout << "\n\n\t2001 is sending data from internal buffer to the harddrive." <<"";
    cout << "\n" << Buffer_K <<"";
    ofstream DataFile;

```

```

DataFile.open("AAAResult.txt", ios::app | ios::out);
DataFile << "Data" << "\n" << Buffer_K << "";
DataFile.close();
free(Buffer_K);
delete Buffer_K;
return 0;
}

int INFO (void)                                     //function reads from 2001
{
int Device;
Buffer_K= new unsigned char [64001];

Device=ibfind ("2001");
ibwrt(Device,":opt?",5);                            //len of command=11
ibrd(Device,Buffer_K,Mybuffsize);                  //up to here the board has been set up
                                                    while the command has been written
                                                    to the 2001.

ofstream DataFile;
DataFile.open("AAAResult.txt", ios::app | ios::out);
DataFile << "Data" << "\n" << Buffer_K << "";
DataFile.close();
free(Buffer_K);
delete Buffer_K;
return 0;
}

```

**Appendix E –  
Optical displacement of the measurement volume**

### **Optical displacement of the measurement volumes**

The refraction angles of the laser beams at the air/Perspex and Perspex/water interfaces were determined according to Snell's law:

$$n_0 \sin \varepsilon_0 = n_1 \sin \varepsilon_1 = n_2 \sin \varepsilon_2$$

$$\varepsilon_1 = \arcsin\left(\frac{n_0}{n_1} \sin \varepsilon_0\right) \quad (\text{D.1})$$

For the refracted beam in medium 2

$$\varepsilon_2 = \frac{n_1}{n_2} \sin \varepsilon_1 \quad (\text{D.2})$$

Substituting equation D.1 yields

$$\varepsilon_2 = \arcsin\left(\frac{n_0}{n_2} \sin \varepsilon_0\right) \quad (\text{D.3})$$

#### **E.1 Displacement due to different refractive indices**

The deflection of an incident beam at a plane window surface is expressed by an angle that is measured between the refracted light beam and the surface normal,  $\varepsilon$ . Further details are given in Figure 3.15. To assure coincidence of both measurement volume after inclining the probe the spatial locations will be determined in the following. This aspect is important for determining the Reynolds stresses where simultaneous measurements of the velocity fluctuations in both orientations are required.

In the following the refractive indices for all three media, air ( $n_0 = n_0 = 1$ ), water ( $n_2=1.34$ ), and Perspex ( $n_1=1.49$ ) were assumed constant. In the following, all calculations will be shown for water.

With the probe being inclined by  $7.06^\circ$  with respect to the normal of the surface window, the green laser beam enters the Perspex plate under an angle of  $4.7^\circ$ . After propagating through it, the laser beam leaves the Perspex window under the angle  $\varepsilon_{2, \text{water}}$ .

From equation D.3 and with  $\varepsilon_0 = \beta = 7.06^\circ$  this yields  $\varepsilon_{2, \text{water}}^{\text{green}} = 5.3^\circ$ .

The same is applied to the blue beam pair, so that  $\varepsilon_{2, \text{water}}^{\text{blue}} = 2.65^\circ$

For Figure D.1, the following trigonometric relationships are found.

$$y_{2, \text{water}}^{\text{green}} = L_2 \cdot \tan \epsilon_{2, \text{water}}^{\text{green}} \quad (\text{D.10})$$

and

$$y_{2, \text{water}}^{\text{blue}} = L_2 \cdot \tan \epsilon_{2, \text{water}}^{\text{blue}} \quad (\text{D.11})$$

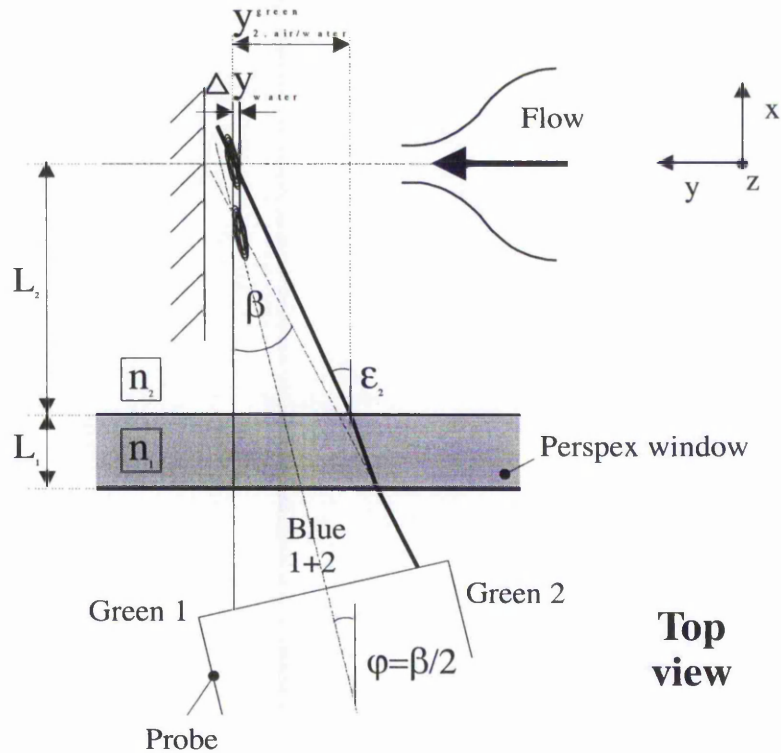


Figure D.1. Schematic of displacement of measurement volume in air/water.

For  $L_2=150\text{mm}$  this yields

$$y_{2, \text{water}}^{\text{green}} = 13.83053\text{mm}$$

and

$$y_{2, \text{water}}^{\text{blue}} = 6.906482\text{mm}$$

Note, that  $y_{2, \text{water}}^{\text{blue}}$  also occurs in the 'x-z' plane so that finally, with D.10 and D.11, the total mismatch between the position of the green and the blue measurement volume is determined as

$$\Delta y_{\text{water}} = y_{2, \text{water}}^{\text{green}} - 2 \cdot y_{2, \text{water}}^{\text{blue}}$$

$$\Delta y_{\text{water}} = 0.017568\text{mm}$$

This represents only 11% of the size of the measurement volume in y-direction, 0.15mm, For this reason the locations of the measurement volumes were considered coincident.

## E.2 Displacement due to astigmatism

Off-axis alignment of an optical LDA-probe may lead to astigmatism which, for large enough angles, may lead to the four beams of a 2D probe no longer intersecting in a single point. Consequently, there might be two focusing points on each refracted laser beam. This aspect was inspected using the exact calculation procedure as proposed by Zhang and Eisele (1995).

Using the theory of geometric optics, the displacement between both intersection points due to astigmatism can be determined from

$$\Delta x_m = \frac{1}{\phi_m} (L_1 \psi_1 + L_2 \psi_2) \quad (\text{D.4})$$

where

$$\phi_m = \tan \varepsilon_{G2} - \tan \varepsilon_{G1} \quad (\text{D.5})$$

and

$$\psi_1 = \frac{K}{\sqrt{n_1^2 - n_0^2} (1 - \cos^2 \varphi \cdot \cos^2 \beta / 2)} - (\tan \varepsilon_{G1} - \tan \varepsilon_{G1}) \quad (\text{D.6})$$

$$\psi_2 = \frac{K}{\sqrt{n_2^2 - n_0^2} (1 - \cos^2 \varphi \cdot \cos^2 \beta / 2)} - (\tan \varepsilon_{G2} - \tan \varepsilon_{G2}) \quad (\text{D.7})$$

where

$$K = n_0 \cdot \cos \varphi \cdot \cos(\beta / 2) \cdot \left[ \tan\left(\alpha + \frac{\beta}{2}\right) - \tan\left(\alpha - \frac{\beta}{2}\right) \right] \quad (\text{D.8})$$

The spatial displacement between both measurement volumes is then

$$\Delta S = \frac{\Delta x_m}{\cos \varepsilon_{0,2}} \quad (\text{D.9})$$

The following values were substituted into equations D.4 to D.9. The thickness of the Perspex window,  $L_1=20\text{mm}$ , and the distance of the measurement plane from the inside of the window surface,  $L_2=150\text{mm}$ .

For the green beam pair, where  $\varphi=\beta/2$  and  $\varepsilon_{0,2}=2.65^\circ$ , the displacement along the centreline of the beam pair was determined to be  $\Delta S_{green}=0.2888\text{mm}$ .

In contrast, the blue beam pair undergoes distortion in two directions. One is due to its on-axis alignment in the 'x-y' plane and the second is due to the probe being tilted by the angle  $\varphi$  with respect to the window surface. Applying the procedure from above, the displacement of the blue measurement volume due to the first effect is  $\Delta S_{1,blue}=0.147\text{mm}$  whereas the second accounts to  $\Delta S_{2,blue}=0.143\text{mm}$ .

The difference between  $\Delta S_{green}$  and  $\Delta S_{blue} = \Delta S_{1,blue} + \Delta S_{2,blue}$  is  $0.001\text{mm}$  and was considered negligible due to the diameter of the measurement volume of  $0.15\text{mm}$ . This agrees well with the findings by Zhang and Eisele (1996) who neglected the effects of astigmatism for cases where the LDA probe was aligned by an angle equal to the half intersection angle between the beams.

**Appendix F –  
ANSYS/FLOTRAN data input file  
for three-dimensional jet impingement model**

**Input file**

File for generating Uwe's 3-d jet impingement model. The following file is run as an "Input file" in the pre-processor stage of ANSYS/FLOTRAN.

Cartesian co-ordinate system

```
csys,0
/angle,wn,90,xm,1
```

Specify element type

```
et,1,142
```

Create keypoints

```
k,1,0,0,0
,2,0.0175,0,0
,3,0.0185,0,0
,4,0.0185,0,0.0185
,5,0,0,0.0185
,6,0,0,0.0175
,7,0,0.05936528,0
/COM, instead of 0.06936528
,8,0.0175,0.06960799,0
,9,0.0185,0.06960799,0
,10,0.0185,0.06960799,0.0185
,11,0,0.06960799,0.0185
,12,0,0.06960799,0.0175
,13,0,0.07,0
,14,0.0175,0.07,0
,15,0.0185,0.07,0
,16,0.0185,0.07,0.0185
,17,0,0.07,0.0185
,18,0,0.07,0.0175
,19,0.08,0,0
,20,0.08,0,0.0185
,21,0.08,0.06898567092,0
,22,0.08,0.06898567092,0.0185
,23,0.08,0.07,0
,24,0.08,0.07,0.0185
,25,0.15,0,0
,26,0.15,0,0.0185
,27,0.15,0.06898567092,0
,28,0.15,0.06863717045,0.0185
,29,0.15,0.07,0
,30,0.15,0.07,0.0185
,31,0,0,0.0875
,32,0,0.067559684,0.0875
,33,0,0.07,0.0875
,34,0,0,0.2835
```

,35,0,0.0669594,0.2835  
 ,36,0,0.07,0.2835  
 ,37,0.02,0,0.0875  
 ,38,0.02,0.0686819792,0.0875  
 ,39,0.02,0.07,0.0875  
 ,40,0.02,0,0.2835  
 ,41,0.02,0.068283695,0.2835  
 ,42,0.02,0.07,0.2835  
 ,43,0.08,0,0.0875  
 ,44,0.08,0.06837082045,0.0875  
 ,45,0.08,0.07,0.0875  
 ,46,0.08,0,0.2835  
 ,47,0.08,0.06797253545,0.2835  
 ,48,0.08,0.07,0.2835  
 ,49,0.15,0,0.0875  
 ,50,0.15,0.0680223192,0.0875  
 ,51,0.15,0.07,0.0875  
 ,52,0.15,0,0.2835  
 ,53,0.15,0.067624035,0.2835  
 ,54,0.15,0.07,0.2835  
 ,55,0.106125,0,0.222625  
 ,56,0.106125,0.07,0.222625  
 ,57,0.09025,0,0.222625

Create lines

1,1,2  
 ,2,3  
 ,3,4  
 ,4,5  
 ,5,6  
 ,6,1  
 ,7,8  
 ,8,9  
 ,9,10  
 ,10,11  
 ,11,12  
 ,12,7  
 ,13,14  
 ,14,15  
 ,15,16  
 ,16,17  
 ,17,18  
 ,18,13  
 /com, create arc  
 larc,2,6,1,0.0175  
 1,8,12  
 1,14,18  
 1,1,7  
 ,2,8

,3,9  
,4,10  
,5,11  
,6,12  
,7,13  
,8,14  
,9,15  
,10,16  
,11,17  
,12,18  
,3,19  
,4,20  
,19,20  
,9,21  
,10,22  
,21,22  
,15,23  
,16,24  
,23,24  
,19,21  
,20,22  
,21,23  
,22,24  
,19,25  
,20,26  
,25,26  
,21,27  
,22,28  
,27,28  
,23,29  
,24,30  
,29,30  
,25,27  
,26,28  
,27,29  
,28,30  
,5,31  
,11,32  
,17,33  
,31,34  
,32,35  
,33,36  
,31,32  
,32,33  
,34,35  
,35,36  
,31,37  
,34,40  
,32,38

,35,41  
,33,39  
,36,42  
,4,37  
,10,38  
,16,39  
,37,40  
,38,41  
,39,42  
,37,38  
,38,39  
,40,41  
,41,42  
,37,43  
,38,44  
,39,45  
,40,46  
,41,47  
,42,48  
,20,43  
,22,44  
,24,45  
,43,46  
,44,47  
,45,48  
,43,44  
,44,45  
,46,47  
,47,48  
,43,49  
,44,50  
,45,51  
,46,52  
,47,53  
,48,54  
,26,49  
,28,50  
,30,51  
,49,52  
,50,53  
,51,54  
,49,50  
,50,51  
,52,53  
,53,54  
/create circle for outlet  
circle,55,0.015875,56,57

Create areas

/com, Volume 1

al,1,19,6

al,1,23,7,22

al,19,23,20,27

al,7,20,12

al,6,22,12,27

/com, Volume 2

al,2,3,4,5,19

al,2,24,8,23

al,3,25,9,24

al,4,25,10,26

al,5,26,11,27

al,8,9,10,11,20

/com, Volume 3

al,7,29,13,28

al,20,29,21,33

al,12,28,18,33

al,13,21,18

/com, Volume 4

al,8,30,14,29

al,9,31,15,30

al,10,31,16,32

al,11,32,17,33

al,14,15,16,17,21

/com, Volume 5

al,3,34,36,35

al,36,43,39,44

al,9,37,39,38

al,24,34,43,37

al,25,35,44,38

/com, Volume 6

al,39,45,42,46

al,15,40,42,41

al,30,37,45,40

al,31,38,46,41

/com, Volume 7

al,47,49,48,36

al,56,49,57,52

al,50,52,51,39

al,43,47,56,50

al,44,48,57,51

/com, Volume 8

al,58,52,59,55

al,53,55,54,42

al,45,50,58,53

al,46,51,59,54

/com, Volume 9

al,4,76,70,60

al,25,76,82,77  
al,10,77,72,61  
al,26,60,66,61  
al,70,82,72,66  
/com, Volume 10  
al,31,77,83,78  
al,16,78,74,62  
al,32,61,67,62  
al,67,72,83,74  
/com, Volume 11  
al,83,80,85,81  
al,74,81,75,65  
al,67,64,69,65  
al,72,80,73,64  
al,73,85,75,69  
/com, Volume 12  
al,82,79,84,80  
al,66,63,68,64  
al,70,79,71,63  
al,71,84,73,68  
/com, Volume 13  
al,38,93,87,77  
al,44,92,98,93  
al,82,86,98,87  
al,35,92,86,76  
/com, Volume 14  
al,87,99,88,83  
al,46,93,99,94  
al,41,94,88,78  
/com, Volume 15  
al,87,96,90,80  
al,98,95,100,96  
al,86,95,89,79  
al,89,100,90,84  
/com, Volume 16  
al,99,96,101,97  
al,88,97,91,81  
al,90,101,91,85  
/com, Volume 17  
al,51,109,103,93  
al,57,108,114,109  
al,102,114,103,98  
al,48,108,102,92  
/com, Volume 18  
al,59,109,115,110  
al,103,115,104,99  
al,54,110,104,94  
/com, Volume 19  
al,102,111,105,95

al,103,112,106,96  
 al,105,116,106,100  
 al,114,111,116,112  
 /com, Volume 20  
 al,104,113,107,97  
 al,106,117,107,101  
 al,115,112,117,113  
 /com,circular outlet area No.85  
 al,118,119,120,121  
 asba,78,85,,keep,keep

Create volumes

va,1,2,3,4,5  
 va,6,7,8,9,10,3,11  
 va,4,12,13,14,15  
 va,11,16,17,18,19,13,20  
 va,21,22,23,24,25,8  
 va,23,26,27,28,29,17  
 va,30,31,32,33,34,22  
 va,32,35,36,37,38,26  
 va,39,40,41,42,43,9  
 va,18,41,44,45,46,47  
 va,47,48,49,50,51,52  
 va,51,43,53,54,55,56  
 va,40,25,57,58,59,60  
 va,44,29,57,61,62,63  
 va,59,53,64,65,66,67  
 va,61,64,48,68,69,70  
 va,34,58,71,72,73,74  
 va,71,38,62,75,76,77  
 va,65,73,85,86,79,80,81  
 va,76,79,68,82,83,84

Specify line divisions and spacing ratios

lesize,22,,,42,0.25  
 ,23,,,42,0.25  
 ,24,,,42,0.25  
 ,25,,,42,0.25  
 ,26,,,42,0.25  
 ,27,,,42,0.25  
 /com,x-lines at wall jet  
 lesize,66,,,16,0.5  
 ,82,,,8,0.5  
 /com,x-lines at the bottom  
 lesize,68,,,10,1  
 ,84,,,8,1  
 ,100,,,8,1  
 ,116,,,8,1  
 /com,x-lines at top and in the middle

```

lesize,43,,,6,1
,44,,,6,1
,56,,,6,1
,57,,,6,1
,98,,,6,1
,114,,,6,1
/com,x-lines near the wall
lesize,28,,,1,1
,29,,,1,1
,30,,,1,1
,31,,,1,1
,32,,,1,1
,33,,,1,1
,45,,,1,1
,46,,,1,1
,58,,,1,1
,59,,,1,1
,67,,,1,1
,69,,,1,1
,83,,,1,1
,85,,,1,1
,99,,,1,1
,101,,,1,1
,115,,,1,1
,117,,,1,1
/com,z-lines in wall jet region
lesize,61,,,28,1
,62,,,28,1
,77,,,28,10
,78,,,28,10
/com,z-lines at middle of wall jet region
lesize,28,,,19,1
,39,,,19,1
,42,,,19,1
,49,,,5,1
,52,,,5,1
,55,,,5,1
/com,z-lines along confining wall
lesize,60,,,28,10
,76,,,28,10
/com,z-lines in middle section
lesize,28,,,10,1
,39,,,10,1
,42,,,10,1
,92,,,6,1
,93,,,6,1
,94,,,6,1
/com,z-lines at right end of section
lesize,108,,,6,1

```

```

,109,,6,1
,110,,6,1
/com,z-lines at the bottom
lesize,63,,8,1
,64,,8,1
,65,,8,1
,79,,8,1
,80,,8,1
,81,,8,1
,95,,8,1
,96,,8,1
,97,,8,1
,111,,8,1
,112,,8,1
,113,,8,1
/com,x,y and z-lines in the stagnation region
lesize,1,,18,1
,6,,18,1
,7,,18,1
,12,,18,1
,13,,18,1
,18,,18,1
,19,,18,1
,20,,18,1
,21,,18,1
,2,,1,1
,5,,1,1
,8,,1,1
,11,,1,1
,14,,1,1
,17,,1,1
,3,,19,1
,4,,19,1
,9,,19,1
,10,,19,1
,15,,19,1
,16,,19,1
/com,x-lines in horizontal wall jet region
lesize,34,,8,1
,35,,5,1
,37,,8,1
,38,,5,1
,40,,12,1
,41,,5,1
,86,,5,0.5
,87,,5,0.5
,88,,5,0.5
,89,,10,1
,90,,8,1

```

```

,91,,,8,1
/com,x-lines in horizontal wall jet region
lesize,102,,,5,1
,103,,,5,1
,104,,,5,1
,105,,,8,1
,106,,,8,1
,107,,,8,1
/com,x-lines in the end of horizontal wall jet region
lesize,47,,,8,1
,48,,,5,1
,42,,,8,1
,51,,,5,1
,53,,,8,1
,54,,,5,1
,70,,,5,1
,71,,,3,1
,72,,,8,1
,73,,,8,1
,74,,,8,1
,75,,,8,1
/com,x-lines in the end of horizontal wall jet region
lesize,118,,,3,1
,119,,,3,1
,120,,,3,1
,121,,,3,1
/view,1,-0.6492,0.7459,-0.1489

```

### Mesh volumes

```

esize,0.5
mshape,1,3D
vmesh,3
vmesh,1
vmesh,4
vmesh,2
vmesh,9
vmesh,10
vmesh,11
vmesh,12
vmesh,5
vmesh,6
vmesh,7
vmesh,8
vmesh,13
vmesh,14
vmesh,15
vmesh,16
vmesh,17
vmesh,18

```

```
vmesh,19
vmesh,20
numcmp,all
```

Define symmetry condition on lines with endpoints, VX=0,1

```
FLST,5,2,4,ORDE,2
FITEM,5,11
FITEM,5,61
CM,_Y,LINE
LSEL,R,,P51X
CM,_Y1,LINE
CMSEL,S,_Y
CMDEL,_Y
```

```
!*
```

```
!*
```

```
DL,_Y1,,VX,0,1
CMDEL,_Y1
```

```
!*
```

/com,define symmetry condition on lines without endpoints, VX=0, 0

```
FLST,5,8,4,ORDE,8
FITEM,5,12
FITEM,5,27
FITEM,5,26
FITEM,5,66
FITEM,5,64
FITEM,5,33
FITEM,5,32
FITEM,5,67
CM,_Y,LINE
LSEL,R,,,P51X
CM,_Y1,LINE
CMSEL,S,_Y
CMDEL,_Y
```

```
!*
```

```
!*
```

```
DL,_Y1,,VX,0,0
CMDEL,_Y1
```

```
!*
```

/com,define symmetry condition on lines with endpoints, VZ=0, 1

```
FLST,5,2,4,ORDE,2
FITEM,5,8
FITEM,5,37
CM,_Y,LINE
LSEL,R,,P51X
CM,_Y1,LINE
CMSEL,S,_Y
CMDEL,_Y
```

```
!*
```

```
!*
```

```

DL,_Y1,,VZ,0,1
CMDEL,_Y1
!*
/com,define symmetry condition on lines without endpoints, VZ=0, 0
FLST,5,8,4,ORDE,8
FITEM,5,7
FITEM,5,23
FITEM,5,24
FITEM,5,43
FITEM,5,50
FITEM,5,29
FITEM,5,30
FITEM,5,45
CM,_Y,LINE
LSEL,R,,P51X
CM,_Y1,LINE
CMSEL,S,_Y
CMDEL,_Y
!*
!*
DL,_Y1,,VZ,0,0
CMDEL,_Y1
!*
/com,define symmetry condition on lines without endpoints, VX=0 and VZ=0, 0
FLST,5,2,4,ORDE,2
FITEM,5,22
FITEM,5,28
CM,_Y,LINE
LSEL,R,,P51X
CM,_Y1,LINE
CMSEL,S,_Y
CMDEL,_Y
!*
!*
DL,_Y1,,VZ,0,0
DL,_Y1,,VX,0,0
CMDEL,_Y1
!*
/com,define symmetry condition on areas without endpoints, VX=0, 0
FLST,5,8,5,ORDE,8
FITEM,5,5
FITEM,5,10
FITEM,5,42
FITEM,5,54
FITEM,5,14
FITEM,5,19
FITEM,5,46
FITEM,5,50
CM,_Y,AREA

```

```

ASEL,R,,,P51X
CM,_Y1,AREA
CMSEL,S,_Y
CMDEL,_Y
!*
!*
DA,_Y1,VX,0,0
CMDEL,_Y1
!*
/com,define symmetry condition on areas without endpoints, VZ=0, 0
FLST,5,8,5,ORDE,8
FITEM,5,2
FITEM,5,7
FITEM,5,24
FITEM,5,33
FITEM,5,12
FITEM,5,16
FITEM,5,28
FITEM,5,37
CM,_Y,AREA
ASEL,R,,,P51X
CM,_Y1,AREA
CMSEL,S,_Y
CMDEL,_Y
!*
!*
DA,_Y1,VZ,0,0
CMDEL,_Y1
!*

```

Definition of non-slip boundary condition at all walls

```

/com, Areas on impingement plate 15,20,27,36,45,63,77,49,69,82
/com, Areas on lateral wall 35,31,75,72,84,81
/com, Areas on semi-confining wall 6,21,30,39,60,74,55,66,86
/com, Areas on bottom plate 56,67,80,52,70,83
FLST,5,31,5,ORDE,31
FITEM,5,15
FITEM,5,20
FITEM,5,27
FITEM,5,36
FITEM,5,45
FITEM,5,63
FITEM,5,77
FITEM,5,49
FITEM,5,69
FITEM,5,82
FITEM,5,35
FITEM,5,31
FITEM,5,75

```

```

FITEM,5,72
FITEM,5,84
FITEM,5,81
FITEM,5,6
FITEM,5,21
FITEM,5,30
FITEM,5,39
FITEM,5,60
FITEM,5,74
FITEM,5,55
FITEM,5,66
FITEM,5,86
FITEM,5,56
FITEM,5,67
FITEM,5,80
FITEM,5,52
FITEM,5,70
FITEM,5,83
CM,_Y,AREA
ASEL,R, , ,P51X
CM,_Y1,AREA
CMSEL,S,_Y
CMDEL,_Y
!*
!*
DA,_Y1,VX,0,1
DA,_Y1,VY,0,1
DA,_Y1,VZ,0,1
D,_Y1,ENKE,0
D,_Y1,ENDS,0
CMDEL,_Y1
!*

```

Define inlet conditions on nozzle exit

```

FLST,5,6,1,ORDE,6
FITEM,5,833
FITEM,5,886
FITEM,5,887
FITEM,5,866
FITEM,5,867
FITEM,5,835
CM,_Y,NODE
NSSEL,R, , ,P51X
CM,_Y1,NODE
CMSEL,S,_Y
CMDEL,_Y
!*
!*
D,_Y1,VX,0

```

```

D,_Y1,VY,4.834
D,_Y1,VZ,0
D,_Y1,ENKE,0.005129
D,_Y1,ENDS,0.240808
CMDEL,_Y1
!*

```

```

FLST,5,4,1,ORDE,4
FITEM,5,885
FITEM,5,1033
FITEM,5,1064
FITEM,5,836
CM,_Y,NODE
NSEL,R, , P51X
CM,_Y1,NODE
CMSEL,S,_Y
CMDEL,_Y

```

```

!*

```

```

!*

```

```

D,_Y1,VX,0
D,_Y1,VY,4.826
D,_Y1,VZ,0
D,_Y1,ENKE,0.005366
D,_Y1,ENDS,0.251918
CMDEL,_Y1
!*

```

```

FLST,5,5,1,ORDE,5
FITEM,5,884
FITEM,5,1034
FITEM,5,1032
FITEM,5,1063
FITEM,5,837
CM,_Y,NODE
NSEL,R, , P51X
CM,_Y1,NODE
CMSEL,S,_Y
CMDEL,_Y

```

```

!*

```

```

!*

```

```

D,_Y1,VX,0
D,_Y1,VY,4.814
D,_Y1,VZ,0
D,_Y1,ENKE,0.005176
D,_Y1,ENDS,0.242982
CMDEL,_Y1
!*

```

```

FLST,5,8,1,ORDE,8

```

```
FITEM,5,883
FITEM,5,1035
FITEM,5,1004
FITEM,5,1002
FITEM,5,1062
FITEM,5,838
FITEM,5,1031
FITEM,5,834
CM,_Y,NODE
NSEL,R,,P51X
CM,_Y1,NODE
CMSEL,S,_Y
CMDEL,_Y
!*
!*
D,_Y1,VX,0
D,_Y1,VY,4.808
D,_Y1,VZ,0
D,_Y1,ENKE,0.004979
D,_Y1,ENDS,0.233759
CMDEL,_Y1
!*

FLST,5,7,1,ORDE,7
FITEM,5,882
FITEM,5,1036
FITEM,5,1005
FITEM,5,1003
FITEM,5,1000
FITEM,5,1030
FITEM,5,1061
FITEM,5,839
CM,_Y,NODE
NSEL,R,,P51X
CM,_Y1,NODE
CMSEL,S,_Y
CMDEL,_Y
!*
!*
D,_Y1,VX,0
D,_Y1,VY,4.801
D,_Y1,VZ,0
D,_Y1,ENKE,0.00541
D,_Y1,ENDS,0.254007
CMDEL,_Y1
!*

FLST,5,13,1,ORDE,13
FITEM,5,881
```



```

D,_Y1,VX,0
D,_Y1,VY,4.753
D,_Y1,VZ,0
D,_Y1,ENKE,0.005696
D,_Y1,ENDS,0.267397
CMDEL,_Y1
!*

```

```

FLST,5,15,1,ORDE,15
FITEM,5,879
FITEM,5,1039
FITEM,5,1008
FITEM,5,1009
FITEM,5,993
FITEM,5,967
FITEM,5,937
FITEM,5,928
FITEM,5,934
FITEM,5,974
FITEM,5,1027
FITEM,5,995
FITEM,5,1058
FITEM,5,842
FITEM,5,1026
CM,_Y,NODE
NSEL,R, , P51X
CM,_Y1,NODE
CMSEL,S,_Y
CMDEL,_Y

```

```

!*

```

```

!*

```

```

D,_Y1,VX,0
D,_Y1,VY,4.721
D,_Y1,VZ,0
D,_Y1,ENKE,0.006147
D,_Y1,ENDS,0.288607
CMDEL,_Y1
!*

```

```

FLST,5,15,1,ORDE,15
FITEM,5,878
FITEM,5,1040
FITEM,5,1010
FITEM,5,988
FITEM,5,964
FITEM,5,932
FITEM,5,927
FITEM,5,922
FITEM,5,933

```

```
FITEM,5,963
FITEM,5,994
FITEM,5,1057
FITEM,5,843
FITEM,5,1025
FITEM,5,839
CM,_Y,NODE
NSEL,R,,P51X
CM,_Y1,NODE
CMSEL,S,_Y
CMDEL,_Y
!*
!*
D,_Y1,VX,0
D,_Y1,VY,4.698
D,_Y1,VZ,0
D,_Y1,ENKE,0.007245
D,_Y1,ENDS,0.34013
CMDEL,_Y1
!*
```

```
FLST,5,15,1,ORDE,15
FITEM,5,877
FITEM,5,1041
FITEM,5,1011
FITEM,5,981
FITEM,5,962
FITEM,5,931
FITEM,5,925
FITEM,5,918
FITEM,5,921
FITEM,5,930
FITEM,5,965
FITEM,5,1056
FITEM,5,991
FITEM,5,844
FITEM,5,1024
CM,_Y,NODE
NSEL,R,,P51X
CM,_Y1,NODE
CMSEL,S,_Y
CMDEL,_Y
!*
!*
D,_Y1,VX,0
D,_Y1,VY,4.653
D,_Y1,VZ,0
D,_Y1,ENKE,0.009739
D,_Y1,ENDS,0.457239
```

CMDEL,\_Y1

!\*  
 !\*

FLST,5,16,1,ORDE,16

FITEM,5,876

FITEM,5,1042

FITEM,5,1012

FITEM,5,982

FITEM,5,960

FITEM,5,929

FITEM,5,919

FITEM,5,901

FITEM,5,917

FITEM,5,926

FITEM,5,935

FITEM,5,966

FITEM,5,1055

FITEM,5,990

FITEM,5,1023

FITEM,5,845

CM,\_Y,NODE

NSEL,R, , P51X

CM,\_Y1,NODE

CMSSEL,S,\_Y

CMDEL,\_Y

!\*  
 !\*

!\*  
 !\*

D,\_Y1,VX,0

D,\_Y1,VY,4.603

D,\_Y1,VZ,0

D,\_Y1,ENKE,0.014145

D,\_Y1,ENDS,0.664069

CMDEL,\_Y1

!\*  
 !\*

FLST,5,17,1,ORDE,17

FITEM,5,875

FITEM,5,1043

FITEM,5,1013

FITEM,5,983

FITEM,5,968

FITEM,5,936

FITEM,5,923

FITEM,5,899

FITEM,5,890

FITEM,5,916

FITEM,5,924

FITEM,5,940

FITEM,5,972

```
FITEM,5,1054
FITEM,5,989
FITEM,5,1022
FITEM,5,846
CM,_Y,NODE
NSEL,R,,P51X
CM,_Y1,NODE
CMSEL,S,_Y
CMDEL,_Y
!*
!*
D,_Y1,VX,0
D,_Y1,VY,4.573
D,_Y1,VZ,0
D,_Y1,ENKE,0.017487
D,_Y1,ENDS,0.820988
CMDEL,_Y1
!*
```

```
FLST,5,17,1,ORDE,17
FITEM,5,874
FITEM,5,1044
FITEM,5,1014
FITEM,5,979
FITEM,5,961
FITEM,5,938
FITEM,5,898
FITEM,5,888
FITEM,5,889
FITEM,5,897
FITEM,5,900
FITEM,5,941
FITEM,5,971
FITEM,5,1053
FITEM,5,987
FITEM,5,1021
FITEM,5,847
CM,_Y,NODE
NSEL,R,,P51X
CM,_Y1,NODE
CMSEL,S,_Y
CMDEL,_Y
!*
!*
D,_Y1,VX,0
D,_Y1,VY,4.539
D,_Y1,VZ,0
D,_Y1,ENKE,0.023697
D,_Y1,ENDS,1.11253
```

```
CMDEL,_Y1
!*

FLST,5,20,1,ORDE,20
FITEM,5,873
FITEM,5,1045
FITEM,5,1015
FITEM,5,984
FITEM,5,969
FITEM,5,914
FITEM,5,902
FITEM,5,891
FITEM,5,892
FITEM,5,893
FITEM,5,894
FITEM,5,895
FITEM,5,896
FITEM,5,903
FITEM,5,915
FITEM,5,970
FITEM,5,986
FITEM,5,1052
FITEM,5,1020
FITEM,5,848
CM,_Y,NODE
NSEL,R,,P51X
CM,_Y1,NODE
CMSEL,S,_Y
CMDEL,_Y
!*
!*
D,_Y1,VX,0
D,_Y1,VY,4.501
D,_Y1,VZ,0
D,_Y1,ENKE,0.034925
D,_Y1,ENDS,1.639651
CMDEL,_Y1
!*

FLST,5,21,1,ORDE,21
FITEM,5,872
FITEM,5,1046
FITEM,5,1016
FITEM,5,980
FITEM,5,944
FITEM,5,920
FITEM,5,904
FITEM,5,905
FITEM,5,906
```

```
FITEM,5,907
FITEM,5,908
FITEM,5,909
FITEM,5,910
FITEM,5,911
FITEM,5,912
FITEM,5,985
FITEM,5,945
FITEM,5,1051
FITEM,5,849
FITEM,5,1019
FITEM,5,869
CM,_Y,NODE
NSEL,R,,P51X
CM,_Y1,NODE
CMSEL,S,_Y
CMDEL,_Y
!*
!*
D,_Y1,VX,0
D,_Y1,VY,4.435
D,_Y1,VZ,0
D,_Y1,ENKE,0.064254
D,_Y1,ENDS,3.016586
CMDEL,_Y1
!*

FLST,5,8,1,ORDE,8
FITEM,5,871
FITEM,5,1047
FITEM,5,1017
FITEM,5,913
FITEM,5,1050
FITEM,5,959
FITEM,5,850
FITEM,5,868
CM,_Y,NODE
NSEL,R,,P51X
CM,_Y1,NODE
CMSEL,S,_Y
CMDEL,_Y
!*
!*
D,_Y1,VX,0
D,_Y1,VY,4.304
D,_Y1,VZ,0
D,_Y1,ENKE,0.154128
D,_Y1,ENDS,7.235966
CMDEL,_Y1
```

!\*  
!

```

FLST,5,18,1,ORDE,18
FITEM,5,870
FITEM,5,1048
FITEM,5,946
FITEM,5,947
FITEM,5,948
FITEM,5,949
FITEM,5,950
FITEM,5,951
FITEM,5,952
FITEM,5,953
FITEM,5,954
FITEM,5,955
FITEM,5,956
FITEM,5,957
FITEM,5,958
FITEM,5,1018
FITEM,5,1049
FITEM,5,851
CM,_Y,NODE
NSEL,R, , ,P51X
CM,_Y1,NODE
CMSEL,S,_Y
CMDEL,_Y

```

!\*  
!

```

D,_Y1,VX,0
D,_Y1,VY,3.642
D,_Y1,VZ,0
D,_Y1,ENKE,0.374739
D,_Y1,ENDS,17.59311
CMDEL,_Y1

```

!\*  
!

```

FLST,5,1,1,ORDE,1
FITEM,5,861
CM,_Y,NODE
NSEL,R, , ,P51X
CM,_Y1,NODE
CMSEL,S,_Y
CMDEL,_Y

```

!\*  
!!\*  
!

```

D,_Y1,VX,0
D,_Y1,VY,2.207
D,_Y1,VZ,0
D,_Y1,ENKE,0.513193

```

D,\_Y1,ENDS,24.0932  
 CMDEL,\_Y1  
 !\*

Define pressure condition at outlet

FLST,2,1,5,ORDE,1  
 FITEM,2,85  
 DA,P51X,PRES,0,0

Definition of solution procedure

FLDATA1,SOLU,TRAN,0  
 FLDATA1,SOLU,FLOW,1  
 FLDATA1,SOLU,TEMP,0  
 FLDATA1,SOLU,TURB,1  
 FLDATA1,SOLU,COMP,0  
 FLDATA1,SOLU,SWRL,0  
 FLDATA1,SOLU,SPEC,0  
 !\*

Definition of execution control

FLDATA2,ITER,EXEC,20000,  
 FLDATA2,ITER,OVER,0,  
 FLDATA2,ITER,APPE,0,  
 FLDATA3,TERM,PRES,1e-008,  
 FLDATA3,TERM,TEMP,1e-008,  
 FLDATA5,OUTP,SUMF,100,  
 !\*

Definition of property based output quantities

FLDATA5,OUTP,DENS,1  
 FLDATA5,OUTP,SPHT,1  
 FLDATA5,OUTP,VISC,1  
 FLDATA5,OUTP,COND,1  
 FLDATA5,OUTP,EVIS,1  
 FLDATA5,OUTP,ECON,1  
 !\*

Definition of derived output quantities

FLDATA5,OUTP,PTOT,1  
 FLDATA5,OUTP,TTOT,1  
 FLDATA5,OUTP,HFLU,1  
 FLDATA5,OUTP,HFLM,1  
 FLDATA5,OUTP,STRM,1  
 FLDATA5,OUTP,PCOE,1  
 FLDATA5,OUTP,MACH,0  
 FLDATA5,OUTP,YPLU,1  
 FLDATA5,OUTP,TAUW,1  
 !\*

Definition of fluid properties

FLDATA12,PROP,DENS,4  
 FLDATA13,VARY,DENS,1  
 FLDATA12,PROP,VISC,4

FLDATA13,VARY,VISC,1  
 FLDATA12,PROP,COND,4  
 FLDATA13,VARY,COND,1  
 FLDATA12,PROP,SPHT,4  
 FLDATA13,VARY,SPHT,1  
 !\*

FLDATA7,PROT,DENS,AIR-SI  
 FLDATA8,NOMI,DENS,-1  
 FLDATA9,COF1,DENS,0  
 FLDATA10,COF2,DENS,0  
 FLDATA11,COF3,DENS,0  
 FLDATA7,PROT,VISC,AIR-SI  
 FLDATA8,NOMI,VISC,-1  
 FLDATA9,COF1,VISC,0  
 FLDATA10,COF2,VISC,0  
 FLDATA11,COF3,VISC,0  
 FLDATA12,PROP,IVIS  
 FLDATA7,PROT,COND,AIR-SI  
 FLDATA8,NOMI,COND,-1  
 FLDATA9,COF1,COND,0  
 FLDATA10,COF2,COND,0  
 FLDATA11,COF3,COND,0  
 FLDATA7,PROT,SPHT,AIR-SI  
 FLDATA8,NOMI,SPHT,-1  
 FLDATA9,COF1,SPHT,0  
 FLDATA10,COF2,SPHT,0  
 FLDATA11,COF3,SPHT,0  
 !\*

Definition of turbulence modelling parameters

FLDATA24,TURB,SCTM,1,  
 FLDATA24,TURB,SCTT,1,  
 FLDATA24,TURB,SCTK,1,  
 FLDATA24,TURB,SCTD,1.314,  
 !\*

FLDATA24,TURB,CMU,0.09,  
 FLDATA24,TURB,C1,1.44,  
 FLDATA24,TURB,C2,1.92,  
 FLDATA24,TURB,KAPP,0.4,  
 FLDATA24,TURB,EWLL,9,  
 FLDATA24,TURB,VAND,26,  
 FLDATA24,TURB,BUC3,1,  
 FLDATA24,TURB,BUC4,0,  
 FLDATA24,TURB,WALL,EQLB  
 FLDATA24,TURB,BETA,0,  
 FLDATA24,TURB,TRAN,11.5,  
 !\*

Definition of solver control features

FLDATA18,METH,ENDS,3  
 FLDATA22,MAXI,ENDS,100,

FLDATA20,SRCH,ENDS,2,  
FLDATA21,CONV,ENDS,1e-005,  
FLDATA23,DELT,ENDS,1e-010,  
!\*

FLDATA18,METH,ENKE,3  
FLDATA22,MAXI,ENKE,100,  
FLDATA20,SRCH,ENKE,2,  
FLDATA21,CONV,ENKE,1e-005,  
FLDATA23,DELT,ENKE,1e-010,  
!\*

FLDATA18,METH,TEMP,3  
FLDATA22,MAXI,TEMP,500,  
FLDATA20,SRCH,TEMP,2,  
FLDATA21,CONV,TEMP,1e-007,  
FLDATA23,DELT,TEMP,1e-010,  
!\*

FLDATA18,METH,PRES,1  
FLDATA19,TDMA,PRES,100,  
!\*

**Appendix G –  
List of Publications**

**Presented at 11<sup>th</sup>  
International Heat Transfer Conference,  
Kyongju, Korea, 23-27 August 1998.**

# FLOW VISUALISATION OF AN IMPINGING WATER JET USING LIQUID CRYSTALS

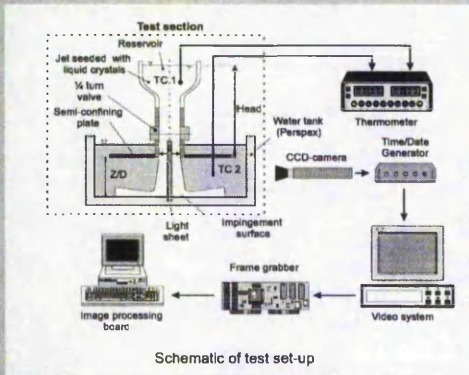
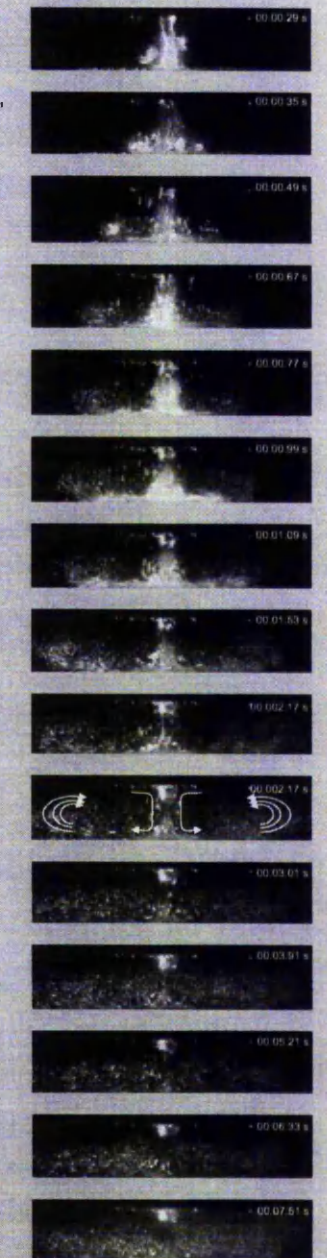
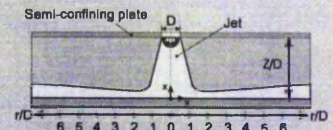
by

S Ashforth-Frost and U W Rüdell  
The Nottingham Trent University, UK.



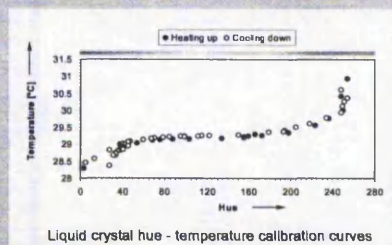
## Overview

Jet impingement flows are widely used in industrial practice due to their excellent heat and mass transfer characteristics. A current research programme concentrates on the effects of Prandtl number on heat transfer in jet impingement. As part of this study, liquid crystal thermography has been shown to be a viable means of visualising flow and temperature distributions, simultaneously. However, hysteresis effects and damage to particles have been identified. The impinging flow was investigated for a mean Reynolds number of 35000 at a nozzle to plate spacing of  $Z/D=3$ .

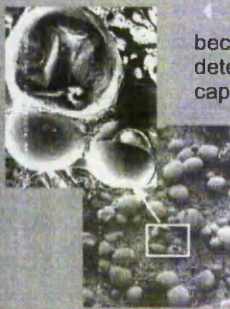


Schematic of test set-up

Thermochromic liquid crystals selectively reflect colours of the visible spectrum on heating as they pass through their cholesteric (i.e. crystalline) phase. A hue-temperature calibration curve was generated which revealed a hysteresis effect between the heating and the cooling process. When cooling down the colours are attributed to higher temperatures. As they cool down they do not always re-align perfectly leading to a change in brightness and calibration. This alignment is dependent on the rate of cooling.

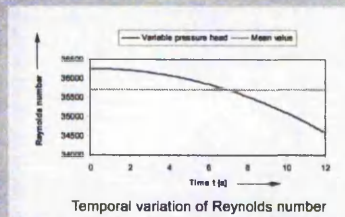


Liquid crystal hue - temperature calibration curves



The liquid crystals proved difficult to apply to forced convection due to their becoming easily mechanically damaged. Microscope photographs revealed a deterioration in the liquid crystals after use; liquid crystals leak from damaged capsules.

Images presented were acquired over the first 8 seconds of the test leading to a high mean Reynolds number of 35000.



Temporal variation of Reynolds number

Vortices are initiated at the exit of the flat round jet, due to prevailing high shear levels, and are transported downstream towards the stagnation region. The deflection of the jet at the impingement surface can be clearly observed. Wall eddies are formed which stretch and diverge in the radial direction and, downstream, the flow begins to resemble that of a developing wall jet. A larger scale recirculation forms, with imposed finer turbulence, as the jet rolls back with complete direction reversal, defining a separation point. The separation point moves continuously downstream manifesting a thickening of the boundary layer. The fast response of the liquid crystals allows even the early stages of the impinging jet to be observed and the thermal development of the turbulent wall jet is also clearly visible. The space between the parallel plates is gradually heated due to entrainment of spent (i.e. already heated) fluid.

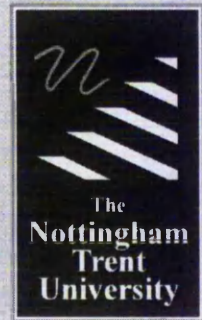
Thermochromic liquid crystals have been demonstrated as a useful tool for simultaneous visualisation of temperature and velocity in a forced convection flow, namely, a turbulent impinging jet. Mechanical damage of the liquid crystal encapsulations can be overcome, however, hysteresis effects in the calibration may become significant where rapid heating and cooling occurs in the same flow domain. For the turbulent Reynolds number considered here, a change in calibration due to hysteresis was less than  $0.25^{\circ}\text{C}$ .

**Presented at  
6<sup>th</sup> National UK Heat Transfer Conference,  
Edinburgh, UK, 15-16 September 1999.**

# THE EFFECTS OF BOUNDARY CONDITIONS ON HEAT TRANSFER TESTING AT MODERATE PRANDTL NUMBERS

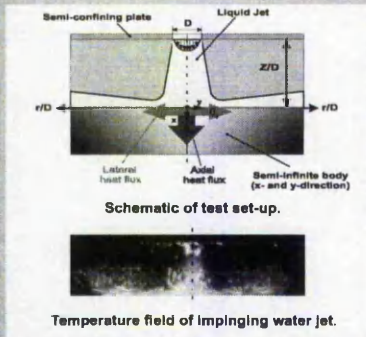
by

U Rüdél, S Ashforth-Frost and K Jambunathan  
The Nottingham Trent University, UK.



## Overview

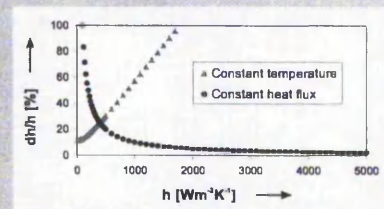
Impinging jets are widely used in industry for heating and cooling applications. In order to exploit their excellent heat transfer characteristics, an improved understanding of their flow and heat transfer distributions is required. There has been extensive heat transfer testing of jet impingement in gaseous (air) jets, but fluids with higher Prandtl number have received much less attention. As part of an ongoing research programme into the effects of Prandtl number on heat transfer in jet impingement, the suitability of different experimental methods has been theoretically assessed. This study provides a direct comparison of experimental approaches in terms of overall uncertainty, reliability, repeatability and ease of use to the measurement of heat transfer beneath impinging jets. Particular attention is paid to the thermal boundary conditions. For jet impingement at moderate Prandtl numbers ( $0.7 \leq Pr \leq 7$ ) the transient heat conduction equation through a semi-infinite body is recommended.



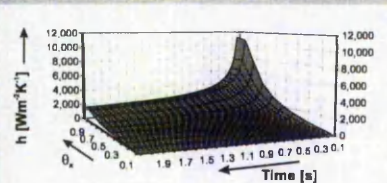
Experimental parameters:  $Re=20,000$  and  $Z/D=2$ .

## Steady-state techniques

For the anticipated heat transfer rates the *constant temperature technique* exhibits increasing uncertainties. This is attributed to the required measurement of surface temperature to within  $0.001^\circ\text{C}$ . Lower uncertainties together with high repeatability and reliability are provided by the *constant heat flux method*. However, long experimental settling times make this approach unsuitable for this investigation.



## One and two-dimensional transient technique



By exposing the impinging surface to a sudden change in temperature and using liquid crystals as surface temperature indicators, the heat transfer coefficient can be obtained by solving the transient heat conduction equation through a semi-infinite solid.

The highest heat transfer coefficients occur at very short transients and at large temperature gradients. This is accompanied by increasing levels of uncertainties for low values of  $\theta_x$ .

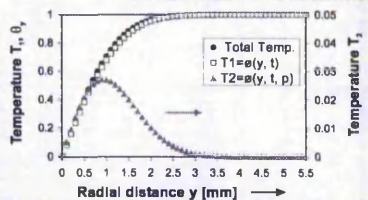
Lateral conduction can be accounted for by assuming a semi-infinite body with initial temperature  $T_0$  and time-dependent surface temperature  $\phi(t)$ .

$$\theta_{\text{Total}} = \theta_x \cdot \theta_y \quad \phi = T_0 e^{\lambda t}$$

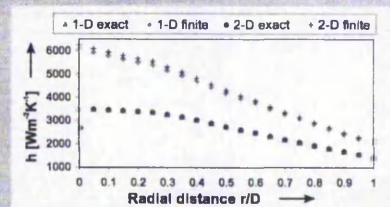
$$\theta_x = \frac{T_s - T_0}{T_j - T_0} = 1 - e^{-\left(\frac{h^2 t}{\rho c_p k}\right)} \text{erfc}\left(\sqrt{\frac{h^2 t}{\rho c_p k}}\right)$$

$$\theta_y = \frac{T_y}{T_0} = T_1 + T_2$$

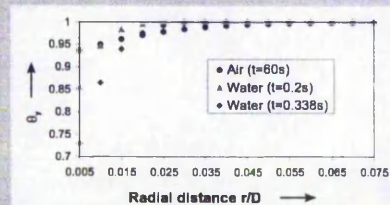
Lateral conduction is mainly composed of heat conducted due to the initial temperature of the plate and heat transport induced by the temporal temperature decay at the stagnation point.



The proposed analytical two-dimensional solution reveals the greatest effects of lateral conduction at the stagnation point.



The high temporal temperature gradient at the stagnation point of a water jet induces greater lateral conduction than comparable air jets.



## Conclusions

The choice of the appropriate thermal boundary condition effectively determines the accuracy and reliability of the overall measurement outcome. Results of an uncertainty analysis demonstrate the suitability of the constant heat flux boundary condition and the transient technique for the measurement of high heat transfer coefficients beneath impinging liquid jets. The effects of lateral conduction in the transient testing of air and water jets are greatest in the immediate proximity of the stagnation point. The design of a transient water experiment requires careful selection of the duration of a test run since it represents a trade-off between low uncertainties associated with longer test intervals and low levels of lateral conduction attributed to short test durations.

C565/067/99

## The effect of boundary conditions on heat transfer testing at moderate Prandtl-numbers

U RÜDEL, S ASHFORTH-FROST, and K JAMBUNATHAN  
 Department of Mechanical and Manufacturing Engineering, The Nottingham Trent University,  
 Nottingham, UK

### Synopsis

Impinging jets are widely used in industry for heating and cooling applications. In order to exploit their excellent heat transfer characteristics, an improved understanding of their flow and heat transfer distributions is required. There has been extensive heat transfer testing of jet impingement, particularly in gaseous (air) jets, but fluids with higher Prandtl number have received much less attention. Often, experimental techniques lead to high uncertainties. This paper provides a direct comparison of experimental approaches and the solution of the associated equations to the measurement of heat transfer beneath impinging jets. Particular attention is paid to the thermal boundary conditions. For jet impingement at moderate Prandtl numbers ( $0.7 \leq Pr \leq 7$ ) the transient heat conduction equation through a semi-infinite body is recommended.

### Nomenclature

A Area of impingement plate, [m<sup>2</sup>]  
 Pr Prandtl number,  $= \nu / \alpha$   
 Q Power, [W]  
 Re Reynolds number,  $= v d / \nu$   
 T Temperature, [°C]  
 c<sub>p</sub> specific heat capacity, [J/(kg K)]  
 d Nozzle diameter, [m]  
 h Heat transfer coefficient, [Wm<sup>-2</sup>K<sup>-1</sup>]  
 i  $= \sqrt{-1}$   
 k Thermal conductivity, [Wm<sup>-1</sup>K<sup>-1</sup>]  
 p  $= -i \sqrt{\lambda}$   
 r/d Radial distance from stagnation point  
 s Thickness of impingement plate, [m]  
 t Time, [s]  
 v Velocity, [m/s]  
 x axial co-ordinate, [m]  
 y radial co-ordinate, [m]

### Greek symbols

$\alpha$  Thermal diffusivity, [m<sup>2</sup>/s]  
 $\gamma = \gamma_p \sqrt{1/\alpha}$   
 $\eta = h^2 t / (\rho c_p k)$   
 $\lambda$  Decay coefficient, [1/s]  
 $\nu$  Kinematic viscosity, [m<sup>2</sup>/s]  
 $\theta$  Non-dimensional temperature  
 $\rho$  Density, [kg/m<sup>3</sup>]

### Subscripts

ad adiabatic  
 B water bath  
 0 initial  
 J Jet  
 S Surface  
 x axial direction  
 y radial direction

## 1 Introduction

Due to its excellent heat and mass transfer characteristics, jet impingement provides an attractive tool for dissipating large heat fluxes in industrial processes. According to the application, there exist many different experimental methods of measuring local heat transfer. The most commonly used boundary conditions are those of uniform heat flux, uniform temperature and transient conditions. Since the thermal boundary condition can affect the measurement and flow condition significantly, it is essential for the designer to be aware of the characteristics of each method and to interpret the results accordingly. For laminar flow over a flat plate, the choice of the constant temperature or constant heat flux boundary condition can result in differences of up to 36% in local heat transfer, Butler and Baughn (1996). For heat transfer problems that involve liquids, deviations are expected to be even higher. In contrast to this Kim *et al.* (1993), in an analytical study on jet impingement, showed that within 2.5 diameters from the stagnation point, local heat transfer is independent of the thermal boundary condition. For liquid jet impingement the boundary conditions may reflect almost ideally the character of real conditions, such as employing the steady state constant heat flux method for modelling the cooling of electronic components. Despite its frequent use in determining heat transfer data of liquid jets, Sun *et al.* (1998), the required steady-state mode imposes long experimental settling times and can lead to errors, caused by the nonuniformities, of up to 30% in electrical power dissipation in a heated foil of uniform thickness, Tarasuk and Castle (1983). The above shortcomings can be overcome by applying a transient wall heating technique, which is well known to be successful in heat transfer measurements, Ireland and Jones (1985). By exposing the impinging surface to a sudden change in temperature and using liquid crystals as surface temperature indicators, the heat transfer coefficient can be obtained. For the specific case of liquid jet impingement, where heat transfer rates are anticipated to exceed  $1000 \text{ Wm}^{-2}\text{K}^{-1}$ , the one-dimensional assumption of the frequently used transient heat conduction method requires further verification. In the open literature, only a few papers exist that have addressed aspects of situations of high heat transfer rates when choosing the transient step wall-heating technique.

It is the purpose of this paper to assess theoretically the suitability of different experimental methods for use in liquid jet impingement heat transfer. An uncertainty analysis was undertaken for each model. For the special case of transient heat conduction through a solid the effects of lateral conduction have been considered.

## 2 Literature review

Only a few papers exist that take into account lateral conduction when obtaining the heat transfer coefficient for transient heat conduction through a solid. Valencia *et al.* (1995) studied the effects of lateral conduction on heat transfer coefficient using liquid crystal thermography (LCT). For flow in a rectangular channel, where longitudinal vortices generated highly non-uniform heat transfer distributions, three types of measurement methods were considered. Results showed that neglecting lateral conduction can lead to uncertainties of more than 100% for the constant wall heat flux boundary condition whereas the errors for the non-steady thin and thick wall technique are approximately 10% and 20%, respectively.

To overcome the problem of lateral conduction, Vedula *et al.* (1988) suggested the use of anisotropic materials with reduced thermal conductivity relative to the conductivity normal to the target surface. For a heat transfer coefficient of  $400 \text{ Wm}^{-2}\text{K}^{-1}$  numerical solutions in the form of a two-dimensional finite element method were presented that corroborated the accuracy of the exact one-dimensional analytical solution. However, no uncertainty analysis was presented.

In a study on the effects of thermal boundary conditions on heat transfer in an incompressible boundary layer, Taylor *et al.* (1989) pointed out that for air flows at 67m/s a measurable difference exists between total, recovery and static temperature. For high Reynolds numbers the constant wall heat flux data are 4% to 5% greater than comparable constant wall temperature data. At the boundary layer origin, the deviations between the two boundary conditions rose up to 15%.

For flows in a turbine blade cooling passage where the heat transfer profile is highly non-uniform and periodic, Chyu *et al.* (1998) compared different methods of evaluating and choosing the appropriate reference temperature. Based on the assumption of invariant local heat flux, the use of the bulk mean temperature as reference temperature, rather than the inlet temperature, yielded the most accurate results. It is interesting to note that the choice of the reference temperature may account for differences in the heat transfer coefficient of up to 40%.

The vast majority of heat transfer data in liquid jet impingement has been acquired using constant heat flux boundary conditions. With regard to the practical application of liquid jets for cooling of electronic components, this is clearly justified and corresponds to the most realistic simulation of the boundary conditions. There are, however, cases where the transient temperature distribution of a relatively thick impingement plate provides better information than those of comparable steady-state methods. To study the importance of surface motion on the heat transfer beneath a planar jet of water, such as in the hot rolling process of steel strips, Zumbrennen *et al.* (1990) employed a transient two-dimensional approach based on a two-dimensional finite difference solution. Heat transfer coefficients in excess of  $25000 \text{ Wm}^{-2}\text{K}^{-1}$  were reported during the initial 12 seconds of a test-run. Using the sequential perturbation method uncertainties of up to 27% were reported.

A few papers exist that report on the use of the one-dimensional transient heat conduction equation for fluids other than air, such as R-12 by Yan *et al.* (1995), diesel spray by Arcoumanis and Chang (1993) and water by Arjocu and Liburdy (1997). Yan and co-authors studied condensing heat transfer coefficients in a glass tube and justified the one-dimensional character of the problem by referring to a work by Dunne (1983) who has shown that materials with small penetration depths have small lateral conduction.

Arcoumanis and Chang (1993) conducted transient heat transfer measurements between a heated plate and an impinging diesel spray. For short test intervals ( $< 1\text{s}$ ) heat transfer rates were inferred from the one-dimensional transient heat conduction equation. This assumption was justified as the temperature gradient normal to the surface was found to be much larger than the lateral one.

von Wolfersdorf *et al.* (1993) presented a hybrid transient step-heating technique that employed a surface heater and liquid crystal thermography. The most striking feature of this method is the fact that the local surface heat flux and the measurement of surface temperatures were eliminated by providing an additional heat flux using a thin surface heater. Nonuniform heating caused by the likelihood of varying foil thickness of the heater is allowed. Liquid crystals are only used to mark the onset of a chosen temperature (colour).

Arjocu and Liburdy (1997) employed the transient step-heating technique to study heat transfer of impinging liquid water jets. Since the nozzle exit Reynolds number was between 300 and 1500, the heat transfer coefficient was less than  $1200 \text{ Wm}^{-2}\text{K}^{-1}$ .

Perera and Baughn (1994) measured variations of the local heat transfer coefficient for sharp edged spirally fluted tubes using the transient heat conduction technique. At the crest and the valley of the flutes, the authors found the effective thickness to be smaller than the penetration depth, which lead them to apply an iterative correction procedure based on a two-dimensional energy balance on a circumferential section of the duct.

### 3 Measurement techniques

The choice of the appropriate surface thermal boundary condition effectively determines the accuracy and reliability of the overall measurement results. In the following section, several experimental techniques are compared and evaluated in terms of overall uncertainty, reliability, repeatability and ease of use. An uncertainty analysis according to Moffat (1985) was undertaken for the most common characterisation of surface thermal boundary conditions.

### 3.1 Steady-state techniques

The practicality of the constant temperature boundary condition, as suggested by den Ouden and Hoogendoorn (1974) for air jets, has been assessed. The governing equation for the uncertainty is given in the Appendix. For the anticipated heat transfer rates results of the uncertainty analysis reveal monotonically increasing uncertainties (see Figure 1.). This is attributed to the required measurement of surface temperature to within  $\pm 0.001^\circ\text{C}$ , which makes this approach inappropriate for the use of liquids.

From Figure 1, it can also be observed that lower uncertainties in the range of interest are provided by the constant heat flux method. This method provides high repeatability and reliability. Although this technique has been widely accepted for the modelling of cooling processes, drawbacks such as possible non-uniformities in power dissipation and long experimental settling times make this approach inflexible. Further results of the uncertainty analysis can be found in Table 1.

### 3.2 Transient techniques

#### 3.2.1 One-dimensional heat conduction technique

The above limitations can be overcome by applying the transient wall heating technique. A detailed description of this technique is given in Ireland and Jones (1985). By exposing the impinging surface to a sudden change in temperature and using liquid crystals as surface temperature indicators, the heat transfer coefficient can be obtained using the transient equation given in Schneider (1959) with a convection boundary condition. The solution is given as follows:

$$\frac{T(x, t) - T_0}{T_1 - T_0} = \theta = 1 - \operatorname{erf} \left[ \frac{x}{\sqrt{4\alpha t}} - e^{\frac{hx}{k} + \eta} \left\{ 1 - \operatorname{erf} \left( \frac{x}{\sqrt{4\alpha t}} + \sqrt{\eta} \right) \right\} \right] \quad (1)$$

If the target plate is sufficiently thick and initially at a uniform temperature then the heat transfer process can be considered to be one-dimensional into a semi-infinite solid. At the surface of the plate, the co-ordinate  $x = 0$  so that

$$\theta_s = \frac{T_s - T_0}{T_1 - T_0} = 1 - e^{\eta} \operatorname{erfc}(\sqrt{\eta}) \quad (2)$$

The adiabatic wall temperature is used as  $T_1$  in equation (2) to account for viscous heating through the boundary layer. The semi-infinite assumption is valid as long as the temperature penetration does not exceed the thickness of the material being used. To maintain the penetration depth much smaller than the effective plate thickness, the guideline for the minimum thickness of the Perspex plate was taken from Schultz and Jones (1973) as

$$x > 4\sqrt{\alpha t} \quad (3)$$

Examination of equation (2) with regard to short transients reveals that the highest heat transfer coefficients occur at very short transients and at large temperature differences between the initial plate temperature and the surface temperature, Figure 2a. Figure 2b shows increasing levels of uncertainties at low values of the non-dimensionalised temperature  $\theta$ . This corroborates observations by Martinez-Botas *et al.* (1995) who reported that, for short measurement intervals with high thermal loads, the highest heat transfer rates occur in the initial stage of the process. Butler and Baughn (1996) pointed out that the more the initial conditions resemble those of a uniform wall temperature (in the present study:  $\theta = 0$ ) the higher are the uncertainties. In contrast to air measurements, where long durations of the transient may allow the semi-infinite substrate assumption to break down, liquid heat transfer coefficients are inferred from much shorter transients. In cases where  $\theta > 0.6$  the uncertainties display significantly lower values. The

contribution to the overall uncertainty for a typical heat transfer situation is given in Table 2. A variation of the transient heat transfer technique using a heating foil and liquid crystals was suggested by von Wolfersdorf *et al.* (1993). Elimination of the local heat flux and the requirement of measuring the surface temperature results in a significant increase in the level of uncertainty. Figure 3a depicts situations where high heat transfer coefficients are obtained at small temperature differences between the wall and the jet. Results of the uncertainty analysis are plotted in Figure 3b. Further examination in the initial stage of the test run reveals that the major contribution to the error results from the uncertainty in recording the start time of the test.

### 3.2.2 Two-dimensional heat conduction technique

Solution to the two-dimensional solution is obtained as a product of two one-dimensional solutions, Incropera and DeWitt (1996).

$$\theta_{\text{total}} = \theta_x \cdot \theta_y \quad (4)$$

In the streamwise direction, the one-dimensional solution is the well-known equation (2) of transient heat conduction through a semi-infinite solid. Lateral conduction can be accounted for by applying the solution given in Carslaw and Jaeger (1959) for a semi-infinite solid with initial temperature  $T_0$  and time-dependent surface temperature  $\phi = \phi(t)$ . Due to the axisymmetric character of round jet impingement heat transfer, only one half of the plate was considered. For the case of the hot target plate being cooled by the jet, the time-dependent surface temperature of the plate can be expressed as

$$\phi = T_0 e^{\lambda t} \quad \lambda < 0 \quad (5)$$

Then,

$$\theta_y = \frac{T_1}{T_0} \quad (6) \quad \text{with} \quad T_1 = T_1 + T_2 \quad (7)$$

where

$$T_1 = \text{erf} \left( \frac{y}{2\sqrt{(\alpha t)}} \right) \quad (8)$$

and

$$T_2 = \frac{1}{2} e^{\lambda t} \left\{ \left[ e^{-y\sqrt{(\lambda/\alpha)}} \right] \text{erfc} \left( \frac{y}{2\sqrt{(\alpha t)}} - \sqrt{(\lambda t)} \right) + \left[ e^{y\sqrt{(\lambda/\alpha)}} \right] \text{erfc} \left( \frac{y}{2\sqrt{(\alpha t)}} + \sqrt{(\lambda t)} \right) \right\} \quad (9)$$

Let  $\lambda = -p^2$ , where  $p$  is a real number so that  $p = -i\sqrt{\lambda}$ . It follows that

$$T_2 = \frac{1}{2} e^{-p^2 t} \left\{ \left[ e^{-y p \sqrt{(t/\alpha)}} \right] \text{erfc} \left( \frac{y}{2\sqrt{(\alpha t)}} - i p \sqrt{t} \right) + \left[ e^{y p \sqrt{(t/\alpha)}} \right] \text{erfc} \left( \frac{y}{2\sqrt{(\alpha t)}} + i p \sqrt{t} \right) \right\}$$

Let  $a = \frac{y}{2\sqrt{(\alpha t)}}$  and  $b = p\sqrt{t}$ . Also put

$$e^{\pm i p \sqrt{(t/\alpha)}} = \cos(y p \sqrt{(t/\alpha)}) \pm i \sin(y p \sqrt{(t/\alpha)}) = \cos \gamma \pm i \sin \gamma \quad (10)$$

and

$$\text{erfc}(z) = \text{erfc}(a + i b) = 1 - \text{erf}(a + i b) = 1 - P - i Q \quad (11)$$

$$\operatorname{erfc}(Z) = \operatorname{erfc}(a - ib) = 1 - \operatorname{erf}(a - ib) = 1 - P + iQ \quad (12)$$

The Gauss error function was implemented using the sum of the following series expansions:

$$P(r, \beta) = \frac{2}{\sqrt{\pi}} \sum_{n=0}^{\infty} \frac{(-1)^n r^{2n+1} T_{2n+1}(\cos \beta)}{(2n+1)n!} \quad (13)$$

$$Q(r, \beta) = \frac{2r \sin \beta}{\sqrt{\pi}} \sum_{n=0}^{\infty} \frac{(-1)^n r^{2n} T_{2n}(\cos \beta)}{(2n+1)n!} \quad (14)$$

where  $T_{2n+1}(\cos \beta)$  and  $U_{2n}(\cos \beta)$  are the Chebyshev's polynomials of the first and second kind, respectively. The expressions P and Q are now calculated by using the recurrence equations and the starting values given in Gradshteyn and Ryzhik (1980).

Substituting equations (10), (11) and (12) into (9) yields

$$T_2 = \frac{1}{2} e^{-r^2} \{ [\cos \gamma - i \sin \gamma] [1 - P + iQ] + [\cos \gamma + i \sin \gamma] [1 - P - iQ] \} \quad (15)$$

Finally, substituting (7), (8) and (15) into (6) leads to

$$\theta_y = \frac{T_y}{T_0} = T_1 + T_2 = \left\{ \operatorname{erf} \left( \frac{y}{2\sqrt{\alpha t}} \right) + e^{-r^2} [(1-P)\cos \gamma + Q \sin \gamma] \right\} \quad (16)$$

To determine the decay coefficient  $\lambda$  experimentally a round semi-confined submerged jet impinging on a heated plate is considered. For the case of air ( $Pr = 0.7$ ) the nozzle diameter is 0.1m while the water jet has similar nozzle exit conditions ( $Re = 20000$ ) but at a nozzle diameter of 0.02m. The experiments were conducted by suddenly exposing a hot impingement plate to a cold jet. In the case of the water jet the test run was initiated by dropping the plate guided by rails along the wall. The surface temperature was measured via a thermocouple attached at the stagnation point of the Perspex plate.

Results of the decay coefficient  $\lambda$  are presented in Figure 4. A least square fit was used to determine the decay coefficient for the air jet to 0.0014 whereas for the water jet  $\lambda$  was determined to be 2.

### 3.3 Numerical approach

In cases of high heat transfer coefficients the heat conduction equation is frequently approximated in a two-dimensional space by employing a finite-difference method, see Zumbrennen *et al.* (1990).

$$\frac{\partial^2 T}{\partial x^2} + \frac{\partial^2 T}{\partial y^2} = \frac{1}{\alpha} \frac{\partial T}{\partial t} \quad (17)$$

The characteristic equation and the corresponding boundary conditions were discretized by using the implicit forward-difference scheme. The resulting set of linear equations is solved by the Gauss-elimination method with row pivoting. The predictive character of the one-dimensional and two-dimensional finite difference approaches was assessed by comparing the solutions to the exact analytical solutions.

### 4 Results and conclusions

The results of uncertainty analyses based on the constant temperature, constant heat flux and transient boundary condition are compared. Results show the unsuitability of the constant temperature method due to monotonically increasing uncertainties at higher heat transfer coefficients. The constant heat flux method displays satisfactory uncertainties, particularly with increasing heat transfer coefficients. Despite its frequent use, long test durations and

nonuniformities in the electrical power dissipation to the heater sheet degrade the overall performance of this method.

An alternative approach is provided by the transient technique, which is widely used for air jet impingement heat transfer. The absence of any heater element allows even complex surfaces to be studied. To illustrate the different effects of experimental parameters, the one-dimensional transient equation for heat conduction through a semi-infinite body was solved and its range of validity systematically mapped. Accurate temporal measurements and, in addition, the selection of the liquid crystal event temperature need to be carefully considered in order to keep uncertainties to a minimum. The approach of providing the surface with an additional heat flux in the form of a thin metal foil was also considered but imposed unacceptable temporal uncertainties.

To account for lateral conduction in transient testing the heat conduction equation was solved in two dimensions using analytically exact methods and using a finite-difference technique. For a typical surface temperature distribution induced by an impinging water jet, the one-dimensional and two-dimensional finite difference method is compared to the exact one-dimensional solution in Figure 5. Results show that both finite difference schemes deliver almost identical trends but over-predict the exact solution by approximately 54%. In both cases, the deviations are greatest at the stagnation point and decline monotonically with increasing  $r/d$ .

Using the two-dimensional solution from equation (4) the two-dimensional profile of the heat transfer coefficient is plotted on the same graph. In contrast to the two-dimensional finite difference scheme, the proposed exact two-dimensional solution, shown in Figure 5, displays lower values of the stagnation point heat transfer coefficient which conforms to expectations of a 'smoothened' heat transfer distribution.

In Figure 6, the effects of lateral conduction in the testing of air and water jets in the immediate proximity of the stagnation point are compared. For short durations typical of air experiments, the non-dimensional temperature  $\theta_{r=0}$  at the stagnation point is reduced by 8%, which coincides with the uncertainty levels reported in the open literature. For water jet experiments at typical time intervals ( $t < 0.5s$ ), the high decay coefficient is counter balanced by the short test interval. For the relatively large nozzle diameter used in this study it can be seen that lateral conduction is confined to the close proximity of the stagnation point.

In the interest of reliable and repeatable results it is essential to carefully select the duration of a transient test run. This represents a trade-off between low uncertainties associated with longer test intervals and low levels of lateral conduction attributable to short test durations.

For the future, use of high speed recording cameras could considerably improve temporal resolution of the temperature measurement.

#### Acknowledgement

The authors would like to thank the Nottingham Trent University and the Engineering and Physical Science Research Council (grant AF/97/0568 to Dr S Ashforth-Frost) for financial support towards this work. The contribution of Dr A Sackfield is gratefully acknowledged.

#### Appendix

Uncertainty analysis for the constant temperature method:

$$\frac{\delta h}{h} = \sqrt{\left(\frac{\delta k}{k}\right)^2 + \left(\frac{-\delta s}{s}\right)^2 + \left(\frac{\delta(T_h - T_s)}{(T_h - T_s)}\right)^2 + \left(\frac{\delta(T_s - T_f)}{(T_s - T_f)}\right)^2} \quad (A1)$$

Uncertainty analysis for the constant heat flux method ( $A=B \cdot L$ ):

$$\frac{\delta h}{h} = \sqrt{\left[ \left( \frac{\delta Q}{Q} \right)^2 + \left( \frac{\delta B}{B} \right)^2 + \left( \frac{\delta L}{L} \right)^2 + \left( \frac{\delta(T_{s,md} - T_f)}{(T_{s,md} - T_f)} \right)^2 \right]} \quad (A2)$$

Table 1. Contribution to overall uncertainty of 10% ( $h=1000 \text{ Wm}^{-2}\text{K}^{-1}$ ).

| Measured Parameter | Typical value | $\pm \delta x$ | $[(\partial h/\partial x)\delta x]/(dh/h)$ [%] |
|--------------------|---------------|----------------|--|
| Q                  | 8800 W        | 500            | 98.78  |
| B, L               | 0.5 m         | 0.0001         | $\Sigma 0.02$                                  |
| $T_{s,md}$         | 40°C          | 0.2            | 0.3  |
| $T_f$              | 20°C          | 0.2            | 0.9  |

Uncertainty analysis for the one-dimensional transient method:

$$\frac{\delta h}{h} = \left[ \left( \frac{\delta t}{2t} \right)^2 + \left( \frac{\delta \sqrt{\rho c k}}{\sqrt{\rho c k}} \right)^2 + \left( \frac{1}{\beta(T_s - T_o)} \right)^2 (\delta T_s^2 + (\theta - 1)^2 \delta T_o^2 + \theta^2 \delta T_f^2) \right]^{0.5} \quad (A3)$$

where  $\beta = 2 \sqrt{\pi} (\pi^{-0.5} - \sqrt{\pi}(1 - \theta))$ .

Table 2. Contribution to overall uncertainty of 8.9% ( $h=992 \text{ Wm}^{-2}\text{K}^{-1}$ ).

| Measured Parameter  | Typical value | $\pm \delta x$ | $[(\partial h/\partial x)\delta x]/(dh/h)$ [%] |
|---------------------|---------------|----------------|--|
| t                   | 0.4s          | 0.05           | 49.2   |
| $\sqrt{\rho c_p k}$ | 566           | 29             | 32.7   |
| $T_s, T_o, T_f$     | 20, 60, 36°C  | 0.2            | $\Sigma 18.1$                                  |

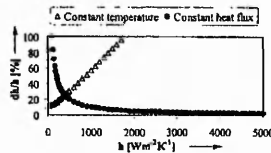


Figure 1. Range of uncertainty of steady-state methods.

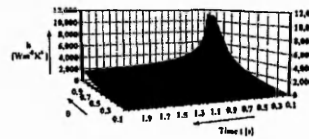


Figure 2a. Range of validity of the 1D-transient technique.

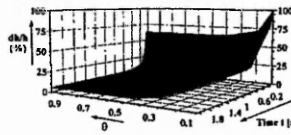


Figure 2b. Range of uncertainty of the 1D-transient technique.

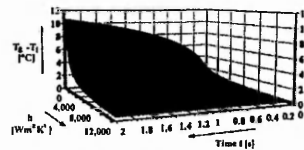


Figure 3a. Range of validity of the 1D-transient technique (additional heat flux).

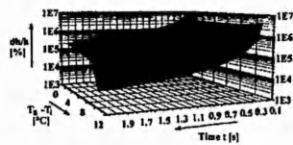


Figure 3b. Range of uncertainty of the 1d-transient technique (additional heat flux).

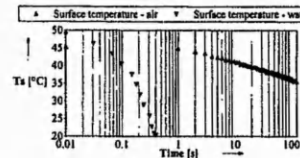


Figure 4. Temporal temperature decay at the stagnation point for air and water.

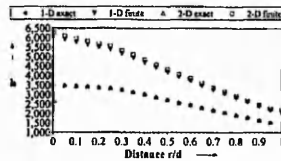


Figure 5. The finite difference technique compared to the exact solutions.

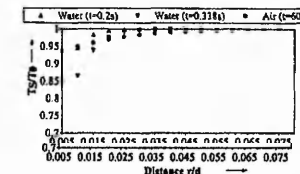


Figure 6. Lateral temperature variation in close vicinity to the stagnation point.

**References**

Arcoumanis, C and Chang, J-C, 1993. Heat transfer between a heated plate and an impinging transient diesel spray. *Experiments in Fluids*, 16, 105-119.

Ajocu, S C and Liburdy, J A, 1997. Influence of elliptical structure on impinging jet array heat transfer performances. *SPIE*, 3172, 130-140.

Bulter, R J and Baughn, J W, 1996. The effect of the thermal boundary condition on transient method heat transfer measurements on a flat plate with a laminar boundary layer. *ASME J. Heat Transfer*, 118, 831-837.

Carslaw, H S and Jaeger, J C, 1959. *Conduction of Heat in Solids*. 2nd ed., Oxford University Press, London, United Kingdom.

Chyu, M K, Ding, H, Downs, J P and Soechting, F O, 1998. Determination of local heat transfer coefficient based on bulk mean temperature using a transient liquid crystals technique. *Experimental Thermal and Fluid Science*, 18, 142-149.

Dunne, S T, 1983. *A study of flow and heat transfer in gas turbine cooling passages*, D. Phil. Thesis, Oxford University, Oxford, United Kingdom.

Gradshteyn, I S and Ryzhik, I M, 1980. *Table of Integrals, Series and Products*. Enlarged and corrected ed., Academic Press, London, United Kingdom.

Incropera, F P and DeWitt, D P, 1996. *Introduction to Heat Transfer*. 3rd ed., John Wiley & Sons, New York, United States of America.

Ireland, P T and Jones, T V, 1985. The measurement of local heat transfer coefficients in blade cooling geometries. *AGARD Conf. Proc.*, 390, paper 28.

Kim, K, Wiedner, B and Camci, C, 1993. Fluid dynamics and convective heat transfer in impinging jets through implementation of a high resolution liquid crystal technique, Part II: Navier-Stokes computation of impulsively starting heat transfer experiments. *Int. Symposium on Air-Breathing engines*, Tokyo, Japan.

- Martínez-Botas, R F, Lock, G D and Jones, T V, 1995. Heat transfer measurements in an annular cascade of transonic gas turbine blades using the transient liquid crystal technique. *J. Turbomachinery*, **117**, 425-431.
- Moffat, R J, 1985. Using uncertainty analysis in the planning of an experiment. *ASME J. Fluids Engineering*, **107**, 173-179.
- Perera, K K and Baughn, J W, 1994. The effect of pitch angle and Reynolds number on local heat transfer in spirally fluted tubes. *ASME HTD* **279**, 99-112.
- den Ouden, C and Hoogendoorn, C J, 1974. Local convective heat transfer coefficients for jets impinging on a plate; experiments using a liquid crystal technique. *Proc. 5<sup>th</sup> Int. Heat Transfer Conf.*, Tokyo, 3-7 Sept., **5**, 293-297.
- Schneider, P J, 1955. *Conduction Heat Transfer*. Addison-Wesley Publishing Co., Inc., Reading, Mass.
- Schultz, D L and Jones, T V, 1973. Heat transfer measurements in short-duration hypersonic facilities. *AGARD-AG-165*.
- Sun, H, Ma, C F and Chen, Y C, 1998. Prandtl number dependence of impingement heat transfer with circular free-surface liquid jets. *Int. J. Heat Mass Transfer*, **41**(10), 1360-1363.
- Tarasuk, J D and Castle, G S P, 1983. Temperature distribution in an electrically heated wide metallic foil. *ASME J. Heat Transfer*, **105**, 210-212.
- Taylor, R P, Coleman, H W, Hosni, M H and Love, P H, 1989. Thermal boundary condition effects on heat transfer in the turbulent incompressible flat plate boundary layer. *Int. J. Heat Mass Transfer*, **32**(6), 1165-1174.
- Valencia, A, Fiebig, M and Mitra, N K, 1995. Influence of heat conduction on determination of heat transfer coefficient by liquid crystal thermography. *Experimental Heat Transfer*, **8**:271-279.
- Vedula, R P, Metzger, D E and Bickford, W B, 1988. Effects of lateral and anisotropic conduction on determination of local convection heat transfer characteristics with transient tests and surface coatings. *ASME Heat Transfer Division*, **104**, 21-28.
- von Wolfersdorf, J, Hoecker, R and Sattelmayer, T, 1993. A hybrid transient step-heating heat transfer measurement technique using heater foils and liquid-crystal thermography. *ASME Journal of Heat Transfer*, **115**, 319-324.
- Yan, X, Baughn, J W, Rabas, T J and Arman, B, 1995. Liquid-crystal transient technique for measurement of in-tube local condensing heat transfer coefficients. *Experimental Heat Transfer*, **8**, 17-32.
- Zumbrunnen, D A, Incropera, F P and Viskanta, R, 1990. Method and apparatus for measuring heat transfer distributions on moving and stationary plates cooled by a planar liquid jet. *Experimental Thermal and Fluid Science*, **3**:202-213.

**Presented at**  
**9<sup>th</sup> International Symposium on Flow Visualization,**  
**Edinburgh, UK, 22-25 August 2000.**



## Flow Visualisation of Submerged Impinging Jets of Different Prandtl numbers

U. Rüdel<sup>1</sup>, S. Ashforth-Frost<sup>1</sup> and K. Jambunathan<sup>1</sup>

Keywords: Prandtl number, impinging jets, CFD

### ABSTRACT

An experimental and numerical investigation was carried out to study the flow field of a confined, submerged jet impinging onto a flat surface over a range of Prandtl numbers. Water at different temperatures and air was used as working fluids. To study the effects of fluid properties on turbulent impinging jet flow, the Reynolds number at the nozzle exit was maintained constant ( $\approx 20,000$ ) over  $0.71 \leq Pr \leq 7$ .

The flow field was modelled at several nozzle-to-plate spacings ( $2 \leq z/d \leq 8.5$ ) using two  $k-\epsilon$  turbulence models, namely the standard  $k-\epsilon$  model and the modified  $k-\epsilon$  model based on renormalisation group (RNG) theory. Results from experimental flow visualisation are in agreement with numerical predictions as the center of the recirculation vortex is predicted to within  $0.3d$ . Measurements of the velocity decay for  $z/d=5$  are in reasonable agreement with numerical predictions. For  $z/d=8.5$  LDA results show that the water jet decays marginally faster than the air jet but shows the same length of the potential core. Beyond the potential core, turbulence levels are higher for the water jet. This is in contrast to the results from the RNG model. The distribution of the turbulent kinetic energy along the impingement wall shows identical values among the Prandtl-number fluids. Effects of variable fluid properties are negligible.

### 1 NOMENCLATURE

|       |  |               |  |
|-------|--|---------------|--|
| Pr    | Prandtl number, $= \mu c_p / \lambda$  | Greek symbols |  |
| Re    | Reynolds number, $= U_{exit} d / \nu$  | $\beta$       | proportionality constant                 |
| $c_p$ | specific heat capacity, [J/(kg.K)]   | $\lambda$     | Thermal conductivity, [W/(m.K)]          |
| d     | Nozzle diameter, [m]   | $\mu$         | Dynamic viscosity, [kg/(m.s)]            |
| k     | Turbulent kinetic energy, $= \sqrt{u'^2 + v'^2} / 2$   | $\nu$         | Kinematic viscosity, [m <sup>2</sup> /s] |
| r/d   | Radial distance from stagnation point  | Subscripts    |  |
| U     | Axial velocity, [m/s]  | cl            | centreline                               |
| V     | Radial velocity, [m/s]   | exit          | conditions at the nozzle exit.           |
| x     | Distance from near wall node to impingement plate, [m]   | J             | Jet                                      |
| y     | Distance from impingement plate surface, [m]   | nw            | near wall                                |
| y+    | Non-dimensional distance from wall to the near wall node, $= 0.09^{1/4} k_{nw}^{1/2} x_{nw} / \nu$ | ref           | reference conditions, 20°C               |
| z     | Nozzle-to-plate spacing, [m]   | T             | Temperature                              |

### 2 INTRODUCTION

The excellent heat and mass transfer characteristics of impinging jets has been extensively exploited in the past for a wide range of industrial applications such as cooling, heating and drying

**Authors:** <sup>1</sup>The Nottingham Trent University  
Department of Mechanical and Manufacturing Engineering,  
Burton Street, Nottingham NG1 4BU, England UK.  
Corresponding author: Uwe Rüdel, [uwe.ruedel@ntu.ac.uk](mailto:uwe.ruedel@ntu.ac.uk)

U. Rüdel, S. Ashforth-Frost and K. Jambunathan

processes. With the advancement in high-performance semi-conductor components it is anticipated that heat fluxes originating from micro-electronic components and electric circuits will steadily increase in the near future. Likewise, the development of new materials is likely to impose large thermal loads on the cooling facilities. Air with its inherent thermal limitations will inevitably be replaced by fluids that are capable of coping with high heat fluxes. It was only recently that jet impingement researchers began to focus attention on the excellent heat transport properties that can be accomplished with liquids. Current applications reflect the diversity and versatility of liquid jet impingement in industrial engineering applications and include the cooling of combustion engines [1], high-performance electrical circuits [2] and highly reflective optical face plates [3]. Further applications include thermal treatment of metal batches [4], [5], cryosurgery [6] and drying processes such as in ink jet printers [7].

The heat transfer coefficients may differ significantly depending on the thermal properties of the fluid. To optimise this process, a full understanding of the flow field with its effects on heat transfer is required. The influence of Prandtl number on convective heat transfer is still one of the least understood aspects for impinging jets [8]. The outcome will be a much more efficient production cycle with higher capacity, higher product quality and higher energy and material savings. Despite jet impingement being a subject of study for decades, the vast majority of correlations have been derived with air as the working fluid, while for other fluids there is a paucity of information. Consequently, the use of correlations originally derived for air jets can lead to errors in designing and optimising processes with fluids other than air. With heat fluxes being anticipated to exceed  $200\text{W}/\text{cm}^2$  within the next decade there is a considerable demand to dissipate these large fluxes. The careful selection of the working fluid, and a full understanding of its physical effects, has great influence on the performance of the heat transfer process in terms of fluid consumption, overall efficiency, pump power, temperature uniformity, electrical conductivity, etc. Jet impingement heat transfer represents a very complex function of several parameters with different weightings. Therefore, it is essential to focus on the impact of the thermal characteristics of the working fluid on the flow and temperature field in order to assess the effects of Prandtl number on jet impingement heat transfer.

In this paper preliminary results of a combined experimental/numerical study into the effects of Prandtl number on the flow field of an impinging turbulent jet are presented. The semi-confined jet (where the nozzle is integral to a flat surface parallel to the impingement surface) impinged orthogonally onto a flat surface at a Reynolds number of 20,000 over  $0.71 \leq \text{Pr} \leq 7$ . Results of flow visualisation are compared to numerical simulations using two widely used  $k-\epsilon$  turbulence models. Some Laser Doppler anemometry (LDA) measurements are presented to characterise the flow behaviour in the axial and radial directions.

### 3 LITERATURE REVIEW

The excellent heat and mass transfer characteristics of impinging jets have attracted considerable research interest over the past two decades. The vast majority of work has dealt with air as the working fluid although fluids of different Prandtl numbers frequently result in heat transfer rates that are several orders of magnitudes higher. The effects of Prandtl number, which expresses the ratio of kinematic viscosity to thermal diffusivity, on convective heat transfer is still one of the least understood aspects of impinging jets [8]. An early analytical study on impinging jets [9] showed that with increasing Prandtl number the thermal boundary layer thinned relative to the hydrodynamic boundary layer. The thermal boundary layer was found to be more sensitive to vortex stretching than the hydrodynamic boundary layer. For air the thermal boundary layer was about 10 times more sensitive to vorticity than the hydrodynamic boundary layer. This effect was greatest for water ( $\text{Pr}=7$ ) and ceased at approximately  $\text{Pr}=100$ . Since small scale eddies are destroyed by viscous dissipation before they reach the boundary layer, the effects of viscosity are more pronounced in the laminar region of the stagnation region. These findings were corroborated by [10] who compared the heat transfer data of water ( $\text{Pr}=3$ ) with those of synthetic oil ( $85 < \text{Pr} < 113$ ). The authors suggested the use of different correlations for liquids whose Prandtl numbers are below or above a value of 100. Effects of variable properties were studied for

FLOW VISUALISATION OF SUBMERGED IMPINGING JETS  
OF DIFFERENT PRANDTL NUMBERS

temperature differences of up to 17.8°K between the surface temperature and the adiabatic wall temperature. FC-77 and water jets were investigated by [11] who focused on the particular case of cooling electronic chip modules. A great influence of the heater dimensions on overall heat transfer data was found which lead the authors to use the geometric size of the heater as the characteristic length as opposed to the characteristic nozzle size. Unsubmerged and submerged jets of water and FC-77 were compared by [12]. Results indicated that heater-average Nusselt numbers were higher under submerged conditions due to the turbulence generated in the shear layer of the jet. In addition, slightly higher heater-average Nusselt numbers were found for the dielectric fluid than for comparable water jets. In a more recent experimental study on unsubmerged jets [8], the heat transfer characteristics of three liquids over a Prandtl-number range of 7 to 262 were investigated. Despite the large Prandtl-number range, the heat transfer coefficient at the stagnation point could be expressed in a single correlation. Existing constant property correlations were found to underpredict for high Prandtl-number fluids by [13]. The authors found that for a sufficiently high Prandtl-number a change in Reynolds number may have little or no effect on Nusselt number. Only a few studies exist that investigated the effects of Prandtl-number on the flow structure beneath impinging jets. The flow pattern beneath an impinging air jet was studied by [14] who found that recirculation currents may exist on a flat plate if there is not sufficient free room for the jet to flow downstream which could cause interference with the formation of the outer peak in heat transfer. In a numerical study [15] investigated the flow field of an impinging jet of FC-77 for various nozzle-to-plate spacings. The computed flow patterns derived from the  $k-\epsilon$  model were in good agreement with experiments but failed to predict secondary recirculation zones. For water and FC-77 jets [16] reported optimum nozzle-to-plate spacings of  $z/d=3$ . This significantly shorter length of the potential core was attributed to the close proximity of the radial wall confinement and the annular collection of the spent fluid. Those effects are believed to enhance turbulent production and to reduce the length of the potential core. The latter study is of particular importance as the confinement of the surrounding walls resembles that of the present study. Near-field velocity and concentration centreline distributions were presented by [17] and supported the general conclusion that the temperature field evolves faster than the velocity field. Measurements were performed of a sodium jet and it was found that the decay of the centreline velocity for sodium to be the same as for fluids of higher Prandtl number. In contrast to that, the centreline temperature was reported to decrease with a power of  $-1$  compared to that of  $-5/3$  for fluids of higher Prandtl number. Different behaviour was attributed to the heat transport process being dominated by molecular diffusion while momentum transport may be characterised by turbulent diffusion. The scalar concentration and velocity field of a round turbulent jet in a coflow was measured by [18]. The length of the potential core was reported to be dependent only on the ratio of ambient velocity to nozzle exit velocity ( $U_a/U_0$ ) and the spreading rate of a jet in stagnant ambient:

$$\frac{x_c}{D} = \frac{\sqrt{1 + U_a / U_0}}{\beta_s (1 - U_a / U_0)} \quad (1)$$

For unsteady boundary layer flow of water [19] found the point of zero skin friction to move downstream with decreasing Prandtl-numbers. Since this point marks the onset of separation when the flow is steady, it can be expected that for heated water flow the flow transition is delayed.

## 4 EXPERIMENTAL METHOD

### 4.1 Experimental techniques

All experimental tests were carried out in a recirculating open water channel as shown schematically in Figure 1. A stainless steel centrifugal pump receives liquid from the main tank and produces a steady stream which can be varied using a gate valve. The liquid is heated in the main tank using two immersion heaters. Temperature is monitored by thermocouples positioned in

U. Rüdél, S. Ashforth-Frost and K. Jambunathan

the main tank and at the entry to the test section. The flow is directed through a filter and a flow straightening section into the test section. To ensure low levels of turbulence intensity at the nozzle exit, the fluid passes through a low-angle diffuser (expansion angle  $8^\circ$ ) and two sets of flow straighteners in the form of tightly packed drinking straws. The flow enters the test section through a bell-shaped contraction with an outlet diameter of 35mm. The test section is made of 20mm-acrylic sheets and has a base area of 0.3m x 0.3m. This places the center of the nozzle 4.3 diameters away from the lateral walls and enables nozzle-to-plate spacings  $z/d$  of up to 8.5 to be studied. After impingement onto a flat plate the flow is discharged through four outlets in the semi-confining plate and is controlled through a ball valve to maintain the liquid level in the test section constant. This ensures that during all experiments the nozzle center is placed 7 diameters from the free surface and the bottom of the test section, respectively. The volume flow rate was maintained steady to within 4%. To maintain the Reynolds number at the nozzle exit constant ( $Re=20,000$ ), the fluids were issued at different nozzle exit velocities.

For  $Pr > 1$ , distilled water was used as the working fluid. The Prandtl number was varied over a temperature range of  $20^\circ C \leq T \leq 50^\circ C$  thus yielding  $3.5 \leq Pr \leq 7$ . It is interesting to note that this large variation in Prandtl number is mainly caused by changes of the dynamic viscosity ( $\mu_{50^\circ C} / \mu_{20^\circ C} = 0.52$ ) while the thermal conductivity and the specific heat capacity vary by no more than 7%. Table 1 lists the relevant transport properties of the fluids under investigation.

| Fluid       | Viscosity $\mu$<br>[kg/(m.s)] | Therm. cond.<br>$\lambda$ [W/(m.K)] | Spec. heat cap.<br>$c_p$ [J/(kg.K)] | Exit velocity<br>[m/s] | Pr   |
|-------------|-------------------------------|-------------------------------------|-------------------------------------|------------------------|------|
| Air, 20°C   | $1.81 \times 10^{-4}$         | 0.02564                             | 1006.1                              | 8.61                   | 0.71 |
| Water, 50°C | $0.549 \times 10^{-3}$        | 0.6405                              | 4182                                | 0.32                   | 3.5  |
| Water, 35°C | $0.723 \times 10^{-3}$        | 0.6221                              | 4179                                | 0.42                   | 4.8  |
| Water, 20°C | $1.005 \times 10^{-3}$        | 0.5996                              | 4182                                | 0.58                   | 7    |

Table 1. Properties of the investigated fluids.

For the experiments with air as the working fluid, the same experimental facility was used. The centrifugal fan was connected to the turbulence management section upstream of the diffuser inlet to allow the airflow to pass the same flow straightening devices as water.

Flow visualisation was conducted using laser sheet illumination of a suspension of hollow glass microspheres having a mean diameter of 60 $\mu$ m and seeding concentration of about 1700 particles/cm<sup>3</sup>. The light sheet was generated using a He-Ne laser ( $\lambda=632.5$ nm) and a circular lens with a focal length of 1.2mm. Still photographs were obtained using a Pentax MX 50mm with a Kodak ISO 400 film at various shutter speeds and apertures between  $f/1.7$  and  $f/2.8$ .

Velocity measurements were performed with a DANTEC four-beam two-colour fiber-optic based 2-dimensional Laser-Doppler anemometer with back-scatter collection optics. The light source is a 150mW Argon-ion laser tuned to 488nm (blue) and 514.5nm (green). With the optical transducer head having a beam separation of 38mm, a front lens of 600mm focal length and a beam expander with an expansion ratio of 1.95 the measurement volume is 0.15mm in diameter and 2.4mm in length. The signals from the photomultipliers were processed by two Burst Spectrum analyzers. The sampling rate was 120Hz over a time interval of 80s. For the liquid flow, silver coated hollow glass spheres with a diameter of 11.9 $\mu$ m were used as seeding particles. The air flow was seeded by employing a seeding generator which provided water/glycerol particles of 2-10 $\mu$ m diameter. Experimental uncertainties are estimated to be within 5% for the mean velocity and 9% for the turbulence intensity.

#### 4.2 Numerical modelling

The flow fields were computed using the commercial finite-element code ANSYS/FLOTRAN. For the modelling of the turbulent flow, two turbulence models were considered in this work, namely the standard high Reynolds number  $k-\epsilon$  model [20] and a modified  $k-\epsilon$  model based on renormalisation group (RNG) theory [21]. The main difference between these two-equation models is the way the various constants and functions are obtained. While the standard  $k-\epsilon$  model's constants are obtained empirically, the RNG  $k-\epsilon$  model's procedure of incorporating small scale

FLOW VISUALISATION OF SUBMERGED IMPINGING JETS  
OF DIFFERENT PRANDTL NUMBERS

phenomena (such as eddies) through a random forcing function into the equations of motion results in a higher degree of accuracy in the vicinity of a wall or in situations of separation or transition. This should predict a longer recirculation zone.

The governing equations for the conservation of mass and energy and transport of momentum are solved with a two-dimensional Cartesian coordinate formulation using a non-uniform, axisymmetric grid. The domain was computed on a 90x99 grid. Computations with 90x58 and 120x99 grids suggest that the results are independent of the grid size. Finer grid spacings were used along the centreline of the jet and in regions of high velocity gradients, such as near the wall and in the stagnation region. The meshing facility in FLOTRAN allows the creation of wedge-shaped elements near the wall so that the requirements of the equilibrium wall function ( $11.5 \leq y^+ \leq 30$ ) are satisfied. The advection term was discretized by the use of a Monotone Streamline Upwind (MSU) approach [22]. Measured jet exit characteristics were specified at the inlet boundary condition of the computational domain.

To study the effects of varying properties on the turbulent flow field, the case of  $Pr=7$  was modelled with varying (case 1) and constant (case 2) fluid properties. Changes in the relevant fluid properties  $\mu$ ,  $k$  and  $c_p$  were expressed using Sutherland's law [22].

## 5 RESULTS

### 5.1 Flow field

Results from numerical predictions using the standard  $k-\epsilon$  model and the RNG  $k-\epsilon$  model in the confined outflow region of different jets of constant Reynolds number are presented. The effects of Prandtl-number, nozzle-to-plate spacing, variable fluid properties and the turbulence model used, on the flow field, are shown. For the specific case of Prandtl-number effects on the centreline velocity decay of the jet, LDA measurements have been included.

The purpose of this study is not to improve predictions of numerical models or codes, but to assess the performance of a turbulence model available in a commercial code against qualitative flow visualisation and quantitative measurements of the flow field using laser Doppler-Anemometry over a range of Prandtl-numbers. The long-term aim of this work will be to use numerical simulations, particularly to investigate higher Prandtl-number liquids ( $Pr \geq 85$ ), when experiments become impractical.

Figure 2 shows the similarities in flow patterns at  $z/d=2$  as the Prandtl-number is decreased from 7 to 3.5. After issuing from the nozzle, the jet develops and impinges on the surface where it is deflected through  $90^\circ$  and accelerates under the influence of a favourable pressure gradient. The pressure gradient helps to 'laminarise' the flow and the streamlines appear parallel to the impingement surface up to  $r/d \approx 1.5$ . By this radial position, transition to turbulence is probably complete. Although not evident in the figure, the formation of small vortices at the edge of the jet (in the mixing layer) were observed. These vortices were transported towards the impingement surface and along the wall jet. The boundary layer appears as wavy streamlines between these vortices and the impingement surface. It is in this region, where other researchers, for example [23], have reported secondary peaks in the local heat transfer profile. Entrainment of spent fluid can be observed where the recirculating vortex transports fluid back towards the centre of the jet. The primary flow patterns are detected well by the standard  $k-\epsilon$  turbulence model, see Figure 3. For the two Prandtl-numbers, the centres of the toroids are predicted to be at identical radial and axial positions and correspond to within  $0.3d$  with the experimental results.

Similar trends are observed for higher nozzle-to-plate spacings. For  $z/d=5$ , Table 2 lists the predictions from the two turbulence models. Despite its inherent feature of predicting longer recirculation regions, the RNG prediction is identical to the results from the standard model. Over the studied Prandtl-number range, no shift in the center of the recirculation vortex becomes apparent.

U. Rüdell, S. Ashforth-Frost and K. Jambunathan

| Pr   | Standard <i>k-ε</i> model |       | RNG <i>k-ε</i> model |       |
|------|---------------------------|-------|----------------------|-------|
|      | r/d                       | y/d   | r/d                  | y/d   |
| 0.71 | 6.145                     | 2.409 | 6.145                | 2.409 |
| 3.5  | 6.145                     | 2.408 | 6.145                | 2.408 |
| 4.8  | 6.145                     | 2.409 | 6.146                | 2.408 |
| 7    | 6.145                     | 2.409 | 6.145                | 2.409 |

Table 2. Center of rotation of the toroidal recirculation flow pattern for  $Re=20,000$  and  $z/d=5$ .

The case of  $z/d=8.5$  (not shown) has been modelled since it represents a distance beyond the potential core of the jet where the mixing layer has spread to the jet axis resulting in an enhancement of heat transfer. For the case of  $Pr=7$ , the stream-functions predicted by the turbulence models are identical. Compared to  $z/d=5$ , the recirculating vortex has moved towards the jet centreline. Considering the other end of the Prandtl-number range,  $Pr=0.71$ , the RNG model places the centre of the toroid radially more outward, away from the centreline and, in the axial direction higher above the target plate than its numerical counterpart. Quantitatively, this difference is small and within expected levels of uncertainty. The streamline plots from the RNG model are qualitatively similar, except for close to the confining plate where more entrainment of spent fluid is observed for water.

## 5.2 Centreline velocity decay and development of the wall jet

Figure 4 compares the velocity profiles at the nozzle exit for four different Prandtl-number fluids together with the turbulence characteristics. All fluids exhibit the same trend, namely at the edge of the jet, in a region of high shear, the turbulence levels are highest and decrease towards the center of the jet.

Numerical results of the decay of axial velocity for  $z/d=5$  is compared with experimental data in Figure 5. All curves exhibit the same trend in that the influence of the impingement plate becomes apparent at a distance of approximately  $0.9d$  from the impingement plate, based on a 95% criterion (dashed line in the graph). Close agreement between experimental and numerical results is observed.

For the case of  $z/d=8.5$ , the axial development of mean velocity and local turbulence intensity is plotted in Figure 6 and allows the effects of Prandtl-number on the length of the potential core to be assessed. The exit velocities of the two jets remain steady over several diameters. Based on a 95% criterion, the length of the potential core for both jets is approximately  $5.8d$ . Beyond the potential core, the water jet decays faster which results in a higher level of turbulence intensity. The numerical results from both turbulence models are plotted in the same graph. There is an initial "overshoot" of the velocity in the potential core and both models underpredict the length of the potential core by  $0.6d$ . The subsequent steep velocity decay is accompanied by a distinct increase in the turbulent kinetic energy, which continues to rise towards the stagnation point where its increase becomes more pronounced. As was previously noted for the streamlines, the results for water coincide for both turbulence models. It is interesting to note that the RNG model's simulations result in a velocity decay of the air jet that is steeper than that of the water jet. This causes the turbulence intensity to increase more sharply than in the case of water.

Numerical simulations for the development of the radial velocity along the target plate are presented in Figure 7, and reveal close agreement between the two turbulence models in the immediate vicinity of the stagnation point, up to  $r/d=0.4$ . Discrepancies between the different Prandtl-number fluids are negligible. The maximum velocity is predicted by both models to occur at  $r/d=0.9$  which is characteristic for a developing wall jet [24]. Beyond this point, the RNG model predicts a radial velocity profile that is up to 8% faster than that from the standard model.

Figure 8 shows the predictions from the turbulence models for the turbulent kinetic energy at the stagnation point. It can be seen that in this region of anisotropic flow, the RNG model predicts better since its predicted turbulence levels are lower. Beyond the stagnation region ( $r/d>1.2$ ) where the flow returns to isotropy the curves of the various Prandtl-number fluids collapse into a single profile for each model. The turbulence levels from the RNG model exceed those from the standard

### FLOW VISUALISATION OF SUBMERGED IMPINGING JETS OF DIFFERENT PRANDTL NUMBERS

model. While the standard turbulence model predicts the peak of  $k$  at  $r/d=0.8$ , the RNG model's lower level of turbulence occurs further downstream,  $r/d=0.9$ . The Figure also shows that the effects of variable fluid properties are negligible.

#### 6 CONCLUSIONS

The flow field of a turbulent, confined and submerged jet over a range of Prandtl-numbers ( $0.71 \leq Pr \leq 7$ ) was studied numerically and experimentally. Two turbulence models, namely the standard  $k-\epsilon$  model and the RNG  $k-\epsilon$  model were used. For the effects of Prandtl number on the decay of axial velocity, numerical results were compared with LDA measurements. Numerical predictions along the impingement plate were compared between the two turbulence models. Results from experimental flow visualisation are in close agreement with numerical predictions in that the centres of the recirculation patterns were positioned correctly to within  $0.3d$ . Quantitative differences between the two models are small throughout the range of studied nozzle-to-plate spacings ( $2 \leq z/d \leq 8.5$ ).

The mean flow parameters, such as axial and radial velocity, are predicted well by both turbulence models and are in close agreement with experimental results. For the case of  $z/d=8.5$ , experimental data show that jets of large differences in Prandtl number, water and air, show approximately identical lengths of the potential core,  $5.8d$ . Beyond the potential core, the faster decaying water jet results in a higher level of turbulence intensity. While the standard turbulence model does not identify any differences, the RNG model predicts the contrary to the experimental results. Negligible Prandtl number effects were found in the development of the wall jet as well as in the development of the turbulent kinetic energy along the impingement plate. The effects of varying fluid properties are negligible.

#### 7 OUTLOOK

Future work will concentrate on validation of the numerical models with experimental data in the near wall region. To clarify the centreline velocity decay, more measurements with a higher spatial resolution will be conducted. Future work will incorporate liquids of higher Prandtl number that will then lead, in the long term, to more detailed understanding of the physical processes that are involved in cooling and heating applications.

#### Acknowledgement

The authors would like to thank Nottingham Trent University and the Engineering and Physical Science Research Council (grant AF/97/0568 to Dr S Ashforth-Frost) for financial support towards this work.

#### 8 REFERENCES

- [1] Kiryu, M., 1986. Development of oil-cooled 750cc motorcycle engine. *Auto. Technol.*, **40**, 1154-1158.
- [2] Garimella, S. V. and Nenaydykh, B., 1996. Nozzle geometry effects in liquid jet impingement heat transfer. *Int. J. Heat Mass Transfer*, **39**(14), 2915-2923.
- [3] Palmer, J. R., 1993. Theoretical model for high power diamond laser optics using high velocity liquid metal jet. *SPIE High Heat Flux Engineering*, **1739**(58), 86-115.
- [4] Zumbrennen, D. A., Incropera, F. P. and Viskanta, R., 1990. Method and Apparatus for measuring heat transfer distributions on moving and stationary plates cooled by a planar liquid jet. *Experimental Thermal and Fluid Science*, **3**:202-213.
- [5] Raudensky, M., Druckmüller, M., and Horský, J., 1998. Inverse Heat conduction Problems and Generalisation of Experimental results. *ASME, Heat Transfer Division, HTD*, Vol. **361-5**, 65-71.
- [6] Filippov, Y. P., 1991. Removal of intensive heat flux with liquid nitrogen jet impingement. In: Fast, R W. ed., *Advances in Cryogenic Engineering*, **37**(A), Plenum Press, 189-196.

U. Rüdél, S. Ashforth-Frost and K. Jambunathan

- [7] Can, M., 1998. Simultaneous convective Heat and Mass transfer in Impingement Ink Drying. *Int. Comm. Heat Mass Transfer*, **25**(6), 863-874.
- [8] Sun, H., Ma, C. F. and Chen, C., 1998. Prandtl number dependence of impingement heat transfer with circular free-surface liquid jets. *Int. J. Heat Mass Transfer*, **41**(10), 1360-1363.
- [9] Sutera, S. P., 1965. Vorticity amplification in stagnation-point flow and its effect on heat transfer. *J. Fluid Mechanics*, **21**(3), 513-524.
- [10] Metzger, D. E., Cummings, K. N. and Ruby, W. A., 1974. Effects of Prandtl number on heat transfer characteristics of impinging liquid jets. *Proc. 5<sup>th</sup> Int. Heat Transfer Conf.*, Tokyo, **2**, 20-24.
- [11] Jiji, L. M. and Dagan, Z., 1988. Experimental investigation of single-phase multijet impingement cooling of an array of microelectronic heat sources. In: Aung, W., ed., *Cooling Technology for Electronic Equipment*. Hemishpere, 333-351.
- [12] Womac, F. P., Ramadhyani, S. and Incropera, F. P., 1993. Correlating equations for impingement cooling of small heat sources with single circular liquid jets. *ASME J. Heat Transfer*, **115**(1), 106-115.
- [13] Leland, J. E. and Pais, M. R., 1999. Free Jet impingement Heat Transfer of a High Prandtl number Fluid under Conditions of Highly varying Properties. *ASME J. Heat Transfer*, **121**, 592-597.
- [14] Meola, C., de Luca, L. and Carlomagno, G. M., 1995. Azimuthal instability in an impinging jet: adiabatic wall temperature distribution. *Experiments in Fluids*, **18**, 303-310.
- [15] Morris, G.K. and Garimella, S. V., 1996. Orifice and impingement flow fields in confined jet impingement. *ASME HTD-Vol. 324*, **2**, 101-106.
- [16] Besserman, D. L., Incropera, F. P. and Ramadhani, S., 1991a. Experimental study of heat transfer from a discrete source to a circular liquid jet with annular collection of the spent fluid. *Experimental Heat Transfer*, **4**(1), 41-57.
- [17] Knebel, J. U., Krebs, L., Müller, U. and Axcell, B. P., 1998. Experimental investigation of a confined heated sodium jet in a co-flow. *J. Fluid Mechanics*, **368**, 51-79.
- [18] Chu, P. C. K., Lee, J. H. and Chu V. H., 1999. Spreading of Turbulent Round Jet in Coflow. *J. Hydraulic Eng.*, **125**(2), 193-204.
- [19] Eswara, A. T. and Nath, G., 1994. Unsteady nonsimilar two-dimensional and axisymmetric water boundary layers with variable viscosity and Prandtl number. *Int. J. Engng. Sci.*, **32**(2), 267-279.
- [20] Launder, B. E. and Spalding, D. B., 1974. The numerical computation of turbulent flows. *Comp. Meth. Appl. Mech. Eng.*, **3**, 269-298.
- [21] Yakhot, V., Orszag, S. A., Thangam, S., Gatski, T. B. and Speziale, C. G., 1992. Development of Turbulence Models for Shear Flows by a Double Expansion Technique, *Phys. Fluids A*, **4**(7), 1510-1520.
- [22] Ansys, 1999. Ansys User's Manual, Vols. 1-4, Release 5.5, SAS IP, Inc.
- [23] Garimella, S. V. and Rice, R. A., 1995. Confined and submerged liquid jet impingement Heat Transfer. *ASME J. Heat Transfer*, **117**(4), 871-877.
- [24] Fitzgerald, J. A. and Garimella, S. V., 1996. Flow fields measurements in confined and submerged jet impingement. *Proc. ASME Heat Transfer Division, HTD-Vol. 333*, **2**, 121-129.

FLOW VISUALISATION OF SUBMERGED IMPINGING JETS OF DIFFERENT PRANDTL NUMBERS

9 APPENDIX

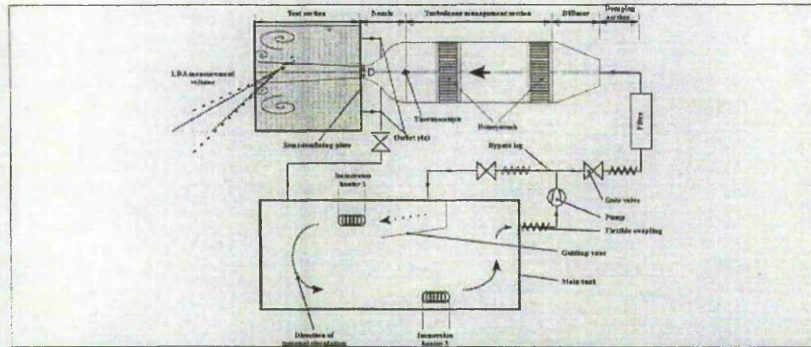


Figure 1 Schematic of the test facility.



Figure 2a. Impinging jet of Pr = 7 and z/d=2 (u/u<sub>ref</sub> = 1).

Figure 2b. Impinging jet of Pr = 3.5 and z/d=2 (u/u<sub>ref</sub> = 0.54).

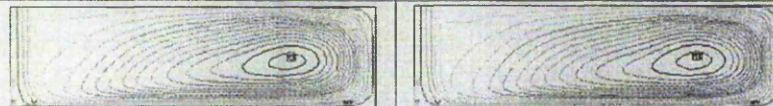


Figure 3a. Predicted stream-functions for Pr=7 (z/d=2) using the k-ε model.

Figure 3b. Predicted stream-functions for Pr=3.5 (z/d=2) using the k-ε model.

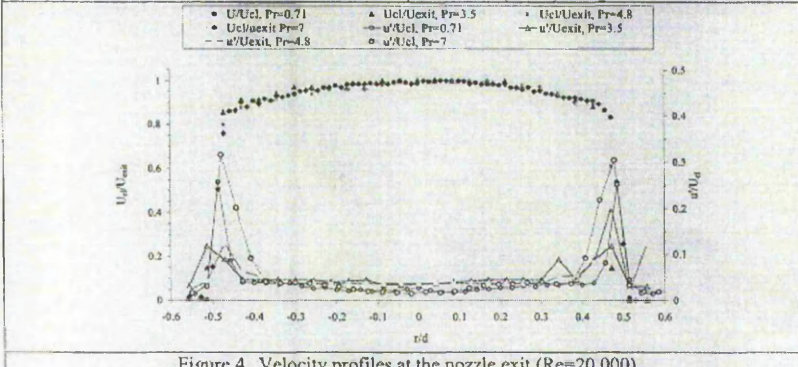


Figure 4. Velocity profiles at the nozzle exit (Re=20,000).

U. Rüdel, S. Ashforth-Frost and K. Jambunathan

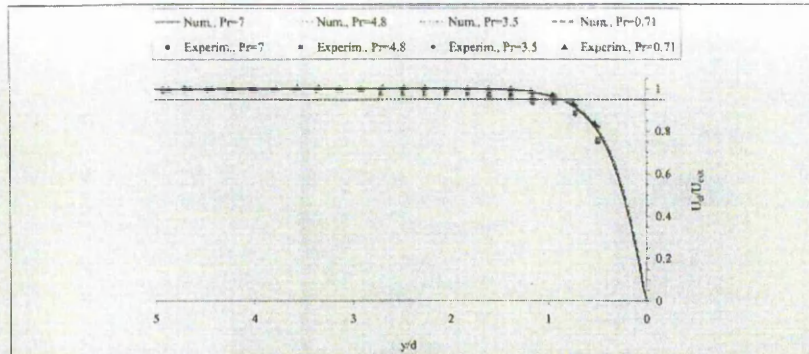


Figure 5. Centreline velocity decay for  $z/d=5$ .

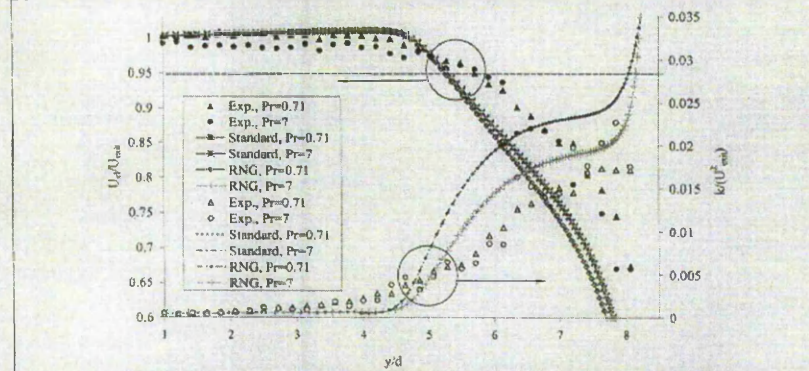


Figure 6. Comparison of LDA-results with predictions from two  $k-\epsilon$  models for the axial velocity decay at  $z/d=8.5$ .

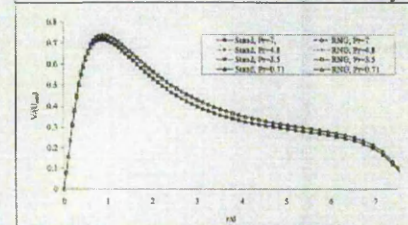


Figure 7. Prediction of the radial velocity for  $z/d=5$ .

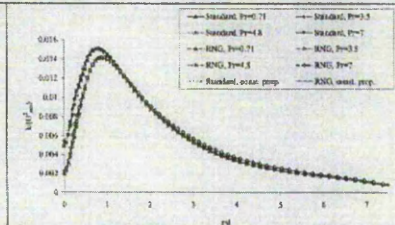


Figure 8. Prediction of turbulent kinetic energy from two  $k-\epsilon$  models along the wall for  $z/d=5$ .